SOLAR AND SPACE WEATHER RADIOPHYSICS

SOLAR AND SPACE WEATHER RADIOPHYSICS
Current Status and Future Developments

Edited by
DALE E. GARY
New Jersey Institute of Technology

CHRISTOPH U. KELLER
National Solar Observatory

Kluwer Academic Publishers
Boston/Dordrecht/London

Contents

List of Figures xiii

List of Tables xxi

Preface xxiii

1
Solar and Solar Radio Effects on Technologies 1
Louis J. Lanzerotti

1 Introduction, and Some History 1
2 Electromagnetic Waves and Wireless 2
3 Solar-Terrestrial Effects on Technologies 5
4 Solar Radio Emissions 7
5 Contemporary Solar Radio and Some Implications for Technologies 8
5.1 Solar noise levels and technologies 8
5.2 Solar noise interference 10
5.3 Statistics of solar radio noise 11
6 Conclusion and Looking to the Future 13
References 15

2
Overview of Solar Radio Physics and Interplanetary Disturbances 17
Monique Pick

1 General Context of the Radio Emissions 19
2 Coronal Magnetography 20
3 Transient Activity and Flares 24
3.1 Energy dissipation 24
3.2 Solar magnetic reconnection in the solar atmosphere and diagnostics on regions of acceleration 25
3.3 Electron acceleration and transport during flares 28
4 Coronal Mass Ejections 30
4.1 Radio signatures of CMEs 31
4.1.1 Lift-off and angular spread in the corona of flare/CME event 32
4.1.2 Relationship with EUV dimming and coronal waves 34
4.1.3 Direct radio CME imaging 34

5 Coronal and Interplanetary Shocks, Flares and CMES 35
6 Interplanetary Coronal Mass Ejections 37
7 Solar Energetic Particle Events 39
8 Concluding Remarks and the Future of Radio Physics 41
References 43

3
The Frequency Agile Solar Radiotelescope 47
T. S. Bastian
1 Introduction and Background 47
2 Preliminaries 49
2.1 Radiative transfer 49
2.2 Radio emission mechanisms 50
3 Overview of FASR Science 52
3.1 Coronal magnetic fields 52
3.2 The physics of flares 53
3.3 Drivers of space weather 55
3.4 The quiet Sun 56
3.5 Synoptic measurements and forecasting 58
4 Description of the Instrument 59
4.1 Operational basis 59
4.2 FASR instrumental requirements 60
4.3 System design overview 62
4.3.1 Antenna configuration 63
4.3.2 Antennas 64
4.3.3 Feeds and front ends 64
4.3.4 Signal transmission 65
4.3.5 Signal processing 66
5 Operational Issues 66
6 Concluding Remarks 67
References 68

4
Radio Spectral Diagnostics 71
Dale E. Gary, G. J. Hurford
1 Introduction 71
2 Characteristic Frequencies of the Solar Atmosphere 73
3 Plasma Emission Diagnostics 75
4 Free-Free Diagnostics 75
5 Gyroresonance Diagnostics 77
6 Gyrosynchrotron Diagnostics 81
7 Exotic Mechanisms 83
8 Conclusion 85
References 86

5
Coronal Magnetic Field Measurements through Gyroresonance Emission 89

Stephen M. White
1 Coronal Magnetic Fields are Intrinsically 3D 90
2 Extrapolations of Surface Magnetic Fields 91
3 The Properties of Gyroresonance Emission 92
3.1 Physical mechanism 92
3.2 Opacity 93
4 Gyroresonance Radio Emission from Active Regions 96
4.1 Radio emission from a dipole magnetic field 96
4.2 The effect of viewing angle 98
4.3 Variation with frequency 98
5 Observational Examples 101
6 Applications of Gyroresonance Emission 104
6.1 Coronal magnetic field measurement 104
6.2 Simulations of FASR magnetic field measurements 106
6.3 Coronal currents 107
6.4 Tests of magnetic extrapolations 108
6.5 Heights of radio sources 111
7 Summary 111
References 112

6
Coronal Magnetic Field Measurements Through Bremsstrahlung 115
G.B.Gelfreikh
1 Introduction 115
2 Basic Formulae 115
2.1 Equations of transfer 115
2.2 Basic expression for isotropic plasma 117
2.3 Basic expression for anisotropic plasma 117
3 Diagnostics of the Coronal Plasma 118
3.1 Diagnostics of the mechanism of the emission generated by thermal bremsstrahlung 118
3.2 Expressions for the magnetic field 119
3.3 Radio measurements of the magnetic field 120
4 Expected Parameters of Polarized Radio Emission 121
4.1 Optically thin regions 121
4.2 Optically thick regions 122
4.3 Combination of optically thin and thick regions 123
5 Radio Magnetograms of Solar Active Regions 124
6 Magnetic Fields in Prominences 125
7 Magnetic Fields in a Coronal Hole 127
8 Magnetic Fields in Coronal Loops 130
9 Future Development of the Method 131
References 133

7
Coronal Magnetic Field Measurements Through QT-Propagation 135
Boris Ryabov

1 Microwave QT-Propagation in the Solar Corona 135
1.1 Introduction 135
1.2 Effects of electromagnetic wave mode coupling 137
1.3 Geometry of QT-propagation 140
2 Results and Prospects of Microwave Observations 140
2.1 Regularities of the inversion phenomenon 141
2.2 Multiple inversion 144
2.3 Linear polarization in the outer corona 145
2.4 Oscillations 145
3 The Technique of Coronal Magnetography Through QT-Propagation 147
3.1 Normalization procedure 147
3.2 The source-QTR distance 148
3.3 Scrutiny of a coronal magnetogram 149
4 Summary and Conclusions 150
References 151

8
Overview of Solar Flares 153
Hugh Hudson, Lyndsay Fletcher, Josef I. Khan and *Takeo Kosugi*
1 Introduction 154
2 New Observational Capabilities 154
2.1 *Yohkoh* 154
2.2 SOHO and TRACE; other facilities 155
3 The Flare Concept 155
3.1 Confined and LDE flares 156
3.2 Flares and CMEs 156
4 Flare Loops 157
4.1 Footpoints, coronal spectroscopy, and evaporation 158
4.2 Arcades 159
4.2.1 “Sigmoids” and filament cavities 162
4.3 Loop-loop interactions 163
5 Particle Acceleration 163
5.1 Footpoint sources 164
5.2 Coronal sources 164
5.3 Energetic ions 166
6 Ejections 166
6.1 Parallel and perpendicular flows 166
6.2 Dimming 167
6.3 Global waves 168
7 Microflares and Nanoflares 169
8 Evolution of Flare Theories and Models 172
9 Conclusions 172
References 173

9
Electron Transport During Solar Flares 179
Jeongwoo Lee
1 Introduction 179

2 The Formulations 182
2.1 Trap-and-precipitation 182
2.2 Trap, bypass, and precipitation 183
3 Electron Trapping And Precipitation 184
3.1 Simple bursts 184
3.2 Trap or precipitation? 184
3.3 Extended and evolving trap 186
3.4 Trap without precipitation 187
4 Electron Pitch Angle Variation 189
4.1 Weak diffusion 189
4.2 Intermediate diffusion 191
4.3 Strong diffusion 193
4.4 Pitch angle scattering and MWR maps 196
5 Electron Energy Variation 197
6 Concluding Remarks 198
References 200

10
Decimeter Burst Emission and Particle Acceleration 203
Arnold O. Benz
1 Introduction 204
2 The Decimeter Range 204
2.1 Spectral types and classifications 205
2.2 High-frequency limit of the decimeter range 209
2.3 Why decimetric radio bursts? 210
3 Hard X-rays and Decimeter Radiation 211
3.1 Decimetric type III bursts 211
3.2 Decimetric narrowband spikes 211
3.3 Drifting pulsating structures 212
3.4 Flares without radio emission 212
4 Flare Physics 214
4.1 Location of source regions 214
4.2 Evidence for reconnection 215
5 Emission Processes 217
5.1 Beam emissions 217
5.2 Emissions from the acceleration site 218
5.3 Decimetric spikes and pulsations 219
6 Conclusions 219
References 220

11
Radio Observations of Coronal Mass Ejections 223
Angelos Vourlidas
1 Coronal Mass Ejections 223
1.1 A brief CME primer 223
1.2 Radio emissions associated with CMEs 225
1.2.1 Thermal free-free 225
1.2.2 Nonthermal gyrosynchrotron 226

1.2.3 Non-thermal plasma emissions 227
2 Radio CME Observations During Cycle 23 227
2.1 CME detection 229
2.2 CME development 229
2.3 Detection of CME-associated structures 231
2.4 Radio prominence eruptions 232
2.5 Type II emission 233
2.6 CME radio precursors 234
2.7 Overview 234
3 FASR Connection 235
3.1 Advantages of radio observations 235
3.2 Disadvantages of current radio observations 236
3.3 Instrument requirements 236
References 239

12
Tomographic 3D-Modeling of the Solar Corona with FASR 243
Markus J. Aschwanden, David Alexander, Marc L. DeRosa
1 Introduction 244
2 Active Region Modeling 245
2.1 Simulation of FASR images 245
2.2 Peak brightness temperature 248
2.3 Temperature and density diagnostic of loops 252
2.4 Radio versus EUV and soft X-ray diagnostics 255
3 Chromospheric and Coronal Modeling 257
4 Future FASR Science 261
References 262

13
Coronal Diagnostics with Radio and EUV/Soft X-Ray Observations 265
Jeffrey W. Brosius
1 Introduction 265
2 2D Coronal Magnetography 267
3 Diagnostics of Quasi-Transverse Layers 270
4 Coronal Iron Abundance 271
5 3D Coronal Magnetography 273
6 Future of Coordinated Radio and EUV/Soft X-ray Observations 281
References 284

14
Radio Observations of the Quiet Sun 287
Christoph U. Keller and *Säm Krucker*
1 Introduction 287
2 Observing the quiet Sun at radio wavelengths 289
3 General appearance of the quiet Sun in radio waves 291
3.1 Submillimeter observations 292
3.2 Millimeter and microwave observations 292
4 Thermal stratification of the quiet Sun 294

5 Filaments and prominences 296
6 Coronal heating events in the quiet Sun 297
7 FASR and the quiet Sun 300
References 301

15
Interplanetary Radio Bursts 305
N. Gopalswamy
1 Introduction 305
2 Type III Bursts 307
2.1 Isolated type III bursts 308
2.2 Complex type III bursts 309
2.2.1 Origin of nonthermal electrons 310
2.2.2 Complex type III bursts and CMEs 311
2.3 Type III storms 312
2.3.1 Cessation and recovery of type III storms 313
3 Type II Bursts 314
3.1 IP shocks, CMEs and type II radio bursts 316
3.1.1 DH type II bursts 317
3.2 Are type II bursts CME-driven? 318
3.3 What is a fast CME? 320
4 Recent Developments 323
4.1 Radio signatures of CME interaction 323
4.1.1 Radio signature solely due to CME interaction 323
4.1.2 Medium modification: Interaction between two fast CMEs 324
4.1.3 Interaction between CMEs with nearly equal speeds 325
4.1.4 What we mean by CME interaction 325
4.2 Unusual radio signatures 328
5 Concluding Remarks 329
References 330

16
Solar Radar 335
William A. Coles
1 Introduction 335
2 Theory 336
3 Other Coronal Observations 342
4 Previous Radar Measurements 345
5 New Observations 348
6 Use of an Imaging Receiver 351
References 352

17
Three-Dimensional Tomography Of Interplanetary Disturbances 355
Bernard V. Jackson, P. Paul Hick
1 Introduction 356
2 Global Data Analyses 358
2.1 IPS measurements 359

2.2 Helios spacecraft Thomson scattering measurements 362
3 Model and Tomographic Analysis 366
3.1 Solar wind model 367
3.2 Computer analysis 368
4 *In-situ* Comparisons 371
4.1 Reconstructed global observations 374
5 Conclusion 381
References 382

Index 387

List of Figures

1.1	Signal strengths and sunspot numbers for 1915–1932	4
1.2	Radio strength vs. sunspot numbers for 1926–1928	5
1.3	Timeline for selected major impacts on technical systems	6
1.4	Variation with time of several solar-originating phenomena measured near Earth during the year 1991	9
1.5	Number of solar burst events per day with amplitudes $> 10^3$ SFU	12
1.6	Number of radio events per day vs. peak flux density	14
2.1	The Sun seen at 17 GHz and EUV	18
2.2	Physical maps from microwave imaging spectroscopy	21
2.3	Coronal magnetic field strength at different heights	23
2.4	The frequency distribution of peak rates in hard X rays	26
2.5	Hard X-ray images of an impulsive west limb flare	27
2.6	Spectrogram of metric spikes (above 320 MHz) and type III bursts (below 320 MHz)	28
2.7	Diagram of a flare model envisioning magnetic reconnection and chromospheric evaporation processes	29
2.8	RHESSI observations of the initial rise of an intense solar gamma-ray line flare	30
2.9	Time-lapse images taken by LASCO-C1 coronagraph in Fe XIV emission line.	32
2.10	Solar manifestations associated with CMEs	33
2.11	Example of an EIT wave from 1997 September 24	35
2.12	Type II emission and CME in the 1998 April 20 event	36
2.13	A hectometric interplanetary type II burst in the 1–14 MHz range	38
2.14	Idealized sketch of a complete radio event (from Wild *et al.* 1963)	40
4.1	Characteristic radio frequencies for the solar atmosphere	74
4.2	A “Universal Spectrum” for free-free brightness temperature	77

4.3	Longitudinal magnetic field from a model atmosphere compared with the field deduced from radio spectra from the model	78
4.4	"Universal Spectra" for gyroresonance emission.	80
4.5	Radio emission spectra at two lines of sight in a model active region, as calculated at 100 frequencies from 1–24 GHz	81
4.6	'Universal Spectra" for gyrosynchrotron emission	83
4.7	Gyrosynchrotron emission from a model coronal magnetic loop	84
5.1	Integrated optical depth of the $s = 2, 3, 4$ gyroresonance layers	95
5.2	Plots of the gyroresonance layers of a dipole sunspot model and the predicted brightness temperatures when the spot is viewed nearly vertically	97
5.3	Same as Figure 5.2, except that now the sunspot is viewed from an angle of 20°	99
5.4	Brightness-temperature profiles across the dipole sunspot model of Figure 5.2 at various frequencies	100
5.5	Spectra of the brightness temperature at different locations across the spot in Figure 5.4	101
5.6	Brightness-temperature profiles across an isolated sunspot observed with the VLA near disk center	102
5.7	VLA observations of a sunspot at 8.0 GHz	103
5.8	Contours of magnetic field strength at the base of the corona plotted on white light, magnetogram and TRACE images of a sunspot	105
5.9	Two examples of radio spectra from an active region model, showing the technique of determining coronal magnetic field	108
5.10	The results of applying the gyroresonance spectral technique to the entire active region model	109
5.11	VLA observations of a complex solar active region reflecting the magnetic field and temperature distribution in the corona over the active region	110
6.1	Radio maps of an AR observed using the Nobeyama radio heliograph	126
6.2	Radio scan of a prominence at a wavelength $\lambda = 2.1$ cm made with the RATAN-600	127
6.3	One-dimensional radio scans of the sun made with the RATAN-600 at eleven wavelengths in the range 1.8–28 cm	129

6.4 Magnetic field of a coronal hole obtained from observations with the RATAN-600 130
6.5 Radio scans of the Sun at 1.8 cm made with the RATAN-600 131
6.6 Radio emission spectra of a CME-associated coronal loop obtained with the RATAN-600 132
7.1 Comparison of radio maps of circular polarization with a longitudinal magnetogram 138
7.2 Simulated geometry of QT-propagation of microwaves 141
7.3 Circularly polarized microwave sources simulated with due regard to the QT-propagation of microwaves 142
7.4 Radio maps in Stokes I and circular polarization taken with the SSRT at 5.7 GHz 143
7.5 Same region as in Figure 7.4, at 17 GHz one day later 144
7.6 Representative geometry of QT-propagation of microwaves 146
7.7 Details of the inversion phenomenon presented in Figure 7.4 148
7.8 Two coronal magnetograms showing the strength of coronal magnetic fields 149
8.1 Soft and hard X-ray observations of the "Masuda flare", 1992 January 13, which nicely illustrates the coronal loop structure of a flare 158
8.2 *Yohkoh* SXT difference image and TRACE image of the arcade flare of 2000 July 14 ("Bastille Day flare") 160
8.3 A beautiful cusp (following an X-class flare) as observed by SXT 161
8.4 Soft X-ray observations of a spiky arcade event exhibiting the "SAD" phenomenon 162
8.5 Disappearing trans-equatorial interconnecting loop (TIL) associated with a blast wave and CME 168
8.6 Soft X-ray signature of a wave event 170
8.7 Energy distributions for microflares observed with the *Yohkoh* SXT 171
9.1 Comparison of the radio time profiles for an event at 17 GHz and 34 GHz with a trap model 185
9.2 Lightcurves at microwaves and hard X rays of a an impulsive burst 186
9.3 Microwave bursts indicative of long-term trapping 188
9.4 Microwave and hard X ray lightcurves during the Bastille Day flare on 2000 July 14 190
9.5 Microwave maps and spectra obtained for the 1993 June 3 flare 192

9.6	The 1999 August 20 flare as a case of the intermediate pitch angle diffusion	194
9.7	A loop top source near the solar limb observed with NoRH at 34 GHz	195
10.1	Broadband spectrogram recorded with the Phoenix-2 showing a rich event in meter and decimeter wavelengths	206
10.2	Dynamic spectrogram of total flux of an intense type III burst (U shape)	207
10.3	Dynamic spectrogram of total flux showing coherent emission	209
10.4	Dynamic spectrograms of 0.3–4.5 GHz total flux observed with the Phoenix-2 and Ondrejov spectrometers	213
10.5	Location of two clusters of decimeteric spikes observed by the Nançay Radioheliograph at 432 MHz	215
10.6	TRACE images overlaid with NRH and Yohkoh/HXT contours of a double-ribbon flare	216
11.1	Halo CME observed by LASCO/C2 and a typical 3-part CME on the west limb	224
11.2	Simulated free-free radio spectra for the quiet Sun and a typical CME	226
11.3	An example of fairly complete spectral coverage of a CME event from 2 GHz to 100 kHz	228
11.4	Radio source progression seen by the NRH at 3 distinct frequencies	230
11.5	Schematic of CME development as inferred from NRH observations.	230
11.6	EIT 195 Å difference image showing the dimming region, overplotted with Nançay 236 MHz contours	231
11.7	Snapshot map of the radio CME loops at 164 MHz	232
11.8	Simulation of CME detection by a temporally redundant array	238
12.1	Potential field extrapolation of SOHO/MDI magnetogram data	246
12.2	Distributions of loop lengths L, loop maximum temperatures $T_{e,max}$, loop minimum densities n_{min}, and maximum densities n_{max}	248
12.3	Simulation of radio brightness temperature maps of an active region at 20 frequencies, from ν=100 to 1258 MHz	249
12.4	Similar representation as in Fig. 12.3, for frequencies of $\nu = 0.8$ to 10 GHz	250

12.5 Radio peak brightness temperature as a function of frequency for the background corona (B), for cool (C) fat loops, and for hot (H) thin loops 251
12.6 Variation of the radio brightness temperature spectrum of a loop with temperature, electron density, and loop width 254
12.7 Enlarged detail of a active region model with a bright loop 256
12.8 Quiet Sun brightness temperature spectrum for an isothermal corona 258
12.9 A compilation of chromospheric and coronal density models 260
12.10 Quiet Sun brightness temperature spectrum for an isothermal corona, for the coronal model by Gabriel (1976), and for a modified Gabriel model 261
13.1 CDS and SERTS spectra from the 1997 November 18 rocket flight 273
13.2 EIT image of NOAA AR 8108 with VLA contours, MDI B_z contours, CDS and SERTS sub-FOV, radio centroids and area for magnetography 274
13.3 $B(T)$ at the centroid of the R component of the 4.866 GHz emission, for four combinations of density distribution 279
13.4 "Slices" of $B(x, y, T)$ along isothermal surfaces 280
13.5 Observed radio maps, with observed and calculated brightness temperature contours 281
13.6 $B(h)$ derived with n_e=constant and different magnetic scale heights 282
13.7 Alfvén speed derived with n_e=constant and p_e=constant 283
14.1 The quiet Sun at different radio wavelengths 291
14.2 Comparison of photospheric magnetogram and 2-cm radio map 293
14.3 Variability of the quiet Sun radio flux at 2 cm 298
14.4 Comparison of network flares in soft X-ray and radio waves at 2 cm 299
15.1 Level of IP radio burst (types II and III) flux compared to cosmic background noise and quiet coronal emission 306
15.2 Hiraiso and Wind/WAVES dynamic spectra showing isolated type III bursts and a type II burst 309
15.3 A complex type III burst that started below about 7 MHz, but was very intense at kilometric wavelengths 310
15.4 Height-time plots of all CMEs that occurred on 2000 November 24, along with the WAVES/RAD2 dynamic spectrum 313

15.5 A hybrid dynamic spectrum consisting of Potsdam and Wind/WAVES data 314
15.6 Type III storm activity observed by Wind/WAVES 315
15.7 IP Type II burst of 2001 September 24-25 316
15.8 Speed, width and acceleration of 132 CMEs associated with DH type II bursts 318
15.9 Histogram of fast CMEs that did not have associated DH type II bursts 319
15.10 Speed distribution of CMEs associated with metric type II bursts as compared to that of general population of CMEs and DH CMEs 320
15.11 Radial profiles of the fast mode speed in the active region and quiet corona 322
15.12 Two CMEs observed by SOHO/LASCO and the associated continuum radio emission detected by Wind/WAVES 324
15.13 SOHO/LASCO difference image showing two interacting CMEs, the associated DH type II bursts, and CME height-time plots 326
15.14 Wind/WAVES dynamic spectrum of the 2001 November 22 events 327
15.15 Wind/WAVES dynamic spectrum of unusual and broadband radio emission that lasted for 4 days 328
15.16 Number of type II bursts that begin in the DH domain and continue to the kilometric domain plotted as a function of time 329
16.1 Plasma density versus solar distance and reflection height versus frequency 337
16.2 Plasma delay and loss versus frequency for the models given in Figure 16.1 338
16.3 Simulation of a spherically symmetric density step of moving outwards at 200 km/s 339
16.4 Simulation of n_e vs radial and tangential distance 341
16.5 Simulation of n_e in the equatorial plane 342
16.6 A relatively simple large CME known as “the lightbulb” as observed by LASCO C2 and C3 343
16.7 Average range distribution of echoes observed with El Campo radar 346
16.8 Annual average radar echo strength 347
16.9 Daily measurements of radar echo strength 347
16.10 Range-Doppler spectra of selected strong echoes 348
16.11 Typical Range-Doppler spectra 349

17.1 Normalized weighting functions for Cambridge and Nagoya interplanetary scintillation (IPS) 361
17.2 Contour plot images obtained from the *Helios* photometers of the 1979 May 07 CME on May 08 and May 09 364
17.3 Thomson-scattering weight function as a function of distance along the LOS 365
17.4 Schematic of a LOS projected as a reference surface on consecutive days 369
17.5 Time series showing a sample of the final velocity and g-level model compared with observations for a time-dependent tomographic run 371
17.6 Time series showing a sample of the final model and photometer brightness comparison for a time-dependent tomographic run for *Helios* 372
17.7 10-day velocity time series from the three-dimensional time-dependent model compared to the velocity and density time series from the ACE spacecraft and its correlation 373
17.8 Comparison plot of heliospheric densities at the *Helios* 2 spacecraft and least squares correlation 374
17.9 View of the corotating component of the plasma density in the inner heliosphere and a three dimensional model projection of the heliosphere 375
17.10 LASCO C2 images and a view of the reconstruction of the halo CMEs 377
17.11 Solwind coronagraph image of the 7 May CME and the remote observer view of heliospheric density 378
17.12 Reconstruction using *in-situ* observations from 5 spacecraft and using the IPS time-dependent Thomson scattering tomography 378
17.13 Carrington synoptic maps of density and velocity during two halo CMEs 379
17.14 Carrington synoptic map of the heliospheric structure at 1 AU on 1979 May 10 380
17.15 Carrington synoptic map of the heliospheric structure at 0.6 AU on 1977 November 25 381

List of Tables

1.1	Impacts of Solar-Terrestrial Processes on Technologies	7
2.1	Principal Radio Bursts	20
3.1	FASR Instrument Requirements	62
8.1	Instruments On Board *Yohkoh*	155
8.2	X-ray Dimming	167
16.1	Comparison of Solar Radar Parameters	350

Preface

This volume is the outgrowth of several international meetings to discuss a vision for the future of solar radio physics: the development of a new radio instrument. From these discussions, the concept for the Frequency Agile Solar Radiotelescope (FASR) was born. Most of the chapters of this book are based on invited talks at the FASR Science Workshop, held in Greenbank, WV in May 2002, and a special session on Solar and Space Weather Radiophysics held at the 200th American Astronomical Society meeting held in Albuquerque, NM in June 2002. Although many of the chapters deal with topics of interest in planning for FASR, other topics in Solar and Space Weather Radiophysics, such as solar radar and interplanetary scintillation, are covered to round out the discipline. The authors have been asked to write with a tutorial approach, to make the book useful to graduate students and scientists new to radio physics.

This book is more than a compilation of FASR science topics. The FASR instrument concept is so revolutionary—by extending capability by an order of magnitude in several dimensions at once (frequency coverage, spatial resolution, dynamic range, time resolution, polarization precision)—that it challenges scientists to think in new ways. The authors of the following chapters have been tasked not only with reviewing the current state of the field, but also with looking to the future and imagining what is possible.

Radio emission is extremely complex because it is generated so readily, and every imaginable plasma parameter affects it. This is both its great strength and its weakness. It offers tremendous diagnostic potential for the study of the quiet and disturbed solar atmosphere and heliosphere, but it also places great demands on the precision and quality of observations needed to interpret the information. FASR will be the first instrument to achieve the necessary precision with simultaneously excellent spatial, spectral, and temporal coverage. Together with observations in other wavelength regimes, both from the ground and from space, FASR will not only unleash the potential for radio diagnostics we are already familiar with—coronal magnetograms, electron acceleration, coronal mass ejections—but it will also allow new science to be addressed. Each author has thought about what will become possible when FASR and the other next-generation solar and heliospheric instruments are available, and has

attempted to describe the discoveries we can expect over the next two decades. To quote N. Gopalswamy (Chapter 15): solar radio astronomy, and solar and heliospheric physics in general, is "poised for a leap."

I would like to thank my wife, Kyle Gary, for her assistance in proof-reading the manuscript. Any errors that remain are mine. Thanks is also due to my co-editor, Christoph Keller, for helping to collect the chapters and for authoring the index terms. My special thanks goes to each of the chapter authors, in particular Tim Bastian, Gordon Hurford, and Stephen White, whose vision and enthusiasm not only made this book possible, but also helped to define FASR and will help to make it a reality.

DALE E. GARY

Chapter 1

SOLAR AND SOLAR RADIO EFFECTS ON TECHNOLOGIES

Louis J. Lanzerotti
Bell Laboratories, Lucent Technologies, Murray Hill, NJ 07974 USA
Center for Solar-Terrestrial Research, New Jersey Institute of Technology, Newark, NJ 07102 USA
ljl@lucent.com; louis.j.lanzerotti@njit.edu

Abstract As technology has vastly expanded in the last century and a half, those technologies that can be affected by the Sun and by solar-produced processes has also increased in number and in their design and operational complexity. A brief history of the influences of solar-produced effects on technologies is provided, beginning with the deployment of the initial electrical telegraph communications systems in the 19th century. An overview is provided of present-day technologies that can be affected by solar-terrestrial phenomena such as galactic cosmic rays, solar-produced plasmas, and geomagnetic disturbances in the Earth's magnetosphere. Some recent considerations of the effects of solar radio noise and bursts on radar and radio communications systems are discussed. New and advanced initiatives in studies of the Sun by radio techniques, especially with the FASR project, will provide important information that will be of considerable relevance to understanding and forecasting space weather.

1. Introduction, and Some History

Very rapidly after the invention and development of the first practical working electrical telegraph in 1835 by Samuel F. B. Morse (patent confirmed by the U.S. Supreme Court in 1854), electrical telegraph systems began to be deployed widely in Europe and the eastern United States. The first line, installed along a railway between Baltimore and Washington, transmitted Morse's initial message ("What hath God wrought?") in 1844 May. This electric-based telegraph system was a vast improvement over previous electrical proposals. And in addition, it certainly provided a more robust resistance to the vagaries of nature in the form of weather and seeing that could plague the optical, semaphore-type,

systems that had been attempted over the prior decades, especially in England and France (see, for example, Standage, 1998). Indeed, Napoleon Bonaparte was a strong proponent of optical telegraphy for military and other purposes, and especially developed a "line" in preparation for a future (which did not occur) invasion of England.

However, in "parallel" with the deployment of the new electrical telegraphs (many of which were also developed in association with the burgeoning new railroad industry), the systems were found to frequently exhibit "anomalous currents" in their wires. As a telegraph engineer with the Midland railroad in England, W. H. Barlow appears to have been the first to systematically study, and record, these currents in an attempt to understand the source of these anomalies (Barlow 1849). Barlow's measurements of the excursions of the galvanometer meters on the Midland Company railway telegraph circuits show a definite diurnal variation (Lanzerotti 2001). Such a variation would certainly suggest an effect of nature on the communication lines. A likely interference of nature was noted by Barlow himself, as he wrote that "... in every case which has come under [his] observation, the telegraph needles have been deflected whenever aurora has been visible." Communication engineers have longed recognized that both of these "nature effects"—aurora and the Earth (telluric) currents—are attributable to electrical currents that flow in the Earth's ionosphere and magnetosphere.

Thus, while the new electrical telegraph allowed communications to avoid many of the afflictions that atmospheric weather imposes on optical telegraphs, the effects of nature's "space weather" now was a factor that had to be dealt with[1]. It would be several decades before the relationship between solar-produced effects and the operations of the electrical telegraph were firmly believed, nearly a century before "space weather" became a wider concern for technology, and more than a century and a half before "space weather" became a term in common engineering and science usage.

2. Electromagnetic Waves and Wireless

The first wireless telegraph signals using electromagnetic waves were sent by Guglielmo Marconi in 1895. Marconi was not only talented in using technology, he was also an astute business person. He clearly recognized that his ship-to-shore wireless enterprizes should be extended to intercontinental distances,

[1]The electrical telegraph did not totally eliminate all of nature's atmospheric weather effects, however. Silliman (1850) noted that "One curious fact connected with the operation of the telegraph is the induction of atmospheric electricity upon the wires ... often to cause the machines at several stations to record the approach of a thunderstorm."

and accomplished this in December 1901 with the reception at St. John's, Newfoundland, of signals transmitted from his Poldhu Station in Cornwall[2].

Marconi's achievement was only possible because of the existence of the ionosphere that reflected the Poldhu-transmitted signal, which otherwise would have propagated off into space. This reflecting layer at the top of Earth's neutral atmosphere was definitively identified some two decades later by the investigations of Briet & Tuve (1925) and by Appleton & Barnett (1925)[3]. Obviously, the physical state of this upper atmosphere conducting layer was of critical importance for the success (or failure) of reliable wireless transmissions.

The same ionosphere electrical currents that could produce "spontaneous" electrical currents within the Earth (and thus disturb the electrical telegraph) could also affect the propagation and reception of the transmitted long-distance wireless signals. This was noted by wireless engineers of the time, and Marconi himself wrote (1928) that "...times of bad fading [of radio signals] practically always coincide with the appearance of large sun-spots and intense aurora-borealis usually accompanied by magnetic storms...." He further significantly noted that these are "...the same periods when cables and land lines experience difficulties or are thrown out of action." Obviously "space weather" was affecting both of these communications technologies.

An example of a study of very long wavelength, long-distance wireless is shown in Figure 1.1 (reproduced from Fagen (1975), which contains historical notes on early wireless research in the old Bell Telephone System; see also Southworth 1962). Shown are the yearly average daylight cross-Atlantic transmission signal strengths for 1915–1932 (upper trace) and the sunspot numbers (lower trace). The intensities in the signal strength curves were derived by averaging the values from about ten European stations that were broadcasting in the 15 to 23 kHz band, after reducing them to a common base[4].

There is clearly an association between the two quantities in Figure 1.1. Wireless engineers at the time could use such information to provide them with some perspectives on expected transmission quality on a year-to-year basis—provided of course, that future sunspot numbers could be forecast. And such a forecast might be possible since the investigation of sunspot numbers and their future values had been an intellectual challenge since the report of Schwabe (in 1851) of an approximately ten year period in spot numbers[5]. The series was subsequently extended back to about 1750 (discussed by, for example, Carrington 1863; Stetson 1937; Clayton 1943, Abetti 1952) and is actively

[2]Guglielmo Marconi was awarded the Nobel Prize in Physics in 1909 for this accomplishment.
[3]Edward V. Appleton was awarded the Nobel Prize in Physics in 1947 for his ionosphere research.
[4]The signal from the transmitter in Nauen, Germany, was used as the base.
[5]He reported sunspot maxima in 1828, 1837, and 1848 (the year following Barlow's study of the anomalous electrical currents in the Midland Railway Company telegraph lines in England), and minima in 1833 and 1843 (Chapman & Bartels 1940).

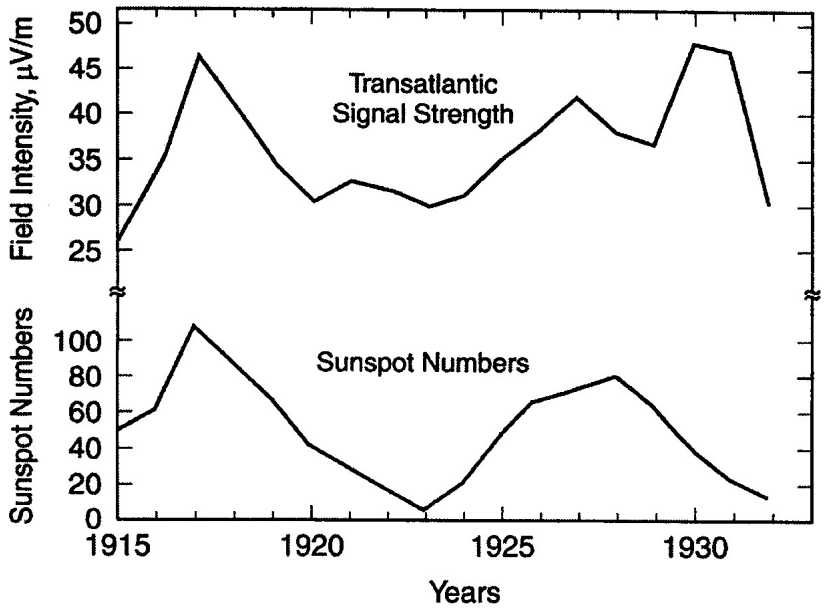


Figure 1.1. Yearly average daylight cross-Atlantic transmission signal strengths and sunspot numbers for the interval 1915–1932.

forecast forward today. Thus, the existence of a "periodicity" could make feasible the forecasting of transmission quality, and is a quantitative feature that is used presently as one of many inputs in a number of space weather products.

Not only did the transmissions of wireless signals seem to depend upon the long-term (order eleven year) trend in sunspot numbers, but the signal strengths also were affected on shorter time periods—month-to-month and year-to-year. This is illustrated in Figure 1.2 for the strength (in mV/m) of a long wavelength (18 kHz) signal recorded in Massachusetts during a two-year period, 1926–1928 (Stetson 1930). The sunspot number is plotted, inverted, as the top trace.

The practical effects of solar-produced disturbances on radio communications was well illustrated by a headline that appeared over a front page article in an issue of *The New York Times*[6]. This headline noted that "Violent magnetic storm disrupts short-wave radio communication." The sub headline related that

[6]Sunday, January 23, 1938.

"Transoceanic services transfer phone and other traffic to long wave lengths as sunspot disturbance strikes."

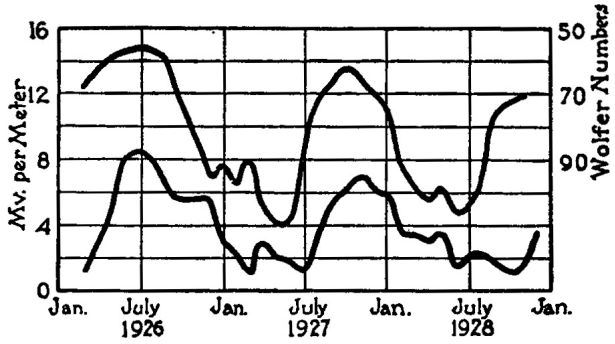


Figure 1.2. Lower trace: Radio field strength (in mV/m) recorded in Boston from station WBBM in Chicago for 1926–1928. Upper trace: Inverted curve of Wolf sunspot numbers.

The engineering work-around that shifted the cross-Atlantic wireless traffic from shorter to longer wavelengths prevented the complete disruption of voice messages at that time. Engineering solutions and engineering work-arounds to ameliorate space weather effects have always been of commensurable importance with deeper scientific understanding of the underlying causes. This is analogous to numerous engineering approaches that are used to address the potential effects of natural hazards on human technologies and infrastructures. For example, understanding the frequency dependence of the amplitudes of ground motions allows civil engineers to design more robust structures in earthquake-prone regions. The employment of lightning rods, pioneered by Benjamin Franklin, aids in reducing—or eliminating—the effects of atmospheric cloud-to-ground discharges on structures.

3. Solar-Terrestrial Effects on Technologies

From the earliest installations of the electrical telegraph systems to the beginnings of wireless communications, from the establishment of inter-connected power grids to the flight in recent decades of humans in space, the role of the solar-terrestrial environment for the successful implementation and operation of many contemporary technologies has continued to increase in importance. Illustrated in Figure 1.3 are selected examples of the times of large solar-originating disturbances on ground and space-based systems.

The operations and survivability of both ground- and space-based technical systems as denoted in Figure 1.3 have often encountered unanticipated surprises because of natural space environmental effects. As technologies continue to increase in sophistication, as well as in miniaturization and in interconnectedness,

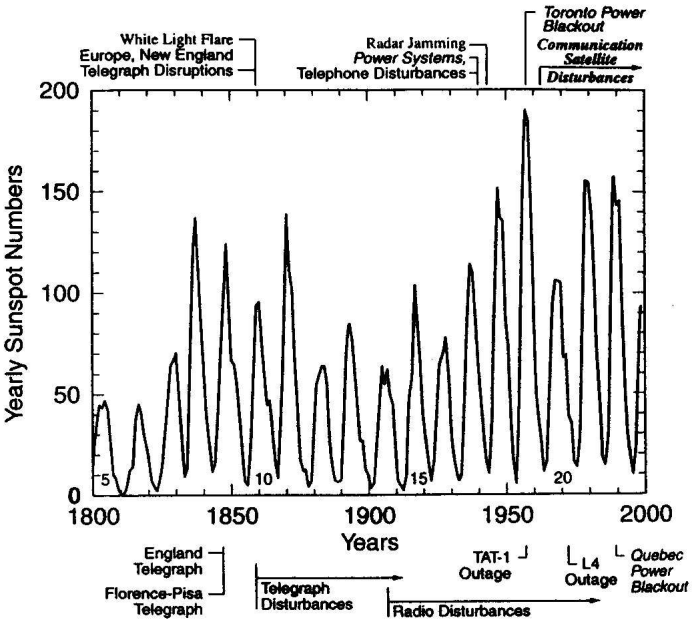


Figure 1.3. Yearly sunspot numbers with indicated times of selected major impacts, or the beginning of major effects, of the solar-terrestrial environment on technical systems (largely ground-based).

more sophisticated understanding of the Earth's space environment continues to be required as well. In addition, the increasing diversity of technical systems that can be affected by solar-terrestrial processes is accompanied by continual changes in the dominance of one technology over another for specific use, both civil and governmental. For example, in 1988 satellites were the dominant carrier of transoceanic messages and data; only about two percent of this traffic was over ocean cable. By 1990, the wide bandwidths provided by fiber optic cables meant that 80% of this traffic had migrated to ocean cables (Mandell 2000). Hence the importance of specific space weather processes is also changing with time and with the technology employed.

Many modern-day technological systems and components that are affected by various aspects of the solar-terrestrial environment are listed in Table 1.1 (Lanzerotti 2001). All of the environmental elements listed have design and/or operational implications for the systems and components indicated. Discussions of the environmental elements and their effects on the systems and components are provided in Lanzerotti *et al.* (1999) and Lanzerotti (2001).

Table 1.1. Impacts of Solar-Terrestrial Processes on Technologies

Solar-Terrestrial Process	Impact	Technologies Affected
Magnetic Field Variations	Induction of electrical currents in the Earth	Power distribution systems Long communications cables Pipelines
	Directional variations	Spacecraft attitude control Compasses
Ionosphere Variations	Reflection, propagation attenuation	Wireless communication systems
	Interference, scintillation	Communication satellites Geophysical prospecting
Solar Radio Bursts	Excess radio noise	Wireless systems Radar systems GPS transmissions
Particle Radiation	Solar cell damage	Spacecraft power
	Semiconductor damage/failure	Spacecraft control
	Faulty operation of semiconductor devices	Spacecraft attitude control
	Charging of surface and interior materials	Spacecraft electronics
	Human radiation exposure	Astronauts Airline passengers
Micrometeoroids and Artificial Space Debris	Physical damage	Solar cells Orbiting mirrors, surfaces, materials Entire vehicles
Atmosphere	Increased drag	Low altitude satellites
	Attenuation/scatter of wireless signals	Wireless communication systems

4. Solar Radio Emissions

The first realization of the existence of radio signals originating from sources other than Earth's atmosphere and human-produced was the discovery of emissions from the Milky Way galaxy by the Bell Laboratories engineer Karl Jansky in the early 1930s (Jansky 1933). The discovery of galactic radio noise by Jansky was made in the course of his studies of radio static on ship-to-shore and transatlantic communications circuits in Holmdel, New Jersey. Although the Illinois-based radio engineer Grote Reber, the only technically-trained individual who readily followed up on Jansky's discovery, attempted to measure

possible radio emissions from the Sun (and other solar system objects), a decade was to pass before there was success (Hey 1973) in this regard.

As in the case of Jansky's discovery, the first measurements of the quiet radio emission of the Sun in June 1942 (Southworth 1945; 1962) and of solar radio bursts in February 1942 (Hey 1946; 1973) were made while each of the engineers were pursuing more practical radio objectives. In the case of Southworth, it was the development of low noise microwave receivers for communications purposes. In the case of Hey, it was the pursuit of the understanding and possible mitigation of the jamming of British radar during the Second World War[7].

Hey (1973) comments on the missed opportunities (following Jansky's work and publications) to detect solar radio emissions. He attributes the "previous failures of other workers to recognize abnormal solar emissions" to the "stultifying effect of clinging to established viewpoints." In any event, the post-war publications of Southworth and of Hey on solar radio stirred a high level of research interest on solar radio physics beginning in the late 1940s. This research established that solar radio emissions can exhibit a wide range of spectral shapes and intensity levels (e.g., Kundu 1965; Guidice & Castelli 1972; Castelli *et al.* 1973; Barron *et al.* 1985). Research on solar radio phenomena remains an active, productive, and important field of study of the Sun today, both in its own right as well in association with studies of other energetic solar phenomena such as solar x-rays, gamma rays, and energetic particle acceleration (Bastian *et al.* 1998).

5. Contemporary Solar Radio and Some Implications for Technologies

5.1 Solar noise levels and technologies

Shown in Figure 1.4 are the time dependencies of a number of solar-originating phenomena measured near Earth during 1991, within the peak years of solar cycle 22 (Lanzerotti *et al.* 1997). The top two panels plot the solar radio emissions (average noontime values) at frequencies $\nu = 1.415$ GHz and $\nu = 15.4$ GHz. For an overall perspective of other physical phenomena emitted by the Sun during this year, sequentially below these traces are plotted the low energy proton fluxes measured by the solar polar-orbiting Ulysses spacecraft and by the near-Earth IMP-8 spacecraft, and the speed of, and interplanetary magnetic field carried in, the solar wind at Earth.

[7]The solar activity that produced the severe jamming in British radar in February 1942 was also the event that produced solar flare-associated particles that were directly measured for the first time. These high-energy particles, now of considerable space weather importance for their effects on space electronics and on humans in space, were detected on February 28 and March 7, 1942, by the ground-based, shielded ionization chambers of Scott Forbush (1946) who was conducting a worldwide program of measurements of "cosmic rays".

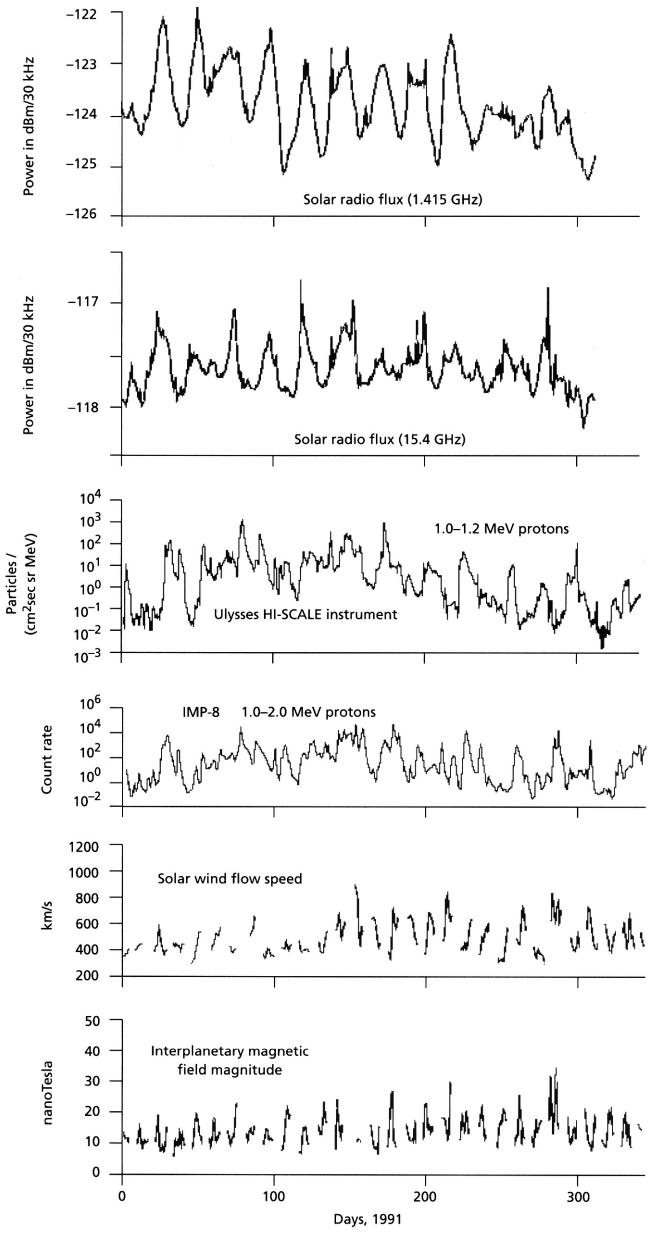


Figure 1.4. Variation with time of several solar-originating phenomena measured near Earth during the year 1991.

There is a wide range of variability in the solar radio emissions in the upper two panels. An analysis showed that during 1991 the average noontime mea-

sured flux at $\nu = 1.145$ GHz and at $\nu = 15.4$ GHz was -162.5 and -156 dBW/(m^2 4kHz), respectively. These values are 6 and 12 dB above the 273 K (Earth's surface temperature) thermal noise of -168.21 dBW/(m^2 4kHz). Further, these average noontime fluxes at Earth are only 20 and 14 dB, respectively, below the maximum flux of 142 dBW/(m^2 4kHz) that is allowed for satellite downlinks by the ITU regulation RR2566. Because this radio noise originates at the Sun in plasma physics processes in the solar photosphere and corona, and is not simple blackbody radiation (e.g., Bastian *et al.* 1998), the emissions may occur in distinct frequency ranges and be neither stationary in time nor have a Gaussian distribution.

An analysis of local noontime solar radio flux data over the last few solar cycles (data from the National Geophysical Data Center (NGDC) of the National Oceanic and Atmospheric Administration (NOAA), Boulder, CO, USA) shows that at 10.2 cm ($\nu = 2.8$ GHz, in one of the contemporary wireless frequency bands), such signals change by about 5.3 dB peak-to-peak during the cycle. They also have a standard deviation around the local one-year mean of 0.7 dB (Lanzerotti *et al.* 1997). The maximum excursion above the local mean was found to be 3.6 dB. It is reasonable to expect, therefore, that emission levels up to two standard deviations above the 1991 levels (at least 5 or 6 dB, and perhaps as high as 7 or 8 dB) might occur at some time during a solar maximum period. Such noise levels would reduce the 14 dB margin at 15.4 GHz to only about 6 or 7 dB.

The solar radio data shown in Figure 1.4 are only local noontime values. Short-term variations with durations of a few seconds can be at least 35 dB higher than these values (Barron *et al.* 1980; Benz 1986; Isliker & Benz 1994). For example, the large flare of 1967 May 23 produced a flux level measured at Earth $> 100,000$ solar flux units (SFU = 10^{-22} W/(m^2 Hz)), and perhaps as high as 300,000 SFU at $\nu \sim 1$ GHz (Castelli *et al.* 1973). This corresponds to -129 dBW/(m^2 4kHz), or 13 dB above the maximum limit of -142 dBW/(m^2 4kHz) noted above.

5.2 Solar noise interference

Solar interference is maximized for geosynchronous (GEO) satellite transmissions in the late February to early April and late August to early October time intervals. The time of maximum interference depends upon the latitude of the receiving station on the ground. For the continental United States this interval is in early March and early October. The duration of interference may last up to thirty minutes or more, depending upon the receiving antenna beam width. Antennae receiving signals from GEO spacecraft in the eastern (western) sky will be subject to inference in local morning (afternoon) hours.

The same morning/afternoon situation for interference times exists for wireless cell sites. An instance of enhanced dropped calls during local morning hours in the base stations of a United States cellular system was shown in Lanzerotti *et al.* (1999) at the time of enhanced solar activity. Unlike the situation of GEO satcoms, interference on ground-based wireless is not seasonally dependent.

Substantial (perhaps up to 10 dB) reduction in received Global Positioning Satellite (GPS) signals can occur under the most intense solar radio bursts. Such occurrences will reduce link margins and degrade signal acquisition. Again, this interference will not be largely seasonally dependent.

Radars are used for tracking and guiding numerous objects in time and across space. Radar antenna tracking at low elevation angles relative to the solar direction can suffer reduced noise floors in their received back-scattered signals, depending upon beam widths and side lobes. Antennae pointing more in the solar direction can result in noise levels far above target signals, causing complete loss of any targets being sought or followed. Interference on several different radars reportedly occurred on several occasions at the time of solar radio bursts during the intense solar activity from 2001 March 24 to April 6 (S. Quigley, Air Force Research Laboratory, private communication, 2001). The radio burst event on 6 April was discussed in the context of its interference potential for wireless communications, using data from the NJIT Owens Valley (California) Solar Array (Lanzerotti *et al.* 2002).

5.3 Statistics of solar radio noise

As discussed in §5.1, short time variations (bursts from milliseconds to many minutes or longer) in solar radio noise levels can attain very large amplitudes, many dB above the quiet Sun background. Since the contemporary knowledge base of the statistics of the occurrence frequency and amplitude distributions of solar bursts did not exist, several recent investigations have been directed toward these objectives (Bala *et al.* 2002; Nita *et al.* 2002). These investigations were motivated by the types of noise level discussions in §5.1, and by other considerations of wireless interference possibilities.

As discussed in Bala *et al.* (2002) (see also Nita *et al.* 2002) the solar flux F_{eq} where the thermal noise levels and the solar noise levels are approximately equal is ~ 960 SFU for a cellular base station operating at 900 MHz and with a gain of ~ 10 for a single polarization antenna. This is more than twice the thermal noise power. $F_{eq} \approx 6000$ SFU for a base station operating at 2.4 GHz with the same antenna gain.

Forty years of solar radio burst data that had been collected by the NGDC were acquired, processed and reformatted for the statistical analyses reported in Bala *et al.* (2002) and in Nita *et al.* (2002). Figure 1.5 shows histograms of the

number of events per day per frequency bin for the forty year period, 1960–1999 (Figures 1.5a, b) and for the three solar cycles (cycles 20, 21, 22) separately (Figures 1.5c–h) as a function of frequency for two separate frequency ranges—1 to 10 GHz and 10 to 20 GHz. In all panels the binned intensities are for bursts $> 10^3$ SFU.

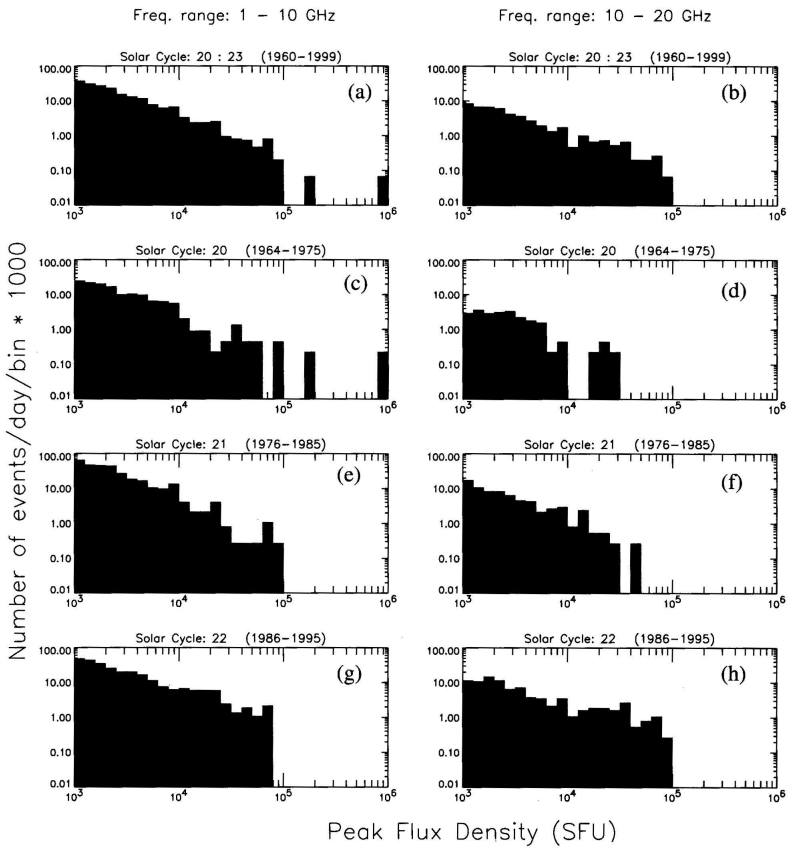


Figure 1.5. Number of solar burst events per day with amplitudes $> 10^3$ SFU (a and b) for 40 years, (c and d) for cycle 20, (e and f) for cycle 21, and (g and h) for cycle 22. The frequency ranges are 1–10 GHz (excluding 10 GHz) shown in the left panels and 10–20 GHz (excluding 20 GHz) in the right panels. Here, the number of events per day per bin is 1000.

The occurrence distributions (Figure 1.5) for events with amplitudes $> 10^3$ SFU decrease with amplitude (peak flux density) approximately as an inverse power law. The implications of such distributions for solar radio emission mechanisms are addressed by Nita *et al.* (2002). In both frequency bands shown, most events have amplitudes $< 10^5$ SFU. The single event with amplitude $> 10^5$

SFU was recorded on 1974 July 04 at Kiel, Germany, at $\nu = 1$ GHz (2.6×10^5 SFU) and $\nu = 1.42$ GHz (8×10^5 SFU).

There is an apparent increase in the number of larger events ($> 10^4$ SFU) in both frequency ranges as one progresses from solar cycle 20 to 22 (Figure 1.5). The physical implications, if any, for this is not understood. Instrumentation effects such as possible changes in the dynamic range sensitivities of the instruments at the various reporting sites cannot be ruled out. Further discussions of these points and others, including changing local time distributions of the global recording sites over the decades, are contained in Nita *et al.* (2002).

The yearly dependence of the daily number of events for events with peak flux densities $> 10^3$ and $> 10^4$ SFU are shown in Figures 1.6a, b, respectively. The frequency bands $\nu =$ 1–2 GHz, 2–4 GHz, and 4–10 GHz are shown with solid, dotted, and dashed lines, respectively. The 11-year sunspot cycle is clearly evident in the statistics. The marked increase in the daily occurrence of larger events in later solar cycles can also be seen. The double peak in the number of radio burst events in the 22nd cycle is clearly evident in geomagnetic storm sudden commencements in this cycle, and somewhat less evident in the number of sunspots (see Solar Geophysical Data, No 668A, 2000).

Taking a solar flux level of 10^3 SFU as a context "threshold", then Figure 1.6 indicates that there can be of the order of one event of this size or larger every $\sim$10–20 days or so on average per year. The event occurrence rate will be larger during solar maximum and smaller during solar minimum. The possibility for interference will also depend upon antenna orientation at a given site.

Considering that an antenna at a given site is most susceptible for ~ 3 h each around local morning and local evening hours, then the chances for interference would reduce to perhaps one event with peak flux density $> 10^3$ SFU or larger every $\sim$ 40 to 80 days, or a few times per year at a given cell site. Since numerous sites will be pointing in the solar direction at the same time, a large service area could be affected by a single burst.

6. Conclusion and Looking to the Future

History has shown that as older technologies are upgraded, or new technologies are introduced, their design features must often be evaluated in the context of the space-affected environments that they will operate in, or operate under the influence of, in order to ensure reliable performance. Thus, many features of the solar and the solar-terrestrial environment must be taken into design and operational consideration in order to ensure the survivability and reliable operations of the technologies. Engineers who at the time were studying other topics in radio physics discovered radio emissions from the Sun. Since these discoveries more than sixty years ago, solar radio emissions have become to be important physical phenomena not only for scientific investigations but also for

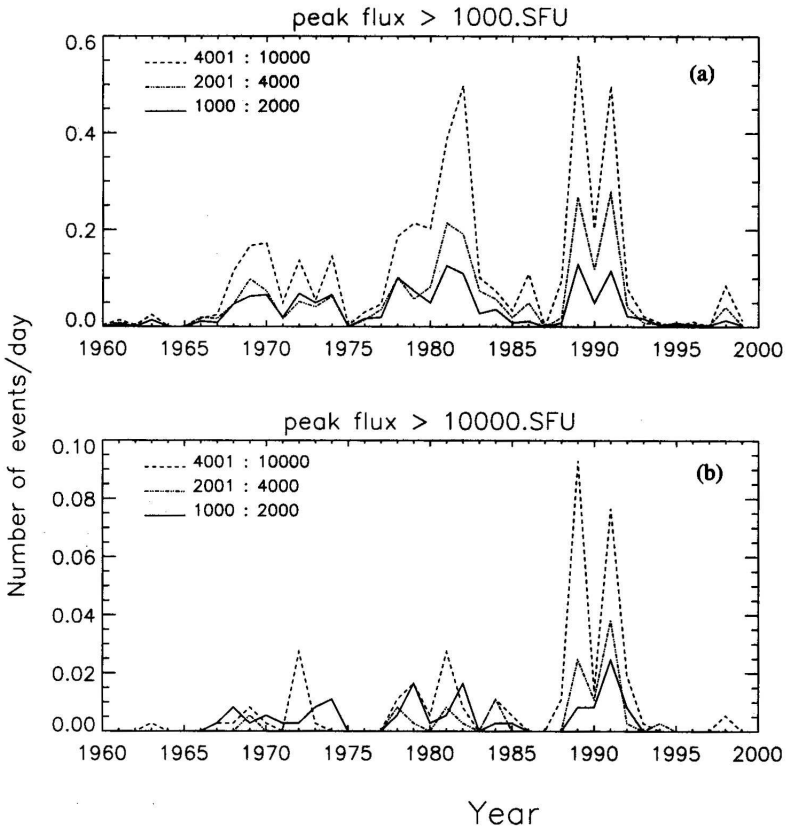


Figure 1.6. Total number of events per day as a function of time in years (a) for peak flux $> 10^3$ SFU and (b) for peak flux $> 10^4$ SFU. The frequency ranges are 1–2, 2–4, and 4–120 GHz.

their role in predicting, in producing, and in mitigating space weather effects on technologies.

A number of new research initiatives, observational as well as theory and modeling, are being discussed, developed, and implemented for the future that will significantly enhance capabilities for understanding, and ultimately forecasting, space weather conditions. A presentation of most of these initiatives is contained in the Decadal Survey study of solar and space physics that was recently carried under the auspices of the National Research Council (NRC) (2003). The report of the study also contains substantial discussion of space weather issues, both research as well as policy challenges. This Survey of the research field and the report on its future makes clear that observational research

on the Sun requires a concerted future effort that must encompass all aspects of solar studies. Investigations discussed and prioritized range from a spacecraft project to fly within a few solar radii of the Sun's photosphere (Solar Probe mission), to a new ground-base solar optical telescope that was previously endorsed in the NRC's decadal survey of astronomy (the Advanced Technology Solar Telescope—ATST).

The highest priority small program in the Solar and Space Physics Survey is the Frequency Agile Solar Radiotelescope (FASR) project. This project, with its multi-frequency imaging array of antennas will be able to yield high spatial resolution images of solar active regions with the time resolution that is critical for understanding the radio bursts and microbursts that can interfere with sensitive communications and radar equipment. FASR will also be of great importance, by itself and in coordination with other solar and space physics initiatives as discussed in the Survey, in understanding the physical processes that underlie phenomena such as the launching of coronal mass ejections from the Sun that, upon reaching Earth, produce the magnetospheric and ionospheric disturbances that can disrupt numerous technologies (Table 1.1).

References

Abetti, G. 1952, The History of Astronomy, Abelard-Schuman, pg. 183ff, New York

Appleton, E. V. & Barnett, M. A. F. 1925, Nature, 115, 333

Bala, B., Lanzerotti, L. J., Gary, D. E. & Thomson, D. J. 2002, Radio Sci., 37, DOI 10.1029/2001RS002481

Barron, W. R., Cliver, E. W., Guidice, D. A. & Badillo, V. L. 1980, Air Force Geophysics Laboratory, Space Physics Division, Project 4643, Hanscom AFB, MA

Barron, W. R., Cliver, E. W., Cronin, J. P. & Guidice, D. A. 1985, in Handbook of Geophysics and the Space Environment, ed. A. S. Jura, Chap. 11, AFGL, USAF

Bastian, T. S., Benz, A. O. & Gary, D. E. 1998, Ann. Rev. Astron. Astrophys., 36, 131

Benz, A. O. 1986, Solar Phys., 104, 99

Breit, M. A. & Tuve, M. A. 1925, Nature, 116, 357

Carrington, R. C. 1863, Observations of the Spots on the Sun from November 9, 1853, to March 24, 1963, Made at Redhill, William & Norgate, London and Edinburgh, 167

Castelli, J. P., Aarons, J., Guidice, D. A. & Straka, R. M. 1973, Proc. IEEE, 61, 1307

Chapman, S. & Bartels, J. 1940, Geomagnetism, Oxford, II, 934

Clayton, H. H. 1943, The sunspot period, in Solar Relations to Weather and Life, ed. H. H. Clayton, Vol. 2, pg. 333
Forbush, S. E. 1946, Phys. Rev., 70, 771
Guidice, D. A. & Castelli, J. P. 1972, in NASA Symp. High Energy Phenomena on the Sun, Goddard Space Flight Center, Greenbelt, MD
Hey, J. S. 1946, Nature, 158, 234
Hey, J. S. 1973, The Evolution of Radio Astronomy, Neale Watson Academic Pub. Inc., New York
Isliker, H. & Benz, A. O. 1994, Astron. Astrophys. Supp. Ser., 104, 145
Jansky, K. 1933, Proc. IRE, 21, 1387
Kundu, M. R. 1965, Solar Radio Astronomy, Interscience, New York
Lanzerotti, L. J., Thomson, D. J. & Maclennan, C. G. 1997, Bell Lab. Tech. J., 2(3), 5
Lanzerotti, L. J. 2001, Space weather effects on technologies, in Space Weather, ed. P. Song, H. Singer, & G. Siscoe, American Geophysical Union, Washington, pg. 11
Lanzerotti, L. J., Gary, D. E., Thomson, D. J. & Maclennan, C. G. 2002, Bell Labs Tech. J., 7(1), 159
Mandell, M. 2000, IEEE Spectrum, April, pg. 50
Marconi, G. 1928, Radio communication, Proc. IRE, 16, 40
National Research Council 2003, The Sun to the Earth - and Beyond, A Decadal Survey of Solar and Space Physics, National Academies Press, Washington, D.C.
Nita, G. M., Gary, D. E., Lanzerotti, L. J. & Thomson, D. J. 2002, Ap.J., 570, 423
Southworth, G. C. 1945, Microwave radiation from the Sun, J. Franklin Inst., 239, 285
Southworth, G. C. 1962, Forty Years of Radio Research, Gordon and Breach, New York
Stetson, H. T. 1930, Man and the Stars, Grosset and Dunlop, New York, pg. 158
Stetson, H. T. 1937, Sunspots and Their Effects, McGraw Hill, pg. 160

Chapter 2

OVERVIEW OF SOLAR RADIO PHYSICS AND INTERPLANETARY DISTURBANCES

Monique Pick
LESIA, UMR CNRS 8109, Observatoire de Paris
monique.pick@obspm.fr

Abstract Solar radio emission has been observed from a few hundred GHz down to a few kHz and has revealed a large variety of phenomena. Thanks to this broad frequency window, solar phenomena can be probed from a fraction of a solar radius out to 1 AU and beyond. This chapter reviews some topics of current interest in which radio astronomy has significantly contributed to transform our knowledge of the physics of the corona and of the interplanetary medium. Special emphasis is placed on the results which have emerged from coordinated studies of radio observations and data obtained in other spectral ranges. The few results presented in this chapter illustrate how major advances can be expected in the future from the Frequency Agile Solar Radiotelescope (FASR) instrument which will provide radio imaging observations covering simultaneously a broad radio spectrum.

Radio observations provide powerful diagnostics on the solar atmosphere and on dynamical phenomena occurring in the solar corona and the interplanetary medium. Radio techniques cover a broad frequency domain from submillimeter to kilometer wavelengths. Observations at different wavelengths sample different heights and physical conditions in the solar atmosphere, with longer wavelengths referring to higher heights above the photosphere. Therefore, a given event and its related effects can in principle be probed from the bottom of the corona to large distances in the interplanetary medium. The first book devoted to Solar Radio Astronomy was written by Kundu (1965) and remains an important contribution on the subject. Historically, radio emission was divided into three categories: the quiet Sun emission, the slowly varying component associated with the transit on the solar disk of structures such as active regions or streamers, and sporadic activity which includes a large variety

of bursts (Figure 2.1). With the progress accomplished in the understanding of the physical processes responsible for radio emission, this classification appears somewhat arbitrary now.

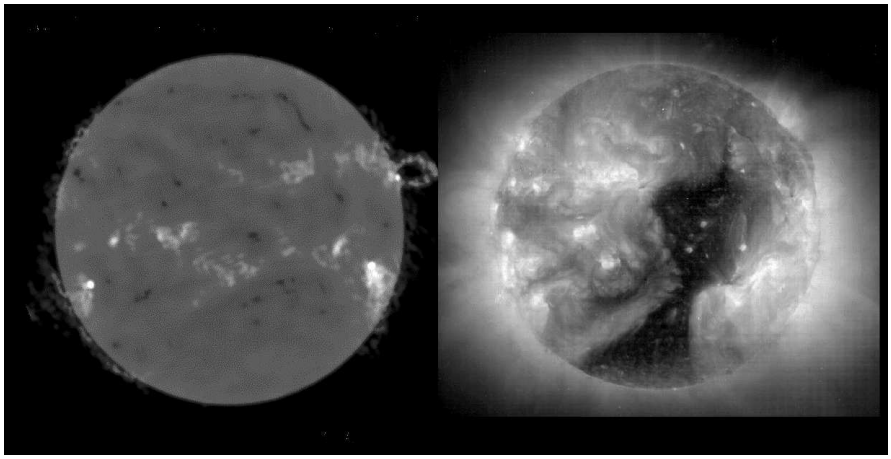


Figure 2.1. The Sun seen at 17 GHz by the Nobeyama Radioheliograph (*left*) and at 195 Åby the Extreme-ultraviolet Imaging Telescope (EIT) on SOHO (*right*); the dark region is a coronal hole.

Important results have emerged over the last two decades from coordinated studies of radio observations and data obtained in other spectral domains. The SMM mission opened a new horizon in solar physics by making available observations covering a large spectral range. Since SMM, many powerful spacecraft such as *Yohkoh*, SOHO, TRACE, GRANAT and recently RHESSI (*Reuven Ramaty High Energy Solar Spectroscopic Imager*) have been launched. Measurements in the interplanetary,medium were obtained jointly by several missions and in particular by ISEE-3, WIND, ACE and Ulysses. Ulysses provided for the first time a 3-D vision of the Sun. Radio imaging observations with high time resolution became available and complemented the spectral data. Tremendous progress was also made on theoretical aspects. For physical processes dealing with scales below the limited resolving power of the instruments, the approach consisted in first elaborating a theoretical scenario and then deducing observational tests to be applied to the data.

I do not intend here to introduce all the topics that will be developed in the following chapters: each author has done it, much better than I could. I have rather decided to select some topics which I believe to be of current interest and in which radio astronomy techniques have already been an important tool, and/or will be of great importance in the coming years.

1. General Context of the Radio Emissions

Radio emission from an undisturbed plasma is generated by thermal bremsstrahlung (free-free) resulting from the Coulomb interaction of the plasma electrons with ions, and by gyroresonance emission of the electrons in the presence of a magnetic field. Thermal gyroresonance emission was introduced independently by Zheleznyakov (1962) and Kakinuma & Swarup (1962); it results from thermal electrons spiraling along coronal magnetic field lines and is emitted at low harmonics of the local electron gyrofrequency ($\nu = s\nu_B$ where s =1, 2, 3 with $\nu_B = 2.8 \times 10^6 B$). Radio emission produced by nonthermal electrons is attributed principally to gyrosynchrotron (at higher harmonics of the gyrofrequency or producing a synchrotron continuum emission, depending on the energy of the electrons) and coherent plasma emission. Their relative contribution depends upon the observing wavelength. Gyrosynchrotron emission usually dominates at frequencies above about 3 GHz. Microwave observations of solar flares reveal the behavior of hot plasmas (thermal emission) and nonthermal high energy electrons (gyrosynchrotron emission). Gyrosynchrotron emission provides diagnostics on the ambient plasma, on the energy range of the radiating electrons and on their evolution.

Coherent plasma emission, which most often dominates at frequencies below 3 GHz, is caused by plasma instabilities driving various wave modes that produce observable radio waves. A wide variety of radio bursts have been reported and classified in the literature. Classification of these bursts and their relation with emission mechanisms remain arbitrary in many aspects. As an introduction to the following chapters, I will however first describe briefly the different kinds of solar radio bursts. Table 2.1 summarizes the principal identified radio bursts. Particularly important are the radio bursts produced by electron beams propagating along the magnetic field; these bursts contain many pieces of information on the electron acceleration, injection and propagation mechanisms, on the beam characteristics and on the ambient medium.

The high brightness temperatures observed in these bursts indicate that the radio signal accurately traces streams of nonthermal electrons in the corona and in the interplanetary medium. For example, type III (also U and J) bursts are due to electron beams propagating along open magnetic field structures and exciting Langmuir waves at each level of the corona and of the interplanetary medium that in turn produce a radio emission at the fundamental or at the second harmonic of the plasma frequency, ν_p. Spike bursts are assumed to be produced by electron cyclotron maser emission (ECME) at the cyclotron ν_B and provide direct information on the magnetic field strength. Type II bursts are caused by electrons accelerated by shocks at the local plasma frequency and/or at its harmonics. Noise storms are the most common form of activity at met-

Table 2.1. Principal Identified Radio Bursts; ν_p = plasma frequency; ν_B = gyro frequency

Incoherent radio emission mechanisms	**Emission mechanism**	**Source**
Microwave and millimeter bursts	free-free emission	Thermal plasma
Type IV bursts continua	Gyrosynchrotron emission	
Millimeter		*Ultrarelativistic elect.*
Microwave and dm-dam		*Relativistic elect.*
Coherent radio emission mechanisms		
Dm-dam type IV bursts	plasma emission	Trapped energetic electrons
Type II bursts	ν_p; $2\nu_p$	Shocks
Type III and V bursts	ν_p; $2\nu_p$	Upward propagating electron beams
Reverse slope bursts	ν_p; $2\nu_p$	Downward propagating electron beams
Type J and U bursts	ν_p; $2\nu_p$	Beams along close loops
Dm-m pulsation	$\nu = s\nu_B$	Loss- cone instability *trapped electrons*
Dm spikes		Loss-cone instability
Dm-m type I storms	plasma emission	trapped and escaping
Dam-Km type III storms		accelerated electrons

ric and decametric wavelengths; they are produced by suprathermal electrons accelerated continuously over time scales of hours or days.

Radioastronomy has significantly contributed to our understanding of the structure of the corona and of the heliosphere (e.g. Bougeret *et al.* 1986).

2. Coronal Magnetography

The physics of the solar corona is governed by the interaction between magnetic fields and plasma. Radio astronomy is the only technique that provides coronal magnetic field measurements.

The polarization characteristics of the observed radio waves are determined by the emission mechanism and by the propagation conditions in the corona. There are two modes of electromagnetic wave propagation in a magnetized plasma: the extraordinary (x-mode) and the ordinary (o-mode). Most of the polarization measurements are made in the microwave domain in the low corona, where the plasma can be optically thick to one of the two mechanisms, brems-

strahlung or gyroresonance. VLA observations showed that the plasma can be optically thick at 20 cm to either thermal bremsstrahlung or gyroresonance emission whereas gyroresonance emission is usually the dominant mechanism above the sunspots at 6 cm. At shorter wavelengths, typically at the observing frequency of the Nobeyama Radioheliograph, 1.76 cm, free-free emission will be dominant for all regions with magnetic fields below 2000 G, which corresponds to the third harmonic of the gyrofrequency (e.g. Grebinskij *et al.* 2000). Several sophisticated methods of diagnostics of the magnetic field have been developed and successfully tested with the available instruments. The following examples illustrate the powerful potentiality of radio observations for measuring coronal magnetic fields.

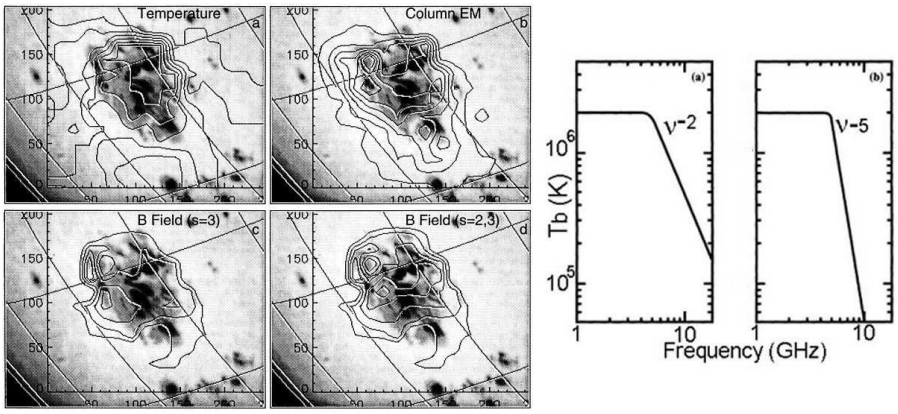


Figure 2.2. Right: Microwave brightness temperature expected for active regions: a) thermal bremsstrahlung; b) thermal gyroresonance emission. *Left*: Physical maps obtained by interpretation of brightness temperature spectra. a) Electron temperature with contour levels 0.9, 1.15, 1.4, 1.9 and 2.09 10^6K. b) Electron column emission measure. c) Total magnetic strength at the base of the corona assuming harmonic $s = 3$ everywhere. The values are as measured from gyroresonance spectra. The contour levels are 200, 400, 600, 800 and 1000 G. d) The same as in c except $s = 2$ has been assumed in upper right part of the active region. The highest contour is in this case 1200 G (from Gary & Hurford 1994).

Owens Valley Solar Array observations at 1.2–7 GHz demonstrated the interest of combining spatial and high spectral resolution (Gary & Hurford 1994). Solar maps were obtained at 22 frequencies by the aperture synthesis method. One of the major results was to show that the brightness temperature spectra generally fall into two easily identifiable types—thermal free-free spectra and thermal gyroresonance spectra—and that their spatial distribution over an active region can be obtained. Interpretation of these spectra provides maps of physical parameters, in particular of the magnetic field strength (Figure 2.2). However, the results were limited by the resolving power of the instrument. Moreover,

variations with time of the structure of active regions cannot be detected by rotational aperture synthesis methods. See the more complete discussion by White (Chapter 5).

Another approach consists in obtaining radio imaging observations at a few discrete frequencies jointly with X-EUV imaging and spectrograph observations. Both kinds of radiations depend on temperature and density but only radio emission depends on magnetic field; X-EUV emission is insensitive to it. EUV and X-ray data allow the determination of physical parameters necessary to calculate the brightness temperature at a particular radio wavelength and to compare it with the observed values. The radio observations can be fitted to a magnetic field model which determines the magnetic field structure. This method was successfully applied using different sets of observations; for example, *Yohkoh* and data from Westerbork Synthesis Radio Telescope (WSRT) provided determination of the magnetic field of a flaring site (Chiuderi-Drago *et al.* 1998). If the two-dimensional distribution of the physical parameters can be obtained for each spatial location, then three-dimensional coronal magnetography can be achieved (Brosius *et al.* 2002). One example is shown in Figure 2.3. More details are given by Brosius (Chapter 13).

The last method of magnetic field measurement is the observation of an inversion of the circular polarization. Circular polarization inversion was observed for the first time by Piddington & Minnett (1951). In the case of weak coupling between the two electromagnetic wave modes, this inversion occurs when the wave crosses a transverse field region (QT). Observations of polarization inversion provide a unique diagnostic on the magnetic field in coronal layers at 0.05–0.4 $R_{\odot}$, well above the height of formation of the microwave emission but the determination of the value of this magnetic field depends on the electron density at the QT level. Therefore, either an arbitrary estimate of the density is performed or another equation is necessary (e.g. Alissandrakis *et al.* 1996, Ryabov *et al.* 1999). Note that this method is independent of the emission mechanism. Further details are given by Ryabov (Chapter 7).

It is interesting to point out that:

- The measured coronal magnetic fields often, but not always, exceed those extrapolated from a simple potential model; this suggests the presence of coronal electric currents.

- Occasional contributions of nonthermal emission in some limited areas of the active regions cannot be excluded (Drago Chiuderi *et al.* 1987). Systematic identification of these regions could be a key factor for understanding the initiation of flare activity, or the origin of the electron acceleration.

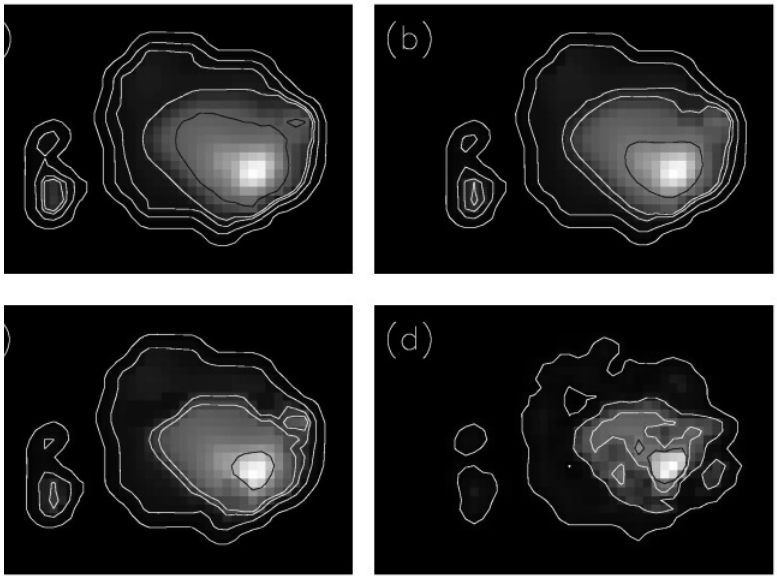


Figure 2.3. Coronal magnetic strength at heights (a) 5000, (b) 10000, (c) 15000 and (d) 25000 km above the photosphere. VLA observations were made at 4.866 and 8.450 GHz. EUV observations were made by SOHO (Coronal Diagnostic Spectrometer, EUV Imaging Telescope and Michelson Doppler Imager). Contour levels are 200, 579, 868, 1005 and 1508 G where the last four values correspond, respectively, to the third harmonic at 4.866 GHz, the second harmonic at 4.866 GHz, the third harmonic at 8.450 GHz and second harmonic at 8.450 GHz (from Brosius *et al.* 2002).

- The uncertainty in the coronal magnetic fields derived through radio observations is usually related to the choice of the best harmonic fitting the results. Most of these uncertainties can be overcome by matching intensity and polarization observations at several frequencies. See Gary & Hurford (Chapter 4). This will not be accomplished until high spatial and spectral radio imaging observations become available. The same holds for the present limitations on the measurement of the inversion of circular polarization. The ambiguity could be in principle suppressed with an instrument covering a wide frequency domain.

- With the new generation of dedicated solar instruments such as FASR (See Bastian, Chapter 3), with its high spatial, spectral and temporal resolution, measurements of the magnetic field and of its evolution outside active regions, as for example, above bright points or filament regions, will become accessible. Finally, quantitative and accurate measurements of the magnetic field made by radio techniques will bring strong con-

straints on the calculation of magnetic fields extrapolated from measured photospheric fields.

3. Transient Activity and Flares

It is generally accepted that several processes encountered in solar and interplanetary physics such as coronal heating, solar wind driving, active region evolution, flare and CME production, particle origin and propagation are governed by magnetic processes. Observations with increasing sensitivity and temporal resolution have shown that the coronal plasma varies continuously. Soft X-ray images reveal many transient phenomena related to magnetic energy release in a broad range of sizes and on temporal scales ranging from a fraction of a second to hours. Heating of the corona, which reaches one million degrees at its bottom, and its high temperature itself may be related to explosive phenomena.

The most spectacular and energetic events occurring in the solar atmosphere are flares and Coronal Mass Ejections (CMEs). See Vourlidas (Chapter 11). Most of the energy that is released locally in the vicinity of active regions during flares is contained in energetic accelerated particles. Energy releases range from 10^{26} ergs for microflares up to 10^{34} ergs for larger flares. The precipitation of energetic particles in the lower atmosphere leads to energy deposition, which produces heating and evaporation of the chromospheric material. Soft X-ray observations provide one of the most direct proofs of the local heating of the plasma: thermal energy radiated by the soft X-rays is the result of the deposition of the nonthermal energy contained in accelerated electrons. CMEs are dynamical events corresponding to the destabilization of a large portion of the corona leading to the expulsion of 10^{15}–10^{16} g of matter. They are recognized as primary drivers of disturbances in the interplanetary medium.

3.1 Energy dissipation

The magnetic energy release in the solar corona is due to a large variety of dynamical processes and is closely connected to the evolution of the solar magnetic field, on all spatial scales, in the highly inhomogeneous and variable coronal plasma. Magnetic reconnection is one of the basic processes proposed for coronal heating and flare energy release. The microscopic and macroscopic processes underlying the mechanism of the energy release are not yet understood. Most recent approaches consider that the coronal heating and the solar activity may result from the superposition of a very large number of incoherent elementary events produced in very small current sheets, the scale of which is too small to be observable. The statistical distribution of these events is an important factor and could be derived, in principle, from observations. The statistical behavior of such complex dynamical systems can be understood by

using the concept of "Self-Organized Criticality" (SOC, Bak *et al.* 1987). This statistical approach has led recently to several promising developments:

- The high temperature of the corona was originally interpreted as arising from the dissipation of waves originating from lower layers. In 1974, Levine proposed that coronal heating may be due to small flares releasing magnetic energy by reconnection. Small brightenings observed above the solar magnetic network of the quiet corona by the *Yohkoh* Soft X-ray telescope (SXT) were first reported by Krucker *et al.* (1997). Through sensitive SOHO and TRACE EUV measurements, microflare events were found in a majority of pixels of the quiet corona. This topic is currently the subject of very intense research. There is a general agreement that the energy distribution of micro events is a power law (index 2.3–2.6) but there are discrepancies on the estimated energy input due to sensitivity limitations and bias in the measurements. At the present stage, it seems that the thermal energy of these micro events, while representing a significant contribution, may not be sufficient to explain the overall coronal heating.

- Radio VLA observations showed similar power-law distributions and also revealed the existence of nonthermal emission for several events (Krucker & Benz 1997). These results established a physical link between the existence of these micro events and flares.

- The SMM Hard X-ray burst spectrometer recorded more than 12000 bursts associated with flares, which in general display a nonthermal spectrum. Figure 2.4 shows that the distribution of the number of hard X-ray flares versus their peak intensity follows a power law (Crosby *et al.* 1993). This suggests that a flare is the result of an avalanche of very small reconnection events as proposed by Lu & Hamilton (1991), who applied the SOC concept to solar flares.

Evidence for fragmented energy release came from radio dynamical spectra (Benz 1985). Sub-millisecond spikes of narrow band coherent emissions are currently observed in the decimetric-metric domain. They aggregate in clusters that can contain up to thousands of them lasting from few seconds to a few minutes. There are many observational signatures favoring the hypothesis that these spikes coincide with the energy release region.

3.2 Solar magnetic reconnection in the solar atmosphere and diagnostics on regions of acceleration

During the ISEE III and SMM missions, joint observations of hard X-ray and dm-m imaging radio emission with a time cadence shorter than one sec-

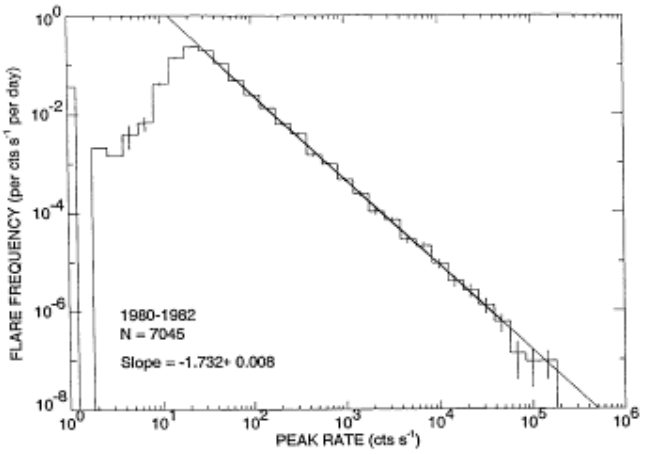


Figure 2.4. The frequency distribution of the peak rates shown for all 7045 HXRBS (Hard X-ray Burst Spectrometer on SMM) flares recorded in 1980–1982. The error bars represent $\pm 1\sigma$ uncertainties based on Poisson statistics on the number of flares in each bin. The straight line through the points above 30 count s^{-1} represents the least-squares fitted power-law function. The turnover below 30 counts s^{-1} corresponds to the HXRBS sensitivity limit. An average background of 40 count s^{-1} was subtracted from the peak rate (including background; from Crosby *et al.* 1993).

ond showed that accelerated electrons during flares originate from the rapid interaction between two or more magnetic structures (Raoult *et al.* 1985).

Microwave and hard X-ray spatially resolved observations were shown to be consistent with emerging flux models of flares with two or more loops interacting together, releasing magnetic energy and producing energetic electrons. Masuda *et al.* (1994) discovered that, in some of the impulsive flares occurring near the limb, a coronal hard X-ray source appeared above the soft X ray bright flare loop located between two foot points. Figure 2.5 shows hard X-ray images of an impulsive flare obtained from the hard X-ray telescope of *Yohkoh*. Since then, a number of observations confirmed that complex magnetic systems, involving often more than two loops, interact and lead to flare onset and development. Shibata *et al.* (1995) found that hot plasma ejections were associated with these X-ray impulsive flares and this result gives a strong support to the reconnection hypothesis.

Many small-scale soft X-ray jets, also showing evidence for magnetic reconnection, were observed in emerging flux regions in association with microflares. Kundu *et al.* (1995) found type III bursts associated with these X-ray jets. This implies that energetic electrons, with velocity of approximately one-third of the light velocity, are accelerated in these small events, similarly to what happens in larger flares.

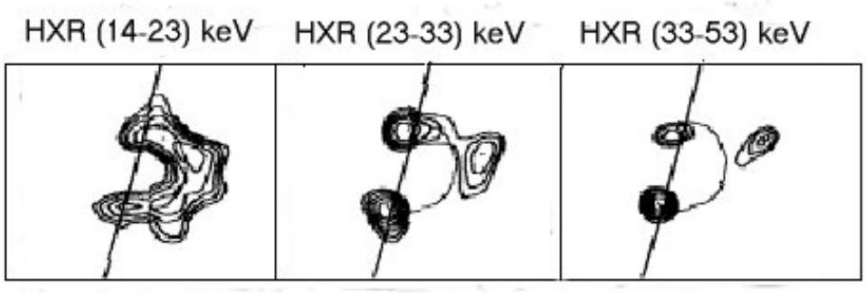


Figure 2.5. Hard X-ray images of an impulsive west limb flare in three energy bands obtained from the hard X-ray telescope on *Yohkoh* (from Masuda *et al.* 1994).

Radio observations in the dm-m wavelength range (see Benz, Chapter 9) also provide information on the acceleration region, which in fact may cover a wide range of heights of the solar corona. The height can, for example, be derived from observations of pairs of type III bursts drifting in opposite directions. Other information is given by metric spikes, which are most often observed just above the starting frequency of type III bursts as illustrated in Figure 2.6; recent spatially resolved observations firmly demonstrate that these spikes are closely related to the electron acceleration region (Benz *et al.* 1996). Due to the high-frequency limit (450 MHz) of the Nançay Radioheliograph (NRH)—the only imaging instrument covering presently the dm-m range—spatially resolved radio observations of spikes are rare.

In summary, the current understanding is that most of the eruptive events observed in the solar magnetized plasmas are due to fast release of magnetically stored energy by breaking and reconnecting the coronal magnetic field structure. Figure 2.7 shows a schematic representation of a flare model derived from X-ray and radio observations. It must be noted that during a flare there may be more than one reconnection site; indeed, radio imaging observations made with VLA and with NRH demonstrated that electron acceleration during flares occurs at discrete sites, the locations of which vary on time scales of the order of a few seconds. Moreover, during energetic electron events for which HXR/GR (hard X-ray/Gamma-ray) spectra were measured, the variability from one HXR/GR peak to the next was shown to be related to the spatial variability observed in the radio images, establishing the link between the characteristics of the accelerated particles and the magnetic configuration in which the particles are produced (e.g. Trottet *et al.* 1998). Furthermore, magnetic reconnection is not necessarily confined to regions located above the active regions or above the

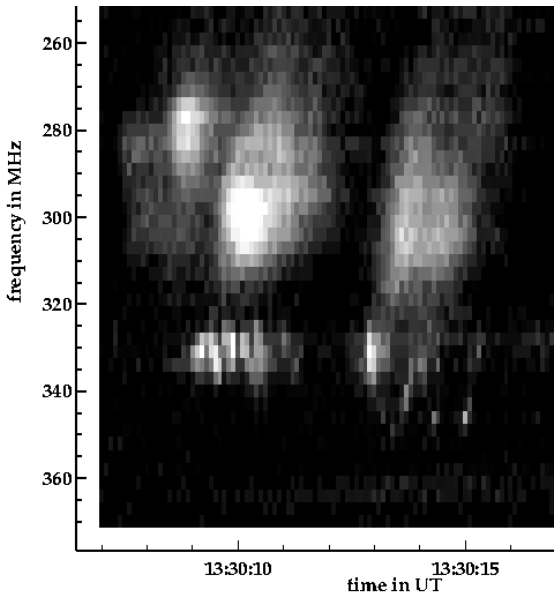


Figure 2.6. Spectrogram of metric spikes (above 320 MHz) and type III bursts (below 320 MHz) observed by the Ikarus, spectrometer near Zurich (Switzerland) (Courtesy A. Benz).

chromospheric bright points. It could involve large scale loop systems as shown by joint soft X-ray and radio studies (Manoharan *et al.* 1996).

3.3 Electron acceleration and transport during flares

Electrons accelerated during flares carry a significant part of the released energy. The most direct evidence for energetic particles comes from hard X-ray, gamma-ray and radio signatures. Radio emission from flares has been recently reviewed by Bastian *et al.* (1998).

- With the high spatial and temporal resolution provided by Nobeyama at 17 GHz, it became possible to study the generation and propagation processes of high energy electrons. Observations and modeling of gyrosynchrotron emission in the centimeter/sub-millimeter wavelength range can provide quantitative measurements on the spectra and on the distribution of energetic electrons ranging from a few hundred keV to a few MeV; it also gives indications on the magnetic field and density in the source regions. The sub-millimetric observations have provided the first evidence of the extension of the gyrosynchrotron spectrum in the frequency domain above 200 GHz (Trottet *et al.* 2002). Spectral and spatial variations and

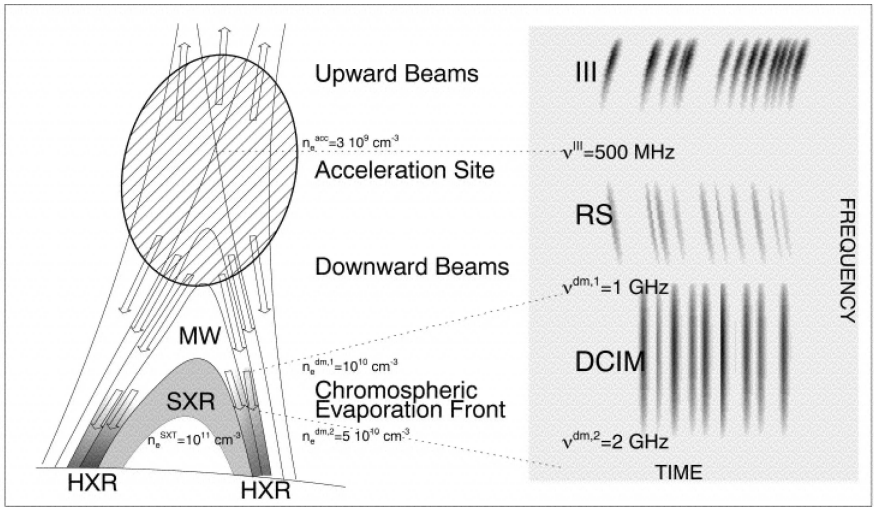


Figure 2.7. Diagram of a flare model envisioning magnetic reconnection and chromospheric evaporation processes. The panel on the right illustrates a dynamic radio spectrum, with radio bursts indicated in a diagram of frequency versus time. The acceleration site is located in the cusp from where electron beams are accelerated in upward (type III) and downward direction (RS). Downward-precipitating electron beams that intercept the chromospheric evaporation front, with a density jump, can be traced as decimetric bursts with almost infinite drift rate in the 1–2 GHz range. The chromospheric upflow fills loops subsequently with wider footpoint separation as the reconnection point rises higher (from Aschwanden & Benz 1997).

the relative timing of temporal features detected at different frequencies are due to the temporal variation of the electron injection spectrum and also to physical conditions controlling the electron transport.

- Peterson & Winckler first investigated the relationship between the HXR and microwave emitting electrons in 1959. After thirty years of debate, the general consensus is that temporal and spectral evolution of X-ray and microwave emissions can be explained by a common source of electrons injected impulsively in trap-and-precipitation regions, i.e. coronal loops. The developed models assume thick target bremsstrahlung for HXR emission and the gyrosynchrotron mechanism for the radio emission.

- With the launch of SMM, GRO and GRANAT missions, measurements of ultra relativistic electrons and gamma ray lines with increasing sensitivity and time resolution became available. In conjunction with radio observations, these measurements provide, simultaneously, unique diagnostics on electrons from 10 keV to above 10 MeV and on ions. Energetic

electrons produce bremsstrahlung continuum emission in the solar atmosphere. Energetic ions, in the energy range 1 MeV/nuc–100 MeV/nuc, interacting with the solar atmosphere produce gamma ray line emission due to nuclear de-excitation, neutron capture and positron annihilation. The simultaneous peaking of emission in the gamma-ray-line domain and HXR emission indicates that the ion acceleration time scales must be less than 1 s.

- High resolution imaging spectroscopy from soft X-rays to gamma rays recently became available with the launch of the RHESSI mission in 2002 (Hurford *et al.* 2002). Figure 2.8 shows observations of a coronal HXR source detected during the initial rise of an intense solar gamma-ray flare; this source has a steep double-power-law spectrum. These observations for the first time provide evidence of coronal acceleration of electrons to tens of keV prior to the impulsive phase of a flare (Lin *et al.* 2003).

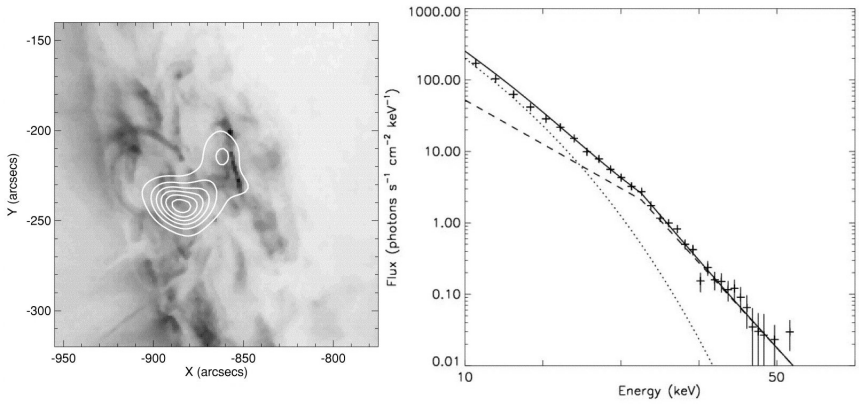


Figure 2.8. RHESSI observations of the initial rise of an intense solar gamma-ray line flare. *Left* 12–30 keV image contour levels superposed on the TRACE 195 Å image. *Right* X-ray spectrum with fit to isothermal (dotted line) and double-power-law (dashed line) spectra and the sum (solid line) (from Lin *et al.* 2003).

4. Coronal Mass Ejections

CMEs discovered during the Skylab mission by Tousey *et al.* (1973) are large scale magnetic structures of plasma expelled from the Sun. They propagate to large distances in the heliosphere, often beyond 1 AU. After three decades of research, we still do not know precisely about them; for instance, what is the initiation mechanism? how do CMEs develop in the low corona? what is their true three-dimensional structure? Typical CMEs seen by coronagraphs

span about 50° in angular extent with a few outstanding events reaching angular extents greater than 100°. CMEs are often associated with eruptive prominences (EP) or disappearing filaments on the solar disk. In that case, the CMEs contain three distinct regions: a bright compression front that surrounds a dark cavity and a bright core inside. The bright core is formed by the material ejected from the cool and dense prominence. CMEs frequently have a much more complex structure than the one just described; they involve multiple magnetic flux systems and neutral lines. CMEs and flares can be produced jointly, but it is now established that there is no causal relationship between these two phenomena. CME speeds can range from a few tens up to 2000 km/s. CMEs associated with EP are accelerated in the corona whereas flare-CME events can propagate with constant speeds that are frequently faster than EP-CMEs. Both kinds of CMEs can reach similar speeds in the upper corona and can be also decelerated later on.

CMEs are associated with on-disk manifestations that have been observed in EUV as large scale dimmings and coronal waves, and in soft X-rays as trans-equatorial loops. Radio observations are sensitive to different aspects of CMEs, depending on the selected observing wavelength domain (see Chapter 11 by Vourlidas).

4.1 Radio signatures of CMEs

Microwave imaging observations are useful for investigating the pre-eruptive and eruptive scenarios of a CME associated with an EP. Figure 2.9 shows the evolution of a prominence, observed with the Nobeyama radioheliograph, that was associated with a CME. An important point is that plots of the speed versus distance are similar for both the leading edge of the CME and the prominence. This suggests that there is no causal relationship and that acceleration has a more global cause, such as loss of MHD stability and restructuring of magnetic field (Srivastava *et al.* 2000). In the metric range, quiescent filaments are observed as a local decrease of brightness due to the low electron density in the cavity surrounding the filament. There is a clear continuity between the radio depression observed in the low corona and the corresponding CME, when observed together. Both of them have identical dynamical behaviors (Marqué *et al.* 2002).

Metric activity is often observed in association with CMEs (e.g. Gopalswamy & Kundu 1994). In the absence of flares, a close spatial and temporal relationship was established between noise storm enhancements and white light transient activity such as CMEs or additional material in the corona at the vicinity of the radio source (Kerdraon *et al.* 1983). Further studies demonstrated that the origin of this nonthermal activity was due to emerging magnetic loops interacting with overlying loops and leading to coronal reconfiguration.

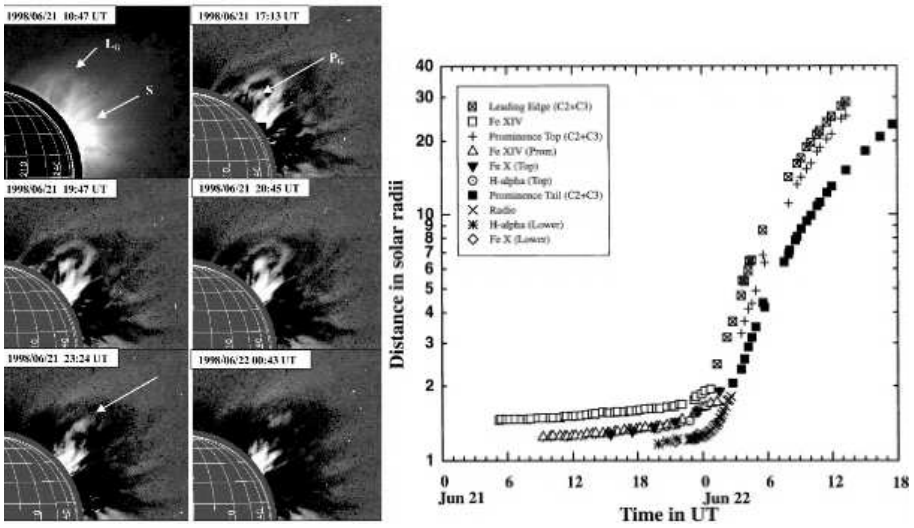


Figure 2.9. Left: Time-lapse images taken by LASCO-C1 coronagraph in Fe XIV emission line. The field of view is 1.1–3 $R_\odot$. All the images shown here have been subtracted from a reference image taken before the occurrence of the CME, except the one at 10:47 UT. The 10:47 UT frame is an on-line image with a nearby continuum and is given in order to show the bright streamer adjacent to the CME. *Right*: Plot of height (on log scale) against time for different features of the CME, viz., the leading edge, the prominence top and the tail, as measured from the images obtained at different wavelengths by various instruments (from Srivastava *et al.* 2000).

In the presence of flares, strong radio bursts are observed over a broad frequency range. Whereas it is well established that flares do not drive CMEs, both of them correspond to different aspects of the same magnetic energy release. In the following, a few radio observations related to flare/CME events are outlined.

4.1.1 Lift-off and angular spread in the corona of flare/CME event.

Many fast flares/CMEs are observed to start with a relatively small angular size and reach their full extent in the low corona (below $2R_\odot$) in a time scale of a few minutes. NRH radio images showed that they initially originate from a rather small coronal region in the vicinity of the flare site and expand by successive magnetic interactions at progressively larger distances from the flare site. Signatures of these interactions are detected by bursts in the dm-m wavelength domain (Maia *et al.* 1999).

The time scale of this progression often corresponds to disturbances with speeds of $\sim$1000 km/s or more. Simultaneous on-the-disk Hα and NRH observations of halo CMEs revealed that the radio sources are associated in space and time with the progression of a Moreton wave. One example is shown in

Figure 2.10. Moreton waves are interpreted as the chromospheric trace of MHD coronal waves. One important output of these studies was to establish that the angular extent of this class of CMEs is linked to the propagation of a coronal wave produced at the time of the flash phase of flares and producing further destabilization and magnetic interactions along its traveling path (Pohjolainen *et al.* 2001).

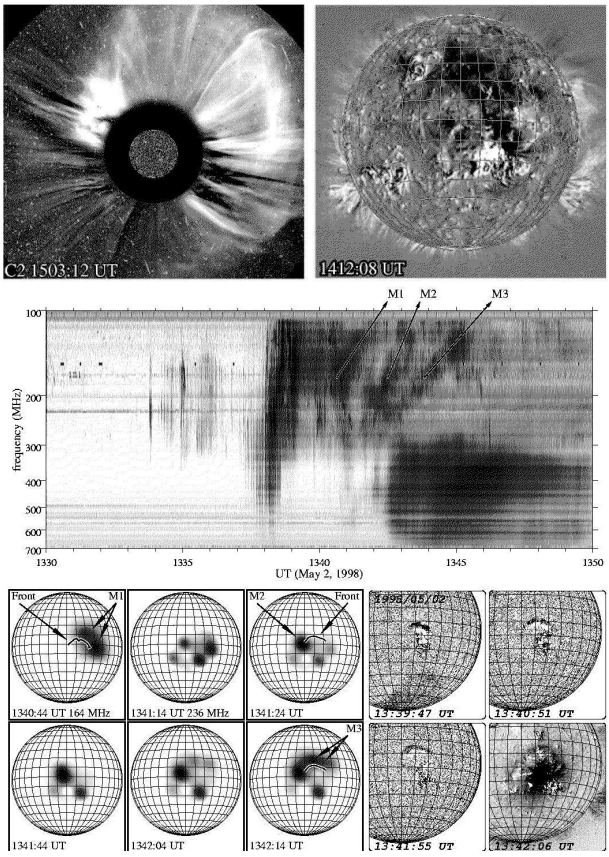


Figure 2.10. Upper panel, left: SOHO LASCO C2 image showing the halo CME on 1998 May 2. *Upper panel right*: SOHO EIT at 195 Å showing the EIT dimming region. *Middle panel*: Artemis IV radio spectra: the spectral drifting type II-like sources are labeled $M1, M2, M3$. *Lower panel, right*: Running differences of respectively Kanzelhöhe Hα images showing the moving wave front (3 frames) and EIT images (1 frame, bottom-right). *Lower panel, left*: Nançay Radioheliograph images at 164 MHz and 236 MHz showing the location of the sources labelled $M1, M2, M3$ (marked by an arrow) at selected times (adapted from Pohjolainen *et al.* 2001).

These interactions lead to the production of secondary coronal shocks detected as radio type II bursts. When a CME erupts, it leaves behind hot, post-eruption arcades or flare loops resulting from reconnection processes. They are often the seat of coronal electron acceleration processes revealed by the presence of nonthermal radio continua (stationary type IV bursts) lasting for several hours and of gradual hard X-ray emissions.

4.1.2 Relationship with EUV dimming and coronal waves. Reconnection processes lead to the opening of the magnetic field, thus allowing other magnetic structures to be evacuated from the corona and to merge and give white light transients. Dimmings seen in EUV were indeed found to be essentially restricted to the region traced by the transit of the Moreton waves. In this sense, the shock is simply a means of promoting reconnection far from the original instability. These conclusions however cannot be generalized. Indeed, for other events, the triggering was initiated by reconnection at a magnetic coronal null point, followed by secondary reconnections in a large coronal volume. These results call for understanding the relationships among EUV coronal waves discovered by Thompson *et al.* (1999), Moreton waves and CMEs. Most of the EUV waves observed by the EIT telescope on SOHO consist of diffuse brightenings having no clear relationship with flares or with type II bursts. The exact nature of these waves is not yet fully understood. It was suggested that they may be attributed to the compression of the plasma in the region surrounding the sudden magnetic field opening (Delanée 2000). The compressive nature of these waves was recently confirmed by the Nobeyama Radioheliograph which detected the thermal emission of these waves due to density enhancements (White *et al.* 2002).

A small number of EUV waves that have sharp bright fronts, like the event shown in Figure 2.11, could be however the coronal counterpart of Moreton waves (Biesecker *et al.* 2002). This was confirmed for two events only, as joint high cadence EUV, Hα and radioheliograph observations are rarely carried out.

4.1.3 Direct radio CME imaging. For events associated with flaring regions located behind the limb, radio imaging data have revealed synchrotron radio emission from CMEs. These radio CMEs are seen in the frequency range of the NRH as an expanding ensemble of loops, filled by energetic radiating electrons, which closely resembles the white light CMEs (see Figure 2.12) (Bastian *et al.* 2001). Detection of radio emission from CME loops offers a number of important diagnostics of CMEs during their early phase, such as constraints on the thermal plasma density.

In conclusion, these results obtained from data analysis of a few individual events illustrate the wide variety of areas where radio observations can bring important and unique contributions to the general understanding of these phe-

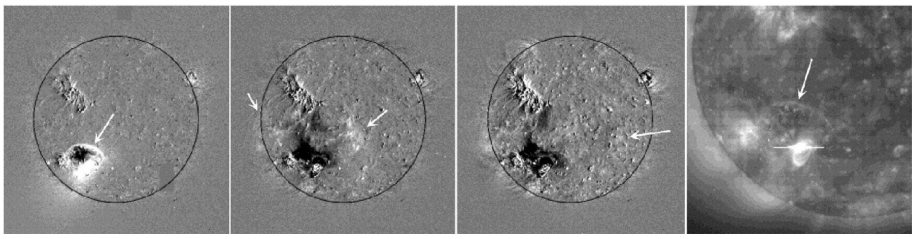


Figure 2.11. Example of an EIT wave from 1997 September 24. The first three panels show successive EIT images at 02:49, 03:03, and 03:23 UT with a pre-event image digitally subtracted from them. Arrows indicate the EIT-wave front(s). The last panel shows a subfield of the first panel (undifferenced), showing an example of a sharp brightening (from Biesecker *et al.* 2002).

nomena. The absence of joint spectral and imaging observations simultaneously covering the microwave, decimetric and metric wavelength domains drastically limit such investigations. Another problem is the matching of theory and modeling efforts with observations: at present, the best approach seems to combine multi-wavelength observations with information on the structure of the magnetic field. This can only be done by using magnetic field extrapolations in order to infer the pre-eruptive topology. This approach provides important information such as the location of the null points, the current sheets, the separatrix layers and the bald patches.

5. Coronal and Interplanetary Shocks, Association with Flares and CMES

Two types of shocks have been considered to produce the type II bursts: the coronal shocks which generate metric type II bursts (see §4, radio signatures of CMEs and Figure 2.10) and the CME-driven shocks which produce hectometric-kilometric type II bursts during their propagation in the interplanetary medium (Cane *et al.* 1987). Coronal shocks are currently interpreted as blast waves; they can however be driven by fast short-lived X-ray ejecta issued from the flare region (Gopalswamy *et al.* 1999) or rapidly expanding structures (Klassen *et al.* 1999). As coronal and interplanetary (IP) type II bursts can be produced during the same event, there has been nevertheless a long-lasting controversy on the relationships among type II bursts, flares and CMEs. Most of the studies were based on the temporal relationship between these events, which required an assumption on the model of density to derive the shock speed parameters. The few studies based on comparison between radioheliograph and coronagraph data showed that when flares and CMEs occur jointly, the positions or the speeds of the metric type II sources are most often not consistent with the

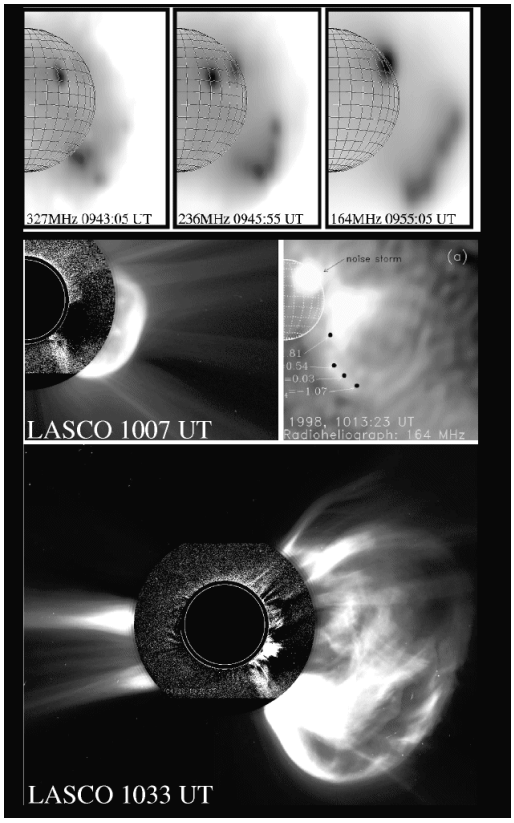


Figure 2.12. 1998 April 20 event. *Upper panel*: Progression of the type II like emission seen at three frequencies (from Maia *et al.* 2000). *Middle and bottom panels*: Composite C1 and C2 LASCO SOHO images showing the images of the CME; Snapshot map of the radio CME at 164 MHz at 10:13 UT; the brightness of the radio image is saturated in the low corona; The emission is gyrosynchrotron. Numbers on the same figure correspond to spectral index measured at four locations and not discussed here (from Bastian *et al.* 2001).

CME bow shock picture. This is consistent with earlier findings (Wagner & Mac Queen 1983) and supports the idea that coronal and IP type II bursts have independent origins. Although the two-shock scenario seems to be the favored view, there are studies supporting a different scenario. The radio receivers on the WIND spacecraft provided, for the first time, observations in the decametric-hectometric wavelength range (D-H) that contributed significantly to resolve the controversy (see Gopalswamy, Chapter 15). First, it was shown that metric type II bursts, which are much more frequent than interplanetary type II bursts, do not generally extend up to hectometric wavelengths (Gopalswamy *et al.* 1998). Second, when CMEs, flares and type II bursts are produced together, the

observed metric and D-H type II frequency have distinct drift rates: a positive correlation was found between the shock speed parameters derived from the D-H radio emissions and the corresponding CME plane-of-the-sky speeds. No similar correlation was found for the metric type II bursts (Reiner *et al.* 2001).

However, recent radio imaging observations showed that some CME-driven shocks can take place at a rather low altitude in the corona. Weak radio type II-like bursts, most often not detected on radio spectrograph data, were observed by the NRH, in close temporal and spatial association with the leading edge of CMEs (Maia *et al.* 2000). One example is displayed in Figure 2.12 (upper panel) which shows the progression of a weak radio source at different frequencies. The corresponding spectrum shows evidence for both fundamental and harmonic emission. This elongated source has a close space and time association with the leading edge of the CME, which propagates with a speed of 1400 km/s. In that case, the CME-driven shock was probably formed at an altitude of the order of 0.7 $R_{\odot}$. One notes that the detection of such events is very rare, due to the simultaneous presence of strong metric emitting sources; this detection is mostly limited to the cases of partly occulted events associated with eruptive regions located behind the solar limb.

In conclusion, these results can suggest the following scenario: in the vicinity of the place where they are launched, fast CMEs are completely wrapped up by a shock wave; in front of the CME nose, energy will be given by the plasma cloud located below which acts as a piston. In the flanks of the CME, the shock will become essentially blast-wave-like and its velocity will decrease with distance. This scenario fits particularly well with white light observations, which revealed shock waves propagating away from high speed CMEs (Sheeley *et al.* 2000; Vourlidas *et al.* 2003).

6. Interplanetary Coronal Mass Ejections

Observations from Ulysses and SOHO missions have provided new insights on dynamical processes in the heliosphere and on their association with solar activity. CMEs were tracked through the corona out to 32 $R_{\odot}$ by the SOHO coronagraphs. Interplanetary CME (ICME) is the term used to describe the CME-like disturbances in the solar wind which, most often, when sampled by *in-situ* observations, include an IP shock preceding a turbulent plasma sheath and an ejecta. The term magnetic cloud refers to ICMEs for which ejecta are characterized by a smooth and continuous rotation of the magnetic field (flux rope) (Burlaga 1981). The propagation and evolution of ICMEs depend strongly on the ambient solar wind and on its structure. Interplanetary disturbances are distorted by the slow and fast solar winds.

Complex solar wind flows were suspected to be caused by multiple interactions between multiple CMEs. (Burlaga *et al.* 1987). Interaction between a

fast and a slow CME have been, indeed, recently identified by long-wavelength radio and white light observations: the radio signature is an intense continuum occurring at the low-frequency end of the D-H type II burst (Figure 2.13). Gopalswamy *et al.* (2001) interpreted this radio enhancement as a consequence of shock strengthening when the shock, located in front of the fast CME, meets the core of the slow CME (see Gopalswamy, Chapter 15).

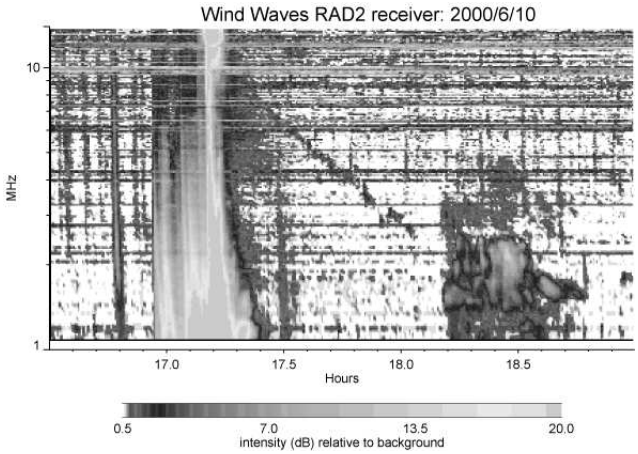


Figure 2.13. Example of a hectometric interplanetary type II burst observed by the Wind/WAVES spectrograph in the 1–14 MHz range. The thin dashed feature is a type II burst. A bright emission is detected between 18.12 and 18.48 UT (from Gopalswamy *et al.* 2001).

ICMEs propagate on long distances before being detected by spacecraft instruments and it is often difficult to relate the *in-situ* observations to the CMEs observed at the sun. Their transit time from the sun to the earth range between 2 and 5 days. Earth directed CMEs, called front-side halos, can reach the earth and generate severe geoeffects. To establish the solar origin of interplanetary disturbances, on-disk observations are of crucial importance. Signatures of CMEs are provided by imaging observations made in EUV and X-rays, in Hα, and in radio.

Radio techniques are the only means that allow the sampling of a large range of altitudes and to track precisely the propagation of these disturbances. In the interplanetary medium, the location of the type II emissions associated with ICMEs can be obtained by triangulation. Another method consists in the measurement of the interplanetary scintillation. See Jackson & Hick (Chapter 17).

Interplanetary scintillation (IPS) arises when the radiation from a distant compact radio source is scattered by electron density irregularities in the so-

lar wind, producing a random diffraction pattern on the ground. An increase in scintillation is observed when the line of sight passes through an ICME. By observing a large number of radio sources, distributed around the Sun, IP disturbances can be detected. Furthermore, if the scintillation is observed by multiple stations, an estimation of the solar wind speed can be obtained. One of the major advantages of IPS techniques is that ICMEs are tracked continuously in the IP. Tokumaru *et al.* (2000), showed that the propagation speed depends on both the latitude and longitude.

7. Solar Energetic Particle Events

Solar Energetic Particle events in the interplanetary medium (SEP) detected from GeV down to keV energies, are usually divided into two groups, currently referred to as "impulsive" and "gradual" events.

Evidence for these two classes, with two characteristic time scales, was mainly based on charge states and composition measurements of SEP events at low energies, typically below 25 MeV (see e.g. Cliver 2000). Impulsive SEP events (accompanied by short SXR bursts, < 1 h) are electron-rich and ^{3}He-rich and show high ionic charge states while gradual SEP events (accompanied by long duration, SXR bursts, >1 h) are proton-rich and show normal coronal abundance and charge states corresponding to quiet coronal temperatures. Both classes were originally attributed to flare processes. This picture mainly originated in the classification of radio emissions introduced by Wild *et al.* (1963), who related the time scale of flare emissions to the particles observed in the interplanetary medium. Due to this classification, it has long been believed that well developed flares show two successive phases: an "impulsive" phase with typical duration of a few minutes characterized by impulsive hard X ray and microwave bursts and by dm-dam activity, including type III bursts; a subsequent "gradual" phase, occurring only in large flares and initiated directly by the first phase, with typical duration of tens of minutes and characterized by gradual hard X-ray bursts and radio-continua (type IV); then, metric activity (continua then noise storms) lasting for many hours is also frequently observed. In this model (see Figure 2.14), the shock wave (type II) produced during the impulsive phase, creates conditions suitable for the acceleration of particles to very high energies which will be partly trapped in coronal loops or will escape into the interplanetary medium.

However, electromagnetic signatures of interacting electrons observed during long duration events, in a wide spectral range from HXR to dam wavelengths, contradicted this model (Pick 1986; Trottet 1986): the energy release and the electron acceleration processes are continuous through all these phases. Gamma ray observations of a few events have also revealed that relativistic ions

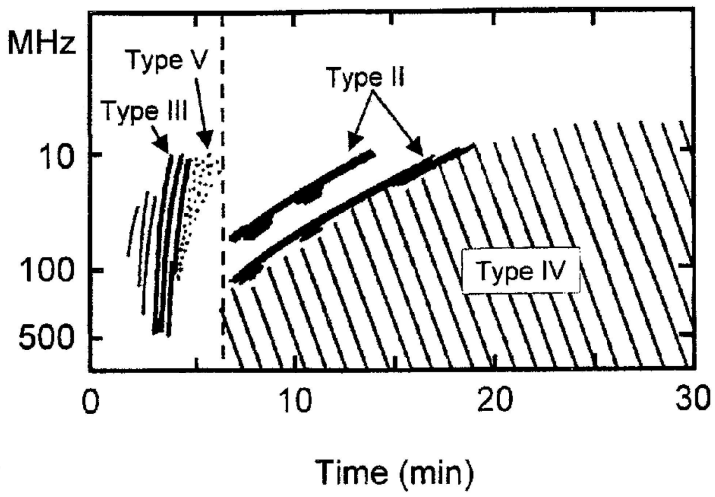


Figure 2.14. Idealized sketch of a complete radio event (from Wild *et al.* 1963).

may be accelerated over several hours at the Sun (e.g. Kanbach *et al.* 1993). The present understanding is rather that acceleration processes are associated with large-scale eruptive phenomena that include flares, filament eruptions, CMEs and interplanetary shocks, which often occur simultaneously. This coincidence emphasizes the difficulty of understanding the link between solar processes and SEP events measured in the interplanetary medium. Radio observations, though restricted to investigations on the origin of accelerated electrons, can however bring important contributions to this problem: they can detect shocks in the corona and the interplanetary medium; they can also identify the regions where the magnetic field interacts during flares or CME development and propagation.

In the new, current, two-class paradigm that has been proposed by Reames (1999), the flare process accounts for acceleration in "impulsive" events, while prolonged acceleration by CME driven shocks dominates "gradual" events. There is however some evidence that some "hybrid" SEP events may contain both particles from flares and from CME-shock origin. The current debate focusses on the possible role played by flares in the gradual SEP events, either by direct particle injections or as a source of seed particles for the shocks. Furthermore, an alternative or additional possibility, which did not attract much attention up to now, is that particle acceleration could be due to magnetic reconnection of coronal structures triggered for example by coronal or CME driven shocks during the CME development (see §4). This point of view is supported by recent findings:

- Maia *et al.* (2001) showed that, in addition to the CME bow shocks, coronal sites of electron acceleration contribute significantly to populating the interplanetary medium with energetic electrons over several hours; this may even be the case, although controversial, for relativistic protons as suggested by Klein *et al.* (2001). Similar ideas were proposed by Cane *et al.* (2002), who showed that, for major proton events, the energetic electrons are associated with type III bursts groups detected at low frequencies in the higher corona. They concluded that these electrons are unlikely to be shock accelerated and probably originate in the reconnection regions below fast CMEs.

- Impulsive relativistic electrons escaping in the interplanetary medium are often related to impulsive flares and type III bursts, but there is a second class of events, that are released after the impulsive phase of the flare; these are possibly related to coronal shocks (Krucker *et al.* 1999) or to CME-driven shocks (Haggerty & Roelof 2002). For most of these delayed electron events, Pick *et al.* (2003) found nonthermal radio signatures in the corona at the estimated time of the electron release. These signatures correspond to the passage of a coronal wave or CME bow shock through local magnetic structures. The height in the corona at which such acceleration takes place varies considerably from one event to another one. The late electron release is explained because the acceleration region in the corona is complex and has a connection to different points in the interplanetary medium, while the electrons are detected by the spacecraft in only one of these points. Similarly it was found that many SEP events occur at times of CME interaction (Gopalswamy *et al.* 2002).

8. Concluding Remarks and the Future of Radio Physics

In the preceding sections, I have attempted to show how solar radio studies have contributed to transform our knowledge of the physics of the corona and of the interplanetary medium, and have been instrumental in the field of solar-terrestrial research. Major spectacular advances can be expected in the future from multi-wavelength observations covering a large spectral range if, however, some specific extensions in radio instrumentation are achieved. The present situation is, indeed, not fully satisfactory: too many results have been obtained using only partial spectral or spatial data; this may lead to uncertain or even to erroneous interpretations. The most obvious current need is for complete radio imaging observations of the Sun covering simultaneously a broad radio spectrum. The few imaging instruments that are presently available have only a restricted frequency bandwidth and, given their geographical location, no simultaneous observations can be obtained. Multifrequency imaging observa-

tions must also be complemented by radio spectral data, which contribute to the complete specification of the radio bursts; although during the last two decades many sophisticated and fruitful radio spectrographs were constructed at different locations, no adequate spectral coverage (compulsory for many studies) is yet achieved, even when gathering all the available data.

The Frequency Agile Solar Radiotelescope (FASR) will provide, for the first time, comprehensive coverage of radio imaging and spectral observations in the frequency range from 100 MHz to 24 GHz. This instrument will allow us to explore in a new way radio emissions from the bottom of the corona up to a few solar radii. It will open a new window, not yet explored by imaging instruments, in the frequency range 1 GHz–500 MHz, where coherent plasma emission plays a dominant role and is rich in diagnostics as briefly recalled in the preceding sections. It is probable that observations obtained with FASR correlated on the one hand, with optical, XUV, and X-ray observations of the corona and on the other hand, with in-situ measurements of the interplanetary medium, will make a significant contribution to our understanding of fundamental problems such as coronal heating, energy dissipation, the link between activity on the Sun's surface and the resulting evolution of the corona, the origin of electron acceleration and transport in the corona, and the shock formation. Study of the interactions between loop systems and of their evolution will be an important means of understanding processes leading to CMEs and flares. Regular monitoring of filaments, active regions, and coronal holes at different wavelengths will provide key parameters for synoptic studies. FASR will be an important complementary tool for the future space missions. For example, Ulysses has identified relatively small structures of the solar wind plasma anchored at the Sun that maintain their identity beyond 4 AU. These structures channel the propagation of solar electron beams, which produce Langmuir waves and type III bursts (Buttighoffer 1998). Such a result demonstrates the close link between the corona and the inner heliosphere at large distances from the Sun.

Optimizing the science return of FASR will require a cooperative effort from a large community around the world and access to the fully processed data similar to what is available from space-borne instruments. Furthermore, as mentioned above, the construction on a site near FASR of a radio spectrograph covering the entire radio spectrum will be necessary not only to complement FASR but also for space-borne radio spectrographs observing at longer wavelengths. The achievement of FASR and of an accompanying new radio spectrograph will represent a major step forward in the organization of international cooperation on solar-terrestrial physics. Further instrumentation dedicated to this research field would be to implement subsystems of FASR at other geographical locations and of similar radio spectrographs. Finally, it is important to underscore once again the complementarity of radio techniques: radio heliography, radio

scintillation and radar instruments. I will close this introductory chapter by a french saying “l’union fait la force”.

Acknowledgments I thank F. Drago-Chiuderi and A. Kerdraon for a critical reading of the manuscript.

References

Aschwanden, M. J., Hudson, H. S., Kosugi, T., & Schwartz, R. A. 1996, ApJ, 464, 985

Aschwanden, M. J., & Benz A. O. 1997, ApJ, 480, 825

Alissandrakis C. E., Borgioli F., Chiuderi Drago, F., Hagyard, M., & Shibasaki, K. 1996, Solar Phys, 167, 167

Bak, P., Tang, C., & Wiesenfeld, K. 1987, Phys. Rev. Lett, 59, 381

Bastian, T. S., Pick, M., Kerdraon, D., Maia, D. & Vourlidas, A. 2001, ApJ, 20, L65

Bastian, T. S., Benz, A. O., & Gary, D. E. 1998, ARAA, 36, 131

Benz, A. O. 1985, Solar Phys., 96, 357

Benz, A. O., Csillaghy, A., & Aschwanden, M. J. 1996, A&A, 309, 291

Biesecker, D. A., Myers, D. C., Thomson, B. J., Hammer, D. M., & Vourlidas, A. 2002, ApJ, 569, 1009

Bougeret, J. L., Hoang, S., & Steinberg J. L. 1986, The Sun and heliosphere in Three dimensions, R. G. Marsden (ed.), 213

Brosius, J. W., Landi, E., Cook, J. W., Newmark, J. S., Gopalswamy, N., & Lara, A.. 2002, ApJ, 574, 453

Burlaga, L. F., Sittler, E., Mariani, F., & Schwenn, R. 1981, EOS Transactions, 82, 39, 433

Burlaga, L. F., Sittler, E., Mariani, F, & Schwenn, R. 1987, JGR, 86, 6673

Buttighoffer, A., 1998, A&A, 335, 295

Bruggman, G., Vilmer, N., Klein, K. L., & Kane, S. R. 1994, Solar Phys, 149, 1, 171

Cane, H. V., Sheeley Jr., N. R., & Howard, R. A. 1987, JGR, 92, 9869

Cane, H. V., Erickson, W. C., & Prestage, N. P. 2002, JGR, 107, A10, 14

Chiuderi-Drago F., Alissandrakis, C. E., Bentley, R. D., & Philips, A. T. 1998, Solar Phys, 182, 459

Cliver, E. W. 2000, ACE-2000 Symposium, AIP Conference Proceedings, Eds. R. A. Mewaldt et al. 528, 21

Crosby, N. B., Aschwanden, M. J., & Dennis, B. R. 1993, Solar Phys, 143, 275

Delanée, C. 2000, ApJ, 545, 512

Drago, F. Chiuderi, Alissandrakis, C., & Hagyard, M. 1987, Solar Phys, 112, 89

Gary, D. E., & Hurford, G., J. 1994, ApJ, 420, 903

Gopalswamy, N., Kundu, M. R., & St Cyr, O.C. 1994, A&A, 424, 2, L135
Gopalswamy, N., & 9 coauthors 1998, JGR, 10, 307
Gopalswamy, N., Nitta, N., Manoharan P. K., Raoult A., & Pick, M. 1999, A&A, 347, 684
Gopalswamy, N., Yashiro, S., Kaiser, M. L., Howard, R. A., & Bougeret, J. L. 2001, ApJ, 548, L91
Gopalswamy, N., & 7 coauthors 2002, ApJ, 572, 103
Grebinskij, A., Bogod, V., Gelfreikh, G., Urpo, S., Pohjolainen, S., & Shibasaki, K. 2000, A&ASuppl. Ser., 144, 169
Haggerty, D. K. & Roelof, E. C. 2002, ApJ, 579, 841
Hurford, G. J., & 13 coauthors 2002, Solar Phys, 210, 61
Kakinuma, T., & Swarup, G. 1962, ApJ, 39, 5
Kanbach, G. & 9 coauthors 1983, A&A, 97, 349
Kane, S., & 6 coauthors 2003, Adv. Space Res., 32, 12, 2503
Kerdraon, A., Pick, M., & Trottet, G. 1983, A&A, 265, L19
Klassen, A., Aurass, H., Klein, K-L, Hofmann, A, & Mann, G. 1999, A&A, 343, 287
Klein, K. L., Trottet, G., Lantos, P., & Delaboudiniere, J. P. 2001 A&A, 373, 1073
Krucker, S., Benz, A. O., Bastian, T. S., & Acton, L. W. 1997, ApJ, 488, 499
Krucker, S., Larson, D. E., Lin, R. P., & Thomson, B. J. 1999, ApJ, 519, 864
Kundu, M. R. 1965, *Solar Radio Astronomy*, Interscience Publishers (Wiley and sons).
Kundu, M. R., Raulin, J. P., Pick, M., & Strong, K. T. 1995, ApJ, 444, 2, 922
Lee, J., & Gary, D. E. 2000, ApJ, 543, 457
Levine, R. H. 1974, ApJ, 190, 457
Lin, R. P., & 12 coauthors 2003, ApJ, 595, L69
Lu, T. L., & Hamilton, R. J. 1991, ApJ, 380, L89
Maia, D., Vourlidas, A., Pick, M., Howard, R., Schwenn, R., & Magalhaes, A. 1999, JGR, 104, 12, 57
Maia, D., Pick, M.,Vourlidas, A.,and Howard, R. 2000, ApJ, 528, L49
Maia, D., Pick, M., Hawkins III , S. E., Formichev, V. V., & Jiricka, K. 2001, Solar Phys, 204, 199
Manoharan, P. K., van Driel-Gesztelyi, Pick, M., amd Demoulin, P. 1996, ApJ, 468, L73
Marqué C., Lantos, P., & Delaboudiniere, J. P. 2002, A&A, 387, 317
Masuda, S., Kosugi, T., Hara, H., Tsuneta, S., Ogawara, Y. 1994, Nature, 371, 6497, 495
Peterson, L. E., & Winckler, J. 1959, JGR, 64, 697
Pick, M. 1986, Solar Phys, 104, 19
Pick, M., Maia, D., Wang, S. J., Lecacheux, A., & Hawkins III, S. E. 2003, Adv. Space Res., 32, 12, 2527

Piddington, J. H. & Minett, N. C. 1951, Australian J. Sci. Res., 4, 131
Pohjolainen, S. D., & 9 coauthors. 2001, ApJ, 556, 421
Raoult, A., Pick, M., Dennis, B. R., & Kane, S. R. 1985, ApJ, 299, 1027
Reames, D. V. 1999, Space Science Rev., 90, 413
Reiner, M. J. & 6 coauthors 2001, JGR, 106, 25279
Ryabov, B. I., Pilyeva, C. E., Alissandrakis, C. E., Shibasaki, K., Bogod, V. M., Gariamov, V. I., & Gelfreikh, G. 1999, Solar Phys, 185, 157
Sheeley, N. R., Hakala, W. N., & Wang, Y. M. 2000, JGR, 105, A3, 5081
Shibata, K., & 7 coauthors 1995, ApJ, 451, L83
Srivastava, N., Schwenn, R., Inhester, B., Martin, S. F., & Hanaoka, Y. 2000, ApJ, 534, 468
Thompson, B. J., & 9 coauthors 1999, A&A, 517, L151
Tokumaru, M., Kojima, M., Fujiki, K., & Yokobe, A. 2000, JGR, 105, 10435
Tousey, R. & 8 coauthors 1973, Solar Phys, 33, 265
Trottet, G. 1986, Solar Phys, 104, 145
Trottet, G., Vilmer, N., Barat, C. *et al.* 1998, A&A, 334, 1099
Trottet, G., Raulin, J. P., Kaufmann, P., Siarkowski, M., Klein, K. L., & Gary, D. E 2002, A&A, 381, 694
Vourlidas, A., Wu, S. T., Wang, A. H., Subramanian, P., & Howard, R. A. 2003, ApJ, 598, 1392
Wagner, W. J., & Mac Queen, R. M. 1983, A&A, 120, 136
White, S. M., 2002, Workshop on Solar Radio Physics with FASR, Green Bank, USA, May 2002
Wild, J. P., Smerd, S.F., & Weiss, A. A. 1963, ARAA, 1, 291
Zheleznyakov, V. V. 1962, Soviet Astron., 6, 3

Chapter 3

THE FREQUENCY AGILE SOLAR RADIOTELESCOPE

T. S. Bastian
National Radio Astronomy Observatory[*]*, Charlottesville, VA 22903, USA*
tbastian@nrao.edu

Abstract The Frequency Agile Solar Radiotelescope (FASR) will be a ground based solar-dedicated radio telescope designed and optimized to produce high resolution, high-fidelity, and high-dynamic-range images over a broad range of radio frequencies ($\sim$ 0.05–24 GHz). That is, FASR will perform broadband imaging spectroscopy, producing unique data and enabling a wide variety of radio-diagnostic tools to be exploited to study the Sun from the mid-chromosphere to coronal heights. FASR will address an extremely broad science program, including the nature and evolution of coronal magnetic fields, the physics of flares, drivers of space weather, the quiet Sun, and synoptic studies. FASR may also play an important role in forecasting solar activity and space weather. An important goal is to mainstream solar radio observations by providing a number of standard data products for use by the wider solar physics and space weather communities.

1. Introduction and Background

Radio observations have played an important role in solar physics for many decades. Beginning in the late 1940s, radio observations were first used to directly measure the kinetic temperature of the solar corona (Pawsey 1946), which is optically thick at meter wavelengths. Early radio interferometric techniques were first devised and applied to studies of compact, nonthermal radiation associated with sunspot groups (McCready, Pawsey & Payne-Scott 1947). These techniques were further refined, forming the underpinnings of modern Fourier synthesis imaging techniques (§4). In the intervening years, solar observations at radio wavelengths has proceeded along two lines:

[*]The National Radio Astronomy Observatory is a facility of the National Science Foundation operated under cooperative agreement by Associated Universities, Inc.

Spectroscopic observations of the Sun have been pursued primarily at decimeter, meter, and decameter wavelengths. These have been used to discover a rich taxonomy of radio burst activity that has been used to probe a wide variety of physical processes in the solar corona, including energy release, electron beams, shocks, and coronal magnetic fields. More recently, spectroscopic observations at centimeter wavelengths have matured, yielding insights on electron acceleration and transport in flares and the structure of active regions (e.g., Gary & Hurford 1994; Lee, Chapter 9). With the advent of space-borne instrumentation, spectroscopic observations were extended to hectometer and kilometer wavelengths, wavelengths that are inaccessible to study from the ground owing to the ionospheric frequency cutoff near 10 MHz. Space-based observations have allowed interplanetary electron beams and shocks to be studied as they propagate from the outer solar corona to 1 AU and beyond.

Imaging observations of the Sun and solar phenomena at discrete radio frequencies have been performed for decades from the ground, but are not yet available from space. The prevailing imaging technique is Fourier synthesis imaging (§4) although other techniques have been used in past years (e.g., "J_0 synthesis" was employed by the Culgoora Radioheliograph, as described in McLean & Labrum 1985). The Sun is routinely imaged with arcsecond resolution using Fourier synthesis imaging techniques at centimeter wavelengths with instruments like the Very Large Array (VLA; Thompson *et al.* 1983) or the Nobeyama Radioheliograph (NoRH; Nakajima *et al.* 1992), or with arcminute resolution at decimeter and meter wavelengths by the Nançay Radioheliograph (NRH; Delouise & Kerdraon 1997).

However, in order to exploit the information embodied in radio emission from the Sun requires fully wedding spectroscopic and imaging capabilities in a single instrument. Moreover, these capabilities must be available on time scales commensurate with those relevant to physical processes on the Sun. This is the motivating factor behind the Frequency Agile Solar Radiotelescope: an instrument that performs broadband imaging spectroscopy.

The Frequency Agile Solar Radiotelescope (FASR) had its genesis in an international workshop organized in 1995 at San Juan Capistrano in California. There, the solar physics and solar radiophysics communities first outlined the science requirements for the instrument. Since then, the instrument has gained support throughout the solar and space weather communities, culminating in the recent recommendations of decadal reviews by the Astronomy and Astrophysics Survey Committee (2001) and the Solar and Space Physics Survey Committee (2003), both sanctioned by the National Research Council. The latter survey ranked FASR as the number one small project ($< \$250$M). On this basis, plans are underway to design and build the instrument.

This chapter serves as an introduction to FASR. In the next section, some preliminary concepts relevant to radio observations are outlined. Key drivers of the FASR science program are summarized in §3. More detailed discussions of radio diagnostic techniques and radio science that will be addressed with FASR are presented elsewhere in this volume. A summary of FASR's operational basis is given in §4. The instrumental requirements and a strawman design are summarized in §5. Some operational issues are discussed in §6 and concluding remarks are presented in §7.

2. Preliminaries

In order to understand the rationale for wedding imaging with spectroscopy in a single instrument, it is useful to revisit briefly elementary concepts of radiative transfer at radio wavelengths and to review relevant radio emission mechanisms.

2.1 Radiative transfer

At radio frequencies $h\nu \ll k_B T$ (in the Rayleigh-Jeans regime), where h is Planck's constant, ν is the (cyclic) radio frequency, k_B is Boltzmann's constant, and T_e is the effective temperature of the emitting material. In this regime, the specific intensity $\mathcal{I}_\nu$ and the source function $\mathcal{S}_\nu$ can be expressed in terms of the brightness temperature T_b and the effective temperature T_e through $\mathcal{I}_\nu = k_B T_b \nu^2/c^2$ and $\mathcal{S}_\nu = (\eta_\nu/\kappa_\nu) k_B T_e \nu^2/c^2$, respectively. The quantities η_ν and κ_ν are the radio emissivity and absorption coefficient, respectively; these embody the microphysics of radio emission and absorption for any given mechanism.

The radiative transfer equation for continuum radio emission is conveniently expressed along a given line of sight as

$$T_b = \int_0^{\tau_\nu} T_e(\tau'_\nu) e^{-\tau'_\nu} d\tau'_\nu + T_{b\circ} e^{-\tau_\nu} \tag{3.1}$$

where $\tau_\nu = \int \kappa_\nu dl$ is the optical depth. In the simple case of an isolated source where T_e is constant, Eq. 3.1 becomes $T_b = T_e(1 - e^{-\tau_\nu})$. When $\tau_\nu \gg 1$ the source is optically thick and $T_b = T_e$. When $\tau_\nu \ll 1$ the source is optically thin and $T_b \approx \tau_\nu T_e$.

For spatially unresolved radio observations the flux density, S_ν, is expressed in units of Jansky. In the case of solar observations, a more convenient unit is the *solar flux unit*, with 1 sfu = 10^4 Jy = 10^{-22} W m^{-2} Hz^{-1}. The total flux density S_ν of a radio source is related to T_b through

$$\mathrm{S}_\nu = \frac{2 k_B \nu^2}{c^2} \int T_b d\Omega \tag{3.2}$$

where $d\Omega$ is the differential solid angle. In the case of an imaging instrument, observations are limited in angular resolution to a solid angle Ω_{bm}, referred to as the "beam" in radio astronomy, the value of which is intrinsic to the instrument. The measured quantity is then the flux density per beam: $\langle \mathrm{S}_\nu \rangle_{bm} = 2k_B \langle T_b \rangle \nu^2 \Omega_{bm}/c^2$ where $\langle T_b \rangle_{bm}$ is the mean source brightness over Ω_{bm}. The total flux density per beam is therefore an estimate of the specific intensity.

Spectroscopy is, of course, a powerful tool in all wavelength regimes. In the case of solar radio emission, bound-bound and bound-free atomic and molecular transitions play no role. Instead, free-free, wave-particle, and wave-wave interactions are responsible for the emission and absorption of radio waves. Even so, spectroscopy is a critical tool for identifying emission mechanisms and for diagnosing physical conditions in the source. In most cases, broadband, low-dispersion radio spectroscopy is the desired tool.

For an unresolved source the total, or integrated, spectrum can be measured as S_ν. As noted in §1, such measurements have been employed for many years using swept-frequency spectrometers or, more recently, broadband digital spectrometers. Typically, time-resolved spectra are used to construct a *dynamic spectrum* over some frequency range. Dynamic spectroscopy has been employed to characterize and study a variety of radio bursts from decimeter to decameter wavelengths on the ground (e.g., the classical radio bursts of types I–V) and from decameter to kilometer wavelengths in space (e.g., interplanetary radio bursts of type II and type III). Broadband dynamic spectroscopy has also been employed to study microwave bursts: e.g., the Owens Valley Solar Array.

While high resolution images of the Sun have also been available for many years from instruments like the VLA and the NoRH, these instruments can only produce images at a small number of widely spaced frequencies, which is insufficient for spectroscopy. What is needed is the ability to combine imaging with broadband spectroscopy in order to acquire time-resolved *brightness temperature spectra* everywhere in the source. The most effective way to satisfy this need is to design and build a solar-dedicated instrument which performs broadband imaging spectroscopy. This is the fundamental innovation of FASR.

2.2 Radio emission mechanisms

Radio emission mechanisms are discussed elsewhere in this volume by Gary & Hurford (Chapter 4) and will therefore be only touched on here. The radio spectrum from centimeter to meter wavelengths is rich in diagnostic possibilities because (1) a variety of coherent and incoherent emission processes occur; (2) both the optically thin and optically thick portions of emission spectra are accessible to study. Hence, tremendous observational leverage is available to measure or otherwise constrain the plasma temperature and density, the magnetic

field, the electron distribution function, and importantly, the spatio-temporal evolution of these observational parameters.

There are two classes of incoherent emission mechanism that are important on the Sun: bremsstrahlung (or free-free) radiation and gyromagnetic (or magneto-bremsstrahlung) radiation.

- *Thermal free-free emission*, due to collisions between thermal electrons and ions, is ubiquitous on the Sun. Thermal free-free radiation can be used to diagnose physical conditions in the quiet Sun, active regions, and the decay phase of certain flares.

- *Thermal gyroresonance emission* is due to the gyromotion of thermal electrons in the presence of a magnetic field. In active regions, the magnetic field can be strong enough to render the corona optically thick to gyroresonance absorption at frequencies in the range 1–18 GHz. It is therefore a powerful tool for measuring magnetic fields in solar active regions.

- *Thermal and nonthermal gyrosynchrotron emission* play a dominant role in energetic phenomena such as flares. Extremely hot electrons or a nonthermal distribution of electrons emit a broadband continuum that strongly dominates the radio emission at frequencies $\nu >$ 1–2 GHz. Gyrosynchrotron radiation provides powerful diagnostics of physical conditions in flaring sources.

In addition to incoherent radiation from thermal and nonthermal distributions of electrons by the above mechanisms, coherent radiation due to wave-particle and wave-wave interactions plays a prominent role on the Sun at frequencies $\nu <$ 1–2 GHz:

- *Plasma radiation* is the result of a two-stage process wherein the electron distribution function becomes unstable to the production of plasma waves—due, for example, to the two-stream instability resulting from the passage of an electron beam, to the passage of a coronal shock, or to a loss-cone instability. The plasma waves are then converted to electromagnetic waves at the electron plasma frequency $\nu_{pe} = \sqrt{n_e e^2/\pi m_e} \approx 9\sqrt{n_e}$ kHz or its harmonic $2\nu_{pe}$. Examples of radio bursts that emit plasma radiation include those of type II and type III.

- *Other coherent mechanisms* include the electron cyclotron maser (Melrose & Dulk 1982; Melnikov & Fleishman and references therein) and possibly transition radiation (Fleishman & Kahler 1992). Additional, as yet unidentified coherent emission mechanisms, may prove to play a role in the Sun's radio repertoire.

3. Overview of FASR Science

In this section, key FASR science goals are summarized. The science background, motivations, and relevant radio diagnostics and techniques are discussed in greater detail elsewhere in this volume. The relevant chapters will be indicated where appropriate. The identification of FASR key science goals has been motivated by (i) the recognition of outstanding problems in solar physics by the wider scientific community, and (ii) the unique and innovative observational role that FASR can play in attacking these problems. FASR is therefore expected to play a central role in the following key science areas:

- The measurement of coronal magnetic fields
- The physics of flares
- The drivers of space weather
- The quiet Sun

In addition to these four key science areas, FASR could play an important role in synoptic studies (§3.5) . An independent, but nevertheless very important, role that FASR data products could play is in forecasting or "nowcasting" solar activity, and in providing new observational tools for assessing its potential impact on the near-Earth environment (§3.6).

3.1 Coronal magnetic fields

It is widely recognized that an understanding of the nature and evolution of coronal magnetic fields is of fundamental importance to acquiring a deeper understanding of a wide variety of outstanding problems, including coronal heating and the origin of the solar wind, solar flares, coronal mass ejections, and particle acceleration and transport. Yet quantitative measurements of the coronal magnetic field have remained elusive. A key capability of FASR will be to exploit a number of diagnostics to measure, or otherwise constrain, coronal magnetic fields. Because of the paucity of such measurements to date, and because of the difficulty of measuring coronal fields at other wavelengths, the impact of FASR may be greatest in its ability to measure fields through a variety of techniques.

Magnetic fields in active regions of strengths > 150 G can be measured using *gyroresonance absorption* (see White, Chapter 5). A measurement of the magnetic field at the base of the corona is straightforward. Extraction of the three-dimensional magnetic field remains a research problem that will be solved through inversion techniques, forward modeling, or other means.

The longitudinal component of weak magnetic fields can be measured using the difference between the free-free absorption coefficient for the ordinary (o) and extraordinary (x) magneto-ionic modes. This difference manifests itself as

circularly polarized emission, the magnitude of which depends on the longitudinal component of the coronal magnetic field. Gelfreikh (Chapter 6) discusses the technique in some detail, which can be exploited to constrain magnetic fields in both active and quiet regions on the Sun.

Propagation effects can also be exploited to measure or constrain the coronal magnetic field. Ryabov (Chapter 7) discusses the propagation of the the x- and o-modes through the solar corona and the consequences of strong and weak coupling between the two modes for the observed spatial distribution of circularly polarized radiation as a function of frequency. These effects can be used to constrain the strength and topology of the coronal magnetic field above and near solar active regions.

Solar activity also yields a number of diagnostic tools for measuring coronal magnetic fields. These include the use of gyrosynchrotron radiation to measure magnetic fields in flaring loops (Bastian 1999; Gary & Hurford, Chapter 4) and in the expanding loops of certain coronal mass ejections (Bastian *et al.* 2001). Statistical studies of the polarization properties of solar radio bursts at meter wavelengths have been used to constrain the macroscopic coronal magnetic field (e.g., Dulk 1976). With the availability of imaging spectroscopy, polarization measurements of specific radio bursts and their trajectories will yield magnetic field measurements in specific regions of the solar corona.

Clearly, FASR magnetic field measurements will often benefit from the use of complementary data. Soft X-ray (SXR) and extreme-ultraviolet (EUV) observations, provide powerful plasma density diagnostics and provide excellent constraints on the magnetic field topology, if not quantitative measurements. Brosius (Chapter 13) reviews the use of multiwavelength observations to measure coronal magnetic fields.

3.2 The physics of flares

FASR will be a superb instrument for investigating the physics of flares. FASR will be sensitive to both thermal and nonthermal emissions, will sample both coherent and incoherent emissions, and span both the optically thick and optically thin spectral regimes. Hence, a large number of radio diagnostics will be brought to bear on solar flares which are expected to yield significant new insights to energy release in flares, the acceleration and transport of electrons, magnetic fields in flares, and the origin of energetic particles in the interplanetary medium.

At frequencies $\nu < 1$–2 GHz, plasma radiation plays an extremely important role. At frequencies less than 200–300 MHz (meter wavelengths) the classical radio bursts will be imaged over a broad frequency range. Burst locations and, importantly, trajectories will be identified and their association with, and relation to, solar flares will be clarified. Pioneering work in this regard has been

made by the NRH at discrete frequencies in the range of 150–450 MHz (see Chapter 2 and references therein, for example). Particularly important are radio bursts of type II (due to a coronal piston-driven or blast-wave shock), type III (due to suprathermal electron beams), and type IV (due to trapped populations of energetic electrons). At frequencies $0.3 < \nu <$ 1–2 GHz (decimeter wavelengths), coherent plasma radiation from type III-like bursts and type IV bursts plays an important role. These are believed to be associated with energy release, but their source regions have not been adequately imaged before, let alone imaged over a frequency range sufficient to exploit the spectral diagnostic power they offer. Also intriguing are the meter-wavelength and decimeter-wavelength narrow-band spikes. Meter-wavelength spikes are associated with metric type IIIs and may be a signature of energy release. Benz reviews decimeter wavelength radio emissions in Chapter 10.

At frequencies $\nu >$ 1–2 GHz (decimeter/centimeter wavelengths) incoherent gyrosynchrotron radiation from electrons with energies of 10s of keV to several MeV is the dominant mechanism. This is the same electron population responsible for hard X-ray (HXR) and γ-ray (continuum) radiation, although the emission mechanisms for hard X-ray, γ-ray, and radio radiation are quite different. HXR and continuum γ-ray radiation over this energy range are due to nonthermal electron bremsstrahlung resulting from collisions of energetic electrons with dense (mostly chromospheric) plasma, while the radio emission results from the gyromotion of these electrons in the magnetic field of the flaring source. Radio and HXR observations of flares are therefore highly complementary. Radio emission is sensitive to emission by nonthermal electrons everywhere in the source. With imaging spectroscopy, it is a powerful diagnostic of the electron distribution function, of the ambient plasma, and of the coronal magnetic field in the source. Gary & Hurford (Chapter 4) outline how some of these measurements are made. Time-resolved imaging spectroscopy will allow the spatio-temporal evolution of the electron distribution function and other physical parameters of the source to be observed. Lee (Chapter 9) demonstrates how time-resolved microwave spectroscopy provides key insights into the problem of electron acceleration and transport.

An extremely important aspect of FASR's capabilities will be the fact that it will provide a *comprehensive* and *integrated* ensemble of data over a wide wavelength range. FASR will provide simultaneous observations of tracers of energy release in the corona at decimeter wavelengths, of energetic, nonthermal electrons at centimeter wavelengths, of associated type II and/or type III radio bursts at meter wavelengths, and of the thermal response of the solar atmosphere at decimeter and centimeter wavelengths (see below). Hence, new insights into the way in which each of these phenomena are coupled to the others will likely emerge.

3.3 Drivers of space weather

The term "space weather" refers to a vast array of phenomena that can disturb the interplanetary medium and/or affect the Earth and near-Earth environment. This includes recurrent structures in the solar wind (fast solar wind streams, co-rotating interaction regions), the ionizing radiation and hard particle radiations from flares, radio noise from the Sun, coronal mass ejections, and shock-accelerated particles. These drivers result in geomagnetic storms, changes in the ionosphere, and atmospheric heating which can, in turn, result in a large variety of effects that are of practical concern to our technological society: ground-level currents in pipelines and electrical power grids, disruption of civilian and military communication, spacecraft charging, enhanced atmospheric drag on spacecraft, etc. A historical perspective of solar and solar radio effects on technologies is presented by Lanzerotti in Chapter 1. The drivers of space weather—fast and slow solar wind streams, flares, and coronal mass ejections—are solar in origin. An understanding of space weather phenomena lies, in part, in gaining a fundamental understanding the origin of these drivers.

Interest in coronal mass ejections (CMEs) has been particularly strong because they are associated with the largest geo-effective events and the largest solar energetic particle (SEP) events. With the detection of synchrotron radiation from CMEs (Bastian *et al.* 2001) a new tool has become available to detect, image, and diagnose the properties of CMEs. Fits of a simple synchrotron model to two- and three-point spectra at various locations in the source yield not only the magnetic field in the CME, but the ambient density of the thermal plasma as well. Radio CMEs may be significantly linearly polarized by the time they propagate to several solar radii from the Sun. Detection of linearly polarized radiation from radio CMEs would provide additional leverage on the magnetic field in CMEs. CMEs can be detected by other means (Bastian & Gary 1997). Using the Clark Lake Radio Observatory, Gopalswamy & Kundu (1993) report observations of thermal radiation signatures of a CME near the plasma level at 38.5, 50, and 73.8 MHz. More recently, thermal emission from CMEs (Kathiravan *et al.* 2002), and coronal dimmings resulting from the launch of a CME (Ramesh and Sastry 2000) have been reported in observations made by the Gauribidanur Radioheliograph between 50–65 MHz. Vourlidas provides a more comprehensive overview of radio signatures of CMEs in Chapter 11.

Coronal waves, possible analogs to chromospheric Moreton waves, were discovered by the SOHO/EIT instrument (Thompson *et al.* 1999; 2000; Biesecker *et al.* 2002) although examples have since been discovered in SXR (Khan & Aurass 2002). They represent the dynamical response of the corona to a flare and/or an associated CME. An associated phenomenon is a coronal dimming, observed in SXR (e.g., Sterling & Hudson 1997) and EUV (Harra & Sterling 2001), believed to result from the removal of coronal material due to the lift-

off of a CME. A radio counterpart to an "EIT wave" was recently detected by the NoRH at 17 GHz (White & Thompson 2004). Observations of radio counterparts to EIT waves and of coronal dimmings mentioned above, suggests that FASR will provide a rather complete view of chromospheric and coronal waves, dimmings, and the interaction of waves with surrounding structures such as active regions (e.g., Ofman and Thompson 2002) and filaments.

It is generally accepted that type II radio bursts are a tracer of fast MHD shocks. The shocks that produce coronal type II radio bursts may be driven by fast ejecta (Gopalswamy *et al.* 1997), by a blast wave (Uchida 1974, Cane & Reames 1988), or by a CME (Cliver *et al.* 1999; Classen & Aurass 2002). Fast ejecta and/or a blast wave are produced by a flare; a CME produces a piston-driven shock wave. The relationship between these shocks, their radio-spectroscopic signature, and other phenomena such as Moreton waves and "EIT waves" remain matters of considerable interest and controversy. Gopalswamy reviews interplanetary type II radio bursts and their relation to interplanetary shocks and CMEs in Chapter 15. With its unique ability to perform imaging spectroscopy, FASR will in some cases be able to simultaneously image the basic shock driver (flare or CME), the response of the atmosphere to the driver (chromospheric and coronal waves and coronal dimmings), and shocks which may form due to the flare and/or the CME. The emphasis placed on FASR's ability to provide an integrated picture of flare phenomena in §3.2 applies equally to CMEs and associated phenomena (type II radio bursts, EIT and Moreton waves, filament eruptions). As an instrument that images coronal energy release and particle acceleration in the middle corona, tracers of coronal shocks, and the onset and ejection of certain coronal mass ejections, simultaneously, FASR will also provide key observations that will help resolve the important and controversial problem of the origin of solar energetic particles in the interplanetary medium.

3.4 The quiet Sun

Radio emission from the quiet Sun is reviewed by Keller & Krucker (Chapter 12). One of the fundamental questions in solar physics is how the solar corona maintains its high temperature of several $\times 10^6$ K. The leading theoretical ideas for how the corona is heated involve either some form of resonant wave heating (e.g., Ofman, Klimchuk, & Davila 1998) or "nanoflares" (Parker 1988), although there exist other models. Wave heating models make specific predictions of where and on what time scales energy deposition occurs in coronal magnetic loops. FASR will provide a detailed history of the temperature, density, and magnetic field in coronal loops in active regions, from which the rate of energy deposition can be calculated as a function of position and time. The role of nanoflares—tiny, flare-like releases of energy from small magnetic

reconnection events—depends critically on the rate at which such events occur. At radio wavelengths Gary, Hartl & Shimizu (1997) established that the 10^{27}-erg SXR events in active regions studied by Shimizu (1995) are accompanied by nonthermal electrons; i.e., they are flare-like. FASR will greatly improve on previous work by providing vastly better frequency coverage and a sensitivity comparable to the VLA under some circumstances (e.g., Krucker *et al.* 1997). The instrument's full-Sun capability should allow FASR to obtain accurate counting statistics on the occurrence rate of these events, and to determine whether that rate increases enough at low energies to contribute significantly to the corona's energy budget.

The structure and heating of the solar chromosphere is also an outstanding problem in solar physics. To date, most chromospheric models have been static. The semi-empirical models of, e.g., Vernazza *et al.* (1981), Fontenla *et al.* (1993) were calculated under the assumption of hydrostatic equilibrium and employ observations of non-LTE UV/EUV lines and disk-averaged IR/submm/mm continuum observations. Separate models are calculated for active region, network, and cell interior contexts. However, observations of CO near 4.7 μm show that the low-chromosphere contains a substantial amount of cool material while broadband microwave (1–18 GHz) spectroscopy of the quiet Sun (Zirin *et al.* 1991) convincingly demonstrate that the semi-empirical models include an overabundance of warm chromospheric material (Bastian *et al.* 1996). Moreover, observations have emphatically shown that the chromosphere is a dynamic entity. Carlsson & Stein (2002, and references therein) have explored dynamic models of the solar chromosphere, wherein acoustic waves are driven through the atmosphere using a sub-photospheric piston. The acoustic waves increase in amplitude as they propagate upward and steepen into shocks at a height of ~ 1000 km where they produce temperature differences as great as 10^4 K. The dynamic model therefore yields material at temperatures considerably higher than that found in the static model chromospheres. However, high temperature material exists only relatively briefly, so that the mean atmosphere in these models is a relatively constant throughout most of the chromosphere.

The FASR design will allow the thermal structure of the chromosphere to be probed down to the height where $\mathrm{T_e} \approx 8000$ K. The sensitivity of the FASR, as presently conceived, will allow the time variability of the thermal structure of the solar chromosphere to be studied in a single frequency band on a time scale < 1 min ($\Delta T_b \sim 100$ K). Over a period of several hours, the FASR will provide high quality maps of the mean thermal state of the chromosphere over its entire frequency range. FASR observations will therefore provide a comprehensive specification of the thermal structure of the chromosphere—in coronal holes, quiet regions, enhanced network, plages—as an input for modern models of the inhomogeneous and dynamic chromosphere.

3.5 Synoptic measurements and forecasting

The Sun occupies a unique position in astronomy and astrophysics because it has a direct impact on life on Earth and in space. Aside from the obvious fact that the Sun makes life on Earth possible, it is the vagaries of the Sun's activity cycle that may cause climatic change (e.g., the Maunder minimum in the late 17th C.). Moreover, as we have come to rely on both ground and space based technologies—for distribution of electrical power, gas and oil pipelines, fixed and mobile communications, navigation, weather and geological information—we have become more vulnerable to disruptions by transient phenomena on the Sun (see Lanzerotti, Chapter 1). Long-term studies of solar activity and both short- and long-term forecasting of solar activity are therefore of pressing interest.

FASR is designed to be flexible enough to carry out a wide variety of research programs requiring specialized data, but in addition it will carry out a strong synoptic role and produce certain data products that will be available in real-time, near real-time, or archivally. The forecasting community, ionospheric physicists, aeronomists and other interested parties will be free to download these products as they become available. As an example, the solar 10.7 cm flux has been used for many years as a proxy indicator of solar activity due to its close correlation with other diagnostics such as sunspot number and area, the emission in Lyα, Mg II, and EUV fluxes, and the total solar irradiance. The 10.7 cm flux remains the solar measurement in highest demand from NOAA/SEC. Schmahl & Kundu (1997) have shown that multi-radio-frequency measurements can be combined to yield superior proxies for both sunspots and irradiance. FASR will provide well-calibrated multifrequency observations suitable for exploiting such proxies.

It is possible that FASR will play a prominent role in forecasting or "now-casting" solar activity and space weather. FASR could produce a number of quicklook data products in near-realtime for this purpose. What is difficult to predict at present, given the unique character of the data that FASR will produce, is which radio diagnostics will prove to be the most useful and robust for forecasting. It is likely that a number data products and/or indices based on the data will prove to be useful. While their utility as forecasting tools remains speculative at this point, examples of such data products include:

- Synoptic maps of the solar atmosphere at various frequencies; synoptic maps of derived physical quantities: temperature, density, magnetic field.

- Maps of the magnetic field strength at the base of the corona in active regions.

- Measures of coronal magnetic activity. Strong gradients and/or high values and/or rapid evolution of the coronal magnetic field may be used as indicators of probable activity.

- Maps of brightness variance at selected frequencies. A high variance is indicative of evolving and/or emerging magnetic flux, local heating, and may be an indicator of probable activity.

- Lists of flare events, erupting prominences, and CMEs; their location, size, and spectral properties as they occur.

4. Description of the Instrument

We now turn to the nature of the instrument itself. It is useful to digress briefly in order to sketch the operational basis of imaging instruments at radio wavelengths in general before discussing FASR specifically.

4.1 Operational basis

High-angular resolution images of celestial sources are formed at radio wavelengths using interferometric techniques. This is because of the fundamental limitation imposed by Rayleigh resolution: the angular resolution of an aperture of diameter D is $\theta \sim \lambda/D$, where λ is the wavelength of the radiation. For example, if an angular resolution of $\theta = 1''$ is desired at a wavelength of $\lambda = 2$ cm ($\nu = 15$ GHz), an aperture $D \approx 4$ km is required. To build a single large antenna of this diameter is impractical. A far more elegant solution is to effectively break the large reflector into an array of many small patches (antennas), each of diameter $d \ll D$, distributed over the desired aperture of diameter D. The basic element of such an array is a pair of antennas, an interferometer. The distance between a given pair of antennas is the antenna baseline b. The interferometer is sensitive to radio emission on an angular scale $\theta = \lambda/b$. Hence, the angular resolution of the array is determined by the maximum baseline $b_{max} = D$, the instrumental beam (§2.1) being $\Omega_{bm} \sim (\lambda/D)^2$. The field of view of the array is determined by the diameter d of the individual antennas: $FOV \sim \lambda/d$.

Most modern radio imaging arrays employ Fourier synthesis imaging. FASR will be no exception. The function of an interferometer is to multiply the signals measured at each antenna. This operation is performed in a device called a correlator. A given interferometer measures a single Fourier component—an amplitude and a phase—of the Fourier transform of the radio brightness distribution within the field of view of a single antenna at a spatial frequency b/λ. A given measurement of a Fourier component is referred to as a complex visibility. An array of N antennas distributed over a two-dimensional domain provides $N_{tot} = N(N-1)/2$ interferometers with baselines of vary-

ing length and orientation and, hence, N_{tot} visibility measurements. One can think of the ensemble of interferometers as constituting a sampling function, a field of delta-functions which multiplies the Fourier transform of the radio brightness distribution within the field of view. The sampling function is the auto-correlation function of the antenna locations. The measurement domain is referred to as the "*uv* plane", where *u* and *v* are the spatial frequency coordinates. The inverse Fourier transform of the sampling function $\mathbf{S}$ is referred to as the "dirty beam" $\mathbf{B}$. It is the point spread function (PSF) of the array. Fourier inversion of the ensemble of measured visibilities therefore yields $\mathbf{I}' = \mathbf{B} \star \mathbf{I} + \mathbf{n}$, where $\mathbf{I}$ is the true radio brightness distribution, $\mathbf{n}$ is instrumental noise, and $\star$ denotes a convolution. A variety of deconvolution and estimation techniques can be used to recover $\mathbf{I}$ from $\mathbf{I}'$.

It is worth pointing out that general purpose radio telescopes such as the VLA can exploit Earth rotation aperture synthesis. If a radio source is static in time—effectively the case for many cosmic radio sources—then the rotation of the Earth can be used to improve the sampling function. This is possible because the projected antenna array geometry, as viewed from a radio source, changes in time as the Earth rotates. Instead of sampling a single point in the Fourier domain, a given interferometer traces out an elliptical path in the Fourier domain time. In the case of solar observations, it is often not possible to use Earth rotation aperture synthesis because the solar radio emission varies significantly on short time scales: e.g., during a solar flare. Solar observations must therefore rely largely on the instantaneous sampling (snapshot imaging) provided by the array for transient phenomena, although Earth rotation aperture synthesis observations can be exploited to observe slowly varying phenomena.

4.2 FASR instrumental requirements

The instrumental requirements for FASR are determined by the scientific requirements, which have been addressed by the wider solar physics community in a number of workshops. The most recent of these was an international workshop at the NRAO in Green Bank, WV, in 2002. These requirements will be revisited periodically until construction of the instrument begins. In this section, we summarize current specifications and discuss the rationale for choices made in general terms. Specific choices are not justified in detail here.

1 *Imaging:* Radio emission from the Sun must be imaged with high dynamic range, fidelity, and angular resolution, with good sensitivity to both compact and extended emission. As discussed in the previous section, FASR will require good snapshot imaging performance, requiring a large number of antenna baselines, optimally distributed.

2 *Field of view*: A full disk imaging capability is desired up to a frequency of 18 GHz. This requirement is determined by the upper frequency limit

to which gyroresonance emission is expected to be relevant. A field of view of ~ 10 $R_\odot$ is required at frequencies < 500 MHz, determined by the requirement that radio CMEs and related phenomena must be imaged.

3 *Angular resolution:* An angular resolution of $1''$ at a frequency of 20 GHz is required, and must be available whenever the Sun exceeds 30° in elevation. For a fixed array, the angular resolution scales linearly with frequency, yielding $10''$ at 2 GHz, and so on. This is believed to be comparable with the limit on angular resolution at radio wavelengths imposed by scattering in the solar corona (Bastian 1994).

4 *Frequency coverage:* The overall frequency range sampled by FASR is of critical importance. It must be sufficient to address each of the key FASR science areas described in §3. Coronal magnetography requires frequency coverage from 1–18 GHz; the physics of flares requires coverage from 0.5–24 GHz, or higher; the drivers of space weather require coverage from $\lesssim 50$–500 MHz.

5 *Frequency agility:* The cost of correlating roughly three decades of frequency bandwidth is very high and is, in any case, unnecessary so long as the broadband radio spectrum is fully sampled on a time scale commensurate with the phenomenon under study. FASR will therefore be *frequency agile*.

6 *Time resolution:* Radio spectra must be obtained at a sufficient rate to resolve the time scale on which phenomena evolve: 10 ms at decimeter wavelengths and 100 ms at centimeter wavelengths and meter wavelengths.

7 *Spectral resolution:* Radio spectra must be sampled with sufficient spectral resolution to resolve spectral features due to a variety of emission mechanisms: as high as 0.1% at decimeter wavelengths and 1% at centimeter and meter wavelengths.

8 *Polarimetry:* Observations of the Stokes polarization parameters I, Q, U, and V must be supported. The instrument must be optimized for measurements of Stokes I and V. In some instances it will be of interest to measure Stokes Q and U. It will not be necessary to measure all four Stokes parameters simultaneously.

9 *Data channels:* At least 2 independent data channels, one for each orthogonal sense of polarization, are required. For operational flexibility, 2–4 pairs of data channels are needed. The net instantaneous frequency bandwidth of the data channels will be of order 1 GHz.

10 *Calibration:* Calibration of the instrument should provide an accuracy of 5% in the absolute flux calibration and an accuracy of $1''$ in absolute position at centimeter wavelengths. This can be relaxed to 10% and $5''$, respectively, at decimeter wavelengths.

These general requirements are reflected in Table 3.1. We now turn to a somewhat more detailed discussion of the FASR instrument.

Table 3.1. FASR Instrument Requirements

Frequency range	0.05–24 GHz
Frequency bandwidth	2×1 GHz per data channel
Frequency resolution	$<$ 300 MHz: 1%
	0.3–2.5 GHz: 0.1%
	$>$ 2.5 GHz: 1%
Time resolution	$<$ 300 MHz: 100 ms
	0.3–2.5 GHz: 10 ms
	$>$ 2.5 GHz: 100 ms
Number antennas	HFA: ~ 100
	IFA: ~ 70
	LFA: ~ 50
Size antennas	HFA: 2 m
	IFA: 6 m
	LFA: LP dipoles/other
Angular resolution	$20''/\nu_{\rm GHz}$
Field of view	HFA: $8^\circ.5/\nu_{GHz}$
	IFA: $2^\circ.8/\nu_{GHz}$
	LFA: $\sim 70^\circ$
Polarization	IQUV
Absolute positions	$1''$
Absolute flux	5%

4.3 System design overview

FASR will be a Fourier synthesis telescope. To image the Sun's radio brightness distribution with excellent dynamic range and fidelity requires many visibility measurements. Since the Sun's brightness varies continuously in time—sometimes dramatically so—Earth rotation aperture synthesis is not always possible. Hence, the instantaneous *uv* coverage—that is, the sampling function in the measurement domain—must be extremely good, and optimized to the solar imaging problem. This implies that a large number of optimally configured antennas is required.

FASR antennas will be designed to track the Sun every day from sunrise to sunset. From an operational standpoint, it is highly undesirable to remove antennas from the array for maintenance or repair during daylight hours. Given the large number of antennas to maintain, FASR antennas must be highly reliable in the field. This suggests that the antenna and front end electronics should be of a simple and robust design and that a minimum of signal processing should be done in the field. The bulk of the signal processing will be carried out at a central location. This has the added advantage that future upgrades to signal processing capabilities can be accomplished more conveniently.

Turning to the source itself, the Sun differs from weak sidereal sources in important respects. First, it is an extremely powerful radio source, so much so that it completely dominates the system noise. This has two consequences: (1) the front-end electronics need not be cooled to cryogenic temperatures, as is commonly done with sensitive, general purpose radio telescopes like the VLA; (2) large antennas are not needed for sensitivity. Second, the Sun's radio emission is highly variable. Depending on the frequency, the Sun's total radio flux may vary by as much as 40 dB. The variability can occur on short time scales, as implied in Table 3.1, and display narrowband structures. FASR must be designed to process such highly variable emission.

One of the most challenging aspects of the FASR project is the very large instrument bandwidth that must be sampled and processed on short time scales. It appears unlikely that a single antenna and feed can optimally support the total instrument bandwidth at low cost. FASR will therefore be composed of three separate arrays of antennas, each designed to support a sub-range of frequencies. The low-frequency array (LFA) will cover 50–350 MHz; the intermediate-frequency array (IFA) will cover roughly 300 MHz to 2.5 GHz; the high-frequency array (HFA) will cover 2.5–24 GHz. Several aspects of the instrument design from the antennas to the correlator are now discussed. Readers that are not interested in a moderately technical discussion are encouraged to skip the remainder of this section.

4.3.1 Antenna configuration. The number and configuration of antennas in each array is of critical importance. The criteria by which antenna configurations are assessed depend on the imaging problem at hand. Each of the arrays described above must image the Sun with high degrees of dynamic range and fidelity over roughly a decade of bandwidth with a fixed configuration. The FASR array configuration is therefore a challenging optimization problem, one that is presently under study.

The angular resolution with which one can image the Sun is limited by scattering on inhomogeneities in the overlying corona: "coronal seeing" (e.g., Bastian 1994). Seeing limitations are frequency dependent and also depend

sensitively on the details of the coronal medium (e.g., an active region source, a quiet region, whether the source is on the limb, whether the Sun is near maximum or minimum levels of activity, etc).

These considerations lead to a requirement that the angular resolution of the HFA is $1''$ at a reference frequency of 20 GHz, which requires a projected baseline of 3 km. To meet this requirement over a significant range of hour angle (source elevation $> 30^\circ$) implies that a maximum antenna baseline of 6 km is required. Since the angular resolution of a fixed array configuration varies linearly with wavelength, the angular resolution requirement varies between $0.8''$–$10''$ in the HFA and, if the configuration footprints are similar for the IFA and LFA, the angular resolutions will be $7''$–$80''$ and $1'$–$3.5'$, respectively. Both observations (e.g., Leblanc *et al.* 2000) and theory (e.g., Bastian 1994) suggest that the proposed extent of the array is a good match to the expected variation in coronal seeing with frequency.

The snapshot imaging capabilities of the instrument, and hence the instantaneous *uv* coverage, must be excellent. Work to date suggests that of order 100 antennas in the HFA, 70 in the IFA, and 50 in the LFA—yielding 4950, 2415, and 1225 instantaneous complex visibility measurements, respectively—will be needed to accomplish this goal. These will be configured in "self-similar" array configurations (Bastian *et al.* 1998; Conway 1998; 2000). The scale-free nature of self-similar configurations is ideal for imaging over wide frequency bands. An example of a self-similar configuration is one composed of logarithmic spirals (Conway 1998).

4.3.2 Antennas. Multiple arrays are needed to meet the joint requirements of supporting a large instrument bandwidth, excellent imaging, and a large field of view. FASR will therefore employ three arrays of antennas using three separate antenna designs. Each will cover roughly a decade in frequency—corresponding roughly to meter, decimeter, and centimeter wavelengths—with an appropriate degree of overlap between each for cross-calibration.

The LFA will employ non-steerable, non-reflecting antennas: i.e., fixed log-periodic dipoles or Vivaldi-type antennas while the IFA and HFA will employ steerable, parabolic reflectors. The IFA will employ symmetric 6 m paraboloids. These have a field of view of $\sim 9^\circ$–1° from 0.3–2.5 GHz. The HFA will employ symmetric 2 m paraboloids, which have a field of view of $\sim 3.5^\circ$–0.5° from 2.5–18 GHz. Future studies will address the optimum choices for the antenna mounts and drives (IFA and HFA).

4.3.3 Feeds and front ends. Both the IFA and HFA will employ broadband, dual-linear feedsfeed. The precise nature of the feeds—log-periodic dipoles, log-periodic zig-zags (e.g., Engargiola 2002), sinuous feeds, or variants thereof—requires a development and evaluation effort. The feeds will not

be mechanically moved during observations to improve focus, but will be optimized for focus near the high-frequency end. The 5–10% loss of efficiency at low frequencies may be acceptable if other losses are well controlled.

FASR will employ tightly integrated broadband front end packages. Because the Sun is a highly variable source the signal must be attenuated by variable amounts. A switched step attenuator will be placed after the first low-noise amplifier. The attenuator step size depends on how constant the input into the optical link and digitizers needs to be. One suggestion is to employ two stages of attenuation: one would be used to ensure that the second stage amplifier remained linear; the second attenuator would ensure constant power into the digitizers. A calibration signal may be needed—e.g., a switchable noise diode—but this remains uncertain until calibration of the instrument is better understood. While the front end need not be cooled to cryogenic temperatures, it does need to be thermally stabilized. This will likely be accomplished using inexpensive Peltier coolers.

Given the relatively small size of the antennas and the simplicity of their front ends, the cost of each antennas is expected to be low.

4.3.4 Signal transmission. Signal transmission will be via bundles of single mode optical fibers over runs of several km. The fiber bundles will be buried to sufficient depth to eliminate diurnal temperature variations and hence, minimize daily variations in length. In the interest of designing as simple, inexpensive, and stable an instrument as possible, it is worth avoiding implementation of a round-trip phase measurement scheme, if possible. To this end, it may be sufficient to simply equalize fiber lengths.

The signals will be transmitted in analog form. The complexity and expense of digitizing the signals at the antenna, not to mention the need to carefully shield the requisite electronics at each antenna, outweighs the advantages of gaining full control over the signal at the antenna. The bandwidths of the LFA and the IFA are such that relatively inexpensive optical modems can be used to transmit the entire radio frequency (RF) band. No frequency conversions are required at the antenna.

In the case of the HFA, the bandwidth is too large for optical modems currently available. The maximum bandwidth for low-cost units for the foreseeable future is 12 GHz, although progress in broader bandwidth optical links is being monitored. Assuming that 12 GHz is the maximum transmittable band, sub-bands must be transmitted. One approach is to perform a single frequency conversion and, in effect, transmit two halves of the total HFA bandwidth. This could be accomplished by means of a direct photonic local oscillator at a frequency near 12 GHz. A switch and single optical modem could be used to handle both sub-bands, or a pair of modems could be used to transmit both si-

multaneously. Support of frequencies > 24 GHz would require a second local oscillator in this scheme.

4.3.5 Signal processing. The RF signal observed by each antenna over its entire nominal frequency range will be transmitted in analog form to a central processing location via optical fiber. There, the desired frequency and bandwidth will be selected and the signal will be converted and digitized prior to further processing.

FASR will be designed to perform "low-dispersion" spectroscopy. A correlator that supports a large number of spectral line channels is not needed on scientific grounds. However, since, like most other modern radio telescopes, FASR will sample a relatively large instantaneous bandwidth, exposure to radio frequency interference (RFI) is a concern. RFI signals are typically narrowband ($< 0.1\%$) and can be very strong (up to 40 dB above quiet Sun levels at low frequencies). The system will require sufficient spectral resolution and dynamic range to isolate and remove sources of RFI in the band. It is therefore important to digitize the signal with a sufficient number of bits to ensure adequate dynamic range. It is expected that 8-bit sampling will be needed for frequencies below 2.5 GHz; 3 bits will likely be sufficient for frequencies > 2.5 GHz.

While alternative signal processing architectures are possible, FASR lends itself to an "FX-like" architecture wherein considerable signal processing will be applied to the signal from each antenna prior to correlation. While the station-based nature of the F part of an FX approach is attractive, the use of a Fourier transform is unattractive in the presence of RFI because the frequency response is too broad. Isolation and excision of undesirable narrowband signals would be problematic. An alternative is to build a digital filter bank using polyphase filters (Bunton 2003). The use of polyphase filtering techniques is attractive because they can be implemented efficiently and yield sharply defined spectral channels. It should be relatively cheap to implement because the frequency resolution requirements of FASR are relatively modest. Another attraction of the digital filter bank approach is that it could adapt to the changing RFI environment dynamically. The output would be clean, narrowband channels. The delay correction and correlation requirements would be therefore be small.

If an FX-like approach is adopted, with frequency-domain signal processing performed in a station-based manner prior to signal correlation, the correlator itself can be relatively small. One-bit, two-level sampling, or two-bit, three-level sampling will likely be sufficient.

5. Operational Issues

An important goal of the FASR project is to "mainstream" the use of radio data by the wider solar physics and related communities. Much as the *Yohkoh* mission mainstreamed the use of SXR and HXR data, the SOHO mission main-

streamed the use of UV and coronagraph data, and the TRACE mission has mainstreamed the use of EUV data, FASR operations will be designed to provide users with the data and data analysis tools that maximize the utility of the data for the greatest number of users.

General purpose radio telescopes such as the VLA, the Very Long Baseline Array, the Giant Meterwave Radio Telescope, and others require a great deal of users. They must prepare detailed scripts for carrying out their observations, they must calibrate their data, and they must carefully image and deconvolve the telescope PSF from their maps. For this reason, radio astronomy has acquired the reputation of being unduly complicated. To achieve the goal of mainstreaming the use of FASR data requires shifting the burdens of data acquisition, calibration, imaging, and deconvolution from the user to facility operations. This goal, while ambitious, is necessary in order to allow users that have not been initiated into the craft of radio interferometry to nevertheless effectively exploit radio observations.

In considering this goal it is worth noting that distinct advantages lie in the fact that FASR, in contrast to a general purpose instrument, will be dedicated to a single radio source. This greatly simplifies daily operations and eliminates the need for user involvement in most observations. (It is quite likely, however, that while users would not be involved in routine FASR operations, users could nevertheless propose special-purpose observing modes.) There is cause for optimism in the fact that the NoRH and the NRH have both made significant progress in automating many operations functions and making data products available to the community in a relatively transparent manner. Given the breadth and diversity of the FASR science program, though, the difficulty of automating data calibration and pipelining imaging and deconvolution should not be underestimated.

6. Concluding Remarks

FASR is an ambitious project involving the national observatories, university partners, and international collaborators. The instrument is being carefully designed and optimized to exploit radio diagnostics of solar radio emission in order to measure a wide variety of physical parameters, many of them unique. FASR will therefore address an extremely broad science program and is expected to serve as a key research facility for solar radiophysics and the wider solar physics and space weather communities. Moreover, it is anticipated that FASR will contribute to forecasting and "nowcasting" of solar activity and space weather.

Acknowledgments

I thank my colleagues D. E. Gary, S. M. White, G. J. Hurford, as well as J. Webber, R. Bradley and many others at the NRAO, for frequent and insightful discussions on myriad aspects of FASR. A preliminary study of the FASR concept was supported in part by NSF grant AST-0138317 to New Jersey Institute of Technology.

References

Ayres, T. R., & Rabin, D. 1996, ApJ, 460, 1042
Bastian, T. S. 1994, ApJ, 426, 774
Bastian, T. S. 1999, in Proc. Nobeyama Symp. Solar Physics with Radio Observations, eds. T. S. Bastian, N. Gopalswamy, & K. Shibasaki, NRO Report 479
Bastian, T. S., & Gary, D. E. 1997, JGR, 102, 14031
Bastian, T. S., Benz, A. O., & Gary, D. E. 1998, ARAA, 38, 136
Bastian, T. S., Maia, D., Pick, M., & Kerdraon, A. 2001, ApJ, 558, L65
Bastian, T. S., Dulk, G. A., Leblanc, Y. 1996, ApJ, 473, 539
Benz, A. O, & Krucker, S. 1999, A&A, 341, 286
Bunton, J. 2003, ALMA Memo. 447
Cane, H. V., & Reames, D. V. 1988, ApJ, 325, 895
Cane, H. V., Erickson, W. C., & Prestage, N. P. 2002, JGR, 107, (A10) 1315
Classen, H. T., & Aurass, H. 2002, A&A, 384, 1098
Cliver, E. W., Webb, D. F.,& Howard, R. A. 1999, Solar Phys, 187, 89
Conway, J. 1998, ALMA Memo. 291
Conway, J. 2000, ALMA Memo. 216
Engargiola, G. 2002, ATA Memo. 45
Fleishman, G. D., & Kahler, S. W. 1992, ApJ, 394, 688
Fleishman, G., & Melnikov, V. 2003a, ApJ, 584, 1071
Gary, D. E., Hartl, M., Shimizu, T. 1997, ApJ, 477, 958
Gopalswamy, N., & Kundu, M. R. 1993, Solar Phys, 143, 347
Gopalswamy, N., Kundu, M. R., Manoharan, P. K., Raoult, A., Nitta, N., & Zarka, P. 1997, ApJ, 486, 1036
Gopalswamy, N. 2000, in Radio Astronomy at Long Wavelengths, eds. R.G. Stone, K. W. Weiler, M. L. Goldstein & J.-L. Bougeret, AGU, p. 123
Gopalswamy, N., Lara, A., Kaiser, M. L., & Bougeret, J.-L. 2001, JGR, 106, 25261
Harra, L. K., & Sterling, A. C. 2001, ApJ, 561, L215
Isliker, H., & Benz, A. O. 1994, A&A, 104, 145
Kathiravan, C., Ramesh, R., Subramanian, S. R. 2002, ApJ, 567, L93
Klassen, A., Aurass, H., Mann, Thompson, B. 2000, A&A Supp., 141, 357
Krucker, S., Benz, A. O. Bastian, T. S., & Acton, L. 1997, ApJ, 488, 499

Leblanc, Y., Dulk, G. A., Vourlidas, A., & Bougeret, J.-L. 2001, JGR, 106, 25301
Melrose, D. B., & Dulk, G. A. 1982, ApJ, 259, 844
Napier, P. J., Thompson, A. R., & Ekers, R. D. 1983, Proc. IEEE 71, 1295
Ofman, L., Klimchuk, J. A., & Davila, J. M. 1998, ApJ, 493, 474
Ofman, L., & Thompson, B. J. 2002, ApJ, 574, 440
Parker, E. N. 1988, ApJ, 330, 474
Pick, M. 1999, in Solar Physics with Radio Observations, eds. T. S. Bastian, N. Gopalswamy, & K. Shibasaki, NRO Report 479, p. 187
Ramaty, R. 1969, ApJ, 158, 753
Ramesh, R., & Sastry, Ch. V. 2000, A&A, 358, 749
Reames, D. 1999, Space Sci. Rev., 90, 413
Schmahl, E.J., & Kundu, M.R. 1998, in Synoptic Solar Physics, edited by K.S. Balasubramanian, J. W. Harvey, & D. M. Rabin, ASP Conf. Series 140, 387-398
Shimizu, T. 1995, Publ. Astron. Soc. Japan, 47, 251
Solar & Space Physics Survey Comm. 2002, The Sun to the Earth – and Beyond: A Decadal Research Strategy for Solar & Space Physcs, National Academy Press, Washington, DC
Stein, R. A., & Carlsson, M. 1997, in SCORe '96: Solar convection and oscillations and their relationship, Eds. F.P. Pijpers, J. Christiansen-Dalsgaard, & C. S. Rosenthal, Astrophys. Sp. Sci. Lib. v. 225, Kluwer, P. 261
Thompson, B. J., & 9 others 1999, ApJ, 517, L151
Thompson, B. J., Reynolds, B., Aurass, H., Gopalswamy, N., Gurman, J. B., Hudson, H. S., Martin, S. F., & St. Cyr, O. C. 2000, Solar Phys, 193, 161
White, S. M., & Thompson, B. J. 2004, in preparation.
White, S. M., & Kundu, M. R. 1997, Solar Phys, 174, 31
Zirin, H., Baumert, B. M., & Hurford, G. J. 1991, ApJ, 370, 779

Chapter 4

RADIO SPECTRAL DIAGNOSTICS

Dale E. Gary
Center for Solar-Terrestrial Research, New Jersey Institute of Technology, Newark, NJ 07102 USA
dgary@njit.edu

G. J. Hurford
Space Sciences Laboratory, University of California, Berkeley, CA 94720
ghurford@ssl.berkeley.edu

Abstract We review solar radio emission from the perspective of imaging spectroscopy. Radio emission mechanisms differ in their spectral properties, which can be used to determine parameters of the emitting particles and the ambient solar atmosphere in the emitting volume. After generation, the propagation of radiation in the solar atmosphere leads to changes in the spectrum that can be exploited to gain further information about the atmospheric parameters along the line of sight.

1. Introduction

Spectral diagnostics have a long history of importance in astrophysics. In fact, the "new science" of astrophysics was born from astronomy with the advent of spectroscopy in the mid-19th century. Solar radio physics was strongly influenced from the beginning by the spectral viewpoint, with the discovery and classification of burst types by Wild & McCready (1950; types I–III), Boischot (1959; type IV), and Wild *et al.* (1959; type V), based on their appearance on spectrographs. Multifrequency radiometers and radio spectrographs, which measure the spatially-integrated flux density from the Sun, have been and will continue to be important for solar diagnostics, but their use for quantitative work, especially for incoherent emission processes, is often frustrated by the inhomogeneity of the Sun and the inability to spatially associate sources with observations at other wavelengths. Radioheliographs (e.g. Nançay Radiohelio-

graph and Nobeyama Radioheliograph) and synthesis telescopes (e.g. Westerbork Synthesis Radio Telescope and Very Large Array) can make high-quality images of the Sun, but operate at only a few widely-spaced frequencies. The only instrument that combines imaging with frequency resolution and coverage adequate for spectral diagnostics is the Owens Valley Solar Array (OVSA), but its small number of antennas and limited spatial resolution fall short of what is needed to fully exploit the diagnostic potential of radio imaging spectroscopy.

The Frequency Agile Solar Radiotelescope (FASR) is envisioned as the first solar radio instrument to combine the spectral and spatial capabilities needed to fully exploit this diagnostic potential. Many of the preceding chapters discuss the multiple-frequency imaging capabilities envisioned for FASR, but this chapter focuses on an alternative viewpoint which, while equivalent, can yield important new insights. Instead of considering the data-cube as a stack of independent images whose morphology changes with frequency, we view the data-cube vertically and consider each pixel in the images to have an associated spectrum.

Such a spectrum is referred to as a *brightness temperature spectrum*, since, for a spatially-resolved image, it is the spectrum of surface brightness, expressed in units of temperature. This is in contrast to the spatially-integrated spectrum. The two are related by the Rayleigh-Jeans approximation for the Planck function

$$S_\nu = \int \frac{2k_B T_b \nu^2}{c^2} d\Omega, \tag{4.1}$$

where S_ν is the flux density (W m^{-2} Hz^{-1}) at frequency, ν (Hz), from an element of solid angle, $d\Omega$, and k_B is the Boltzmann constant. The brightness temperature T_b is the "temperature equivalent brightness" of the emission, and is the essential quantity that contains all of the physics. For example, in the case of optically thick thermal emission it is just the electron temperature. For optically thick nonthermal emission it is an "effective" temperature related to the energy $k_B T_{\rm eff}$ of the emitting electrons. As we will discuss in more detail shortly, a surprisingly large number of physical parameters can be deduced from a precisely measured brightness temperature spectrum.

In using the terms thermal and nonthermal, above, we restrict ourselves to incoherent emission, where each electron produces radiation independently of the others in the source. However, emission is possible from electrons that act coherently, in phase with the wave mode exciting the electron motion. The brightness of such coherent emission loses its diagnostic power for determining electron energies, but rather reflects the growth rate of the responsible waves, which may be Langmiur waves, electron-cyclotron waves or others. However, when the mechanism responsible for such coherent emission can be identified, the emitting frequency, polarization, and timescale for brightness changes can

provide diagnostics on the ambient density, magnetic field strength, speed of the disturbance, inherent size of the source, and perhaps other parameters.

2. Characteristic Frequencies of the Solar Atmosphere

To gain an overview of the power of radio spectral diagnostics, it is necessary to have an appreciation for radio emission processes in the Sun and solar wind over more than 6 decades in frequency, from < 30 kHz (typical plasma frequency at Earth) to > 30 GHz. FASR will cover approximately the upper half of these 6 decades of frequency. Although a bewildering variety of emission mechanisms vie for dominance over this wide spectral range, much of the apparent complexity exhibited by solar bursts can be understood in terms of three characteristic frequencies (Gary & Hurford 1988). The three relevant frequencies (Hz) are the plasma frequency,

$$\nu_p = 8.98 \times 10^3 \sqrt{n_e}, \tag{4.2}$$

the frequency at which free-free emission reaches optical depth unity

$$\nu(\tau_{\rm ff} = 1) \approx 0.5 n_e T_e^{-3/4} L^{1/2}, \tag{4.3}$$

and the electron gyrofrequency

$$\nu_B = 2.8 \times 10^6 B. \tag{4.4}$$

In equations (4.2–4.4), n_e is the electron density in cm^{-3}, T_e is the electron temperature in K, L is the relevant scale length in cm for free-free emission (the density scale height in the case of an isothermal corona), and B is the magnetic field strength in G.

Figure 4.1 relates these characteristic frequencies to height in the solar atmosphere for a nominal solar model, providing a heuristic indication for why emission mechanisms change with height. In general, the characteristic frequency that appears highest in the figure determines the emission mechanism. Broadly speaking, plasma emission dominates at frequencies from 30 kHz to several hundred MHz, covering heights greater than 0.2 $R_\odot$ above the photosphere. The dominance of plasma emission over this range is simply because the plasma level lies above the $\tau_{\rm ff} = 1$ level at these frequencies. At decimetric frequencies (200 MHz–1 GHz), the plasma level in active regions is generally below the $\tau_{\rm ff} = 1$ level, but plasma emission may still be important because of the inhomogeneity of the corona in this height range, and the extremely high brightness of the coherent plasma emission, which can reach an intrinsic brightness of 10^{15} K. Outside of bursts, the emission in this range is thermal or slightly nonthermal, but burst emission is still dominated by coherent plasma emission.

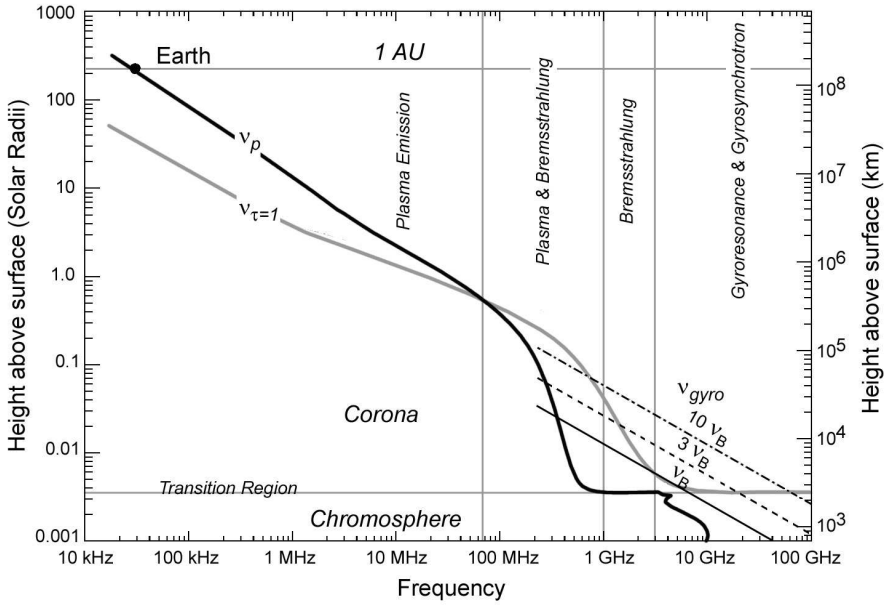


Figure 4.1. Characteristic radio frequencies for the solar atmosphere. The upper-most characteristic frequency at a given frequency determines the dominant emission mechanism. The plot is meant to be schematic only, and is based on a model of temperature, density, and magnetic field as follows: The density is based on the VAL model B (Vernazza *et al.* 1981), extended to 10^5 km by requiring hydrostatic equilibrium, and then matched by a scale factor to agree with 5 $\times$ the Saito *et al.* (1970) minimum corona model above that height (the factor of 5 was chosen to give 30 kHz as the 1 AU plasma frequency). Temperature was based on the VAL model to about 10^5 km, then extended to 2×10^6 K by a hydrostatic equilibrium model. The temperature is then taken to be constant to 1 AU. The magnetic field strength was taken to be the typical value for active regions given by Dulk & McLean (1978), $B = 0.5(R/R_\odot - 1)^{1.5}$. For the $\nu(\tau_{\rm ff} = 1)$ curve, a scale height L is needed. We used $L = H_0(T/T_0)(R/R_\odot)^2$ where $H_0 = 0.1R_\odot$ and $T_0 = 2 \times 10^6$ K. Near the Sun, the curves apply to active regions.

Three lines are shown for gyroemission, representing the cyclotron frequency and its harmonics. The cyclotron line ($\nu = \nu_B$) is generally not relevant for the solar corona within active regions, but rather the emission occurs typically at the third harmonic $\nu = 3\,\nu_B$. Figure 4.1 shows that the $3\,\nu_B$ line lies above the $\tau_{\rm ff} = 1$ level down to 1–2 GHz, and extends up in frequency to ~ 20 GHz—both of which agree well with the observed range. During bursts, gyroemission is more typically at $\nu = 10\,\nu_B$, from which we see that gyroemission during bursts can extend to 800–900 MHz in the decimetric range. At mm wavelengths ~ 100 GHz, bursts can be dominated by either free-free or gyroemission, depending on the number and energy of emitting particles. Outside of flares, the emission above 20 GHz is entirely due to free-free emission.

3. Plasma Emission Diagnostics

As we mentioned above, the brightness temperature due to coherent mechanisms does not provide a diagnostic of the electron energy distribution, as incoherent mechanisms do. But as discussed in more detail in Chapter 10, other features of the spectrum are rich in diagnostics. A prime example is the frequency drift rate of type III bursts. These are due to beams of electrons traveling upward or downward in the solar corona, which generate emission at the plasma frequency or its second harmonic. Hence, the emission frequency depends only on the local electron density, according to equation 4.1. Given a model of density vs. height, the frequency drift rate can be converted to beam velocity, which is typically of order $0.1c$. Alternatively, imaging observations at many frequencies, such as FASR will give the trajectory of the beam and hence the run of electron density along the trajectory. When type III bursts with both positive and negative frequency drifts are seen (see Figure 2.7 of Chapter 2, and Figure 10.1 of Chapter 10), imaging observations should pinpoint the location of the acceleration site.

Type II bursts, also due to plasma emission, are excited by the passage of a shock wave. Similar to the case of type III bursts, the frequency drift rate, combined with spectral imaging, gives the ambient density and speed of the shock. Some type II bursts show "herring bone" structure due to excitation of electron beams from the shock front. Spectral imaging of such bursts should give rich diagnostics of particle acceleration at shocks by giving the local direction of the magnetic field along the shock (from the trajectories of the type IIIs) and the ambient density along the shock (from the frequency of emission).

As described in Chapter 10, many other types of coherent emission occur in the decimetric and metric wavelength ranges, for which spectral imaging may provide new plasma diagnostics. However, much more must be learned about the emission mechanisms before the full diagnostic potential can be realized. Quasi-periodic pulsations, for example, can potentially give magnetic field diagnostics if the oscillating magnetic loop geometry is known from imaging observations. FASR's combined spatial and spectral capabilities will yield new insights into the myriad coherent burst types, and perhaps give a better understanding of the emission mechanisms necessary for new diagnostics that are not yet possible.

4. Free-Free Diagnostics

At radio wavelengths, free-free emission, or bremsstrahlung, is derived from consideration of collisions of electrons on ions in the small-angle approximation. An expression for free-free opacity from thermal electrons, relevant to

conditions of the solar atmosphere, was given by Dulk (1985) as

$$\kappa_\nu \approx \sum_i \frac{1}{3c}\left(\frac{2}{\pi}\right)^{1/2}\frac{\nu_p^2}{\nu^2}\frac{4\pi Z_i^2 n_i e^4}{m_e^{1/2}(k_B T)^{3/2}}\frac{\pi}{\sqrt{3}}G(T,\nu) \tag{4.5}$$

$$\approx 9.78\times 10^{-3}\frac{n_e}{\nu^2 T^{3/2}}\sum_i Z_i^2 n_i \times \begin{cases} 18.2 + \ln T^{3/2} - \ln\nu & (T < 2\times 10^5 K) \\ 24.5 + \ln T - \ln\nu & (T > 2\times 10^5 K) \end{cases} \tag{4.6}$$

where ν_p is the plasma frequency (eq. 4.2), Z_i and n_i are the ion charge and number density, respectively ($\sum_i Z_i^2 n_i \approx 1.2 n_e$ for the solar corona), m_e is the electron mass, and G is the free-free "gaunt factor" related to the Coulomb logarithm. As discussed in Chapter 6, for free-free emission from the solar atmosphere the corona has an appreciable optical thickness at low frequencies, becoming optically thin at higher frequencies whereby the lower-lying chromosphere becomes visible. As frequency increases further, we see to slightly lower depths in the chromosphere, but it remains optically thick to the highest radio frequencies. Even at submillimeter wavelengths the chromosphere is optically thick well above the temperature minimum region (Bastian *et al.* 1993).

The equation of radiative transfer becomes

$$T_b = T_{\rm chr}\exp^{-\tau_{cor}} + T_{\rm cor}(1-\exp^{-\tau_{\rm cor}}) \tag{4.7}$$

where $T_{\rm chr}$ is the electron temperature of the chromosphere, $T_{\rm cor}$ is the electron temperature of the corona, and $\tau_{\rm cor} = \int \kappa\ dl$ is the optical depth of the corona. Figure 4.2 shows the spectral shape that results from an isothermal corona at $T_{\rm cor} = 10^6$ K overlying an isothermal chromosphere at $T_{\rm chr} = 10^4$ K (solid line), and after subtracting the background chromosphere (dotted line).

Changing the temperature and density (or column emission measure $\int n^2 dl$) of the corona merely shifts the (dashed) spectrum in the directions indicated by the arrows in Figure 4.2, *without changing the spectral shape.* The lengths and directions of the arrows indicate the effect of quadrupling the relevant parameter labeling the arrows. Gary & Hurford (1988) called such spectra "Universal Spectra," to indicate that the shape is invariant to changes in plasma parameters. The Universal Spectra are strictly valid only for homogeneous sources, and variations along the line of sight can change the spectral shape. An example of the use of this spectral diagnostic to deduce coronal temperature and density as a function of position in an active region was given by Gary & Hurford (1994—See Fig. 2.2 of Chapter 2).

FASR will produce far higher quality brightness temperature spectra, at much better spatial resolution, than any previously available. As noted in Chapter 6, the polarization characteristics of such spectra provide a diagnostic of the longitudinal magnetic field strength. The more precise measurements from FASR will permit more realistic modeling of the line-of-sight variations of tempera-

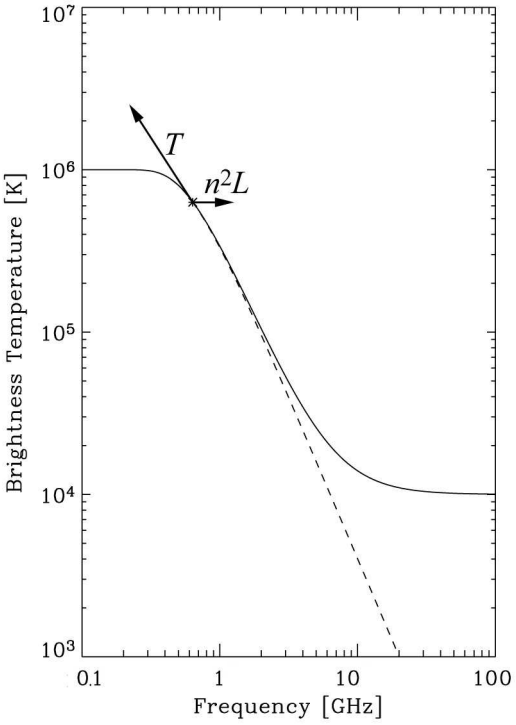


Figure 4.2. A "Universal Spectrum" for free-free brightness temperature. The solid line shows the spectrum for a 10^6 K corona and 10^4 K chromosphere. The dashed line shows the spectrum for the coronal contribution alone.

ture and density than assuming a single-temperature corona. The fact that the optically thick part of the spectrum gives directly the electron temperature as a function of frequency, and hence height, can be used to determine the LOS variation. In fact, Grebinskij *et al.* (2000; see also Chapter 6) show that precise measurement of the spectral slope and the degree of polarization are sufficient to determine the longitudinal component of B. Figure 4.3 demonstrates that this simple technique works amazingly well, at least for model data. The relatively low degree of polarization, and the need for smooth and accurate brightness temperature spectra, make this a challenging but rewarding observational application for FASR.

5. Gyroresonance Diagnostics

The free-free emission diagnostics can be used everywhere in the solar atmosphere that the magnetic field is not too strong ($B \leq 100$ G). However, in

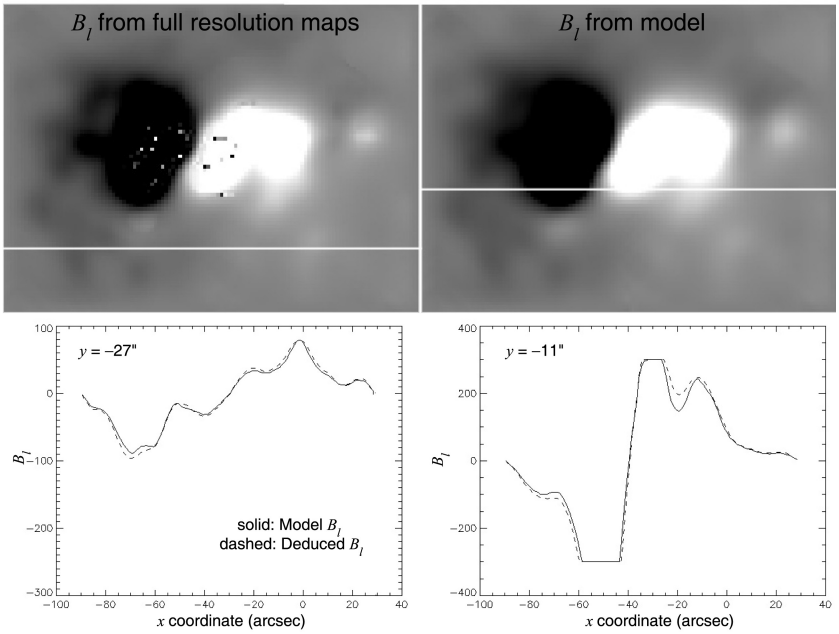


Figure 4.3. Longitudinal magnetic field from the model atmosphere given by Mok *et al.* (2003), compared with the field deduced from radio spectra from the model. The model is shown on the upper right, and the deduced longitudinal magnetogram is shown on the upper left. The salt and pepper in the deduced field map is due to failure of the algorithm in regions of high field strength, where gyroresonance emission strongly affects the spectrum. The horizontal white lines indicate the locations of the 1-dimensional profiles shown in the lower panels, for quantitative comparison. The excellent quantitative comparison (see Gary 2003) shows that the method, from Grebinskij *et al.* (2000) works very well.

the lower corona above active regions a different mechanism, gyroresonance emission, dominates as detailed in Chapter 5. The expression for gyroresonance opacity from thermal electrons, is given by Dulk (1985) as

$$\kappa_\nu(s,\theta) = \frac{\pi^2}{4c}\frac{1}{\mu_\sigma \partial(\omega\mu_\sigma)/\partial\omega}\frac{\nu_p^2}{\nu}\frac{s^2}{s!}\left(\frac{s^2\beta^2\sin^2\theta}{2}\right)^{s-1}\frac{1}{\beta|\cos\theta|} \tag{4.8}$$

$$\times \exp\left[-\frac{(1-s\nu_B/\nu)^2}{(2\mu_\sigma^2\beta^2\cos^2\theta)}\right](1-\sigma|\cos\theta|)^2 \tag{4.9}$$

where μ_σ is the refractive index for magneto-ionic mode σ ($\sigma = +1$ for o-mode and -1 for x-mode), $\beta = k_B T/m_e c^2$, θ is the direction of the magnetic field to the line of sight, and the other parameters are as defined earlier. Spectra from

gyroresonance sources, again assuming an isothermal corona, are characterized by a flat optically thick portion at low frequencies, becoming optically thin and falling steeply at high frequencies. The frequency at which the steep decline occurs is $\nu = s\nu_B$, where s is the highest optically thick harmonic, typically $s = 3$ for x-mode and $s = 2$ for o-mode, and ν_B is the gyrofrequency for the highest magnetic field strength along the line of sight that remains at coronal temperatures, as discussed by White in Chapter 5. Note that gyroresonance measures the total magnetic field, as distinct from longitudinal component of magnetic flux, discussed in the previous section.

Neglecting variations of T_e along the line of sight, the spectral shape for thermal gyroresonance emission is again invariant. The Universal Spectrum for this mechanism is as shown in Figure 4.4, where the arrows again indicate the shift in the position of the spectrum for factor of 4 changes in T_e and B. Note that the electron density and the angle, θ, that B makes to the line of sight also affect the shape, but in a discrete way by changing which harmonic is optically thick. The spectrum shown by the dashed line illustrates a typical change in shape when density or angle θ (both assumed constant along the line of sight) drops enough that the $s = 3$ layer becomes only partially optically thick, but $s = 2$ remains optically thick. In this case, the spectrum falls steeply at frequency $\nu = 2\nu_B$, to the brightness temperature $T_b = T_{\rm cor}\tau$, where $\tau < 1$ is the optical depth at the $s = 3$ layer. The arrow on the horizontal branch of the dashed spectrum shows the shift expected for an increase in $n_e(\sin\theta)^{2s-2}$ by a factor of 4. Because the optical depth of o-mode emission is less than that of x-mode, both spectral shapes in Figure 4.4 can occur along the same line of sight, with the solid line representing the x-mode, and the dashed line representing the o-mode. More complicated spectra are possible in which both x-mode and o-mode spectra may display harmonic changes. In any case, key diagnostic information can be gleaned from measuring spectra in both circular polarizations, which essentially give two independent, but mutually consistent diagnostics of plasma parameters along the line of sight. Such spectral features have been observed with OVSA when the spatial geometry could be accounted for, either by modeling (Hurford & Gary 1986) or by direct imaging (Gary & Hurford 1994—see Chapter 2, Fig. 2.2).

FASR will produce the first brightness temperature spectra of sufficient spatial and spectral resolution that the spectral discontinuities of the type shown by the dashed line in Figure 4.4 will be well resolved on a routine basis. The spectra in Figure 4.5 are derived from an active region model by Mok *et al.* (2004). The model parameters of B, n_e, and T were used to calculate radio emission maps at 100 frequencies, and the figure shows the resulting spectra at two points in the active region, in both right and left circular polarization, after folding through the expected FASR instrumental response. Such spectra will be available at every resolution element in the maps. This demonstrates that

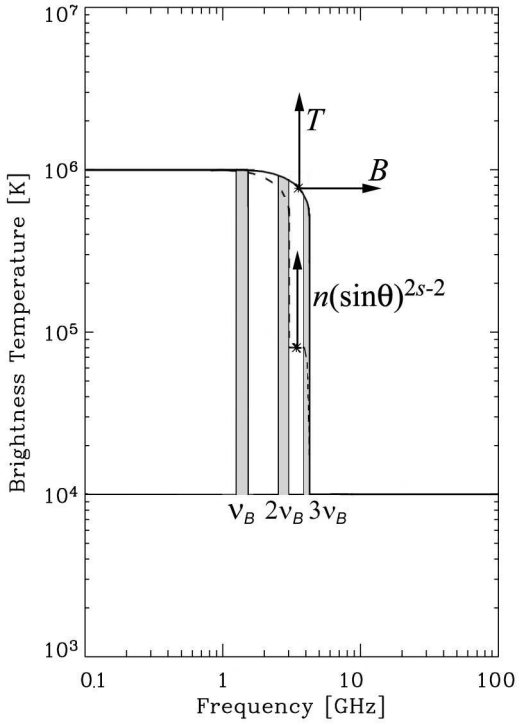


Figure 4.4. "Universal Spectra" for gyroresonance emission. See text for details.

parameters of electron temperature and magnetic field strength can be simply determined directly from such spectra. Thus, FASR will provide precise diagnostics without the need for assumptions of constant T_e, n_e, or $\sin\theta$ along the line of sight.

In the more general case, the optically thick spectral shape will be a sensitive measure of the variations of T_e as a function of B, while the spectral shapes of optically thin "plateaus" will indicate changes in n_e and θ with B. In practice, the dependence on θ is rather steep and will likely swamp the linear dependence on n_e. Time variations in the shape of these plateaus will provide a sensitive measure of large-scale oscillations in the direction of the magnetic field, as has already been shown with single- and dual-frquency observations (Shibasaki 2001; Nindos *et al.* 2002). The conversion of variations of T_e as a function of B to T_e as a function of absolute distance along the line of sight, of course, requires a knowledge of the dependence of B along the line of sight, which is an unsolved problem. Careful analysis based on photospheric field extrapolations, indications from observations at other wavelengths, and physical relationships

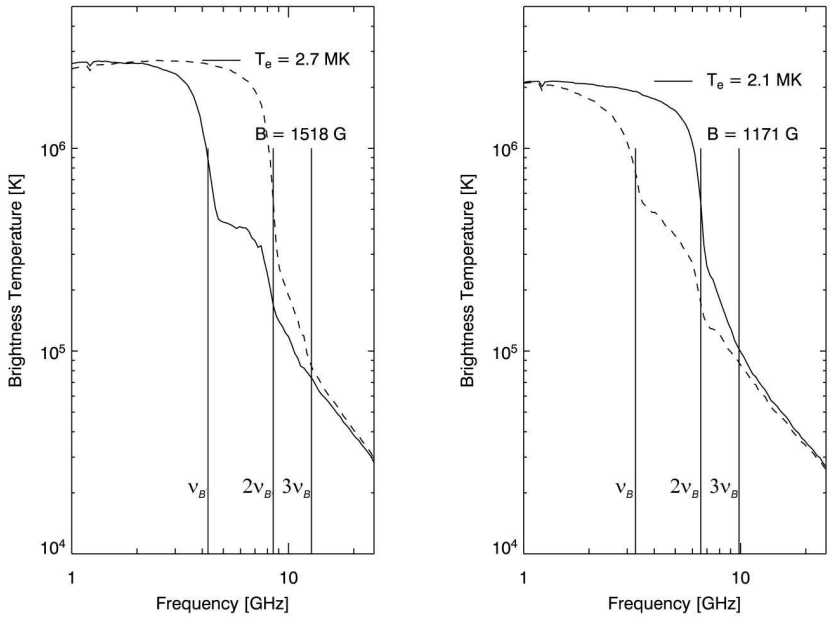


Figure 4.5. The right-hand circular polarization (RCP, solid curve) and left-hand circular polarization (LCP, dashed curve) radio emission spectra at two lines of sight in a model active region, as calculated at 100 frequencies from 1–24 GHz, after folding through the instrumental response. The electron temperature of the corona can be read directly from the spectra at low frequencies, where the emission is optically thick. The frequency at which abrupt drops in brightness occur are identified with different harmonics of the gyrofrequency (vertical lines), allowing the magnetic field strength to be unambiguously determined.

such as pressure balance and continuity offer the prospect that a full 3-D model of the solar active region atmosphere could be obtained. This lofty goal has not been accomplished to date, but efforts are underway (e.g. Mok *et al.* 2001; 2004).

6. Gyrosynchrotron Diagnostics

The main emission mechanism during solar flares, at least at frequencies > 3 GHz, is gyrosynchrotron emission from mildly-relativistic electrons of order several hundred keV. For such energies, the theoretical expressions must be solved numerically. The spectral shapes expected from thermal and powerlaw nonthermal isotropic electron distributions were given by Dulk (1985), along with empirical powerlaw expressions for emissivity, opacity, effective temperature, degree of polarization, and others, obtained from fits to the numerical

results. For powerlaw electron distributions, the spectral shapes remain invariant with such parameters as number density of fast electrons, magnetic field strength and direction, but the slopes of the spectrum do vary with electron powerlaw index δ. The concept of Universal Spectra can still be used for homogeneous sources in this case, so long as the variation in spectral slope with δ is specified.

Figure 4.6 shows the resulting Universal Spectra, again for homogeneous sources, for both thermal and powerlaw nonthermal distributions (left and right panels respectively). The arrows indicate the direction and magnitude of shift for increases in the labeled parameter by a factor of 4. The positive slope on the optically thick (low frequency) side of the brightness temperature spectrum is due to the rising effective energy, E, of the electrons producing the emission, $T_b = E/k_B$. Changes in the column density, $N_e L$ shift the spectra nearly parallel to this rising slope. The optically thin (high frequency) slope is directly proportional to the powerlaw index of the electron energy distribution. The spectra in each panel shown by the dashed lines schematically indicate the o-mode emission, to show the typical spectral pattern of circular polarization expected from a homogeneous source.

However, several effects can alter these simple relationships, even for a homogeneous source. On the optically thick side, the ambient medium can affect the shape either because of extra absorption by co-spatial thermal plasma (e.g. Benka & Holman (1992), or by suppression of the emission due to Razin Suppression (at frequencies $\nu < 20 n_e/B$). On the optically thin side, recent work by Fleishman & Melnikov (2003ab) shows that non-isotropic pitch angle distributions for the electrons can significantly alter the high-frequency slope, and greatly change the polarization. Observationally, flaring loops have been imaged typically at two frequencies (e.g. Dulk *et al.* 1986; Nindos *et al.* 2000; Melnikov *et al.* 2002), although some events have been imaged at many frequencies (e.g. Lim *et al.* 1994; Wang *et al.* 1994; 1995; 1996) with moderate spatial resolution. Observations of the spectral and spatial dynamics of flaring loops (Lee *et al.* 2000; Lee & Gary 2001; Melnikov *et al.* 2002) are particularly useful as diagnostics of the evolution of accelerated electrons (see Chapter 9).

FASR will give spatially resolved spectra with sufficient quality and spatial resolution to measure the detailed changes in the spectrum at different points along flaring loops. The peak frequency of such spectra alone is enough to constrain the relative magnetic field strength along the loop, as shown in Figure 4.7. The optically thin slope directly yields the energy distribution of electrons, and possible changes with position in the loop due to transport effects, collisions, and wave-particle interactions.

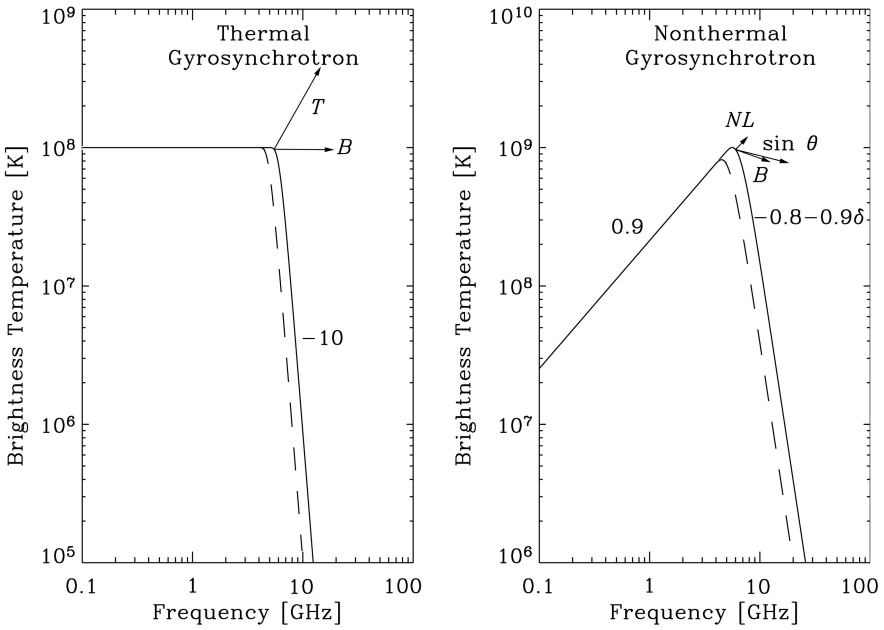


Figure 4.6. "Universal Spectra" for gyrosynchrotron emission, for a homogeneous source with thermal (left panel) or powerlaw (right panel) electron energy distributions. The solid lines show the x-mode spectra, while the dashed lines schematically show the o-mode spectra. Thermal spectra are distinguished by their flat optically thick slope, and very steep optically thin slope.

7. Exotic Mechanisms

In addition to these standard mechanisms, others have been proposed to explain certain kinds of observed emission. Here we briefly mention the Electron Cyclotron Maser (ECM) mechanism and Transition Radiation.

ECM (Holman *et al.* 1980; Melrose & Dulk 1982) is expected to operate in convergent magnetic fields in the legs of loops, where downward moving electrons escape the magnetic trap. The remaining particles form an anisotropic pitch angle distribution, which is unstable to ECM emission. The coherent emission occurs in clusters of short duration ($\sim$ 10 ms), narrowband ($\sim$ 10 MHz), high brightness ($\sim 10^{12}$ K) bursts called spike bursts. Too little is known about the spatial and spectral characteristics of ECM emission to develop spectral diagnostics (in fact, there is uncertainty whether spike bursts are due to ECM or other wave instabilities—see Chapter 10), and it may be that any such diagnostics would relate only to the detailed microphysics in the source region. Accounting for the generation and escape of the radiation may yield constraints on the surrounding plasma, however.

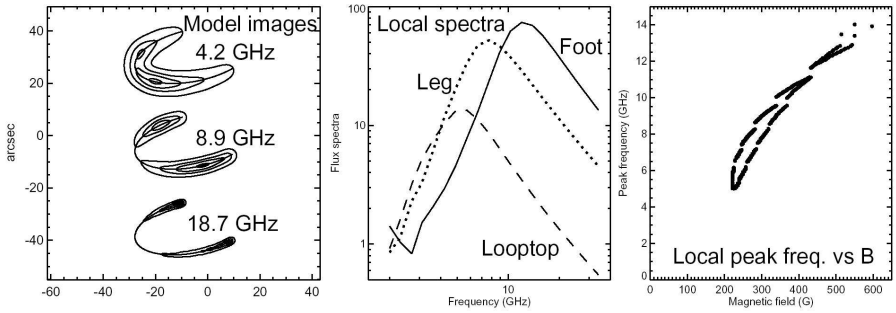


Figure 4.7. Gyrosynchrotron emission from a model coronal magnetic loop. The panel at left shows how the appearance of the loop changes from low optically thick frequencies (4.2 GHz) where the loop dominates to high optically thin frequencies (18.7 GHz) where the footpoints dominate. The thin solid line inicates the spine of the loop in each case. In the middle panel are plotted local radio spectra at three different locations within the loop: at a footpoint (solid line), at the top of the loop (dashed line), and at a location half-way up the leg of the loop (dotted line). In the right panel we plot the frequency of the peak of the radio spectrum versus the local magnetic field, showing that there is a nearly linear dependence of the spectral peak on the local magnetic field and thus spatially-resolved spectroscopy can be used to measure the variation of magnetic field along the loop. Figure by S. White, private communication.

Transition Radiation (TR) arises not due to the usual electron accelerations, but rather due to electrons moving with constant velocity through a medium with inhomogeneities or discontinuities in the dielectric constant of the medium. Although the TR theory is quite old, a full understanding of the observational characteristics had to await more recent developments in the theory (Platonov & Fleishman 1994; Platonov & Fleishman 2002). The intensity of transition radiation had been predicted to be very small and perhaps unobservable, until Platonov & Fleishman (1994) discovered that the intensity is greatly enhanced at frequencies just above the local plasma frequency. The radiation in this form is referred to as resonant transition radiation (RTR), since the plasma response to the external excitation is strengthened around the resonant frequency of the medium (Platonov & Fleishman 1994; Platonov & Fleishman 2002). The RTR emission is observable for any source when a sufficient level of small-scale inhomogeneity is present, and the emission is observed at frequencies covering the characteristic plasma frequency of the source. These conditions are met in the decimetric frequency range in the solar corona. Thus, fast electrons accelerated in solar flares can be expected to produce observable RTR in certain conditions. The problem is to recognize it in the presence of simultaneously occurring competing mechanisms, such as gyrosynchrotron emission, electron-

cyclotron emission, or coherent plasma emission. The theory of transition radiation generated by fast particles is discussed in detail in a recent review paper by Platonov & Fleishman (2002).

8. Conclusion

This chapter has reviewed mechanisms relevant to solar radio emission with emphasis on the resulting spatially-resolved spectra. The regimes of applicability of these different mechanisms are explained in terms of the relative values of the local plasma frequency, gyrofrequency and the frequency at which free-free emission becomes optically thick. In the case of incoherent emission (free-free, gyroresonance, thermal and nonthermal gyrosynchrotron), so-called "Universal Spectra" show that *for uniform source parameters along a line of sight*, the spectral shapes are invariant, with spectral parameters readily related to the electron and magnetic field parameters. Changes in these physical parameters from point to point in the solar atmosphere merely act to shift the location of the Universal Spectra while maintaining their shape. For non-uniform parameters along the line of sight, the shapes can change due to superposition of contributions of the invariant spectra for a given mechanism, or even contributions from multiple mechanisms. However, we also outline basic approaches whereby such contributions can be inverted, given the high quality spectra expected from FASR, so that 3-dimensional solar radio diagnostics can be anticipated. A key reason that this can be done for radio emission, in contrast to the case of X-ray or EUV emission, is that the radio emission is optically thick at some frequencies and optically thin at others. Thus, the "line of sight" is really many lines of sight of different lengths at different frequencies, giving extra information about the distribution of plasma parameters along the line of sight. As we mentioned earlier, additional information can be gleaned from measuring spectra in both circular polarizations, which essentially give two independent, but mutually consistent diagnostics of plasma parameters along the line of sight.

The "Universal Spectra" approach that we have outlined is thus meant to be schematic only, to demonstrate the basics of using the radio spectrum to deduce both parameters of the solar atmosphere and characteristics of energetic particles in flaring regions. The high spatial and spectral resolution FASR data will permit far more sophisticated analysis, yielding a diagnostic precision far greater than any so far available. In fact, the anticipation of FASR observations is already spurring theoretical and modeling efforts to explore the range of new diagnostics that FASR will make possible, some of which are described in this book. Even more exciting, the FASR data will undoubtedly show many puzzling features that will not agree with our naive models, and so will lead to new understanding of the solar atmosphere and flaring loops.

Acknowledgments

This work was supported by NASA grant NAS5-11875 to the New Jersey Institute of Technology (NJIT) and by NSF grant AST-0138317 to NJIT with subcontract to University of California/Berkeley.

References

Bastian, T. S., Ewell, M. W., & Zirin, H. 1993, ApJ, 415, 364
Benka, S. G. & Holman, G. D. 1992, ApJ, 391, 854
Boischot, A. 1959, Ann. Astrophys. 21, 273
Dulk, G. A. & McLean, D. J. 1978, Solar Phys, 57, 279
Dulk, G. A. 1985, ARAA, 23, 169
Dulk, G. A., Bastian, T. S., & Kane, S. R. 1986, ApJ, 300, 438
Fleishman, G. D. & Melnikov, V. F. 2003*a*, ApJ, 584, 1071
Fleishman, G. D. & Melnikov, V. F. 2003*b*, ApJ, 587, 823
Gary, D. E. & Hurford, G. J. 1994, ApJ, 420, 903
Grebinskij, A., Bogod, V., Gelfreikh, G., Urpo, S., Pohjolainen, S., & Shibasaki, K. 2000, A&AS, 144, 169
Holman, G. D., Eichler, D., & Kundu, M. R. 1980, IAU Symp. 86: Radio Physics of the Sun, 86, 457
Hurford, G. J. & Gary, D. E. 1986, Coronal and Prominence Plasmas, 319
Hurford, G. J., Gary, D. E., & Garrett, H. B. 1985, Radio Stars; Proceedings of the Workshop on Stellar Continuum Radio Astronomy, 379
Lee, J. & Gary, D. E. 2000, ApJ, 543, 457
Lee, J., Gary, D. E., & Shibasaki, K. 2000, ApJ, 531, 1109
Lim, J., Gary, D. E., Hurford, G. J., & Lemen, J. R. 1994, ApJ, 430, 425
Melnikov, V. F., Reznikova, V. E., Yokoyama, T., & Shibasaki, K. 2002, The 10th European Solar Physics Meeting, (Ed. A. Wilson.), ESA SP-506, Vol. 1. 339
Melrose, D. B. & Dulk, G. A. 1982, ApJ, 259, 844
Mok, Y., Lionello, R., Mikic, Z., & Linker, J. 2004, ApJ, submitted
Mok, Y., Lionello, R., Mikic, Z., & Linker, J. 2002, American Astronomical Society Meeting, 200, abstract #2.12
Mok, Y., Lionello, R., Mikic, Z., & Linker, J. 2001, American Geophysical Union, Spring Meeting 2001, abstract #SH41A-20, 41
Nindos, A., White, S. M., Kundu, M. R., & Gary, D. E. 2000, ApJ, 533, 1053
Nindos, A., Alissandrakis, C. E., Gelfreikh, G. B., Bogod, V. M., & Gontikakis, C. 2002, A&A, 386, 658
Platonov, K. Y. & Fleishman, G. D. 1994, Journal of Experimental and Theoretical Physics, 79, 572
Platonov, K. Y. & Fleishman, G. D. 2002, Uspekhi Fizicheskikh Nauk, 45, 235

Saito, K., Makita, M., Nishi, K., & Hata, S. 1970, Annals of the Tokyo Astronomical Observatory, 12, 51
Shibasaki, K. 2001, ApJ, 550, 1113
Vernazza, J. E., Avrett, E. H., & Loeser, R. 1981, ApJ Supp., 45, 635
Wang, H., Gary, D. E., Zirin, H., Nitta, N., Schwartz, R. A., & Kosugi, T. 1996, ApJ, 456, 403
Wang, H., Gary, D. E., Zirin, H., Kosugi, T., Schwartz, R. A., & Linford, G. 1995, ApJ, 444, L115
Wang, H., Gary, D. E., Lim, J., & Schwartz, R. A. 1994, ApJ, 433, 379
Wild, J. P. & McCready, L. L. 1950, Aust. J. Sci. Res., A-3, 387
Wild, J. P., Sheridan, K. V., & Trent, G. H. 1959, in Paris Symp. on Solar Radio Astronomy, Ed. R.N. Bracewell, Stanford Univ. Press, 176

Chapter 5

CORONAL MAGNETIC FIELD MEASUREMENTS THROUGH GYRORESONANCE EMISSION

Stephen M. White
Department of Astronomy, University of Maryland
College Park MD 20742 USA
white@astro.umd.edu

Abstract This article reviews the use of gyroresonance emission at radio wavelengths to measure coronal magnetic fields. The spiralling motion of electrons in the 200–2000 G fields in the solar corona produces sufficient opacity to render the corona optically thick, making it easy to recognize such sources in microwave images from their coronal brightness temperatures. Where gyroresonance sources are present they may be used as sensitive probes of the magnetic field strength above active regions, and this unique capability is one of the strengths of radio observations. Typically a gyroresonance radio source shows the temperature on an optically thick surface of constant magnetic field within the corona. Since each radio frequency corresponds to a different magnetic field strength, the coronal structure can be "peeled away" by using different frequencies.

Keywords: Sun, solar corona, solar magnetic fields, solar radio emission

Introduction

Since the realization in the early 1960s (Ginzburg & Zheleznyakov 1961; Kakinuma & Swarup 1962; Zheleznyakov 1962) that the strong radio emission observed from solar active regions was associated with gyroresonance opacity, radio observations have provided a direct measurement of magnetic field strengths in the solar corona. It is a happy coincidence that the low harmonics of the range of magnetic field strengths found in the corona (up to 2500 G) correspond to the range of microwave frequencies (1–20 GHz) for which atmospheric transmission is not an issue and high spatial resolution radio observations are

readily feasible. In this review we discuss the ideas behind the use of radio observations to determine the magnetic field strength in the corona.

Both of the mechanisms responsible for opacity in the active region corona at radio wavelengths, gyroresonance emission and bremsstrahlung (free electrons deflected by ions and remaining unbound, hence also known as free-free emission), are sensitive to the magnetic field. Bremsstrahlung emission in a magnetic field is polarized because the magnetic field breaks the degeneracy in properties of the two natural wave modes, so that information on the field is contained only in the polarized signal. In gyroresonance emission the effect is much more direct: it is the acceleration of electrons by the $\mathbf{v} \times \mathbf{B}$ magnetic force itself which produces the opacity, so that each polarization by itself independently contains information on the magnetic field. Thus bremsstrahlung and gyroresonance emission provide quite different diagnostics. At frequencies below ~ 3 GHz bremsstrahlung tends to dominate active region emission, making the corona optically thick at heights above the gyroresonance layers. At these low frequencies bremsstrahlung is usually the only emission available for coronal magnetic field diagnostics, and the application of bremsstrahlung for these purposes is discussed in Chapter 6, by Gelfreikh. Chapter 13, by Brosius, describes techniques by which both bremsstrahlung and gyroresonance diagnostics can be combined in investigating coronal magnetic fields. Another relevant effect is the change in polarization induced by propagation through the magnetized plasma of the solar atmosphere, discussed in Chapter 7, by Ryabov.

In the next section we briefly contrast the problems of measuring photospheric and coronal magnetic fields, then discuss the basic properties of thermal gyroresonance emission (also known as cyclotron emission), and show how these properties determine the radio appearance of solar active regions. We also discuss some of the limitations of radio observations. Many people have contributed over the years to our understanding of gyroresonance emission from the corona, and we will not attempt to ascribe credit for each specific development. Previous papers covering similar topics include Zlotnik (1968a, b), Zheleznyakov (1970), Lantos (1972), Gelfreikh & Lubyshev (1979), Alissandrakis, Kundu & Lantos (1980), Krüger, Hildenbrandt & Fürstenberg (1985), Hurford (1986), Brosius & Holman (1989), Lee, Hurford & Gary (1993), Vourlidas (1996), and White & Kundu (1997).

1. Coronal Magnetic Fields are Intrinsically 3D

An important aspect of coronal magnetic fields that needs to be appreciated is that they are intrinsically three dimensional, and this makes their measurement a fundamentally different problem from that of measuring magnetic fields at the solar photosphere. The solar photosphere is a well-defined two-dimensional surface at which the solar atmosphere becomes optically thin to photons at op-

tical wavelengths. To quite a good approximation, the photosphere is spherical: the largest deviations from a sphere occur in the Wilson depressions in the umbrae of large sunspots, which may be several hundred km below the normal radius of the photosphere (e.g., Bray & Loughhead 1964). Thus observations of the Zeeman effect in optical lines can be safely assumed to come from a sharp two-dimensional surface, and the magnetic field strengths measured from such data come from a known height (although often radiative transfer in the lower atmosphere must be taken into account in order to untangle complicated Zeeman profiles). Even in the case of chromospheric and transition region lines, the thickness of the emitting layer is small compared to the transverse dimension of a typical resolution element.

This is far from true in the case of the corona, where densities of 10^9 cm^{-3} can be found at heights of 10^5 km. One would like to be able to measure the magnetic field strength at all heights along a given line of sight, at least to within the horizontal resolution of the data: a set of coronal magnetic field strength measurements should be three dimensional. It is difficult to see how this can be achieved with optically thin line diagnostics alone, because most of the optical, IR and EUV lines are proportional to the square of the plasma number density and thus are heavily weighted to the brightest emission feature along any given line of sight: this feature will dominate the Zeeman signal in a given pixel and no information on the field strength at other heights an be retrieved. In this case even stereo observations offer little improvement, since each pixel in both images will be dominated by the brightest feature along that line of sight and effectively one can at best double the number of points in the volume at which B is measured. If we take the notion of the dynamic corona seriously then tomography also offers little help in this regard: it is precisely the fields that change most rapidly that are often most interesting scientifically, but these are the fields for which tomography does not work since it assumes constant fields.

One of the attractions of gyroresonance emission for the measurement of coronal magnetic fields is that it is not optically thin: different magnetic field strengths are optically thick at different frequencies and thus by tuning the frequency we can peel away the corona in a truly three-dimensional nature. The vertical scale height is not easily retrieved form the radio data as we will see, but vertical information is present.

2. Extrapolations of Surface Magnetic Fields

In principal, one can determine the coronal magnetic field distribution from the photospheric magnetic field distribution under certain assumptions. Given a complete measurement of the vector magnetic field $\mathbf{B}$ at a surface, one can solve a boundary value problem for the distribution of $\mathbf{B}$ throughout the volume above the boundary using the nonlinear equations $(\nabla \times \mathbf{B}) \times \mathbf{B} = 0$ and

$\nabla \cdot \mathbf{B} = 0$. Here the assumption that the coronal field is force-free has been made, i.e., these equations are valid for a quasi-static corona in which any $\mathbf{J} \times \mathbf{B}$ forces perpendicular to magnetic field lines have been allowed to act and the corona has relaxed to a force-free state. In particular, any currents present in the corona must flow along field lines. The evolutionary timescales for the solar magnetic field outside flares and other explosive phenomena involving reconnection in the corona are slow enough that this assumption should be valid most of the time. The system of equations plus a boundary measurement set constitutes a mixed elliptic-hyperbolic boundary value problem which has proven remarkably difficult to solve (Gary 1989; McClymont & Mikić 1994; Amari *et al.* 1999). One can write generally $\nabla \times \mathbf{B} = \alpha(\mathbf{r})\mathbf{B}$ and solve for the scalar $\alpha(\mathbf{r})$, which is constant along field lines since $\mathbf{B} \cdot \nabla\alpha(\mathbf{r}) = 0$. Common approximations are the potential approximation ($\nabla \times \mathbf{B} = 0$, $\mathbf{B} = \nabla\phi$, where ϕ is a scalar potential), only valid if no currents are present, and the "linear force-free solution" (α is a constant everywhere). Unfortunately the observations indicate that α is not a constant in a given coronal region.

Numerical methods for solving the full nonlinear force-free equations have been developed. To ensure a well-posed problem, one needs a measurement of the vertical component of the magnetic field everywhere and the value of $\alpha(\mathbf{r})$ at the boundary for one polarity. Relaxation techniques have had considerable success at producing an accurate solution to the equations, as judged by comparisons with observed magnetic field lines (Jiao, McClymont, & Mikić 1997) and measured coronal magnetic field strengths (Lee *et al.* 1998), but there are some limitations: the direction of the transverse component of the magnetic field in the corona cannot be determined unambiguously (to within 180°) (e.g., Semel & Skumanich 1998); errors in measurements of the photospheric magnetic field affect the reconstruction of the coronal field (Klimchuk & Canfield 1994); and the photospheric values of α may not be appropriate in the corona since the photosphere is not force-free (Metcalf *et al.* 1995). In the future measurements of the chromospheric magnetic field may avoid this latter difficulty.

3. The Properties of Gyroresonance Emission

3.1 Physical mechanism

A collisionless plasma such as the solar corona (where a typical collision frequency, e.g., for density n_e = 10^{10} cm^{-3} and temperature $T = 2 \times 10^6$ K, is 200 Hz) may be characterized by two frequencies corresponding to electron resonances: the frequency of oscillation of electrons in the electric field of the ions, known as the plasma frequency, $\nu_p = 8980\sqrt{n_e}$ Hz; and the gyro frequency, which is the frequency of rotation of an electron about the magnetic field due to the $\mathbf{v} \times \mathbf{B}$ Lorentz force, $\nu_B = 2.80 \times 10^6\, B$ Hz, where B is measured in G. For typical conditions in gyroresonant sources above active regions

($n_e = 10^{10}$ cm^{-3} and $B \gtrsim 300$ G), $\nu_B > \nu_p$. In such a plasma the propagating electromagnetic modes corresponding to the free-space radiation modes are circularly polarized under most conditions. One of the modes, known as the *extraordinary* or x mode, gyrates about the magnetic field with the same sense of rotation as an electron, and therefore resonates strongly with the thermal electron population; the other mode, known as the *ordinary* or o mode, gyrates about the magnetic field direction with the sense opposite to that of the electron, and correspondingly interacts much less strongly. Since a radio telescope can generally detect both modes independently, as opposite circular polarizations, this difference in the strength of interaction of the two modes provides a powerful diagnostic.

The frequency width of a given cyclotron resonance $\propto \mu^{-1/2} s\nu_B$, where $\mu = m_e c^2/k_B T$. Since $\mu \approx 3000$ in the corona, the cyclotron resonances are very narrow and, for a given value of ν_B, opacity is only significant at frequencies very close to discrete harmonics $s\nu_B$, s = 1,2,3,... (at much higher temperatures the individual resonances have significant width and may overlap). Equivalently, if we are observing an inhomogeneous corona at a frequency ν, gyroresonance opacity is only significant at those discrete points along the line of sight at which $\nu_B = \nu/s$, s = 1,2,3,... The thermal width of the cyclotron resonance at coronal temperatures is such that B varies by less than 2% across a resonant layer, corresponding to a physical width of less than 200 km for typical coronal magnetic gradients (scale length $\sim 10^4$ km). The narrow physical thickness of the gyroresonant layers is an important feature of this mechanism: since they are much smaller than relevant gradients in n_e, B and T (except possibly in the vicinity of current sheets), these physical properties may be regarded as constant across any given gyroresonant layer.

3.2 Opacity

The formal expression for gyroresonance opacity is discussed in many places (Zheleznyakov 1970; Melrose 1980; Robinson & Melrose 1984) and will not be derived here. Instead we will simply quote the expression for the optical depth τ of a gyroresonance layer (the absorption coefficient integrated through the layer) as a function of the frequency ν, the harmonic number s (which determines $\nu_B = \nu/s$ and hence B in the layer), and the angle θ between the magnetic field direction and the line of sight:

$$\tau_{x,o}(s,\nu,\theta) \;=\; .0133\,\frac{n_e\,L_B(\theta)}{\nu}\,\frac{s^2}{s!}\left(\frac{s^2\,\sin^2\theta}{2\,\mu}\right)^{s-1} F_{x,o}(\theta) \qquad (5.1)$$

where $L_B(\theta)$ is the scale length of the magnetic field ($B/\frac{\partial B}{\partial l}$) evaluated along the line of sight. For simplicity we have set the refractive index to be unity

in (5.1). $F_{x,o}(\theta)$ is a function of angle which is of order unity for the x mode near $\theta = 90^\circ$, but decreases sharply at smaller θ, and is smaller in the o mode than in the x mode. At angles θ away from 90° it is often approximated by

$$F_{x,o}(\theta) \approx \left(1 - \sigma \cos\theta\right)^2 \tag{5.2}$$

with $\sigma = -1$ for the x mode and $\sigma = 1$ for the o mode. However, this approximation is really only appropriate when the two natural electromagnetic modes are perfectly circularly polarized, and at the low harmonics (s = 1,2,3,4) relevant to the corona this is rarely a good assumption. Zlotnik (1968a) presents accurate expressions for $F_{x,o}(\theta)$ which correctly handle the mode polarization properties. (Note that Zlotnik's formulae are presented in the limit that the refractive index is unity, and require a small correction when $\nu_p \sim \nu_B$.)

In Figure 5.1 we present exact calculations of τ, the optical depth of a gyroresonant layer, for typical coronal conditions ($T = 3 \times 10^6$ K, $L_B = 10^9$ cm) and a fixed frequency of 5 GHz at the appropriate harmonics s = 2, 3 and 4. Both the x (solid lines) and o (dashed lines) modes are shown. For comparison, we also plot the approximation represented by (5.2) (dotted lines).

A number of features should be noted in this figure:

- For typical coronal conditions, the x mode is optically thick ($\tau \geq 1$) in the s = 2 and 3 layers over a broad range of angles θ. The o mode is optically thick over most of the s = 2 layer, and may be at least marginally optically thick over a small portion of the s = 3 layer if θ is large. Harmonics greater than s = 4 do not have any significant optical depth in the quiet solar corona.

- At each harmonic and angle the o mode opacity is always at least an order of magnitude smaller than the x mode opacity, despite the fact that (5.2) predicts that they should be nearly equal for a range of θ around 90°. The approximation (5.2) is adequate for the x mode at small θ, but is poor for the o mode at all θ, being easily a factor of 2 or more in error even at small angles.

- The opacity drops sharply towards small θ in both modes. At angles very close to 90°, the o mode opacity dips sharply since it must be a factor of μ smaller than the x mode opacity exactly at θ = 90° (e.g., Bornatici *et al.* 1983, Robinson 1991). By (5.1), the opacity is zero at θ = 0° for $s > 1$. The $\sin^{2s-2}\theta$-dependence of (5.1) causes the fall-off towards small θ to be much more rapid as s increases.

- For each increase of s by 1, the opacity in a given mode at a given angle drops by slightly more than 2 orders of magnitude. This is largely due to the μ^{-s} dependence of (5.1). The importance of this large change in

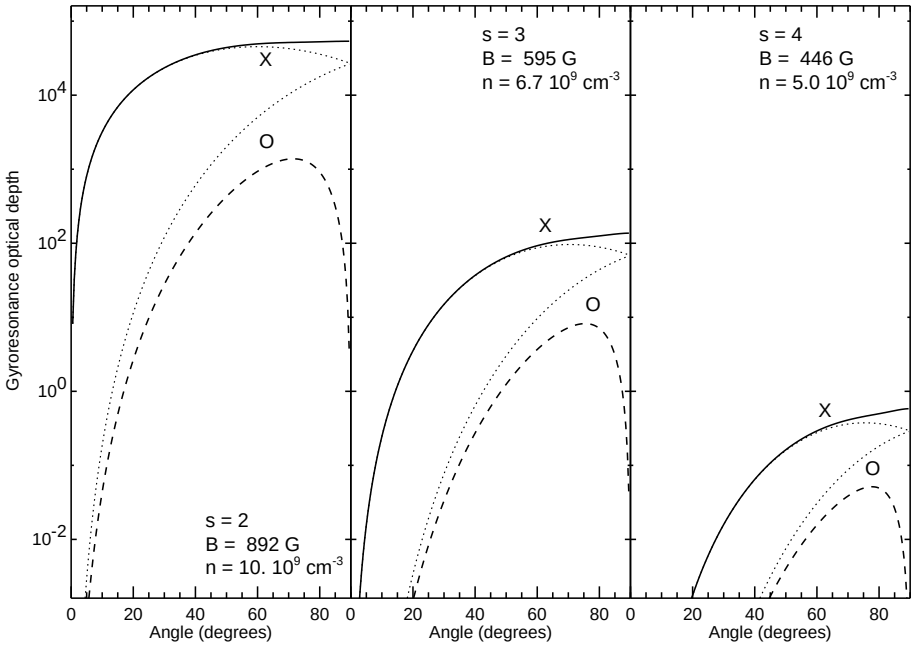


Figure 5.1. The (integrated) optical depth of the $s = 2, 3, 4$ gyroresonance layers at 5 GHz (left, middle and right panels, respectively) as a function of the angle θ between the line of sight and the magnetic field direction. The temperature in the source is 3×10^6 K, and the magnetic scale height L_B is 10^9 cm. In each panel the solid line is the optical depth of the layer in the x mode, and the dashed line is the optical depth in the o mode. The dotted lines show the optical depth obtained using the circularly-polarized mode approximation (5.2). The density used for this calculation was decreased as s increases to simulate the decrease of n_e with height: the values are shown in each panel.

opacity from one layer to the next is that a given harmonic layer is likely to be either optically thick over a wide range of angles θ, or else optically thin everywhere.

An important point to be emphasized is that gyroresonance observations are sensitive to the absolute magnetic field strength B, whereas conventional (Babcock or Leighton style) optical magnetographs measure only the line-of-sight component of the magnetic field, $B\cos\theta$, and thus are of limited value for regions near the solar limb. Further, in many cases magnetographs measure magnetic flux averaged over a resolution element (a pixel or a seeing cell) and are thus affected by the filling factor of the magnetic field within the resolution element; radio observations are not affected by this filling factor.

4. Gyroresonance Radio Emission from Active Regions

4.1 Radio emission from a dipole magnetic field

Here we will use a dipole magnetic field (vertically-oriented and seen looking directly onto one pole, often used as a model for isolated sunspots) to illustrate the ways in which the properties of gyroresonance emission affect the appearance of solar active regions at microwave frequencies. Figure 5.2 shows the expected appearance of a a perfectly dipolar field (of peak surface field strength 2500 G) at a frequency of 5 GHz. The upper panel shows the four lowest gyroresonant layers (s = 1, 2, 3, 4, corresponding to B = 1785, 892, 595 and 446 G, respectively), with the line-type indicating whether the layer is optically thick in a given mode. A solid line in the upper panel indicates that the layer is optically thick at both x and o modes; a dashed line indicates that only the x mode is optically thick; and a thin dotted line represents a region of the layer optically thin in both modes. The thin solid lines are magnetic field lines. In the bottom panel we plot the brightness temperature (Chapter 13, by Brosius, summarizes radiative transfer terminology) seen by an observer looking straight down on the dipole. In this panel the solid line represents the x mode brightness temperature, which the observer will see as one circular polarization (right circular polarization if the spot is of positive magnetic polarity), while the dashed line represents the o mode (seen by the observer as the opposite circular polarization).

A height of zero in the atmospheric model used for this calculation corresponds to the base of the corona. The density is 10^{10} cm^{-3} at the base and decreases exponentially with a scale height of 5000 km. The temperature is 6000 K below the corona and 1.0×10^6 K at the base, increasing to 3.0×10^6 K at a height of about 15000 km. The morphology of the radio emission can easily be understood by referring to the gyroresonance (GR) layers and the details of the temperature model, and recalling that along any given line of sight we only see down to the highest optically thick layer:

- Neither mode is optically thick in the $s = 4$ layer, but at the outer edges of this layer there is enough opacity in the x mode to produce a brightness temperature of order 10^5 K, which provides the outer boundary of the radio source.

- On the $s = 3$ layer, the o mode is only (marginally) optically thick at the low-lying outer edge of the layer where θ is largest, but the temperature is relatively low there because of the low altitude. The x mode is optically thick in the $s = 3$ layer to within $\sim$ 5000 km from the center of the umbra, and the peak brightness temperature in the x mode occurs close to the inner edge of this optically-thick region since the height of the layer, and therefore the temperature, is maximum there.

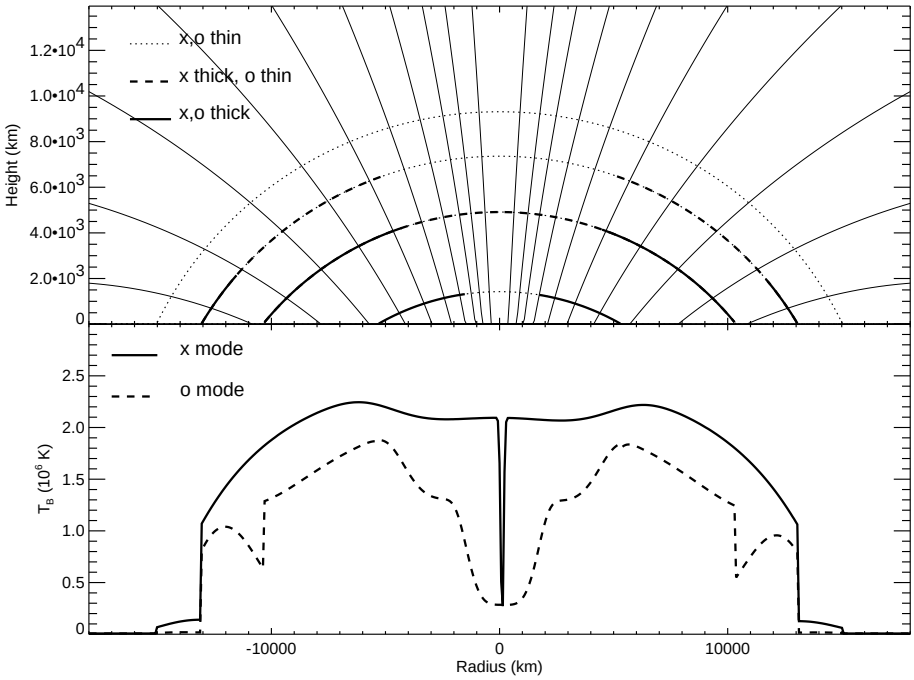


Figure 5.2. Plots of the gyroresonance layers of a dipole sunspot model (upper panel) and the predicted brightness temperatures resulting from an observation of such a spot (lower panel), viewed nearly vertically (actually 1° off vertical). In the upper panel the thin solid lines are magnetic lines of force and the dotted lines are the $s = 1, 2, 3, 4$ gyroresonance layers, with $s = 4$ the highest and $s = 1$ the lowest layer. Where the gyroresonance layers are optically thick (i.e., $\tau \geq 1$) in the o mode, they have been overplotted with a thick solid line. Except in the $s = 1$ layer where the x mode does not propagate, a layer which is optically-thick in the o mode is also thick in the x mode. If a gyroresonance layer is optically thick in the x mode but not in the o mode, it is overplotted with a thick dashed line. In the lower panel, the x-mode brightness temperature is shown by a solid line and the o mode brightness temperature by a dashed line. The frequency is 5.0 GHz, the dipole is buried at a depth of 1.2×10^9 cm, and the maximum field strength at the surface is 2500 G. In the model temperature increases with radial height from 1.0×10^6 K at the base of the corona (zero height in this case) to 3.0×10^6 K at about 15000 km.

- At smaller radii where the $s = 3$ layer is optically thin, the main contribution to the x mode comes from the $s = 2$ layer which is lower and therefore at a lower temperature: this shows up as a drop in brightness temperature at small radii.

- In the very center of the $s = 2$ layer where the line-of-sight is along the field line, the x mode is optically thin and there is a narrow low-

temperature feature. However, it is only a fraction of an arcsecond across and would be difficult to observe.

- In the o mode the central depression in brightness temperature due to the transparency of the $s = 2$ layer at small θ is much broader, and at the center of the spot even the $s = 1$ layer is optically thin in the o mode, but still has sufficient opacity to maintain the brightness temperature at 3.0×10^5 K.

- The sharp features in the o mode profile at radii of order 10^4 km are due to the gap between the radius at which the optically thick $s = 2$ layer drops beneath the corona and the radius at which θ increases sufficiently for the $s = 3$ layer to become (in this case only marginally) optically thick.

4.2 The effect of viewing angle

Since the angle θ is so important in determining the opacity of a GR layer, changing the viewing angle can have a dramatic effect on the appearance of the radio source and this is shown in Figure 5.3, where we view the same dipolar coronal field at an angle 20° to the vertical. The format of the figure is identical to that of Fig. 5.2 except that the dipole and the surface have been tilted to show them as the observer would see them. On the far side of the spot from the observer (the left side of this figure) the field lines at the outer edge of the GR layers are nearly orthogonal to the line of sight and this leads to a large opacity in both modes in the $s = 3$ layer there and consequently a relatively small difference in brightness temperature between the two modes. Because the $s = 3$ layer is optically thick to a greater height on the far side where θ is larger, peak brightness temperatures are higher there than on the near side, where the o mode in particular shows structure due to changes in opacity and differences in temperature between the different layers.

4.3 Variation with frequency

The change in appearance of the radio emission as frequency changes may be seen in Figure 5.4, where we plot the radio profiles across the dipolar field viewed from directly above in the x (upper panel) and o (lower panel) modes at frequencies from 4 GHz (outermost curve) to 16 GHz (innermost curve) at an interval of 1 GHz. Since higher frequencies correspond to stronger magnetic fields, source size decreases as frequency rises. In the o mode the sharp edges at the outer boundaries of the $s = 3$ and $s = 2$ layers are readily evident, changing in dimension as frequency and correspondingly the appropriate value of magnetic field strength change. In the x mode the outer edges of the $s = 3$ and $s = 4$ layers are evident at lower frequencies, while the outer edge of

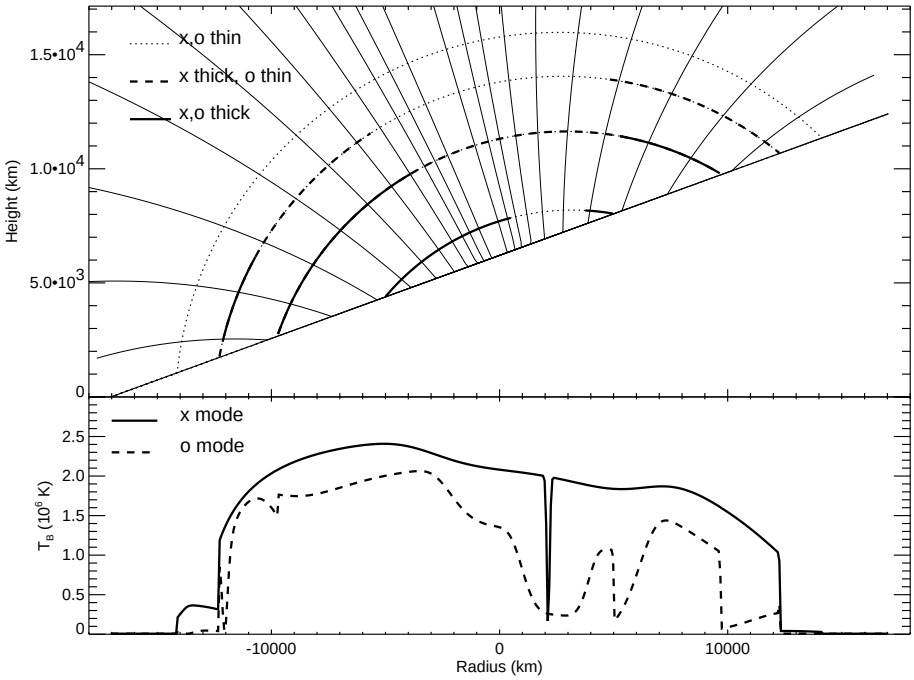


Figure 5.3. A plot in format identical to Figure 5.2, except that now the sunspot is viewed from an angle at 20° to the axis of the dipole (the observer is again at the top of the page). The brightness temperature profiles in the bottom panel are shown as the observer would see them in projection.

the $s = 2$ layer becomes apparent at higher frequencies. There is a dramatic drop in the peak brightness temperature of the x mode near the center of the spot when the $s = 2$ layer drops below the corona, since the $s = 3$ layer is optically thin at these small viewing angles. The general drop in brightness temperature as frequency rises is due to the fact that at higher frequencies the GR layers are lower in the corona and therefore, in this model, lie in regions of lower temperature.

Spectra at four different radii and the area-weighted spectrum of the whole spot are shown in Figure 5.5. Each individual local x mode spectrum is fairly smooth at low frequencies where we simply see the third-harmonic GR layer move down the temperature gradient as ν and therefore B increases. The local o mode spectra show more structure due to the different harmonic resonance layers along each line of sight, while the averaged spectrum shows essentially no structure. In all cases for this model the x mode is brighter than the o mode since, on average, the x mode opacity occurs higher up the temperature gradient. In other models this need not be the case: in situations where the x mode is

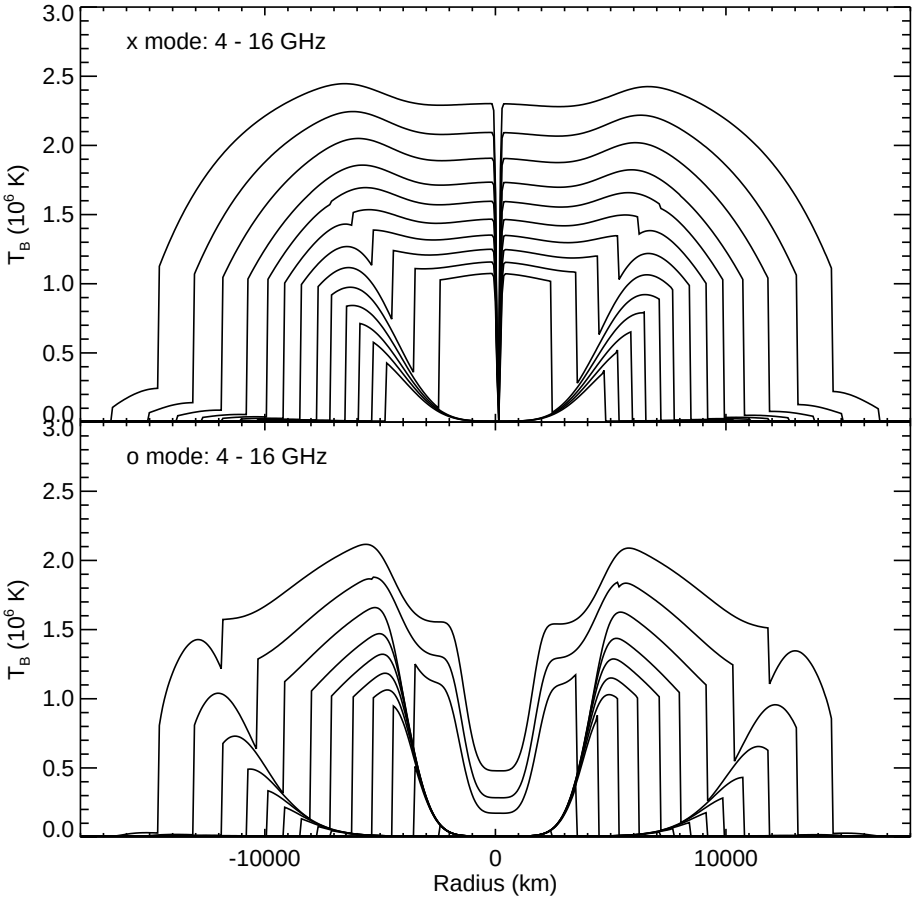


Figure 5.4. Brightness-temperature profiles across the dipole sunspot model of Figure 5.2 at frequencies spaced by 1 GHz from 4 to 16 GHz. The upper panel shows the x mode profiles and the lower panel the o mode. In each panel the lowest-frequency profiles are the outside profiles.

optically thick in the $s = 3$ layer but the highest layer in which the o mode is optically thick is $s = 2$, the overall emission will be polarized in the sense of the o mode if the temperature structure is such that the deeper $s = 2$ layer is hotter than the $s = 3$ layer. Vourlidas (1996) interprets a detection of o mode polarization from a sunspot in terms of a temperature structure of this type.

The structure revealed at many closely-spaced frequencies in these models shows that appropriate observations contain a great deal of information about both the magnetic field and temperature of the corona. The contrast between the local spectra and the mean spectrum of the spot indicates the value of high spatial resolution in studies of this kind.

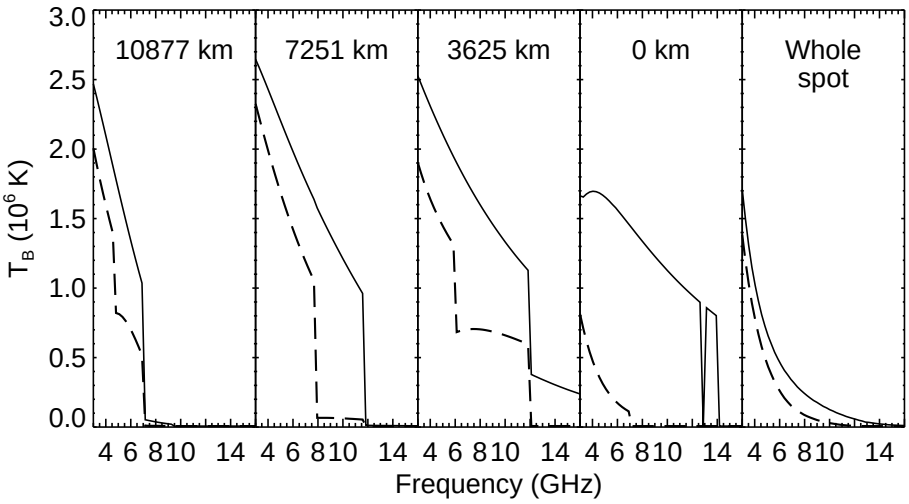


Figure 5.5. Spectra of the brightness temperature at 4 different locations across the spot in Figure 5.4 (first 4 panels) and a spectrum averaged across the whole spot (last panel). The spectra are labelled according to their distance from the center of the spot. The x mode brightness temperature is plotted with a solid line and the o mode brightness temperature with a dashed line.

5. Observational Examples

We have used a dipolar magnetic field with simple temperature gradients as examples here because they are particularly straightforward to calculate, but the basic principles apply to all gyroresonance emission. Rarely do actual observations show the straightforward structure of our models. Isolated sunspots viewed near the center of the disk can show the basic pattern of a symmetric ring of emission, with low brightness temperatures over the umbra where θ is small. An example of profiles from such a sunspot is shown in Figure 5.6, taken from Zlotnik *et al.* (1996).

This is a VLA[1] observation with data at the frequencies 4.5, 5.0, 8.0, 8.4, 14.7 and 15.0 GHz. At the two highest frequencies there are no optically-thick GR layers in the corona and brightness temperatures remain low. In general we see that the brightness temperature decreases steadily as frequency increases, and the x mode brightness temperature everywhere exceeds the o mode brightness temperature at the same frequency. As discussed in the previous section, this combination of properties suggests a positive gradient of temperature with height, at least over the range of heights covered by these observations. The

[1]The VLA is a facility of the National Radio Astronomy Observatory, which is operated by Associated Universities, Inc., under cooperative agreement with the National Science Foundation.

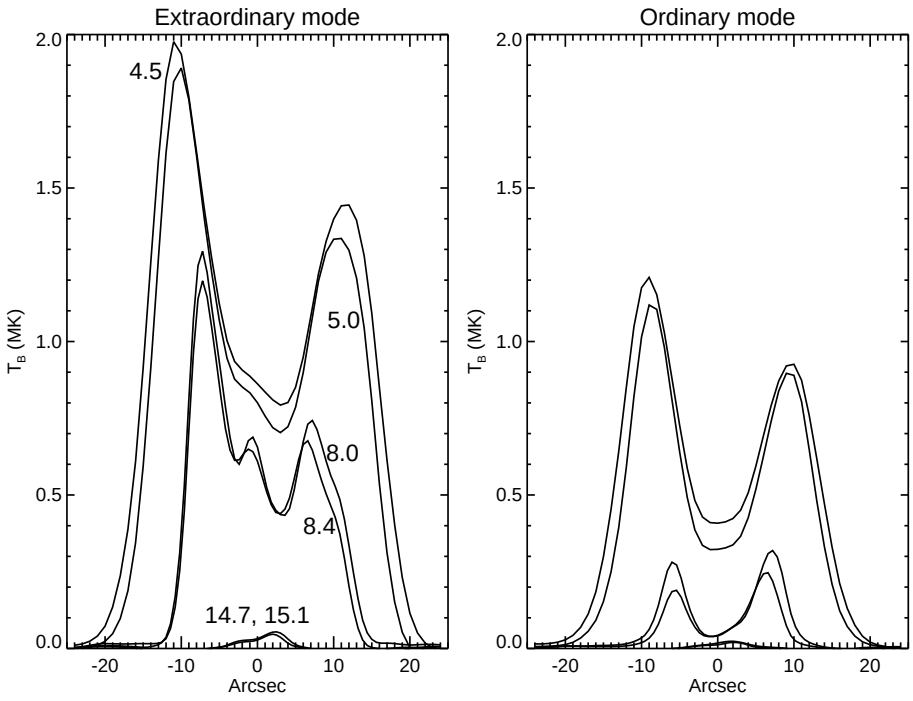


Figure 5.6. Brightness-temperature profiles across an isolated sunspot observed near disk center (actually 13° north-west of disk center) with the VLA by Zlotnik *et al.*(1996). The 6 curves each show the brightness temperature along a cut across the source at a different frequency, starting with 4.5 GHz as the outermost curve, and 14.7 & 15.0 GHz as the two innermost curves. The curves are labelled according to frequency in the left panel which shows the x mode; the right panel shows the corresponding o mode profiles, which are present in the same order as in the left panel.

central depression in the x mode is far broader than the corresponding feature in Fig. 5.4. This can be explained if the temperature has a radial dependence, i.e., the corona over the umbra is cooler than over the penumbra (in Fig. 5.4 the temperature has no radial dependence). Another feature which is not consistent with the simple models is that the radio emission is brighter on the eastern side, closer to disk center, whereas in an atmosphere with a positive temperature gradient viewed at a moderate angle (e.g., Fig. 5.3), we expect the side away from disk center to have brighter radio emission. In these observations, the spatial resolution, although excellent (several arcseconds), is probably inadequate to see the sharp edges at resonance layer jumps seen in Figure 5.4.

Figure 5.7 shows another simple sunspot observed by the VLA at 8.0 GHz, in which a resonance jump may be visible. The sunspot was located 240″ west of disk center. The x mode image is quite round with a relatively flat

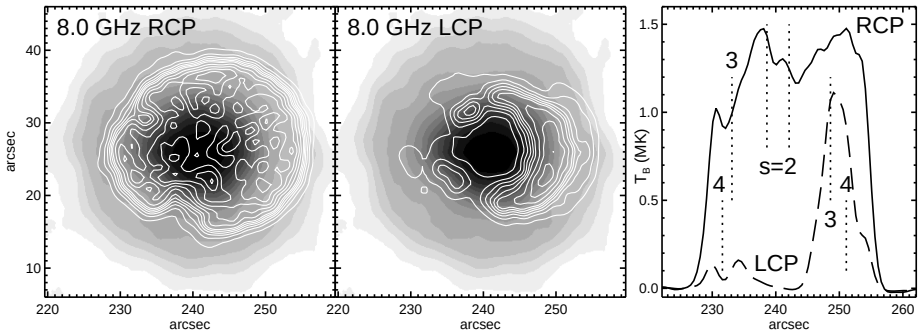


Figure 5.7. VLA observations of a sunspot on 2001 July 17 at 8.0 GHz. The left panel shows contours of right circularly polarized (RCP, the x mode for this spot) emission superimposed on a white light image, while the middle panel shows contours of left circular polarization (LCP, o mode) on the white light image. Contours are at brightness temperatures of .05, .15, ..., .55, .75, .95, ..., 1.75×10^6 K, and the resolution is $2''$. The x mode is optically thick everywhere, while the o mode shows the classic ring structure due to the fact that the opacity is low where the line of sight is parallel to the magnetic field direction and increases outwards from that point as the magnetic field lines in the corona fan outwards. The right panel shows horizontal profiles (units of 10^6 K) through the radio images at a vertical coordinate of $25''$for RCP (solid line) and LCP (dashed line), showing the presence of a number of sharp edges. For comparison, the locations of the s = 2, 3 and 4 harmonics along the same path determined from the SOHO/MDI longitudinal magnetogram in the photosphere are marked by vertical dotted lines.

brightness temperature profile across the spot, indicating that it is optically thick everywhere. It shows the typical sharp drop at the outer edges of the source where the gyroresonance layers drop out of the corona. As in Fig. 5.6, the x mode is everywhere brighter than the o mode, and the x mode source is much larger than the o mode source. The o mode image shows a nice ring structure that is markedly asymmetric, with the brightest emission on the west side of the spot. This behaviour is in perfect agreement with the earlier models: in the o mode opacity is lower than in the x mode, and it is only substantial on the far side of the spot where, by geometry, the angle between $\mathbf{B}$ and the line of sight is larger because the field lines coming out of the spot fan out as they go upwards. Another interesting feature of the o mode image is that in addition to the brightest rim of emission to the west of the umbra, there is another fainter rim of emission further west which we can attribute to the next higher harmonic, which is much fainter because it has much less opacity than the lower harmonic.

The examples used here are of simple sunspots since they most closely resemble our model calculation and therefore most straightforwardly illustrate the concepts discussed earlier. Most simple sunspots show considerable structure in the radio emission that does not fit the symmetric patterns of model dipoles, most active regions of interest are far more complicated, and the previous pub-

lished radio images of active regions (too numerous to refer to here: see White *et al.* 1992 for a list of studies published prior to 1992) show the full range of complexity. However, we emphasize that there is no difference in principle between the simple dipole model and a real active region: in the latter, as in the former, it is the interplay between the the structure of the GR layers (particularly the variation of θ over the layers) and the temperature and density structure of the corona that determines the appearance of an active region at microwave frequencies. Much of the diagnostic potential of gyroresonance emission lies in the fact that at a given frequency it reveals specific well-defined layers, and this is equally true of simple dipolar sunspots and real active regions with more convoluted GR layers.

6. Applications of Gyroresonance Emission

6.1 Coronal magnetic field measurement

One of the simplest uses of radio observations is the determination of magnetic field strengths at the base of the corona (e.g., Hurford 1986). The absolute value of the coronal magnetic field strength is important for understanding the energetics of the corona, and the availability of free energy stored in coronal magnetic fields which may be used in flares and coronal heating. Figs. 5.2–5.5 demonstrate that where the optically-thick GR layer corresponding to a given frequency and mode drops below the corona, the radio brightness temperature at that frequency and corresponding polarization shows a sharp drop from coronal to approximately chromospheric values. (Note that the transition region is not expected to be detected via gyroresonance emission if its thickness is less than $1''$ as energy balance models predict, because its signature would be confined to the line at the intersection of the $< 1''$-thick surface of the transition region with the typically $< 0''.2$-thick GR surface, and the thickness of this line is likely to be so narrow as to be undetectable.) Observationally it is a simple matter to detect such a signature. Thus the locations of the outer edges of the radio sources at differing frequencies contain information on the magnetic field strength at the base of the corona. With data such as those shown in Figs. 5.4–5.5, several harmonics can be identified unambiguously in each mode and therefore the appropriate values of s can be identified, which is essential to determine absolute values of B. In this way, it is straightforward to map the distribution of B over the base of the corona wherever the radio emission is dominated by bright gyroresonance emission. This technique has been convincingly demonstrated with the Owens Valley Solar Array (Gary & Hurford 1994).

When only a few frequencies are available, as in VLA observations such as Figure 5.8, it is possible to map the extent of the region in the corona in which the magnetic field exceeds the values which correspond to the frequencies observed. High-frequency observations allow us to estimate the maximum

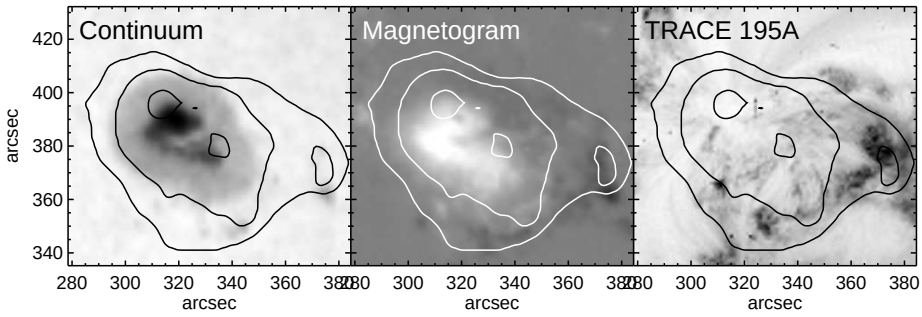


Figure 5.8. Contours of magnetic field strength at the base of the corona plotted on white light (left), magnetogram (middle) and TRACE 195 Å Fe XII (right) images of a sunspot observed on 1999 May 13. The coronal contours are plotted at 500, 900 and 1700 G, corresponding to the radio images at 4.5, 8.0 and 15.0 GHz used to construct the coronal magnetogram. Note the displacement of the 1700 G coronal magnetic field strength from the strongest photospheric fields, due in part to projection effects resulting from the height of the radio-emitting layer. Axes are labelled in arcseconds from apparent disk center.

magnetic field strength in the corona. This can be obtained from the maximum frequency ν_m GHz at which coronal brightness temperatures are observed, using the assumption that this will take place in the x mode in the $s = 3$ layer at the base of the corona where the field strength is maximum. (One feature illustrated by Figure 5.1 is that only in extreme conditions is the $s = 4$ layer optically thick, and therefore $s = 3$ is generally appropriate for this purpose.) On this assumption, the maximum field strength is $120\,\nu_m$ G. For example, if as in White *et al.* (1991) there are coronal brightness temperatures at 15 GHz, the coronal magnetic field must reach at least 1800 G. When the 17 GHz Nobeyama radioheliograph measures coronal brightness temperatures from an active region, the coronal magnetic field must exceed 2000 G (Shibasaki *et al.* 1994). When many closely-spaced frequencies have been observed, as is possible with the Owens Valley Solar Array and RATAN-600, fairly tight limits can be placed on the maximum magnetic field strength (Akhmedov *et al.* 1982; Lee *et al.* 1993; Gary & Hurford 1994).

A common argument applied to coronal magnetic field strengths is as follows: magnetic flux in the (high-β) solar photosphere tends to be concentrated in small regions of intense (kG) field strength. As this flux rises into the low-β solar corona it will expand laterally, thus diminishing the strength of the field. This argument is the basis for the wide-spread belief that coronal magnetic fields are much weaker than the fields measured in the photosphere. The argument appears to be valid for the quiet-Sun fields concentrated in small flux tubes in the cell network: if these fields reached the solar corona with strengths of order of hundreds of G or more, we would see clear signatures in radio images

of the Sun in the form of features over the network at coronal temperatures. Such signatures are not seen (e.g., Gary *et al.* 1990). However, present upper limits for magnetic field strengths in the corona above quiet-Sun regions are well above the field strengths expected from the flux expansion argument.

On the other hand, the argument does not apply to active regions fields. Field strengths of 2000 G or more can be found in the corona, particularly over large sunspots (Shibasaki *et al.* 1994): in active regions there is so much flux that there is little field-free volume to expand into, and so field strength declines much less rapidly with height than simple models tend to predict (Akhmedov *et al.* 1982). The example in Fig. 5.8 shows a coronal magnetogram deduced from VLA data and therefore suffering from poor resolution in B. In this particular sunspot the maximum line-of-sight field in the photosphere is not much more than 2000 G, yet coronal fields of 1800 G are found to be present in the VLA observations. The recent coronal line measurements above active regions at the limb agree with this conclusion (Lin *et al.* 2000), as does the fact that loop width measurements find that coronal loops tend to have constant widths, rather than showing expansion at greater heights (McClymont & Mikić 1994, Klimchuk 2000).

6.2 Simulations of FASR magnetic field measurements

The crude coronal magnetogram shown in Figure 5.8, with just 3 contours from 600 to 1800 G, is the best we can do with VLA data due to the limited number of discrete frequencies available for observations. The Frequency Agile Solar Radiotelescope (FASR) will make images of solar active regions at high spatial resolution at many different frequencies simultaneously, in order to be able to measure coronal magnetic fields continuously over a broad range of field strengths. Gary, Lee, Giordano & Mok (2004, in preparation) have demonstrated how to convert such observations into measurements of the coronal field strength at the base of the corona by resolving the ambiguities of harmonic number. As described above, sharp jumps in the brightness temperature along a given line of sight are expected if where a harmonic layer drops out of the corona. Thus sharp drops in the brightness temperature spectra indicate harmonic numbers. If two such sharp edges are present along a given line of sight then the ratio of the frequencies of the two edges provides a unique identification of the harmonics corresponding to both edges, because we can safely assume that they are adjacent harmonics in the ratio of 2:1, 3:2 or 4:3. It is a great advantage that we can measure spectra in both the x and the o modes as opposite circular polarizations, because different edges may appear in either polarization.

This approach has been tested using a physical model of an active region. The model is a potential field model extrapolated from an actual vector magne-

togram. The thermal structure (density and temperature as a function of position throughout the volume) was computed self-consistently assuming a plasma heating model in which the volumetric heating rate is directly proportional to the local magnetic field strength (Mok *et al.* 2004). Given a three-dimensional model, we can simply predict the radio emission that would be observed. The radio images are folded through the FASR instrument response function, adding a realistic noise level. Maps at 100 frequencies are produced and the spectra analyzed on a point by point basis.

Examples of the resulting spectra are shown in Figure 5.9. In both these cases, one sharp edge is detected in each polarization and the two edges have a frequency ratio of 2:1, implying that they are the first and second harmonics. Once the harmonic number and the frequency of the edge are known, the magnetic field at the base of the corona is uniquely determined. It is straightforward to apply this method to two-dimensional data, as shown in Figure 5.10. The agreement between the input model fields and the values derived from realistic radio data is excellent.

6.3 Coronal currents

An extension of this simple measurement is the identification of coronal currents. Coronal currents occur in regions of highly sheared magnetic fields and therefore elevate coronal field strengths above the values expected from simple potential-field (i.e., current-free) extrapolations of surface measurements. They will also produce a characteristic reversal of field direction with position as one moves across the current layer. Both these features are in principle observable in radio images. Relatively little has been done in this area due to the difficulties of obtaining well-calibrated, unsaturated photospheric magnetogram data simultaneous with suitable radio data (i.e., at high spatial resolution and covering the appropriate frequency range), and the problem of identifying the height of the radio source (Alissandrakis *et al.* 1980; Schmahl *et al.* 1982; Alissandrakis & Kundu 1984; Chiuderi Drago *et al.* 1987; Schmelz *et al.* 1994). Figure 5.11 shows an example of the radio emission from a complex of sunspots at three different frequencies. The three frequencies correspond to three different magnetic field strengths: these are x mode images corresponding to the 450 G surface at 5 GHz, 750 G at 8.4 GHz and 1350 G at 15 GHz (these correspond to the fourth harmonic surface being optically thick since the temperature in the corona was very high for this active region). Note that, as should be the case, the optically thick region becomes smaller at higher frequencies corresponding to larger magnetic field strengths. At the lower frequencies the optically thick surface covers the whole active region; at the highest frequency several discrete sources are found. One of them (the bright source in the center of panel d, over the neutral line) has been shown to be the result of highly non-potential

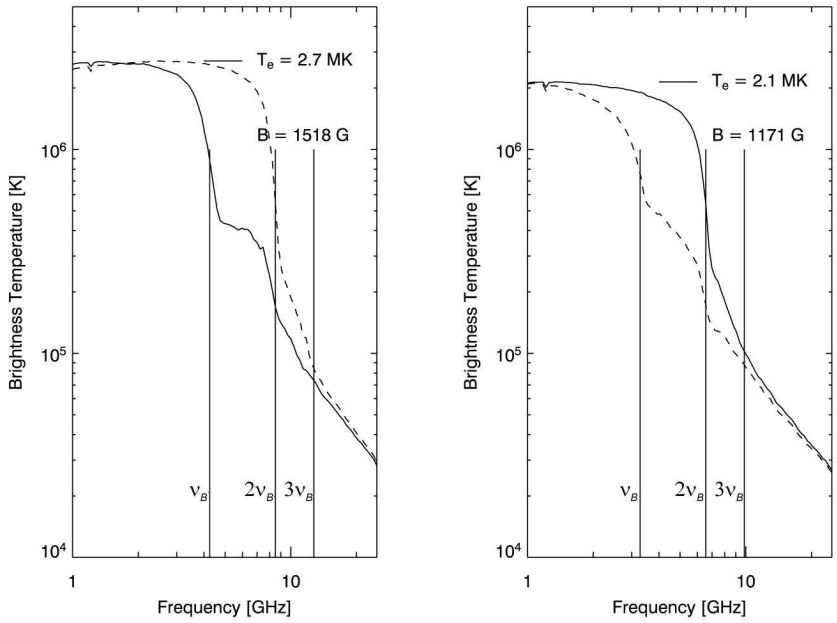


Figure 5.9. Two examples of radio spectra arising from the thermal active region model of Mok *et al.* (2004). The solid line is for one sense of circular polarization and the dashed line is for the opposite polarization: in the left panel the dashed line is the x mode, while in the right panel it is the o mode. In both cases the harmonic ratio is 2:1, allowing identification of the magnetic field in each case as labelled; fiducial vertical lines indicating the locations of the harmonics are shown on each panel.

fields at this location (Lee *et al.* 1997). Potential extrapolations of photospheric magnetic fields were unable to explain the presence of a 15 GHz radio source at this location above a neutral line even with the conservative assumption that the 4th harmonic layer could have sufficient opacity to be optically thick (requiring 1330 G fields). In this case a photospheric vector magnetogram also indicates the presence of a strong current with footpoints in the photosphere on either side of the neutral line and consistent with a coronal current crossing the neutral line in the corona at the location inferred from the radio data.

6.4 Tests of magnetic extrapolations

Extrapolations of magnetic field measurements from the lower atmosphere into the corona are likely to become an increasingly important tool in the near future, and in conjunction with the radio measurements are expected to provide a powerful means for studying coronal fields. One important area where the techniques interact is in testing extrapolation algorithms: as described earlier,

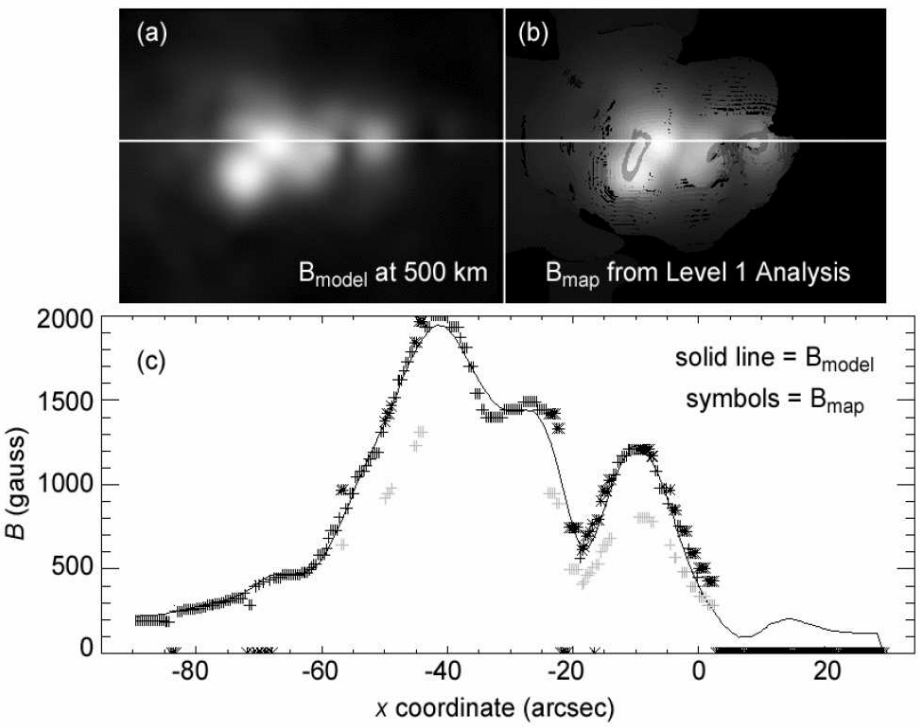


Figure 5.10. The results of applying the gyroresonance technique to model data. The top left panel shows the magnetic field in the input model at a height of 500 km, representative of the base of the corona (in the thermal model the actual height of the base of the corona varies). The top right panel shows the values derived from the radio technique of identifying harmonics from spectra in each pixel and using the frequency ratio to determine the harmonic numbers. The lower panel shows a more detailed comparison of the model (line) and radio-derived (symbols) fields along the horizontal line in the upper panels. The technique occasionally fails when edges are not sufficiently sharp and a 3:2 ratio can be mistaken for a 2:1 ratio (grey symbols). From Gary, Lee, Giordano & Mok (2004, in preparation).

extrapolation is a very difficult procedure and many different approaches have been tried. It is clearly valuable to be able to test the success of a given extrapolation technique, and radio data provide one way of doing so. The preceding subsection described such tests involving magnetic field strengths. Another important test involves the topology of magnetic field lines derived from the extrapolations. For the same region described above, Lee *et al.* (1999) compared the temperatures measured on the same field lines at two different frequencies, corresponding to two different locations (field strengths) on the same field lines. Since heat transport parallel to the magnetic field is so much faster than it is across magnetic field lines, one expects that temperatures measured at two different locations on a field line should be very well correlated. Lee *et al.* (1999)

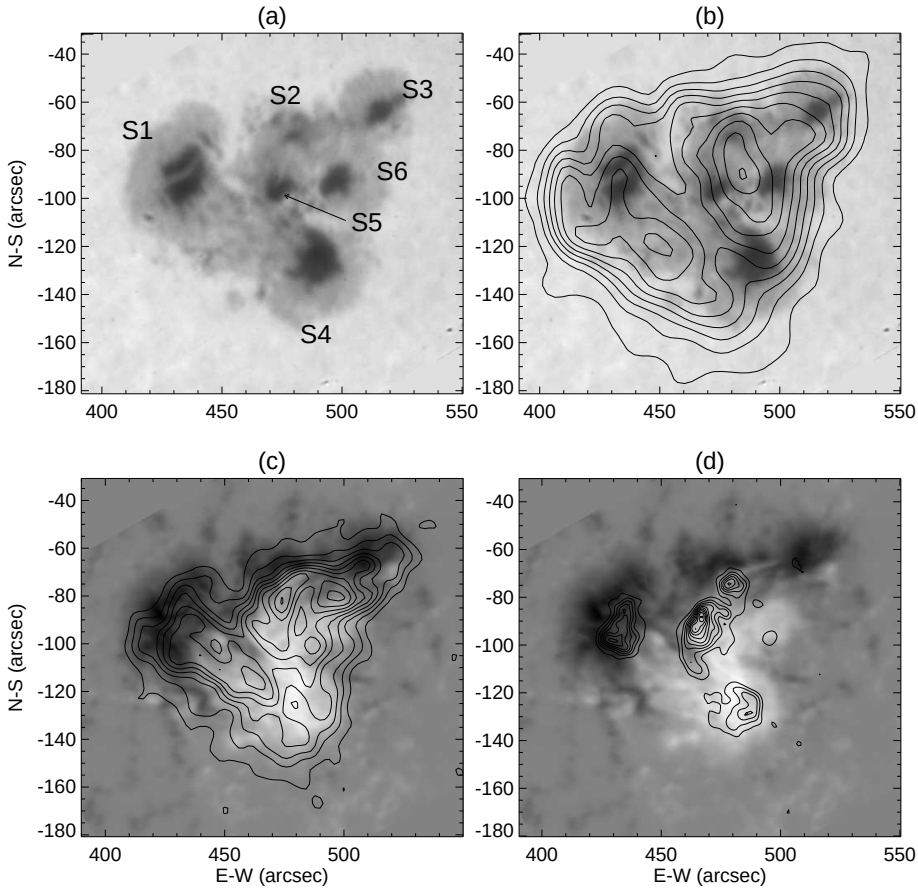


Figure 5.11. VLA observations of a complex solar active region reflecting the magnetic field and temperature distribution in the corona over the active region. The white-light image (a) shows a number of spots within the same penumbra. In panel (b) contours of the VLA 5 GHz emission are overlaid on the white-light image: since the radio emission is due to the gyroresonance process, the radio image corresponds to the electron temperature distribution on the surface in the corona where the magnetic field B equals 450 G. Panels (c) and (d) show contours of the 8.4 GHz (B = 750 G) and 15 GHz emission (B = 1350 G), respectively, overlaid on a longitudinal photospheric magnetogram which indicates the direction of the magnetic field at the surface (white = upgoing, black = downgoing field). The maximum brightness temperatures in the radio images are 4.4×10^6 K at 4.9 GHz, 4.6×10^6 K at 8.4 GHz, and 1.8×10^6 at 15 GHz, respectively. Contours begin at 10% of the maximum brightness temperature and then are 10% apart. From Lee *et al.* (1997).

compared this correlation for the field lines from potential, linear force-free and nonlinear force-free extrapolations using brightness temperatures measured at 5 and 8 GHz and showed that indeed the correlation was extremely good for the nonlinear force-free extrapolation and much poorer for the other extrapo-

lations. The radio data were also useful for resolving the well-known problem of the 180° ambiguity in the vector magnetogram measurements. The techniques of radio measurements and surface extrapolations, particularly when better chromospheric magnetograms become available, are expected to provide complementary information necessary to study coronal magnetic fields.

6.5 Heights of radio sources

Perhaps the major shortcoming of gyroresonance emission as a diagnostic is the fact that it does not yield height information directly. (Other coronal diagnostics such as X-ray imaging share this shortcoming.) A single radio observation at multiple frequencies is sensitive to emission from many different GR layers in the corona, but is largely insensitive to the distance between the layers, and for this reason does not easily lend itself to height determination. When two observations at different times are combined, the change in perspective produced by solar rotation permits stereoscopy to be used to estimate source heights (Aschwanden & Bastian 1994). However, to carry this out correctly for gyroresonance emission requires both that the physical properties of the corona not change between the observations and that the changes in appearance expected from the dependence on θ be taken into account carefully, which is far from trivial.

In principle there is information present on the heights of the GR layers due to the dependence of the optical depth (5.1) on L_B, and the fact that we know the magnetic field strength in each layer. L_B must be consistent with the height separation of isogauss layers of different field strengths. If L_B could be determined from the data, it may be possible to use the combination of L_B, the fundamental law $\nabla \cdot \mathbf{B} = 0$ and the fact that B is constant within a layer to reconstruct the heights of the GR layers, at least approximately. However, in (5.1), L_B is coupled with the electron density, and it may be difficult to separate these two parameters from radio data alone: EUV observations which provide independent information on n_e, and improved extrapolations of surface fields which provide an estimate of L_B, may help with this separation.

7. Summary

This chapter has reviewed the radio technique of using gyroresonance emission to measure magnetic field strengths in the solar corona. These measurements have the potential to determine fields in solar active regions above field strengths of order 200 G, and thus provide important information for studying changes in coronal magnetic fields and their role in flares, eruptions and coronal heating. A major advance in the application of this technique will be provided by the construction of the Frequency Agile Solar Radiotelescope, which is being designed to make routine high-resolution coronal magnetic field measurements

as one of its primary science goals. In addition, the data acquired by FASR will be ideal for going beyond the techniques described here and starting to exploit the full extent of the three-dimensional information present in the radio data.

Acknowledgments

Solar research at the University of Maryland is supported by NSF grants ATM 99-90809 and ATM 02-33907 and NASA grants NAG 5-11872, NAG 5-12860 and NAG 5-10175.

References

Akhmedov, Sh. B., Gelfreikh, G. B., Bogod, V. M., & Korzhavin, A. N. 1982, Solar Phys, 79

Alissandrakis, C. E. & Kundu, M. R. 1984, A&A, 139, 271

Alissandrakis, C. E., Kundu, M. R., & Lantos, P. 1980, A&A, 82, 30

Amari, T., Boulmezaoud, T. Z., & Mikic, Z. 1999, A&A, 350, 1051

Aschwanden, M. J. & Bastian, T. S. 1994, ApJ, 426, 425

Bornatici, M., Cano, R., de Barbieri, O., & Engelmann, F. 1983, Nucl. Fusion, 23, 1153

Bray, R. J. & Loughhead, R. E. 1964, Sunspots, Chapman & Hall, London

Brosius, J. W. & Holman, G. D. 1989, ApJ, 342, 1172

Chiuderi Drago, F., Alissandrakis, C. E., & Hagyard, M. 1987, Solar Phys, 112, 89

Gary, D. E. & Hurford, G. J. 1994, ApJ, 420, 903

Gary, D. E., Zirin, H., & Wang, H. 1990, ApJ, 355, 321

Gary, G. A. 1989, ApJ Supp., 69, 323.

Gelfreikh, G. B. & Lubyshev, B. I. 1979, Sov. Astron., 23, 316

Ginzburg, V. L. & Zheleznyakov, V. V. 1961, Sov. Astron., 5, 1

Hurford, G. J. 1986, in Solar Flares and Coronal Physics Using P/OF as a Research Tool, (Tandberg-Hanssen, E., Wilson, R. M., and Hudson, H. S., eds.), NASA Conf. Pub. 2421, 191

Jiao, L., McClymont, A. N., & Mikić, Z. 1997, Solar Phys, 174, 311

Kakinuma, T. & Swarup, G. 1962, ApJ, 136, 975

Klimchuk, J. A. 2000, Solar Phys, 193, 53

Klimchuk, J. A. & Canfield, R. C. 1994, in Solar Active Region Evolution: Comparing Models with Observations, (Balasubramanian, K. S. & Simon, G. W., eds.), PASP Conf. Ser. 68, 233

Krüger, A., Hildebrandt, J., & Fürstenberg, F. 1985, A&A, 143, 72

Lantos, P. 1972, Solar Phys, 22, 387

Lee, J., McClymont, A. N., Mikić, Z., White, S. M., & Kundu, M. R. 1998, ApJ, 501, 853

Lee, J., White, S. M., Gopalswamy, N., & Kundu, M. R. 1997, Solar Phys, 174, 175

Lee, J., White, S. M., Kundu, M. R., Mikić, Z., & McClymont, A. N. 1999, ApJ, 510, 413

Lee, J. W., Hurford, G. J., & Gary, D. E. 1993, Solar Phys, 144, 45

Lin, H., Penn, M. J., & Tomczyk, S. 2000, ApJ, 541, L83

McClymont, A. N. & Mikić, Z. 1994, ApJ, 422, 899

Melrose, D. B. 1980, Plasma Astrophysics, Gordon and Breach, New York

Metcalf, T. R., Jiao, L., McClymont, A. N., Canfield, R. C., & Uitenbroek, H. 1995, ApJ, 439, 474

Mok, Y., Lionello, R., Mikic, Z., & Linker, J. A. 2004, ApJ, submitted.

Robinson, P. A. 1991, Solar Phys, 136, 343

Robinson, P. A. & Melrose, D. B. 1984, Aust. J. Phys., 37, 675

Schmahl, E. J., Kundu, M. R., Strong, K. T., Bentley, R. D., Smith, J. B., & Krall, K. R. 1982, Solar Phys, 80, 233

Schmelz, J. T., Holman, G. D., Brosius, J. W., & Willson, R. F. 1994, ApJ, 434, 786

Semel, M. & Skumanich, A. 1998, A&A, 331, 383

Shibasaki, K., Enome, S., Nakajima, H., Nishio, M., Takano, T., Hanaoka, Y., Torii, C., Sekiguchi, H., , Kawashima, S., Bushimata, T., Shinohara, N., Koshiishi, H., Shiomi, Y., Irimajiri, Y., Leka, K. D., & Canfield, R. C. 1994, Publ. Astron. Soc. Japan, 46, L17

Vourlidas, A. 1996, Ph. D. thesis, New Mexico Inst. of Mining and Technology, unpublished.

White, S. M. & Kundu, M. R. 1997, Solar Phys, 174, 31

White, S. M., Kundu, M. R., & Gopalswamy, N. 1991, ApJ, 366, L43

White, S. M., Kundu, M. R., & Gopalswamy, N. 1992, ApJ Supp., 78, 599

Zheleznyakov, V. V. 1962, Sov. Astron. J., 6, 3

Zheleznyakov, V. V. 1970, Radio Emission of the Sun and the Planets, Pergamon Press Ltd., Oxford

Zlotnik, E. Ya. 1968*a*, Sov. Astron., 12, 245

Zlotnik, E. Ya. 1968*b*, Sov. Astron., 12, 464

Zlotnik, E. Ya., Kundu, M. R., & White, S. M. 1996, Radiophysics and Quantum Electronics, 39, 255

Chapter 6

CORONAL MAGNETIC FIELD MEASUREMENTS THROUGH BREMSSTRAHLUNG EMISSION

G.B.Gelfreikh
Central (Pulkovo) Astronomical Observatory RAS. St.Petersburg 196140, Russia
GBG@GG1623.spb.edu

Abstract Basic concepts are presented of the theory of thermal bremsstrahlung in the anisotropic plasma of the solar atmosphere. Formulas are given describing the polarization resulting from the solar magnetic field, from which the longitudinal component of the magnetic field can be found through analysis of the polarization spectra of the thermal radio emission. The application of the method is illustrated with examples pertaining to solar faculae, prominences, coronal holes and coronal loops. The observations were carried with large, modern radio telescopes such as the Nobeyama Radioheliograph (Japan) and the RATAN-600 (Russia).

1. Introduction

Many forms of electromagnetic emission arise as a result of the acceleration of charged particles. In the case under consideration here, the acceleration is caused by the electrostatic field of ions and the emitting particles are electrons. In some approximation this process may be considered as particle collisions. This mechanism is usually called bremsstrahlung, although the term free-free emission is also used in the astrophysical literature. In fact, this mechanism for generating radio emission may be considered the main one produced by a thermal plasma (e.g. see Benz 1993), since it is always present.

2. Basic Formulae

2.1 Equations of transfer of the thermal emission in anisotropic plasma

For the intensity of the emission we have the equation of transfer:

$$I(\nu) = \int \eta(l)\, e^{-\tau(l)}\, dl, \tag{6.1}$$

where the emissivity $\eta(\nu)$ is the energy emitted per unit volume per unit solid angle per unit interval of the wave frequency ν. Absorption coefficient $\kappa(\nu)$ is the relative decrease of intensity per unit length of the ray. The optical thickness is the integral of κ along the ray path:

$$\tau = \int \kappa(l)\, dl. \tag{6.2}$$

If the emitting particles have a thermal distribution (that is, have Boltzmann's distribution in energy space, or Maxwell's distribution in velocity space) then the emissivity η and absorption coefficient κ are connected by a simple relation (Kirchhoff's law)

$$\frac{\eta}{\kappa} = B(T) = \frac{2kT}{\lambda^2} = \frac{2kT\nu^2}{c^2}, \tag{6.3}$$

where $B(T)$ is the Planck function. The Rayleigh-Jeans approximation to the Planck function (valid in the radio regime) has been used in the above equation.

For observations in the radio wave range the intensity usually is given in units of brightness temperature defined by the relation

$$I = \frac{2kT_b}{\lambda^2} = \frac{2kT_b\nu^2}{c^2}. \tag{6.4}$$

This implies that the brightness temperature T_b is equal to the temperature of the black body producing the same intensity (or having the same brightness). In these terms the equation of transfer has the form

$$T_b = \int T(\tau) e^{-\tau} d\tau. \tag{6.5}$$

The values η and κ are also functions of plasma parameters such as

- electron density n_e and/or of other particles n_i (ions and neutral particles);
- electron temperature T_e;
- magnetic field $\mathbf{B}$, its strength and direction.

In magneto-ionic theory, when the approximation of geometrical optics is valid, two types of waves—called the ordinary and extraordinary modes—can propagate in a plasma. They correspond approximately to the two orthogonal circular polarizations. Thus, in an anisotropic (i.e. magnetized) plasma we must write two separate equations of transfer for ordinary (o) and extraordinary (x) modes:

$$\begin{aligned} T_b^o &= \int T(\tau^o)\, e^{-\tau^o}\, d\tau^o \\ T_b^x &= \int T(\tau^x)\, e^{-\tau^x}\, d\tau^x. \end{aligned} \tag{6.6}$$

In most cases we treat these "normal modes" as left-handed and right-handed circular polarization.

We should keep in mind that $T_b(\nu)$ is also a function of temperature, density, magnetic field and other plasma parameters in the region of generation and propagation of the electromagnetic waves. The goal of plasma diagnostics is the evaluation of these parameters. To get these we deal with the solution of the equations of the form:

$$F(T, n_e, \mathbf{B}, \dots) = T_b(\nu). \tag{6.7}$$

In general, even with high-resolution imaging, the values n_e, $\mathbf{B}$, T, etc., that we wish to find are in fact averaged along the line of sight at some position in the object of study.

2.2 Basic expression for the case of the isotropic plasma

For the absorption coefficient in isotropic plasma we can use the expression

$$\kappa = \frac{\zeta n_e^2}{T^{3/2}\nu^2}, \tag{6.8}$$

which is a simplification of the full expression (4.6) given in Chapter 4. The coefficient ζ only slightly (logarithmically) depends on the plasma parameters. In most cases of solar interest, its value is within the range 0.12–0.2. In the following discussion we will consider it a constant. Generally speaking, in determining the value of ζ the chemical composition and degree of ionization of the plasma must be taken into account.

Since we here consider only the case of thermal emission, we can use Kirchhoff's law to evaluate the expression for the emissivity using (6.8):

$$\eta = \frac{2\zeta k}{c^2}\frac{n_e^2}{\sqrt{T}}. \tag{6.9}$$

2.3 Basic expression for the case of anisotropic plasma

Now we present the expressions for the absorption coefficient for an anisotropic plasma in the presence of a magnetic field $\mathbf{B}_0$. In this case the absorption coefficient becomes:

$$\kappa_{o,x} = \frac{\zeta n_e^2}{T^{3/2}(\nu \pm \nu_B|\cos\alpha|)^2}, \tag{6.10}$$

where ν_B is the electron gyrofrequency. For the two types of the circular polarization of normal modes

$$\kappa_{L,R} = \frac{\zeta n_e^2}{T^{3/2}(\nu \pm \nu_B \cos\alpha)^2}. \tag{6.11}$$

In all equations above we assume that the refractive index $\tilde{n} = 1$. This can be checked if necessary using the expression

$$\tilde{n}^2 = 1 - \frac{\nu_p^2}{\nu^2} = 1 - \frac{n_e e^2}{\pi m_e \nu^2}, \tag{6.12}$$

where m_e and e are the mass and charge of an electron.

3. Diagnostics of the Coronal Plasma

The central point of our discussion here is to measure the magnetic field using spectral-polarization observations of the radio bremsstrahlung of the thermal plasma. One of the serious problems of the method is identification of the mechanism generating the observed structure on the radio map of the Sun.

3.1 Diagnostics of the mechanism of the emission generated by thermal bremsstrahlung

From the frequency dependence of opacity given by (6.8), the equation of transfer (6.1) can be analyzed with the known spectral index for optical depth:

$$\tau(\lambda) \propto \lambda^2. \tag{6.13}$$

At the same time, to a good approximation the emissivity, η, in (6.9) does not depend on the wavelength λ (or frequency ν). And so, it follows that

$$\frac{\partial I}{\partial \lambda} \leq 0. \tag{6.14}$$

For shorter wavelengths, where $\tau \ll 1$

$$I(\lambda) = const. \tag{6.15}$$

This flat flux density spectrum is an important characteristic of bremsstrahlung by which to identify the radio emission mechanism. Another important property is the limit in brightness temperature to be expected of thermal emission:

$$T_b \leq T_e, \tag{6.16}$$

where T_e is the electron temperature. If the emission mechanism is thermal bremsstrahlung, then the brightness temperature must not exceed reasonable

values of the electron temperature for the plasma. The value of T_e refers to some point in the emitting plasma structure. For the case of optically thick regions a reasonable approximation is

$$T_b(\lambda) = T_e \qquad (\tau(\lambda) \geq 1) \tag{6.17}$$

We shall refer to this condition later. We should also notice that κ and especially η depend strongly on electron density and inversely on temperature (see 6.8 and 6.9). Thus, observations of bremsstrahlung are most effective in the denser, cooler regions of the solar atmosphere.

So far in the diagnostics of the mechanism of thermal bremsstrahlung we have used expressions for isotropic plasma. However in reasonably good approximation this assumption works also for anisotropic plasma if the magnetic fields are not too strong.

3.2 Expressions for the magnetic field

Now, once we have come to the conclusion that the mechanism responsible for the observed radio emission is indeed thermal bremsstrahlung, from analysis of its intensity (brightness) spectrum, the next step is to analyze its polarization—the main source of information on the magnetic field within the source. The analysis is based on the equations of transfer for an anisotropic plasma (6.6), from which we can derive the equation giving the strength of the magnetic field in the source region generating the thermal bremsstrahlung.

We define the degree of polarization as

$$P = \frac{T_b^R - T_b^L}{T_b^R + T_b^L}, \tag{6.18}$$

where the brightness temperatures for the two types of the circular polarization as a function of the wavelength λ are to be determined by the equations of transfer (6.6). Optical thickness $\tau^{R,L}$ is found using (6.10) and (6.11). For the case of the optically thin region we have, to a good approximation,

$$T_b^{x,o} = T_e \, \tau_{x,o} \qquad (\tau \ll 1), \tag{6.19}$$

or

$$T_b^{L,R} = T_e \, \tau_{L,R} \, . \tag{6.20}$$

Then follows

$$P = \frac{T_b^x - T_b^o}{T_b^x + T_b^o} = \frac{\tau_x - \tau_o}{\tau_x + \tau_o} \approx 2\frac{\nu_B}{\nu} |\cos\alpha| \, , \tag{6.21}$$

or, taking into account the sign of polarization,

$$P = \frac{T_b^R - T_b^L}{T_b^R + T_b^L} = \frac{\tau_R - \tau_L}{\tau_R + \tau_L} = 2\frac{\nu_B}{\nu}\cos\alpha \ . \tag{6.22}$$

In the case of optically thick plasma the brightness temperature is $T_b = T_e$ — some (density weighted) mean value of the electron temperature along the line of sight. For isothermal plasma

$$T_b^x = T_b^o = T_e \tag{6.23}$$

and $P = 0$ —no polarization is observed and no magnetic field measurements are possible. The existence of a gradient in temperature with height, however, changes the situation. The optical thickness for ordinary mode $\tau^o < \tau^x$ for extraordinary mode and so we look into deeper, usually colder, layers of the solar atmosphere. The resulting equation for polarization can be found from the equations of transfer using the approximation of the weak magnetic field:

$$P = n\frac{\nu_B}{\nu} \mid \cos\alpha \mid \ . \tag{6.24}$$

Here spectral index n is given by the equation

$$n \equiv -\frac{\partial(\log T_b)}{\partial(\log\nu)} = \frac{\partial(\log T_b)}{\partial(\log\lambda)} \ , \tag{6.25}$$

and can be measured directly from spatially resolved spectral observations. If the sign of polarization is taken into account, then instead of (6.24) we have

$$P = n\frac{\nu_B}{\nu}\cos\alpha \ . \tag{6.26}$$

Recalling that the electron gyrofrequency is $\nu_B = 2.8 \times 10^6 B$, and noting that $B\cos\alpha = B_l$ is the longitudinal component of the magnetic field, (6.26) becomes

$$P = n\frac{2.8 \times 10^6}{\nu}B_l \ . \tag{6.27}$$

3.3 Radio measurements of the magnetic field

These expressions may be successfully used to measure the longitudinal component of magnetic fields in the solar atmosphere, keeping in mind that they refer to an average over the line of sight, weighted by n_e^2 and $T_e^{-3/2}$. To this end it is reasonable to write them in terms of the strength of the longitudinal component of the magnetic field. For the optically thin region, where we expect the spectral slope $n = 2$, we have

$$B_l = \frac{54}{\lambda}P\% \ . \tag{6.28}$$

In this case the longitudinal component of the magnetic field B_l can be found from observations at one wavelength. In fact, however, spectral observations in this case are also necessary to confirm the bremsstrahlung nature of the radio emission and that we really deal with an isolated optically thin region (for example as viewed above the solar limb).

The longitudinal component of the magnetic field in the more general situation may be written in the form

$$B_l = \frac{107}{\lambda \cdot n} P\% \, . \tag{6.29}$$

Both $P\%$ and n can be found from observations. So, we have come to a viable method of performing radio magnetography, provided $P\%$ and n can be measured with sufficient precision.

4. Expected Parameters of Polarized Radio Emission from the Solar Plasma

Using (6.29), we can measure the longitudinal component of the magnetic field both in the solar corona and upper chromosphere, including the transition region. The method is applicable, both on the disk and above the solar limb, to most plasma structures in the upper solar atmosphere that are organized by sufficiently strong local magnetic fields. Such fields are not easily accessible to traditional optical methods, such as Zeeman splitting of spectral lines or the Hanlé effect, except in special cases. Infrared techniques are currently being developed which may provide Zeeman measurements above the limb.

4.1 Optically thin regions

According to (6.13), (6.20) and (6.21) we have in this case

$$\begin{array}{lll} T_b & \propto & \lambda^2 \\ P & \propto & \lambda \end{array} \tag{6.30}$$

It follows that the sensitivity to the magnetic field increases with the wavelength λ. However, at the same time the optical depth of coronal structures increases for longer wavelengths and so weakens the polarization. Another important limitation in applicability of the method is the possible simultaneous presence of other radio emission mechanisms typical for the solar active regions. The central role here belongs to the thermal cyclotron (gyroresonance) emission (see Chapter 5). This mechanism becomes effective at frequencies corresponding typically to the third harmonic of the electron gyrofrequency. In this case, the magnetic field can be estimated according to the equation

$$B(\nu = 3\nu_B) = \frac{3570}{\lambda(\mathrm{cm})} = 119 \, \nu_{\mathrm{GHz}} \, . \tag{6.31}$$

While for the sunspots this kind of radio emission is usually important at wavelengths $\gtrsim 2$ cm, for the weaker fields elsewhere in the active region it may be important from $\gtrsim 5$ cm. These sources are identified by strong polarization and high brightness, and so can be excluded from the analysis of thermal bremsstrahlung.

One may conclude that the study of magnetic fields with thermal bremsstrahlung complements their study via the gyroresonance mechanism. Thermal bremsstrahlung can be used in coronal structures and parts of ARs where the magnetic field is weaker than 100–200 G, where the radio brightness and degree of polarization are rather low. The coronal condensations (increases in density) can be studied both behind the limb and on the disk. With the sensitivity of, say 0.1% at $\lambda = 5$ cm, we achieve the sensitivity in the coronal magnetic fields of about 1 G. This high precision is not easy to achieve with present techniques but, on the other hand, there are no principal limitations to its achievement.

4.2 Optically thick regions

In the case $\tau \gg 1$ the polarization is determined by the gradient of temperature in the emitting layers of the solar atmosphere. A good approximation for the short cm and mm wavelength ranges (where the hot corona gives a negligible background solar radio emission) is given by (6.17). The excess of brightness for the x-mode above the o-mode is

$$\Delta T_b = T_e(\tau_x = 1) - T_e(\tau_o = 1) \; . \tag{6.32}$$

At short cm wavelengths a typical value for spectral index from observations (see 6.25) is $n \approx 1$. That implies

$$\Delta T_b / T_b \approx \Delta\nu / \nu \; . \tag{6.33}$$

So, according to (6.29), the sensitivity to the magnetic field in this case is approximately a factor of two lower than in the case of transparent coronal structures.

The magnetic field in the case under consideration can be found from (6.29). In this case we also need to use spectral observations to find the spectral index n (see 6.25). This reflects the level of the gradient of temperature in the emitting layer, mostly at the depth of $\tau = 1$. At the short cm waves for the quiet Sun, $n \approx 1$. For better accuracy n certainly should be measured simultaneously with the degree of polarization.

In contrast with the previous case of coronal condensations the magnetic field measured in the chromosphere refers to a rather thin layer defined by (6.17). So the approximation of homogeneous magnetic field seems to be reasonable. Below we illustrate this method in the chromosphere of ARs (see §6).

An interesting point in the case under consideration is that the presence of the magnetic field may produce a polarized component without significant spatial variation of total intensity. The reason is that the presence of a magnetic field shifts the effective emitting level for the two modes (two circular polarizations) in different directions: the x-mode becomes optically thick in hotter, higher levels of the solar atmosphere, while the o-mode comes from lower cooler levels.

4.3 Combination of optically thin and thick regions

This situation is quite common when we observe a bright source on the disk that is due to the emission of some condensation of coronal material. For short cm waves it is usually optically thin. This can be checked from an analysis of the spectrum in the intensity channel, which may be dominated by the almost flat chromospheric spectrum. The polarized flux in this situation, however, may be significantly affected by both emission of the condensation and the lower opaque solar atmosphere (chromosphere levels). This may be checked by spectral observations. If the polarized emission T_b^V does not follow the law

$$T_b^V = \frac{1}{2}(T_b^R - T_b^L) \propto \lambda^3 \ , \tag{6.34}$$

then it is significantly affected by both emissions.

However, the spectral observations may help to solve the problem and allow the effective magnetic fields to be found separately for the chromosphere below the radio source and that in the coronal condensation. The observed brightness temperature is the sum of the cold background and hot but transparent region in the overlying corona.

$$\begin{aligned} T_b^I(\lambda) &= T_{b,chr}^I(\lambda)(1-\tau_1\lambda^2) + T_e\tau_1\lambda^2 \\ T_b^V(\lambda) &= T_{b,chr}^V(\lambda)(1-\tau_1\lambda^2) + T_e\tau_1\lambda^2 \cdot 2\lambda/\lambda_B \ . \end{aligned} \tag{6.35}$$

To a reasonable approximation these equations can be written in the following forms. For the intensity:

$$T_b^I(\lambda) = T_1 \cdot \lambda^n + T_2 \cdot \lambda^2 \tag{6.36}$$

and for the circular polarization:

$$T_b^V(\lambda) = T_1 \cdot \frac{\lambda^{n+1}}{\lambda_B^{chr}} + T_2 \cdot \frac{\lambda^3}{\lambda_B^{cor}} \ . \tag{6.37}$$

Equation (6.36) can be used to find parameter n from spectral observations, reflecting the gradient of temperature in the emitting layers of the chromosphere. Then (6.37) gives as the value of λ_B, equivalent of magnetic field,

based on polarization measurements. In this case the longitude component of the magnetic field strength is

$$B_l = \frac{10800}{\lambda_B} \ . \tag{6.38}$$

This can be found from spectral polarization observations separately for the chromosphere λ_B^{chr} and corona λ_B^{cor}.

5. Radio Magnetograms of Solar Active Regions

At short cm waves the radio emission of an active region is mostly generated by thermal mechanisms outside of flaring periods. The magnetic field at the level of the upper chromosphere and the CCTR can be deduced, as has been shown above using (6.29). The radio observations made at the RATAN-600 in the wavelength range of 2–4 cm with the high one-dimensional resolution demonstrated effectiveness of the method on an example of a flocculus (Bogod & Gelfreikh 1980). The magnetic field of about 50 G was measured with the accuracy of about 10 G, the latter being in good agreement with the optical observations. The spectral index in the range of $n = 0.7$–1.0 was found for the flocculus region.

The most effective radio magnetography of solar ARs today is based on the Nobeyama Radioheliograph observations at $\lambda = 1.76$ cm (Shibasaki *et al*. 1994), where both intensity and circular polarization maps are regularly obtained with 2D resolution of about 15 arc sec. Two mechanisms of the generation of the thermal radio emission should be taken into account—gyroresonance (or cyclotron) emission and bremsstrahlung. From numerous modeling computations one knows that the emission at the third and second harmonics of the electron gyrofrequency plays the main role in the observed radio emission of ARs (see Chapter 5). For $\lambda = 1.76$ cm, the second and third harmonics of the electron gyrofrequency correspond to magnetic field strengths of 2000 and 3100 G, respectively.

It is clear that a gyroresonance radio source can be observed with Nobeyama only above sunspots in which strong magnetic fields of $B \approx 2000$ G penetrate into the corona (3100 G needed for the second harmonic is a very rare case). In any case, emission at the third harmonic of the gyrofrequency is strongly polarized, so such radio sources are easy to identify and consider separately.

To measure the magnetic field, we use (6.29). It follows that besides measurements of degree of polarization, which we can get from the I and V radio maps of Nobeyama, we need also some spectral observations in order to measure the spectral index n in (6.25). This is certainly the main limitation of the Nobeyama Radioheliograph data. We may try to overcome this difficulty using some approximations/assumptions. If we look at a typical radio map of

an active region (Figure 6.1) we see no significant increase of brightness over most of it. That implies no significant difference exists in the thermal structure of the solar atmosphere at the levels from which we observe the emission. So, as a reasonable approximation we use the same spectral index of about $n \approx 1$ that is known for the quiet Sun and weak plage regions at $\lambda = 1.76$ cm, being in reasonable agreement with the RATAN-600 data (Bogod & Gelfreikh 1980). Next, we use the assumed value for the Nobeyama brightness temperature for the quiet sun $T_b \equiv 10^4$ K. Using these approximations we can see that (6.29) becomes simply

$$B_l = \frac{107}{\lambda} \frac{V}{I} \times 100 \approx T_b^V \ . \tag{6.39}$$

From this relation one can conclude that V radio maps of the Nobeyama radio heliograph can be used directly as approximate magnetograms of the active regions. So, we have come to a possible method of simple and effective magnetography of the ARs using Nobeyama radio heliograms.

The next problem we deal with is that of sensitivity. The most often used time averaging at Nobeyama is 10 s—just such maps in FITS format are accessible from Nobeyama. The sensitivity of these is about 1% and, according to (6.39), the accuracy of such magnetograms is about 100 G. That is not very good for our goal. However, we can improve our sensitivity by using longer averaging of the images, say for 10 min instead of 10 s. An example of the resulting magnetogram of an active region is shown in the Figure 6.1.

To check the extent to which the method leads to reasonable results, we compared the radio magnetogram with the optical one, averaged with the beam pattern of the radio heliograph (see Figure 6.1). For this case and some others the results seem to be in reasonable agreement, not only in structure but in the values of the magnetic field strength as well (Gelfreikh & Shibasaki 1999).

On all the magnetograms we can clearly see the sunspots as the regions of the highest degree of polarization (some tens of percent). The polarized signal in this case, however, did not show such good correlation with the strength of the magnetic field of the spot (at photospheric level).

6. Magnetic Fields in Prominences

The physics of prominences plays an important role in modern understanding of all types of solar activity because they reflect the position of the neutral lines of the photospheric magnetic field, both in its global and local AR structures. In the latter case it represents the location of the highest flare activity. The complicated plasma and magnetic structure of the surrounding regions is of great interest for studying the nature of the solar flares and other processes of the solar energy release.

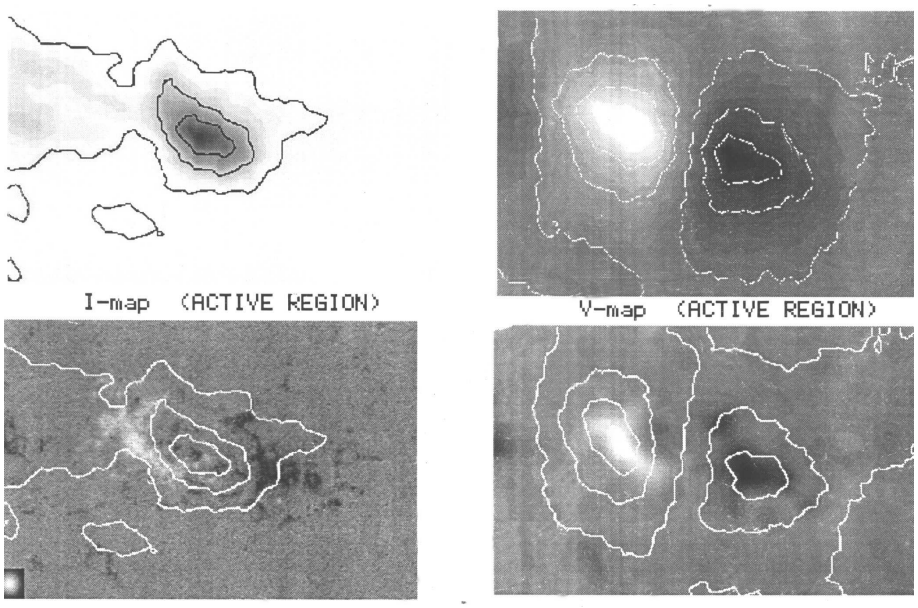


Figure 6.1. Radio maps of the AR observed on June 09, 1995 using Nobeyama radio heliograph at $\lambda = 1.76$ cm. Contours present the brightness distribution . Maximum in I channel ($T_b = 27 \cdot 10^3 K$). Maximum in V-channel $T_b^V = 440K$. Maximum degree of polarization $P = 2.8\%$. The region maps are overlapped by gray scale magnetograms . For V-maps they are averaged by the scale of the Nobeyama radio heliograph beam (shown below on the left). The upper V-map present brightness T_b^V , the lower one—percentage $P\%$ of polarization.

Radio observations of free-free emission offer a new method of measuring the magnetic field inside prominences, though at present the combination of spatial and spectral resolution of the radio observations is not sufficient for detailed study. Measurements of the prominence magnetic fields have been made using the 22 meter dish RT-22 of the Crimean Astrophysical Observatory at the wavelengths of 8 and 13.5 mm. A dozen prominences were analyzed in 1993 (Apushkinsky *et al.* 1996). The longitudinal component of the magnetic field was found to be in the range from 7 to 30 G, depending on the prominence. This result is in reasonable agreement with the optical data. The maximum value of the field usually was found at higher regions within the prominences, where in fact one can expect the maximum of the longitudinal component.

A similar conclusion, but with stronger magnetic field, was found with the RATAN-600. In figure 6.2 we see a one-dimensional scan of the limb of the solar disk at wavelength $\lambda = 2.1$ cm, both in intensity and circular polarization. The quiet Sun level has already been subtracted. The bright source behind the west limb is due to the prominence and surrounding plasma structures in the

solar corona (at $\lambda = 2.1$ cm they are weak). The maximum polarization signal $P = (6 \pm 1)\%$ coincides with the upper part of the prominence where probably the plasma is already optically thin. The resulting magnetic field we get is $B_l \approx 150 \pm 25$ G. This field is an order of magnitude higher than in the previous case based on observations made with the RT-22. One possible reason is due to the higher resolution of the RATAN-600. Alternatively, it may be due to a stronger AR in which the prominence appeared.

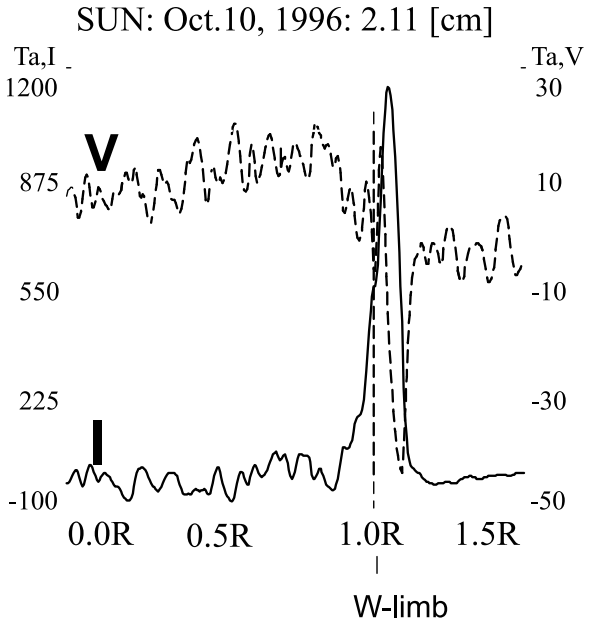


Figure 6.2. Radio scan of the prominence at a wavelength $\lambda = 2.1$ cm made with the RATAN-600 on 1996 October 11. Intensity (I) and circular polarization (V) are shown. The level of the quiet Sun has been excluded from the intensity curve. The upper part of the prominence is polarized: $P = (6 \pm 1)\%$

7. Magnetic Fields in a Coronal Hole

The coronal holes (CH) are important structures of the solar corona both from the point of the solar activity and the nature of plasma structures. They are known to be the regions of acceleration of fast geoeffective solar wind. They are the regions of lower density and temperature as well as the lower gradient of temperature in the transition region. They reflect open magnetic field structures, unlike the closed-field regions of the surrounding solar atmosphere.

The CHs are directly observed in soft X-rays and EUV from space. In the ground-based observations they are identified mostly in the He I line 10830 Å

(the "reflections" in the chromosphere). At the limb CHs are clearly identified in the green coronal line. As far as the radio observations are concerned they appear as dark regions at dm wavelengths (see figure 6.3). At short centimeters the input emission of the corona is too weak and at meter waves the large optical thickness of the corona smoothes the effect.

As follows from (6.9) and (6.20), in the case of optically thin emission the brightness $T_b \propto n_e^2/\sqrt{T_e}$. So, it only slightly depends on the coronal temperature, and the lower electron density in the CH produces the main contrast observed on a radio map. The brightness depression really amounts to some tens of percent but for measurements of magnetic field we must detect some much smaller polarization effects, which are accessible only to a few of the largest instruments in the world. We could expect magnetic field in the corona of a CH to be of the order of 10 G or even lower (the CH are generally observed outside the solar ARs). For $\lambda \approx 30$ cm this would result in degree of polarization of $P \approx 2\%$ (see 6.28), implying the necessary sensitivity of the instrument to polarization measurements of about 0.1%.

In fact, at present only one case of publication of the radio measurements of the magnetic fields in a CH is registered (Borovik *et al.* 1999). The observations have been carried out with the reflector radio telescope RATAN-600. Figure 6.3 illustrates the observations of a coronal hole made with the RATAN-600. Observations of the same CH in EUV (line FeXII 195 Å) is also presented. From the Figure 6.3 it is clearly seen that the CH is well registered at dm wavelengths ($\lambda \geq 10$ cm).

The magnetic field strength (averaged longitudinal component) was found from (6.29) using the observations made with the radio telescope RATAN-600. The logarithmic spectral index n was found as a function of wavelength (see 6.25): $n = 0.9$ at 9–11 cm, $n = 1.04$ at 14–18 cm and $n = 1.7$ at 27–30 cm (measured on October 12, 1996). The magnetic field strength in the CH according to expression above is presented in Figure 6.4. Taking into account the magnetic field measurements at the photosphere level (Stanford data) we have concluded that the longitudinal component of the magnetic field in the coronal hole increases with height from 0.2 G at the photospheric level to 7–10 G at the level of the generation of radio emission at 18 cm. In this wavelength range practically all of the emission is due to coronal plasma and the obtained value of B_l is a mean one weighted by the distribution of n_e^2. At shorter wavelengths, a contribution from the chromosphere is expected. That implies a lower strength of the field in the chromosphere-photosphere level, in good agreement with the optical data.

One can hope that the problem of the 3D-structure of the magnetic field in coronal holes and related solar wind acceleration phenomena may be successfully resolved using radio astronomical instruments providing both high spatial resolution and high sensitivity for polarization measurements. Spectra

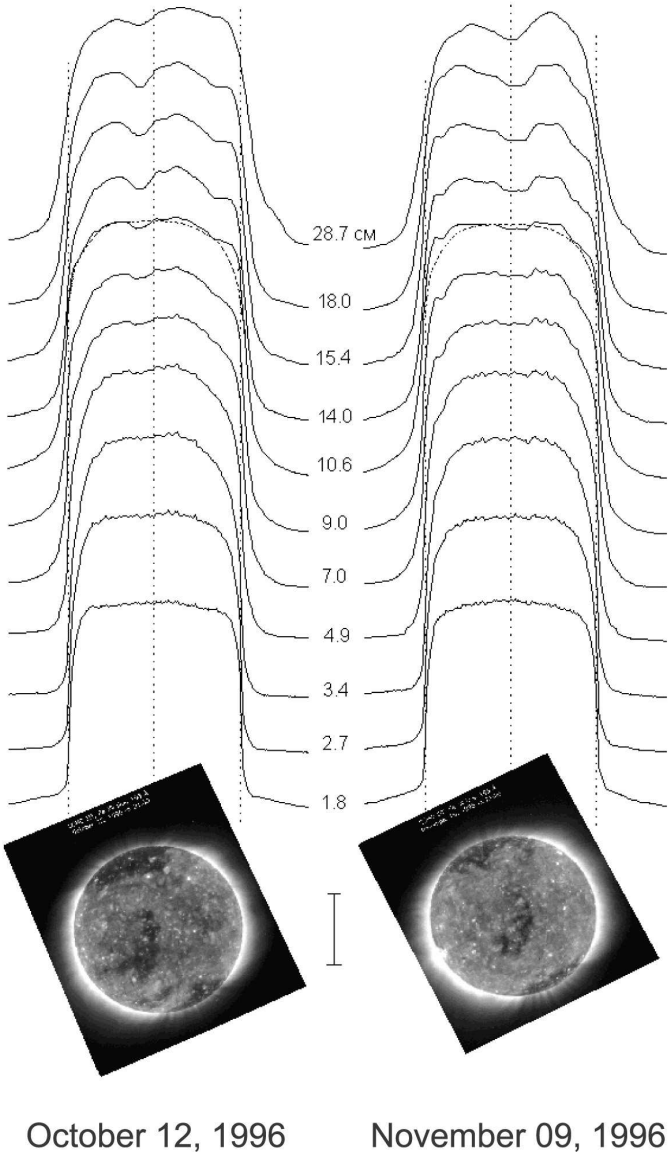


Figure 6.3. One-dimensional radio scans of the sun made with the RATAN-600 at eleven wavelengths in the range 1.8–28 cm for 1996 Oct 12 and Nov 9. Coronal holes are seen as brightness depressions at dm waves. For identification of the CHs at the bottom the EUV maps of the Sun (SOHO data) are shown.

at the short cm wavelengths in this case could be used for magnetography at the chromospheric level.

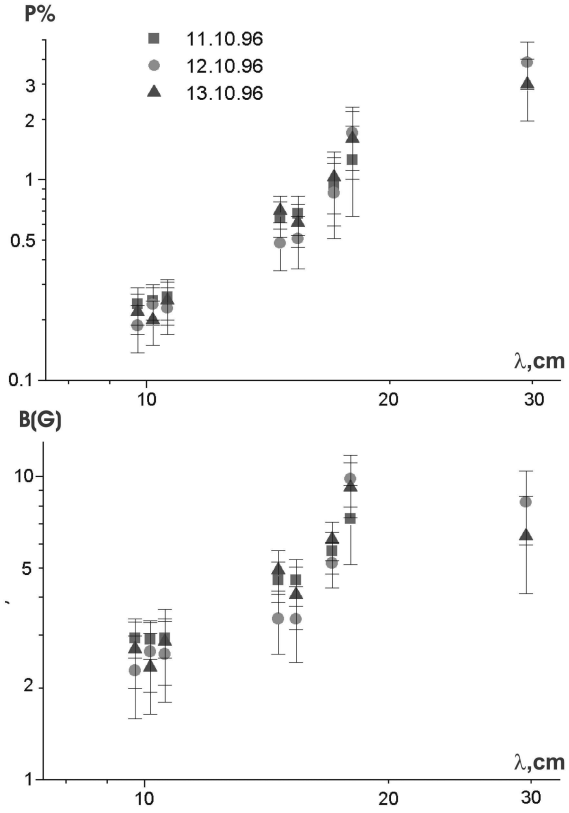


Figure 6.4. Percentage of circular polarization (upper curve) and effective value of the magnetic field (lower curve) for the coronal hole obtained from observations made with the RATAN-600. The observations were made on 1996 October 11, 12, 13.

8. Magnetic Fields in Coronal Loops

As we have discussed already for an optically thin plasma the emissivity for the thermal bremsstrahlung $\eta \propto n_e^2/\sqrt{T_e}$ (see 6.9). So, the emission is heavily weighted to high density regions in the solar corona and the radio maps are expected to reflect any type of plasma structures in the upper parts of the solar atmosphere. In contrast to the solar images obtained in the EUV lines, e.g. obtained with SOHO, the radio emission is weakly ($\propto T^{-1/2}$) dependent on the electron temperature. The longitudinal component of the magnetic field in this case is found using (6.28) based on polarization measurements. It represents the averaged value of the field weighted by n_e^2. We illustrate the method with

an example of a coronalarch (Figure 6.5) observed on the disk and connected with the CME (Borovik *et al.* 2002).

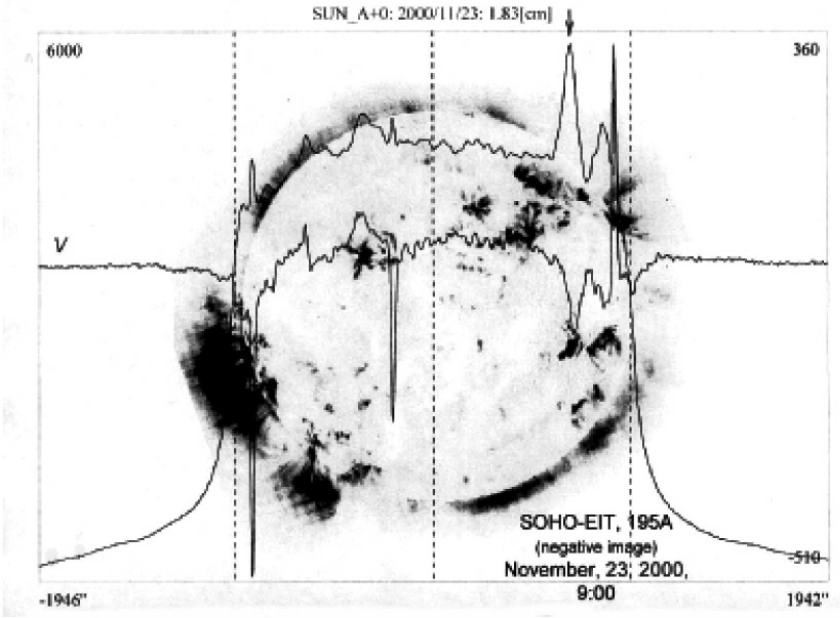


Figure 6.5. Radio scans of the Sun on 2000 November 23. The observations at the wavelength $\lambda = 1.8$ cm in intensity (I) and circular polarization (V) were made with the RATAN-600. The bright region at 195 Å according the SOHO data are shown for comparison. The coronal loop connected with the CME is marked by an arrow.

From the spectra presented at the Figure 6.6 one can conclude that the emission is really produced by the thermal bremsstrahlung from an optically thin coronal structure. The corresponding magnetic field strength was found in the range of 200–250 G. Similar values for the same structure were found from the Nobeyama radio heliograph data. An increase of the field from 150 to 200 G was registered, probably connected with the CME event. The next day the source of the coronal arch disappeared.

9. Future Development of the Method

The examples above demonstrated high effectiveness of the method of measuring magnetic fields in the solar chromosphere and corona based on analysis of bremsstrahlung radio emission. These include such coronal structures as prominences, coronal holes, CMEs, loops, and arches. The potential sensitivity of the method exceeds 1 G. The magnetic fields of few gauss in the corona have already been reported using the RATAN-600 spectral-polarization

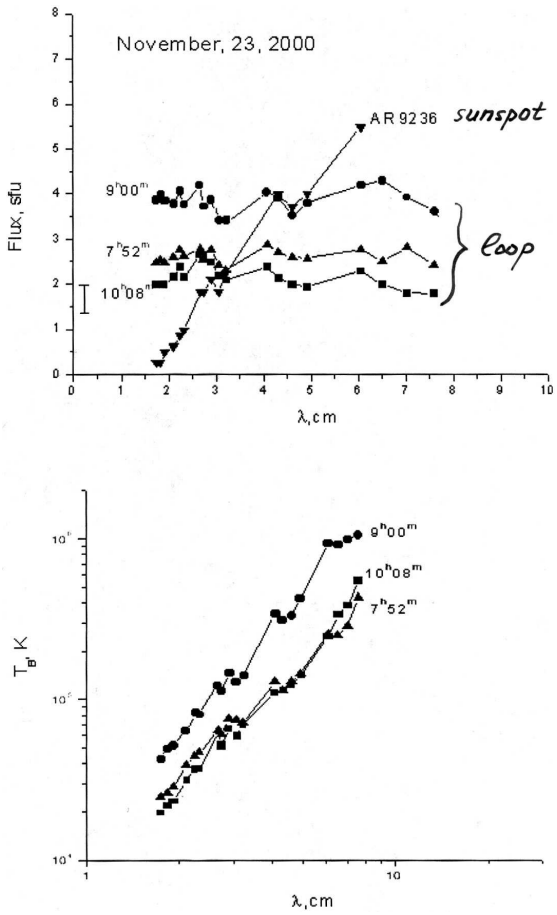


Figure 6.6. The spectra of the radio emission of the CME-associated coronal loop obtained with the RATAN-600 on 2000 November 23 for three times. The upper curves represent the spectra of intensity. For comparison also a spectra of the sunspot-associated source is shown. At the bottom, the spectra of brightness for the same loop are shown.

observations. In contrast to the method based on the observations of the gyroresonance emission (see Chapter 5, by White), the bremsstrahlung method is applicable to measurement of weaker magnetic fields (see Chapter 4, by Gary & Hurford), and presents an average of the longitude component of the field weighted by n_e^2.

In comparison with the method based on the observation of the inversion of the sign of the circular polarization (chapter 7) bremsstrahlung does not require a special region of quasi-transverse propagation and, being comparable in sensitivity, may have more general applications.

However, the method under discussion needs much higher sensitivity for polarization analysis and some spectral observations. So, at the moment numerous structures were accessible only to observations made with the instrument of high collecting area—RATAN-600. Stronger magnetic fields in active regions could be analyzed using the modern radio heliograph at Nobeyama, resulting in 2D radio magnetography. The future development of these approaches, using a combination of high spatial and spectral resolution, may give a new observational basis for the theory of the solar plasma. This is of great scientific interest because most of the energetic processes in the corona are directly due to the interaction of magnetic structures, and no other means to measure magnetic fields in the corona are available.

Acknowledgments

The results presented in this chapter were partially made with the support of the grants of the RFBR 02-02-16548 and INTAS 00181.

References

Apushkinsky, G. P., Tochilo, N. A., Tsyganov, A. N. & Nesterov, N. S. 1996, Astron. Nachr. 317, No. 6, 317

Benz, A. O. 1993, Plasma Astrophysics, Kluwer Academic Publishers.

Bogod, V. M. & Gelfreikh, G. B. 1980, Solar Phys, 67, 29

Bogod, V. M., Grebinskij, A. S. & Garaimov, V.I. 1998, Solar Phys, 182 139

Borovik, V. N., Medar, V. G. & Korzhavin, A. N. 1999, Astronomy Letters, 25, No.4, 250

Borovik, V. N., Gelfreikh, G. B., Medar, V. G. & Grigorieva, I. Y. 2002, Proc. 10th European Solar Physics Meeting, (Noordwijk: ESA Publ.), ESA SP-506, 431

Brosius, J. W., Davila, J. M., Thomas, R. J. & White, S. M. 1997, ApJ, 488, 488

Gelfreikh, G. B. 1994, IAU Colloq. 144, (VEDA Publ. Company, Bratislava), 21

Gelfreikh, G. B. 1998, Proc. of Nobeyama Symposium, NRO report No. 479, 41

Gelfreikh, G. B. & Shibasaki, K. 1999, Proc. 9th European Meeting on Solar Physics, ESA SP-448, 1139

Grebinskij, A., Bogod, V. M., Gelfreikh, G. B., Urpo, S., Pohjolainen, S. & Shibasaki, K. 2000, A&A Suppl., 144, 169

Shibasaki K., Enome S., Nakajima H., Nishio M., Takano T., Hanaoka Y., Torii C., Sekiguchi H., Kavbashina S., Bushimata T., Shinchara N., Koshiishi H., and Shiomi Y. 1994, Proc. Kofu Symposium, NRO Report No. 360, 45

Chapter 7

CORONAL MAGNETIC FIELD MEASUREMENTS THROUGH QUASI-TRANSVERSE PROPAGATION

Boris Ryabov
Institute of Astronomy of the Latvian University, Riga, Latvia
Ventspils International Radio Astronomy Center, Riga, Latvia
ryabov@latnet.lv

Abstract The QT-propagation of microwaves as a means to measure coronal magnetic fields and the inversion of circular polarization as an observational proof of the QT-propagation are discussed. The first part of the chapter briefly outlines the relevant geometry and mathematical relations. Then the state of the art in the coronal magnetography and some possibilities are demonstrated. We discuss use of the technique for coronal magnetography and give some estimates concerning the coronal magnetography with the forthcoming Frequency Agile Solar Radiotelescope.

Keywords: Sun: corona, Sun: radio, magnetic field

1. Microwave QT-Propagation in the Solar Corona

1.1 Introduction

As early as 1951, the phenomenon of polarization inversion in solar microwave sources was discovered (Piddington & Minnett 1960). It was correctly attributed to result from the quasi-transverse (QT-) propagation of microwaves (Cohen 1960). However, so far it has been a difficult task to use the effect of QT-propagation for magnetic field measurements in a coronal region, although the position of the QT region is defined by the coronal magnetic structure.

The first problem a solar physicist encounters is the correct identification of the observed polarization inversion. Other effects, in addition to QT-propagation, can give rise to polarization inversion in microwaves. Some alternatives are a temperature gradient inverted with height in a gyroresonance source (Zlotnik

1999), propagation angle variations in a source at the top of a coronal loop (Alissandrakis & Preka-Papadema 1984), and energetic (nonthermal) electrons trapped in a magnetic loop. In this chapter we seek to list the regularities of the inversion due to QT-propagation to assist the search of its manifestations.

The next problem is an adequate analysis of polarization inversion. The interplay between the position of an active region (AR) on the solar disk and the frequency dependence of the QT-propagation leads to the observed variety of polarization inversions in microwaves. Multiple polarization inversions may also occur at cm wavelengths as a result of multiple passages of microwave emission through the coronal regions of QT propagation (QTRs) (Bogod *et al.* 1993; Alissandrakis *et al.* 1996). The sporadic radio observations at only a few frequencies do not necessarily enable us to analyze the multiple inversion with sufficient certainty. The Frequency Agile Solar Radiotelescope (FASR), which will provide arcsecond-resolution full-disk images of the Sun, is well suited for the in-depth analysis and coronal magnetography. We attempt to demonstrate some advantages of this analysis and the benefits a solar physicist may get from it. Radio measurements in the QTR inherently involve the magnetic fields of the key topological regions. The points of fundamental interest in an active region magnetosphere, such as neutral points and solar flares may be probed using these techniques.

A persisting problem is the accurate value of the distance between the microwave source and the QTR. The distance or the height of the QTR above the photosphere is the only unknown coordinate of the measured magnetic field. The model extrapolations of the magnetic field to coronal heights (Alissandrakis *et al.* 1996; Lee *et al.* 1998) and the direct determinations of the height from the inversion rate (Bezrukov *et al.* 2004) do not seem to yield agreement.

Since 1963, when the mathematical relation between coronal magnetic field in the QTR and the observed circular polarization was deduced (Zheleznyakov & Zlotnik 1963), the two-dimensional (2D) coronal magnetography in the QTR at a single frequency has been made possible. Up to now, analysis of QT propagation has dealt only with the line of zero circular polarization (polarization inversion line). It has not taken into account the portion of the microwave source that is partly depolarized by a QTR. Since solar observations with the Nobeyama Radioheliograph (NoRH), the Siberian Solar Radio Telescope (SSRT), and the Very Large Array (VLA) give 2D measurements with a high angular resolution, we suggest the development of 2D coronal magnetography based on the effect of QT-propagation of microwaves (Ryabov *et al.* 1999). To this end, the normalization procedure should be improved. We mean the procedure of a radio image reduction requires that that the image be subjected to the QT-propagation effect only.

1.2 Effects of electromagnetic wave mode coupling

In this section a few definitions and mathematical relations are cited to carry out the analysis of polarization inversion at microwaves. We restrict our discussion to the cases appropriate for solar observations at cm wavelengths.

An electromagnetic wave at a given frequency can be expressed as a linear combination of the ordinary (o) and extraordinary (x) wave modes (Stix 1962). The polarization in these two modes is of opposite senses and tends to be circular in the outer solar corona for most values of the angle θ between the coronal magnetic field $\mathbf{B}$ and the line of sight $\mathbf{s}$ (quasi-linear propagation, QL). The polarization becomes linear in the regions where the angle θ is in the range near 90° (quasi-transverse propagation, QT; Zheleznyakov 1970).

The sense of circular polarization of these modes corresponds to the sign of longitudinal component of magnetic field in a source of microwave emission. As the x-mode prevails for most sources of thermal microwave emission in the Sun, the polarization of a sunspot-associated source can be related with the sign of sunspot magnetic fields. Right-circularly polarized (RC) emission corresponds to N (positive) magnetic fields, while left-circularly polarized (LC) emission corresponds to S (negative) magnetic fields. However, the sense of circular polarization as intrinsically emitted may become inverted due to passage through the corona, by the time that the wave reaches the observer.

Polarization inversions have been detected in some microwave sources (Piddington & Minnett 1960; Peterova & Akhmedov 1974) and throughout the cm wavelength range (Peterova & Akhmedov 1974; Gelfreikh *et al.* 1987) (Figure 7.1). No corresponding changes of magnetic polarity in the photosphere have been observed. It appears that the polarization is strongly affected by propagation conditions on the way through the solar corona to the observer. The wave mode coupling theory (Cohen 1960; Zheleznyakov 1970) deals with the propagation and interaction (coupling) between o- and x-mode waves. The sense of circular polarization is inverted when the waves cross the region of transverse magnetic fields, where the sign of the longitudinal component changes. However, if the transverse magnetic fields are weak enough, electromagnetic waves at high frequencies do not "respond" to them and they do not change the sense of circular polarization. The o and x wave modes strongly interact in this case. The transverse fields of intermediate strengths cause the depolarization, so far as circular polarization is converted to linear (Zheleznyakov 1970).

The wave mode-coupling theory offers a rigorous treatment of this wave mode interaction. The efficiency of the interaction is determined by the parameter $\delta_\circ$ (Zheleznyakov & Zlotnik 1963) :

$$2\,\delta_\circ \approx 1.15 \times 10^{-25} B^3 n_e L_d \lambda^4\,, \tag{7.1}$$

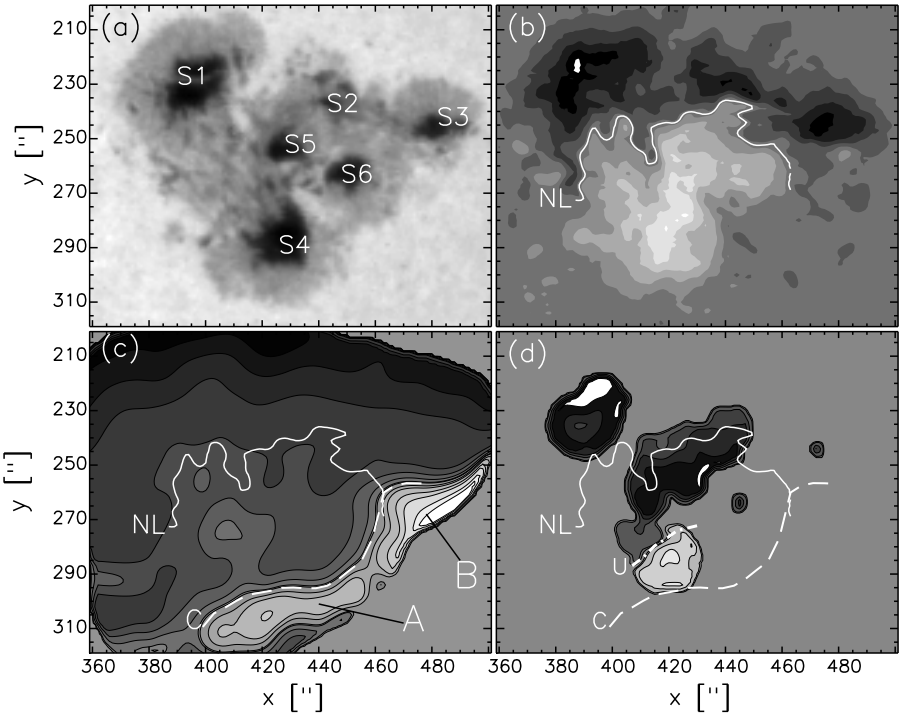


Figure 7.1. AR 6615. Radio maps of the circular polarization degree taken with the VLA at 4.9 GHz and 15 GHz (lower row) together with a white-light picture and a longitudinal magnetogram (upper row). At both frequencies the sense of circular polarization does not correspond to magnetic polarity in the region above the sunspot S5. The depolarization lines, $V = 0$, at 4.9 GHz (dashed line C) and at 15 GHz (dot-dashed line U) are noticeably shifted from a zero line of longitudinal photospheric magnetic fields (solid line NL). (From Lee *et al.* 1998).

where B is the strength of coronal magnetic fields, n_e is the electron density, L_d is the field divergence in the coronal QT-region, $L_d = \theta \mid d\theta/d\mathbf{s}|^{-1}$, and λ is the operational wavelength (hereafter, all units are in CGS). Notice that $2\,\delta_\circ$ differs from the coupling parameter C (Zheleznyakov & Zlotnik 1963; Bandiera 1982) by a factor of the order of unity.

If $\rho_\circ^V$ is the degree of circular polarization of the wave incoming the region of quasi-transverse propagation (QTR; $\theta \approx 90^\circ$), the circular polarization ρ^V after passing through the QTR reads (Zheleznyakov & Zlotnik 1963):

$$\rho^V = \rho_\circ^V \left[2 \, \exp(-2\delta_\circ) - 1 \right] . \tag{7.2}$$

When the QTR is crossed by an electromagnetic wave, there are the following cases:

$2\,\delta_\circ << 1$: strong wave mode coupling, $\rho^V \approx \rho_\circ^V$,
$2\,\delta_\circ = \ln 2$: critical wave mode coupling, $\rho^V = 0$,
$2\,\delta_\circ >> 1$: weak wave mode coupling, $\rho^V \approx -\rho_\circ^V$.

Let us rewrite (7.1) and (7.2) with $n_e L_d = 10^{18}$ cm^{-2} :

$$B \approx 2.05 \times 10^2 \, \lambda^{-4/3} \left[- \ln \left(\frac{\rho^V / \rho_\circ^V + 1}{2} \right) \right]^{1/3} . \tag{7.3}$$

The above cases might be simplified and expressed in terms of the strength B of the magnetic field in the QTR, provided the factor $n_e L_d$ is constant:

$B << B_\circ$: weak magnetic fields; circular polarization is preserved,
$B = B_\circ$: critical value of magnetic fields; depolarization,
$B >> B_\circ$: strong magnetic fields; inversion of circular polarization.

In the same way the cases above might be classified in terms of frequencies (wavelengths) of electromagnetic waves. Let us define the transition frequency ν_t as a frequency of zero circular polarization, $\rho^V(\nu_t) = 0$.

It appears that other kinds of the wave mode interactions and corresponding coupling parameters (see Gopalswamy *et al.* 1994 as a review) are mainly applicable beyond cm wavelength range. Some cases of an apparent disagreement with the coupling theory are reported in decimetric and metric wavelength ranges (Gopalswamy *et al.* 1991; White *et al.* 1992). Gopalswamy *et al.* (1994) have proposed to overcome the above difficulties by considering a specific mode coupling in a coronal current sheet which has been detected at 1.5 GHz.

We will use Eq. (7.3) along with the specified terms in the analyses and measurements of coronal magnetic fields. The polarization value is most sensitive to the strength B of coronal fields under the condition $\rho^V = 0$. More precisely, the highest sensitivity of the measurements corresponds to

$$\rho^V = \rho_\circ^V \left[2 \, \exp(-\frac{2}{3}) - 1 \right] \approx 0.0268 \, \rho_\circ^V \, , \tag{7.4}$$

which was obtained by solution of the equation $\partial^2 \rho^V / \partial B^2 = 0$, implying the maximum of the function $\left| \partial \rho^V / \partial B \right|$.

1.3 Geometry of QT-propagation

To illustrate the interplay between the location of the QTR in an active region and the dominant parameters in (7.1) and (7.2), that is, the wavelength of observations and the coronal magnetic field, let us introduce a QT-surface. The surface is the central part of the QTR, where the propagation angle θ is strictly equal 90°. It should be noted that the thickness of the QTR , $2\pi^{-1} L_d \sqrt{u} \approx 10^8 - 10^9$ cm (Kravtsov & Naida 1976), is small compared with the solar active region size.

It is important to note that the shape and the location of the QT-surface depend on the direction of the line of sight (Figure 7.2). In the case of a magnetically unchanging active region, the shape of the QTR is modified only due to solar axis rotation. On a large scale the QTR appears as an inclined conical surface in the case of uniform magnetic fields of a single sunspot. As the photospheric neutral line satisfies the condition $B_l = 0$—that is $\theta = 90^\circ$—the line is always the lower border of the QT-surface. The location of all the magnetic neutral points, $B = 0$, on a QT-surface can be deduced similarly.

When the source is near the solar disk center, the QT-surface is crossed by microwaves higher up in the corona, where the magnetic field B is weak and the resulted polarization ρ^V is the same as in front of the QTR, that is, $\rho_\circ^V$ in (7.2). As the Sun rotates, a microwave source moves towards the west solar limb. The QTR is crossed by microwaves lower in the corona (Figure 7.2) and the sign of the resulted circular polarization is reversed (Figure 7.3).

Another case is a bipolar active region with the axis directed along a solar meridian. This geometry seems to promote the QT-propagation of microwaves from sources most distant from the solar equator. The inverted sign of circular polarization may remain for many days within such a bipolar active region.

2. Results and Prospects of Microwave Observations

Prior to analysis in terms of coronal magnetography, it should be tested whether the polarization inversion is due to the QT-propagation. The test depends on whether the inversion is observed at a single wavelength over time or it is observed at many microwave frequencies at a single time. Spectral-polarization observations with a high angular resolution, such as FASR will produce, are preferable for the correct identification and precise analysis of the polarization inversion.

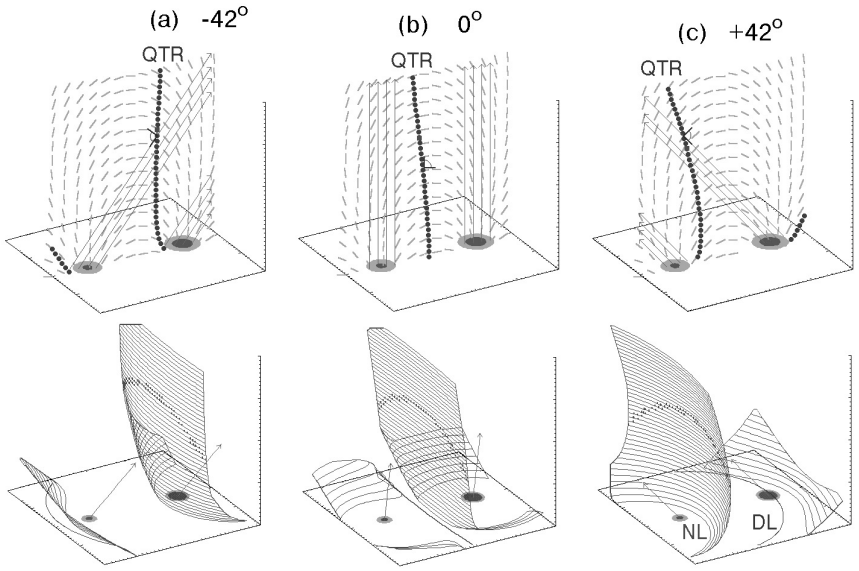


Figure 7.2. Simulated geometry of QT-propagation of microwaves in a bipolar active region in the vertical section (upper row) and in 3D representation (lower row). Two microwave sources over sunspots of opposite magnetic polarities emit the radiation at 5.7 GHz circularly polarized in opposite sense. The observed circular polarization (presented in Figure 7.3) is quite different for each of the three longitudinal displacements from the central solar meridian (a) -42°, (b) 0°, and (c) $+42^\circ$ depending on whether the QTR is crossed higher or lower than the line of the critical value $B_\circ = 20$ G of coronal magnetic fields. The 20 G isogauss contour projected to the plane of the sources appears as a depolarization line, $V = 0$, at 5.7 GHz (line DL).

2.1 Regularities of the inversion phenomenon

As mentioned earlier, an inversion in the sign of circular polarization of a microwave source might be caused by a variety of factors. Before dealing with coronal magnetography one needs the unambiguous evidence of the manifestation of the QT-propagation of microwaves in the solar corona. The following regularities summarize some radio observations (Peterova & Akhmedov 1974) and model simulations of the polarization inversion due to the QT-propagation:

(1) the sunspot-associated microwave source nearest to the solar limb is the first that inverts its sign of circular polarization in an AR.

The regularities for the western solar hemisphere are as follows:

(2) the closer an AR is to the W solar limb, the shorter is the wavelength required to detect the polarization inversion;

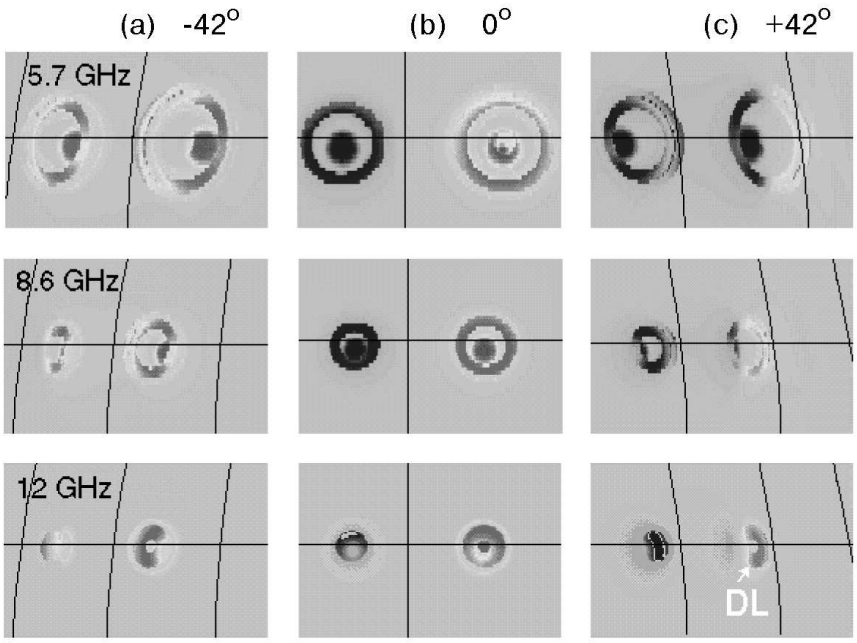


Figure 7.3. Transformations of the circularly polarized microwave sources simulated with due regard to the QT-propagation of microwaves using the geometry in Figure 7.2. Each row represents the sources simulated at 5.7 GHz (upper row), 8.6 GHz, and 12 GHz (lower row). Each panel in the rows depicts the sources at the longitudinal displacement from the central solar meridian: (a) -42°, (b) 0°, and (c) +42°.

(3) the depolarization line, $\rho^V = 0$, moves toward the W solar limb while the polarization inversion is observed at a fixed operational wavelength;

(4) the post-inversion value of the degree of circular polarization, as a rule, does not exceed the pre-inversion one.

The regularities for the eastern solar hemisphere are as follows:

(5) the farther an AR is from the E solar limb, the longer is the wavelength required to detect the polarization inversion;

(6) the depolarization line, $\rho^V = 0$, moves toward the W solar limb while the polarization inversion is observed at a fixed operational wavelength;

(7) if the microwave source of circularly polarized emission is a loop-associated source, as is often the case at long wavelengths, the regularities of polarization inversion seem to be similar to those of a sunspot-associated

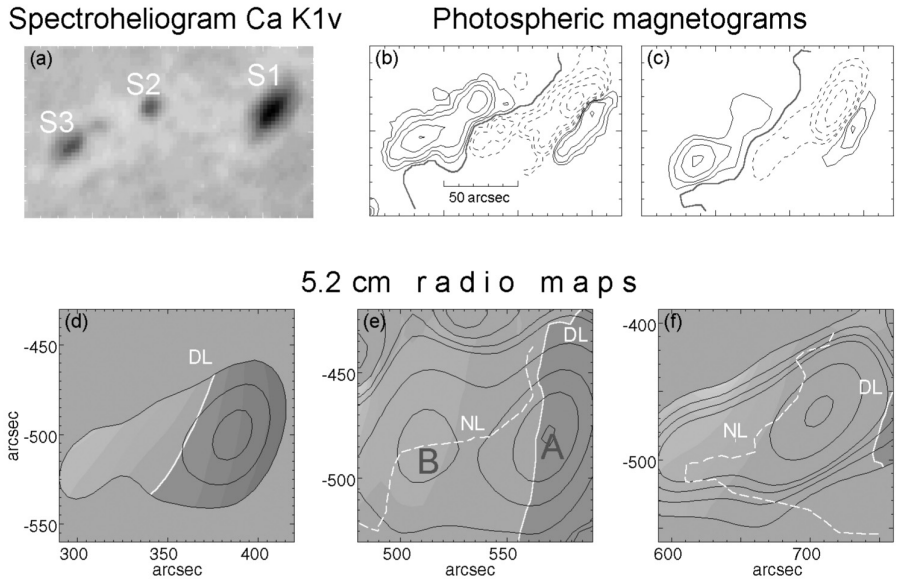


Figure 7.4. AR8365. Three radio maps taken with the SSRT at 5.7 GHz (lower row) on (d) October 21, (e) October 22, and (f) 1998 October 23, together with a spectroheliogram CaII K1v on (a) October 22 and the longitudinal magnetograms on (b) October 22 and (c) October 23. RC (brighter halftones) and LC (darker halftones) radio polarizations are separated by depolarization line DL. Note the displacement of the depolarization line above the western sunspot-associated microwave source A. A zero line of longitudinal photospheric magnetic fields is marked by dashed white line NL. (From Ryabov *et al.* 2004).

source. The initial sign of circular polarization corresponds to the sign of the longitudinal component of the magnetic field B_l. The analyses of the polarization inversion at a given wavelength with time must take into account both the QT-propagation and the displacement of the coronal neutral line, $B_l = 0$, within the loop (Alissandrakis and Preka-Papadema, 1984).

The above regularities immediately follow from (7.1), (7.2) and from the geometry of QT-surface in a bipolar AR with the magnetic meridian approximately in the east-west direction. Figures 7.4, 7.5 give an example of how the polarization inversion proceeds in a slightly polarized microwave source with time and frequency.

The FASR telescope will give the opportunity to provide the test of QT-propagation by the spectral-polarization observation inspection. During these observations with the FASR it is necessary that the above observational find-

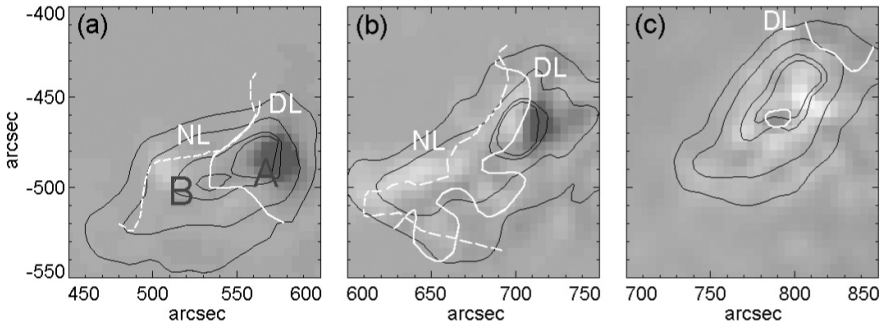


Figure 7.5. The representation of the AR8365 (similar to Figure 7.4) but at the frequency of 17 GHz a day later. Radio maps in Stokes I (black contours) and the degree of circular polarization V/I (grayscale) taken with the NoRH at 17 GHz ($\lambda = 1.76$ cm) on (a) 1998 October 22, (b) October 23, and (c) October 24. RC (brighter halftones) and LC (darker halftones) polarization are separated by the depolarization line DL. (From Ryabov *et al.* 2004).

ings be taken into consideration. The detailed analysis of QT-propagations is promising. Some possibilities of the coronal magnetography application are examined in § 2.2–2.4.

2.2 Multiple inversion

The multiple inversion through the cm wavelength range has emerged from one-dimensional spectral-polarization observations with the RATAN-600 telescope. Bogod *et al.* (1993) have detected the double inversion of the circular polarization sign over a cm wavelength range in a sunspot-associated source. Schmelz *et al.* (1994) and Alissandrakis *et al.* (1996) have reported the double inversion for a part of a microwave source. The latter inversions are revealed from model analyses of radio maps made at a single wavelength. How may we test the applicability of QT-propagation, and determine the number of possibly multiple inversions of this type?

An appropriate examination is provided by some model simulations of QT-surfaces and numerical restrictions on ρ^V to be derived from (7.1) and (7.2). Let $\varepsilon \leq 0.03$ be the wavelength spacing, $\lambda_{i+1} = \lambda_i + \varepsilon\,\lambda_i$ in the case of the FASR telescope. The normalized degree of circular polarization P reads (Ryabov, 1997):

$$P(\lambda_{i+1}) \equiv \frac{\rho^V(\lambda_{i+1})}{\rho^V_\circ(\lambda_{i+1})} = 2^{1-(1+\varepsilon)^4} - 1\,. \qquad (7.5)$$

We can observe that the normalized degree of circular polarization at the wavelength λ_{i+1} adjacent to the wavelength λ_i of zero polarization, $\rho^V(\lambda_i) = 0$, is suppressed to the known value. If we assume $\varepsilon = 0.03$, we get $P \approx -0.083$. It is advisable to have the FASR accuracy high enough to resolve the above 8% of the normalized circular polarization, which is difficult to attain having a slightly polarized source $\mid \rho^V_\circ(\lambda_{i+1}) \mid \ll 1$. It is self-evident that the restriction on P is necessary but it is not a sufficient condition for the polarization inversion to be determined by QT-propagation.

The multiple inversion as a result of QT-propagation seems to be promising for coronal magnetography at a set of coronal heights simultaneously. The magnetic structure in the vicinity of a magnetic neutral point (NP) is supposed to produce a double polarization inversion (Figure 7.6). It is expected that a NP will occur as $10'' - 30''$ oppositely polarized intrusion into the microwave source situated behind, and FASR will provide a unique tool to observe such a NP.

2.3 Linear polarization in the outer corona

It appears that linear polarization can be detected within a narrow bandwidth if the QTR, where circular polarization is transformed to linear, is at a sufficient height that the Faraday rotation does not smear the linear polarization to zero.

In 1993 the linear polarization was detected by Alissandrakis and Chiuderi Drago (1994) above the AR 7530 in the course of circular polarization sign inversion due to QT-propagation. The observations were made with a multi-channel spectral line receiver at the Westerbork Synthesis Radio Telescope (63 channels 19.6 kHz wide in a 1.2 MHz bandwidth around $\nu = 4995$ MHz). The angular resolution of the WSRT is $3'' \times 9''$ at this wavelength of 6 cm. The linear polarization components, Stokes U, Q, measured close to the depolarization line, $V = 0$, show a sinusoidal trend as a function of λ^2 in accordance to the Faraday rotation (Alissandrakis & Chiuderi Drago 1994). Using the current-free assumption for AR coronal magnetic fields the height of the QTR is estimated to be 10^{10} cm above the photosphere (Alissandrakis *et al.* 1996).

It is interesting to note that the analyses of full Stokes vector (I, Q, U, V) by Segre and Zanza (2001) retrieve both the strength of the coronal field $B = 12.8 - 11.2$ G and the factor $n_e L_d = (1.4 - 2.1) \times 10^{18}$ cm^{-2} from those observational data.

2.4 Oscillations

The depolarization line is the most convenient line in the field of view to trace polarization inversion. It is clearly seen in V radio maps and it is not subjected

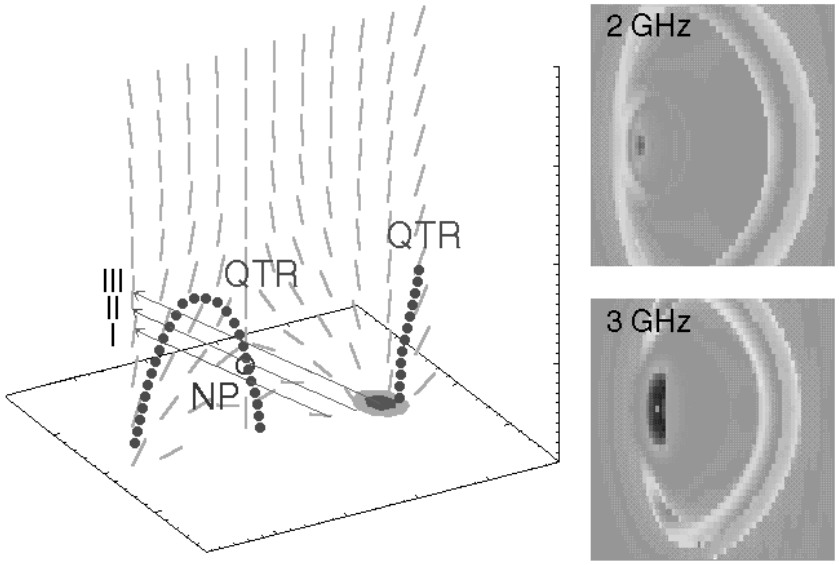


Figure 7.6. Representative geometry of QT-propagation of microwaves throughout the vicinity of the neutral point (NP; circle) of the coronal magnetic fields. The total number N of the polarization sign inversions at 2 GHz along the ray paths: I, $N = 2$; II, $N = 1$; III, $N = 0$. A result of the twofold QT-surface is the elliptic dark patch of opposite polarization at long cm wavelengths. Double sign inversion is expected in the patch over a cm wavelength range.

to alteration by the normalization procedure, that is, $\rho^V/\rho_\circ^V$. As discussed above, $\rho^V = 0$ is the polarization degree that is most sensitive to the coronal magnetic field. If the coronal fields oscillate, the depolarization line is bound to oscillate too.

Recently the oscillations of $\rho^V = 0$ points were found in the radio scans taken with the SSRT at the wavelength 5.2 cm (Gelfreikh *et al.* 2002). Oscillations with the characteristic time of about 13 min were detected in the course of polarization inversion in a sunspot-associated source of the AR 6412.

According to (7.1) and (7.2), $\rho^V = 0$ at $\lambda = 5.2$ cm is produced by the coronal field of about 20 G with $n_e L_d = 10^{18}$ cm^{-2} in the QTR. The depolarization line oscillations provide an accurate account of the oscillations of the coronal magnetic field.

3. The Technique of Coronal Magnetography Through QT-Propagation

This coronal magnetography begins with the proof that the QT-propagation is responsible for the polarization inversion and ends with the analyses of 2D coronal magnetograms. It is (7.3) that enables us to evaluate 2D coronal magnetograms.

3.1 Normalization procedure

According to (7.3), the distribution $\rho^V(x,y)$ normalized to the circular polarization degree $\rho^V_\circ(x,y)$ of initial radiation results in 2D coronal magnetograms $B(x,y)$, provided the factor n_eL_d is given. Since $\rho^V_\circ$ is modified in the QTR during the polarization inversion, the inherent polarization of a source is not known. We propose some practical substitutes for $\rho^V_\circ$:

(1) circular polarization degree observed at the day of the absence of QT-propagation effects. A limitation of this normalization is quite obvious: the AR evolves and $\rho^V_\circ$ alters with time;

(2) circular polarization calculated by the model simulations of the microwave source under study. Not only the sunspot-associated microwave source, but also a coronal condensation should be taken into account at long cm wavelengths.

We will illustrate the process of choosing $\rho^V_\circ$ for the normalization procedure (Figure 7.7). The depolarization line, $V=0$, moves across the western source in the sequence of the maps. In the first map the depolarization line roughly marks the border between two microwave sources of the opposite polarization not affected by the QT-propagation. Hence the first map is taken to be a $\rho^V_\circ(x,y)$ map. If a set of sampled maps covers the overall process of inversion with time, the polarization is only slightly suppressed in the starting map and the inverted polarization attains its maximum value in the last map.

With $\rho^V_\circ$ chosen according to the first substitute, the $\rho^V(x,y)$ maps should be shifted to the position of $\rho^V_\circ(x,y)$ on the solar disk. Finally, the normalized maps $P=\rho^V/\rho^V_\circ$ are expressed in gauss units according to (7.3). The resulted coronal magnetograms are depicted in Figure 7.8. The borders of the coronal magnetograms are determined by the limitation $\mid P \mid \leq 1-\sigma$, where σ is the accuracy of the observed ρ^V.

A reference coronal magnetogram is introduced in Ryabov *et al.* (1999) as a convenient intermediate result. The reference magnetogram is a magnetogram calculated by means of Eq. (7.3) with the constant value of n_eL_d factor. Taking into account the opposite sense of the variations of n_e and L_d with height, and the evaluation of n_e and L_d in Segre & Zanza (2001), the constant value of $n_eL_d = 10^{18}$ cm^{-2} is reasonable. It is easy to correct the reference magnetogram if a

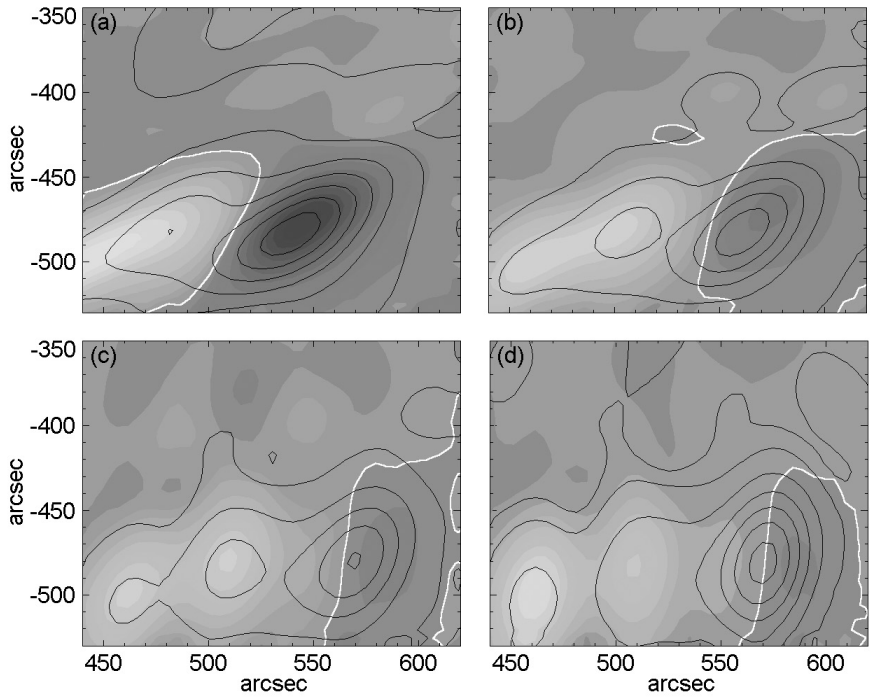


Figure 7.7. Details of the inversion phenomenon presented in Figure 7.4. AR8365. Radio maps in Stokes I (black contours) and V (grayscale) taken with the SSRT at 5.7 GHz ($\lambda = 5.2$ cm) on 1998 October 22 at (a) 2:54 UT, (b) 3:54 UT, (c) 5:54 UT, and (d) 6:54 UT. RC (bright halftones) and LC (dark halftones) polarization are divided by depolarization line (solid white line). (From Ryabov *et al.* 2004).

more precise distribution of electron density n_e or the divergence of the magnetic field L_d is known.

3.2 The source-QTR distance

There are generally three methods to evaluate the distance between the microwave source and the QTR or the height of the measured coronal field.

According to the first method, the distance is geometrically determined from the depolarization line displacements or from the time over which the polarization inversion lasts. The height of the transverse magnetic fields that screen the microwave source is assumed to be constant in the QTR during the inversion (Gelfreikh *et al.* 1987).

The second method calculates the distance between the source and the QTR by means of the magnetic field extrapolations to coronal heights. This extrap-

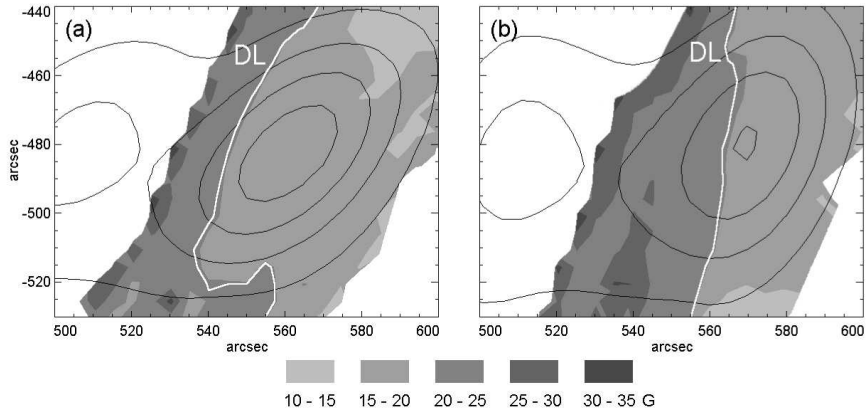


Figure 7.8. AR8365. Two coronal magnetograms (grayscale) show the strength of coronal magnetic fields on 1998 October 22 at (a) 3:54 UT and (b) 5:54 UT. The halftones corresponding to the coronal fields 10–30 G are clearly seen. The radio depolarization line $V = 0$ at 5.7 GHz is marked by a white line DL. (From Ryabov *et al.* 2004).

olation should be consistent with the radio observations (Alissandrakis *et al.* 1996; Lee *et al.* 1998).

The third method suggests that the observed distance between the radio depolarization line and the photospheric neutral line is converted to the height of the QTR in the frame of the dipole approximation of an active region magnetosphere(Bandiera 1982; Kundu & Alissandrakis 1984).

The uncertainty of the distance estimates is rather high and may reach the factor 2 if the results of any two methods are compared. Lee *et al.* (1998) have attributed the uncertainty to the specific geometry of the QTR: a QT surface may be inclined nearly along the line of sight direction. It is worth noting that the coronal magnetograms relate to the coronal fields in the QTR which are not necessarily located directly above a microwave source.

3.3 Scrutiny of a coronal magnetogram

Any coronal magnetogram shows the features intrinsic to the magnetic field distribution in the QTR projected to the plane of view. We will specify some apparent features in terms of $P = \rho^V / \rho_\circ^V$ to observe the normalization procedure results.

(a) Since the photospheric neutral line is a lower border of the QTR, it is evident that the projection of the strongest coronal field $(-1 < P < 0)$

should be closer to the neutral line than that of the weakest field $(0 < P < 1)$. This is true as far as the frequency of observations is concerned: the higher the frequency is, the closer the depolarization line, $P = 0$, lies to the neutral line (Figure 7.1).

(b) The weaker the field in the QTR $(P > 0)$, the faster the movement of its projection will be during the polarization inversion (Figure 7.8). The strong coronal field $(P < 0)$ at a low height is responsible for a slow movement of its projection.

(c) The depolarization line, as well as any $P = constant$ line in the plane of view, tends to move toward the W solar limb during the polarization inversion (Figure 7.8).

Some small-scale structural peculiarities of an AR magnetosphere, such as neutral points, are supposed to be watched with the coronal magnetograms in hand.

A QT surface itself is a significant geometrical feature. It presents a large-scale outline of an AR magnetosphere, if the direction of the line of sight is also taken into consideration. The FASR telescope will enable us to get not only a full-range coronal magnetography, but also to retrieve the 3D geometry of the QTR throughout an AR magnetosphere.

4. Summary and Conclusions

The experience accumulated suggests that the frequency range around 7 GHz is convenient for the measurements in the QT region (Peterova & Akhmedov 1974; Gelfreikh *et al.* 1987). A fairly polarized sunspot-associated source at 7 GHz can be differentiated from a loop-associated source with its distinct internal magnetic structuremagnetic,structure (Alissandrakis & Preka-Papadema 1984). The higher the circular polarization of a microwave source, the more reliable is the distribution of polarization over the source and hence the more reliable is the resulting coronal magnetogram. As far as the feasibility of coronal field measurements at cm wavelengths using the polarization inversion phenomenon is concerned, the measurements have proved to be effective up to 17 GHz (Ryabov *et al.* 1999; Ryabov *et al.* 2004). The coronal fields of 20–40 G at the heights of (7.0–5.5)$\times 10^9$ cm (Alissandrakis 1999; Lee *et al.* 1998) and of 100 G at 3.5×10^9 cm (Alissandrakis 1999; Ryabov *et al.* 1999) may be cited as characteristic values, though the natural height variations from one active region to another are high.

An occasional character of the polarization inversion and the required availability of a polarized source beneath the QTR are the drawbacks of the measurements from the QT-propagation. The inversion predictions based on the known regularities (§ 2.1) and the analyses of the sizable polarized sources for

the coronal magnetography service are under development now (Ryabov *et al.* 2004; Bezrukov *et al.* 2004).

The measurements discussed above are complementary to the radio measurements through gyroresonance emission, discussed in Chapter 5, by White and bremsstrahlung emission, discussed in Chapter 6, by Gelfreikh. The former are complemented by the evaluation of weaker magnetic fields (down to 1 G at cm wavelengths), and the latter are complemented by the determination of transverse magnetic fields. It should be noted that the measurements through the QT-propagation do not depend on the emission mechanism operating in a polarized source.

The 2D coronal magnetography through the QT-propagation is a new technique. The subsequent coronal magnetic field measurements with the NoRH, the SSRT, and the VLA have shown the application areas and limitations of the technique. The essential part of this technique, the normalization procedure, should improve radically given more complete spectral and spatial observations.

The wave propagation theory being developed by Segre and Zanza (2001) shows that much more information can be gained in the course of polarization inversion from the radio observations in the four Stokes parameters. For example, the detection of Faraday rotation above the line of zero circular polarization (Alissandrakis & Chiuderi Drago 1994) provides magnetic fields higher in the solar corona than other measurements do. The product of electron density and the scale of the magnetic field divergence involved in the coronal magnetography (see equation 7.3) can also be determined along with the magnetic field strength in the QTR (Segre & Zanza 2001).

A potent technique of coronal magnetography could be based on nearly simultaneous radio mappings over a wide range of frequencies. A set of zero polarization lines detected within a microwave source at a number of frequencies will ensure a full-range magnetogram and provide the highest sensitivity to coronal magnetic fields in the QTR. The forthcoming Frequency Agile Solar Radiotelescope will promote the coronal magnetography technique as well as an allow in-depth study of other aspects of the inversion phenomenon.

Acknowledgments

This work has been supported by INTAS grants 00-0181 and 00-0543.

References

Alissandrakis, C. E. 1998, Proc. Nobeyama Symp., Kiyosato, Japan, (T.Bastian, N.Gopalswamy and K.Shibasaki, eds.), NRO Report No. 479, 53

Alissandrakis, C. E., Borgioli, F., Chiuderi Drago, F., Hagyard, M., Shibasaki, K. 1996, Solar Phys, 167, 167

Alissandrakis, C. E. & Chiuderi Drago, F. 1994, ApJ, 428, L73

Alissandrakis, C. E. & Preka-Papadema, P. 1984, A&A, 139, 507
Bandiera, R. 1982, A&A, 112, 52.
Bezrukov, D. A., Ryabov, B. I., Bogod, V. M., Gelfreikh, G. B., Maksimov, V. P., Drago, F., Lubyshev, B. I., Peterova, N. G., Borisevich, T. P. 2004, Baltic Astronomy, submitted
Bogod, V. M., Gelfreikh, G. B., Ryabov, B. I., Hafizov, S. R. 1993, ASP Conference Series, 46, 302
Cohen, M. H. 1960, ApJ, 131, 664
Gelfreikh, G. B., Peterova, N. G., Ryabov, B. I. 1987, Solar Phys, 108, 89
Gelfreikh, G. B., Ryabov, B. I., Peterova, N. G., Drago, F., Agalakov, B. V., Borisevich, T. P., Lubyshev, B. I., Maksimov, V. P. 2002, Abstracts of the Russsian conf. "Active Processes on the Sun and stars," July 2–6, St. Petersburg (in Russian)
Gopalswamy, N., White, S. M., Kundu, M. R. 1991, ApJ, 379, 366
Gopalswamy, N., Zheleznyakov, V. V., White, S. M., Kundu, M. K. 1994, Solar Phys, 155, 339
Kravtsov, Yu. A. & Naida, O. N. 1976, Soviet.Phys., 44, 122 (1976, JETP, 71, 237)
Kundu, M. R. & Alissandrakis, C. E. 1984, Solar Phys, 94, 249
Lee, J., White, S. M., Kundu, M. R., Mikic, Z., McClymont, A. N. 1998, Solar Phys, 180, 193
Peterova, N. G. & Akhmedov, Sh. B. 1974, Soviet. Astron., 17, 768
Piddington, J. H. & Minnnett, H. C. 1951, Austral. J. Sci. Res., A4, 131
Ryabov, B. I. 1997, Baltic Astronomy, 6, 651
Ryabov, B. I., Maksimov, V. P., Lesovoi, S. V., Shibasaki, K., Nindos, A., Pevtsov, A. A. 2004, Solar Phys, submitted
Ryabov, B. I., Pilyeva N. A., Alissandrakis, C. E., Shibasaki, K., Bogod, V. M., Garaimov, V. I., Gelfreikh G. B. 1999, Solar Phys, 185, 157
Schmelz, J. T., Holman, G. D., Brosius, J. W., Willson, R. F. 1994, ApJ, 434, 786
Segre, S. E. & Zanza, V. 2001, ApJ, 554, 408
Stix, T. H. 1962, The theory of plasma waves, New-York: Mc Graw-Hill.
White, S. M., Thejappa, G., Kundu, M. R. 1992, Solar Phys, 138, 163
Zheleznyakov, V.V. 1970, Radio Emission of the Sun and Planets, Oxford: Pergamon Press.
Zheleznyakov, V. V., Zlotnik, E. Ya. 1963, Astron. Zhurn., 40, 633 (1964, Soviet Astron., 7, 485)
Zlotnik, E. Ya. 1999, Proc. 9th European Meeting on Solar Physics, Florence, ESA, SP-448, 1239

Chapter 8

OVERVIEW OF SOLAR FLARES

The Yohkoh Perspective

Hugh Hudson
Space Sciences Laboratory, UC, Berkeley CA USA 94720
hhudson@ssl.berkeley.edu

Lyndsay Fletcher
Dept. of Physics & Astronomy, University of Glasgow, Glasgow G12 8QQ, Scotland, U.K.
lyndsay@astro.gla.ac.uk

Josef I. Khan
Dept. of Physics & Astronomy, University of Glasgow, Glasgow G12 8QQ, Scotland, U.K.
jkhan@spd.aas.org

Takeo Kosugi
Institute for Space and Astronautical Sciences, Sagamihara, Kanagawa, Japan
kosugi@solar.isas.jaxa.jp

Abstract This chapter reviews the physics of solar flares, with special emphasis on the past decade. During this decade first *Yohkoh* and then TRACE have drastically improved our observational capabilities for flares, with contributions also from the essentially non-flare instrumentation on SOHO and of course the ground-based observatories. In this review we assess how these new observations have changed our understanding of the basic physics of flares and consider the implications of these results for future observations with FASR. The discussion emphasizes flaring loops, flare ejecta, particle acceleration, and microflares.

Keywords: Flares, X-rays, ejecta, corona

1. Introduction

The physics of solar flares seems too broad a subject to review adequately within the confines of a single chapter, so we have adopted an alternate strategy here. We pick several key topics and for each briefly review its history, its development in the *Yohkoh* era (mainly the decade of the 1990s), and its potential for development via future observations. We hope to have touched upon the most important new developments related to solar flares, and regret that space does not allow a complete description of any of them.

A solar flare is a sudden brightening in the solar atmosphere, typically spread across all atmospheric layers and involving substantial mass motions and particle acceleration. Brightening implies energy dissipation, and the consensus now holds that the energy for a flare had been stored magnetically in the corona prior to the event. This energy builds up relatively gradually as the result of deep-seated convective motions that deliver magnetic stress into the corona in the form of non-potential magnetic fields; the twist representing this non-potentiality may reside in an emerging flux system. Radio observations from the 1950s, and then X-ray and γ-ray observations from space from the 1960s, revealed that solar flares begin with high-energy processes. The key elements are accelerated particles, the "evaporation" of large masses of high-pressure plasma into coronal magnetic loops, and (frequently) magnetic eruptions as observed in a variety of wavelengths. While almost all of these components had been known prior to the launch of the *Yohkoh* observatory in August, 1991, the decade that followed saw great clarification of the observational situation.

The specific topics discussed here are the *flare concept*, flare loops, particle acceleration, ejections (including global waves), and microflares. We start with a brief review of new observational capabilities (*Yohkoh*, SOHO, and TRACE), and end with a discussion of how flare models and theories have changed. In this limited review we cannot cite the literature comprehensively, but we do try to give both early and modern references wherever possible. Finally we do not generally discuss FASR's capability, because other chapters cover this, but our choice of topics emphasizes areas where FASR will contribute in major ways. *Yohkoh* has made major contributions to identifying and understanding the wealth of radio observations of the solar corona.

2. New Observational Capabilities

2.1 *Yohkoh*

Yohkoh carried two imaging instruments, the Hard X-ray Telescope (HXT; 15–93 keV) and the Soft X-ray Telescope (SXT; $\sim$3–50Å), as well as two instruments for spectroscopy (WBS and BCS), as summarized in Table 8.1. The observations extended from 1991 September to 2001 December.

The SXT used grazing-incidence mirrors and a CCD readout (Tsuneta *et al.* 1991), and thus was a second-generation instrument following the film readouts of the Skylab soft X-ray telescopes. The new instrument had lower scattered-light levels, better spectral selection, better off-axis angular resolution, and (most important) the CCD. The linearity and speed of this type of detector readily allowed movie representations of the data. This made motions easier to recognize, and small-scale motions turned out to be almost ubiquitous, as suggested by the Skylab data (Gerassimenko *et al.* 1974).

The HXT (Kosugi *et al.* 1991) followed the earlier hard X-ray imagers on the Solar Maximum Mission and Hinotori. Its innovations consisted of speed (large effective area), plus a four-channel spectral capability extending over ∼15–93 keV.

Table 8.1. Instruments On Board *Yohkoh*[a]

Instrument	Type	Spectral range
HXT	Synthesis imaging	15–93 keV (4 channels)
SXT	Direct imaging	∼3–50Å (5 filters)
BCS	X-ray line spectroscopy	SXV, CaXIX, FeXXV, FeXXVI
WBS	Broad-band spectroscopy	∼3 keV–20 MeV

[a] Svestka & Uchida 1991

2.2 SOHO and TRACE; other facilities

The Solar and Heliospheric Observatory (SOHO), launched in 1995, carries instruments not optimized for flare research, but which have produced copious new results on flares; TRACE, launched in 1998 (Handy *et al.* 1999) remedied the lack of time resolution for UV and EUV observations and has also produced extensive flare observations. RHESSI, launched in 2002 (Lin *et al.* 2002), unfortunately does not overlap with the *Yohkoh* observations. The other facilities contributing greatly to our understanding during the *Yohkoh* era have been for the most part ground-based observatories, including the radioheliographs at Nançay, Nobeyama, and Owens Valley, and the VLA.

3. The Flare Concept

A general definition of "solar flare" was given in the Introduction. In this section we discuss the current state of knowledge of the geometry and physics of a solar flare in order to introduce concepts and terminology. The following sections then discuss what we think are the most relevant outstanding issues related to future observations with FASR: magnetic loop structure, particle acceleration, ejection and magnetic-field restructuring, and microflares. In

much of the discussion we make use of the language of the "standard model" of a flare (or a CME), namely that of large-scale magnetic reconnection. In the *Yohkoh* literature this is often referred to as the CSHKP model (Carmichael-Sturrock-Hirayama-Kopp-Pneuman). (See Aschwanden 2002; Priest & Forbes 2002 for modern descriptions).

3.1 Confined and LDE flares

The Skylab data led to a two-element classification of solar flares into *confined* and *eruptive* categories (Pallavicini *et al.* 1977), and this classification appears to work well enough for the *Yohkoh* data as well (§ 6). The confined flares typically appear as small bright loops with little large-scale motion other than that attributed to evaporation flows along the loops; the eruptive flares tend to lead to long-decay events (LDEs; MacCombie & Rust 1979) with an arcade of loops, and to be more strongly associated with coronal mass ejections (CMEs). In both cases one can have a full development of radiative signatures across the whole spectrum, in the extreme ranging from kilometer wavelengths to high-energy γ-radiation, plus the emission of energetic particles from the Sun.

As has been well-known from the classical Hα observations of solar flares, even powerful eruptive events can sometimes occur in essentially quiet regions or in active regions so feeble as not to support sunspots. Such events were observed with Skylab in soft X-rays, forming the extreme end of the LDE population, and in the *Yohkoh* era we often refer to these as "global restructurings." These events appear in soft X-ray images as giant arcades, sometimes extending more than one solar radius in length. They generally arise in filament channels, and the largest ones occur in the polar-crown filament regions. We identify them with two-ribbon structures analogous to those of eruptive flares but outside active regions, as observed in the chromosphere (Harvey *et al.* 1986).

3.2 Flares and CMEs

The relationships between flares and CMEs have excited extensive discussion and some controversy. See Cliver & Hudson (2002) for recent impressions of this subject. Briefly speaking, flare physics is best known through radiation signatures, and CMEs through motions of coronal material seen with a coronagraph or other coronal imager. The eruptive flares involve mass motions as well, and often the same structures (filaments) can be identified in both flares and CMEs. Flares occur more frequently than CMEs; most of the powerful flares (GOES X-class) have closely-associated CMEs with comparable total energy, although a few do not. Similarly a few of the most spectacular CMEs have negligible flare effects in the low corona, most famously the event of 1997 January 07 (Webb *et al.* 1998). The flare/CME association involves high-energy

particle signatures well studied via coronal radio emission at metric and longer wavelengths (see Chapter 2) and by *in-situ* observations in the heliosphere.

The flares/CME connection became controversial in the 1990s, when there were suggestions that CMEs directly caused flaring, leading to the confusing usage "post-eruption loops" as a synonym for "eruptive flare." The *Yohkoh* era has seen much more detailed study of the relationship between flare and CME processes, to the extent that we now do not know which causes which, if either. It may depend upon the type of event, since the data clearly show more than one kind of CME. While unquestionably signatures of a coming eruption (e.g., the activation and slow rise of a filament) may precede the main flare effects, the actual eruptions appear to go hand-in-hand with the flare's radiation effects (Hudson & Webb 1997; Zarro *et al.* 1999). Zhang *et al.* (2002) have confirmed the close simultaneity of CME acceleration and flare brightening found originally from the *Yohkoh* observations of expanding loops and dimmings. We now recognize that CME acceleration may coincide well with the impulsive phase of its associated flare (Nitta & Akiyama 1999; Zhang *et al.* 2002). But even with our superior new data it seems premature to decide on the direction of causality, and indeed the flare and CME processes may be too closely intertwined physically to make this a meaningful exercise (Hudson & Cliver 2001; Zhang *et al.* 2001).

4. Flare Loops

The corona consists, we believe, of a volume-filling magnetic field populated by hot plasma (the corona) in an intermittent manner. From the Skylab era we have known that there is no such thing as a smooth background corona, and that magnetic loops define structures everywhere within the coronal volume. When a flare occurs, soft X-ray observations typically show the sudden formation of bright closed loops; this brightening results from the expansion of new hot plasma from below into already well-defined coronal structures (Figure 8.1). The footpoints of the flare loops first become bright across a wide spectral range, and then the whole loop appears in high-temperature observations. The cooling post-flare loops fade gradually with time as the gas pressure decreases and the excess mass eventually drains back out of the corona. In this gradual or decay phase of a flare there is a definite temporal relationship between density and temperature, as discovered in numerical simulations by Serio *et al.* (1991): $n_e^2 \propto T_e$ (Takahashi *et al.* 1996), where n_e, T_e are the electron density and temperature respectively.

A flare observed in soft X-rays consists mainly of one or more magnetic loops; in every event these include almost stationary loops that appear (footpoints first) and then fade with time. In the LDEs (Long Decay Events) this gradual phase (fading) may be protracted to the extent that energy input must continue, since

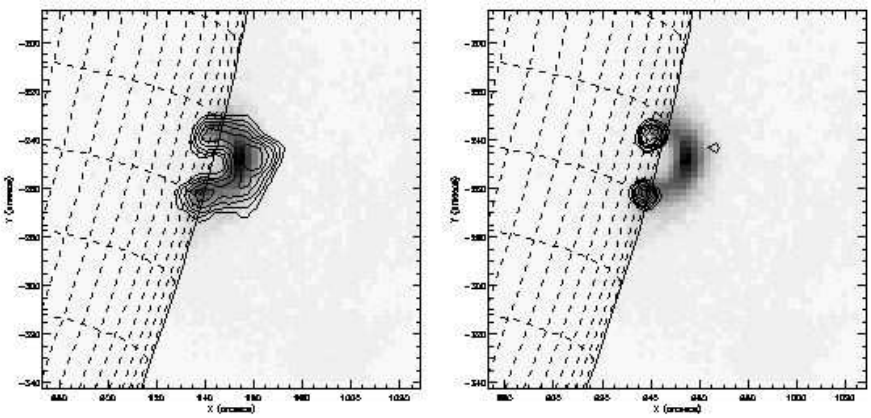


Figure 8.1. Soft and hard X-ray observations of the "Masuda flare", 1992 January 13, which nicely illustrates the coronal loop structure of a flare. Background image: soft X-rays (1992 January 13; reversed color table) from *Yohkoh* SXT. Contours: left, 15–23 keV; right, 23–33 keV from *Yohkoh* HXT. The contour above the soft X-ray loop shows the location of the Masuda source, and the contours at the ends of the soft X-ray loop show the hard X-ray footpoints. Although the contours tend to obscure them in this representation, the footpoints are also bright in soft X-rays.

the observed cooling time exceeds that expected theoretically (MacCombie & Rust 1979; van Driel-Gesztelyi *et al.* 1997) over the lifetime of the loops. New loops must be appearing successively in the gradual phase, giving the (illusory) appearance of slow loop growth. This requirement helped to drive the development of the large-scale reconnection models, in which field lines opened during the flare process would then close, releasing magnetic energy to power the late phase of the flare.

In eruptive events some loops are violently ejected during the impulsive phase (Canfield *et al.* 1992; de Jager *et al.* 1984); this topic is deferred until § 6.

4.1 Footpoints, coronal spectroscopy, and evaporation

The footpoints of the flare loops often brighten impulsively (Figure 8.1). While this was known from earlier observations (Hoyng *et al.* 1981), the HXT data established the presence of this process for flares of GOES class C or above, and have allowed interesting time-resolved studies (Sakao *et al.* 1998; Masuda *et al.* 2001). Related impulsive brightenings take place all across the spectrum, including the "white light flare" phenomenon; the SXT observations clearly established this relationship (Hudson *et al.* 1992) and also show impulsive emission in soft X-rays as well (McTiernan *et al.* 1993; Hudson *et al.* 1994).

The footpoints show where chromospheric material is being heated, ionized, and channeled into the corona by the magnetic field (Neupert 1968). The existence of such a phenomenon has long been inferred (more or less indirectly, in the absence of direct imaging) from the observation of EUV line shifts (e.g., Acton *et al.* 1982; Bentley *et al.* 1994).

The Bragg Crystal Spectrometer (BCS) on board *Yohkoh* continued the work of high-resolution X-ray spectroscopy of solar-flare plasmas (Culhane *et al.* 1991). *Yohkoh* lacked imaging spectroscopy, but SOHO instruments overcame this problem to a certain extent. Unfortunately they were not optimized for rapid time variability, and the SOHO spectroscopic instruments tended to avoid flare observations. However the evaporation flow has now also been imaged spectroscopically via SOHO (Czaykowska *et al.* 1999) even though a direct association with particle precipitation remains problematic (Czaykowska *et al.* 2001), at least in the late phase of an LDE.

The soft X-ray emission lines in flares typically show "nonthermal broadening;" the line widths exceed those expected from the thermal motions of the emitting ions. Determining the physical location of this signature (loop top or footpoints?) clearly would help us to understand flare evolution; if the nonthermal broadening results from small-scale turbulence, this might be identified with the site of the energy conversion. Without spatial resolution, *Yohkoh* efforts to localize the nonthermal broadening made use of limb occultation. Khan *et al.* (1995) studied a sequence of nearly homologous flares that were successively occulted by the limb, and found no substantial difference in nonthermal broadening. On the other hand Mariska *et al.* (1996) studied a different (but still small) sample of events, finding a tendency for the nonthermal broadening to be greater in the footpoints of the flare loops. Similarly the interpretation of the time-series development of nonthermal broadening (Alexander *et al.* 1998) is ambiguous. Alexander *et al.* (1998) and Harra *et al.* (2001) argue that the nonthermal broadening may appear *prior to* the impulsive hard X-rays, thus suggesting an early turbulent phase of energy release; Mariska & McTiernan (1999) and Ranns *et al.* (2001) on the other hand, find a closer relationship between the two signatures. These results are therefore ambiguous, but there is hope — Solar-B will have much better EUV imaging spectroscopy and should overlap with FASR.

4.2 Arcades

In many flares an elongated arcade of loops develops, probably never more spectacularly than in the "Bastille Day flare" of 2000 (Figure 8.2). These constitute one of the two categories of flare noted by Pallavicini *et al.* (1977), namely the compact loop flares and the eruptive flares, and this categorization appears to have a counterpart in the morphology of solar energetic particles (SEPs) ob-

served in the heliosphere (e.g., Reames 1999). The loop and footpoint behavior of these two types of flare do not separate into any kind of bimodal distribution, since a compact flare loop has two footpoints equivalent to short ribbons. Bimodal behavior is seen more strongly in the SEP events—"impulsive" and "gradual" SEP events do occur, with the former associated more strongly with impulsive flares and the latter with CMEs (Reames 1999).

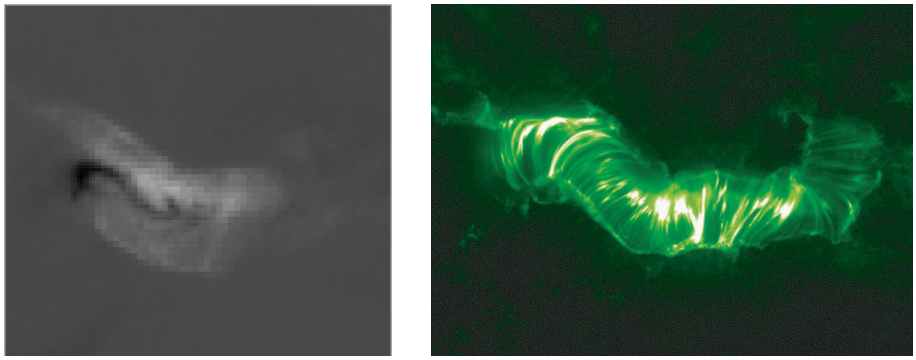


Figure 8.2. Yohkoh SXT difference image (left) and TRACE image (right) of the arcade flare of 2000 July 14 ("Bastille Day flare"), not to scale. The SXT difference images shows (as black) the pre-flare sigmoid, and (as white) the flare arcade. The TRACE image shows the full development of the large arcade, at lower temperatures.

The arcade morphology extends beyond the eruptive flares and into the domain of filament eruptions ("spotless flares") from the quiet corona (Harvey *et al.* 1986). More properly these might be called "quiescent filament-channel eruptions," since the role of the filament itself in the flare dynamics remains unclear (note though that Low 2001, emphasizes the importance of the filament mass as an anchor for a flux rope that otherwise might rise via buoyancy). See Engvold (1994) for a description of filament channels. *Yohkoh*, EIT (the EUV Imaging Telescope), and TRACE (the Transition Region and Coronal Explorer) have observed many such arcade events, which may appear in GOES non-imaging X-ray data as long-decay events (LDEs)—or they may not; they are cooler and fainter than active-region events and frequently cannot be detected in whole-Sun X-ray data above the background, even if their X-ray images are striking. We suggest that similar physics, including the nonthermal aspects (e.g., Dennis & Zarro 1993), extends through this category of flare as well as through the active-region events.

The SXT observations of arcades revealed something not obvious in the EUV images: cusp-shaped structures, as shown in Figure 8.3. Because these resem-

ble the general geometry of large-scale reconnection (and also the geometry of coronal streamers in particular) this observation immediately supported flare models involving reconnection (possibly, from the streamer analogy, between field lines which have been opened; see Hiei *et al.* 1993). Further evidence came from (i) the temperature structure observed by SXT in certain flares which suggested the pattern of slow shocks in the Petschek regime (Tsuneta 1996*a*; Tsuneta 1996*b*), and (ii) the presence of shrinkage within the cusp described by Hiei *et al.* (1997)—it is this "dipolarization" of newly closed loops that actually converts the stored magnetic energy into kinetic energy (Svestka *et al.* 1987; Forbes & Acton 1996).

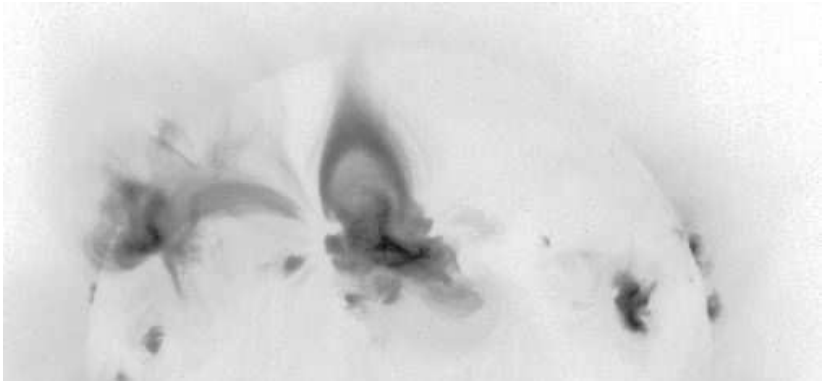


Figure 8.3. A beautiful cusp (following an X-class flare of 2000 June 07), as observed by SXT. This image shows the northern hemisphere of the Sun, and the scale can be judged from the limb.

In the latter half of the *Yohkoh* observations, as a result of improvements in the observing program, observations of a velocity fields around the arcade began to be noticed, as expected from the dimming signatures (§ 6.2). Yokoyama *et al.* (2001), for example, reported horizontal inward flows in a cusp geometry towards the apparent reconnection point. This observation made use of both EIT and SXT data, showing the temperature structure clearly, and an estimate of the inflow speed put it at on the order of 10^{-3} times the Alfvén speed.

While an inflow consistent with coronal reconnection has been reported only for the single event of Yokoyama *et al.* 2001, outflows (downward, towards the arcade) also consistent with the standard reconnection model have been detected many times by *Yohkoh* (McKenzie 2000) and now by TRACE as well (Gallagher *et al.* 2002). These flows are known as a "Supra-Arcade Downflows" or SAD events (Figure 8.4). The first observations (McKenzie & Hudson 1999) showed dark intrusions streaming down in between a spiky structure extending above the late-phase arcade (Švestka *et al.* 1998); such spikes form in a fraction of

the arcade events and appear to map to individual loops of the arcade below. The downward velocities are much smaller than the inferred Alfvén speed, and usually smaller than the free-fall speed as well (McKenzie 2000). The intrusions are voids (Innes *et al.* 2003) and occur in the impulsive phase, in association with hard X-ray bursts (Asai *et al.* 2004), as well as the gradual phase. This downward velocity field should be distinguished from that of the well-known "coronal rain," which occurs in the legs of an arcade as it cools. The logical interpretation of the SADs would be in terms of reconnection ouflow jets, but several aspects of the observations remain puzzling (Why a spiky arcade? Why sub-Alfvénic downflow speeds? Why do voids appear in the flow?)

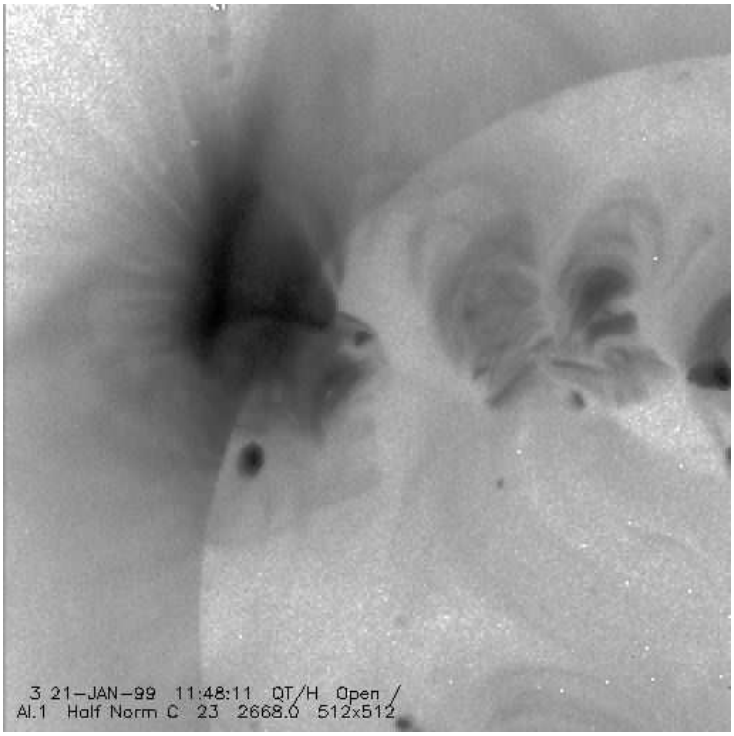


Figure 8.4. Left, soft X-ray observations of a spiky arcade event. The spikes extend above the NE limb to heights on the order of one solar radius; such events exhibit the "SAD" phenomenon described in the text.

4.2.1 "Sigmoids" and filament cavities. The association of S-shaped coronal soft X-ray features with eruptivity is a well-established, if not one-to-one, relationship (Sterling & Hudson 1997; Canfield *et al.* 1999; Gibson *et al.* 2002). Figure 8.2 shows the disappearance of a sigmoid during the eruption

of the Bastille Day 2000 flare. This "sigmoid-to-arcade" development is a characteristic pattern for such events (Sterling *et al.* 2000), with the simple interpretation that the sigmoid structure represents magnetic twist associated with field-aligned coronal current flow. Hagyard *et al.* (1984) had already found such regions to have enhanced flare probability. The sigmoid features probably consist of elongated flux ropes analogous to filament cavities (Engvold 1994), which often appear as stable features of the quiet corona and which may have enormous spatial scales.

4.3 Loop-loop interactions

The SXT images of flares typically show multiple loops to be involved. In many cases *three* footpoints appear, showing two loops possibly interacting within one of them. This morphology was known from the Solar Maximum Mission (Machado *et al.* 1988) and from VLA observations, but was greatly extended with *Yohkoh* and Nobeyama observations (Hanaoka 1997; Nishio *et al.* 1997). In such cases flaring in a primary compact loop sometimes appears to trigger a response in a larger-scale loop, and the configuration is often referred to as a "loop-loop interaction." Such a geometry could also explain flares with apparently over-bright footpoints (e.g., Fárník *et al.* 1997), by hypothesizing that such a footpoint actually would consist of an unresolved bipolar loop structure. Although an analysis of loop-loop behavior can be made by assuming that the loops are discrete entities (Melrose 1997), the common assumption is that the coronal magnetic field fills the entire volume, so that bright loops (in the low-β limit) may not really be distinct structures. It should be noted that cases of independent loop brightenings in flares also occur, with no apparent physical contact between the loops.

5. Particle Acceleration

Nonthermal particles play a fundamental role in solar flares and in CMEs. We can detect them directly in the heliosphere or remotely via their radiation signatures in various wavelength ranges. Hard X-rays from solar flares show the presence of energetic (semi-relativistic) electrons, accelerated by an as yet unidentified acceleration mechanism that operates in the impulsive phase of the flare. The significance of these observations follows from the large energy inferred to be present in the nonthermal electrons of the impulsive phase (Kane & Donnelly 1971).

Imaging observations in the hard X-ray range ($>$10 keV) only began with the SMM and *Hinotori* spacecraft in the 1980s, and then only over a limited energy range. This imaging showed that fairly short (10^9 cm scale) magnetic loops could be the site of energy release even for some of the most powerful

flares; these loops revealed their presence by double footpoint sources (Hoyng *et al.* 1981). In the footpoint region of a flaring loop, virtually every observable wavelength may show an impulsive emission component—cm-wave radio, white light, EUV, and soft X-rays as well as hard X-rays. Thus the phenomenon occurring in these regions must be highly nonthermal, consistent with the precipitation of the impulsive-phase energetic electrons from the corona in the form of directed beams.

5.1 Footpoint sources

The hard X-ray imager HXT on *Yohkoh* has greatly expanded our knowledge of the nonthermal particle populations in solar flares. In particular the images showed two footpoints in the majority of the many flares observed (Sakao 1994), as illustrated in Figure 8.1. In other cases HXT only showed a single brightening, which could be interpreted as unresolved footpoints; in other cases more than two footpoints appeared. In most cases the soft X-ray images from SXT showed coronal loop structures connecting pairs of footpoints.

Sakao (1994) noted a tendency towards footpoint asymmetry, in the sense that the brighter footpoint of a conjugate pair tended to have the weaker photospheric magnetic field as inferred from a magnetogram. This would be consistent with the magnetic mirror force restricting the electron propagation. More interestingly still, Sakao *et al.* (1998) found that the footpoints moved during the flare development, but not always in the direction (greater separation) expected from the standard reconnection model. This has opened an active field of research, in which the footpoint motions are interpreted in terms of their coronal connectivity (Somov & Kosugi 1997; Fletcher & Hudson 2001; Saba *et al.* 2001; Qiu *et al.* 2002; Somov *et al.* 2002). The observations in principle help in understanding not only the geometry of the magnetic restructuring causing the flare, but also its energetics since the nonthermal electrons carry such a large fraction of the total flare energy.

A ubiquitous "soft-hard-soft" pattern of spectral evolution (Parks & Winckler 1969; Fletcher & Hudson 2002) appears in the hard X-ray footpoint sources. There exists a theoretical description (Benz 1977; Brown & Loran 1985) based upon stochastic acceleration. Theories of impulsive-phase particle acceleration involving large-scale shock waves (Tsuneta & Naito, 1998) or acceleration actually in the reconnection region (Litvinenko 2000) need to be shown consistent with this soft-hard-soft pattern.

5.2 Coronal sources

Yohkoh soft X-ray observations show us the active behavior of all domains in the solar corona, and so the X-ray counterparts of the metric burst classification (types I through V) have all been identified. The results are clearest for the

type II and type III bursts, as described elsewhere in this Chapter. Furthermore significant progress has been made in our understanding of the highly complex decimetric band, in particular the drifting pulsating sources (Kliem *et al.* 2000; Khan *et al.* 2002). The "Masuda flare" phenomenon (Masuda *et al.* 1995) has had a substantial impact on our thinking about the physical mechanisms at work in solar flares. Briefly this refers to the presence of a hard X-ray source in the corona *above* the soft X-ray loops, visible during the impulsive phase of a flare as illustrated in Figure 8.1. The only feasible explanation for this phenomenon appears to be the presence of a sufficient target density in the emitting region (Fletcher 1995; Wheatland & Melrose, 1995; Conway *et al.* 1998), in order that the inefficient thin-target bremsstrahlung process would be detectable. The need for high density can be mitigated by trapping (Fletcher & Martens 1998), but this depends upon the unknown field geometry as well as on the acceleration mechanism. The standard reconnection models envision low-field regions (actually nulls in 2D models) which could serve as particle traps. The Masuda source occurs during the impulsive phase of a flare but appears to be unusual, in that surveys (Petrosian *et al.* 2002; Aschwanden 2002) only revealed a handful of such Masuda events among *Yohkoh*'s many flares. The prototype flare of 1992 January 13 (Figure 8.1) appears to have a high trapping efficiency (Aschwanden *et al.* 1999), which could be consistent with the time scale needed for the evaporation of sufficient material to form a dense bremsstrahlung target. Metcalf & Alexander (1999) have carried out a detailed analysis of the target density requirement in view of the spectral evolution in the Masuda source.

Upon its discovery the Masuda source was immediately interpreted in terms of the standard reconnection model (Masuda *et al.* 1995) involving a fast-mode MHD shock terminating the reconnection outflow. The hard X-ray source could arise in particle acceleration either at the shock itself via the Fermi mechanism, with trapping by the paired slow-mode shock structures present in the standard (2D) reconnection model (Tsuneta & Naito, 1998). This attractive idea has the added advantage that the particle acceleration takes place not at the point of reconnection, which may have a low density (the "number problem"; see Brown & Melrose 1977), but in a closed loop structure that may already contain electrons or else gain additional electrons via the mechanism of chromospheric evaporation driven by the overall process. A stochastic acceleration model in a similar geometry (Larosa *et al.* 1996; Jakimiec *et al.* 1998) could also be consistent with the presence of energy conversion above the loop top.

In addition to the Masuda sources, closely related to the impulsive phase and to the flare loops themselves, there are other coronal hard X-ray sources more closely associated with eruption and CME development (Cliver *et al.* 1986 and references therein). To observe coronal hard X-ray sources with good sensitivity, it is best to study flares for which the bright footpoint sources are occulted (e.g., Tomczak 2001). A recent *Yohkoh* example has been discussed by

Sato (2001), who found good evidence for the trapping of nonthermal electrons in coronal loops. Hudson *et al.* (2001) also found a moving source from an over-the-limb flare on 2001 April 18. The hard X-ray source emerged from behind the limb in the form of a compact structure identifiable with a microwave source, and moved outwards at $\sim 10^3$ km s^{-1}.

5.3 Energetic ions

The energetic ion component ($>$1 MeV) of a solar flare, as revealed by its γ-ray line emission spectrum, may contain energy rivaling that of the impulsive-phase electrons and therefore of the entire flare process (Ramaty *et al.* 1995). *Yohkoh* confirmed the existence of two types of solar γ-ray bursts (Yoshimori *et al.* 1999), namely the normal events and the so-called "electron-rich" events. We expect substantial progress in γ-ray line spectroscopy from RHESSI (the Reuven Ramaty High-Energy Solar Spectroscopic Imager, launched in February 2002; see Lin *et al.* 2002).

6. Ejections

Flares originally were called "eruptions" by Hale, and we know now that this was apt terminology: an explosive restructuring of the coronal magnetic field often plays a key role in the physical development of a flare. Almost invariably, for the most powerful flares, this involves loop ejections, global wave generation, and the occurrence of a CME. De La Beaujardière *et al.* (1995) and Green *et al.* (2002) have shown, however, that even major flares sometimes consist of "confined eruptions" that have no significant counterparts in the upper corona.

6.1 Parallel and perpendicular flows

Movie representations of the images often show motions both perpendicular and parallel to the inferred field direction. *Yohkoh* observations in particular immediately revealed parallel flows in the form of X-ray jets, previously unknown, often with apparent velocities on the order of 10^3 km s^{-1} (Shibata *et al.* 1992; Strong *et al.* 1992). These jets are highly-collimated plasma flows emerging from the vicinity of flaring loops (microflares; see § 7), often found in the leading-polarity region of a sunspot group (Shimojo *et al.* 1998). They also apparently mark the locations of channels for certain type III radio bursts (Aurass *et al.* 1994; Kundu *et al.* 1995).

The perpendicular motions (restructurings) occur in strong association with CMEs (Nitta & Akiyama 1999), but also at lower speeds in expanding active regions (Uchida *et al.* 1992). Flares, especially major ones, frequently exhibit high-speed ejections (Hudson *et al.* 1996; Ohyama & Shibata 1998; Innes *et al.* 2001). It is worth emphasizing that *non-radial* motions may characterize the

early development of a flare ejection; this is often the appearance from *Yohkoh* images, although one cannot be sure because of the geometrical projection effects, but it can be demonstrated with full 3D reconstructions using high-resolution spectroscopic imaging (e.g., Penn 2000).

6.2 Dimming

Dimming at soft X-ray and EUV wavelengths has become a prominent signature of coronal mass ejections, analogous to the "coronal depletions" seen in white light (Hansen *et al.* 1974). Because they have broad temperature response, both the white-light and X-ray decreases suggest a simple explanation: the dimmed material has been released to expand into the solar wind. We can distinguish four types of dimming (Hudson & Webb 1997), all of which closely match the increase of flare brightening (Table 8.2) in temporal development.

Table 8.2. Soft X-ray Coronal Dimming

Type	Prototype	Reference
Transient coronal hole	1997 October 23	Rust 1983
Diffuse	1992 February 21	Hudson *et al.* 1995
Loop expansion	1994 November 13	Nitta & Akiyama 1999
Disappearing TIL[a]	1998 May 06	Khan & Hudson 2000

[a] Transequatorial interconnecting loop system.

From the original observations it was clear that the dimming time scale was inconsistent with cooling time scales, and hence must involve expansion of the field (Hudson *et al.* 1996); in some cases this expansion appears to be arrested (de La Beaujardière *et al.* 1995; Green *et al.* 2002), but normally it involves the opening of active region magnetic field lines into the interplanetary medium as a part of a CME. The SXT data show unambiguously that the temporal pattern of the dimming reflects that of the flare brightening, a result significant for discussions of flare/CME relationships (§ 3.2).

The trans-equatorial interconnecting loops (TILs) link active regions, or their near vicinities, across the solar equator (e.g., Svestka *et al.* 1977, Pevtsov 2000). These TILs tend to have greater visibility in soft X-rays than in the lower-temperature EUV observations from EIT (as do the sigmoids; see §4). This points to the existence of a heating mechanism that may differ from that responsible for bright loops in active regions, which have small spatial scales, short time scales, and originate in strong-field regions. Note that filament channels, which also contain long field lines, tend to be cool and dark in soft X-rays. In a striking observation Khan & Hudson (2000) found that such a loop structure may suddenly disappear (Figure 8.5). The event of 1998 May 06 (see also

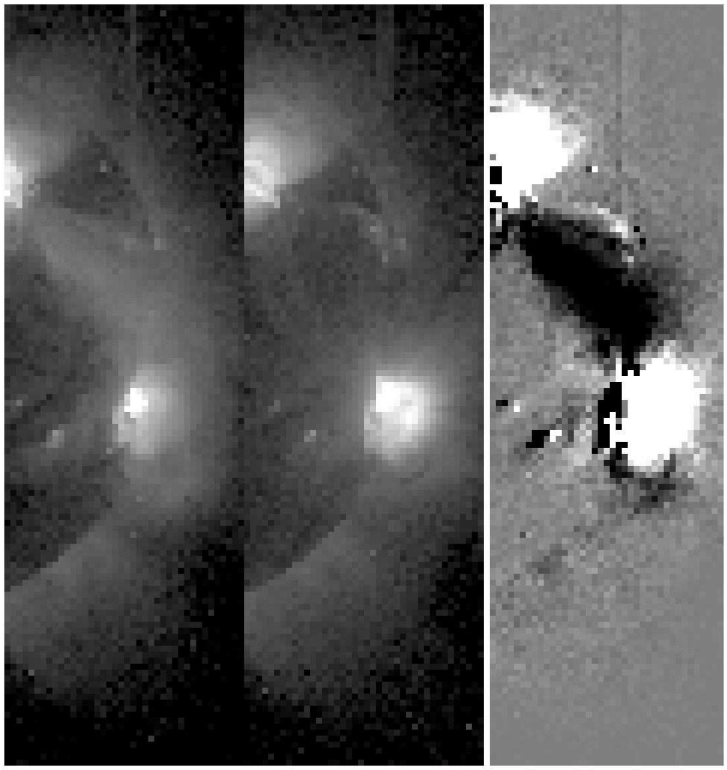


Figure 8.5. Disappearing trans-equatorial interconnecting loop (TIL) associated with the blast wave and CME of the flare of 1998 May 06 (Khan & Hudson 2000). The left two panels show the W limb of the Sun before and after the disappearance; the right panel shows the difference at higher image contrast; the dark outline of the TIL represents dimming.

§ 6.3) was the first of a set of three nearly homologous disappearances. Khan & Hudson (2000) found that the timing suggested a disruption of the TIL by the flare blast wave; the TIL morphology closely agreed with the initial appearance of the CME as viewed by the LASCO coronagraphs.

6.3 Global waves

Prior to the 1990s, we knew of the existence of global coronal shock waves (analogous to supernova shocks) via their Moreton wave and meter-wave type II radio signatures. The obvious prediction for *Yohkoh* was there: SXT could observe the solar corona directly in its soft X-ray emission, and therefore the weak fast-mode MHD shock responsible for a type II burst (see Uchida 1968), because it was compressive, should produce a bright ripple visible in a flare movie sequence.

In fact it required almost a decade before such sources were clearly identified (Khan & Aurass 2002; Narukage *et al.* 2002; Hudson *et al.* 2003). The reasons for this delay are complex, but in the meanwhile the EIT instrument on SOHO had made clear detections of related coronal waves (Moses *et al.* 1997, Thompson *et al.* 1998). Although considerable debate has accompanied the development of consensus on this point (e.g., Cliver & Hudson 2002), we now feel sure that two types of large-scale waves occur. The immediate blast wave begins in the magnetic-restructuring disturbance at the onset of the flare impulsive phase; as it moves outward it develops into a fast-mode MHD shock wave and "ignites" as a type II burst at metric wavelengths (e.g., Vršnak 2001). At the same time the CME, if one occurs, moves outward and drives an interplanetary shock ahead of it. This wave, unlike the blast wave, can continue as long as the CME propagates supersonically; when it arrives at the Earth it makes a clear signature in the geomagnetic field (the "storm sudden commencement").

The observations of the 1998 May 06 wave event in soft X-rays (Figure 8.6) allowed us to study its development within 10^9 cm of the flare core. In fact, the wave did not appear to originate at the core loops of the flare, but rather from a radiant point significantly displaced from it. This tends to rule out a "pressure pulse" explanation for the wave formation, and instead points to the field restructuring itself as the direct cause—not an implausible situation in what is believed to be plasma at low β, where gas pressure itself should have a negligible effect.

The "EIT wave"EUV,wave phenomenon (Thompson *et al.* 1998) actually now appears to comprise both blast waves and restructurings (Delannée 2000). The fastest of the waves have a strong correlation with flares and type II bursts and thus agree with Uchida's unifying theory of type IIs and Moreton waves (Biesecker *et al.* 2002).

7. Microflares and Nanoflares

"Microflares," in the sense of flare-like events with total energies on the order of 10^{26} erg, were already evident in the GOES data, a B1 event being about 10^{-4} the energy of a GOES X10 event. Theoretical insight (Parker 1988) and hard X-ray observations (Lin *et al.* 1984) suggested that tiny nonthermal events might play a major energetic role in active regions or even the entire corona. But to do so required "nanoflares," even tinier events whose numbers and frequency might merge into the appearance of a continuous heating of the coronal plasma. Hudson (1991) pointed out that the microflare observations (from various sources) in fact showed occurrence-frequency distributions of total flare energy W for which $N(W) \sim W^{-\alpha}$, with $\alpha < 2$. The energy in such distributions is dominated by large events, not small ones, and so the

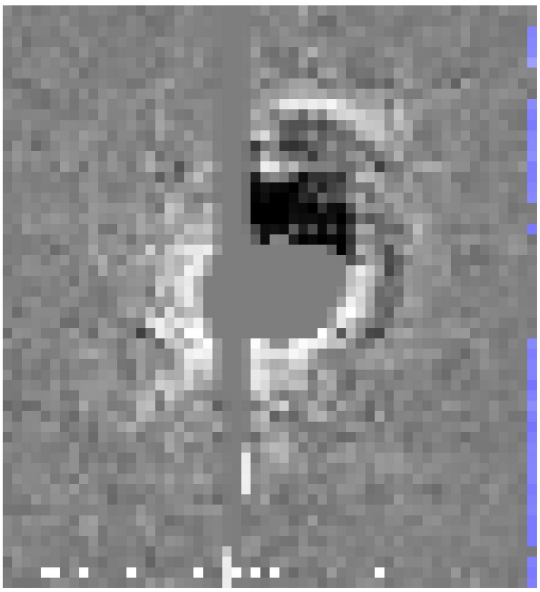


Figure 8.6. Soft X-ray signature of 1998 May 06 wave. The image shows a difference image at a 40 s spacing from the SXT AlMg filter with $10''$ pixels, at a time several minutes after the initiation time of the event as determined by its radiant (Hudson *et al.* 2003). The neutral gray area, including the vertical spike, show regions of CCD saturation; field-of-view $\sim 10'$.

nanoflare phenomenon needed to be found in events not strictly resembling the flares and microflares. The SXT observations provided the first good imaging X-ray data for this purpose with adequate temporal sampling.

The *Yohkoh* soft X-ray imaging immediately revealed the locations of the smallest GOES events, which for the most part turned out to be flare-like brightenings in active regions (Shimizu *et al.* 1992). These then were the soft X-ray counterparts of the hard X-ray microflares originally observed by Lin *et al.* 1984. Detailed studies in soft X-rays (Shimizu *et al.* 1994) and at other wavelengths (White *et al.* 1995; Gary *et al.* 1997; Shimizu *et al.* 2002) have subsequently provided little evidence to suggest the presence of any substantially different physics represented; hence "microflare" seems a reasonable name for a flare-like event on such a scale. The microflares occur in a power-law distribution with total energy in a manner consistent with flare observations (e.g., Hudson 1991; as shown in Figure 8.7 they span the energy range down to about 10^{27} ergs before a roll-over attributable to selection effects for the smaller events.

Despite these results some controversy has continued to simmer, as EUV observations of these microflares and of still smaller "micro-events" in the quiet Sun (e.g., Berghmans *et al.* 1998; Parnell & Jupp 2000; Aschwanden & Char-

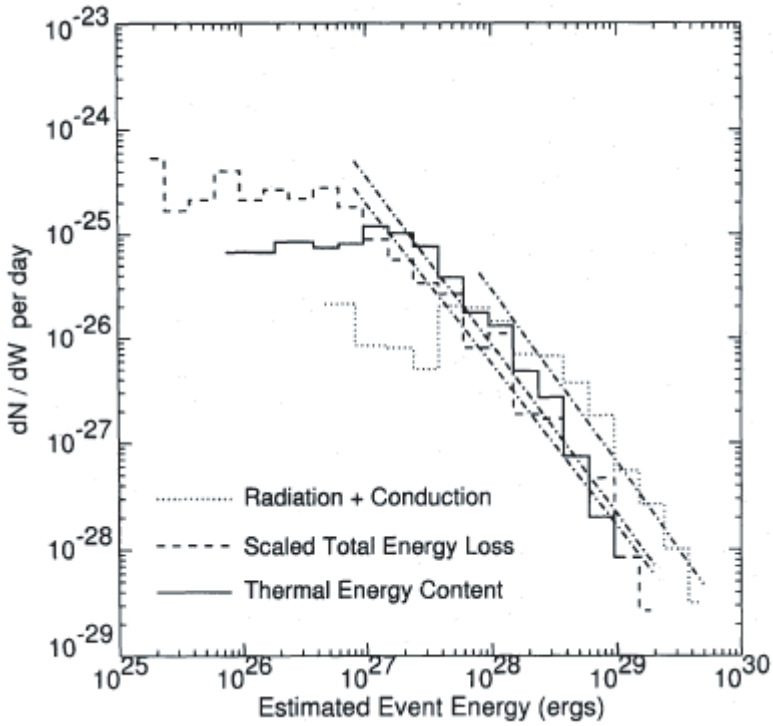


Figure 8.7. Energy distributions for microflares observed with the *Yohkoh* SXT (Shimizu 1995), incorporating plausible physical models to scale the total energy. The flattening of the distribution for small event energies represents detection threshold.

bonneau 2002; Benz & Krucker 2002) became available. Partly this may have stemmed from the more complex morphologies of the EUV observations but the ambiguities of the modeling needed to interpret the observations physically also seems to have contributed to the continuing discussion. Can the microflares themselves be taken as a signature of coronal heating? The flatness of the distribution function suggests not (Hudson 1991), but the conversion from any observable signature to the total energy of an event requires extensive model-dependent adjustments and we may not know how to do it correctly. To answer this question one must deal correctly with sampling bias—the equivalent of the cosmologist's "Malmquist bias" (Aschwanden & Charbonneau 2002). Our current knowledge of the energies and distributions of flare-like events, at present, suggests that they have little to do with the heating of the general corona.

8. Evolution of Flare Theories and Models

Theories of flares and CMEs, often indistinguishable in their essence, have generally followed the line of the standard large-scale reconnection (CSHKP) model. This involves either an ideal MHD catastrophe or a dissipative process that opens the magnetic field of an active region, allowing it to re-form with energy release into the cusped arcade structure made familiar with *Yohkoh* images (Priest & Forbes 2002). Theoretical treatments of these phenomena based upon MHD will always have trouble with self-consistency, however, because of the strong effects of particle acceleration. Recent work has emphasized the 3D nature of the phenomena, the topology of the coronal magnetic field in terms of separatrices or "quasi-separatrix structures" that separate domains of connectivity, the role of statistical sub-processes working in a self-organizing manner, and the physics of magnetic helicity.

At the simplest level of this theoretical work, there is now convincing evidence, in the late phases of eruptive flares, for the large-scale reconnection picture presented by CSHKP models. Current thinking distinguishes between eruptions occurring from "tether-cutting" reconnection (Moore & Labonte 1980) which can occur in an essentially bipolar magnetic configuration, and eruptions requiring more complex connectivity (e.g., the "breakout" model of Antiochos 1998). One apparent problem of all such magnetic models is the need to circumvent the "Aly conjecture," which suggests that the open configuration of the field has greater energy than the closed configuration. Opening the field therefore would absorb energy, rather than releasing it as observed during a flare. How to avoid this problem remains unclear, but there are suggestions that the problem does not exist for partial eruptions of the field (Sturrock *et al.* 2001), or that the conjecture itself may simply be wrong (Choe & Cheng 2002).

The idea that magnetic energy stored slowly in the corona can be released suddenly to power a flare or CME is almost unanimous. Unfortunately we have only sketchy knowledge of the coronal magnetic field because of the extreme difficulty of direct observations and because extrapolation from the photospheric magnetograms has fundamental uncertainties. Thus it has recently become interesting to make use of the flare observations to define both the connectivity and also infer something about the site of energy storage and release. In particular Aschwanden (2002) has developed a comprehensive view of flare structure including the use of accelerated particles both as tracers in the lower atmosphere and also as time-of-flight guides to the middle corona where energy may be stored.

9. Conclusions

Even though many of the *Yohkoh* observations were merely nice refinements of earlier discoveries, many also have had "breakthrough" quality. This decade-

long flood of wonderful observations has taught us a great deal, and from the data archive many research workers around the world are still finding new things. With RHESSI to fill in some of the gaps and to extend our knowledge in the key area of nonthermal particle behavior, the epoch beginning in 1991 will no doubt be recognized as the most important yet for our understanding of flare physics. From the theoretical point of view, we are now beginning to study the 3D geometry of the flare catastrophe, and it is very interesting—FASR will help greatly on this score, because of its capability to make direct coronal magnetic-field measure (see Chapter 12). This suggests the possible development of coronal loop seismology (see Roberts 2000 and references therein) leading to inference of coronal properties such as the magnetic field intensity (Nakariakov & Ofman 2001).

Acknowledgments

NASA supported the work of HSH under NAS 5-98033, and he thanks the Astronomy and Astrophysics Group of the University of Glasgow for hospitality during the writing of this Chapter.

References

Acton, L. W., Leibacher, J. W., Canfield, R. C., Gunkler, T. A., Hudson, H. S., & Kiplinger, A. L. 1982, ApJ, 263, 409

Alexander, D., Harra-Murnion, L. K., Khan, J. I., & Matthews, S. A. 1998, ApJ, 494, L235

Antiochos, S. K. 1998, ApJ, 502, L181

Asai, A., Yokoyama, T., Shimojo, M., & Shibata, K. 2004, ApJ, 605, L77

Aschwanden, M. J. 2002, Space Sci. Rev., 101, Nos. 1-2, Kluwer Academic Publishers, Dordrecht.

Aschwanden, M. J. & Charbonneau, P. 2002, ApJ, 566, L59

Aschwanden, M. J., Fletcher, L., Sakao, T., Kosugi, T., & Hudson, H. 1999, ApJ, 517, 977

Aurass, H., Klein, K.-L., & Martens, P. C. H. 1994, Solar Phys, 155, 203

Bentley, R. D., Doschek, G. A., Simnett, G. M., Rilee, M. L., Mariska, J. T., Culhane, J. L., Kosugi, T., & Watanabe, T. 1994, ApJ, 421, L55

Benz, A. O. 1977, ApJ, 211, 270

Benz, A. O. & Krucker, S. . 2002, ApJ, 568, 413

Berghmans, D., Clette, F., & Moses, D. 1998, A&A, 336, 1039

Biesecker, D. A., Myers, D. C., Thompson, B. J., Hammer, D. M., & Vourlidas, A. 2002, ApJ, 569, 1009

Brown, J. C. & Loran, J. M. 1985, MNRAS, 212, 245

Brown, J. C. & Melrose, D. B. 1977, Solar Phys, 52, 117

Canfield, R. C., Hudson, H. S., Leka, K. D., Mickey, D. L., Metcalf, T. R., Wuelser, J., Acton, L. W., Strong, K. T., Kosugi, T., Sakao, T., Tsuneta, S., Culhane, J. L., Phillips, A., & Fludra, A. 1992, PASJ, 44, L111
Canfield, R. C., Hudson, H. S., & McKenzie, D. E. 1999, GRL, 26, 627
Choe, G. S. & Cheng, C. Z. 2002, ApJ, 574, L179
Cliver, E. W., Dennis, B. R., Kiplinger, A. L., Kane, S. R., Neidig, D. F., Sheeley, N. R., & Koomen, M. J. 1986, ApJ, 305, 920
Cliver, E. W. & Hudson, H. S. 2002, J. Atm. & Terr. Phys., 64, 231
Conway, A. J., MacKinnon, A. L., Brown, J. C., & McArthur, G. 1998, A&A, 331, 1103
Culhane, J. L., Bentley, R. D., Hiei, E., Watanabe, T., Doschek, G. A., Brown, C. M., Cruise, A. M., Lang, J., Ogawara, Y., & Uchida, Y. 1991, Solar Phys, 136, 89
Czaykowska, A., Alexander, D., & De Pontieu, B. 2001, ApJ, 552, 849
Czaykowska, A., de Pontieu, B., Alexander, D., & Rank, G. 1999, ApJ, 521, L75
de Jager, C., Boelee, A., & Rust, D. M. 1984, Solar Phys, 92, 245
de La Beaujardière, J.-F., Canfield, R. C., Hudson, H. S., Wulser, J.-P., Acton, L., Kosugi, T., & Masuda, S. 1995, ApJ, 440, 386
Delannée, C. 2000, ApJ, 545, 512
Dennis, B. R. & Zarro, D. M. 1993, Solar Phys, 146, 177
Engvold, O. 1994, IAU Colloq. 144, Solar Coronal Structures, p297
Fárník, F., Hudson, H., & Watanabe, T. 1997, A&A, 324, 433
Fletcher, L. 1995, A&A, 303, L9
Fletcher, L. & Hudson, H. S. 2001, Solar Phys, 204, 69
Fletcher, L. & Hudson, H. S. 2002, Solar Phys, 210, 307
Fletcher, L. & Martens, P. C. H. 1998, ApJ, 505, 418
Forbes, T. G. & Acton, L. W. 1996, ApJ, 459, 330
Gallagher, P. T., Dennis, B. R., Krucker, S., A., S. R., & Tolbert, A. K. 2002, Solar Phys, 210, 341
Gary, D. E., Hartl, M. D., & Shimizu, T. 1997, ApJ, 477, 958
Gerassimenko, M., Golub, L., Kahler, S., & Petrasso, R. 1974, Coronal Disturbances, IAU Symp. 57, 501
Gibson, S. E., Fletcher, L., Del Zanna, G., Pike, C. D., Mason, H. E., Mandrini, C. H., Démoulin, P., Gilbert, H., Burkepile, J., Holzer, T., Alexander, D., Liu, Y., Nitta, N., Qiu, J., Schmieder, B., & Thompson, B. J. 2002, ApJ, 574, 1021
Green, L. M., Matthews, S. A., van Driel-Gesztelyi, L., Harra, L. K., & Culhane, J. L. 2002, Solar Phys, 205, 325
Hagyard, M. J., Teuber, D., West, E. A., & Smith, J. B. 1984, Solar Phys, 91, 115
Hanaoka, Y. 1997, Solar Phys, 173, 319

Handy, B. N. *et al.* 1999, Solar Phys, 187, 229
Hansen, R. T., Garcia, C. J., Hansen, S. F., & Yasukawa, E. 1974, PASP, 86, 500
Harra, L. K., Matthews, S. A., & Culhane, J. L. 2001, ApJ, 549, L245
Harvey, K. L., Sheeley, N. R., & Harvey, J. W. 1986, Solar-Terrestrial Predictions, (P.A. Simon *et al.* eds.), 2, 198
Hiei, E., Hundhausen, A. J., and Sime, D. G. 1993, GRL, 20, 2785
Hiei, E., Hundhausen, A. J., & Burkepile, J. 1997, ASP Conf. Ser. 111, Magnetic Reconnection in the Solar Atmosphere, 383
Hoyng, P., Duijveman, A., Machado, M. E., Rust, D. M., Svestka, Z., Boelee, A., de Jager, C., Frost, K. T., Lafleur, H., Simnett, G. M., van Beek, H. F., & Woodgate, B. E. 1981, ApJ, 246, L155
Hudson, H. S. 1991, Solar Phys, 133, 357
Hudson, H. S., Acton, L. W., Alexander, D., Freeland, S. L., Lemen, J. R., & Harvey, K. L. 1995, Solar Wind Conference, p58
Hudson, H. S., Acton, L. W., & Freeland, S. L. 1996, ApJ, 470, 629
Hudson, H. S., Acton, L. W., Hirayama, T., & Uchida, Y. 1992, PASJ, 44, L77
Hudson, H. S. & Cliver, E. W. 2001, JGR, 106, 25199
Hudson, H. S., Khan, J. I., Lemen, J. R., Nitta, N. V., & Uchida, Y. 2003, Solar Phys, 212, 121
Hudson, H. S., Kosugi, T., Nitta, N. V., & Shimojo, M. 2001, ApJ, 561, L211
Hudson, H. S., Strong, K. T., Dennis, B. R., Zarro, D., Inda, M., Kosugi, T., & Sakao, T. 1994, ApJ, 422, L25
Hudson, H. S. & Webb, D. F. 1997, Geophysical Monographs, 99, 27.
Innes, D. E., Curdt, W., Schwenn, R., Solanki, S., Stenborg, G., & McKenzie, D. E. 2001, ApJ, 549, L249
Innes, D. E., McKenzie, D. E., & Wang, T. 2003, Solar Phys, 217, 247
Jakimiec, J., Tomczak, M., Falewicz, R., Phillips, K. J. H., & Fludra, A. 1998, A&A, 334, 1112
Kane, S. R. & Donnelly, R. F. 1971, ApJ, 164, 151
Khan, J. I. & Aurass, H. 2002, A&A, 383, 1018
Khan, J. I., Harra-Murnion, L. K., Hudson, H. S., Lemen, J. R., & Sterling, A. C. 1995, ApJ, 452, L153
Khan, J. I. & Hudson, H. S. 2000, GRL, 27, 1083
Khan, J. I., Vilmer, N., Saint-Hilaire, P., and Benz, A. O. 2002, A&A, 388, 363
Kliem, B., Karlický, M., & Benz, A. O. 2000, A&A, 360, 715
Kosugi, T., Masuda, S., Makishima, K., Inda, M., Murakami, T., Dotani, T., Ogawara, Y., Sakao, T., Kai, K., & Nakajima, H. 1991, Solar Phys, 136, 17
Kundu, M. R., Raulin, J. P., Nitta, N., Hudson, H. S., Shimojo, M., Shibata, K., & Raoult, A. 1995, ApJ, 447, L135
Larosa, T. N., Moore, R. L., Miller, J. A., & Shore, S. N. 1996, ApJ, 467, 454

Lin, R. P., Schwartz, R. A., Kane, S. R., Pelling, R. M., & Hurley, K. C. 1984, ApJ, 283, 421
Lin et al., R. P. *et al.* 2002, Solar Phys, 210, 3
Litvinenko, Y. E. 2000, Solar Phys, 194, 327
Low, B. C. 2001, JGR, 106, 25141
MacCombie, W. J. & Rust, D. M. 1979, Solar Phys, 61, 69
Machado, M. E., Moore, R. L., Hernandez, A. M., Rovira, M. G., Hagyard, M. J., & Smith, J. B. 1988, ApJ, 326, 425
Mariska, J. T. & McTiernan, J. M. 1999, ApJ, 514, 484
Mariska, J. T., Sakao, T., & Bentley, R. D. 1996, ApJ, 459, 815
Masuda, S., Kosugi, T., Hara, H., Sakao, T., Shibata, K., & Tsuneta, S. 1995, PASJ, 47, 677
Masuda, S., Kosugi, T., & Hudson, H. S. 2001, Solar Phys, 204, 55
McKenzie, D. E. 2000, Solar Phys, 195, 381
McKenzie, D. E. & Hudson, H. S. 1999, ApJ, 519, L93
McTiernan, J. M., Kane, S. R., Loran, J. M., Lemen, J. R., Acton, L. W., Hara, H., Tsuneta, S., & Kosugi, T. 1993, ApJ, 416, L91
Melrose, D. B. 1997, ApJ, 486, 521
Metcalf, T. R. & Alexander, D. 1999, ApJ, 522, 1108
Moore, R. L. & Labonte, B. J. 1980, IAU Symposium 91, 207
Moses, D., *et al.* 1997, Solar Phys, 175, 571
Nakariakov, V. M. & Ofman, L. 2001, A&A, 372, L53
Narukage, N., Hudson, H. S., Morimoto, T., Akiyama, S., Kitai, R., Kurokawa, H., & Shibata, K. 2002, ApJ, 572, L109
Neupert, W. M. 1968, ApJ, 153, L59
Nishio, M., Yaji, K., Kosugi, T., Nakajima, H., & Sakurai, T. 1997, ApJ, 489, 976
Nitta, N. & Akiyama, S. 1999, ApJ, 525, L57
Ohyama, M. & Shibata, K. 1998, ApJ, 499, 934
Pallavicini, R., Serio, S., & Vaiana, G. S. 1977, ApJ, 216, 108
Parker, E. N. 1988, ApJ, 330, 474
Parks, G. K. & Winckler, J. R. 1969, ApJ, 155, L117
Parnell, C. E. & Jupp, P. E. 2000, ApJ, 529, 554
Penn, M. J. 2000, Solar Phys, 197, 313
Petrosian, V., Donaghy, T. Q., & McTiernan, J. M. 2002, ApJ, 569, 459
Pevtsov, A. A. 2000, ApJ, 531, 553
Priest, E. R. & Forbes, T. G. 2002, Astron. Ap. Revs., 10, 313
Qiu, J., Lee, J., Gary, D. E., & Wang, H. 2002, ApJ, 565, 1335
Ramaty, R., Mandzhavidze, N., Kozlovsky, B., & Murphy, R. J. 1995, ApJ, 455, L193
Ranns, N. D. R., Harra, L. K., Matthews, S. A., & Culhane, J. L. 2001, A&A, 379, 616

Reames, D. V. 1999, Space Sci. Rev., 90, 413
Roberts, B. 2000, Solar Phys, 193, 139
Rust, D. M. 1983, Space Sci. Rev., 34, 21
Saba, J. L. R., Gaeng, T., & Tarbell, T. D. 2001, *Yohkoh* 10th Ann. Meeting., 96
Sakao, T. 1994, Ph.D. Thesis, U. Tokyo
Sakao, T., Kosugi, T., & Masuda, S. 1998, ASSL Vol. 229, 273
Sato, J. 2001, ApJ, 558, L137
Serio, S., Reale, F., Jakimiec, J., Sylwester, B., & Sylwester, J. 1991, A&A, 241, 197
Shibata, K., Ishido, Y., Acton, L. W., Strong, K. T., Hirayama, T., Uchida, Y., McAllister, A. H., Matsumoto, R., Tsuneta, S., Shimizu, T., Hara, H., Sakurai, T., Ichimoto, K., Nishino, Y., & Ogawara, Y. 1992, PASJ, 44, L173
Shimizu, T. 1995, PASJ, 47, 251
Shimizu, T., Shine, R. A., Title, A. M., Tarbell, T. D., & Frank, Z. 2002, ApJ, 574, 1074
Shimizu, T., Tsuneta, S., Acton, L. W., Lemen, J. R., Ogawara, Y., & Uchida, Y. 1994, ApJ, 422, 906
Shimizu, T., Tsuneta, S., Acton, L. W., Lemen, J. R., & Uchida, Y. 1992, PASJ, 44, L147
Shimojo, M., Shibata, K., & Harvey, K. L. 1998, Solar Phys, 178, 379
Somov, B. V. & Kosugi, T. 1997, ApJ, 485, 859
Somov, B. V., Kosugi, T., Hudson, H. S., Sakao, T., & Masuda, S. 2002, ApJ, 579, 863
Sterling, A. C. & Hudson, H. S. 1997, ApJ, 491, L55
Sterling, A. C., Hudson, H. S., Thompson, B. J., & Zarro, D. M. 2000, ApJ, 532, 628
Strong, K. T., Harvey, K., Hirayama, T., Nitta, N., Shimizu, T., & Tsuneta, S. 1992, PASJ, 44, L161
Sturrock, P. A., Weber, M., Wheatland, M. S., & Wolfson, R. 2001, ApJ, 548, 492
Svestka, Z., Krieger, A. S., Chase, R. C., & Howard, R. 1977, Solar Phys, 52, 69
Svestka, Z. & Uchida, Y. 1991, The YOHKOH (Solar-A) Mission (Dordrecht: Kluwer Academic Publishers)
Svestka, Z. F., Fontenla, J. M., Machado, M. E., Martin, S. F., & Neidig, D. F. 1987, Solar Phys, 108, 237
Takahashi, M., Watanabe, T., Sakai, J., Sakao, T., Kosugi, T., Sakurai, T., Enome, S., Hudson, H. S., Hashimoto, S., & Nitta, N. 1996, PASJ, 48, 857
Thompson, B. J., Plunkett, S. P., Gurman, J. B., Newmark, J. S., St. Cyr, O. C., & Michels, D. J. 1998, GRL, 25, 2465
Tomczak, M. 2001, A&A, 366, 294
Tsuneta, S. 1996*a*, ApJ, 456, 840

Tsuneta, S. 1996*b*, ApJ, 464, 1055
Tsuneta, S., Acton, L., Bruner, M., Lemen, J., Brown, W., Caravalho, R., Catura, R., Freeland, S., Jurcevich, B., & Owens, J. 1991, Solar Phys, 136, 37
Tsuneta, S. & Naito, T. 1998, ApJ, 495, L67
Uchida, Y. 1968, Solar Phys, 4, 30
Uchida, Y., McAllister, A., Strong, K. T., Ogawara, Y., Shimizu, T., Matsumoto, R., & Hudson, H. S. 1992, PASJ, 44, L155
Švestka, Z. . K., Fárník, F. ., Hudson, H. S., & Hick, P. 1998, Solar Phys, 182, 179
van Driel-Gesztelyi, L., Wiik, J. E., Schmieder, B., Tarbell, T., Kitai, R., Funakoshi, Y., & Anwar, B. 1997, Solar Phys, 174, 151
Vršnak, B. 2001, JGR, 106, 25249
Webb, D. F., Cliver, E. W., Gopalswamy, N., Hudson, H. S., & St. Cyr, O. C. 1998, GRL, 25, 2469
Wheatland, M. S. & Melrose, D. B. 1995, Solar Phys, 158, 283
White, S. M., Kundu, M. R., Shimizu, T., Shibasaki, K., & Enome, S. 1995, ApJ, 450, 435
Yokoyama, T., Akita, K., Morimoto, T., Inoue, K., & Newmark, J. 2001, ApJ, 546, L69
Yoshimori, M., Shiozawa, A., & Suga, K. 1999, Proc. Nobeyama Symposium, Kiyosato, Japan, (T. S. Bastian, N. Gopalswamy & K. Shibasaki, eds.), NRO Report 479, 353
Zarro, D. M., Sterling, A. C., Thompson, B. J., Hudson, H. S., & Nitta, N. 1999, ApJ, 520, L139
Zhang, J., Dere, K. P., Howard, R. A., Kundu, M. R., & White, S. M. 2001, ApJ, 559, 452
Zhang, M., Golub, L., DeLuca, E., & Burkepile, J. 2002, ApJ, 574, L97

Chapter 9

ELECTRON TRANSPORT DURING SOLAR FLARES

Jeongwoo Lee
Physics Department, New Jersey Institute of Technology, Newark, NJ 07102, U.S.A. *
leej@njit.edu

Abstract In this chapter we discuss microwave observation as a tool for investigating kinetic process of high energy electrons in solar flares. An ultimate goal of such studies is determination of electron evolution as a result of acceleration and transport in the presence of inhomogeneous magnetic field, and our focus is on why microwave radiation should be adequate for achieving this goal. The microwave studies devoted to such problems are briefly reviewed, and the main paradigms are expressed in simple formulations for so-called trap-and-precipitation systems. These formulations are then taken as a basis for organizing and illuminating contemporary ideas that recently emerged, including direct precipitation, various pitch angle scattering, and energy variation. The ideas enlarged from the discussions may guide the use of the FASR as an exceptional tool for solar flare study.

Keywords: acceleration of particles — Sun: flares — Sun: radio radiation — Sun: magnetic fields — radiation mechanisms: nonthermal

1. Introduction

Solar flares are an important example in the study of astrophysical particle acceleration, because they present a number of radiative characteristics indicative of kinetic processes of high energy particles in details unparalleled with other astronomical observations (Miller *et al.* 1997). As observational characteristics become known in increasing numbers, we, however, encounter an ambiguity as to whether the observed characteristic is directly due to acceleration or alternatively due to some transport effect (see Petrosian 1990). The ability to

*This work was supported by NASA grants NAG 5-10891 and NAG-11875

identify each of these two physical effects from observations therefore appears to be a key to further advancement in the study of kinetic processes in solar flares. During the last three decades, the problem of electron acceleration and transport has been discussed largely with Hard X Ray (HXR) observations (Aschwanden 2003) and partly with observations at microwaves (Bastian, Benz, & Gary 1998; Gary 2000) and other radio wavelengths (Wild & Smerd 1972; Dulk 1985). In this chapter we mainly discuss Microwave Radiation (MWR), as a tool for exploring the electron acceleration and transport processes during solar flares.

In 1966, Takakura & Kai formulated MWR spectral evolution as an electron transport problem for the first time, taking into account Coulomb collisions and synchrotron losses. Later several authors (Crannell *et al.* 1978; Cornell *et al.* 1984) found that lightcurves of MWR and HXR share an overall similarity, but MWR reaches its maximum in a delayed time and decays over an extended period. In a more systematic study, Lu & Petrosian (1988) found both short and relatively longer delays between 17 GHz and HXR, which they interpreted as due to transport and acceleration effects, respectively. Since then, further efforts have been made to interpret MWR observations using the ideas developed in HXR studies such as spectral hardening in the trapped electrons (Melrose & Brown 1976) and energy dependent time delay under Coulomb collisions (Bai & Ramaty 1979). Along this line, Melnikov (1990; 1994) presented for the first time microwave spectral evolution under Coulomb collisions, using Melrose & Brown's (1976) model. Similar studies followed, to account for the frequency-dependent time delays between MWR peaks as well as the relative delay of MWR to HXR peaks within the physics of Coulomb collisions (Bruggman *et al.* 1994; Bastian & Aschwanden 1997; Melnikov & Magun 1998; Silva, Wang, & Gary 2000).

Besides the time correlations, some authors compared MWR flux with proton flux (Bai 1982; Kai, Kosugi & Nitta 1985; Daibog *et al.* 1989; Melnikov *et al.* 1991; Daibog, Melnikov & Stolpovskii 1993), and with HXR fluxes (Kosugi, Dennis & Kai 1988; Melnikov 1990; 1994). They commonly found that extended (gradual) flares tend to show excess MWR flux, implying accumulation of electrons in a trap. Kai (1985) proposed that MWR is emitted by directly precipitating electrons in an attempt to resolve the problem of inconsistent numbers of electrons deduced from HXR and from MWR. Klein, Trottet, & Magun (1986) showed that use of a common injection function for both HXR and MWR can help in resolving the number problem too. The understanding that has emerged from these correlative studies is that MWR and HXR electrons share a common origin but, depending on whether they are emitted by the trapped or precipitating electrons, different fluxes and numbers may result.

While the above studies mainly deal with the effect of Coulomb collisions on the electron energy, more recent studies add the effects of Coulomb collisions on electron pitch angles together with magnetic mirroring. Lee & Gary (2000) and Lee, Gary & Shibasaki (2000) have analyzed a burst of which spectral evolution is due to not only collisional energy loss but pitch angle diffusion. Kundu *et al.* (2001a) studied time profiles of simple impulsive MWR bursts in comparison with HXR lightcurves, and explained the relative difference within the trap-and-precipitation model (Melrose & Brown 1976). Lee *et al.* (2002) studied an impulsive MWR event with rather long tail, using direct precipitation and a time-dependent injection spectrum inferred from HXR.

Transport effects have also been discussed with imaging observations. VLA observations have shown that in many flares the MWR source starts at the loop top and moves apart towards footpoints, which could be regarded as direct indication of the main energy release and subsequent propagation (see review by Marsh & Hurford 1982). Petrosian (1982) presented a more general consideration for the loop-top MWR source, including the radiative efficiency and particle kinetics. Holman *et al.* (1982) proposed that a loop top source and its expansion (Marsh & Hurford 1980) represent an instantaneous trap of the high energy electrons and subsequent pitch angle diffusion. Kundu *et al.* (1995) observed an asymmetric pair of MWR sources and interpreted it as due to asymmetric precipitation of nonthermal electrons under weak diffusion. The asymmetric MWR source presented in Lee, Gary & Shibasaki (2000) and Lee & Gary (2000) was also interpreted as due to magnetic mirroring under weak pitch angle diffusion. Melnikov, Shibasaki & Reznikova (2002, 2003) studied MWR loop-top sources at 17 and 34 GHz, which they found to represent an actual concentration of electrons rather than a radiative transfer effect.

Another type of imaging study has been made by Hanaoka (1996; 1997), Nishio *et al.* (1997), and Kundu *et al.* (2001b) using Nobeyama 17 GHz imaging data together with HXR images from the *Yohkoh* satellite, who argue for reconnection of interacting loops, inferred from their multiple footpoints. Lee *et al.* (2003) found spatial coincidence of the MWR sources with the magnetic separatrix inferred from a magnetogram and Hα ribbons in an impulsive flare. These studies have suggested some gross properties of magnetic reconnection, which is responsible for the particle acceleration, and resulting propagation away from the acceleration site.

In summary, we see that the early spectral/time studies suggested that MWR and HXR are related to trap-and-precipitation, respectively, and this can be known from the electron energy variation. However some of the recent imaging observations (Kundu *et al.* 2001a, b; Lee *et al.* 2002; Melnikov *et al.* 2002; 2003) suggest that electron pitch angles and inhomogeneous magnetic fields are also important elements in the transport problem. In the rest of this chapter, we

will discuss key issues in electron acceleration and transport within the latter paradigm.

2. The Formulations

Let us present a simplest possible formulation with which we can illustrate the recent and past picture of trap-and-precipitation in a unified fashion. Suppose electrons are injected into a trap by the quantity Q and leave the trap at a rate ν, in which case the Fokker-Planck equation will be in the form:

$$\frac{\partial N}{\partial t} = [\dots] - \nu N + Q \ ,$$

where $[\dots]$ should include all the variations in momentum and space. The solution to this equation takes a form of $N = K \otimes Q$, where the kernel function K accommodates all the terms in the right hand side except the injection. Our problem is therefore how to deconvolve Q from the resulting electron distribution function N obtained from the observed radiation. In general all of these quantities N, Q, and K involve time, energy and pitch angle as arguments, and not only the solution but even the formulation is not always expressed in a convenient closed form. Here we consider a simple case where all the terms in $[\dots]$ can be ignored, which corresponds to a collisionless trap where there is no loss of particles other than that due to escape (νN) and its pitch angle-dependence is implicitly handled. In this case the kernel function is simply an exponential function, and solution for trapped electrons is in the form $N = \int_0^t e^{-\nu(t-t')} Q(E,t') dt'$, where the transport effect is solely described by the property of the escape rate ν (as used in Aschwanden 1998; Kundu *et al.* 2001a; Lee *et al.* 2002).

2.1 Trap-and-precipitation

The above N alone provides electrons in a perfect trap, with ν, representing some loss rate. Melrose & Brown (1975) presented a model in which the trap region (thin target) is connected to a precipitating region (thick target) and therefore the escape rate ν is set as the precipitation rate which in turn becomes an injection rate into the thick target region. To express this idea under our simplifying assumption given above, we have

$$\begin{array}{rcc} N & = & \int_0^t e^{-\nu(t-t')} Q(E,t') dt' \\ \dot{n} & = & \nu N(E,t) \end{array} \ , \qquad (9.1)$$

where N is the number density in the trapped electrons (thin target) and $\dot{n}$ is injection rate into the thick target region. In this model, ν is the central quantity whose magnitude and energy dependence governs the lives of the

trapped electrons (N) and precipitating electrons ($\dot{n}$). As a major advantage, the N and $\dot{n}$, which are believed to be responsible for MWR and thick-target HXR, respectively, can be related to each other via the single physical effect of pitch angle scattering. As a limitation, however, the model predicts that the time evolution of the HXR electrons ($\sim \dot{n}$) should be well correlated with that of the MWR electrons ($\sim N$), whereas HXR often appear with a shorter timescale than the MWR.

2.2 Trap, bypass, and precipitation

As an important step forward, Aschwanden (1998) included another component in to the formulation, a population associated with direct precipitation ("by-passing the trap" in other words). To illustrate this idea, we split the injected particles Q into two parts, according to whether the initial pitch angles are greater or smaller than the loss-cone angle, i.e., $Q(\phi^+)$ and $Q(\phi^-)$, where $\phi^+(\phi^-)$ represents the electron pitch angles greater (smaller) than the loss-cone angle, ϕ_L (cf. MacKinnon 1991). The loss-cone angle is set by the magnetic mirror ratio of the flaring loop, $\phi_L = \sin^{-1}(B_1/B_2)$, with B_1 and B_2 representing the magnetic field strength at the loop top and a footpoint, respectively. Since the particles with ϕ^- can *directly* precipitate without being trapped, (9.1) should be modified to the following form:

$$\begin{array}{rcl} N & = & \int_0^t e^{-\nu(t-t')} Q(E, \phi^+, t') dt' \\ \dot{n} & = & Q(E, \phi^-, t) \; + \; \nu N \end{array} \quad . \tag{9.2}$$

Note that (9.2) will reduce to (9.1) in the limit of $\phi_L \rightarrow 0$, i.e. all particles are initially trapped and then are able to precipitate. We can thus say that (9.1) is valid to the extent that ϕ_L can be ignored. Another limit in which both equations approach to each other is at $\nu \rightarrow \infty$. In this case $N \rightarrow 0$ and $\dot{n} \rightarrow Q$, which means that observed radiation is a direct consequence of acceleration with no transport effect. These two cases represent the entirely trapped (transport-dominated) and entirely untrapped (acceleration-dominated) cases, respectively.

Equation (9.2) shows, on a minimum basis, how the magnetic field and pitch angle distribution comes into the context of trap-and-precipitation. Under this model, we can treat the following issues: (1) The injection function can, at least in the portion $Q(\phi^-)$, be subject directly to observations rather than treated as a free parameter. (2) The precipitating population can behave differently from the trapped one if the bypassing component $Q(\phi^-)$ dominates over the secondary precipitation νN. As a result, we can have an impulsive HXR and more extended MWR in an event. (3) The finite magnetic field comes into the context, at a minimum, in the form of mirror ratio. (4) Since N and $\dot{n}$ can have different time behaviors, the combination of these two terms can produce various

types of MWR lightcurves, especially, a burst with impulsive rise and extended decay. In the next section we will apply these ideas to actual observational data.

3. Electron Trapping And Precipitation

In this section, we consider various classes of MWR activities as evidence of the trap-and-precipitation system as formulated above.

3.1 Simple bursts

When a flare produces a single or small number of bursts in HXR and is accompanied by more extended MWR emission, we expect that the HXR would be a result of direct precipitation and thus would represent injection, while MWR will be given by a convolution of the HXR profile with the kernel function. Such events were recently studied by Kundu *et al.* (2001a) and Lee *et al.* (2002). We show a result presented by Kundu *et al.* (2001a) in Figure 9.1. In the figure, the authors compare the NoRH lightcurves at 17 and 34 GHz with HXR from HXT/Yohkoh. Both HXR and MWR has the same initial rise and the core part of the impulsive peak is similar in both radiations. Such coincidence (excluding the time-of-flight effect as studied by Aschwanden and his colleagues) can be taken as evidence for direct precipitation. Then the extended tail of the MWR is interpreted as due to trapped electrons. Kundu *et al.* reproduced its time behaviors using a convolution of HXR which has been taken as injection. In our notation, this is to say that the HXR represents the direct precipitation into a thick target $\sim Q(\phi^-)$, and the MWR is contributed by both trapped and directly precipitating electrons $\sim K \otimes Q(\phi^+) + Q(\phi^-)\,\ell/u$, where ℓ/u is the transit time for an electron of speed u in a loop of length ℓ.

The distinction between injection and trapping was made possible here because the HXR emission is dominated by thick target emission while MWR is from both components. MWR responds to both components because of its greater sensitivity to energetic electrons, whether they are located in the dense chromosphere or tenuous corona. Therefore the relative difference between MWR and HXR serves as a measure of transport effects. A similar conclusion is presented by Lee *et al.* (2002) in which a HXR spectrum is used to derive an injection function in a time dependent spectrum, and this is used to reproduce MWR bursts, taking into account full radiative transfer as electrons pass through an inhomogeneous magnetic loop.

3.2 Trap or precipitation?

Many solar flares show multiple peaks in MWR and HXR, in which case there may form a smooth envelope underneath the impulsive peaks. In this case, the trapping and direct precipitation could be attributed to the smooth envelope and superposed pulses, respectively. The individual MWR peaks

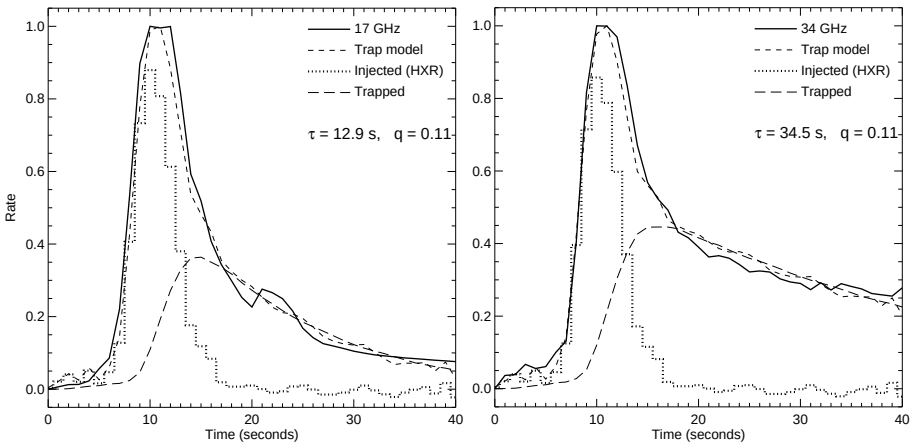


Figure 9.1. Comparison of the radio time profiles for the event on 1998 June 13 for (left) 17 GHz and (right) 34 GHz with a trap model (short-dashed line) derived using the Yohkoh/HXT 53–93 keV hard X-ray time profile (dotted histogram) as an injection function. The radio time profile is modeled as the sum of a component identical to the hard X-ray time profile (the injection function) and a trapped component (long-dashed line) derived by integrating over the injection function convolved with an exponential kernel function. τ and q denoted in this figure are respectively equivalent to ν^{-1} and $Q(\phi^-)/Q(\phi^+)$ in our notation. (From Kundu *et al.* 2001*a*).

themselves may not be much delayed or extended compared with those of HXR, but the presence of the underlying envelope in MWR may obscure the similarity expected between the two radiations. We show such an example in Figure 9.2. The solid lines are MWR and HXR lightcurves, and the dashed lines are fit by eye to the background envelope. The result difference profiles give a set of short pulses. Since they show peak-to-peak correspondence between two radiations, we regard them as representing the direct precipitation ($\sim Q(\phi^-)$) during the event. As we regard the smooth envelope as the trapped population, we require it to be reproduced by convolution of the net impulsive peaks with some kernel function. Although the exact account of this calculation depends on how one sets the background, we do indeed find a rough fit to the observed HXR envelope at $\nu = 1.2 \times 10^{-2}$ s^{-1}. The MWR envelope is more extended and the fit is made at a much lower value of $\nu = 5.1 \times 10^{-3}$ s^{-1}, implying a longer lifetime of electrons compared with the HXR case.

The two different values of ν for MWR and HXR could simply reflect an energy dependence of the precipitation rate, given the expectation that the MWR and HXR are contributed by electrons with different energies. It is also possible that the effective emitting region for HXR has different physical parameters than that for MWR or that the envelopes in HXR and MWR represent the secondary

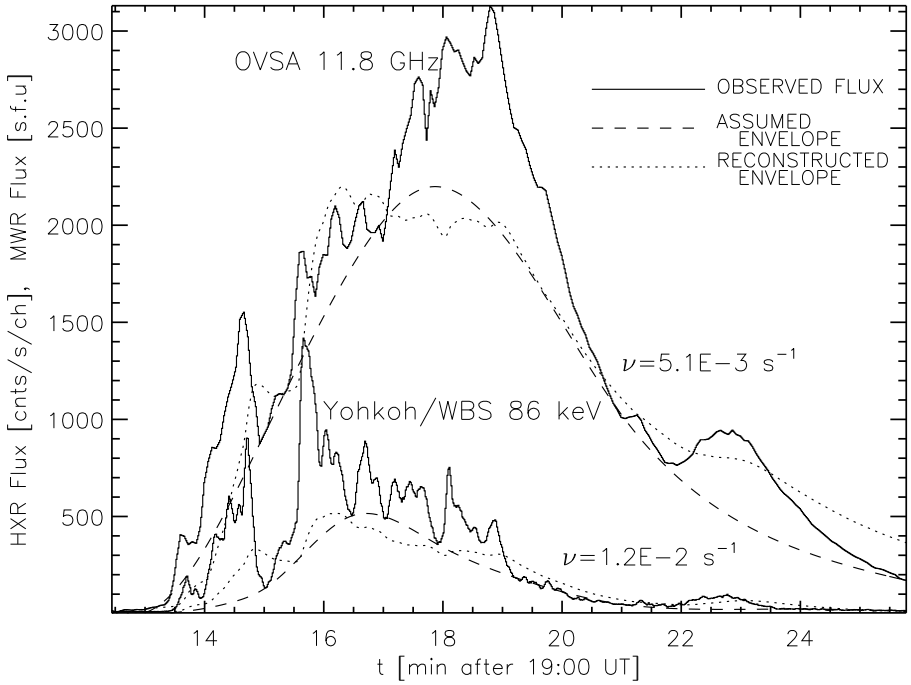


Figure 9.2. An impulsive burst that occurred on 2001 April 6. The solid lines are lightcurves at MWR at 11.8 GHz and HXR 86 KeV from Yohkoh/WBS. The dashed lines are the envelope of each curve obtained by smoothly connecting the local minima of the curves. The fluctuation above the envelope shows a peak-to-peak correspondence and is regarded as due to direct precipitation. This is then convolved with a kernel function in an attempt to self-consistently reproduce the envelope, shown as dotted lines.

precipitation, νN, and trapped electrons, N, respectively. With the temporal profile alone, we have no way to distinguish among these or other possibilities. However, HXT/*Yohkoh* imaging data available for this event showed that the HXR sources appear on the footpoints, by which we could conclude that the smooth HXR envelope is due to secondary precipitation while the MWR envelope is due to the trapped component. In this case also, the relative difference between MWR and HXR serves as a measure of trapping.

3.3 Extended and evolving trap

Large flares usually show temporally extended MWR activity, as do the accompanying soft X-rays and HXRs. Naively speaking, a large flare is powered by a larger amount of energy, and therefore activity can be extended in time. Alternatively the extended activity may be a result of long term trapping associ-

ated with the large physical extent of such a flare. This leads to a long standing question as to whether the extended activity is due to prolonged acceleration or efficient trapping, in other words, whether it is due to a longer τ_a or smaller ν.

An example of extended MWR bursts, the 1991 March 22 flare, is shown in Figure 9.3. The left panel shows the MWR lightcurves at multiple frequencies and the right panel, MWR spectra at selected times (symbols) together with a model fit (solid lines). Note that the extent of the activity is not equally long at all frequencies, but varies rapidly across frequencies. Based on the idea presented in the previous section, we speculate that the short-period activity at the highest frequency (18 GHz) represent the injection-related component ($\sim Q(\phi^-)\,\ell/u$) and longer period activity toward lower frequencies represent the more extended trapped component ($\sim N$). This then means that the extended activity in this event is not due to injection (which was impulsive) but due to efficient trapping, i.e., $\tau_a \ll \nu^{-1}$, where τ_a is the timescale for acceleration. Such a good trap condition may be realized simply because the ambient density in the coronal magnetic loop may be very low (for Coulomb collisions) or the mirror ratio may be high so that ϕ_L is small, or both.

We draw further attention to the frequency-dependence of the MWR activity. If Coulomb collisions dominated, and if the MWR frequency is simply proportional to the electron energy, the flux at a high frequency should have been longer than that at a low frequency, as opposed to the observation. Lee, Gary & Zirin (1994) made a model to fit such a spectral variation as shown in the right panels in Figure 9.3, in which the MWR source at the maximum phase spans the entire loop encompassing highly inhomogeneous magnetic fields, and then the trap gradually shrinks to a smaller region with weaker fields, i.e., the loop top. In such a model, the high frequency flux has short duration because it is emitted by directly precipitating electrons that are passing through the strong magnetic fields near the footpoints, and the gradual decay toward lower frequencies is, in fact, due to *harder* electrons surviving longer in the loop top. This type of burst demonstrates how significant the magnetic inhomogeneity can be to the evolution of MWR in a solar flare.

3.4 Trap without precipitation

In some events the correlation between MWR and HXR is so poor that we are puzzled about the common origin for MWRs and HXRs. A good example can be found in the famous Bastille Day flare as shown in Figure 9.4. In the top panel we compare the HXR and MWR lightcurves and in the bottom two panels, EUV images at 195 Å from Transition Region and Coronal Explorer (TRACE) before and after the impulsive phase. The HXR reached its maximum at t_1 and then diminished whereas the MWR has multiple peaks remaining strong throughout the flare. This temporal behavior differs from that shown in Figure 9.2 in

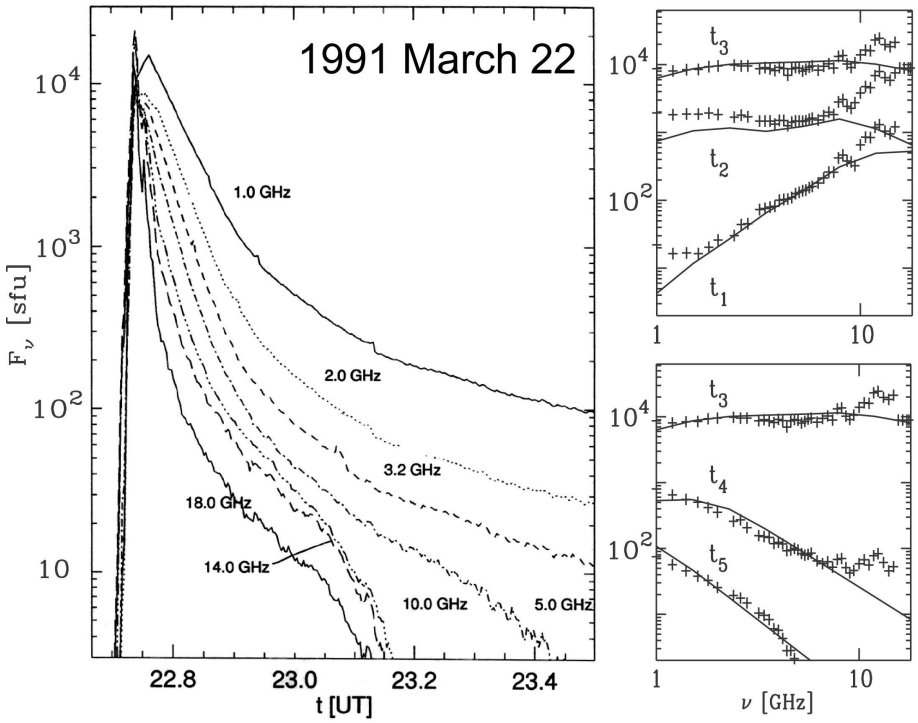


Figure 9.3. MWR bursts indicative of long-term trapping. In the leftmost panel, the 1991 March 22 flare shows an impulsive rise and extended decay, but with an obvious frequency-dependence. The right panels show MWR spectra at selected times (symbols) and a model fit (solid lines). $t_1 - t_5$ respectively refer to 22:43:20, 43:50, 44:10, 55:00, and 23:30:00 UT. The model assumes gradual shrinkage of the electron trap into smaller regions centered at the loop top, together with softening of the electrons in the decay.

that there is no HXR counterpart after t_1. It is also different from that in Figure 9.3 in that the continued MWR activity indicates multiple occurrences of additional acceleration rather than just efficient trapping. Aschwanden & Alexander (2001) had shown that the HXR peak (which is taken as evidence of precipitation in this chapter) is accompanied by soft X rays and EUV in gradually delayed time profiles, indicative of energy cascade from 30 MK to 1 MK. The MWR electrons therefore participate in this energy transfer to low atmosphere only at time t_1 but not afterwards, $t_{2,3,\ldots}$.

Such decoupling of MWR from other (precipitation-oriented) radiations is expected, within the current framework of (9.2), when either $\phi_L(t)$ gets smaller or $Q(\phi, t)$ becomes more anisotropic at times $\{t_1, t_2, \ldots\}$. The former can happen as a result of the loop rising with the same footpoints (or some magnetic restructuring) so that the magnetic mirroring force will increase, so that a larger

fraction of particles return back to the coronal trap. We find some clue for the magnetic field change in the TRACE EUV loops shown in the bottom panels. The bright features in the left panel are thought to be low-lying magnetic loops in an arcade, which grow outward after the flare to form the newly formed, relaxed loops shown in the right panel. Alternatively the rapid drop of precipitation could be due to a change in the ratio of the injected electrons within or outside of loss cone, $Q(\phi^+)/Q(\phi^-)$, which was moderate at t_1 but could have increased at $t_{2,3,...}$ by a large factor. This could therefore imply that the electron acceleration mechanism had changed so as to produce more electrons with a perpendicular momentum distribution (see §4.3). Also in this case, the electron loss in the coronal trap would not be due to precipitation but some other mechanism. An appropriate loss mechanism may be escape associated with the upward ejecta or propagation into interplanetary space.

To conclude this section, the framework of trapped and directly precipitating electrons such as (9.2) leads us to a physical interpretation of a variety of MWR and HXR lightcurves. However, quantitative assessment of the similarities and differences requires a knowledge of the electron pitch angle and magnetic field, ideally to be deduced from observations.

4. Electron Pitch Angle Variation

We have thus far discussed the role of the initial electron pitch angle distribution, $Q(\phi)$, in the evolution of the electrons in a trap-and-precipitation system (the evolution of N and $\dot{n}$). Changes in pitch angle during transport can also significantly influence the evolution of N and $\dot{n}$. In many studies, the electron pitch angle diffusion due to scattering has been directly related to the precipitation rate, ν. We, however, present in this section an alternative view that stronger pitch angle diffusion does not necessarily imply more efficient precipitation. Rather, we show that relating the electron pitch angle diffusion to the magnetic field loop structure leads to an independent tool for studying the acceleration and transport characteristics.

4.1 Weak diffusion

Weak pitch angle diffusion has been defined as the condition in which the loss cone is empty. As a result the loss cone size has not been considered a factor in the precipitation and the precipitation is expected to increase in proportion to the scattering rate. However, such an assumption overlooks the fact that at a given scattering rate a large loss cone is more difficult to fill compared to a small loss cone. Also, the scattering rate itself should depend on pitch angle, which varies along the electron motion according to the ambient magnetic field, under conservation of the magnetic moment (first adiabatic invariant) $\mu_\perp^2/2B$

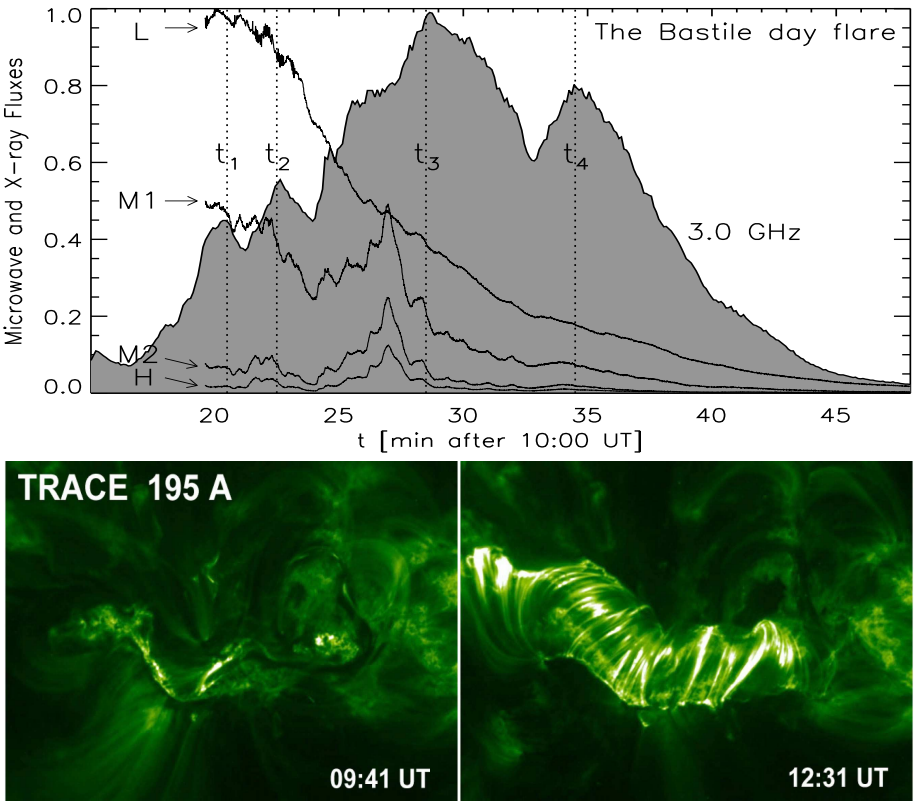


Figure 9.4. The top panel shows MWR and HXR lightcurves during the Bastille Day flare on 2000 July 14. The HXR lightcurves are from *Yohkoh* HXT at four energy channels, L, M1, M2, and H, and the 3.0 GHz MWR flux is from Ondrejov Solar Radio Telescope shown as the filled curve. Note the poor correlation between MWR and HXR lightcurves. The bottom panels show closeup views of the magnetic loops in the active region before and after the flare, as observed in 195 Å images obtained with the TRACE spacecraft.

(Melrose 1980). For these two reasons, pitch angle scattering even under weak diffusion cannot entirely be free from the magnetic field (see Lee & Gary 2000). The term weak diffusion has also been used to refer to a case where Coulomb collisions dominate, in the sense that Coulomb collisions always exist and any other scattering mechanism, if added, will make the scattering no longer weak. In this case the precipitation is given by the electron deflection time so that $\nu \approx 10\, n_9 E^{-3/2}\ \mathrm{s}^{-1}$ where E is in units of keV and n_9 is the ambient electron density in $10^9\ \mathrm{cm}^{-3}$ (Trubnikov 1965; Spitzer 1967). A comprehensive review and result of analysis that leads to a diagnostic of the trap density can be found in Aschwanden *et al.* (1997).

In an alternative, but perhaps more insightful, approach to reveal the presence of weak diffusion, Melrose & White (1979) suggested that spatial morphology of MWR could be asymmetric under weak diffusion because of asymmetric magnetic mirroring. Kundu *et al.* (1995) found an asymmetric spatial distribution of MWR sources and explained the observation within this context (see also Sakao 1995). Lee, Gary & Shibasaki (2000) and Lee & Gary (2000) reported an asymmetric MWR source in a magnetic loop, which is reproduced in Figure 9.5. The top panel shows that one of the double MWR sources is found at a footpoint and the other MWR source is some distance above the conjugate footpoint. Since the latter footpoint has stronger field, the asymmetric MWR source positions along the loop implies there are regions where electrons do not have access because of magnetic mirroring. The bottom panels show MWR spectral hardening during the decay phase, which indicates the influence of Coulomb collisions on the electron energy distribution. The theoretical modeling becomes more complicated in this case, since pitch angle and magnetic field inhomogeneity needs to be taken into account. Through a simplified simulation including electron pitch angles and a specific magnetic field structure of the loop, Lee & Gary (2000) found that a model fit to the observed spectral variation required an anisotropic pitch angle distribution in the injected electrons. Not only does the MWR spectrum show great sensitivity to the electron pitch angle distribution, but also the slow changes in the collisionless coronal trap. This allowed Lee & Gary (2000) to deduce the pitch angle distribution of the initial injection. This underscores the importance of MWR observations for the study of the properties of the coronal population, including pitch angle distributions.

4.2 Intermediate diffusion

In contrast to weak diffusion, Melrose & Brown (1975) defined the case of the loss cone being filled with scattered particles as "strong" diffusion. We shall instead call this "intermediate" diffusion to save the term "strong" diffusion for another case to be discussed in the next section (see Bespalov, Zaitsev & Stepanov 1991). If the loss cone is continually refilled, the rate of precipitation will be limited by the size of the loss cone, and is expressed as $\nu = \alpha_0^2 u/2\ell$, where α_0 is the loss-cone angle (Kennel 1969). The scattering rate is thus proportional to u (or $E^{1/2}$) independent of the scattering mechanism. While weak diffusion offers a number of interesting spatial structures associated with magnetic mirroring, intermediate diffusion would erase any such features by quickly isotropizing the electron momenta, and the whole loop is evenly occupied by the electrons. As a result, the spatially-averaged Fokker-Planck solution is appropriate in this case.

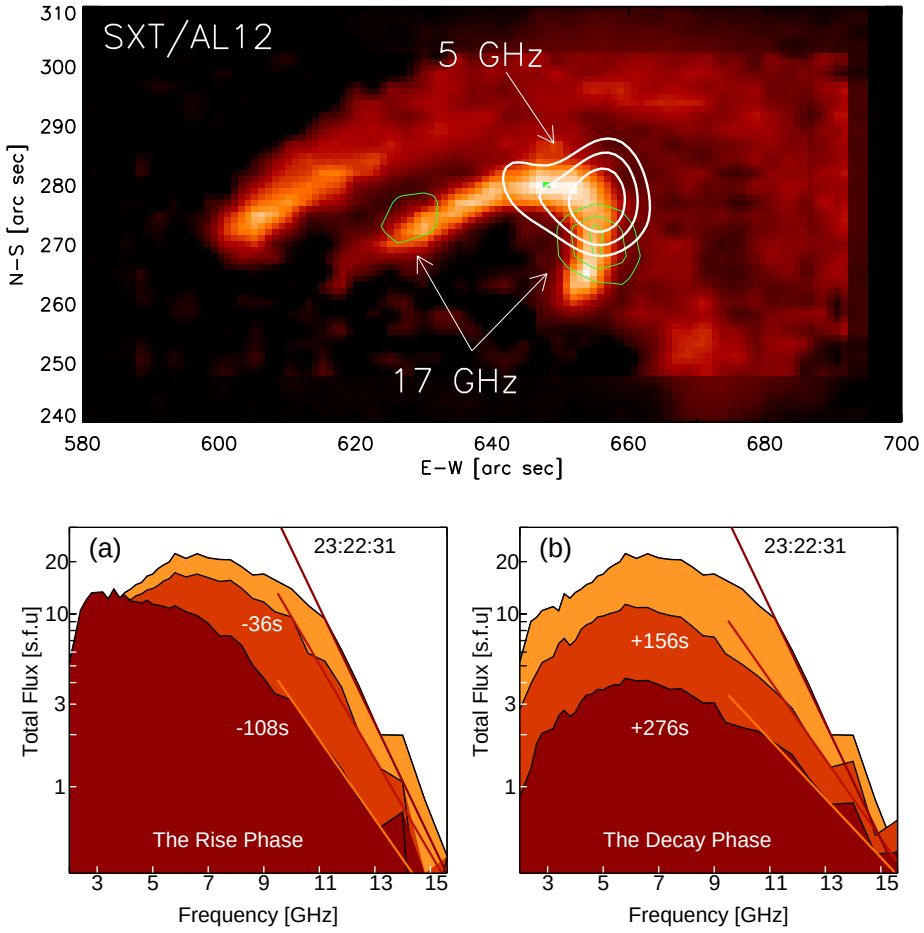


Figure 9.5. MWR maps and spectra obtained for the 1993 June 3 flare. Top: Radio intensity peaks (contours) on top of a soft X-ray image from a filtered *Yohkoh* SXT/AL12 at 23:29 UT. Contours are 80% to 99% of the maximum intensities: 1.8×10^7 K at 5 GHz and 1.2×10^5 K at 17 GHz, respectively. Bottom: Spectral variation in the microwave total power during (a) the rise and (b) the decay phases, at five selected times relative to the time of the maximum flux (23:22:31 UT). The straight lines are guide lines for spectral slope at the corresponding times. (From Lee & Gary 2000)

Figure 9.6 shows a model fit to the MWR fluxes during the 1999 August 20 flare (Lee *et al.* 2002) which led the authors to argue for intermediate diffusion. The OVSA visibility implied a large loop ($\ell \approx 1.4 \times 10^5$ km) entirely filled with accelerated electrons. Since morphology is of little help in the intermediate

diffusion case, the only way to know which pitch angle scattering scenario applies to this flare was to check the energy dependence of the precipitation rate. The authors compared the model predictions made under various energy dependencies with the MWR flux variation with frequency to find that the assumption of $\nu \sim E^{1/2}$ (case (b) in the figure) is the most appropriate. The MWR flux decays only slowly and the loss cone is found to be as small as $\alpha_0 \approx 4.3^\circ$. Thus in spite of the fact that it is not a weak diffusion case, the actual precipitation rate is very low. This is an example in which highly efficient pitch angle diffusion does not imply a high efficiency of precipitation. In retrospect, intermediate diffusion pertains in this event because the loss cone is small and can be easily filled, leading to the precipitation rate becoming independent of the scattering mechanism.

4.3 Strong diffusion

In the above case of "intermediate" diffusion, the precipitation rate depends on the whole loop length, implying that the scattered particles still remember the whole dimension of the loop at least over a few bounce times. Bespalov, Zaitsev & Stepanov (1991) defined another regime for pitch angle scattering as "strong" in which the scattering, for instance, due to the presence of enhanced turbulence, is so strong as to alter pitch angles so quickly that the mean free path is much shorter than the loop length. In this case, defining a loss cone is not meaningful and the electrons are effectively trapped within the scattering source. This is another example for which pitch angle diffusion and precipitation may be two independent, unrelated effects. An important aspect of this strong diffusion is that the region of such strong turbulence, if localized on a flaring loop, could give clues to the spatial location of the acceleration site and properties of the acceleration mechanism. Just as loop-top HXR sources (Masuda *et al.* 1994) have been much debated, the loop-top MWR source has also been a mystery considering the strong dependence of MWR emissivity on magnetic field strength. If the entire loop is optically thick, we may then expect the highest effective temperature of MWR to occur at the loop-top, because that is the location of the lowest field strengths, which are associated with the highest harmonics at a given frequency. This is demonstrated in several flare loop models (Alissandrakis & Preka-Papadema 1984; Klein & Trottet 1984; Lee *et al.* 1994). However if the loop-top source is optically thin, a looptop brightening implies an actual concentration of electrons at the position rather than an apparent radiative effect.

In Figure 9.7 we show an example of a loop top source from NoRH observations (Melnikov, Shibasaki & Reznikova 2003) at two frequencies. It is apparent from the figure that the 34 GHz image outlines a loop over an active

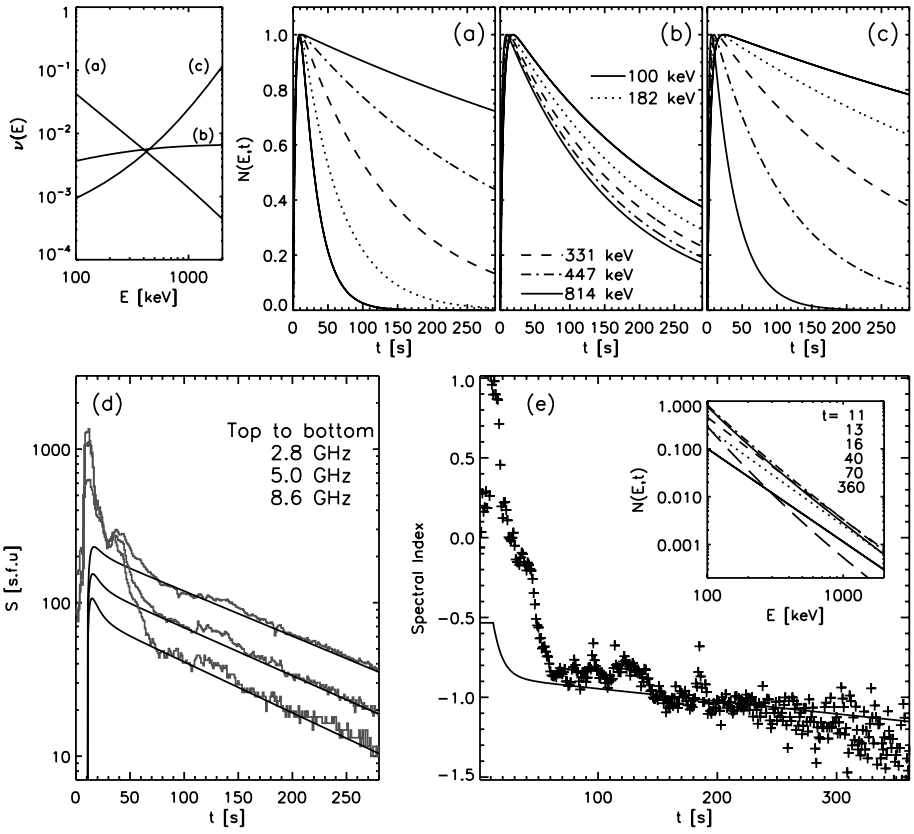


Figure 9.6. The 1999 August 20 flare as a case of intermediate pitch angle diffusion. The top left panel shows the energy dependence of the precipitation rate $\nu(E)$. (a)–(c) Model electron numbers at different energies evolving under the transport effect described by $\nu(E)$, which we refer to as weak, intermediate, and strong scattering, respectively. (d) Model fit to the observed microwave light curves at three frequencies. (e) Model fit to the observed microwave spectral index. The inset in (e) shows the evolution of electron energy spectrum used for the fitting. In (a)–(c), t represents time in the model, and in (d) and (e) t represents time after 23:06 UT. The fit is made at a very small loss cone $\alpha_0 \approx 4.3^\circ$ and a large loop, $l \approx 1.4 \times 10^5$ km. (From Lee *et al.* 2002)

region lying on the limb and is brightest at the loop top. By comparing this 34 GHz intensity with the 17 GHz intensity, this loop-top source is found to be clearly optically thin, and therefore must represent an actual confinement of electrons. A concentration of electrons around the loop top may result from magnetic mirroring. However, Melnikov, Shibasaki & Reznikova (2002) have found that magnetic mirroring alone is insufficient to overcome the increase of MWR toward the footpoints due to field strength (see also Petrosian 1982).

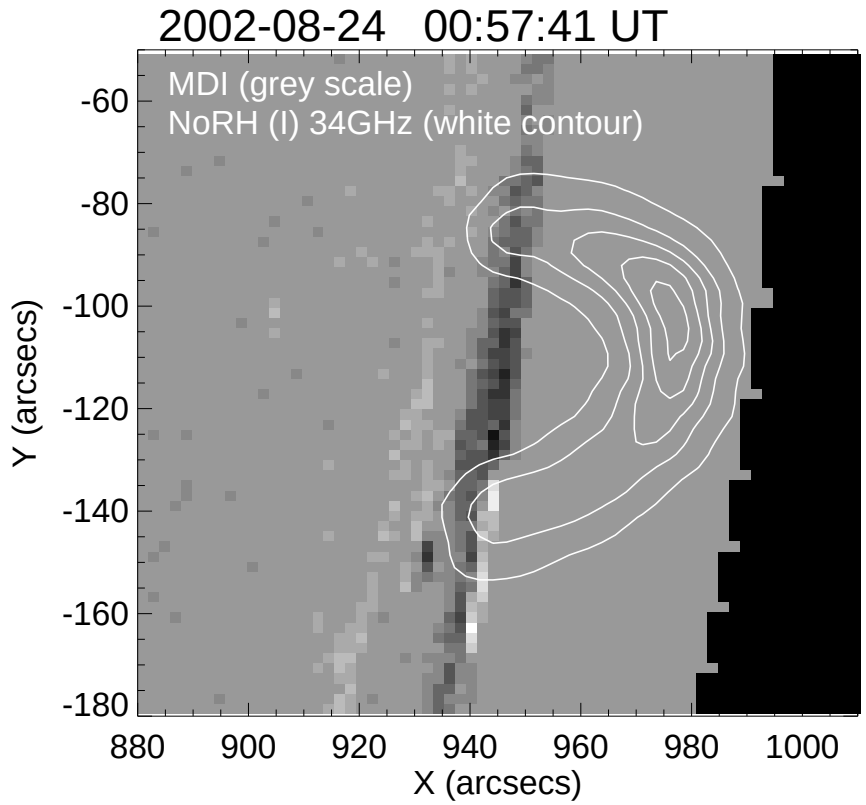


Figure 9.7. A loop top source near the solar limb observed with NoRH at 34 GHz. This MWR source (contours) is found to be optically thin, and therefore represents electrons that are highly concentrated at the loop top. The black and white pixels represent the longitudinal magnetic fields in the active region which lies on the very limb. (From Melnikov, Shibasaki & Reznikova 2003)

Melnikov *et al.* (2002) suggested two possibilities for such local confinement of electrons: either electrons are preferentially accelerated with a perpendicular momentum distribution or the loss of electrons is enhanced at the lower part of the loop. We here consider a third, ad hoc possibility that turbulence leads to strong diffusion and thus the associated trapping is itself localized to the loop top.

4.4 Pitch angle scattering and MWR maps

Each of the above three regimes of pitch angle scattering involve different physics, and it is likely that we can distinguish them in imaging MWR observations. Melrose & White (1979) predicted that, under weak diffusion, asymmetric double peaks will appear on an inhomogeneous magnetic loop (Fig. 9.5), whereas, under intermediate diffusion, electrons are able to access all part of the loop and thus will result in symmetric footpoint emissions. As seen above, electrons can be confined to a localized region under the strong diffusion (Fig. 9.7).

We also expect that the MWR source may move at a speed much slower than the individual particle themselves, so that it can be observable as a moving MWR source. Under the weak diffusion a source may expand toward the footpoints as electrons initially at a restricted range of pitch angles scatter to smaller pitch angles. Under strong diffusion, the electron confinement can expand more rapidly. For instance, Yokoyama *et al.* (2002) observed MWR sources propagating at speed up to $\sim 10^4$ km s^{-1} using the NoRH, which might represent the expansion of a Whistler turbulent region at its phase velocity (Stepanov *et al.* 2003). No actual motion of the microwave source is expected for intermediate diffusion. However we can expect an apparent motion of MWR sources from the loop-top to footpoints in the case where the entire loop is initially optically thick at the maximum phase and becomes optically thin later.

The key diagnostic comes from the spatially resolved MWR spectrum, which we have shown is sensitive to the pitch angle distribution (see Lee & Gary 2000). Nevertheless such investigations are not common for a couple of reasons. First, allowing an evolving pitch angle distribution introduces a number of parameters into calculation of MWR spectrum, which already depends on many largely unknown ambient plasma and accelerated electron parameters. Second, it has been expected that electrons with an anisotropic distribution will be unstable to various instabilities by which they become isotropized quickly (Melrose 1980). Recently, Fleishman & Melnikov (2003ab) addressed this problem by first showing that electrons in an anisotropic pitch angle distribution can be stable against the Cyclotron instablity over a wide range of parameters, although other instabilities are yet to be investigated. In their result, the gyrosynchrotron MWR spectrum from electrons with anisotropic pitch angle and single power-law energy distribution is steeper than that for isotropic electrons (see also Lee & Gary 2000), and furthermore the microwave spectral index itself varies with frequency, unlike the isotropic case. Such spectral diagnostics for anisotropic distributions of electrons may be utilized (and indeed may be necessary) when spatially resolved MWR spectra along a loop become available (e.g. with FASR).

5. Electron Energy Variation

Finally we discuss changes in electron energy during acceleration and transport, which is the main effect that has received attention in the interpretation of both MWR and HXR spectra. To study acceleration using the MWR spectrum, Moghaddam-Taaheri & Goertz (1990) modeled the runaway electrons in the electric field and subsequent pitch angle scattering by turbulence, and compared the predicted MWR spectral evolution with an observation by Marsh *et al.* (1981). Benka & Holman (1992) used a combination of thermal and nonthermal electrons in a model in which a DC field variation results in a typical OVSA spectral variation (Stähli, Gary & Hurford 1990). This acceleration process, in our formulations, amounts to determining $Q(E,t)$. On the other hand, the transport study is usually made assuming a time invariant injection spectrum, $Q(E,t) = q(E)T(t)$ and all spectral changes in the decay are attributed to the energy dependence of ν. The top panels in Figure 9.6 show some examples of such attempts. In many transport studies, efforts are made to confirm that $\nu(E)$ inferred from observations is consistent with the Coulomb collision physics. Such studies have provided some understanding of time delay, spectral hardening, etc. A recent comprehensive study using OVSA spectral data has been made by Melnikov & Silva (1999; 2000) and Silva *et al.* (2000).

Note that not all of these studies on energy dependent processes in phase space employ the trap-and-precipitation paradigm, in spite of the ample evidence for this hypothesis. It will thus be worthwhile to discuss how the paradigm will change once this trap-and-precipitation system is introduced.

1. Time delay and spectral hardening of MWR with respect to HXR are often attributed to the energy dependence of Coulomb collisions. However, the trapped component will always show time delay with respect to the directly precipitating electrons regardless of the scattering mechanism (see top panels of Fig. 9.6). The harder electron distribution in a trap is also possible for other reasons not entirely due to Coulomb collisions. For instance, Lee & Gary (1994) feed a common Whistler turbulence into two regions with weak and strong magnetic fields, which are assumed for MWR and HXR emitting regions, respectively, and find a steeper energy spectrum in the latter region due to the enhanced escape rate there. See also the discussion made in §3.2 for two different values of ν for MWR and HXR. It should therefore be clarified whether the relative differences of MWR and HXR time profiles arise solely due to the energy dependence of the radiations or due to the different conditions in the trap-and-precipitation regions.

2. If the Razin effect, suppression of radiation due to ambient plasma (Ramaty 1969), is observed together with the spectral flattening (cf. Belkora

1997), this may provide additional evidence for the importance of Coulomb collisions.

3. Some studies indicated that the trap region contains higher energy electrons and precipitation is primarily by lower energy electrons. This is consistent with the physics of Coulomb collisions. However, one can be misled by the radiative characteristics of MWR. Even though electrons in the entire energy range are equally trapped and precipitating, the coronal trap has weaker magnetic field and thus emits MWR at higher harmonics. As a result, the loop-top MWR represents relatively higher energy electrons at a given frequency. On the other hand, the precipitating region has stong magnetic field and the MWR from the region is dominated by low harmonics and thus correspondingly low energy electrons (cf. Kosugi *et al.* 1988). It is therefore essential to take into account the ambient magnetic field strength in relating the MWR frequency to electron energy.

4. In some studies, time correlation of MWR and HXR fluxes has been investigated to determine the energy of electrons that contribute most to a given frequency. Note however that the electrons staying in the trap would have a more extended life than the precipitating electrons, even though injected at the same time and energy. The magnetic trap thus acts as a machine to separate the two populations in time as well as in space. Accordingly, such correlation of the two radiations at a fixed time interval may be misleading in the presence of the magnetic trapping.

5. MWR has both optically thick and thin parts, each of which responds to injection spectrum very differently. While a thin MWR flux varies in proportion to the number of electrons like HXR, optically thick MWR represents a mean energy or effective temperature. For instance, if the emitting electrons are nonthermal in a single power-law distribution with index δ, the optically-thick MWR directly responds to δ avoiding confusion with the increase in N (see simplified expression for the effective temperature by Dulk & Marsh 1984). Accordingly, the optically thick MWR is rather important when the injection spectrum changes with time, which has often been ignored in the transport problem. In this case the structure of trap-and-precipitation is important, because direct precipitation is more likely to be optically thick as electrons pass through the strongest fields (see Fig. 8 of Lee *et al.* 2002).

6. Concluding Remarks

In this chapter, we have discussed MWR as an important clue to understand electron kinetic processes occurring in solar flares. Our emphasis was on the trap-and-precipitation paradigm, which naturally arises in the presence of in-

homogeneous magnetic fields on the Sun and is responsible for the relative differences between MWR and HXR. It is this framework that we take as a means to distinguish the acceleration from the transport, which is otherwise a difficult deconvolution problem. The pitch angle and energy variation have also been discussed within this framework, which puts us in a better position to derive physical properties of the acceleration and transport mechanisms.

Based on the ideas discussed in this chapter, we briefly comment on the traditionally suggested utility of MWR in the study of solar flares. MWR has often been regarded as appropriate for trapped electrons while HXR relate more to acceleration (Melnikov 1994). We found that the MWR well represents the trapped electrons because of its greater sensitivity to energetic electrons in the absence of cooler ambient plasma. We have shown that this sensitivity can be used, on the contrary, to derive information on the acceleration properties. To summarize: (1) MWR helps to locate those electrons produced in the high tenuous corona that are not precipitating into lower atmosphere and therefore are largely undetected by HXR and other lower energy radiations. (2) In some events, the slowly evolving nature of trapped electrons as measured in MWR allows us to investigate injection properties, within the instrumental time resolution. (3) The field strength dependence of MWR provides a strong constraint on the electron spatial distribution on a magnetic loop. (4) MWR spectra have both optically thick and thin emission, which provides diagnostics on N and δ, respectively. This is particularly useful when the acceleration spectrum changes with time. There has been a concern that inversion of MWR to flare parameters is more complicated than that of HXR, as it involves many parameters (Gary 2000). We however recognize that this complexity arises from two major ingredients in the electron transport problem: the magnetic field and electron pitch angles. We therefore suggest that future advance in MWR study would depend on how well we can use MWR observations to address the pitch angle and magnetic fields.

Until now, the diagnostics discussed in this chapter have not been fully exploited, largely due to the absence of high spatial and spectral resolution imaging spectroscopy. The ideas about trapping were proposed some time ago (Melnikov 1990; 1994), but the identification of direct precipitation in MWR was begun only recently (Kundu *et al.* 2001a; Lee *et al.* 2002). Imaging and spectral MWR observations for the study of pitch angle diffusion and associated acceleration properties is just beginning (Lee & Gary 2000; Melnikov *et al.* 2002; 2003). A topic that is closely related to the present context but not discussed here is the MWR study for multi-loop interactions (Hanaoka 1996; 1997; Nishio *et al.* 1994; 1997; Kundu *et al.* 2001b). This has direct implications for magnetic reconnection (see also Kundu *et al.* 1982ab), and therefore is significant in relating the electron kinetics to solar flare magnetohydrodynamics. Electron

propagation in a magnetic reconnection region may be handled by extending the present paradigm to a multiple system of trap-and-precipitation (Aschwanden *et al.* 1999). Currently the effort to achieve these goals is shared by OVSA with spectral capabilities and the VLA and Nobeyama Radioheliograph with imaging capability. The FASR, as an instrument targeted to this spectral imaging capability, will therefore not only integrate all the currently available knowledge but also achieve a new level of MWR study to advance our knowledge of kinetic processes during solar flares.

References

Alissandrakis, C. E. & Preka-papadema, P. 1984, A&A, 139, 507
Aschwanden, M. J. 2003, Particle Acceleration and Kinematics in Solar Flares, Reprinted from SPACE SCIENCE REVIEWS, Volume 101, Nos. 1-2, Kluwer Academic Publishers, Dordrecht
Aschwanden, M. J. 1998, ApJ, 502, 455
Aschwanden, M. J., Bynum, R. T., Kosugi, T., Hudson, H., and Schwartz, R.A. 1997, ApJ, 487, 936
Aschwanden, M. J., & Alexander, D. 2001 Solar Phys, 204, 93
Aschwanden, M. J., Schwartz, R. A., & Dennis, B. R. 1998, ApJ, 502, 468
Aschwanden, M. J., Kosugi, T., Hanaoka, Y., Nishio, M., & Melrose, D. B. 1999, ApJ, 526, 1026
Bai, T. & Ramaty, R. 1979, ApJ, 227, 1072
Bai, T. 1986, ApJ, 308, 912
Bastian, T. S. & Aschwanden, M. J. 1997, BAAS, Vol. 29, p.922
Bastian, T. S., Benz, A. O., & Gary, D. E. 1998, ARAA, 36, 131
Belkora, L. 1997, ApJ, 481, 582
Benka, S. G. & Holman, G. D.: 1992, ApJ, 391, 854
Bespalov, P. A., Zaitsev, V. V., & Stepanov, A. V. 1991, ApJ, 374, 369
Brown, J. C., Conway, A. J., & Aschwanden, M. J. 1998, ApJ, 509, 911
Bruggmann, G., Vilmer, N., Klein, K.-L., & Kane, S. R.: 1994, Solar Phys, 149, 171
Cornell, M. E., Hurford, G. J., Kiplinger, A. L., & Dennis, B. R. 1984, ApJ, 279, 875
Crannell, C. J., Frost, K. J., Saba, J. L., Maetzler, C. & Ohki, K. 1978, ApJ, 223, 620
Daibog, E. I., Mel'Nikov, V. F., Stolpovskii, V. G. 1993, Solar Phys, 144, 361
Daibog, E. I., Stolpovskii, V. G., Melnikov, V. F., Podstrigach, T. S. 1989, Soviet Astr.Lett.(Tr:PISMA) V.15, NO. 6/NOV, 432
Dulk, G. A. 1985, ARAA, 23, 169
Dulk, G. A. & Marsh, K. A. 1982, ApJ, 259, 350
Fleishman, G. D. & Melnikov, V. F. 2003a, ApJ, 584, 1071

Fleishman, G. D. & Melnikov, V. F. 2003*b*, ApJ, 587, 823
Gary, D. E. 2000, in High Energy Solar Physics-Anticipating HESSI, ASP Conf. Ser. 206, 297
Ginzburg, V. L. & Syrovatskii, S. I. 1965, ARAA, 3, 297
Hanaoka, Y. 1997, Solar Phys, 173, 319
Hanaoka, Y. 1996, Solar Phys, 165, 275
Holman, G. D., Kundu, M. R., & Papadopoulos, P. 1982, ApJ, 257, 354
Kai., K. 1986, Solar Phys, 104, 235
Kai, K. Kosugi, T., & Nitta, N. 1985, PASP, 37, 155
Kennel, C. F. 1969, Rev. Geophys. Space Phys., 7, 379
Klein, K.-L., Trottet, G., & Magun, A. 1986, Solar Phys. 104, 243
Klein, K.-L. & Trottet, G. 1984, A&A, 141, 67
Kosugi, T., Dennis, B. R., & Kai, K. 1988, ApJ, 324, 1118
Kundu, M. R., White, S. M., Shibasaki, K., Sakurai, T., & Grechnev, V. V. 2001*a*, ApJ, 547, 1090
Kundu, M. R., Grechnev, V. V., Garaimov, V. I., & White, S. M. 2001*b*, ApJ, 563, 389
Kundu, M. R., Nitta, N., White, S. M., Shibasaki, K., Enome, S., Sakao, T., Kosugi, T., & Sakurai, T. 1995, ApJ, 454, 522
Kundu, M. R., Schmahl, E. J., Vlahos, L., & Velusamy, T. 1982b, A&A, 108, 188
Kundu, M. R., Schmahl, E. J., & Velusamy, T. 1982a, ApJ, 253, 963
Lee, J., Gallagher, P. T., Gary, D. E., Nita, G. M., Choe, G. S., Bong, S.-C., & Yun, H. S. 2003, ApJ, 585, 524
Lee, J. & Gary, D. E. 1994, Solar Phys, 153, 347
Lee, J., Gary, D. E., & Zirin, H. 1994, Solar Phys, 152, 409
Lee, J., Gary, D. E., & Shibasaki, K. 2000, ApJ, 531, 1109
Lee, J. & Gary, D. E. 2000, ApJ, 543, 457
Lee, J., Gary, D. E., Qiu, J., & Gallagher, P. T. 2002, ApJ, 572, 609
Lu, E. T. and Petrosian, V. 1988, ApJ, 327, 405
MacKinnon, A. L. 1991, A&A, 242, 256
Marsh, K. A., Hurford, G. J., Zirin, H., Dulk, G. A., Dennis, B. R., Frost, K. J., & Orwig, L. E. 1981, ApJ, 251, 797
Marsh, K. A. & Hurford, G. J., 1982, ARAA, 20, 497
Marsh, K. A. & Hurford, G. J., 1980, ApJ, 240, L111
Masuda, S., Kosugi, T., Hara, H., Tsuneta, S., & Ogawara, Y. 1994 Nature, 371, 495
Melnikov, V. F. 1990, Ph.D. Thesis, Radiophysical ResearchInstitute, Nizhniy Novgorod, Russia
Melnikov, V. F., Podstrigach, T. S., Daibog, E. I., Stolpovskii, V. G. 1991, CosRe 29, 95
Melnikov, V. F. 1994, Radiophys. Quant. Electron. 37, 557

Melnikov, V. F. & Magun, A. 1998 Solar Phys, 178, 153
Melnikov, V. F., Shibasaki, K., & Reznikova, V. E. 2002, ApJ, 580, L185
Melnikov, V. F., Shibasaki, K., & Reznikova, V. E. 2003, ApJ, in preparation
Melnikov, V. F. & Silva, A. V. R. 1999, Ninth European Meeting on Solar Physics: Magnetic Fields and Solar Processes. Florence, Italy, 12-18 September, 1999. Proceedings published in ESA SP Series (SP-448), ed. A. Wilson.
Melnikov, V. F. & Silva, A. V. R. 2000, in High Energy Solar Physics-Anticipating HESSI, ASP Conf. Ser. 206, 371
Melrose, D. B. 1980, Plasma Astrophysics, (New York: Gordon and Breach)
Melrose, D. B. & Brown, J. C. 1976, MNRAS, 176, 15
Melrose, D. B. & White, S. M. 1979, Proc Astron. Soc. Australia, 3, 369
Moghaddam-Taaheri, E. & Goertz, C. K. 1990, ApJ, 352, 361
Miller, J. A., Cargill, P. J., Emslie, A. G., Holman, G. D., Dennis, B. R., LaRosa, T. N., Winglee, R. M., Benka, S. G., & Tsuneta, S. 1997, JGR, 102, 14631
Nishio, M., *et al.* 1994 PASJ 46, L11
Nishio, M., Yaji, K., Kosugi, T., Nakajima, H., & Sakurai, T. 1997, ApJ, 489, 976
Petrosian, V. 1990, in Basic plasma processes on the sun (A92-30901 12-92). Dordrecht, Netherlands, Kluwer Academic Publishers, p. 391
Petrosian, V. 1982, ApJ, 255, L85
Petrosian, V. 1981, ApJ, 251, 727
Preka-Papadema, P., & Alissandrakis, C. E. 1992, A&A, 257, 307
Ramaty, R. 1969, ApJ, 158, 753
Sakao, T. 1994, Ph.D. thesis, University of Tokyo
Silva, A. V. R., Wang, H., & Gary, D. E. 2000, ApJ, 545, 1116
Spitzer, L. 1967, The Physics of Fully Ionized Gases (2d ed., New York: Interscience)
Stähli, M., Gary, D. E., & Hurford, G. J. 1990, Solar Phys., 125, 343.
Stepanov, A. V., Melnikov, V. F., Yokoyama, T., Nakajima, H., & Shibasaki, K. 2003, in preparation
Takakura, T. & Kai. K. 1966, PASJ 18, 57
Trottet, G. & Vilmer, N. 1984, Adv. in Space Res. 4 (2-3), 153
Trubnikov, B. A. 1965, Rev. Plasma Phys., 1, 105
Vilmer, N., Kane, S. R., & Trottet, G. 1982, A&A, 108, 306
Yokoyama, T., Nakajima, H., Shibasaki, K., Melnikov, V. F., & Stepanov, A. V. 2002, ApJ, 576, L87
Wild, J.P. & Smerd, S.F. 1972, ARAA, 10, 159

Chapter 10

DECIMETER BURST EMISSION AND PARTICLE ACCELERATION

Arnold O. Benz
Institute of Astronomy, ETH, Zurich, Switzerland
benz@astro.phys.ethz.ch

Abstract The radio emission of solar flares at decimeter wavelengths includes a variety of emission processes of a plasma thought to have a high beta. Very intense coherent emissions are observed at frequencies smaller than about 9 GHz. They are caused by plasma instabilities driving various wave modes that in turn may emit observable radio waves. Particularly important are type III bursts, caused by electron beams exciting Langmuir waves. Their sources may be used to trace the path of the electrons back in the corona to the acceleration region. Less known are radio emissions from trapped electrons driving loss-cone unstable waves, suspected for type IV bursts. These types of coherent radio emission give clues on the geometry and plasma parameters near the acceleration region.

More speculative are emissions that are directly produced by the acceleration process. A possible group of such phenomena are narrowband, short peaks of emission. Narrowband spikes are seen sometimes at frequencies above the start of metric type III events. There is mounting evidence for the hypothesis that these spikes coincide with the energy release region. Much less clear is the situation for decimetric spikes, which are associated with hard X-ray flares. More frequently than spikes, however, there is fluctuating broadband decimetric emission during the hard X-ray phase of flares. The use of these coherent radio emissions as a diagnostic tool for the primary energy release requires a solid understanding of the emission process. At the moment we are still far away from an accepted theory. Complementary observations of energetic electrons and the thermal coronal background in EUV lines and soft X-rays can put coherent emissions into context and test the different emission scenarios. In combination with other wavelengths, spectroscopic imaging by FASR would provide exciting possibilities for the diagnostics of the acceleration process.

1. Introduction

The total solar radio emission in meter and decimeter waves occasionally brightens up by more than an order of magnitude during flares. These radio sources thus outshine the thermal radiation of the rest of the Sun and are called bursts. Meterwave emissions have been studied since the late 1940s and are reviewed in the book by McLean & Labrum (1985). Observationally, they are classified as type I through V bursts, and there are more or less accepted scenarios for each of them.

First spectral observations in the decimeter range were made already in the early 1960s by (Young *et al.* 1961), exploring the spectral region beyond 300 MHz up to 1 GHz. In addition to type III bursts continuing into the decimeter range, these observers noted a rich variety of "type III-like" features later termed pulsations and fine structures in type IV bursts, such as drifting parallel bands and intermediate drift bursts[1]. The decimeter range has been systematically studied only in the 1980s when digitally recording spectrometers became available resolving the fast temporal changes and narrowband spectral structure. In the 1990s the spectral coverage was extended finally beyond 3 GHz where coherent emissions were found to become weak and rare. Today several spectrometers observe in the decimeter range and the spectral properties of coherent emissions have been well explored in the past decade. Some of the decimeter wave observations have been reviewed by Bastian *et al.* (1998) and in Benz (2002). These observations have revealed a new field of solar emissions with potential diagnostic value for flare physics, CME origin, particle acceleration and propagation, coronal heating and more.

We still do not know much about the locations of decimeter bursts, and thus cannot superpose them easily on images of the thermal corona, such as observed in EUV lines and soft X-rays, since imaging instruments in this wavelenths are sparse. The lack of imaging severely limits progress in the field and will hopefully change in the next cycle of solar activity, when solar dedicated interferometers such as FASR will be put into operation. This review thus is a summary of current observations which are still so incomplete that the inferences on flare physics and particle acceleration are limited.

2. The Decimeter Range

The radio emission of flares at wavelengths from millimeter to decameter waves includes a large variety of radiation processes. They can be considered as different diagnostic tools particularly suited for the analysis of nonthermal electron distributions, enhanced levels of various kinds of plasma waves and

[1] Decimeter type IV fine structures have later been renamed zebra patterns and fiber bursts, but we use here the names given by the discoverers.

dynamic plasma phenomena. Incoherent gyrosynchrotron emission dominates at millimeter and centimeter wavelengths. Its peak frequency is usually above 3 GHz. At lower frequencies it is self-absorbed and can sometimes be detected down to 1 GHz. The existence of gyrosynchrotron emission at meter waves was widely accepted until the 1970s, but has never been confirmed. Gyrosynchrotron radiation is discussed in Chapters 4 and 9, and will not be discussed further here. Much more intense emissions in the decimeter range with smaller bandwidth than produced by the gyrosynchrotron process (Benz & Tarnstrom 1976) are the subject of this Chapter.

An example of an event rich in various emissions is shown in Figure 10.1. Note that meter wave emissions marked as "metric" appear distinct from the decimeter bursts. The event starts with a group of metric type III bursts at 200–400 MHz. Later and about simultaneously, metric type V activity, type III bursts in the range 350–750 MHz, decimetric pulsations and gyrosynchrotron emissions start. The type III bursts are termed "metric" because they appear to be very similar to metric bursts in other flares shifted to higher frequencies in this case. They drift upward in the corona (negative drift rate). The type III bursts at even higher frequencies, extending up to 3400 MHz, have predominantly positive drift rate if measurable at all. An extremely broadband type III burst about in the middle of the figure is bidirectional, drifting up above 1400 MHz and down below. The fact that this frequency corresponds to the center frequency of the pulsations is interesting and deserves further investigation. The emission marked as narrowband spikes consists in fact mostly of a continuum with some interspersed spikes. For all decimetric burst types, durations generally decrease with increasing frequency.

2.1 Spectral types and classifications

For a long time, decimetric emissions were the least studied radio phenomena of solar flares. They appear more diverse than their counterparts in the meter range. In spectrograms every burst appears different. The first observers with broadband analog spectrographs already reported complex and unresolved features (Young *et al.* 1961). Differences between decimetric and metric bursts were remarked very early (Kundu *et al.* 1961). Nevertheless, the classification of the metric bursts has generally been applied to the decimeter waves whenever possible. For the other bursts, in particular broadband pulsating structures, narrowband spikes, patches of continuum emission as well as unresolved events, the abbreviation DCIM has been used by some observers.

As long as there is no definite way to relate burst types to emission processes, any classification into types and subtypes remains an artificial and accidental task. Nevertheless, ordering the decimetric bursts by similarity of their shape in the dynamic spectrum is necessary for theoretical work. It has become

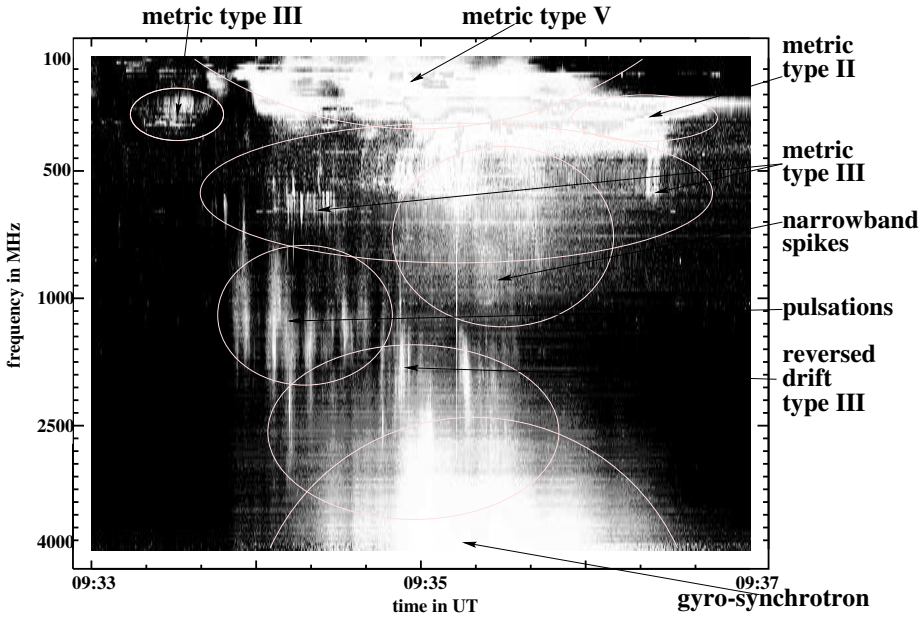


Figure 10.1. Broadband spectrogram recorded with the Phoenix-2 spectrometer of ETH Zurich on 2001/12/10 showing a rich event in meter and decimeter wavelengths. Enhanced radio flux density is indicated bright. The solar background is subtracted. Various types of emissions are identified and discussed in the text.

meaningful with sufficient resolution by digital spectrometers in the 1980s and 1990s. Extended surveys and classifications were made by Güdel and Benz (0.3–1.0 GHz, 1988), Isliker and Benz (1.0–3.0 GHz, 1994), Bruggmann *et al.* (6.5–8.5 GHz, 1990). Statistics on the occurrence rate can be found in Jiricka *et al.* (2002). The usual classification criteria taken into account are: *bandwidth, duration, drift rate, substructures, impulsiveness, order, and shape in the spectrogram*. Well over 90% of the events can be assigned to 5 classes:

1. Decimetric type III bursts: type III bursts, drifting rapidly in frequency as time progresses, are well-known at meter and decameter wave lengths. They are generally interpreted as the signature of electron beams propagating through the corona and interplanetary medium. As the beam excites plasma waves at the local plasma frequency, the frequency changes with source density. type III bursts thus trace the path of the beam from near the acceleration site toward the final destination of the electrons as long as the beam is capable to excite radio emission. Many decimetric emissions are shaped similar to metric type IIIs: Short duration (about 0.5–l.0 s), impulsive onset, high drift rates (usually $>$100 MHz/s), groups of some tens to hundreds (Staehli & Benz, 1987; Benz *et al.* 1992; Meléndez *et al.* 1999). Reverse drift bursts are as common as normal drift

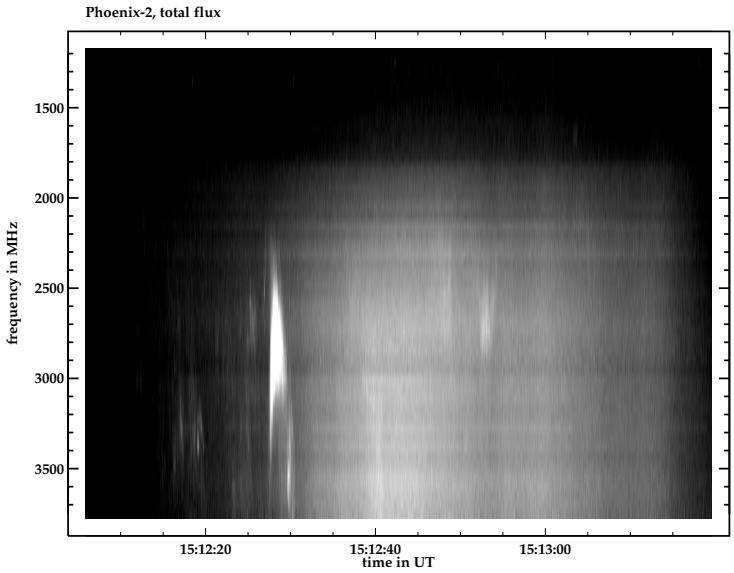


Figure 10.2. Dynamic spectrogram of total flux observed on 2001/09/09. An intense type III burst (U shape) occurred at 15:12:28 UT. More diffuse and peaking at 15:12:40, the low-frequency part of the gyrosynchrotron emission is visible.

bursts and dominate above about 1 GHz. type III bursts are generally interpreted as electron beams interacting with the ambient coronal plasma to excite a bump-on-tail instability of Langmuir waves. The electromagnetic emission is assumed to be produced at the local plasma frequency or its harmonic. Type III bursts, then, are a diagnostic of the electron density of the plasma traversed by the beam.

In broadband overview spectrograms type III emission is frequently observed before or in the early phase of an event. Figure 10.2 shows a case where the decimetric type III emission suggests that the electrons have propagated in a loop, propagating first up and then down (forming a U burst in metric terminology).

2. Decimetric type IV events are continua of tens of minutes duration occurring in the 0.3–5 GHz range. The emission is usually modulated in time on scales of 10 s or less, and is strongly polarized. Often, the emission carries fine structures in frequency and time (catalogued by Bernold 1980). The decimetric type IV observations in the 1970s were made below 1 GHz. The characteristic shape and fine structures were found to exist beyond 4 GHz (e.g. Benz & Mann 1998; Wang *et al.* 2001). The phenomena are generally interpreted by electrons trapped in loop-shaped magnetic fields (Stepanov 1974; Kuijpers 1975).

3. Diffuse continua occur most frequently in the 1–3 GHz range, have various forms and sometimes drift in frequency. Their characteristic duration is between one and some tens of seconds, too long for a type III burst and too short for a type IV burst. They have also been noted in the 0.3–1 GHz range and have been called "patches" in the literature. The circular polarization is usually weak. Continua have been interpreted as continuous injection of electrons (Bruggmann *et al.* 1990) or as proton beams destabilized by impacting the transition layer (Smith & Benz 1991).

4. Pulsations are broadband emissions (several 100 MHz) with periodic or irregular short fluctuations. They are sometimes quasi-periodic with pulses of 0.1 to 1 s separations, occurring in groups of some tens to hundreds and lasting some seconds to minutes. The drift rates exceed the type III bursts by at least a factor of 3. Also different from type III bursts are the well defined upper and lower boundaries in frequency. There are significant differences in modulation depths of pulsations, and some (termed drifting pusating structures) gradually drift to lower frequency in the course of the event.

5. Spikes of narrowband emissions last only a few tens of microseconds (review by Benz, 1986). Individual spikes are very short ($<$0.1 s), extremely narrowband (some MHz) intense emissions forming broadband clusters of some tens to ten thousands during some tens of seconds to about a few minutes. Clusters are sometimes organized in small subgroups or chains. In some cases, harmonic structure is present. Metric spikes at 250–700 MHz form a different class of spike bursts, common near the starting frequency of metric type III bursts.

Figure 10.3 is meant to be a warning concerning the classification. The coherent emission seen before the main phase has very short time structure, not resolved in the observation sampled at a rate of 10 Hz. No drift is discernible, and the circular polarizaion is nearly fully right circular. Some harmonic structure is barely recognizable. These properties are typical for narrowband spikes, however the bandwidth is of the order of 500 MHz, about an order of magnitude larger than usual for spikes. Thus the coherent emission in Figure 10.3 combines properties of both narrowband spikes and pulsations.

There are probably more burst types among the decimetric bursts, although some may be just borderline cases. It must be pointed out that the classification is influenced by spectral and temporal resolution. A few peculiar events have been noted that did not fit at all into any of these classes, such as the drifting type II-like events (Benz 1976; Allaart *et al.* 1990) and fine structure in type IV bursts (Karlicky *et al.* 2001). Nevertheless, the above five major classes plus the gyrosynchrotron type may be used to tentatively classify most 0.3–8 GHz observations.

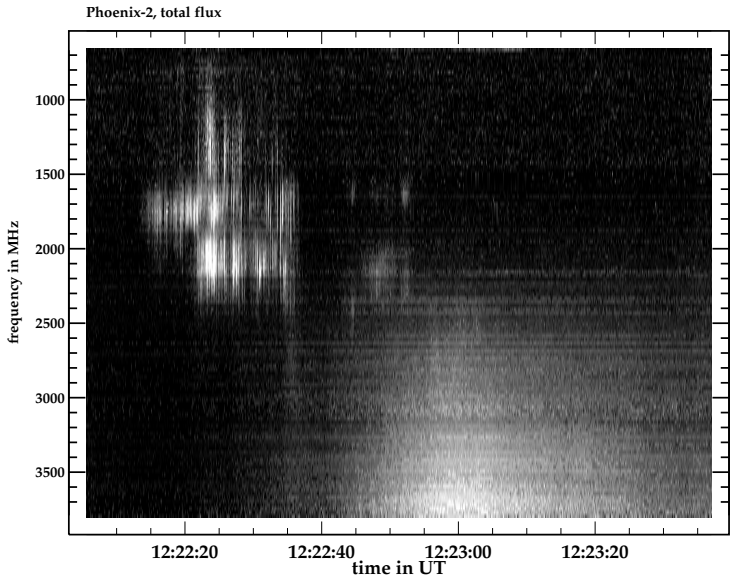


Figure 10.3. Dynamic spectrogram of total flux observed on 2001/10/19. Coherent emission occurred around 12:22:30 UT, before the main flare phase marked by diffuse gyrosynchrotron emission peaking at 12:23:00 UT.

2.2 High-frequency limit of the decimeter range

As seen in Figure 10.1, the lower frequency limit to the burst type referred to as "decimetric" is between 300 and 700 MHz. Above that frequency, the metric types from I to V disappear except for the type III bursts, and new types of bursts appear. Thus one may wonder where the upper limit of these coherent bursts could be. The upper limit puts an important constraint on the emission and propagation processes, but is difficult to determine since the quiet and slowly varying radio backgrounds increase with frequency, the absorption by collisional damping becomes more severe, and coherent emissions become generally weaker.

Benz *et al.* (1992*a*) have reported narrow-band spikes at 6.5–8 GHz, and Benz *et al.* (1992*b*) recorded a group of type III bursts exceeding the observing limit of 8.5 GHz. Both cases were strongly polarized, which has been interpreted by the authors as an effect of selective mode propagation. The highest peak flux measured at 8.2 GHz was 60 sfu. Levin *et al.* (1994) have reported "steps" in pre-flare emission at 8–12 GHz.

Two new observations are reported here for the first time: The frequency-agile Phoenix-2 spectrometer has been modified to observe at 10–12 GHz in 1999 March 13 to 31, 2000 March 16–April 15, and 2000 October 9–22. The

antenna had a diameter of 0.8 m, observing the full Sun. The channel bandwidth was 10 MHz, sampling time 0.1 s and integration time 0.5 ms. The rms noise of these observations was 0.0095 times the quiet Sun. Using the observed SGMH values for calibration, the detection threshold (5σ) was about 22 sfu. During 1100 observing hours, including 322 flares reported by NOAA, no event was found other than consistent with broadband gyrosynchrotron emission.

A more sensitive observation was made at ETH Zurich from 2000 July 1–11, using an acousto-optic multichannel spectrometer in the 10.7–11.7 GHz band. The time resolution was 0.1 s and frequency channels were 1 MHz separated by 3.9 MHz. The sampling time and integration time were 40 ms and equal, yielding a sensitivity of 12 sfu (5σ). The sensitivity has been improved by integrating to 5MHz$\times$0.08s pixels yielding a sensitivity of 4 sfu. In 200 observing hours, including 72 flares, no burst other than broadband emission was observed. Thus the present observations suggest that the high-frequency limit of coherent solar flare emission is 9–10 GHz.

2.3 Why decimetric radio bursts?

The emission frequency of coherent emission is tightly related to the source plasma and not to the exciting electrons. It is one of the characteristic frequencies of the background plasma, the plasma frequency or electron gyrofrequency, that determine the emitted radio frequency. Thus it is immediately clear that the most direct diagnostic value of coherent emission concerns the source plasma. The plasma frequency is given by

$$\omega_p \;=\; \sqrt{\frac{4\pi e^2 n_e}{m_e}} \;=\; 2\pi\ 890\sqrt{\frac{n_e}{10^{10}\mathrm{cm}^{-3}}}\ \ [\mathrm{MHz}], \qquad (10.1)$$

where e is the elementary charge, m_e the electron mass and n_e the electron density. The electron cyclotron frequency is

$$\Omega_e \;=\; \frac{eB}{m_e c} \;=\; 2\pi\ 280\left(\frac{B}{100\ \mathrm{G}}\right)\ \ [\mathrm{MHz}], \qquad (10.2)$$

where B is the magnetic field strength. Radio emission is produced at these frequencies (fundamental) or second harmonic (and higher for some gyromagnetic emissions).

The decimeter range (0.3 to 9 GHz) thus corresponds to source densities of 3×10^8 to 3×10^{11} cm^{-3}, assuming harmonic plasma emission. This is the range of densities where the primary energy release of flares is expected to take place.

3. Hard X-rays and Decimeter Radiation

What radiation is observed during major hard X-ray (HXR) flares in the decimeter range? The two wavelengths must be compared exactly in time and the spatial location of the emissions should be close. This has been done only partially and very recently in a few cases. Here I review studies in which have a certain type of radio burst has been selected and searched for associated HXR.

3.1 Decimetric type III bursts

Temporal correlations have been first made for type III bursts. Only 3% of meter wave type III bursts are correlated with impulsive HXR emission (Kane 1981), however the correlation increases with increasing type III start frequency and with intensity. Since metric type III bursts originate high above active regions and propagate mostly upwards, it is perhaps not surprising that they are poorly correlated with HXR events. Aschwanden *et al.* (1985) show that 48% of reverse-drift type III bursts at decimeter wavelengths are correlated with HXR bursts, consistent with the expectation that downward-directed electron beams should correlate better with thick target HXR emission than upward-directed beams. However, not every HXR peak is associated with a radio burst. Aschwanden *et al.* (1995) find an associated type III burst in 31% of individual HXR pulses. In a more recent study of C-class flares in active region 9830, out of 11 only 7 events showed radio emission recorded by the Phoenix-2 radio spectrometer between 100 MHz and 4 GHz, 5 of them type III radio bursts. Two were associated with decimeter wave emissions of unknown origin (Benz & Grigis, unpublished). Most surprising in these recent investigations is the large range of observed ratios between coherent radio emission and X-ray flux. The range exceeds 9 orders of magnitude from intense groups of meter wave type III bursts without X-ray counterpart to large HXR events without coherent radio emission at meter and decimeter waves.

Some flare electron beams emit coherent radio waves on their path from the acceleration site down to the chromosphere where they are stopped and emit HXRs. The correlation of radio waves from down-going electrons with HXR thick target emission is well established (Dennis *et al.* 1984; Sawant *et al.* 1990; Aschwanden *et al.* 1993), although a comprehensive correlation analysis is still missing and the spatial relation between the radio sources and HXR has not yet been investigated.

3.2 Decimetric narrowband spikes

The situation is much less clear for narrowband spikes at *decimeter* wavelength. Originally, they were reported to occur in the rise phase of centimeter radio bursts and thus to be associated with major flares (Slottje 1978). The as-

sociation rate with HXR flares is high (Benz & Kane 1986; Güdel *et al.* 1991). Narrowband spikes have been discovered also in decimeter type IV bursts occurring after the HXR emitting phase of flares (Isliker & Benz 1994). Contrary to their relatives at meter waves, however, decimetric spikes do not correlate with type III bursts and are extremely rare (2% of all HXR flares, Güdel *et al.* 1991). An association analysis is reviewed in §4.

3.3 Drifting pulsating structures

Much more often than narrowband spikes, decimetric pulsations are associated with a HXR event. Figure 10.4 shows an example together with gyrosynchrotron emission visible at high frequencies above about 3 GHz and reported up to 15 GHz in *Solar Geophysical Data*. The HXR emission peaks simultaneously with the first decimeter pulsations occurring in the range 0.45–3 GHz (marked A in Figure 10.4, top). The pulsations precede the first metric type III bursts (B) in this event. The bulk of the pulsations drift gradually to lower frequencies and have a second peak (E) possibly related to weak HXR emission at 12:21 UT.

The decimetric pulsations in Figure 10.4 have a nonthermal spectrum that is too narrow for gyrosynchrotron emission. Thus a coherent process is probably responsible. The emission is pulsating irregularly and does not have a smooth spectrum, thus it has a "noisy" appearance.

Kliem *et al.* (2000) have studied a deeply modulated, drifting, pulsating structure in the 0.6–2 GHz range before the HXR peak. In the main HXR phase, the intensity increases and the pulsations become less regular. The decimeteric pulsations drift slowly to lower frequency during the event. The authors propose a model in which the pulsations of the radio flux are caused by quasi-periodic particle acceleration episodes that result from magnetic reconnection in a large-scale current sheet. Under these circumstances, reconnection is dominated by repeated formation and subsequent coalescence of magnetic islands. The process is known as secondary tearing or impulsive bursty regime of reconnection.

3.4 Flares without radio emission

Considering that flares generally accelerate nonthermal electrons capable of coherent emissions, one may expect that all flares are accompanied by coherent radio emissions. As mentioned before, reality is different and more complex: (i) Simnett and Benz (1986) have pointed out that some 15% of large flares do not show radio emission in meter and decimeter wavelengths. This percentage needs to be revised using modern broadband spectra that cover also the range above 1 GHz. Nevertheless, the fact remains that the coherent radiation is sometimes much weaker than expected. (ii) Coherent radio emission appears in

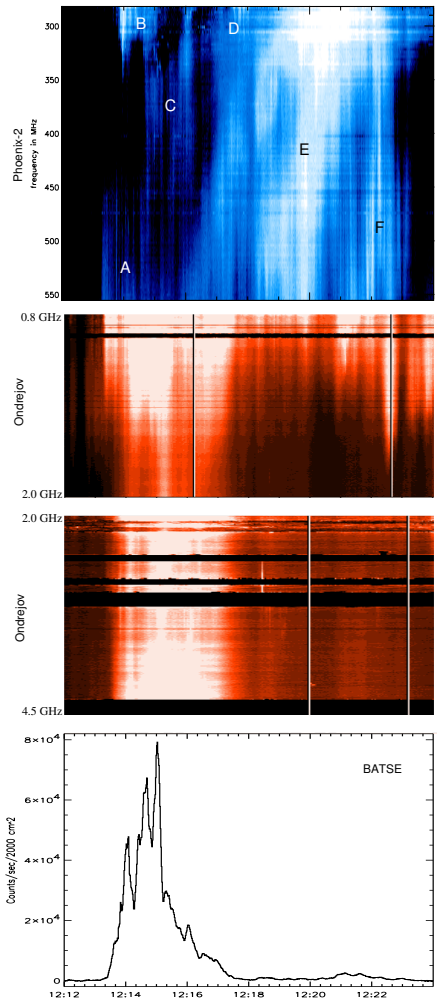


Figure 10.4. Dynamic spectrograms of 0.3–4.5 GHz total flux observed with the Phoenix-2 and Ondrejov radio spectrometers on 1999/09/08 compared with HXR observations by BATSE in the 25–1000 keV range. In the top part of the figure, various emissions are marked that are discussed in the text (from Saint-Hilaire & Benz 2003).

many different spectral forms, varying enormously in bandwidth, polarization, fluctuation, duration and frequency drift. The cause of these widely different emissions does not appear to be identical and several emission mechanisms seem to be at work. It is thus not immediately clear which emission originates from the main acceleration region, refers to escaping or trapped electrons, or is produced by some secondary shocks.

4. Flare Physics

The evidence increases that some of the coherent radio emissions in the short wavelength meter radiation is emitted near or within the HXR flare region. Most are drifting, broadband pulsations rather than narrowband spikes. Little is firmly known about the emission process. Even if this first step is not yet achieved, some conclusions on the acceleration physics can be inferred. In particular, proposed acceleration processes can be tested on their general predictions for radio emission. Mechanisms that necessarily produce excessive coherent radio emission can be excluded. Examples are electron acceleration producing monoenergetic beams or electron beams proposed as sources of powerful low-frequency waves. Such beams are unstable and would produce intense coherent radio emission in all cases, which is not observed. More direct inferences may become possible when the emission mechanisms of narrowband spikes and broadband drifting pulsations will be known.

Secondary emissions, such as type III bursts, also can contribute to understanding acceleration. They have been used to locate the energy release site of small flares in the high corona. Their role in major flares is not clear.

4.1 Location of source regions

Imaging observations of coherent radio emissions will allow in the near future to put them into the context of the HXR emission and the thermal coronal plasma as outlined in EUV lines and soft X-rays. The location of the source relative to coronal loops allows testing the predictions of some emission models. Thus it will soon become possible to distinguish emissions by trapped electrons from radiations originating near or at the acceleration site. The existing EIT, TRACE and RHESSI observations are promising ingredients for a new era of research in coherent radio emission.

First imaging observations have recently been reported. Benz *et al.* (2002) have recently located clusters of narrowband decimetric radio spikes that occur in the decay phase of solar flares at low decimeter frequencies (327–430 MHz). Contrary to previous observational claims and leading theoretical expectations, most of the observed spike clusters reported occurred well outside the main energy release region of the flare and not at the feet of magnetic loops (Figure 10.5). Instead, the observations suggest that the electrons for these radio bursts are accelerated at secondary sites high in magnetic fields adjacent to the main flare site, as these fields adjust in response to the flare. In at least two cases the spikes were found near loop tops. Similarly, reversed drifting type III bursts occurring at frequencies above a spike cluster, suggesting electron beams propagating downward from the spike source presumably at high altitude, were found in sensitive observations (Benz *et al.* 2001).

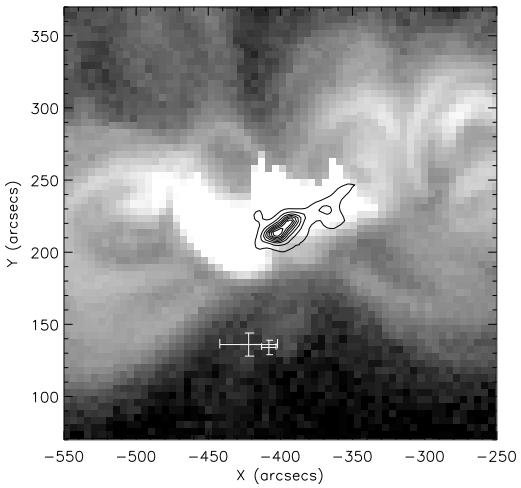


Figure 10.5. Location of two clusters of decimeteric spikes observed by the Nançay Radioheliograph at 432 MHz (error bars) in the course of the X1.9 event on 2000/07/12 superposed on an SXT/Yohkoh image. The image coordinates are in arcseconds from Sun center (from Benz *et al.* 2002).

The role of spike emission in the decimeter range is not settled. It is still possible that they reveal a property of acceleration in general. However, if decimetric spikes do represent the main acceleration site as previously assumed, this could be only for spikes at high decimetric frequency. The above arguments do not exclude the spike source as a secondary energy release above the main event. The better transparency of the high corona to radio waves emitted at the local plasma frequency and their direct interplanetary influence make high-altitude events particularly interesting.

Figure 10.6 displays the positions of the emissions shown in the spectrum in Figure 10.4 at the time marked C, thus near the main HXR peak. The emissions at 410 and 432 MHz correspond to decimetric pulsations, located less than 20″from the HXR sources, presumably two footpoint sources situated on the two flare ribbons. The 327 MHz source appears to be a type III burst originating from an escaping electron beam.

4.2 Evidence for reconnection

Bidirectional type III bursts have been detected by Aschwanden *et al.* (1995) in radio spectra. The acceleration site was concluded to be at a plasma frequency of about 300–500 MHz. The range was based on a limited set of data. Thus a density in the acceleration site of 3×10^8 to $3 \times 10^9 \mathrm{cm}^{-3}$ was inferred. The

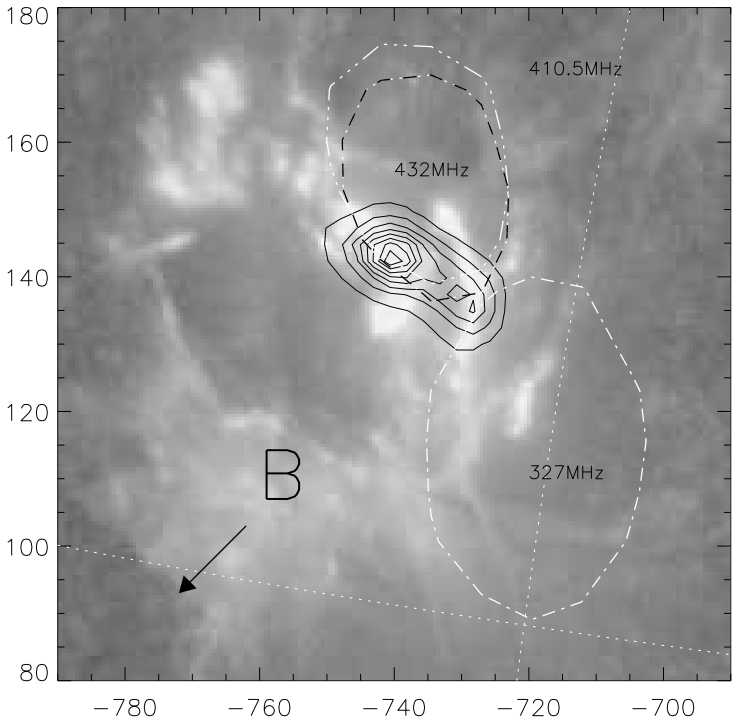


Figure 10.6. TRACE 1600Å images with NRH contours (98% level) at various frequencies, and Yohkoh/HXT (23–33 keV band) overlay (black isophotes) of the 1999/09/08 double-ribbon flare (for the spectrum see Fig.10.4). The units of the axes are arcseconds from Sun center. The arrow marked B indicates an ejecta and its motion (from Saint-Hilaire and Benz, 2003).

bidirectional burst in Figure 10.1 rather suggests a density of 6.2×10^9 cm^{-3} (second harmonic emission assumed). Robinson & Benz (2000) interpreted the general weakness and slower drift of the down-going branch by the combination of beam properties and magnetic geometry.

Imaging observations have shown that the type III sources often do not emerge from a single location. Klein *et al.* (1997) have reported that down-propagating branches of metric type III bursts are sometimes double sources. Their simultaneous existence suggests a common origin. Paesold *et al.* (2001) have found double type III sources to diverge in upward propagation from the same spike source. The multiplicity of the beam paths is consistent with the predictions of the reconnection scenario for magnetic energy release where magnetic field lines from four different directions meet closely.

5. Emission Processes

The common characteristic of these emissions is that they are not produced by individual electrons as in free-free emission (bremsstrahlung) or synchrotron radiation, but by collective motions due to waves and instabilities in the plasma. The wave introduces an organization in the plasma that allows particles to emit in phase, thus coherently. Coherent emissions are generally more efficient in converting kinetic particle energy into radiation than incoherent emission by single particles. Thus coherent emissions are bright and indicate the presence of particle oscillations in plasma waves. The waves that can give rise to radio emissions must be of high frequency, above the local plasma frequency, and are generally excited by some plasma instability. Thus coherent emissions indicate the presence of a cause of such instability such as a beam of electrons, magnetically trapped electrons having a loss-cone velocity distribution, a shock, or a strong current.

5.1 Beam emissions

Currently type III bursts are the most useful and important coherent bursts since their physics is at least qualitatively understood. The recent interest in type III bursts is motivated by their use as a diagnostic for the acceleration process of electrons in flares and furthermore as tracers of the magnetic field lines along which they propagate and the ambient density of the corona they traverse.

The type III emission by energetic electrons is generally agreed to be caused by three basic processes:

- Beam formation: If the acceleration process does not intrinsically produce a beam, propagation will. As particles propagate along field lines the fastest ones will arrive first at a remote location and there constitute a hump on the tail of the ambient electrons.

- Plasma instability: As soon as a positive gradient in velocity space beyond about three times the local thermal electron velocity, v_{te}, develops, the bump-on-tail instability sets in. It drives electrostatic plasma waves to grow exponentially. They are approximately Langmuir waves with a phase velocity equal to the particle velocities of positive gradient. The frequency of the Langmuir waves is slightly above the plasma frequency, ω_p, of the ambient medium. The distance Δz to reach instability depends on how rapidly the acceleration occurs, i.e. on the e-folding acceleration time τ. For a Maxwellian distribution at the acceleration site, it is

$$\Delta z \approx 27(v_{te}/v_{th})^2 v_{te}\tau \ , \tag{10.3}$$

where v_{th} is the thermal velocity of the hot electrons (Benz 2002). Eq. (10.3) demonstrates that instable beams form after a few thousand kilometers for acceleration times less than one second.

- Wave conversion: The Langmuir waves are transformed into transverse electromagnetic waves observable in the radio regime in at least two ways as has been realized early from the observation of occasional simultaneous type III bursts with a frequency ratio of 1:2. The harmonic emission is well accepted to be the result of coalescence of two Langmuir waves into a radio wave ($L + L' \rightarrow t$). The dominant emission process at the fundamental is still in discussion. In interplanetary type III bursts the decay of a Langmuir wave into an ion sound wave and a transverse wave ($L + s \rightarrow t$) has been found to be the most significant process by *in-situ* measurements.

The appearance of high-frequency type III bursts is surprising for two reasons: (i) The escape of radio emission from high density plasma is much reduced by free-free absorption. Even the second harmonic cannot escape from the 7 GHz level in a spherically symmetric atmosphere at coronal temperatures. (ii) The densities for such plasma emission is at least 10^{11} cm^{-3}. If coronal, such densities are astonishing considering the early flare phase to which they refer. Whether the bursts occur in the transition region and what this would imply, warrants further studies.

It must be noted here that there is no quantitative theory yet of coronal type III bursts. Type III bursts appear under such different conditions than in interplanetary space that accepted theories may not simply be applied to coronal counterparts.

5.2 Emissions from the acceleration site

If $\Omega_e \gtrsim \omega_p$, an instability, called electron cyclotron maser emission, exists that converts free energy in a velocity distribution increasing in perpendicular velocity into electromagnetic emission at the electron gyrofrequency and its harmonics (Wu & Lee 1979). As it can escape directly from the corona as radio emission, the maser process is extremely efficient. It is the generally accepted emission process for the terrestrial kilometric radiation and Jupiter's decametric radiation. For the Sun, however, it has become doubtful, as the above requirement is beyond all magnetic fields inferred up to now.

Of particular interest are waves that are predicted by existing acceleration models. For reconnection models requiring anomalous resistivity, some current instability is usually invoked. The low-frequency waves excited by currents are mostly of the ion acoustic or lower hybrid type. They may emit radio emission by the coalescence process described above if accelerated electrons provide the Langmuir waves. Such models have been proposed by Benz & Wentzel

(1981) and Benz & Smith (1987), respectively, to interpret narrowband radio emissions.

A very popular acceleration model for solar flares is transit-time-damping (Miller *et al.* 1997, Schlickeiser 2002). The waves assumed in this model are even lower in frequency and are unlikely to couple into radio waves. Other models, in particular those based on electron beams producing waves to accelerate ions (e.g. Temerin & Roth 1992), are prone to predict intense radio emission. Whether or not coherent radio emission is emitted is therefore an observable criterion for the validity of acceleration models.

Narrowband radio bursts must be coherent and can only be emitted from localized sources, as the relevant frequency, either the plasma frequency or the electron gyrofrequency, cannot have variations more than the observed bandwidth, $\Delta\nu$. One can express this in the form

$$\Delta\nu \lesssim \nu\frac{\Delta s}{H_f} \ , \tag{10.4}$$

where Δs is the size of the source and H_f is the scale length of the relevant frequency.

5.3 Decimetric spikes and pulsations

Narrowband bursts require very small source sizes. Therefore, they cannot be produced by propagating beams that tend to disperse in space and cause relatively large and thus broadband sources.

The emission process of decimetric spikes is still controversial. Originally, the loss-cone instability of trapped electrons has been proposed to produce electron cyclotron maser emission at the footpoints of flare loops (Holman *et al.* 1980; Melrose & Dulk 1982). To avoid the assumption of high magnetic field strength in the source, the model has been changed to emission of upper-hybrid and Bernstein modes (Willes & Robinson 1996). The scheme can interpret occasional harmonic emission in decimeter spikes (Benz & Güdel 1987). Alternatively, Tajima *et al.* (1990) and Güdel & Wentzel (1993) proposed the spike sources to be in the acceleration regions of flares and to result from waves produced by the acceleration process. The emission of decimeteric pulsations has also been interpreted by a loss-cone instability of trapped electrons (Aschwanden and Benz 1988).

6. Conclusions

Decimetric type III bursts, irregular pulsations and narrowband spikes have been observed in close correlation with HXR events. They constitute potential diagnostics for flare energy release and electron acceleration. Two main ingredients are still missing: Their location in relation to the main flare is poorly

known and at the moment we are still far from an accepted theory for decimetric spikes and pulsations. Only careful comparisons with complementary observations of energetic electrons and the thermal coronal background in EUV lines and soft X-rays can put coherent emissions into context and test the different scenarios. The comparison with HXR, millimeter and centimeter observations will be necessary to derive quantitative results on energy release. In combination with other wavelengths and their recent imaging capabilities, exciting new possibilities are now opening for radio diagnostics.

Acknowledgments

I would like to thank the organizers for taking the initiative for this meeting far remote of the well trodden paths. Thomas Wentzler and Christian Monstein have built the equipment for 10–12 GHz observations that are reported here for the first time. The construction of the ETH spectrometers is financed by the Swiss National Science Foundation grant 20-67995.02.

References

Allaart M.A.F., van Nieuwkoop J., Slottje C., Sondaar, L.H. 1990, Solar Phys., 130, 183

Aschwanden, M. J., Wiehl, H. J., Benz, A. O., Kane, S. R. 1985, Solar Phys. 97, 159

Aschwanden M. J., Benz A. O. 1988, ApJ, 111, 113

Aschwanden M. J., Benz A. O., Schwartz R.A. 1995, ApJ, 417, 790

Bastian T. S., Benz A. O., Gary D. E. 1998, Ann. Rev. Astr. Astrophys., 36, 131

Benz A. O. 1976, Kleinheubacher Berichte, 20, 376

Benz, A. O., Tarnstrom, G. L. 1976, ApJ, 204, 597

Benz A. O., Wentzel D.G. 1981, A&A, 94, 100

Benz A. O. 1986, Solar Phys., 104, 99

Benz A. O., Kane S.R. 1986, Solar Phys., 104, 179

Benz A. O., Güdel M. 1987, Solar Phys., 111, 175

Benz A. O., Smith D. F. 1992a, Solar Phys., 107, 299

Benz A. O., Su H., Magun A., Stehling W. A&A Supplement Series, 93, 539 (1)

Benz A.O., Magun A., Stehling W., Su H. 1992b, Solar Phys., 141, 335

Benz A. O., Mann G. 1998, A&A, 333, 1034

Benz A. O., Messmer P., Monstein C. 2001, A&A, 366, 326

Benz A. O. 2002, Plasma Astrophysics: Kinetic Processes in Solar and Stellar Coronae, 2nd edition, (Kluwer, Dordrecht)

Benz A.O., Saint-Hilaire P., Vilmer N. 2002, A&A, 383, 67

Bernold T. 1980, A&A, 42, 43

Bruggmann G., Benz A.O., Magun A., Stehling W. 1990, A&A, 240, 506

Dennis, B. R., Benz, A. O., Ranieri, M., Simnett, G. M. 1984, Solar Phys., 90, 383
Güdel M., Benz A.O., 1988, A&A, 75, 243
Güdel M., Aschwanden M.J., Benz A.O. 1991, A&A, 251, 285
Güdel M., Wentzel D.G. 1993, ApJ, 415, 750
Holman G.D., Eichler D., Kundu M.R.: In 1980, Radio Physics of the Sun, Kundu M.R. and Gergeley T.E. (eds.), IAU Symp., Vol., 86, 457
Isliker H., Benz A.O. 1994, A&A Sup. Ser., 104, 145
Jiřička K., Karlický M., Meszarosova H., Snizek, V. 2001, A&A, 375, 24
Kane S.R. 1981, ApJ, 247, 1113
Karlický, M., Bárta, M., Jiřička, K., Mészárosová, H., Sawant, H. S., Fernandes, F. C. R., & Cecatto, J. R. 2001, A&A, 375, 638
Klein K.-L., Aurass H., Soru-Escaut I., Kalman B. 1997, A&A, 320, 612
Kliem B., Karlický M., Benz A.O. 2000, A&A, 360, 715
Kuijpers J. 1975, Solar Phys., 44, 173
Kundu M.R., Roberts J.A., Spencer C.L., Kniper J.W. 1961, ApJ 133, 255
Levin B. N., Fridman V. M., Sheiner O. A. 1994, ApJ Supplement Series, 90, 713
McLean D. J., Labrum N. R. Solar Radiophysics: Studies of emission from the sun at metre wavelengths. Cambridge University Press, Cambridge (1985)
Meléndez J. L., Sawant H. S., Fernandes F. C. R., Benz, A. O. 1999, Solar Phys., 187, 77
Melrose D.B., Dulk G.A. 1982, ApJ, 447, 844
Miller J.A. & 8 others 1997, J. Geophys. Res., 491, 14631
Paesold G., Benz A.O., Klein K.-L., Vilmer N. 2001, A&A, 371, 333
Robinson P.A., Benz A.O. 2000, Solar Phys., 194, 345
Saint-Hilaire, P., Benz, A. O. 2003, Solar Phys.,in press
Sawant, H. S., Lattari, C. J. B., Benz, A. O., Dennis, B. R. 1990, Solar Phys., 130, 57
Schlickeiser R. 2002, Cosmic ray astrophysics, Berlin, Springer
Simnett G.M., Benz A.O. 1986, A&A, 165, 227
Slottje C. 1978, Nature, 275, 520
Smith D.F., Benz A.O. 1991, Solar Phys., 131, 352
Staehli M., Benz A.O. 1987, A&A, 175, 271
Stepanov A.V. 1974, Soviet Astronomy AJ, 17, 781
Tajima T., Benz A.O., Thaker M., Leboeuf J.N. 1990, ApJ, 353, 666
Temerin M., Roth I. 1992, ApJ, 391, L105
Wang, S., Yan, Y., Zhao, R., Fu, Q., Tan, C., Xu, L., Wang, S., & Lin, H. 2001, Solar Phys., 204, 153
Willes A.J., Robinson P.A. 1996, ApJ, 467, 465
Wu C. S., Lee L.C. 1979, ApJ, 230, 621
Young C. W., Spencer C. L., Moreton G.E., Roberts J.A. 1961, ApJ, 133, 243

Chapter 11

RADIO OBSERVATIONS OF CORONAL MASS EJECTIONS

Angelos Vourlidas
Solar Physics Branch, Naval Research Laboratory, Washington, DC
vourlidas@nrl.navy.mil

Abstract In this chapter we review the status of CME observations in radio wavelengths with an emphasis on imaging. It is an area of renewed interest since 1996 due to the upgrade of the Nançay Radioheliograph in conjunction with the continuous coverage of the solar corona from the EIT and LASCO instruments aboard *SOHO*. Also covered are analyses of Nobeyama Radioheliograph data and spectral data from a plethora of spectrographs around the world. We will point out the shortcomings of the current instrumentation and the ways that FASR could contribute. A summary of the current understanding of the physical processes that are involved in the radio emission from CMEs is be given.

Keywords: Sun: Corona, Sun: Coronal Mass Ejections, Sun: Radio

1. Coronal Mass Ejections

1.1 A brief CME primer

A coronal mass ejection (CME) is, by definition, the expulsion of coronal plasma and magnetic field entrained therein into the heliosphere. The event is detected in white light by Thomson scattering of the photospheric light by the coronal electrons in the ejected mass. The first CME was discovered on 1971 December 14 by the OSO-7 orbiting coronagraph (Tousey 1973) which recorded only a small number of events (Howard *et al.* 1975). *Skylab* observations quickly followed and allowed the first study of CME properties (Gosling *et al.* 1974). Observations from many thousands of events have been collected since, from a series of space-borne coronagraphs: *Solwind* (Michels *et al.* 1980), *SMM*/ CP (MacQueen *et al.* 1980) and currently *SOHO*/LASCO (Brueckner *et al.* 1995). The average properties of CMEs are now well established (Hundhausen *et al.*

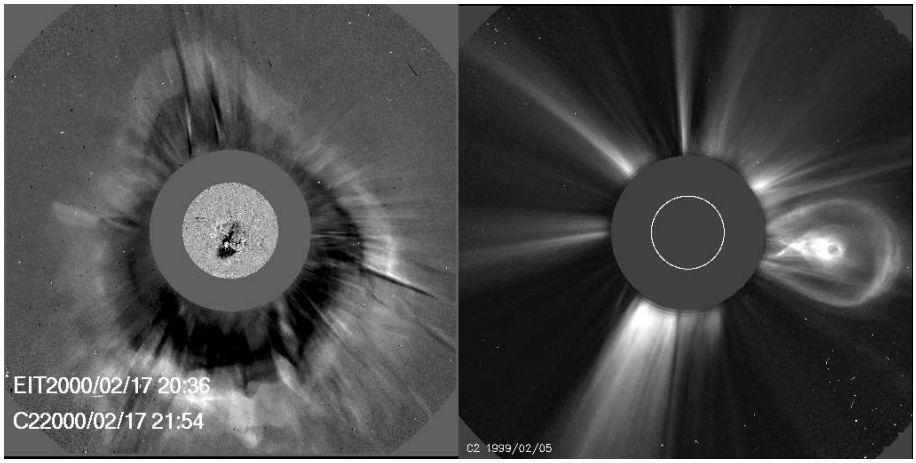


Figure 11.1. Left panel: Halo CME observed by LASCO/C2 on 2000 February 17. An EIT 195 Å difference image is inserted to show the extent of the dimming in the low corona. Both images are differences between subsequent frames. *Right panel:* A typical 3-part CME along the western limb.

1984; Howard *et al.* 1985; Hundhausen 1999; St Cyr *et al.* 1999; Vourlidas *et al.* 2002). Earth-directed CMEs, called "halo" CMEs because the ejected material surrounds the coronagraph occulter like a halo, were first recognized in *Solwind* images (Howard *et al.* 1982). The left panel of Figure 11.1 shows a typical example of a halo CME as observed by the LASCO/C2 coronagraph. Coronal ejections come in many shapes but one of the simplest forms (and hence usually refer to as "typical") is the 3-part CME comprising a leading edge, followed by a dark cavity and a bright core (Fig 11.1, right panel).

In the years since their discovery, CMEs have come to be recognized as an important means of energy release in the solar corona and halo CMEs, in particular, as the major driver of the physical conditions in the Sun-Earth system (Webb *et al.* 2000; Webb *et al.* 2001; Plunkett *et al.* 2001). For an alternative view see (Cane, Richardson & StCyr 2000). In an average event, $10^{14} - 10^{16}$ g of material is ejected into the heliosphere with speeds ranging from 100 to 2000 km/s (Howard *et al.* 1985; Hundhausen, Burkepile & StCyr 1994). CMEs might play an important role in the evolution of solar magnetism (Low 2001) since an amount of solar magnetic flux (not directly measured but potentially significant) is removed during the ejection process. Due to their large propagation speeds, CMEs can also drive interplanetary (IP) shocks (Cane 1984; Sheeley *et al.* 1985). IP shocks could be the sources of the accelerated particles (Reames 1999) that together with Earth-directed CME mass and entrained magnetic field can severely affect geospace. Consequently, their study is very important for understanding and ultimately predicting space weather conditions. For a more

detailed review of CMEs refer to the articles in the *Coronal Mass Ejections* monograph (Crooker, Joselyn & Feynman 1997) and references therein.

CMEs are almost exclusively observed by white-light orbiting coronagraphs, which by design occult the solar disk. Thus, the initiation and early stages of the event are not visible and observations from other instruments, such as EUV imagers, must be employed. However, data analysis has been hampered by varying instrument cadences, small fields of view, and telemetry restrictions. A thorough understanding of the CME phenomenon still eludes us. This is an area where radio astronomy can help. Radio telescopes can observe both the solar disk and the corona out to a few solar radii, at many frequencies and with high cadence (< 1 s), while data acquisition issues are easily handled for ground-based instruments.

I begin with a short summary of the types of radio emissions that can be detected. In the next section, I review the work on radio CME observations since the launch of the SOHO satellite (Domingo, Fleck & Poland 1995). I conclude with a discussion of the issues confronting current radio CME observations and how they can be addressed by future instrumentation, such as the Frequency Agile Solar Radiotelescope (FASR) to bring radio observations to the forefront of CME science.

1.2 Radio emissions associated with CMEs

For the sake of the current discussion, we can divide radio emissions into two classes, thermal and nonthermal, based on the frequency dependence of the source radio flux density, $S(\nu)$, or, for spatially resolved measurements, the brightness temperature, $T_b(\nu)$ (Gary & Hurford, Chapter 4). For optically-thin thermal sources, $T_b(\nu) \propto \nu^{-2}$ while for optically-thin non-thermal ones, $T_b(\nu) \propto \nu^{-\alpha}, \alpha > 2$. In the case of CMEs, there are possibly three relevant radio emission mechanisms; thermal free-free, non-thermal gyrosynchrotron and plasma emission. Here, I give only a very brief account of the relevant mechanisms as they pertain to CMEs. Complete discussion of the radio emission from the Sun can be found elsewhere (Dulk 1985).

1.2.1 Thermal free-free. The plasma entrained in the expanding magnetic field of the CME will produce optically thin free-free emission. The characteristics of this process are well understood and are described in detail in this volume (Gary & Hurford, Chapter 4; Gelfreikh, Chapter 6). The free-free emitting structures will look very similar to the structures seen by the white light coronagraphs since both correspond to multi-thermal plasmas and depend on the emission measure of the electrons; namely, $\int n_e dl$ for Thomson scattering and $\int n_e^2 dl$ for free-free, where n_e is the density of the coronal electrons. Besides the electron density, one may also derive the inhomogeneity of the emitting structures from a detailed comparison between the two regimes.

CMEs have coronal temperatures and low densities and hence their free-free emission is expected to be very optically thin and difficult to observe, especially in the presence of the much brighter emissions from non-thermal mechanisms (Figure 11.2).

1.2.2 Nonthermal gyrosynchrotron. Gyrosynchrotron emission is routinely observed in flares (Bastian, Benz & Gary 1998) and could be present in CMEs, since they are capable of accelerating electrons to high energies (Kahler *et al.* 1986). The gyrosynchrotron emission from even a small number of non-thermal electrons, entrained in the CME magnetic field, can easily exceed the thermal emission by a few orders of magnitude. Therefore, it is much easier to detect. Due to the dependence of gyrosynchrotron emission on the magnetic field, the brighter signal will correspond to the locations of the strongest magnetic field within the CME but the overall morphology will be similar to the white light CME. Gyroemission at low frequencies is suppressed in the presence of plasma where the index of refraction deviates from unity (Razin-Tsytovich suppression). This effect can be used as an additional diag-

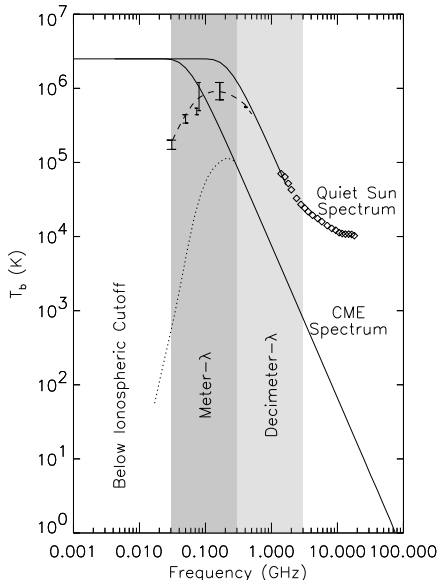


Figure 11.2. Simulated free-free radio spectra for the quiet Sun and a typical CME ($n_e = 3.5 \times 10^7$ cm^{-3}, $T_e = 2.5$ MK, $L = 4.4 \times 10^{10}$ cm). The effects of refraction and reflection at the plasma layer are shown by the dashed and dotted lines, respectively. Diamonds are measurements by Zirin, Baumert & Hurford (1991). The bars, below 1 GHz, represent the range of measurements at a few relevant frequencies from Lantos *et al.* (1980) and Wang, Schmahl & Kundu (1987). From Bastian & Gary (1997).

nostic of the density of the ambient (thermal) electrons and the magnetic field strength.

1.2.3 Non-thermal plasma emissions. Plasma emission is the most prevalent emission from CME structures and involves the efficient conversion of electron energy into a natural wave-mode of the plasma (e.g., trapped Langmuir waves) and the subsequent conversion to transverse waves that can escape to space as plasma radiation. This occurs at the plasma frequency and its second harmonic but rarely at higher harmonics. It is important mostly for frequencies below a few hundred MHz. Due to optical thickness effects, the plasma radiation is strongly reabsorbed at high frequencies (above 0.1–0.3 MHz for the fundamental and 2–5 GHz for the 2nd harmonic). It is the accepted emission mechanism for type II and IV-IVm solar bursts. Type II bursts are associated with shocks driven by CME fronts and flares (Cane 1984; Gopalswamy *et al.* 1998*a*; Cliver, Webb & Howard 1999) while type IV are stationery bursts that seem to be associated with the CME material following the leading edge. Moving type IVs (IVm) are outward-moving radio blobs and are also associated with CMEs. They occur very rarely and are classified in three types: isolated plasmoids (Wagner *et al.* 1981), expanding arches and advancing fronts (Stewart 1985). It should be noted that plasma emission is not the only possible emission mechanism for IVm bursts. An alternative explanation is gyrosynchrotron emission.

Imaging observations of such bursts at a single or few widely spaced frequencies are of rather limited use. First, the source morphology is entirely different from the white-light CME because plasma emission arises near the plasma level or its second harmonic, making it difficult to directly compare structures. Second, plasma radiation tends to be very bright and can easily mask the much weaker thermal free-free emission. Third, it is very difficult to derive information on the physical parameters of the emitting sources because of the complexity of the plasma emission processes. However, imaging over many closely spaced frequencies over the relevant frequency range, as FASR will do, will provide spatially resolved spectra over the entire emitting volume and may allow for a more complete interpretation of such events.

2. Radio CME Observations During Cycle 23

The concept of ejection of coronal material has been around for a long time (Morrison 1954; Gold 1955) owing mainly to the early radio observations of moving type IV (Boichot 1957) and type II (Payne-Scott, Yabsley & Bolton 1947) bursts. However, the true extent of the CME phenomenon became apparent with the white light observations from orbiting coronagraphs in the last 30 years. Joint imaging radio and white light CME analyses have been rare because of the limited observing windows between ground-based and earth-

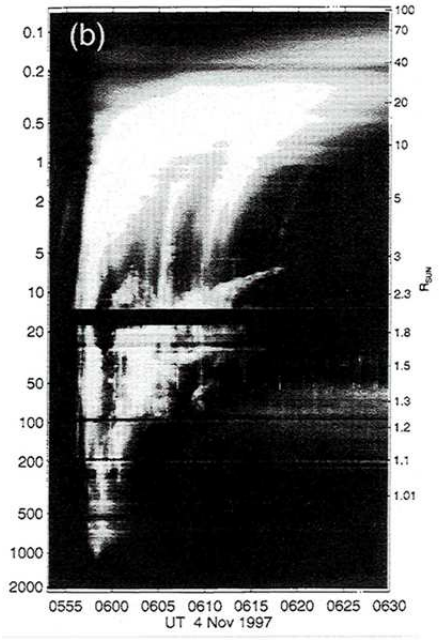


Figure 11.3. Example of a fairly complete spectral coverage of a CME event from 2 GHz to 100 kHz. The frequency axis on the left is in MHz units and the heliocentric distance axis on the right is in solar radii. From Dulk *et al.* (2000)

orbiting instruments. Since 1996, this situation has greatly improved with the operation of the LASCO coronagraphs aboard the SOHO satellite which monitor the Sun continuously from the L1 point. Moreover, new and/or upgraded radio instruments have become operational in the last few years. They include solar imaging interferometers such as the Nobeyama Radioheliograph (NoRH; Nakajima *et al.* 1994) observing at 17 and 34 GHz, the upgraded Nançay Radioheliograph (NRH; Kerdraon & Delouis 1997) observing at up to 10 frequencies between 164–435 MHz, and the addition of 74 MHz capability at the Very Large Array (VLA). CME observations have also been reported from the Gauribidanour Radioheliograph (GRH; Ramesh *et al.* 1998) and Ooty (Manoharan *et al.* 2001). On the spectral front, there have been important advances in the study of IP bursts with the addition of space-based observations at frequencies below 14 MHz from the WAVES instrument (Bougeret *et al.* 1995) aboard the WIND satellite. Several ground-based spectrometers have also been upgraded (Potsdam, Odrejov, IZMIRAN) or constructed (BIRS, SRBL, Artemis, Oporto). We can now track the radio emission spectrum from the chromosphere (a few GHz) all the way to the Earth (a few kHz) (Figure 11.3).

Combined radio/EUV/LASCO observations have led to new insights on the physics of CMEs. For these reasons, this chapter is focused on the significant amount of radio work during the rising phase of solar cycle 23. The emphasis is on direct radio imaging of CME structures but work on what can be considered as indirect imaging (e.g., type II sources, spectroscopic observations, etc.) is also discussed. We present the most important results in the following.

2.1 CME detection

Direct CME detection in radio has great potential for important contributions to space weather studies because of the ability to track the event from its nascent stages on the disk to the outer corona. Despite the availability of better instrumentation there has been no detection of the thermal emission from CMEs so far. Gary *et al.* (1998) made the first science observations with the new 74 MHz VLA band searching specifically for CME thermal signatures. Two CMEs occurred during this observing period. Despite the radio data's excellent sensitivity (signal-to-noise ratio of 3000:1), no signatures of the CMEs were detected. Faint sources from several CME fronts were detected at NRH frequencies (Maia *et al.* 2000). Figure 11.4 is the best example. The sources moved at speeds comparable to the CME white light front and had brightness temperatures consistent with thermal sources (a few $\times 10^4$ K). The polarization and spectral behavior, however, clearly showed that they were non-thermal sources. These results do not support the earlier detections of thermal CME emission (Gopalswamy & Kundu 1992; Sheridan *et al.* 1978) although those were made at very low frequencies (< 80 MHz), which are not easily accessible with today's imaging instrumentation. The opening of the overlying streamer during the early stages of a CME was imaged by GRH at 109 MHz and an estimate of the mass at the leading edge was derived (Kathiravan, Ramesh & Subramanian 2002). Unfortunately, GRH lacks the capability to follow the event in time. It appears, therefore, that a radio instrument finely tuned to CME characteristics is needed. We will return to this point later.

2.2 CME development

Thermal emission is not the only probe into the physics of CMEs. As we mentioned earlier, nonthermal emissions are easily detectable and their imaging can tell us a great deal about the development of the CME in the low corona.

The main advantages of coronal radio observations over other wavelengths are the high cadence (< 1 s) and large field of view (active region scales to 2–3 $R_\odot$, depending on observing wavelength). The first joint analysis of a CME with LASCO and the upgraded NRH (Maia *et al.* 1998; Pick *et al.* 1998) revealed multiple loop systems participating in the eruption process. The development

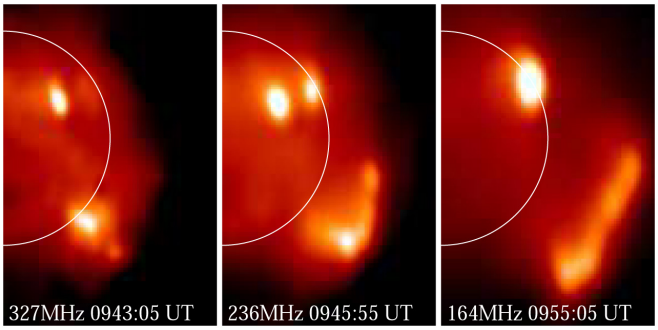


Figure 11.4. 1998 April 20 : Radio source progression seen by the NRH at 3 distinct frequencies. The sources is likely associated with the front of the white-light CME (Vourlidas *et al.* 1999).

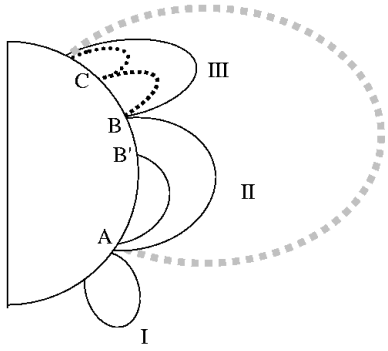


Figure 11.5. 1997 November 06: Schematic of the CME development as inferred from the NRH observations. From Maia *et al.* 1999.

of the eruption was shown more clearly in the imaging of the 1997 November 06 event (Maia *et al.* 1999), where activated loop systems were traced from the flare site to the south of the equator to a active region behind the limb and north of the equator (Figure 11.5). Most importantly, most of the low-corona CME development took place within 4–5 min, much faster than the cadence of the LASCO or EIT instruments. In another large event, the radio sources spread through the solar disk in < 15 min (Maia *et al.* 2001). A similar analysis of a halo CME (Pohjolainen *et al.* 2001) verified the above conclusions. In addition, they showed that part of the ejected loops can be traced by their radio emission before their liftoff. The radio observations imaged a set of transequatorial loops that lifted as part of the CME, leaving an EUV dimming behind (Figure 11.6).

This result demonstrates the capability of radio imaging in tracing the source regions of the Earth-directed CME ejecta and consequently the possibility of estimating the mass and magnetic field in these ejecta, perhaps through the use

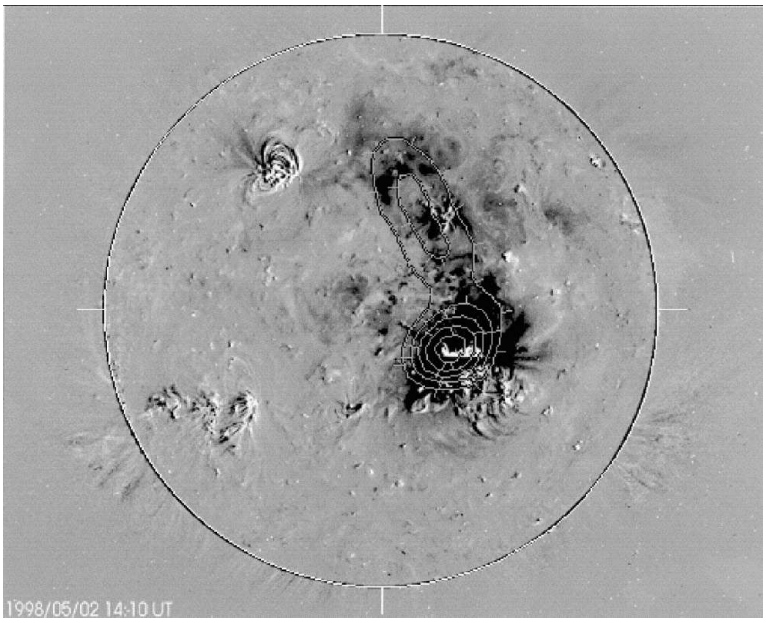


Figure 11.6. 195Å difference image on 1998 May 2 showing the EIT dimming region position at 14:10 UT. The Nançay 236 MHz image at 13:48:21 UT is overplotted in contours. At the time of the EIT image, this radio source had already disappeared. From Pohjolainen *et al.* (2001).

of auxiliary observations (EUV, SXR). The radio observations also reveal the sites of coronal electron acceleration which continues long after the CME has left the low corona (Pick 1986).

2.3 Detection of CME-associated structures

EUV waves emanating from sites of active region transients have been recently detected with EIT (Thompson *et al.* 1999). They are closely correlated with CMEs (Biesecker *et al.* 2002) but flares and metric type II bursts also occur during these events (Klassen *et al.* 2000; Classen & Aurass 2002). What is the trigger or the nature of these waves is still unclear. In that respect, radio imaging of these phenomena may shed some light. For example, Gopalswamy *et al.* (2000) reported the imaging of a type II source at 164 MHz coincident with the location of a brow-shaped EIT wave. The thermal radio counterpart of another EIT wave was detected at 17 GHz (White & Thompson 2002). These two observations suggest that there might be two classes of EIT waves. Waves with sharp fronts may be MHD, flare-associated waves while EIT waves with diffused fronts nay be associated with CMEs and might trace material pile-up low in the corona.

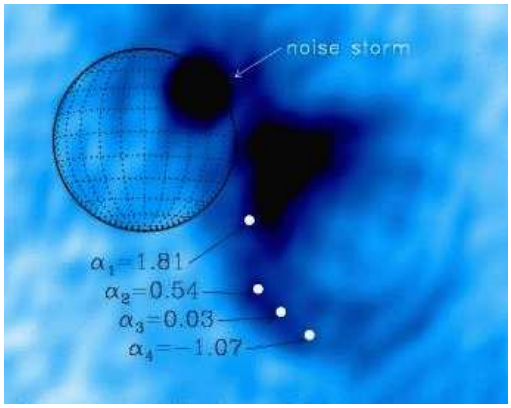


Figure 11.7. Snapshot map of the radio CME loops at 164 MHz. The background disk emission has been removed. A noise storm is present at the northwest. The spectral indices at a few locations are also shown. From Bastian *et al.* (2001).

Bastian *et al.* (2001) carefully analyzed the faint emissions from the 1998 April 20 CME and were able to detect, for the first time, radio loops behind the CME front (Figure 11.7). The emission was found to be nonthermal gyrosynchrotron from 0.5–5 MeV electrons. The detection of the loops in several of the NRH frequencies enabled the calculation of spectral indices along the loops. By fitting these lines of sight, Bastian *et al.* (2001) derived additional physical parameters (e.g., density of thermal electrons, magnetic field). Observations of this type will open the possibility of more accurate diagnostics (e.g., thermal density, filling factors) for CME structures.

Gopalswamy, Hanaoka & Lemen (1998) report the detection of a flare-associated plasmoid at 17 GHz. This is likely the highest frequency type IVm burst detected, and gives information on nonthermal electrons in the cores of CMEs. Plasmoids were detected at 164 MHz in the wake of large eruptions (Vourlidas /etal/ 1999), and they were suggested as the possible sources of some IP bursts.

2.4 Radio prominence eruptions

Hα prominence eruptions have long been used as proxies to coronal ejections (Morrison 1954). The Hα emission depends critically on the temperature of the plasma and therefore provides an incomplete picture of the eruption. Because of their low temperature ($\sim$ 8000 K) and high density ($\sim 10^{10} - 10^{11}$ cm^{-3}), prominences are optically thick at most microwave frequencies and can be easily observed even at 17 GHz (Gopalswamy & Hanaoka 1998). During eruption, the prominence heats and expands, resulting in changes in its bright-

ness temperature and optical thickness (Gopalswamy, Hanaoka & Lemen 1998). Because prominences are likely to become the white light CME core (Illing & Hundhausen 1985), their analysis is important. In such a study, Hori (2000) found that the appearance or not of a CME core depends on the density of the radio prominence. Estimates of the prominence mass and the dynamics of the early eruption can also be derived from radio data (Gopalswamy & Hanaoka 1998; Gopalswamy *et al.* 1999). These mass estimates are of limited value, however, as the amount of material that drains back to the surface is unknown. It is worth noting that the analysis of a filament eruption at 5 GHz is one of the first results to come out from the renovated Siberian Solar Radio Telescope (Uralov *et al.* 2002).

In addition, careful data reduction of NRH observations of filament eruptions at 410 MHz (Marqué *et al.* 2002) demonstrated that both the filament and the precursor to the white light CME cavity can be imaged and their development followed with high cadence. These results demonstrate that two elements (cavity and core) of the three-part structure of the nominal CME (front, cavity and core) can be imaged and analyzed from radio observations of prominence eruptions. More work in needed in this area to exploit the full potential of these observations.

2.5 Type II emission

Type II bursts are frequency drifting radio emissions caused by a physical agent propagating outwards in the solar corona (Wild & McCready 1950). Their agent is considered to be an MHD shock (Uchida 1960). They were among the first discoveries in radioastronomy (Payne-Scott, Yabsley & Bolton 1947) and have been used as a proxy for solar eruptive phenomena ever since, so a very large literature on type II emission has developed. Gopalswamy 2000 gives a recent in-depth review of this phenomenon. Here we focus on a couple of issues that relate to the type II/CME analyses. The correlation between type II bursts and CMEs remains controversial (Gopalswamy *et al.* 1998*b*; Cliver, Webb & Howard 1999). The main reason is that the relative timing of flares, CMEs and type II bursts cannot be established sufficiently accurately with the current instrumentation, although some efforts have been made (Leblanc *et al.* 2001). The connection between metric and decimetric type IIs is also unclear. Leblanc *et al.* (2001) argue that type IIs can be followed from the Sun to the Earth, while Reiner *et al.* (2001) conclude that two independent shocks are needed to explain the observations. The rarity of type II imaging during CME events (Gary *et al.* 1984) contributes to the confusion. Most type IIs appear at frequencies below those that can currently be imaged routinely (164 MHz at NRH). GMRT is in principle capable of observing at 50 MHz but this feature has not been implemented yet. Besides, GMRT is not a solar-dedicated instrument.

This area of research needs to be addressed by future instrumentation because type II bursts can tell us a lot about shocks and their evolution in IP space and could have important implications for space weather studies.

2.6 CME radio precursors

Radio observations of the corona can contribute also to the search for CME precursors, which are needed for operational applications. In a recent work Aurass *et al.* (1999) proposed that faint drifting continua might indicate the opening of the coronal structures just before the eruption takes place. Their conclusion is based on only two events, however. More extensive searches for these faint radio signatures are needed before drawing firmer conclusions. Another possible candidate are noise storms (Elgaroy 1977). This radio emission is associated with coronal changes such as mass addition (Kerdraon *et al.* 1983), large scale magnetic field restructuring (Habbal *et al.* 1996) and filament disappearance (Lantos *et al.* 1981; Pick *et al.* 1995; Marqué *et al.* 2001). A recent statistical study (Ramesh & Sundaram 2001) on the temporal correlation between noise storms and CMEs has been inconclusive. Another study, Chertok *et al.* (2001), found that sharp decreases of the noise storm radio emission are correlated with the passage of the CME material. It seems that the two phenomena are somehow interrelated but the details of the relationship (physical, temporal and/or spatial) are still unclear.

2.7 Overview

The above review hopefully demonstrates the importance of radio observations to many aspects of the CME phenomenon. Their contributions to our still incomplete, understanding of these events can be summarized into a "typical radio CME":

- It takes less than 15 minutes to fully develop in the low corona. By "fully develop," I mean that the CME and its associated disturbances have spread throughout the solar disk.
- During its evolution, multiple loop systems, at distant locations (active regions), become active and participate in the eruption by contributing to the ejecta. Determining the participating systems can also help in selecting viable CME initiation models (Maia *et al.* 2003).
- The ejections continue for tens of minutes, even after the main CME body (as witnessed by the white light observations) has left the corona. This suggests that particle acceleration also continues in the wake of the CME. The delayed ejections can drive shocks, interact with the earlier ejecta and therefore may be important for understanding *in-situ* observations and space weather.

- Structures that are commonly used as CME proxies (EIT waves) might not be related to CMEs at all but rather to co-temporal flares.
- Both the cavity and the core of a typical 3-part white light CME can be imaged in a radio CME. The much higher cadence, provided by the radio instruments, allow us to follow the early phases of the eruption in detail. The core of a typical CME is part of an ejected prominence and its mass can be estimated from the radio measurements.
- Well-defined loops can still be seen within the CME at large heights (2–3 $R_\odot$), and contain energetic particles with energies of the order of 1 MeV interacting with $\sim$ 1 G magnetic fields.

3. FASR Connection

The solar activity that mostly affects the interplanetary space and consequently the Earth environment is the CME activity as seen through white light observations. As such, white light coronagraphs carry the bulk of the research effort. However, their principle of operation—occulting the solar disk—is also their major shortcoming. The birth, drivers and initial stages of the ejection event cannot be monitored. The best solution, so far, has been accomplished by the LASCO and EIT instruments observing the ejections from the disk to the outer corona. These two instrument suites, working as a complement, have contributed to coronal physics and space weather studies to such a degree that future solar NASA missions (STEREO, SDO) require an EUV disk imager/whitelight coronagraph suite. However, this approach has some shortcomings. Space-based observations are restricted by the available telemetry and therefore the observing cadence and data gathering ability are compromised compared to ground-based instruments. EUV telescopes are only able to image the solar disk over a narrow temperature range and might miss CME activity outside of their bandpass. Coronagraphs able to image the corona below about 1.5 $R_\odot$ are very complex and therefore expensive to build. For these reasons, it is difficult to identify and follow CME structures from the EUV to the white light fields of view. This ambiguity plagues the CME modeling efforts, for example.

Radio instruments have their own problems when they are used for CME observations. But they also have the potential to contribute to the areas where space-based instruments cannot.

3.1 Advantages of radio observations

From the work discussed in the previous section, one can derive several key areas radio observations offer (or have the potential to offer) significant insights in the problem of CMEs.

- Accurate timing of CME initiation.

- Positional information on type II/shock.
- Identification of the electron acceleration sites.
- Capability to follow an event from the low corona to the Earth.
- When the emission mechanism is thermal or gyrosynchrotron, derivation of physical parameters (e.g., electron density, magnetic field, energy distribution) inside the CME is possible.

3.2 Disadvantages of current radio observations

- Incomplete spectral coverage.
- Difficulties in combining different spectrometer data due to their varying sensitivity, calibration, frequency coverage, RFI environment, etc.
- Imaging unavailable in many frequencies.
- Higher sensitivity is needed for both imaging and spectral observations.
- Physical interpretation of important radio emissions, such as type IIs, is still incomplete. It reduces the scientific return of these radio observations (for modeling purposes, for example).

3.3 Instrument requirements

Clearly, we need an instrument capable of both broadband spectroscopy and imaging. The requirements that such an instrument must satisfy are:

(a) It should be able to image the bulk of the ejected material for both limb and Earth-directed CMEs. This requires the detection of thermal free-free emission over the background disk emission and the much stronger nonthermal emissions that accompany CMEs. Because the brightness of the thermal CME is frequency-dependent, there is a range of frequencies that would be optimum for detection (Figure 11.2). This range lies between about 0.2–2 GHz where a dynamic range of ~ 10 is sufficient to detect CMEs over the disk background. Nonthermal emission can easily reach brightness temperatures of 10^9 K (e.g. plasma emission). Since the thermal CME emission is expected to be about $10^4 - 10^5$ K, a dynamic range of at least 10^4 is needed in this case.

(b) The thermal emission should be imaged at a cadence sufficient to follow the CME evolution on the disk and low corona and to provide meaningful speed measurements. Given that a typical CME takes about 15 min to develop, a radio map of the full disk every minute or two with the dynamic range stated in (a) should be sufficient.

(c) We already know from the Nançay observations (Maia *et al.* 1999; Pohjolainen *et al.* 2001) that nonthermal sources exhibit significant evolution over 1 sec timescales (loop illuminations, short-lived bursts, etc.). Thus, snapshot images every few seconds would allows us a better understanding of the high energy processes involved in the CME, pinpointing shock origins, the relation between flare and CME evolution, etc.

(d) The instrument should have a large field of view to image CMEs beyond the disk. This will provide the connection to the white light coronagraph field of view, which generally starts at $\sim 2R_{\odot}$, and so will allow the study of the acceleration profile and the dynamics of the events and help elucidate the large scale implications of CMEs, such as effects on streamers.

(e) Finally, the instrument must be able to observe in as many frequencies as possible and to switch among them in a rapid fashion. In this way, terrestrial interference and confusing (bright) solar emissions can be avoided and the observations can be tailored to individual events. Another advantage of multi-frequency capability is the use of frequency synthesis techniques (Conway, Cornwell & Wilkenson 1990) to improve the quality of the maps with a minimum impact on hardware.

An instrument that can satisfy all these requirements is an interferometric array designed for Fourier synthesis imaging (e.g., like the VLA). Such an instrument has been proposed under the name Frequency Agile Solar Radiotelescope (FASR) (Bastian, Gary & White 1999) and has been received very well by the community. It is now the number one recommendation of the Solar and Space Physics Survey Committee. The instrument concept and implementation is presented in this volume (Bastian, Chapter 3).

Although the design details (e.g., number of antennas, array shape, etc) have not been finalized yet, the viability of CME detection by such an array has been assessed by Bastian & Gary 1997. They simulated an off-limb CME ($\sim 10^{16}$ g of material) and used three different methods to detect it: (i) direct snapshot imaging at a single frequency, (ii) vector subtraction of CME visibilities between two snapshots (the radio equivalent of running difference) and (iii) vector subtraction for a temporally redundant array. In other words, an array that has identical uv coverage for images taken at a certain cadence, Δt where Δt is of the order of several minutes. It turns out that the last technique achieves the best results (Figure 11.8) based on a 73-element array (split into two subarrays of 37 elements each).

Detection of CMEs against the solar disk is one of the more important tasks for FASR. Based on the observations reviewed in §2 and the simulations above, it appears that an array with a large number of elements, frequency agility, large

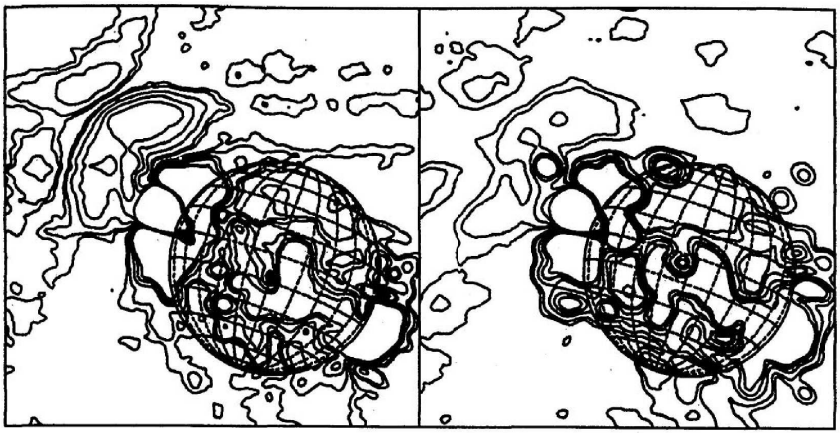


Figure 11.8. Simulation of CME detection by a temporally redundant array. Left panel: Results from a 73-element array. Right panel: Results from a 37-element array. The contour levels are 1, 2, 5, 10, 20 $\times 10^5$ K. From Bastian & Gary (1997).

bandwidth and fast cadence will be able to detect disk CMEs. One should not underestimate source motion as an important factor in pattern recognition. An observer can distinguish a traveling feature in the presence of noise, even if the feature is not readily detectable in a single frame. The detection of EIT waves is a superb example of the power of this technique. These waves are usually undetectable in normal EIT images and barely visible in single difference frames. In a movie sequence of difference, though, the wave becomes visible and can be analyzed. The discussion so far concerned mainly the thermal radio emission. On-disk nonthermal sources (e.g. gyrosynchrotron) are expected to be easily detectable even with a relatively small number of non-thermal electrons entrained in the CME (Figure 8 in Bastian & Gary 1997).

In conclusion, the power of radio observations lies in their flexibility and access to the many facets of coronal mass ejections (bulk material, shocks, waves, prominence eruptions). The ability to obtain information on the physical parameters of the CME and the processes that initiate these phenomena has been demonstrated above. The next step is to design, build and operate FASR, a radio instrument that will exploit this potential.

Acknowledgments

I wish to thank N. Gopalswamy and S. Plunkett for useful discussions. A.V. research is supported by various NASA and ONR grants. SOHO is an international collaboration between NASA and ESA and is part of the International Solar Terrestrial Physics Program. LASCO was constructed by a consortium of institutions: the Naval Research Laboratory (Washington, DC, USA), the University of Birmingham (Birmingham, UK), the Max-Planck-Institut für

Aeronomie (Katlenburg-Lindau, Germany) and the Laboratoire d'Astronomie Spatiale (Marseille, France).

References

Aurass, H., Vourlidas, A., Andrews, M. D., Thompson, B. J., Howard, R. H. & Mann, G. 1999, ApJ, 511, 451
Bastian, T. S. & Gary, D. E. 1997, JGR, 102, 14031
Bastian, T. S., Benz, A. O. & Gary, D. E. 1998, ARAA, 36, 131
Bastian, T. S., Gary, D. E. & White, S. M. 1999, Report to the Astronomy and Astrophysics Survey Committee
Bastian, T. S., Pick, M., Kerdraon, A., Maia, D. & Vourlidas, A. 2001, ApJ, 558, L65
Bastian, T. S., Chapter 3, this volume
Biesecker, D. A., Myers, D. C., Thompson, B. J., Hammer, D. M. & Vourlidas, A. 2002, ApJ, 569, 1009
Boichot, A. 1957, Compt. Rend. Acad. Sci., 244, 1326
Bougeret, J.-L., *et al.* 1995, Space Sci. Rev., 71, 231
Brueckner, 1995, Solar Phys, 163, 357
Cane, H. V. 1984, A&A, 140, 205
Cane, H. V., Richardson, I. G. & St Cyr, O. C. 2000, GRL, 27, 3591
Chertok, I. M., Kahler, S., Aurass, H. & Gnezdilov, A. A. 2001, Solar Phys, 202, 337
Classen, A. T. & Aurass, H. 2002, A&A, 384, 1098
Cliver, E. W., Webb, D. F., Howard, R. A. 1999, Solar Phys, 187, 89
Conway, J. E., Cornwell, T. J. & Wilkenson, P. N. 1990, MNRAS, 246, 490
Crooker, N., Joselyn, J. A. & Feynman, J. (eds), 1997, Coronal Mass Ejections, AGU Geophys. Mon. 99, (AGU: Washington, DC)
Dulk, G. A. 1985, ARAA, 23, 169
Dulk, G. A., Leblanc, Y., Bastian, T. S., Bougeret, J.-L. 2000, JGR, 105, 27343
Domingo, V., Fleck, B. & Poland, A. I. 1995, Solar Phys, 162, 1
Elgaroy, O. 1977, Solar Noise Storms, (Oxford: Pergammon Press)
Gary, D. E., Dulk, G. A., House, L., Illing, R., Sawyer, C., Wagner, W. J., McLean, D. J. & Hildner, E. 1984, A&A, 134, 222
Gary, D. E., Bastian, T. S., Vourlidas, A. 1998, BAAS, SPD meeting 30, SH-32A-11
Gary, D. E. & Hurford, G. J., Chapter 4, this volume.
Gelfreikh, G. B., Chapter 6, this volume.
Gopalswamy, N. & Kundu, M. R. 1992, ApJ, 390, L37
Gopalswamy, N. and 11 co-authors 1998*a*, GRL, 25, 2485
Gopalswamy, N., Kaiser, M. L., Lepping, R. P., Kahler, S. W., Ogilvie, K., Berdichevsky, D., Kondo, T., Isobe, T., Akioka, M. 1998*b*, JGR, 103, 307

Gopalswamy, N. & Hanaoka, Y. 1998, ApJ, 498, L179
Gopalswamy, N., Hanaoka, Y. & Lemen, J. R. 1998, in New Perspectives in Solar Prominences, IAU Coll. 167, eds D.F. Webb, B. Schmieder & D.M. Rust (San Francisco: ASP)
Gopalswamy, N. 1999, in Solar Physics with Radio Observations, Proc. of the Nobeyama Symp. eds. Bastian, T. S., Gopalswamy, N. & Shibasaki, K.,p. 141
Gopalswamy, N., Kaiser, M. L., Sato, J., Pick, M. 2000, in High Energy Solar Physics: Anticipating HESSI, ASP Conf. Ser. 206, eds. R. Ramaty & N. Mandshavidze, 351
Gopalswamy, N. 2000, in Radio Astronomy at Long Wavelengths, AGU Geophys. Mon. 119, eds. R.G. Stone, K.W. Weiler, M.L. Goldstein & J.-L. Bougeret (Washington, DC: AGU), p. 123
Gopalswamy, N., Yashiro, S., Kaiser, M. L., Howard, R. A., Bougeret, J.-L. 2001, ApJ, 548, L91
Gold, T. 1955, in Gas Dynamics of Cosmic Clouds, IAU, 2, (N.Holland Publ. C: Amsterdam), p.238
Gosling, J. T., Hildner, E., MacQueen, R. M., Munro, R. H., Poland, A. I., Ross, C. L. 1974, JGR, 79, 4581
Habbal, S. R., Mossman, A., Gonzalez, R., Esser, R. 1996, JGR, 101, 19943
Hori, K. 2000, ApJ, 543, 1011
Howard, R.A. *et al.* 1975, World Data Center Report UAG, 48A
Howard, R. A., Michels, D. J., Sheeley, N. R., Jr., Koomen, M. J. 1982, ApJ, 263, L101
Howard, R. A., Sheeley, N. R., Jr., Michels, D. J., Koomen, M. J. 1985, JGR, 90, 8173
Hundhausen, A. J., Sawyer, C. B., House, L., Illing, R. M. E., Wagner, W. J. 1984, JGR, 89, 2639
Hundhausen A. J., Burkepile, J.T. & StCyr, O. C. 1994, JGR, 90, 6543
Hundhausen, A. J., 1999, in The Many Faces of the Sun, eds. K.T. Strong, J.L.R. Saba, B.M. Haisch & J.T. Schmelz (New York: Springer), p.143
Illing, R. M. E. & Hundhausen, A. J. 1985, JGR, 90, 275
Kahler, S. W., Cliver, E. W., Cane, H. V., McGuire, R. E., Stone, R. G., Sheeley, N. R., Jr. 1986, ApJ, 302, 504
Kathiravan, C., Ramesh, R. & Subramanian, K. R. 2002, ApJ, 567, L93
Kerdraon, A. & Delouis, J. M. 1997, in Coronal Physics from Radio and Space Observations, ed. G. Trottet (Berlin: Springer) 192
Kerdraon, A., Pick, M., Trottet, G., Sawyer, C., Illing, R., Wagner, W., House, L. 1983, ApJ, 265, L21
Klassen, A., Aurass, H., Mann, G., Thompson, B. J. 2000, A&ASupp., 141, 357

Landos, P. 1980, in Radio Physics of the Sun, Kundu, M.R. & Gergely, T.E. (eds), (Norwell, MA: D. Reidel), 41
Lantos, P., Kerdraon, A., Rapley, G. G., Bentley, R. D. 1981, A&A, 101, 33
Leblanc, Y. *et al.* 2000, JGR, 105, 18225
Leblanc, Y., Dulk, G. A., Vourlidas, A., Bougeret, J.-L. 2001, JGR, 106, 25301
Low, B. C. 2001, JGR, 106, 25141
MacQueen, R. M., Csoeke-Poeckh, A., Hildner, E., House, L., Reynolds, R., Stanger, A., Tepoel, H., Wagner, W. 1980, Solar Phys, 65, 91
Maia, D. *et al.* 1998, Solar Phys, 181, 121
Maia, D., Vourlidas, A., Pick, M., Howard, R., Schwenn, R. & Magalhães, A. 1999, JGR, 104, 12507
Maia, D., Pick, M., Vourlidas, A. & Howard, R. 2000, ApJ, 528, L49
Maia, D., Pick, M., Hawkins, S. E., Fomichev, V. V. & Jiřička, K. 2001, Solar Phys, 204, 197
Maia, D., Aulanier, G., Wang, S. J., Pick, M., Malherbe, J.-M. & Delaboudinière, J.-P. 2003, A&A, 405, 313
Manoharan, P. K., Tokumaru, M., Pick, M., Subramanian, P., Ipavich, F. M., Schenk, K., Kaiser, M. L., Lepping, R. P., Vourlidas, A. 2001, ApJ, 559, 1180
Marqué, C., Lantos, P., Klein, K.-L. & Delouis, J. M. 2001, A&A, 374, 316
Marqué, C., Lantos, P. & Delaboudinière, J. P. 2002, A&A, 387, 317
Michels, D. J., Howard, R. A., Koomen, M. J., Sheeley, N. R., Jr. 1980, in Radio Physics of the Sun, IAU 86, eds Kundu, M.R. & Gergely, T., (Hingman: D. Reidel)p. 439
Morrison, P. 1954, Phys. Rev., 95, 440
Nakajima, H. *et al.* 1994, Proc. IEEE, 82, 705
Payne-Scott, R., Yabsley, D. E. & Bolton, J. G. 1947, Nature, 160, 256
Pick, M. 1986, Solar Phys, 104, 19
Pick, M., Buttighoffer, A., Kerdraon, A., Armstrong, T. P., Roelof, E. C., Hoang, S., Lanzerotti, L. J., Simnett, G. M., Lemen, J. 1995, Sp. Sc. Rev.,72, 315
Pick, M. and 12 co-authors 1998, Solar Phys, 181, 455
Plunkett, S. P., Vourlidas, A., Simberová, S., Karlický, M., Kotrc, P., Heinzel, P., Kupryakov, Yu. A., Guo, W. P., Wu, S. T. 2001, Solar Phys, 194, 371
Pohjolainen, S., Maia, D., Pick, M., Vilmer, N., Khan, J. I., Otruba, W., Warmuth, A., Benz, A., Alissandrakis, C., Thompson, B. J. 2001, ApJ, 556, 421
Ramesh, R., Subramanian, K. R., Sundararajan, M. S., Sastry, Ch. V. 1998, Solar Phys, 181, 439
Ramesh, R. & Shanmugha Sundaram, G. A. 2001, Solar Phys, 202, 355
Rames, D. V. 1999, Space Sci. Rev., 90, 413
Reiner, M. J., Kaiser, M. L., Gopalswamy, N., Aurass, H., Mann, G., Vourlidas, A., Maksimovic, M. 2001, JGR, 106, 25279
Sheeley, N. R., Jr., Howard, R. A., Michels, D. J., Koomen, M. J., Schwenn, R., Muehlhaeuser, K. H., Rosenbauer, H. 1985, JGR, 90, 163

Sheridan, K. V., Jackson, B. V., McLear, D. J. & Dulk, G. A. 1978, Proc. Astr. Soc. Aus., 3, 249

St. Cyr, O. C., Burkepile, J. T., Hundhausen, A. J. & Lecinski, A. R. 1999, JGR, 104, 12493

Stewart, R. T. 1985, in Solar Radiophysics, McLean, D.J & Labrum, N.R. eds, (London:Cam. Univ. Press), p. 361

Thompson, B. J., Gurman, J. B., Neupert, W. M., Newmark, J. S., Delaboudinière, J.-P., St. Cyr, O. C., Stezelberger, S., Dere, K. P., Howard, R. A., Michels, D. J. 1999, ApJ, 517, L151

Tousey, R. 1973, in Space Research XIII, ed. M.J. Rycroft & S.K. Runcorn (Berin:Academie-Verlag), p.173

Uchida, Y. 1960, PASJ, 12, 376

Uralov, A. M., Lesovoi, S. V., Zandanov, V. G. & Grechnev, V. V. 2002, Solar Phys, 208, 69

Vourlidas, A., Maia, D., Pick, M., Howard, R. A. 1999, in Proc. of the 9th Eur. Mtg on Solar Physics, ed. R. Willson, ESA SP-448, 1003

Vourlidas, A., Howard, R. A., Morrill, J. S., Munz, S. 2002, in Solar-Terrestrial Magnetic Activity & Space Enviroment, COSPAR Coll. Ser. 14, Wang, H.N. & Xu, R.K. (eds), (London: Pergammon), p. 201

Wang, Z., Schmahl, E.J. & Kundu, M. R. 1987, Solar Phys, 111, 419

Wagner, W. J., Hildner, E., House, L. L., Sawyer, C., Sheridan, K. V. & Dulk, G. A. 1981, ApJ, 244, L123

Webb, D. F., Cliver, E. W., Crooker, N. U., St. Cry, O. C., Thompson, B. J. 2000, JGR, 105, 7491

Webb, D. F. *et al*. 2001, in Space Weather, AGU Geophys. Mon. 125, Song, P., Singer, H.J. & Siscoe, G.L. (eds), 123

White, S. M. & Thompson, B. J. 2002, AAS Meeting, 200.2904

Wild, J. P. & McCready, L. L. 1950, Aus. J. Sci. Res., A3, 387

Zirin, H., Baumert, B. M. & Hurford, G. J., 1991, ApJ, 370, 779

Chapter 12

TOMOGRAPHIC 3D-MODELING OF THE SOLAR CORONA WITH FASR

Markus J. Aschwanden
Lockheed Martin Advanced Technology Center, Solar & Astrophysics Laboratory
aschwanden@lmsal.com

David Alexander
Rice University
dalex@rice.edu

Marc L. DeRosa
Lockheed Martin Advanced Technology Center, Solar & Astrophysics Laboratory
derosa@lmsal.com

Abstract The Frequency-Agile Solar Radiotelescope (FASR) literally opens up a new dimension, in addition to the 3D Euclidian geometry—the frequency dimension. The 3D geometry is degenerated to 2D in all images from astronomical telescopes, but the additional frequency dimension allows us to retrieve the missing third dimension by means of physical modeling. We call this type of 3D reconstruction Frequency Tomography. In this study we simulate a realistic 3D model of an active region, composed of 500 coronal loops with the 3D geometry $[x(s), y(s), z(s)]$ constrained by magnetic field extrapolations and the physical parameters of the density $n_e(s)$ and temperature $T_e(s)$ given by hydrostatic solutions. We simulate a series of 20 radio images in a frequency range of $\nu = 0.1-10$ GHz, anticipating the capabilities of FASR, and investigate what physical information can be retrieved from such a dataset. We discuss also forward-modeling of the chromospheric and Quiet Sun density and temperature structure, another primary goal of future FASR science.

Keywords: Sun : corona — Sun : chromosphere — Sun : radio

1. Introduction

Three-dimensional (3D) modeling of solar phenomena has always been a challenge with the available two-dimensional (2D) images, but is an utmost necessity to test physical models in a quantitative way. Since solar imaging telescopes have never been launched on multiple spacecraft that separate to a significant parallax angle from the Earth, no true 3D imaging or solar tomography (Davila 1994; Gary, Davis, & Moore 1998; Liewer *et al.* 2001) has been performed so far. The Solar Terrestrial Relations Observatory (STEREO), now being assembled and planned for launch in 2005 November, will be the first true stereoscopic facility, mapping the Sun with an increasing separation angle of 22° per year. Alternative approaches of 3D reconstruction methods utilize the solar rotation to vary the aspect angle (Altschuler 1979; Berton & Sakurai 1985; Koutchmy & Molodensky 1992; Aschwanden & Bastian 1994ab; Batchelor 1994; Hurlburt *et al.* 1994; Zidowitz 1999; Koutchmy, Merzlyakov & Molodensky 2001), but this method generally requires static structures over several days. An advanced form of solar rotation stereoscopy is the so-called *dynamic stereoscopy* method (Aschwanden *et al.* 1999; 2000a), where the 3D geometry of dynamic plasma structures can be reconstructed as long as the guiding magnetic field is quasi-stationary. Of course, 3D modeling with 2D constraints can also be attempted if a-priori assumptions are made for the geometry, e.g. using the assumption of coplanar and semi-circular loops (Nitta, VanDriel-Gestelyi & Harra-Murnion 1999).

A new branch of 3D modeling is the combination of 2D images $I(x, y)$ with the frequency dimension ν, which we call *frequency tomography*. There have been only a very few attempts to apply this method to solar data, mainly because multi-frequency imaging was not available or had insufficient spatial resolution. There are essentially only three published studies that employ the method of frequency tomography: Aschwanden *et al.* (1995); Bogod & Grebinskij (1997); Grebinskij *et al.* (2000.).

In the first study (Aschwanden *et al.* 1995), gyroresonance emission above a sunspot was observed at 7 frequencies in both polarizations in the frequency range of $\nu = 10$–14 GHz with the Owens Valley Solar Array (OVSA) during 4 days. From stereoscopic correlations the height levels $h(\nu)$ of each frequency could be determined above the sunspot. Correcting for the jump in height when dominant gyroresonance emission switches from the second ($s = 2$) to the third harmonic ($s = 3$), the magnetic field $B(\nu) = 357(\nu_{GHz}/s)$ [G] could then be derived as a function of height, $B(h)$, and was found to fit a classical dipole field $B(h) = B_0(1 + h/h_D)^{-3}$. Moreover, from the measured brightness temperature spectrum $T_b(\nu)$ using the same stereoscopic height measurement $h(\nu)$, the temperature profile $T(h)$ as a function of height above the sunspot could also be determined. This study represents an application of frequency

tomography, additionally supported with *solar rotation stereoscopy*, and thus is subject to the requirement of quasi-stationary structures.

In the second study (Bogod & Grebinskij 1997), brightness temperature spectra $T_b(\nu)$ were measured in 36 frequencies in the wavelength range $\lambda = 2$–32 cm ($\nu = 0.94 - 15$ GHz) with RATAN-600, from quiet-Sun regions, active region plages, and from coronal holes. A differential deconvolution method of Laplace transform inversion was then used to infer the electron temperature $T(\tau)$ as a function of the opacity τ. This method does not yield the temperature as a function of an absolute height h, but if an atmospheric model $[T(h), n_e(h)]$ is available as a function of height, the temperature as a function of the free-free (bremsstrahlung) opacity $T(\tau)$ can be calculated and compared with the observations.

In the third study (Grebinskij *et al.* 2000), the brightness temperature in both polarizations is measured as a function of frequency, i.e. $T_b^{RCP}(\nu)$ and $T_b^{LCP}(\nu)$. Since the magnetic field causes a slightly different refractive index in the two circular polarizations (see Chapter 6, by Gelfreikh), the free-free (bremsstrahlung) opacity is consequently also slightly different, so that the magnetic field $B(\nu)$ can be inferred. Again, a physical model $[T(h), n_e(h), B(h)]$ is needed to predict $B(\nu)$ and to compare it with the observed spectrum $T_b(\nu)$.

The content of this chapter is as follows: In §2 we simulate an active region, with the 3D geometry constrained by an observed magnetogram and the physical parameters given by hydrostatic solutions, which are used to calculate FASR radio images in terms of brightness temperature maps $T_b(x, y, \nu)$, and test how the physical parameters of individual coronal loops can be retrieved with FASR tomography. In §3 we discuss a few examples of chromospheric and quiet-Sun coronal modeling to illustrate the power and limitations of FASR tomography. In the final §4 we summarize some primary goals of FASR science that can be pursued with frequency tomography.

2. Active Region Modeling

2.1 Simulation of FASR images

Our aim is to build a realistic 3D model of an active region, in the form of 3D distributions of the electron density $n_e(x, y, z)$ and electron temperature $T_e(x, y, z)$, which can be used to simulate radio brightness temperature maps $T_b(x, y, \nu)$ at arbitrary frequencies ν that can be obtained with the planned Frequency-Agile Solar Radiotelescope (FASR).

We start from a magnetogram recorded with the Michelson Doppler Imager (MDI) instrument onboard the Solar and Heliospheric Observatory (SOHO) on 1999 May 08, 0–1 UT. We perform a potential field extrapolation, with the magnetogram as the lower boundary condition of the photospheric magnetic

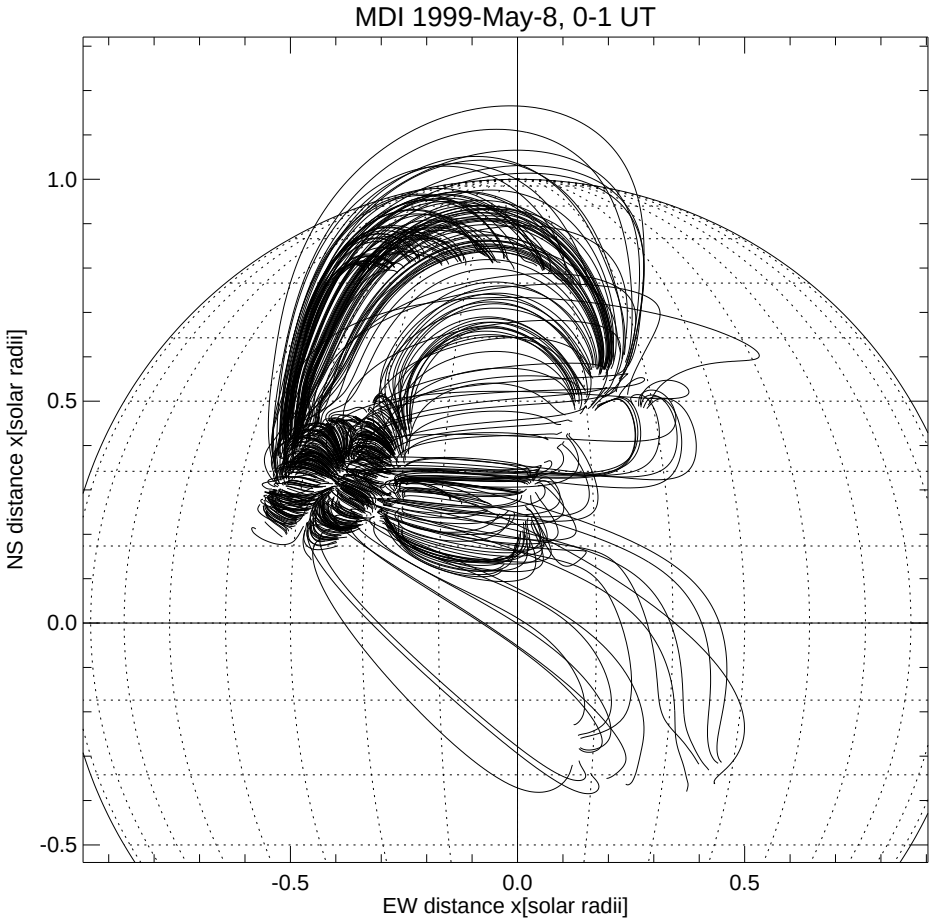


Figure 12.1. Potential field extrapolation of SOHO/MDI magnetogram data from 1999 May 08, 0–1 UT.

field, to obtain the 3D geometry of magnetic field lines. We apply a threshold for the minimum magnetic field at the footpoints, which limits the number of extrapolated field lines to $n = 500$. The projection of these 3D field lines along the line of sight onto the solar disk is shown in Figure 12.1. We basically see two groups of field lines, (1) a compact double arcade with low-lying field lines in an active region in the north-east quadrant of the Sun, and (2) a set of large-scale field lines that spread out from the eastern active region to the west and close in the western hemisphere. From this set of field lines we have constrained the 3D geometry of 500 coronal loops, defined by a length coordinate $s(x, y, z)$.

In a next step we fill the 500 loops with coronal plasma with density $n_e(s)$ and temperature functions $T_e(s)$ that obey hydrostatic solutions. For accu-

rate analytical approximations of hydrostatic solutions we used the code given in Aschwanden & Schrijver (2002). Each hydrostatic solution is defined by three independent parameters: the loop length L, the loop base heating rate E_{H0}, and the heating scale height s_H. The momentum and energy balance equation between the heating rate and radiative and conductive loss rates, i.e. $E_H(s) + E_{rad}(s) + E_{cond}(s) = 0$, yields a unique solution for each parameter set (L, s_H, E_{H0}). For the set of short loops located in the compact double arcade, which have lengths of $L \approx 4 - 100$ Mm, we choose a heating scale height of $s_H = 10$ Mm and base heating rates that are randomly distributed in the logarithmic interval of $E_{H0} = 10^{-4}, ..., 10^{-2}$ erg cm^{-3} s^{-1}. For the group of long loops with lengths of $L \approx 100 - 800$ Mm, we choose near-uniform heating ($s_H = 800$ Mm) and volumetric heating rates randomly distributed in the logarithmic interval of $E_{H0} = 0.5 \times 10^{-7}, \ldots, 0.5 \times 10^{-5}$ erg cm^{-3} s^{-1}. This choice of heating rates produces a distribution of loop maximum temperatures (at the loop tops) of $T_e \approx 1 - 3$ MK, electron densities of $n_e \approx 10^8, \ldots, 10^{10}$ cm^{-3} at the footpoints, and $n_e \approx 10^6, \ldots, 10^9$ cm^{-3} at the loop tops. We show the distribution of loop top temperatures, loop base densities, and loop top densities in Figure 12.2. These parameters are considered to be realistic in the sense that they reproduce typical loop densities and temperatures observed with SOHO and TRACE, as well as correspond to the measured heating scale heights of $s_H \approx 10 - 20$ Mm (Aschwanden, Nightingale, & Alexander 2000*b*), for the set of short loops.

For the simulation of radio images we choose an image size of 512×512 pixels, with a pixel size of 2.25″, and 21 frequencies logarithmically distributed between $\nu = 100$ MHz and 10 GHz. To each magnetic field line we attribute a loop with a width (or column depth) of $w \approx 10^8, \ldots, 10^9$ cm. For each voxel, i.e. volume element at $\mathbf{x} = (x_i, y_j, z_k)$, we calculate the free-free absorption coefficient κ_{ff} (e.g. Lang 1980, p.47),

$$\kappa_{ff}^{\nu}(x_i, y_j, z_k) = 9.78 \times 10^{-3} \frac{n_{e,ijk}^2}{\nu^2 T_{e,ijk}^{3/2}} [24.2 + \ln(T_{e,ijk}) - \ln(\nu)] \ , \quad (12.1)$$

and integrate the opacity τ_{ff}^{ν} along the line of sight (LOS) z,

$$\tau_{ff}^{\nu}(x_i, y_j, z_k) = \int_{-\infty}^{z} \kappa_{ff}^{\nu}(x_i, y_j, z_k) dz' \ , \quad (12.2)$$

to obtain the radio brightness temperature $T_b^{\nu}(x_i, y_j)$ with the radiative transfer equation (in the Rayleigh-Jeans limit),

$$T_b^{\nu}(x_i, y_j) = \int_{-\infty}^{+\infty} T_{e,ijk} \exp^{-\tau_{ff}^{\nu}((x_i, y_j, z_k)} \kappa_{ff}^{\nu}(x_i, y_j, z_k) dz \ , \quad (12.3)$$

The simulated images for the frequency range of $\nu = 100$ MHz to 10 GHz are shown in Figures 12.3 and 12.4. The approximate instrumental resolution is

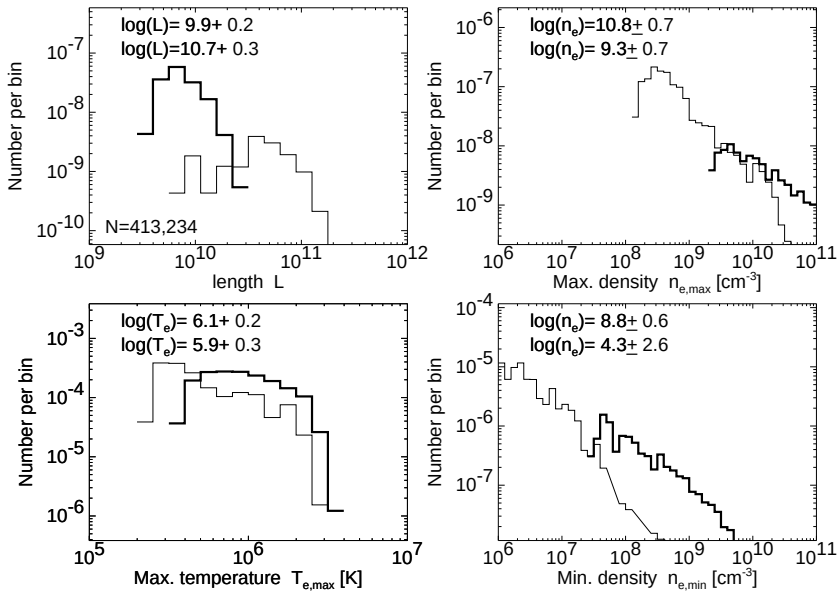


Figure 12.2. Distributions of loop lengths L, loop maximum temperatures $T_{e,max}$, loop minimum densities n_{min}, and maximum densities n_{max}. The distributions with thick linestyle correspond to ≈ 400 loops in the compact arcade, while the distributions with thin linestyle correspond to the group of ≈ 100 large-scale loops.

rendered by smoothing the simulated images with a boxcar that corresponds to the instrumental resolution of FASR,

$$w_{res} = \frac{20''}{\nu_{GHz}}. \tag{12.4}$$

A caveat needs to be made, that the real reconstructed radio images may reach this theoretical resolution only if a sufficient number of Fourier components are available, either from a large number of baselines (which scale with the square of the number of dishes) or from aperture synthesis (which increases the number of Fourier components during Earth rotation proportionally to the accumulation time interval). Also, we did not include here the effects of angular scattering due to turbulence or other coronal inhomogeneities (Bastian 1994, 1995).

2.2 Peak brightness temperature

The intensity of radio maps is usually specified in terms of the observed brightness temperature T_b. We list the peak brightness temperature in each map in Figures 12.3 and 12.4. We see that a maximum brightness is observed in the

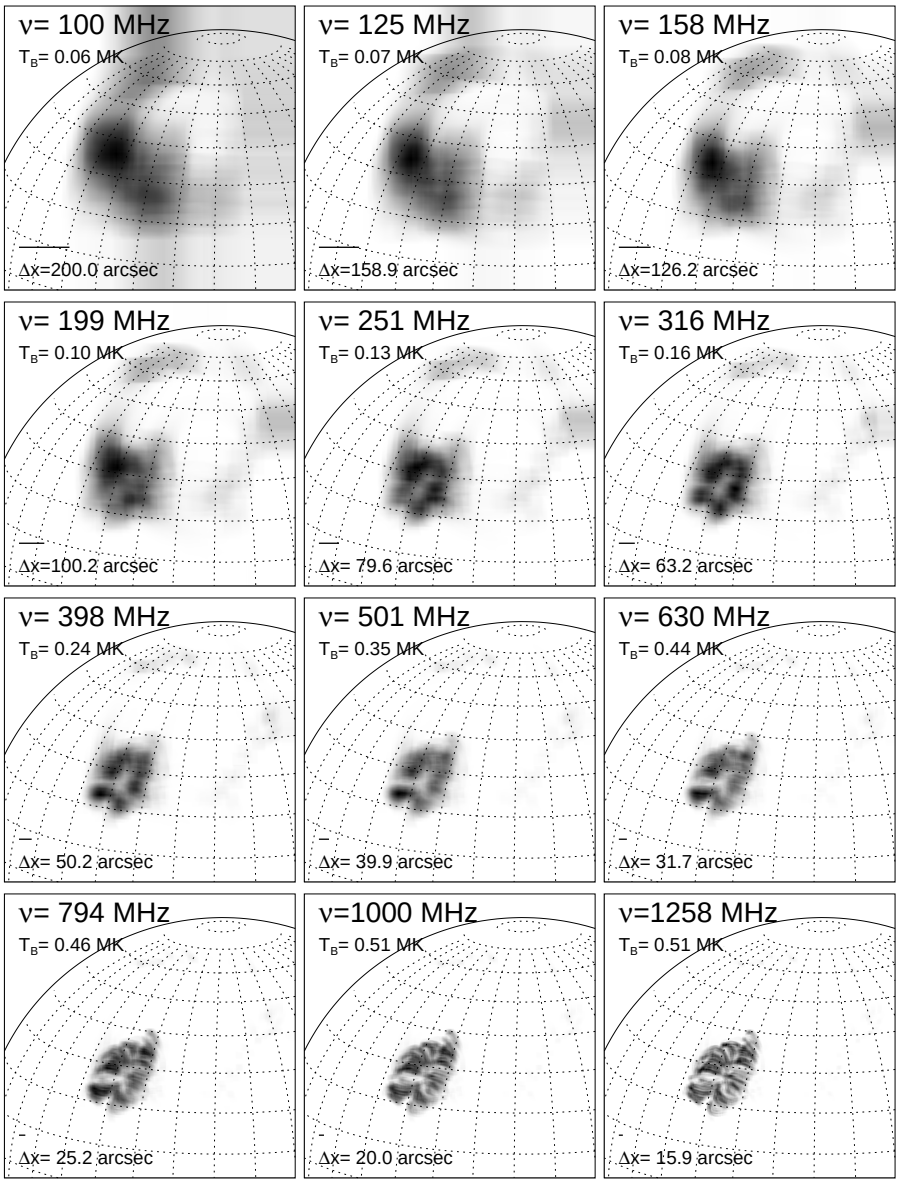


Figure 12.3. Simulation of radio brightness temperature maps of an active region at 20 frequencies, from $\nu = 100$ to 1258 MHz. The maximum brightness temperature (T_b) and the angular resolution Δx are indicated in each frame.

second-last map in Figure 12.4, with $T_b = 1.85$ MK at a frequency of $\nu = 7.94$ GHz. Let us obtain some understanding of the relative brightness temperatures

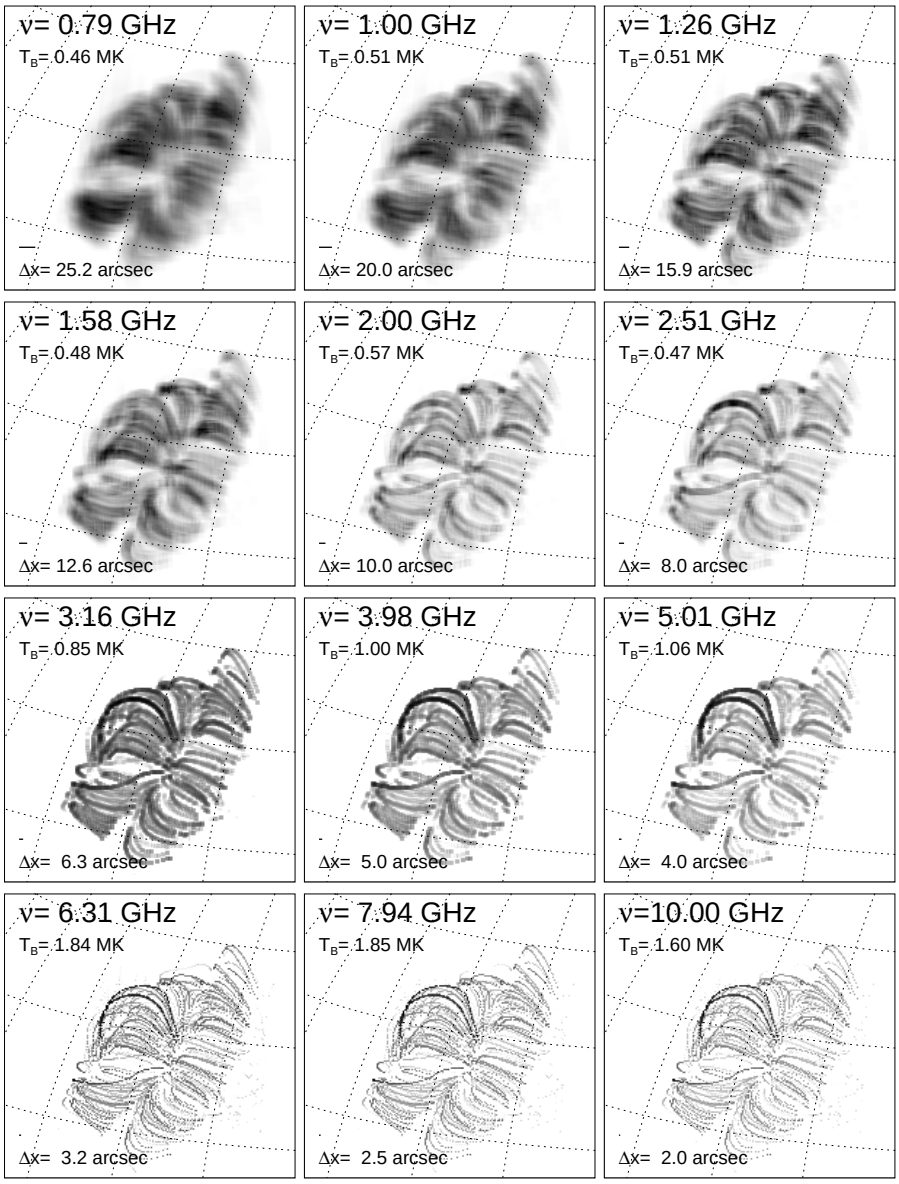


Figure 12.4. Similar representation as in Fig. 12.3, for frequencies of ν=0.8 to 10 GHz, with a smaller field of view than in Fig. 12.3. The brightness is shown on linear scale in the first two rows, and on logarithmic scale in the last two rows (with a contrast of 1:100 in the third row and 1:1000 in fourth row).

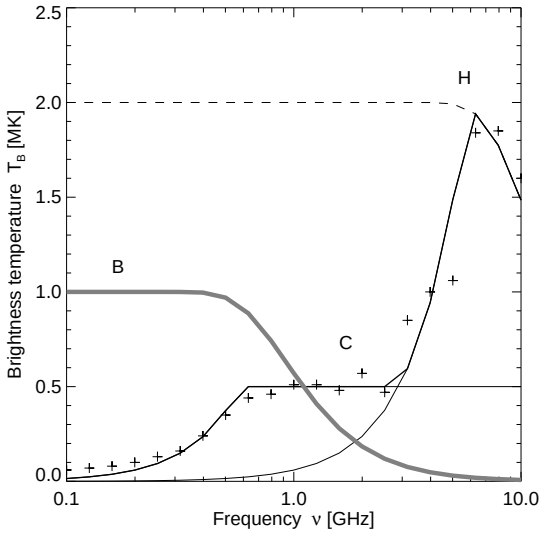


Figure 12.5. The radio peak brightness temperature T_b is shown as function of frequency ν: for the background corona (B), for cool (C) fat loops ($T = 0.5$ MK, $n_e = 10^{11}$ cm^{-3}, $w = 25$ Mm), and hot (H) thin loops ($T = 2.0$ MK, $n_e = 10^{11}$ cm^{-3}, $w = 2.5$ Mm). The cross symbols indicate the peak brightness temperatures observed in the simulated maps (Figures 12.3 and 12.4), while the medium-thick line represents the combined model of hot and cool loops. The dashed line indicates the expected brightness temperature of hot loops if no beam dilution due to the instrumental angular resolution would occur. The thick grey curve (B) indicates a model of the background corona.

$T_b(\nu)$ as function of frequency ν, in order to facilitate the interpretation of radio maps. We plot the peak brightness temperature $T_b(\nu)$ of the simulated maps as function of frequency in Figure 12.5 (cross symbols). There are two counteracting effects that reduce the brightness temperature: First, the loops become optically thin at high frequencies as a result of the ν^{-2}-dependence of the free-free opacity (Eq. 12.1). Hot loops with a temperature of $T = 2.0$ MK, a density of $n_e = 10^{11}$ cm^{-3}, and a width of $w = 2.5$ Mm are optically thick below $\nu \lesssim 5$ GHz, so the brightness temperature would match the electron temperature $T_b = T_e$ (dashed line in Figure 12.5), but falls off at higher frequencies, i.e. $T_b(\nu > 5\ \mathrm{GHz}) < T_e$.

The second effect that reduces the brightness temperature is the beam dilution, which has a ν^2-dependence below the critical frequency where structures are unresolved. The effectively observed brightness temperature $T_b^{eff}(\nu)$ due

to beam dilution for a structure with width w is

$$T_b^{eff}(\nu) = T_b \times \begin{cases} \left(\frac{\nu}{\nu_{crit}}\right)^2 & \text{for } \nu < \nu_{crit}(w) \\ 1 & \text{for } \nu > \nu_{crit}(w) \end{cases} \tag{12.5}$$

where the critical frequency $\nu_{crit}(w)$ depends on the width w of the structure and, according to Eq. (12.4), is for FASR,

$$\nu_{crit}(w) = \frac{20''}{w''}\ [GHz]\ . \tag{12.6}$$

Because the brightness drops drastically below $\nu_{crit} \approx 5$ GHz in Figure 12.5, we conclude that the width of the unresolved structures is about $w'' = 20''/5 = 4'' = 3$ Mm. Therefore we can understand the peak brightness temperaturestemperature,brightness in the maps, as shown in Figure 12.5 (crosses) in the range of $\nu \approx 3 - 10$ GHz via a combination of these two effects, free-free opacity and beam dilution.

Below a frequency of $\nu \lesssim 3$ GHz, we see that another group of loops contributes to the peak brightness of the maps. We find that the peak brightness below 3 GHz can adequately be understood by a group of cooler loops with a temperature of $T = 0.5$ MK, densities of $n_e = 10^{11}$ cm^{-3}, and widths of $w = 25$ Mm (Figure 12.5). Thus cool loops dominate the brightness at low frequencies, and hot loops at higher frequencies.

In the simulations in Figures 12.3 and 12.4 we have not included the background corona. In order to give a comparison of the effect of the background corona we calculate the opacity for a space-filling corona with an average temperature of $T = 1.0$ MK, an average density of $n_e = 10^9$ cm^{-3}, and a vertical (isothermal) scale height of $w \approx \lambda_T \approx 50$ Mm. The brightness temperature of this background corona is shown with a thick gray curve (labeled B) in Figure 12.5. According to this estimate, the background corona overwhelms the brightest active region loops at frequencies $\nu \lesssim 1$ GHz. From this we conclude that it might be difficult to observe active region loops at decimetric frequencies $\nu \lesssim 1.0$ GHz, unless they are very high and stick out above a density scale height, i.e. at altitudes of $h \gtrsim 50$ Mm. In conclusion, the contrast of active region loops in our example seems to be greatest at a frequency near $\nu \approx 5$ GHz, but drops at both sides of this optimum frequency (see Figure 12.5).

2.3 Temperature and density diagnostic of loops

FASR will provide simultaneous sets of images $I(x, y, \nu)$ at many frequencies ν. In other words, for every image position (x_i, y_j), a spectrum $T_b^{ij}(\nu)$ can be obtained. A desirable diagnostic capability is the determination of temperature and density in active region loops. Let us parameterize the projected position of a loop by a length coordinate s_k, $k = 1, ..., n$, e.g.

$[x_i = x(s_k), y_j = y(s_k)]$. If we manage to determine the temperature $T_e(x_i, y_j)$ and density $n_e(x_i, y_i)$ at every loop position (x_i, y_j), we have a diagnostic of the temperature profile $T(s)$ and density profile $n_e(s)$ of an active region loop. Thus, the question is whether we can extract a temperature T_e and density n_e from a brightness temperature spectrum $T_b(\nu)$ at a given pixel position (i, j). In order to illustrate the feasibility of this task, we show the brightness temperature spectrum $T_b(\nu)$ of a typical active region loop in Figure 12.6, and display its variation as a function of the physical (T_e, n_e) and geometric (w) parameters.

We define a typical active region loop by an electron temperature $T_e = 1.0$ MK, an electron density $n_e = 10^{10}$ cm^{-3}, and a width $w = 10$ Mm. Such a loop is brightest at frequencies of $\nu \approx$1.5–3.0 GHz (Figure 12.6; thick curve). The loop is fainter at higher frequencies because free-free emission becomes optically thin, while it is optically thick at lower frequencies. The reason that the loop is also fainter at low frequencies is because of the beam dilution at frequencies where the instrument does not resolve the loop diameter. If we increase the temperature, the brightness temperature increases, and vice versa decreases at lower electron temperatures (Figure 12.6, top). If we increase the density, the critical frequency where the loop becomes optically thin shifts to higher frequencies, while the peak brightness temperature decreases for lower densities (Figure 12.6, middle panel). If we increase the width of the loops, the brightness temperature spectrum is bright in a much larger frequency range, because we shift the critical frequency for beam dilution towards lower frequencies, while the overall brightness temperature decreases for a smaller loop width (Figure 12.6, bottom). Based on this little tutorial, one can essentially understand how the optimization works in spectral fitting (e.g. with a forward-fitting technique) to an observed brightness temperature spectrum $T_b(\nu)$.

To demonstrate how the density and temperature diagnostic works in practice, we pick a bright loop seen at $\nu = 5.0$ GHz in Figure 12.4, which we show as an enlarged detail in Figure 12.7 (left panel). We pick three locations (A, B, C) along the loop and extract the brightness temperature spectra $T_b(\nu)$ from the simulated datacube $T_b(x, y, \nu)$ at the locations (A, B, C), shown in Figure 12.7 (three middle panels). Each spectrum shows two peaks, which we interpret as two cospatial loops. For each spectral peak we can therefore roughly fit a loop model, constrained by three parameters each, i.e. $[T_e, n_e, w]$. We can now fit a brightness temperature spectrum $T_b^{\mathit{eff}}(\nu)$ to the observed (or simulated here) spectrum $T_b^{obs}(\nu)$, physically defined by the same radiation transfer model for free-free emission as in Eqs. (12.1–12.5), but simplified by the approximation of constant parameters (T_e, n_e), and thus a constant absorption coefficient $\kappa_{\mathit{ff}}(\nu)$, over the relatively small spatial extent of a loop diameter w,

$$\kappa_{\mathit{ff}}(\nu) = 9.78 \times 10^{-3} \frac{n_e^2}{\nu^2 T_e^{3/2}} [24.2 + \ln(T_e) - \ln(\nu)] \,, \tag{12.7}$$

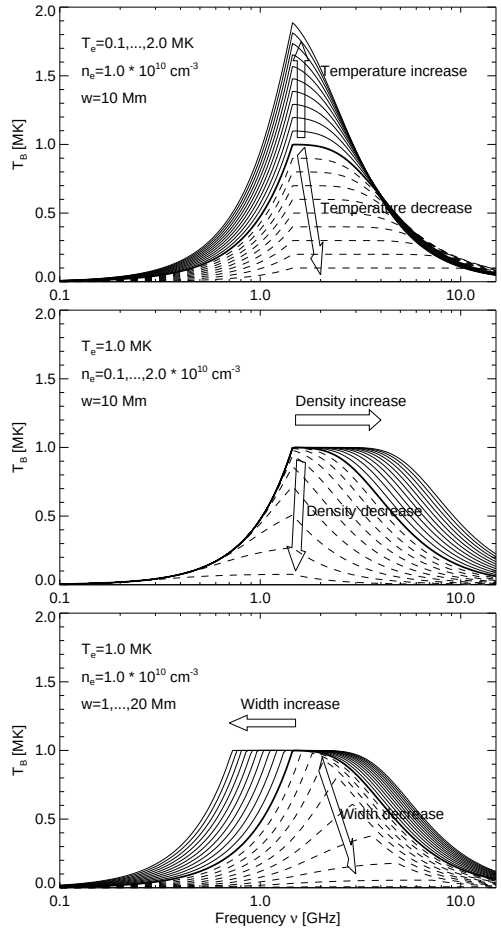


Figure 12.6. The variation of the radio brightness temperature spectrum $T_b(\nu)$ of a loop by varying the temperature T_e (top panel), the electron density n_e (middle panel), and the loop width w (bottom panel). In each of the three panels, one parameter is varied from 10%, 20%, ..., 90% (dashed curves) to 110%, 120%,... , 200% (solid lines). The reference curve with parameters $T_e = 1.0$ MK, $n_e = 10^{10}$ cm^{-3}, and $w = 10$ Mm is indicated with a thick line. The arrows indicate the spectral shift of the peak.

$$\tau_{ff}(\nu) = \kappa_{ff}(\nu)\, w\ , \tag{12.8}$$

$$T_b(\nu) = T_e \left(1 - \exp^{-\tau_{ff}(\nu)}\right), \tag{12.9}$$

$$T_b^{eff}(\nu) = T_b \times \begin{cases} \left(\frac{\nu}{\nu_{crit}}\right)^2 & \text{for } \nu < \nu_{crit}(w) \\ 1 & \text{for } \nu > \nu_{crit}(w) \end{cases}. \tag{12.10}$$

What can immediately be determined from the observed brightness temperature spectra $T_b^{obs}(\nu)$ are the frequencies of the spectral peaks (Figure 12.7, middle panels), which are found around $\nu_{peak} = 1.2$ and 6.0 GHz. Based on the tutorial given in Figure 12.6 it is clear that these spectral peaks demarcate the critical frequencies where structures become unresolved. Thus we can immediately determine the diameters of the two loops with Eq. (12.6), i.e. $w_1 = 20''/1.2 = 17'' = 12.0$ Mm and $w_2 = 20''/6.0 = 3.3'' = 2.4$ Mm. The only thing left to do is to vary the temperature and density and to fit the model (Eqs. 12.7–12.10) to the observed spectrum. For an approximate solution (shown as smooth curves in the middle panels of Figure 12.7) we find $T_1 = 3.0$ MK and $n_1 = 4 \times 10^{10}$ cm^{-3} for the first loop (with width $w_1 = 2.5$ Mm and spectral peak at $\nu_1 = 6.0$ GHz), and $T_2 = 2.9$ MK and $n_2 = 1.9 \times 10^9$ cm^{-3} for the second loop (with width $w_2 = 12$ Mm and spectral peak at $\nu_1 = 1.2$ GHz). The resulting temperature $T_e(s)$ and density profiles $n_e(s)$ along the loops are shown in Figure 12.7 (right panels). This approximate fit is just an example to illustrate the concept of forward-fitting to FASR tomographic data. More information can be extracted from the data by detailed fits with variable loop cross-section along the loop and proper deconvolution of the projected column depth across the loop diameter (which is a function of the aspect angle between the LOS and the loop axis). For a proper determination of the inclination angle of the loop plane, the principle of *dynamic stereoscopy* can be applied (Aschwanden *et al.* 1999; see Appendix A therein for coordinate transformations between the observers reference frame and the loop plane). Of course, our example is somehow idealized. In practice there will be confusion by adjacent or intersecting loops, as well as confusion by other radiation mechanisms, such as gyroresonance emission, which competes with free-free emission at frequencies of $\nu \gtrsim 5$ GHz near sunspots. Polarization measurements and other spectral features can help to sort out contributions by other radiation mechanisms, however.

2.4 Radio versus EUV and soft X-ray diagnostics

We can ask whether temperature and density diagnostic of coronal loops is better done in other wavelengths, such as in EUV and soft X-rays (e.g. Aschwanden *et al.* 1999), rather than with radio tomography. Free-free emission in EUV and soft X-rays is optically thin, which has the advantage that every loop along a LOS is visible to some extent, while loops in optically thick plasmas can be hidden at radio wavelengths. On the other side, the LOS confusion in optically thin plasmas is larger in EUV and soft X-rays, in particular if multiple loops along the same LOS have similar temperatures. Different loops along a LOS can only be discriminated in EUV and soft X-rays if they have significantly different temperatures, so that they show different responses in lines with different ionization temperatures. Two cospatial loops that have

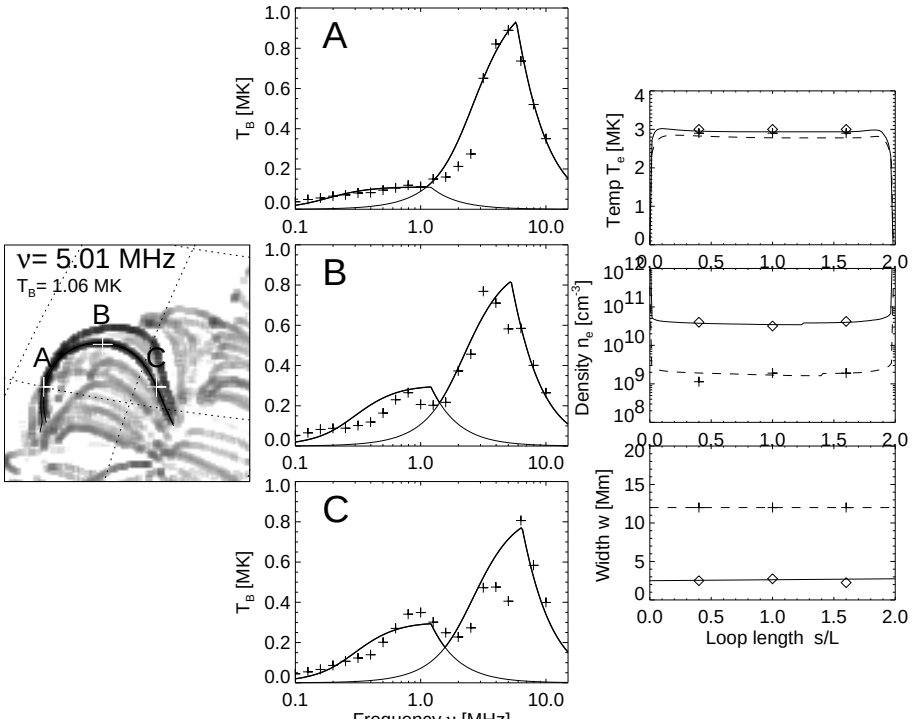


Figure 12.7. Enlarged detail of the active region with a bright loop (left panel). From the measured brightness temperature spectra $T_b(\nu)$ (crosses in middle panels) at the three loop locations (A, B, C) we fit theoretical spectra and determine the temperatures (right top panel), densities (right middle panel), and loop widths (right bottom panel) at the three loop locations (A, B, C).

similar temperatures but different widths cannot be distinguished by EUV or soft X-ray detectors. In radio wavelengths, however, even cospatial loops with similar temperatures, as the two loops in our example in Figure 12.7 ($T_1 = 3.0$ MK and $T_2 = 2.9$ MK), can be separated if they have different widths. The reason is that they have different critical frequencies $\nu_{crit}(w)$ where they become resolved, and thus show up as two different peaks in the brightness temperature spectrum $T_b^{eff}(\nu)$. Radio tomography has therefore a number of unique advantages over loop analysis in EUV and soft X-ray wavelengths: (1) a ground-based instrument is much less costly than a space-based instrument, (2) a wide spectral radio wavelength range (decimetric, centimetric) provides straightforwardly diagnostic over a wide temperature range, while an equivalent temperature diagnostic in EUV and soft X-rays would require a large number of spectral lines and instrumental filters, (3) optically thick radio emission is most sensitive to cool plasma, which is undetectable in EUV and soft X-rays,

except for absorption in the case of very dense cool plasmas, and (4) radio brightness temperature spectra can discriminate multiple cospatial structures with identical temperatures based on their spatial scale, which is not possible with optically thin EUV and soft X-ray emission.

3. Chromospheric and Coronal Modeling

The vertical density and temperature structure of the chromosphere, transition region, and corona has been probed in soft X-rays, EUV, and in radio wavelengths, but detailed models that are consistent in all wavelengths are still unavailable. Comprehensive coverage of the multi-thermal and inhomogeneous solar corona necessarily requires either many wavelength filters in soft X-rays and EUV, or many radio frequencies, for which FASR will be the optimum instrument.

We illustrate the concept of how to explore the vertical structure of the chromosphere and corona with a few simple examples. We know that the corona is highly inhomogeneous along any LOS, so a 3D model has to be composed of a distribution of many magnetic fluxtubes, each one representing a mini-atmosphere with its own density and temperature structure, being isolated from others due to the low value of the plasma-beta, i.e. $\beta = p_{thermal}/p_{magn} = 2n_e k_B T_e/(B^2/8\pi) \ll 1$. The confusion due to inhomogeneous temperatures and densities is largest for lines of sight above the limb (due to the longest column depths with contributing opacity), and is smallest for lines of sight near the solar disk center, where we look down through the atmosphere in vertical direction.

The simplest model of the atmosphere is given by the hydrostatic equilibrium in the isothermal approximation, $T(h) = const$, where the hydrostatic scale height λ_T is proportional to the electron temperature T, i.e.

$$\lambda_T = \frac{k_B T}{\mu m_p g_\odot} = \lambda_0 \Big(\frac{T}{1\ \mathrm{MK}} \Big) \tag{12.11}$$

with $\lambda_0 = 47$ Mm for coronal conditions, with μm_p the average ion mass (i.e. $\mu \approx 1.3$ for H:He = 10:1) and $g_\odot$ the solar gravitation. The height dependence of the electron density is for gravitational pressure balance,

$$n_e(h) = n_0\ \exp\big[-\frac{(h - h_0)}{\lambda_0 T} \big]\ . \tag{12.12}$$

where $n_0 = n(h_0)$ is the base electron density. This expression for the density $n_e(h)$ can then be inserted into the free-free absorption coefficient $\kappa(h, \nu)$, with $T(h) = const$ in the isothermal approximation,

$$\kappa_{ff}(h, \nu) = 9.78 \times 10^{-3} \frac{n_e^2(h)}{\nu^2 T(h)^{3/2}} [24.2 + \ln T(h) - \ln(\nu)]\ , \tag{12.13}$$

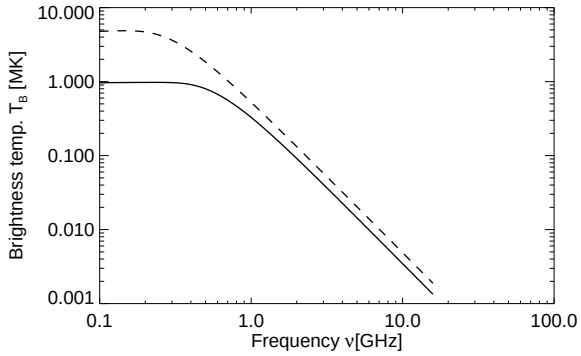


Figure 12.8. Quiet Sun brightness temperature spectrum for an isothermal corona with $T = 1.0$ MK (solid line) or $T = 5.0$ MK (dashed line) with a base density of $n_0 = 10^9$ cm^{-3}.

At disk center, we can set the altitude h equal to the LOS coordinate z, so that the free-free opacity $\tau_{ff}(h, \nu)$ integrated along the LOS $h = z$ is,

$$\tau_{ff}(h, \nu) = \int_{-\infty}^{h} \kappa_{ff}(h', \nu)\, dh' \,, \tag{12.14}$$

and the radio brightness temperature $T_b(\nu)$ is then

$$T_b(\nu) = \int_{-\infty}^{0} T(h) \exp^{-\tau_{ff}(h,\nu)} \kappa_{ff}(h, \nu) dh \,. \tag{12.15}$$

With this simple model we can determine the mean temperature $T(h)$ by fitting the observed brightness temperature spectra $T_b(\nu)$ to the theoretical spectra (Eq. 12.15) by varying the temperature $T(h) = const$ (in Eqs. 12.13–12.14). The expected brightness temperature spectra for an isothermal corona with temperatures of $T = 1.0$ MK and $T = 5.0$ MK and a base density of $n_0 = 10^9$ cm^{-3} are shown in Figure 12.8 (See also Fig. 4.2 of Chapter 4). We see that the corona becomes optically thin ($T_b \ll T_e$) at frequencies of $\nu \gtrsim 1 - 2$ GHz in this temperature range that is typical for the Quiet Sun.

These hydrostatic models in the lower corona, however, have been criticized because of the presence of dynamic phenomena, such as spiculae, which may contribute to an extended chromosphere in the statistical average. The spicular extension of this dynamic chromosphere has been probed with high-resolution measurements of the Normal Incidence X-Ray Telescope (NIXT) (Daw, DeLuca, & Golub 1995) as well as with radio submillimeter observations during a total eclipse (Ewell *et al.* 1993). Using the radio limb height measurements at various mm and sub-mm wavelengths in the range of 200-3000 μm (Roellig *et al.* 1991; Horne *et al.* 1981; Wannier *et al.* 1983; Belkora

et al. 1992; Ewell *et al.* 1993), an empirical Caltech Irreference Chromospheric Model (CICM) was established, which fits the observed limb heights between 500 km and 5000 km in a temperature regime of $T = 4410$ K to $T = 7500$ K (Ewell *et al.* 1993), shown in Figure 12.9. We see that these radio limb measurements yield electron densities that are 1-2 orders of magnitude higher in the height range of 500-5000 km than predicted by hydrostatic models (VAL, FAL, Gabriel 1976), which was interpreted in terms of the dynamic nature of spicules (Ewell *et al.* 1993). This enhanced density in the extended chromosphere has also been corroborated with recent RHESSI measurements (Aschwanden, Brown & Kontar 2002). Hard X-rays mainly probe the total neutral and ionized hydrogen density that governs the bremsstrahlung and the total bound and free electron density in collisional energy losses, while the electron density $n_e(h)$ inferred from the radio-based measurements is based on free-free emission, and shows a remarkably good agreement in the height range of $h \approx 1000-3000$ km. The extended chromosphere produces substantially more opacity at microwave frequencies than hydrostatic models (e.g. Gabriel 1976).

The atmospheric structure thus needs to be explored with more general parameterizations of the density $n_e(h)$ and temperature $T_e(h)$ structure than hydrostatic models provide. For instance, each of the atmospheric models shown in Figure 12.9 provides different functions $n_e(h)$ and $T_e(h)$. Observational tests of these models can be made simply by forward-fitting of the parameterized height-dependent density $n_e(h)$ and temperature profiles $T_e(h)$, using the expressions for free-free emission (Eqs. 12.13–12.15). In Figure 12.10 we illustrate this with an example. The datapoints (shown as diamonds in Figure 12.10) represent radio observations of the solar limb at frequencies of $\nu = 1.4$–18 GHz during the solar minimum in 1986-87 by Zirin, Baumert, & Hurford (1991). We show in Figure 12.10 an isothermal hydrostatic model for a coronal temperature of $T_e = 1.5$ MK and a base density of $n_e = 10^9$ cm^{-3}, as well as the hydrostatic model of Gabriel (1976), of which the density profile $n_e(h)$ is shown in Figure 12.9. The Gabriel model was calculated based on the expansion of the magnetic field of coronal flux tubes over the area of a supergranule (canopy geometry). The geometric expansion factor and the densities at the lower boundary in the transition region (given by the chromospheric VAL and FAL models, see Figure 12.10) then constrains the coronal density model $n_e(h)$, which falls off exponentially with height in an isothermal fluxtube in hydrostatic equilibrium. We see that the Gabriel model roughly matches the isothermal hydrostatic model (see Figure 12.10), but does not exactly match the observations by Zirin *et al.* (1991). However, if we multiply the Gabriel model by a factor of 0.4, to adjust for solar cycle minimum conditions, and add a temperature of $T_e = 11,000$ K to account for an optically thick chromosphere (similar to the values determined by Bastian, Dulk & Leblanc 1996), we find a reasonably good fit to the observations of Zirin (thick curve in Fig-

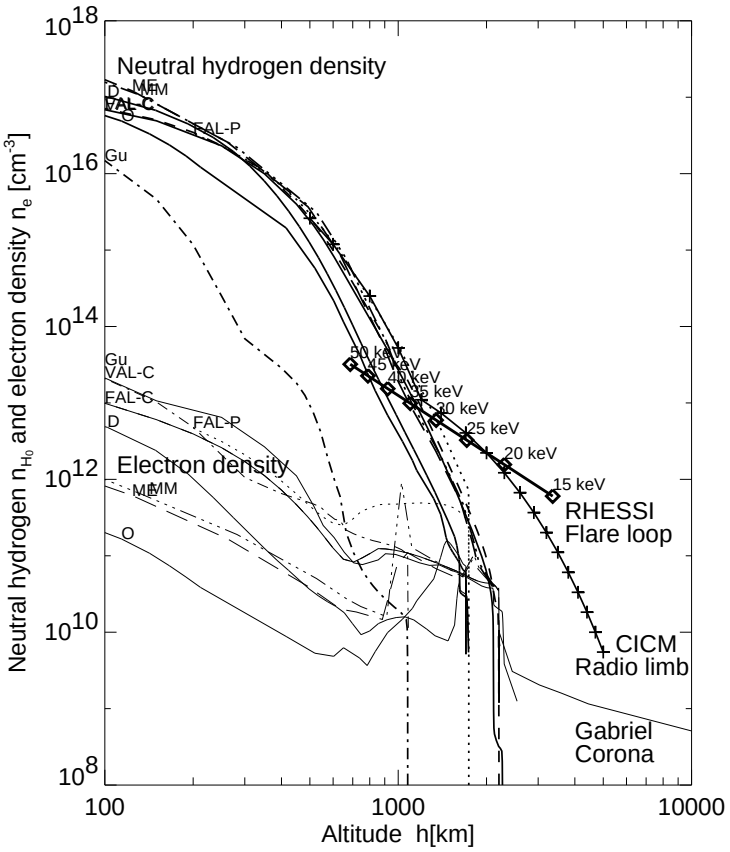


Figure 12.9. A compilation of chromospheric and coronal density models: VAL-C = Vernazza, Avrett, & Loeser (1981), model C; FAL-C = Fontenla, Avrett, & Loeser (1990), model C; FAL-P = Fontenla, Avrett, & Loeser (1990), model P; G = Gu, Jefferies *et al.* (1997); MM = Maltby *et al.* (1986), model M; ME = Maltby *et al.* (1986), model E; D = Ding & Fang (1989); O = Obridko & Staude (1988); Gabriel = Gabriel (1976), coronal model; CICM = Caltech Irreference Chromospheric Model, radio sub-millimeter limb observations (Ewell *et al.* 1993), RHESSI flare loop (Aschwanden, Brown, & Kontar 2002).

ure 12.10). This example demonstrates that radio spectra in the frequency range of $\nu \approx 1$–10 GHz are quite sensitive as a probe of the physical structure of the chromosphere and transition region.

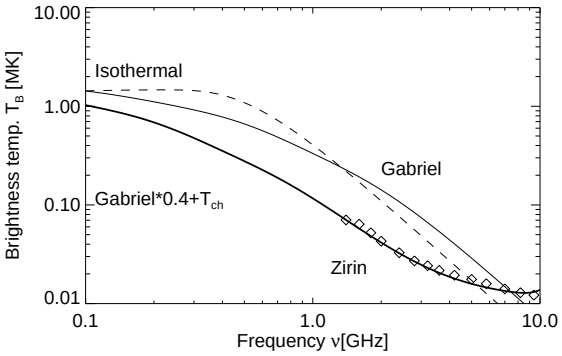


Figure 12.10. Quiet Sun brightness temperature spectrum for an isothermal corona with $T = 1.5$ MK with a base density of $n_0 = 10^9$ cm^{-3} (solid thin line), for the coronal model by Gabriel (1976) (thin solid line), and for a modified Gabriel model (thick solid line).

4. Future FASR Science

With our study we illustrated some basic applications of frequency tomography as can be expected from FASR data. We demonstrated how physical parameters from coronal loops in active regions, from the quiet-Sun corona, and from the chromosphere and transition region can be retrieved. Based on these capabilities we expect that the following science goals can be efficiently studied with future FASR data:

(1) The electron density $n_e(s)$ and electron temperature profile $T_e(s)$ of individual active region loops can be retrieved, which constrain the heating function $E_H(s)$ along the loop in the momentum and energy balance hydrodynamic equations. This enables us to test whether a loop is in hydrostatic equilibrium or evolves in a dynamic manner. Detailed dynamic studies of the time-dependent heating function $E_H(s,t)$ may reveal the time scales of intermittent plasma heating processes, which can be used to constrain whether AC or DC heating processes control energy dissipation. Ultimately, such quantitative studies will lead to the determination and identification of the so far unknown physical heating mechanisms, a long-thought goal of the so-called *coronal heating problem*. Radio diagnostics are most sensitive to cool dense plasma, but are also sensitive continuously up to the highest temperatures, and in this way nicely complements EUV and soft X-ray diagnostic.

(2) Because coronal loops are direct tracers of closed coronal magnetic field lines, the reconstruction of the 3D geometry of loops, as mapped with multi-frequency data from FASR in a tomographic manner, gives infor-

mation that can be used to test theoretical models based on magnetic field extrapolations from the photosphere. The circular polarization of free-free emission contains additional information on the magnetic field (Grebinskij *et al.* 2000; Gelfreikh 2002; Brosius 2002; Chapter 6, this volume), while gyroresonance emission provides direct measurements of the magnetic field by its proportionality to the gyrofrequency (Lee *et al.* 1998; White 2002; Ryabov 2002, Chapter 5, this volume). Ultimately, such studies may constrain the non-potentiality and the localization of currents in the corona.

(3) The density $n_e(h)$ and temperature profile $T_e(h)$ of the chromosphere, transition region, and corona can be determined in the Quiet Sun from brightness temperature spectra $T_b(\nu)$, with least confusion at disk center. Parameterized models of the density and temperature structure, additionally constrained by the hydrodynamic equations and differential emission measure distributions, can be forward-fitted to the observed radio brightness temperature spectra $T_b(\nu)$. This provides a new tool to probe physical conditions in the transition region, deviations from hydrostatic equilibria, and diagnostic of dynamic processes (flows, turbulence, waves, heating, cooling) in this little understood interface to the corona.

(4) Since free-free emission is most sensitive to cool dense plasma, FASR data will also be very suitable to study the origin, evolution, destabilization, and eruption of filaments, which seem to play a crucial role in triggering and onset of *coronal mass ejections* (Vourlidas 2002; see Chapter 11, this volume). Ultimately, the information to forecast CMEs may be chiefly exploited from the early evolution of filaments.

Previous studies with multi-frequency instruments (VLA, OVRO, Nançay, RATAN-600) allowed only crude attempts to pioneer tomographic 3D-modeling of the solar corona, because of the limitations of a relatively small number of Fourier components and a sparse number of frequencies. FASR will be the optimum instrument to faciliate 3D diagnostics of the solar corona on a routine basis, which is likely to lead to ground-breaking discoveries in long-standing problems of coronal plasma physics.

References

Altschuler, M. D. 1979, in Image Reconstruction from Projections, (ed. G. T. Herman, Berlin:Springer), p.105

Aschwanden, M. J. & Bastian, T. S. 1994*a*, ApJ, 426, 425

Aschwanden, M. J. & Bastian, T. S. 1994*b*, ApJ, 426, 434

Aschwanden, M. J., Lim, J., Gary, D. E., & Klimchuk, J. A. 1995, ApJ, 454, 512

Aschwanden, M. J., Newmark, J. S., Delaboudiniere, J. P., Neupert, W. M., Klimchuk, J. A., Gary, G. A., Portier-Fornazzi, F., & Zucker, A. 1999, ApJ, 515, 842
Aschwanden, M. J., Alexander, D., Hurlburt, N., Newmark, J. S., Neupert, W. M., Klimchuk, J. A., & G. A. Gary 2000*a*, ApJ, 531, 1129
Aschwanden, M. J., Nightingale, R. W., & Alexander, D. 2000*b*, ApJ, 541, 1059
Aschwanden, M. J. & Schrijver, K. J. 2002, ApJ Supp., 142, 269
Aschwanden, M. J., Brown, J. C., & Kontar, E. P. 2002, Solar Phys, 210, 383
Bastian, T. S. 1994, ApJ, 426, 774
Bastian, T. S. 1995, ApJ, 439, 494
Bastian, T. S., Dulk, G. A., & Leblanc, Y. 1996, ApJ, 473, 539
Batchelor, D. A. 1994, Solar Phys, 155, 57
Belkora, L., Hurford, G. J., Gary, D. E. & Woody, D. P. 1992, ApJ, 400, 692
Berton. R. & Sakurai, T. 1985, Solar Phys, 96, 93
Bogod, V. M., & Grebinskij, A. S. 1997, Solar Phys, 176, 67
Brosius, J. W. 2004, (Chapter 13, this volume)
Davila, J. M. 1994, ApJ, 423, 871
Daw, A., DeLuca, E. E., & Golub, L. 1995, ApJ, 453, 929
Ding, M. D. & Fang, C. 1989, A&A, 225, 204
Ewell, M. W. Jr., Zirin, H., Jensen, J. B., & Bastian, T. S. 1993, ApJ, 403, 426
Fontenla, J. M., Avrett, E. H., & Loeser, R. 1990, ApJ, 355, 700
Gabriel, A. H. 1976, Royal Society (London), Philosophical Transactions, Series A, 281, no. 1304, 339
Gary, A., Davis, J. M., & Moore, R. 1998, Solar Phys, 183, 45
Gelfreikh, G. B. 2004, (Chapter 6, this volume)
Grebinskij, A., Bogod, V., Gelfreikh, G., Urpo, S., Pohjolainen, S. & Shibasaki, K. 2000, A&AS, 144, 169
Gu, Y., Jefferies, J. T., Lindsey, C. & Avrett, E. H. 1997, ApJ, 484, 960
Horne, K., Hurford, G. J., Zirin, H., & DeGraauw, Th. 1981, ApJ, 244, 340
Hurlburt, N. E., Martens, P, C. H., Slater, G. L., & Jaffey, S. M. 1994, in Solar Active Region Evolution: Comparing Models with Observations, ASP Conf. Ser., 68, 30
Lang, K. R. 1980, Astrophysical Formulae. A Compendium for the Physicist and Astrophysicist, Berlin: Springer
Lee, J. W., McClymont, A. N., Mikic, Z., White, S. M., & Kundu, M. R. 1998, ApJ, 501, 853
Koutchmy, S., & Molodensky, M. M. 1992, Nature, 360, 717
Koutchmy, S., Merzlyakov, V. L., & Molodensky, M. M. 2001, Astronomy Reports, 45, 10, 834
Liewer, P. C., Hall, J. R., DeJong, M., Socker, D. G., Howard, R. A., Crane, P. C., Reiser, P., Rich, N., Vourlidas, A. 2001, JGR, 106/A8, 15903

Maltby, P., Avrett, E. H., Carlsson, M., Kjeldseth-Moe, O., Kurucz, R. L., & Loeser, R. 1986, ApJ, 306, 284
Nitta, N., VanDriel-Gestelyi, L., & Harra-Murnion, L, K. 1999, Solar Phys, 189, 181
Obridko, V. N. & Staude, J. 1988, A&A, 189, 232
Roellig, T. L., Becklin, E. E., Jefferies, J. T., Kopp, G. A., Lindsey, C. A., Orral, F. Q., & Werner, M. W., 1991, ApJ, 381, 288
Ryabov, V. B. 2004, (Chapter 7, this volume)
Vernazza, J. E., Avrett, E. H., & Loeser, R. 1981, ApJ Supp., 45, 635
Vourlidas, A. 2004, (Chapter 11, this volume)
Wannier, P. G., Hurford, G. J., & Seielstad, G. A. 1983, ApJ, 264, 660
White, S. M. 2004, (Chapter 5, this volume)
Zidowitz, S. 1999, JGR, 104, 9727
Zirin, H., Baumert, B. M., & Hurford, G. J. 1991, ApJ, 370, 779

Chapter 13

CORONAL DIAGNOSTICS WITH COORDINATED RADIO AND EUV/SOFT X-RAY OBSERVATIONS

Jeffrey W. Brosius
The Catholic University of America, Code 682, NASA's Goddard Space Flight Center, Greenbelt, MD 20771
brosius@comstoc.gsfc.nasa.gov

Abstract

A brief review is provided of what has been learned about the solar corona from existing coordinated radio and EUV (or soft X-ray) observations. Topics include: introduction to radio thermal bremsstrahlung and thermal gyroemission; two-dimensional coronal magnetography measurements; measurements of coronal elemental abundances; measurements of physical properties of quasi-transverse (QT) layers in the coronal magnetic field; and three-dimensional coronal magnetography measurements (the primary subject of this Chapter). Results from these studies are used to help focus on coronal diagnostics that can be performed with similar coordinated observations involving FASR, as well as to recommend FASR instrument requirements.

Keywords: active regions, corona, elemental abundances, line emission, magnetic fields, polarization, radio radiation, sunspots, ultraviolet radiation, X-ray radiation

1. Introduction

The brightness temperature T_b of a radio emitting source is the blackbody temperature of that source, related to its measured flux density through Planck's law of radiation in the Rayleigh-Jeans approximation. We use T_b, measured in K (kelvins), in all that follows. It is well known that two mechanisms contribute to the radio emission from quiescent (nonflaring) coronal active region plasma: thermal bremsstrahlung (free-free) and thermal gyroresonance (cyclotron). Textbooks by Kundu (1965), Zheleznyakov (1970), and Golub & Pasachoff (1997) provide further information and references on both of these mechanisms. Thermal bremsstrahlung emission arises from the interaction of

unbound electrons with protons, and corresponds to the minimum possible radio intensity to emanate from the plasma. Thermal bremsstrahlung is present whether or not the emitting plasma is permeated by a magnetic field. Thermal gyroemission arises from thermal electrons spiraling along coronal magnetic field lines, and thus requires a magnetic field in its source region. It is emitted at low harmonics of the local electron gyrofrequency.

A magnetic field in a radio source region forces the radiation from that region to propagate via two oppositely polarized modes (*cf.* Sturrock 1994): the ordinary (o-mode) and the extraordinary (x-mode). The dispersion relation for the o-mode is similar to that for propagation in a field-free plasma (hence the name "ordinary"), while that for the x-mode is different due to a resonance at the gyrofrequency. Thus, for any given radio observing frequency, a different brightness temperature is obtained for each polarization. However, a radio telescope does not directly observe either the x-mode or the o-mode, but rather the handedness (right or left) of the polarization. For a source region in which the magnetic field's longitudinal (line-of-sight) component is directed toward the observer, the right hand (R) circularly polarized component corresponds to x-mode emission while the left hand (L) corresponds to o-mode. Similarly, if the field's longitudinal component is directed away from the observer, the R component corresponds to o-mode while the L component corresponds to x-mode.

The optical thickness $\Delta\tau$ of a source region in either mode of electromagnetic wave propagation at any given radio frequency is the sum of the free-free (f-f) and gyroresonant (g-r) opacities:

$$\Delta\tau^{x,o} = \Delta\tau_{ff}^{x,o} + \Delta\tau_{gr}^{x,o}. \tag{13.1}$$

The free-free optical thickness is given by

$$\Delta\tau_{ff}^{x,o} = \frac{9.786 \times 10^{-21}(CEM)\ln(\alpha/\nu)}{n_\nu T^{1.5}(\nu \mp \nu_B \cos\theta)^2}, \tag{13.2}$$

where $\alpha = 47T$ for temperatures above 3.16×10^5 K and $\alpha = 4.954\times10^{-2}T^{1.5}$ otherwise; CEM is the column emission measure $\int n_e^2 d\ell$ in cm^{-5} (in which n_e is the electron number density and $d\ell$ is an element of path length along the line of sight), T is the electron temperature in K, ν is the observation frequency in GHz, n_ν is the index of refraction for the frequency ν, $\nu_B = 2.797 \times 10^{-3}B$ is the gyrofrequency in GHz (B is the magnetic field strength in gauss), θ is the angle between the magnetic field and the line of sight, and the minus sign refers to the x-mode while the plus sign refers to the o-mode. A reasonable approximation for the gyroresonance optical thickness is given by

$$\Delta\tau_{gr}^{x,o} = 0.052\frac{s^{2s}}{2^{s+1}s!}n_e\nu^{-1}L_B(1.77\times10^{-10}T)^{s-1}(1\pm\cos\theta)^2\sin^{2s-2}\theta, \tag{13.3}$$

where $s = \nu/\nu_B$ is the harmonic number (e.g., 2, 3, 4,...), n_e is the electron density, L_B is the magnetic scale height $B/\nabla B$ in units of 10^9 cm, and the plus sign refers to the x-mode while the minus sign refers to the o-mode. Zlotnik (1968) presents more accurate expressions for the angular dependence. $\Delta\tau_{gr}^{x,o}$ is non-zero only for locations in which the observation frequency is an integral multiple (harmonic) of the local electron gyrofrequency.

For a radio source with electron temperature T and optical thickness $\Delta\tau$ lying below an optical depth τ, the observed radio brightness temperatures will be

$$T_b^{x,o} = T[1 - \exp(-\Delta\tau^{x,o})] \exp(-\tau^{x,o}). \tag{13.4}$$

The opacities and, hence, the radio brightness temperatures for both emission mechanisms depend upon the coronal magnetic field. In addition, the two modes of propagation depend in a different way on that field. The key to measuring coronal magnetic fields is to obtain coronal *plasma* parameters (density, temperature, and emission measure) from observations of optically thin X-ray and/or EUV emission lines (which are insensitive to coronal magnetic fields), and then use these quantities in equations for the thermal bremsstrahlung and gyroresonance opacities so that coronal *magnetic* parameters (field strength and direction) can be obtained from a comparison of observed and "calculated" radio intensities.

This chapter provides summaries of several selected topics pertaining to coordinated radio and EUV/soft X-ray observations, with thoughts on how FASR observations will enable significant improvements. §2 provides a brief history of 2D coronal magnetography, §3 discusses the measurement of physical parameters in a quasi-transverse layer of the coronal magnetic field, §4 presents measurements of coronal elemental abundance, §5 describes 3D coronal magnetography (the main thrust of this Chapter), and §6 summarizes thoughts on the future of coordinated EUV/soft X-ray and radio observations with FASR.

2. 2D Coronal Magnetography

Coordinated radio and X-ray or EUV observations have been carried out since the Skylab era in attempts to garner information about coronal magnetic fields (Kundu, Schmahl & Gerassimenko 1980; Kundu, Schmahl & Rao 1981; Pallavicini, Sakurai & Vaiana 1981; Shibasaki *et al.* 1983; Webb *et al.* 1983, 1987; Holman 1986; Lang *et al.* 1987*ab*; Brosius, Holman & Schmelz 1991; Nitta *et al.* 1991; Brosius *et al.* 1992; 1993; Schmelz *et al.* 1992; 1994). The terms "radio" and "microwave" are frequently used interchangeably in the range relevant to magnetic field measurement.

Brosius *et al.* (1991, 1992) and Schmelz *et al.* (1992, 1994) adapted the Sakurai (1982) potential field extrapolation code to derive two-dimensional ex-

trapolated magnetograms at specified (sometimes numerous and closely spaced) heights in the corona to aid with their analysis of observations obtained during the 1987 Coronal Magnetic Structures Observing Campaign (CoMStOC). This campaign involved coordinated radio observations with the Very Large Array (VLA) and soft X-ray observations with the X-Ray Polychromator (XRP; Acton *et al.* 1980) aboard the Solar Maximum Mission (SMM) satellite. Key results from CoMStOC include (i) the derivation of plasma and magnetic field parameters in individual sunspots and coronal loops, (ii) the demonstration that potential field extrapolations are sometimes adequate, and other times inadequate (yield field strengths that are too small) to explain the observed radio emission, and (iii) evidence for the presence of cool coronal plasma at some locations. Bogod *et al.* (1992) and Lang *et al.* (1993) applied similar adaptations of the Sakurai (1982) code to obtain extrapolated coronal magnetograms. They combined these potential models of the solar coronal magnetic field with constant conductive flux models of the solar atmosphere to compute theoretical radio emission maps for comparison with observations. At some locations their theoretical and observed maps agreed well, demonstrating that the potential extrapolation provided a reasonable approximation of the coronal field. At other locations their theoretical intensities exceeded their observed intensities, suggesting the presence of cool absorbing plasma; at still other locations, their theoretical intensities were less than their observed intensities, indicating a possible role for non-potential coronal fields.

Other authors derived 2D maps of the coronal magnetic field without relying on potential extrapolations from photospheric longitudinal magnetograms. Brosius *et al.* (1993) used coordinated observations obtained with NASA/GSFC's Solar EUV Research Telescope and Spectrograph (SERTS) and the VLA to derive coronal magnetograms in a solar plage area, while Gary & Hurford (1994) used Owens Valley Solar Array (OVSA) multiple wavelength observations to derive coronal magnetograms of a solar active region.

Brosius *et al.* (1993) used 1991 SERTS EUV images of Fe XV at 284.1 Å and Fe XVI at 335.4 Å to determine the two-dimensional temperature and emission measure distribution in a solar plage area under the assumption of an isothermal corona. Using the 2D map of intensity ratios of the Fe XVI to Fe XV emission lines, along with the ionization equilibrium computations of Arnaud & Raymond (1992), they found that the coronal plasma temperature ranged from 2.3 to 2.9 $\times 10^6$ K throughout the region, the maximum value occurring where relatively strong, oppositely-directed magnetic polarities were closely spaced. The temperature map, along with the line intensity maps and the coronal iron abundance of Meyer (1991) and Feldman (1992), were then used to derive a map of the column emission measure; this ranged from 2.5×10^{27} to 1.3×10^{28} cm^{-5}, the maximum value also occurring where the oppositely-directed magnetic polarities were closely spaced. The temperature and emission measure

maps were used to calculate a map of the expected 1.5 GHz thermal bremsstrahlung emission using equations like those in §1. The calculated structure and intensity of this emission was similar to the structure and intensity of the 1.5 GHz radio emission observed by the VLA, thus indicating that neither cool absorbing plasma nor magnetic fields sufficient to produce gyroemission were required. This meant that thermal bremsstrahlung *alone* was responsible for the 1.5 GHz plage emission, thus enabling the derivation of a map of the coronal longitudinal magnetic field from the observed 1.5 GHz polarization.

From (13.2), the optical depth of the thermal bremsstrahlung emission can be written

$$\Delta\tau_{ff}^{x,o} = \Delta\tau_0(1 \mp \frac{\nu_B}{\nu}\cos\theta)^{-2}, \tag{13.5}$$

where $\Delta\tau_0$ is the optical depth of the unmagnetized plasma. In order to extract information about the magnetic field from the free-free emission, it is important that $\Delta\tau_0$ be small enough that the brightness temperatures of the two modes of radio propagation are different. For example, if $\Delta\tau_0$ is large then the radio brightness temperatures of both modes are equal to the electron temperature, and the net polarization is zero. Brosius *et al.* (1993) found an average opacity of 0.1 for the 1.5 GHz emission, appropriate to enable free-free polarization measurements to be used to derived coronal magnetic fields. Inserting the above equation into Eq. (13.4), we obtain an expression for the *predicted* radio brightness temperature

$$T_b^{x,o;pred} = T[1 - \exp(-\Delta\tau_{ff}^{x,o})]. \tag{13.6}$$

Although the brightness temperatures of the two modes depend upon the magnetic field strength, the predicted *total* radio intensity $I^{pred} = (T_b^{x;pred} + T_b^{o;pred})/2$ is independent of the field strength, which means that a map of total predicted free-free intensity can be calculated from a map of $\Delta\tau_0$ values. This was done, and the resulting map reproduced the observed structure and intensity within the measurement uncertainties. Equating the *predicted* polarization

$$P = (T_b^{x;pred} - T_b^{o;pred})/(T_b^{x;pred} + T_b^{o;pred}) \tag{13.7}$$

to the measured value $P = (T_b^R - T_b^L)/(T_b^R + T_b^L)$, and using the definition of the longitudinal component of the magnetic field $B_z = B\cos\theta$, it can be shown that

$$B_z = 258P[1 - \exp(-\Delta\tau_0)]/[\Delta\tau_0\exp(-\Delta\tau_0)]. \tag{13.8}$$

The map of the coronal magnetic field obtained in this way showed that the longitudinal field strength was $\sim$ 30–60 G in the radio emission region, comparable to values obtained with the Sakurai (1982) potential field extrapolation

code for heights of 5,000 and 10,000 km. This suggested that the magnetic field in this region was potential, and that the hot plasma observed by SERTS and the VLA was at heights $\sim$ 5,000 to 10,000 km. Attention was given to relating each mode of circular polarization (R or L) to its appropriate mode of propagation (x or o) to obtain the sign of the magnetic field in the radio emission region.

By observing the whole Sun at numerous radio frequencies whose intensities are dominated by thermal bremsstrahlung, FASR will be able to map the coronal magnetic field strength over the entire solar disk. It is possible that heights could be determined by measuring displacements due to projection effects.

3. Diagnostics of Quasi-Transverse Layers

The *extrapolated* coronal magnetograms derived by Brosius *et al.* (1992) and Schmelz *et al.* (1992) (see §2), although not "true" coronal magnetograms, were essential for treating radio polarization inversion via mode coupling in a quasi-transverse (QT) layer in the coronal magnetic field (Cohen 1961; Zheleznyakov 1970; Bandiera 1982; Ryabov, Chapter 7 of this volume). The QT layer occurs where the angle between the magnetic field and the line of sight (direction of wave propagation) approaches 90°, i.e., the longitudinal field component B_z becomes zero and reverses. Several studies have provided evidence for such polarization inversions (e.g., Kundu *et al.* 1977; Webb *et al.* 1983; Alissandrakis & Kundu 1982, 1984; Brosius *et al.* 1992; Schmelz *et al.* 1992).

The radio polarization is inverted when coupling between the two propagation modes is weak. Zheleznyakov (1970), using the WKB method, obtained the following expression for the coupling parameter, given here in the notation of Bandiera (1982):

$$C_\nu = \frac{2\ln 2}{\pi^2}\frac{(m_e c)^4}{e^5}\frac{(2\pi\nu)^4}{n_e B^3}\left|\frac{d\theta}{ds}\right|, \tag{13.9}$$

where m_e and e are the rest mass and charge on an electron, c is the speed of light, ν is the observation frequency, n_e is the electron number density, B is the magnetic field strength, and $d\theta/ds$ is the gradient of the angle between the field and the line of sight along the ray path; all units are in CGS. The radio emission undergoes a polarization inversion when $C \ll 1$, or

$$4.766 \times 10^{-18}\frac{\nu^4}{n_e B^3}\left|\frac{d\theta}{ds}\right| \ll 1. \tag{13.10}$$

Schmelz *et al.* (1992) used the magnetic properties of the QT layer in the extrapolated coronal magnetic field above an active region to deduce the plasma density in those layers. They found that the *predicted* 1.5 GHz radio intensities calculated with the plasma temperature and emission measure derived from the SMM/XRP soft X-ray observations exceeded the observed values, thus requiring the presence of cooler absorbing plasma overlying the X-ray source.

Absorption in this cooler plasma reduced the predicted intensities to the observed values. However, by virtue of stronger absorption in the x-mode than in the o-mode, the resulting expected polarization was opposite that observed. This polarization would be inverted (to the observed value) in the QT layer if the modes were weakly coupled, so Schmelz *et al.* concluded that $C_{1.5} \ll 1$. Similarly, they found that no polarization inversion was required for the 4.9 GHz emission, and concluded that $C_{4.9} \gg 1$. Then, inserting values for the total field strength B (5.8 G) and the angular gradient along the line of sight $d\theta/ds$ (7.9×10^{-11} rad/cm) for the QT layer derived from the potential extrapolation, Schmelz *et al.* used $C_{4.9} \gg 1$ to place an upper limit $n_e \ll 1 \times 10^9$ cm^{-3} on the plasma density, and $C_{1.5} \ll 1$ to place a lower limit $n_e \gg 1 \times 10^7$ cm^{-3}. Both conditions were satisfied by $n_e \approx 10^8$ cm^{-3} in the QT layer.

4. Coronal Iron Abundance

The intensity of an optically thin emission line (which most solar EUV and soft X-ray lines are) is given by

$$I = \frac{1}{4\pi} \frac{N_E}{N_H} \int G(T)\phi(T)dT \quad \text{erg cm}^{-2}\ \text{s}^{-1}\ \text{sr}^{-1}, \tag{13.11}$$

where N_E/N_H is the abundance of the given element (E) with respect to hydrogen (H), $G(T)$ contains the atomic physics parameters pertaining to the given line (all of which, in principle, are known: excitation rates, spontaneous emission rates, branching ratios, fractional ionization, and energy of the transition), and $\phi(T)$ is the differential emission measure (DEM; $n_e^2 dh/dT$). The DEM provides a measure of the amount of plasma at temperature T (Withbroe 1975; Pottasch 1963). The "formation temperature" of an emission line is the temperature of the plasma from which the maximum contribution to the line's total intensity is emitted; typically, it is also the temperature corresponding to the maximum fractional abundance of the relevant ion. Such abundances are obtained theoretically, for example, under the assumption of ionization equilibrium (e.g., Mazzotta *et al.* 1998; Arnaud & Raymond 1992; Arnaud & Rothenflug 1985).

Measured intensities I_i of EUV and/or soft X-ray lines formed at different temperatures T_i are used to calculate $\phi(T)$ by inverting the above integral: $\phi(T)$ is derived such that theoretical line intensities match the observed ones within the measurement uncertainties. This inversion is non-trivial, and numerous authors have developed different methods to carry it out; see Landi & Landini (1997), Schmelz *et al.* (1999), and the conference proceedings edited by Harrison & Thompson (1991) and references therein.

Note that the DEM depends directly upon the intensities of the emission lines used to obtain it, as well as the abundances of the elements of those lines. Thus, in order to calculate an accurate DEM, the intensities of the emission lines must

be well calibrated, and the abundances of the elements must be known reliably. Unfortunately, coronal elemental abundances are a subject of controversy (e.g., Meyer 1991), and there is evidence that no single set of coronal abundances can be applied to solar active regions under all circumstances (Saba & Strong 1993). This situation inspired White *et al.* (2000) to apply a new technique for measuring the coronal abundance of iron in an active region.

Basically, White *et al.* obtained coordinated, well calibrated EUV and VLA radio observations of an active region with sufficiently weak magnetic fields that the radio emission was due to thermal bremsstrahlung only. The thermal bremsstrahlung condition was established by the facts that the structures in the EUV and radio images mimicked each other closely, the radio polarization was low, and the radio spectrum (determined with the radio frequencies of 1.4, 4.8, and 8.4 GHz) was flat. Using the Coronal Diagnostic Spectrometer (CDS) aboard the NASA/ESA Solar and Heliospheric Observatory SOHO satellite, White *et al.* (2000) measured the intensities of emission lines from eight successive ionization stages of iron (Fe^{+9} = Fe X through Fe^{+16} = Fe XVII) covering the temperature range $1.0 \times 10^6 \leq T_i \leq 4.0 \times 10^6$ K. (In this notation, un-ionized iron is written as Fe I.) These observations were obtained on 1997 November 11, one week before the SERTS cross-calibration underflight. Based upon the coordinated SERTS and CDS observations acquired on 1997 November 18 (see Figure 13.1), Thomas *et al.* (1999) derived modifications to the CDS calibration that were incorporated into the CDS software and applied to the observations of White *et al.* (2000), thus providing a reliable absolute radiometric calibration for the iron line intensities used to calculate the DEM. Thus the only source of uncertainty in the DEM calculation was the iron abundance.

The DEM was derived assuming a given Fe abundance, and used to calculate the thermal bremsstrahlung radio brightness temperature. (See Eq. (13.2), where the column emission measure at temperature T is obtained by integrating the DEM over the temperature range T to $T + dT$.) By equating the observed and calculated thermal bremsstrahlung radio brightness temperatures at all three radio observing frequencies, the coronal iron abundance was determined to be $1.56 \pm 0.31 \times 10^{-4}$, in agreement with Feldman (1992). This value is 4 times the photospheric value, consistent with other measured coronal abundance enhancements for elements of low first ionization potential (FIP; e.g., Meyer 1991, Saba & Strong 1993).

Coronal elemental abundances are important for coronal magnetography because they directly impact the DEM, which is needed to calculate the free-free contribution to the radio brightness temperature in order to accurately determine the observed gyroresonance harmonics (see next section). FASR will enable more frequent observations of weak, thermal bremsstrahlung regions (including quiet-Sun areas) to measure the abundances of iron and other elements when coordinated EUV and/or soft X-ray observations can be obtained.

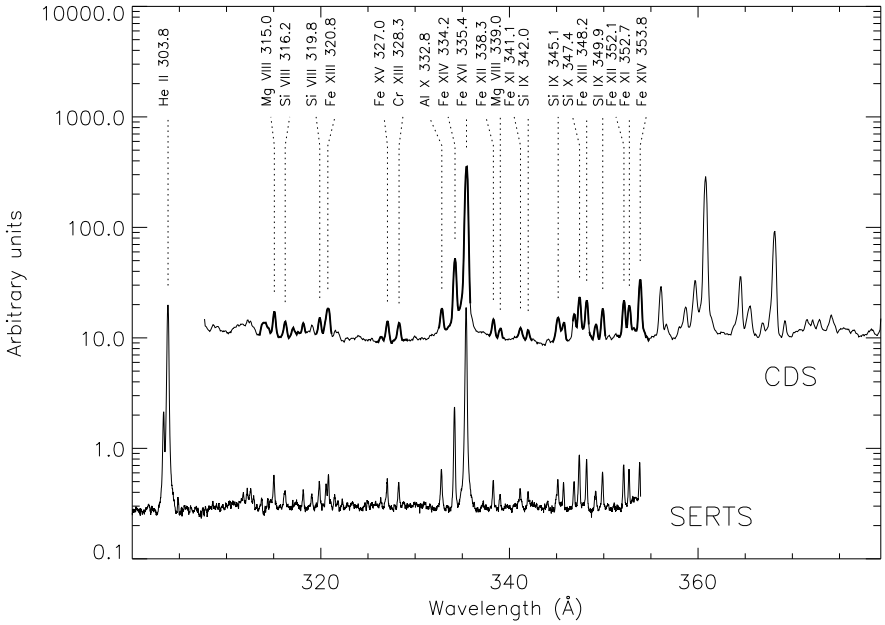


Figure 13.1. CDS and SERTS spectra from the 1997 November 18 rocket flight. Portions of the CDS spectrum in boldface indicate the spectral windows that were observed at the same time as the SERTS flight; other portions of the spectrum were obtained before and after the rocket flight. Lines from six ionization stages of iron (XI–XVI) are marked on the figure; lines from Fe X and XVII are also in this waveband.

With FASR it will be possible to monitor abundance variations with time in emerging and/or decaying active regions. Further, studies of where, when, and how coronal elemental abundances are organized according to FIP will advance our understanding of transport in the solar atmosphere.

5. 3D Coronal Magnetography

It is widely believed that magnetic processes heat the solar corona, drive the solar wind, and trigger solar flares. Therefore, measurements of coronal magnetic fields may provide the key to understanding these phenomena. We describe Brosius *et al.*'s (2002) treatment of coordinated EUV and radio obser-

vations of NOAA Active Region 8108 on 1997 November 18 as an example of three-dimensional solar coronal magnetography.

Radio observations were obtained with the VLA, and EUV observations were obtained with CDS and the Extreme-ultraviolet Imaging Telescope (EIT) aboard SOHO. In addition, coordinated SERTS sounding rocket observations (Brosius *et al.* 2000) provided a reliable cross calibration standard (Thomas *et al.* 1999) for the SOHO instruments, as well as density sensitive line intensity ratios. Finally, the Michelson Doppler Imager (MDI) aboard SOHO was used to obtain photospheric longitudinal magnetograms from which potential extrapolations (Sakurai 1982) were derived for comparison with the 3D fields derived as described below. See Figure 13.2.

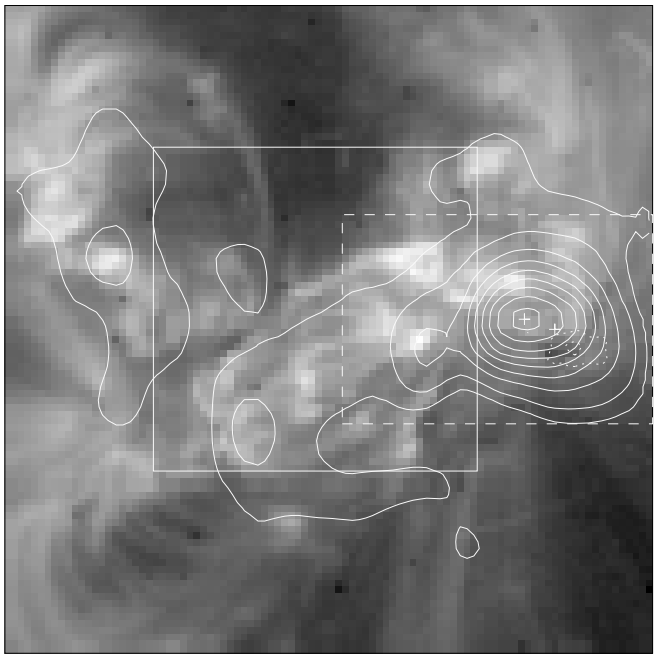


Figure 13.2. Fe XII 195 Å $4' \times 4'$ EIT image of NOAA AR 8108 around 1940 UT on 1997 Nov 18, with (1) VLA T_b^R(5 GHz) contours at 0.1, 0.25, 0.5, 0.75, 1.0, 1.25, 1.5, 1.75, and 2.0 $\times 10^6$ K (solid); (2) MDI B_z contours of +1000 and +1500 G (dotted); (3) CDS and SERTS $2' \times 2'$ sub-FOV (solid); (4) Radio centroids of T_b^R(5 GHz) and T_b^R(8 GHz) (crosses); and (5) $1'.9 \times 1'.3$ area for magnetography (dashed). The heliocentric location of the spot in this image is (-185″, +295″), i.e., north and east of disk center.

The coronal magnetography method developed by Brosius *et al.* (1997, 2002) uses the right-hand (R) and left-hand (L) circularly polarized components of the radio observing frequencies, along with the coordinated EUV observations, in

an iterative procedure to obtain the temperature distribution of the total magnetic field strength $B(x, y, T)$ for each spatial location (x, y) in and around an active region sunspot. Temperature is used as the independent variable since the relationship between height and magnetic field is poorly constrained by the data (e.g., White & Kundu 1997), and the temperature dependence of the derived coronal magnetic field is relatively insensitive to uncertainties on the observed parameters. Ultimately, however, $B(x, y, T)$ is converted to $B(x, y, h)$.

Brosius *et al.* (2002) were the first to apply CDS and EIT data to the problem of coronal magnetography. These data enabled significant improvements over previous coronal magnetography measurements by providing (1) a *measured* (rather than *estimated*, as in Brosius *et al.* 1997) pixel-by-pixel (i.e., two-dimensional) differential emission measure, which enables the treatment of a realistic, non-isothermal corona; and (2) a measured two-dimensional (rather than a single-spectrum average active region) electron density distribution. In addition, Brosius *et al.* (2002) developed and applied a new algorithm to iteratively select the temperature intervals into which the largest, dominant harmonics for each radio observing frequency must be placed in order to reproduce the observed brightness temperatures. Further, through projection effects, the radio observations themselves provided a direct measure of an upper limit on the magnetic scale height L_B as well as evidence that the coronal temperature increased with height. Thus the temperature dependence of the coronal magnetic field was converted to a height dependence with greater confidence than could be done in earlier studies.

The sunspot was located at heliocentric coordinates $(-185'', +295'')$, i.e., north and east of disk center. The centroids of the observed L and R components of 8.450 GHz and the centroids of the observed L and R components of 4.866 GHz shifted systematically to the north and east relative to the photospheric sunspot (see Figure 13.2). This is consistent with the emission of these components being due to thermal gyroemission from successively lower magnetic field strengths occurring at successively greater heights, viewed in projection. The shift, combined with an increase in centroid brightness temperature with increasing displacement, indicated that the coronal temperature increases with height. The shift in centroid displacements was also used to estimate L_B, the magnetic scale height $(B/\nabla B)$. Based upon the sunspot's location, a viewing angle of $20^{\circ}.8$ relative to the line of sight was obtained. This, combined with the measured separations among the various centroids and knowing that the R components were dominated by 3rd harmonic emission (see below) while the L components were dominated by 2nd, yielded a magnetic scale height $L_B \sim 3.8 \times 10^9$ cm. Since there was no guarantee that the centroid shifts were due entirely to projection effects, the measured L_B was interpreted as an upper limit. This is consistent with other measured values of $(2.4 \pm 0.1) \times 10^9$ cm (Aschwanden *et al.* 1995), $> 0.73 \times 10^9$ cm (Gary *et al.* 1993), 0.54×10^9 cm

(Lee, Gary, & Hurford 1993), $(0.74 \pm 0.23) \times 10^9$ cm (Kruger *et al.* 1986). Taking $L_B \sim 1 \times 10^9$ cm as a canonical value, magnetography calculations were performed using two values for L_B: 3.8×10^9 and 1.0×10^9 cm.

Brosius *et al.* (2002) derived 2D arrays of DEM curves with the methods of both Landi & Landini (1997) and Cook *et al.* (1999), using the Feldman (1992) coronal element abundances, the CHIANTI (Dere *et al.* 1997; Young, Landi & Thomas 1998) Version 2.0 atomic physics database (Landi *et al.* 1999), and the Mazzotta *et al.* (1998) ionization equilibrium computations. In addition, they obtained theoretical density sensitive line intensity ratios from the CHIANTI database, and derived a map of the Fe XIV density from intensity images of density sensitive line pairs. Although such ratios were not available over a wide temperature range, they were available for lines formed at temperatures corresponding to the radio brightness temperatures. Calculations were performed using two simple density distributions consistent with the available observations: one in which the density remained constant (the value derived from Fe XIV) with temperature, and the other in which the pressure (derived from Fe XIV) remained constant with temperature. Thus coronal magnetography calculations were performed for a total of four different parameter sets (two different L_B values and two different density distributions).

For each spatial location or, in this case, each $2''.5 \times 2''.5$ image pixel inside the dashed box in Figure 13.2, the solar atmosphere was divided into discrete intervals of uniform temperature (T-intervals) such that the hottest plasma ($\log T = 6.4$) was on top, and the temperature decreased downward (to $\log T = 5.0$). This was the simplest temperature structure that was consistent with the observations described above, and could have been adjusted as needed to satisfy constraints imposed by the coordinated EUV and radio observations. Every image pixel corresponded to a unique line of sight. For each line of sight the angle between the field and the line of sight was taken to increase from 20° (the projection angle) at the top ($\log T = 6.4$) to 45° at $\log T = 5.7$, and remain constant below that. It was important that the angle remained relatively small, or else both modes of any given radio observing frequency would be optically thick in the same harmonic (see Eq. 13.3) in the same T-interval, and the observed difference between the R and L (or between the x and o) components at that frequency could not be reproduced.

The opacity of the i'th interval (at any given radio frequency) is

$$\Delta\tau_i^{x,o} = \Delta\tau_{ff,i}^{x,o} + \Delta\tau_{gr,i}^{x,o}, \tag{13.12}$$

where all parameters have the same meaning as in (13.1). Similarly, the free-free and gyroresonant optical thicknesses of the i'th interval can be adapted from (13.2) and (13.3) by including subscripts i. For brevity they will not be repeated here. The radio emission from each discrete T-interval in the solar atmosphere passes through the overlying intervals prior to exiting the atmosphere, and is

modified by the total opacity of those layers. The total optical depth of each interval is given by the sum of the optical thicknesses of all of the overlying intervals

$$\tau_i^{x,o} = \sum_{j=1}^{i} \Delta\tau_{j-1}^{x,o}, \tag{13.13}$$

and $\tau_0^{x,o} = 0$. The contribution to the total brightness temperature from the i'th interval is

$$\Delta T_{b,i}^{x,o} = T_i[1 - \exp(-\Delta\tau_i^{x,o})] \exp(-\tau_i^{x,o}). \tag{13.14}$$

The total radio brightness temperature is calculated by summing over the contributions from all of the discrete temperature intervals at their corresponding optical depths:

$$T_b^{x,o} = \sum \Delta T_{b,i}^{x,o}. \tag{13.15}$$

The key to deriving coronal magnetic field strengths from solar radio observations is to determine, first of all, the dominant radio emission mechanism. If the emission measure is large enough that the free-free mechanism alone is adequate to produce the observed radio brightness temperatures, then the magnetic field strength may be derived from the observed polarization as described in §13.2. If the emission measure is so small that the free-free mechanism alone is not adequate to produce the observed radio brightness temperatures, then thermal gyroemission must be included, and the appropriate harmonic number for both modes of each radio observing frequency determined. Brosius *et al.* (2002) restricted their solutions to the *greatest* harmonics (which correspond to the smallest magnetic field strengths) that could possibly do the job. (Recall that gyroresonance opacity increases with decreasing harmonic number.) Thus they required that their solution contains the smallest possible magnetic field strengths. They accomplished this by placing a given harmonic (say, 5th) for the x-mode of the smallest radio observing frequency in *every* T-interval along the line of sight, and calculating the corresponding theoretical contributions to the radio brightness temperature from each interval. If the maximum such contribution was less than the corresponding observed value, they tried the next smaller harmonic and repeated the procedure. For a given line of sight, the solution was found when the maximum theoretical radio brightness temperature contribution exceeded the observed value. This harmonic of this frequency along this line of sight was later placed in a *lower* T-interval such that the calculated radio brightness temperature along the line of sight (incorporating free-free as well as gyroemission, and treating both x- and o-modes of the given radio observing frequency simultaneously) matched the observed value.

They then applied an iterative procedure in which the x-mode harmonic at a given frequency was initially placed in a low T-interval and successively moved to higher T-intervals until agreement was reached between the observed

and calculated brightness temperatures. This process was repeated for the o-mode of the same frequency, where contributions from both the x-mode's and o-mode's harmonics were included. (The x-mode is typically optically thick enough that the contribution from the next lower harmonic does not affect the x-mode's brightness temperature.) Free-free contributions were always included, and the procedure was repeated for both frequencies. Thus, for each line of sight, they placed at most four harmonics (four B values) within appropriate T-intervals. The procedure was performed in each $2''.5 \times 2''.5$ (x, y) spatial pixel in the region (the dashed box in Figure 13.2), but was restricted to the radio components whose observed brightness temperatures exceeded both the free-free contribution and a lower limit of 2×10^5 K. Thus for some spatial pixels they placed no B values at all within any T-intervals (which means that the magnetic field in those pixels was less than the measurement threshhold), while in other pixels they placed 1, 2, 3, or 4 values.

For spatial pixels in which two or more B values were placed into T-intervals, the slope $\Delta B/\Delta T$ was derived between T-intervals within which magnetic field values were placed, and a simple linear interpolation performed to derive $B(T)$ between those T-intervals. This yielded $B(x, y, T)$ along the line of sight for field strengths appropriate to the radio observing frequencies. See Figure 13.3. Maps of the coronal magnetic field $B(x, y, T)$ were obtained by combining results for each spatial pixel (x, y) within which $B(T)$ was derived. See Figure 13.4. Field strengths in excess of 580 G were found in the 2×10^6 K plasma, while field strengths in excess of 1500 G were found in the 1×10^6 K plasma. Theoretical radio brightness temperature maps were obtained by integrating along each line of sight, including all harmonics present. Agreement between these and the observed maps (see Figure 13.5) served as a consistency check for the derived coronal magnetic field strength.

For T-intervals above (below) the largest (smallest) T-interval into which a magnetic field strength value (harmonic) was placed, one could extrapolate the magnetic field strength using the same slope that was derived in the other intervals; however, such extrapolations could not be verified because radio observations at the appropriate frequencies were not available. This is one area in which FASR will enable vast improvements: by providing numerous additional radio observing frequencies, it will sample numerous additional magnetic field strengths (and temperatures) along each line of sight. Thus, FASR will not only expand the T-range within which B is measured, but also provide a more dense sampling of B within that range.

The temperature dependence of the coronal magnetic field $B(x, y, T)$ was converted to height dependence $B(x, y, h)$ by calculating the thicknesses of the individual T-intervals along each line of sight. The heights of the various T-intervals were obtained by summing the thicknesses of their underlying

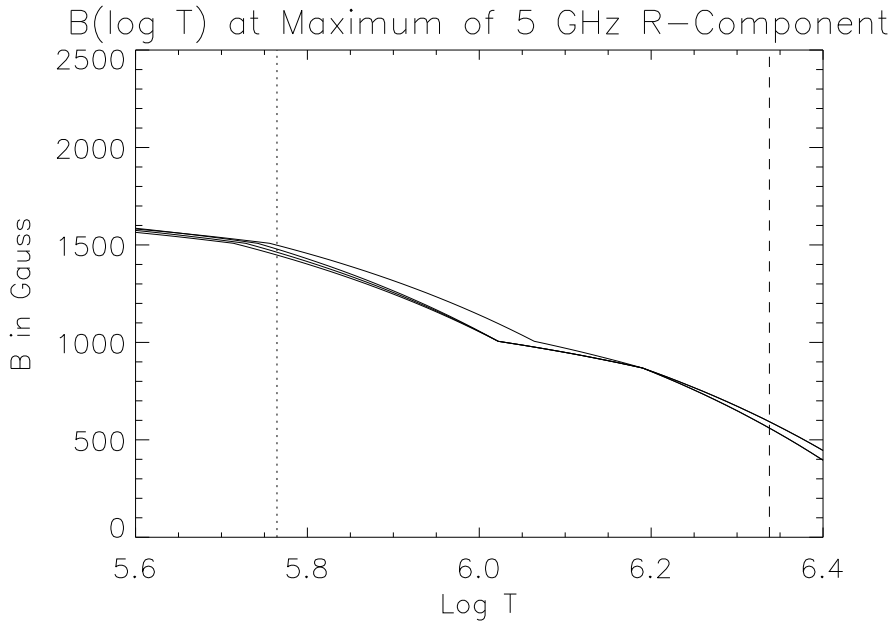


Figure 13.3. $B(T)$ at the centroid of the right-hand circularly polarized component of the 4.866 GHz emission, for all four combinations of density distribution (n_e=constant or p_e=constant, based on Fe XIV) and L_B (1.0 or 3.8 $\times 10^9$ cm). Evident blending of the curves indicates that our solution is relatively insensitive to L_B and the plasma density distribution. Dotted and dashed vertical lines bound the T-range within which B can be reliably determined at this location. Similar figures can be plotted for every spatial pixel in the region. By providing observations at higher and lower radio frequencies, FASR will expand the temperature range within which the magnetic field is reliably measured.

intervals, and assuming that the height of the lowest T-interval above the photosphere was 2000 km.

The thicknesses of the T-intervals were derived using two methods. The first involved the definition of magnetic scale height. For the i'th T-interval, substituting $\nabla B_i = \Delta B_i / \Delta \ell_i$ into $L_B = B_i / \nabla B_i$ yields

$$\Delta \ell_i = L_B \Delta B_i / B_i, \tag{13.16}$$

where ΔB_i, the change in magnetic field strength across the i'th T-interval, was taken to be one half the change in magnetic field strength between the two surrounding T-intervals, i.e., $(B_{i+1} - B_{i-1})/2$. The second method involved the definition of the column emission measure. For the i'th T-interval $CEM_i = n_{e,i}^2 \Delta \ell'_i$, which immediately yields

$$\Delta \ell'_i = CEM_i / n_{e,i}^2. \tag{13.17}$$

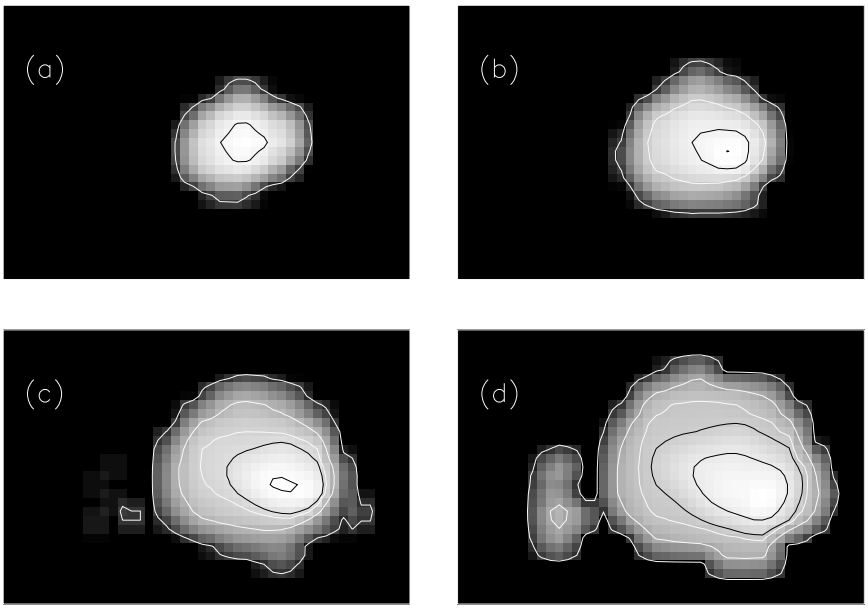


Figure 13.4. "Slices" of $B(x, y, T)$ along isothermal surfaces at (*a*) 2.0×10^6 K, (*b*) 1.5×10^6 K, (*c*) 1.0×10^6 K, and (*d*) 0.5×10^6 K. Contour levels are 100, 580, 870, 1000, and 1500 G, the last four values corresponding to 3rd & 2nd harmonics of 4.866 GHz, and 3rd & 2nd harmonics of 8.450 GHz. Inner contours in these $1'.9 \times 1'.3$ images are drawn in darker color to enhance visibility.

Figure 13.6 shows the height dependence of the coronal magnetic field derived at the centroid of the right-hand circularly polarized component of the 4.866 GHz emission. Heights were derived using both methods above (with two values for L_B in the first), as well as the Sakurai (1982) potential field extrapolation code. Note that $B(h)$ varied significantly with L_B. Based upon $L_B = 3.8 \times 10^9$ cm derived from the relative displacements of the observed radio centroids, magnetic field strengths exceeded 1500 G at heights of 15,000 km, and 1000 G at 25,000 km. Also note that the magnitudes of the potential field strengths are factors of two or more smaller than those derived from the coordinated radio and EUV data. This indicates that the sunspot field was not potential, and that currents must have been present in the corona. Observations of a given target region on several successive days would yield a variety of projection angles, thus enabling a better determination of L_B and, ultimately, $B(x, y, h)$. Continuous, full disk FASR observations would enable vast improvements in this area.

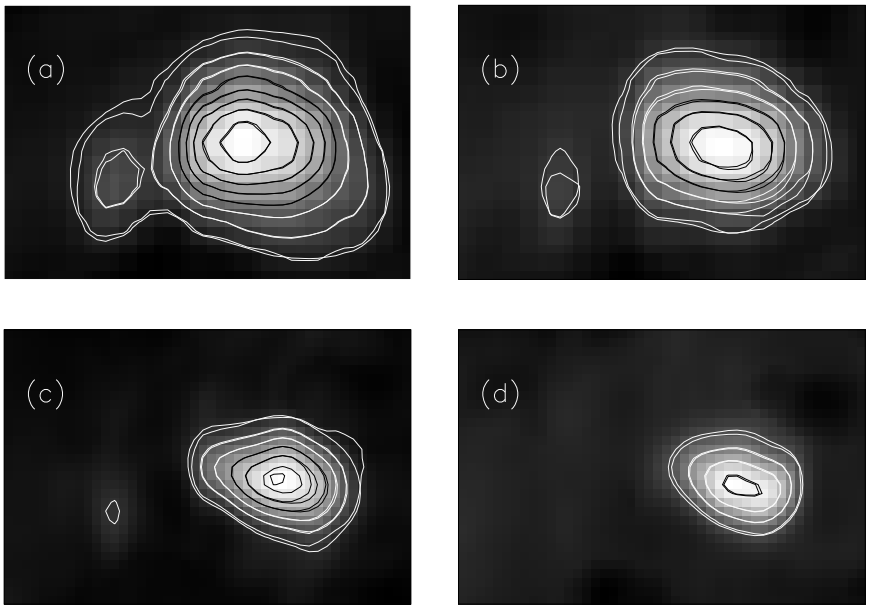


Figure 13.5. Observed radio maps, with observed *and calculated* brightness temperature contours of 0.25, 0.5, 0.75, 1.0, 1.25, 1.5, 1.75, 2.0 MK for (a) the 4.866 GHz x-mode, (b) the 4.866 GHz o-mode, (c) the 8.450 GHz x-mode, and (d) the 8.450 GHz o-mode. The close agreement between the observed and calculated contours supports the reliability of our derived 3D coronal magnetogram $B(x, y, T)$.

Alfvén waves are transverse MHD waves that travel along magnetic field lines at speed $V_A = B[4\pi\rho]^{-1/2}$, where ρ is the mass density of the medium. The Alfvén speed is important because it determines timescales on which wave energy can be deposited (for, e.g., coronal heating), or solar structures may vary. Alfvén speeds between 25,000 and 57,000 km s^{-1} were derived for the 1×10^6 K plasma at the centroids of the radio observing frequencies, consistent with values found by Brosius *et al.* (1992) from CoMStOC observations (10,000 - 40,000 km/s). See Figure 13.7.

6. Future of Coordinated Radio and EUV/Soft X-ray Observations

As a solar-dedicated radio telescope, FASR will provide daily coverage of the entire solar disk over a wide portion of its $0.1 \leq \nu_9 \leq 30$ GHz frequency range, thus providing much more frequent measurements of coronal properties

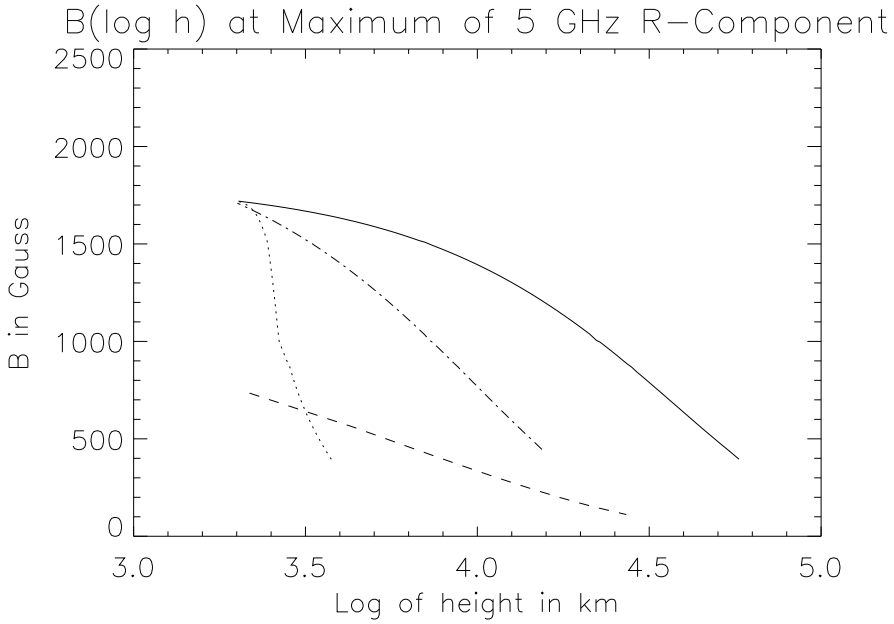


Figure 13.6. $B(h)$ derived with n_e=constant and *(solid curve)* $L_B = 3.8 \times 10^9$, *(dash-dotted curve)* $L_B = 1 \times 10^9$, and *(dotted curve)* CEM/n_e^2. The dashed curve shows the potential field derived from the MDI photospheric longitudinal magnetogram with the Sakurai (1982) code.

than can be obtained with existing radio instrumentation (like the VLA) which must be shared by the entire astronomical community.

Coordinated observations between FASR and future EUV imagers and spectrometers promise vast improvements over our current capabilities for measuring and understanding coronal properties. For example, the Extreme-ultraviolet Imaging Spectrometer (EIS), under construction (as of this writing) for the Solar-B satellite, will provide spectral imaging capability in the 170 - 210 and 250 - 290 Å wavebands. These wavebands include lines from Fe VIII through Fe XVI and S VIII through S XIII (e.g., Brosius *et al.* 1998), which means that EIS observations can be used to obtain maps of DEM curves based upon one or the other of these two elements. The abundances of these two elements can be determined separately by applying the method of White *et al.* (2000). Further, since most active regions will likely emit only thermal bremsstrahlung at FASR's higher radio frequencies, it may be possible to measure element abundances in almost all active regions using this same method. Ultimately, temporal variations in coronal elemental abundances will be measured in active regions and quiet-sun areas. Studies of where, when, and how coronal elemen-

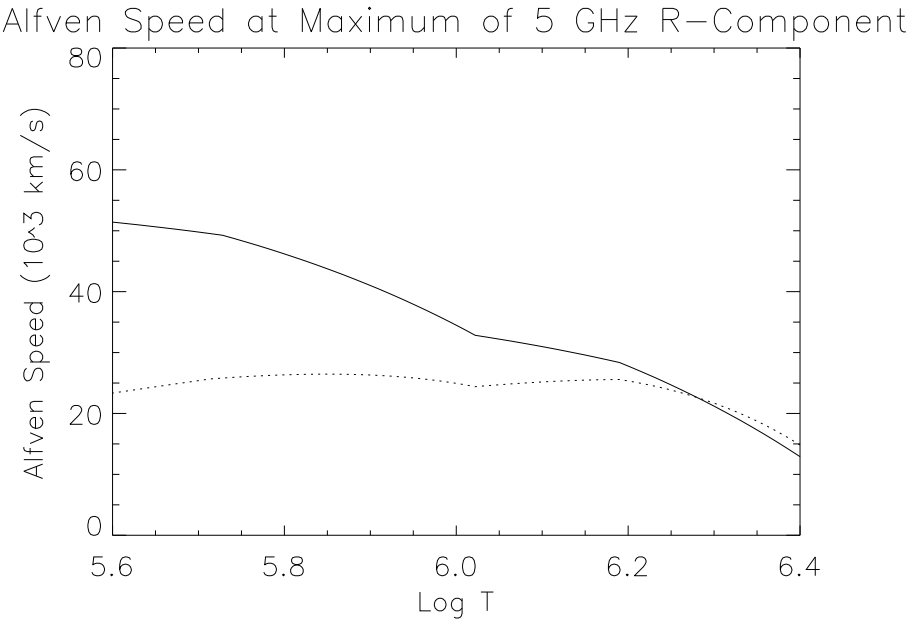


Figure 13.7. Alfvén speed $V_A(T) = B(T)[4\pi\rho(T)]^{-1/2}$ derived with *(solid curve)* n_e=constant and *(dotted curve)* p_e=constant. L_B has very little effect on $V_A(T)$.

tal abundances are organized according to FIP will advance our understanding of transport in the solar atmosphere.

With its wide frequency range of $0.1 \leq \nu_9 \leq 30$ GHz, FASR will be sensitive to coronal magnetic field strengths between 12 and 5400 G (assuming 3rd and 2nd harmonic gyroemission), a wider range than is currently available with the VLA. This will enable the measurement of coronal magnetograms not only in active regions, but in quiet Sun areas as well. FASR will also expand the temperature range within which the coronal magnetic field is measured, and provide a more dense sampling of the field within that range. The coronal magnetography method of Brosius *et al.* (2002) described above will be regularly performed with FASR data both on the disk and above the limb, so that the height dependence (and the magnetic scale height) of the coronal magnetic field will be unambiguously determined. Further, time variations of coronal magnetic fields will be studied for a variety of solar features and conditions, including flares. Since magnetic processes like reconnection are believed to trigger flares, it will be especially valuable to measure coronal magnetic fields in a flaring active region both before and after a flare, to look for changes in the field strength or structure. It is expected that the methods for measuring coronal

magnetograms will improve with time and experience, so that the acquisition of full disk coronal magnetograms may eventually become routine.

Acknowledgments

J. W. B. gratefully acknowledges NASA support through contract NAS5-99145 and grant NAG5-11757.

References

Acton, L. W. & 9 co-authors 1980, Sol. Phys. 65, 53.
Alissandrakis, C. E. & Kundu, M. R. 1982, ApJ 253, L49
Alissandrakis, C. E. & Kundu, M. R. 1984, A&A 139, 271
Arnaud, M. & Raymond, J. 1992, ApJ 398, 394
Arnaud, M. & Rothenflug, R. 1985, A&AS 60, 425
Aschwanden, M. J., Lim, J., Gary, D. E. & Klimchuk, J. A. 1995, ApJ 454, 512
Bandiera R. 1982, A&A 112, 52
Bogod, V. M., Gelfreikh, G. B., Willson, R. F., Lang, K. R., Opeikina, L. V., Shatilov, V. & Tsvetkov, S. V. 1992, Sol. Phys 141, 303
Brosius, J. W., Davila, J. M. & Thomas, R. J. 1998, ApJS 119, 255
Brosius, J. W., Davila, J. M., Thomas, R. J. & White, S. M. 1997, ApJ 488, 488
Brosius, J. W., Holman, G. D. & Schmelz, J. T. 1991, Eos 72, 449
Brosius, J. W., Davila, J. M., Thompson, W. T., Thomas, R. J., Holman, G. D., Gopalswamy, N., White, S. M., Kundu, M. R. & Jones, H. P. 1993, ApJ 411, 410
Brosius, J. W., Landi, E., Cook, J. W., Newmark, J. S., Gopalswamy, N. & Lara, A. 2002, ApJ 574, 453
Brosius, J. W., Thomas, R. J., Davila, J. M. & Landi, E. 2000, ApJ 543, 1016
Brosius, J. W., Willson, R. F., Holman, G. D. & Schmelz, J. T. 1992, ApJ 386, 347
Cohen, M. H. 1961, ApJ 133, 978
Cook, J. W., Newmark, J. S. & Moses, J. D. 1999, Proc. 8th SOHO Workshop, ESA SP-446, 241
Dere, K. P., Landi, E., Mason, H. E., Monsignori-Fossi, B. C. & Young, P. R. 1997, A&AS 125, 149
Feldman, U. 1992, Phys. Scr. 46, 202
Gary, D. E. & Hurford, G. J. 1994, ApJ 420, 903
Gary, D. E., LeBlanc, Y., Dulk, G. A. & Golub, L. 1993, ApJ 412, 421
Golub, L. & Pasachoff, J. M. 1997, The Solar Corona (Cambridge: University Press)
Harrison, R. A. & Thompson, A. M. (editors) 1991, "Intensity Integral Inversion Techniques: a Study in Preparation for the SOHO Mission," RAL-91-092

Holman, G. D. 1986, in "Coronal and Prominence Plasmas," ed. A. I. Poland, NASA CP-2442, 297
Kruger, A., Hildebrandt, J., Bogod, V. M., Korzhavin, A. N., Akhmedov, S. B. & Gelfreikh, G. B. 1986, Sol. Phys. 105, 111
Kundu, M. R. 1965, Solar Radio Astronomy, New York: Wiley & Sons
Kundu, M. R., Alissandrakis, C. E., Bregman, J. D. & Hin, A. C. 1977, ApJ 213, 278
Kundu, M. R., Schmahl, E. J. & Gerassimenko, M. 1980, A&A 82, 265
Kundu, M. R., Schmahl, E. J. & Rao, A. P. 1981, A&A 94, 72
Landi, E. & Landini, M. 1997, A&A 327, 1230
Landi, E., Landini, M., Dere, K. P., Young, P. R. & Mason, H. E. 1999, A&AS 135, 339
Lang, K. R. *et al.* 1993, ApJ 419, 398
Lang, K. R., Willson, R. F., Smith, K. L. & Strong, K. T. 1987a, ApJ 322, 1035
Lang, K. R., Willson, R. F., Smith, K. L. & Strong, K. T. 1987b, ApJ 322, 1044
Lee, J., Gary, D. E. & Hurford, G. J. 1993, Sol. Phys. 144, 349
Mazzotta, P., Mazzitelli, G., Colafrancesco, S. & Vittorio, N. 1998, A&AS 133, 403
Meyer, J.-P. 1991, Adv. Space Res. 11, No. 1, 269
Nitta, N., White, S. M., Kundu, M. R., Gopalswamy, N., Holman, G. D., Brosius, J. W., Schmelz, J. T., Saba, J. L. R. & Strong, K. T. 1991, ApJ 374, 374
Pallavicini, R., Sakurai, T. & Vaiana, G. S. 1981, A&A 98, 316
Pottasch, S. R. 1963, ApJ 137, 945
Saba, J. L. R. & Strong, K. T. 1993, Adv. Space Res. 13, No. 9, 391
Sakurai, T. 1982, Sol. Phys. 76, 301
Schmelz, J. T., Holman, G. D., Brosius, J. W. & Gonzalez, R. D. 1992, ApJ 399, 733
Schmelz, J. T., Holman, G. D., Brosius, J. W. & Willson, R. F. 1994, ApJ 434, 786
Schmelz, J. T., Saba, J. L. R., Strong, K. T., Winter, H. D. & Brosius, J. W. 1999, ApJ 523, 432
Shibasaki, K., Chiuderi-Drago, F., Melozzi, M., Slottje, C. & Antonucci, E. 1983, Sol. Phys. 89, 307
Sturrock, P. A. 1994, Plasma Physics (Cambridge: University Press)
Thomas, R. J., Davila, J. M., Thompson, W. T., Kent, B. J. & Hollandt, J. 1999, BAAS 31, 850
Webb, D. F., Davis, J. M., Kundu, M. R. & Velusamy, T. 1983, Sol. Phys. 85, 267
Webb, D. F., Holman, G. D., Davis, J. M., Kundu, M. R. & Shevgaonkar, R. K. 1987, ApJ 315, 716
White, S. M. & Kundu, M. R. 1997, Sol. Phys. 174, 31

White, S. M., Thomas, R. J., Brosius, J. W. & Kundu, M. R. 2000, ApJ 534, L203
Withbroe, G. L. 1975, Sol. Phys. 45, 301
Young, P. R., Landi, E. & Thomas, R. J. 1998, A&A 329, 291
Zheleznyakov, V. V. 1970, Radio Emission of the Sun and Planets, ed. J. S. Hey (Oxford: Pergamon)
Zlotnik, E. Y. 1968, Soviet Astron. 12, 245

Chapter 14

RADIO OBSERVATIONS OF THE QUIET SUN

Christoph U. Keller
National Solar Observatory, 950 N. Cherry Ave., Tucson, AZ 85719, USA
ckeller@noao.edu

Säm Krucker
Space Sciences Laboratory, University of California, Berkeley, CA 94720, USA
krucker@ssl.berkeley.edu

Abstract While radio observations of the Sun have mostly focused on active region phenomena, they also contribute unique data to our knowledge of the quiet Sun, in particular through accurate measurements of the temperature as a function of height in the atmosphere and through the measurement of nonthermal emissions from chromospheric and coronal heating events. Here we review observations of the quiet Sun using radio telescopes and discuss current science problems that will be addressed with future facilities such as the Frequency Agile Solar Radiotelescope (FASR).

Keywords: quiet Sun, temperature structure, coronal heating, prominence, filament, coronal hole

1. Introduction

An article on the quiet Sun needs to start with a definition of the term "quiet Sun." This is particularly important for radio observations that cover a large range of radial distances from the solar surface. In the context of the present review, we define the quiet Sun as those phenomena in the solar atmosphere that are not related to active regions. It therefore includes stationary structures such as coronal holes and quiescent filaments and prominences as well as transient phenomena such as those believed to be associated with heating of the transition region and the corona above the quiet photosphere.

Studying the quiet Sun has advantages over trying to grasp the complex phenomena in active regions because one deals with less complex magnetic field topologies and a supposedly simpler structure of the stratified atmosphere. In the photosphere and parts of the chromosphere, the quiet Sun is dominated by phenomena related to convection. Any energy input to the nonthermal heating of the upper chromosphere and corona in the quiet Sun must ultimately have the convective energy as its origin. Magnetic fields are considered to be the most likely channels for transporting the energy from the photosphere through the chromosphere and the transition region into the corona.

While most solar radio observations have focused on active region phenomena such as flares and coronal mass ejections, there are several areas in which the radio regime provides particularly important diagnostic capabilities to address questions regarding the quiet Sun:

- Radio observations provide a linear thermometer that can be scanned in height by changing the frequency of the observations;
- Radio observations show nonthermal heating events in the quiet upper chromosphere, the transition region, and the corona;
- Radio observations of the circular polarization are sensitive to the line-of-sight component of the coronal magnetic field.

We will discuss these areas in detail in the following sections. Radio observations of the quiet Sun have also been used to study problems associated with oscillations (e.g. Tsvetkov 1986; Borovik *et al.* 1997), but we will not discuss these observations any further because they have so far not led to fundamentally new insights about the quiet Sun.

Recent reviews of quiet Sun radio physics can be found in the 1998 proceedings of the Japanese National Radio Observatory conference (Bastian *et al.* 1999). In particular, Shibasaki (1999) reviewed microwave (10–30 GHz) and Lantos (1999) reviewed low-frequency (30–400 MHz) quiet Sun studies. Here we concentrate on the higher frequencies and discuss the more recent literature that has appeared since those reviews were prepared.

We start with short discussions of general issues associated with radio observations of the quiet Sun and list present and future radio telescopes that are suitable for quiet Sun studies. The majority of this chapter is divided into three areas: observations of the thermal emission from the quiet Sun to determine average atmospheric properties, observations of quiescent prominences and filaments, and observations of nonthermal emission thought to be connected with heating of the chromosphere and the corona.

2. Observing the quiet Sun at radio wavelengths

Radio emission from the quiet Sun is in the form of continuum radiation without significant spectral lines (but see Dravskikh & Dravskikh 1988 and Boreiko & Clark 1986). The lack of significant spectral lines is no surprise because the emission of plasma waves by atoms is more effective than the emission of ordinary photons in a turbulent plasma (e.g. Kaplan *et al.* 1977). Furthermore, collisional broadening of the closely-spaced energy levels that would be involved at radio wavelengths inhibits bound-bound transitions.

The absence of spectral lines limits the diagnostic capabilities of radio observations. On the other hand, the absence of complicated atomic and radiative transfer processes makes calculations much more simple. Nevertheless, wideband spectra of the intensity and the circular polarization with high temporal resolution are a powerful tool to retrieve physical parameters of the underlying atmosphere. Combinations of radio observations with X-ray, EUV, and optical measurements provide a particularly powerful tool (see Chapter 13 by Brosius).

Radio observations at the shortest wavelengths (sub-millimeter) have historically been performed with single-dish antennas and have therefore been limited in spatial resolution to tens of arcsec, except for those that have been recorded during a solar eclipse, which provides sub-diffraction-limited resolution in one dimension. Interferometric submillimeter arrays that can be pointed at the Sun are under construction (e.g. the Atacama Large Millimeter Array, ALMA), and they will open a new world for solar radio physics because of the sub-arcsecond spatial resolution that they will achieve.

At longer wavelengths many general purpose imaging radio interferometers are useful for studying the quiet Sun with good spatial resolution and high dynamic range, which is required to separate the rather weak signal of the quiet Sun from the strong active region signals that often dominate the measured signals. Since the quiet Sun contains a large number of sources that vary on time scales of minutes, many baselines and therefore many antennas are needed. Earth-rotation synthesis is normally not an option because the solar sources are not constant for a long enough period. Apart from the number of baselines and the receiver noise, the achieved image quality also depends on the accuracy with which phases and amplitudes can be calibrated. Self-calibrating schemes can be very useful to reduce antenna-based phase and amplitude errors, making use of redundancy when a large number of baselines are measured.

The Japanese Nobeyama Radioheliograph is currently the most powerful, solar-dedicated imaging radio telescope. It provides full disk maps of the Sun simultaneously at frequencies of 17 and 34 GHz, with an angular resolution of 10 and 5 arcsec, respectively, and with a time resolution as short as 0.1 seconds. At 17 GHz, both left and right-hand circularly polarized emission is recorded. The array consists of three arms with 28 antennas each. While originally built

to study flare-associated phenomena, it is well suited for full-disk quiet Sun studies (Shibasaki 1999).

The French solar-dedicated Nançay Radioheliograph consists of a cross-shaped 43-antenna array that images the Sun at 6 frequencies between 164 MHz and 432 MHz at a rate of 5 Hz (Avignon *et al.* 1989). These frequencies originate in the corona at heights of 0.1 to 0.5 solar radii above the photosphere.

The general purpose Very Large Array (VLA) in the United States with its 27 antennae in a Y-shaped array is successfully used to observe the Sun when it is in its most compact configurations. There are seven fixed observing wavelengths at 90, 20, 6, 3.6, 2.0, 1.3, and 0.7 cm. Circular and linear polarization measurements can be performed. The VLA is currently being expanded to the Expanded VLA (EVLA). While the addition of far-away antennas does not provide any advantages to solar observations, the much improved spectroscopic capabilities, allowing observations anywhere between 1 and 50 GHz and with more than 250,000 channels, will provide a fantastic solar capability. Its drawbacks include a low duty-cycle on the Sun due to its non-solar-dedicated nature, its limited field of view, and its relatively slow (of order 30 s) change of frequency bands.

The Russian RATAN-600 telescope has a circular arrangement of 895 antenna-segments that operate between 0.61 and 30 GHz. The large frequency range makes it attractive for solar observations in general, but the one-dimensional scans provide only limited information about the structure of the quiet Sun.

The solar-dedicated Owens Valley Solar Array (OVSA) in the United States consists of two 27-m and five 2-m antennae spreading over an area about 1.2 km wide. The receivers can tune to any harmonic of 200 MHz in the range of 1 to 18 GHz, and acquire phase lock in less than 10 ms. The system records left- and right-circularly polarized and linearly polarized radiation. The rapidly tuning receiver system provides near-simultaneous observations of an area of the Sun at many frequencies, allowing observations that require spectroscopic capabilities.

The planned Frequency Agile Solar Radiotelescope (FASR) is a Fourier synthesis telescope designed to perform imaging spectroscopy over an extremely broad frequency range (0.1–30 GHz). The frequency, temporal, and angular resolution of the instrument will be optimized for the many and varied radio phenomena produced by the Sun. Consequently, FASR will the most powerful and versatile radioheliograph ever built. FASR will probe all phenomena in the solar atmosphere from the mid-chromosphere to the outer corona.

The international Atacama Large Millimeter Array (ALMA) is currently under construction in the Chilean Andes. Its 64 antennas can observe in all wavelength ranges between 0.35 and 10 mm that are transmitted by the Earth's atmosphere. Its spatial resolution of down to $0.01''$as well as its spectroscopic

capabilities should make it particularly interesting for solar observations (Bastian 2002).

3. General appearance of the quiet Sun in radio waves

Radio observations are particularly useful for temperature measurements as a function of optical depth because higher frequencies arise from lower layers of the solar atmosphere. Radio waves of a certain frequency can only be observed from regions where the local electron plasma frequency ν_p is equal to or lower than the radio frequency ν. Since the electron density decreases with height, ν_p also decreases with height. Radio observations therefore provide diagnostic data from the chromosphere out to the heliosphere. The lower chromosphere is seen at frequencies of 100–1000 GHz, the middle chromosphere is seen at 20–100 GHz, and the upper chromosphere is seen at frequencies of 2–20 GHz. The corona is seen at frequencies of 2 GHz and below.

At frequencies above 10 GHz, the Sun appears as a rather uniform disk with a brightness temperature of about 11,000 K (see Figure 14.1). Active regions show up as somewhat brighter areas. At frequencies of about 1 GHz, the quiet Sun has a brightness temperature of about 50,000 K, while active regions show brightness temperatures of a few million K, which is due to the coronal component. In coronal holes, the coronal contribution is very small while it may be substantial elsewhere in the quiet Sun. Coronal holes therefore show up as darker areas below about 10 GHz. Paradoxically, coronal holes appear brighter than the quiet Sun (Nindos *et al.* 1999a) at frequencies above about 10 GHz, for reasons that are not well understood. At 0.1 GHz and below, the whole Sun has a brightness temperature of about one million K, and active regions are no longer distinguishable, but higher-laying structures such as coronal streamers show up as bright structures.

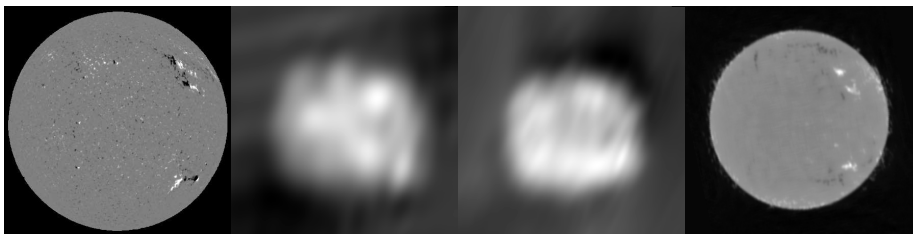


Figure 14.1. The quiet Sun on 1998 February 01 at different radio wavelengths, compared with a photospheric magnetogram. From left to right: Kitt Peak magnetogram, Nançay Radioheliograph at 164 and 327 MHz, and Nobeyama Radioheliograph at 17 GHz.

3.1 Submillimeter observations

Radio images of the Sun at the shortest wavelengths have been obtained at 0.85 mm (a wavelength where the Earth's atmosphere transmits well at high altitudes) with the James Clerk Maxwell Telescope (JCMT) on Mauna Kea (Lindsey *et al.* 1990) and the 10.4 m Caltech Submillimeter Observatory (Bastian *et al.* 1993). These submillimeter full-disk images of the Sun correlate well with images obtained in very strong spectral lines in the visible spectrum such as CaII K, which are again well correlated with maps of the magnetic field. At 0.85 mm, one therefore clearly sees the supergranular network (Lindsey & Jefferies 1991). The resolution of these observations is on the order of $20''$. A better spatial resolution can be obtained at the limb during a solar eclipse when the lunar limb acts as a moving knife-edge. This allows measurements of the limb profile with a spatial resolution of a few arcsec (Ewell *et al.* 1993), which shows a roughly 10% limb brightening in the outer $7''$and a radio limb that extends well beyond the visible limb.

3.2 Millimeter and microwave observations

The time-averaged brightness temperature images of the quiet Sun at frequencies of 5 to 20 GHz also show the chromospheric network (Bastian *et al.* 1996), such as shown in Figure 14.2. However, there are considerable temporal variations in the observed brightness temperature.

Coronal holes at the poles as well as elsewhere on the solar disk show enhanced emission between 17 and 87 GHz (see Nindos *et al.* 1999*b*, and references therein). Outside of this frequency range, the coronal holes either cannot be detected or show reduced emission because of the lower coronal temperature. The enhancement is due to both compact as well as diffuse sources within coronal holes.

At 17 GHz, the diffuse component has 1500 K excess brightness, and the compact sources show a localized excess brightness of about 3500 K (Nindos *et al.* 1999*b*). The cause of the enhancement is not well understood. A comparison of 17-GHz Nobeyama radio observations with simultaneous SOHO EIT images does not show a correlation between the compact radio sources and the bright EUV features (Nindos *et al.* 1999*b*). The temporal variations of the compact microwave sources also did not correspond to any significant changes in EUV emission. This suggests that the origin of the polar brightening is not coronal; it seems that the bulk of the patchy radio emission comes from heights below the 80,000 K layer.

Recent measurements of an equatorial coronal hole combining 17-GHz maps from the Nobeyama Radioheliograph with extreme-ultraviolet, far-ultraviolet, and visible emissions (Moran *et al.* 2001) also do not show an enhanced temperature as measured with UV lines. However, there are indications for an

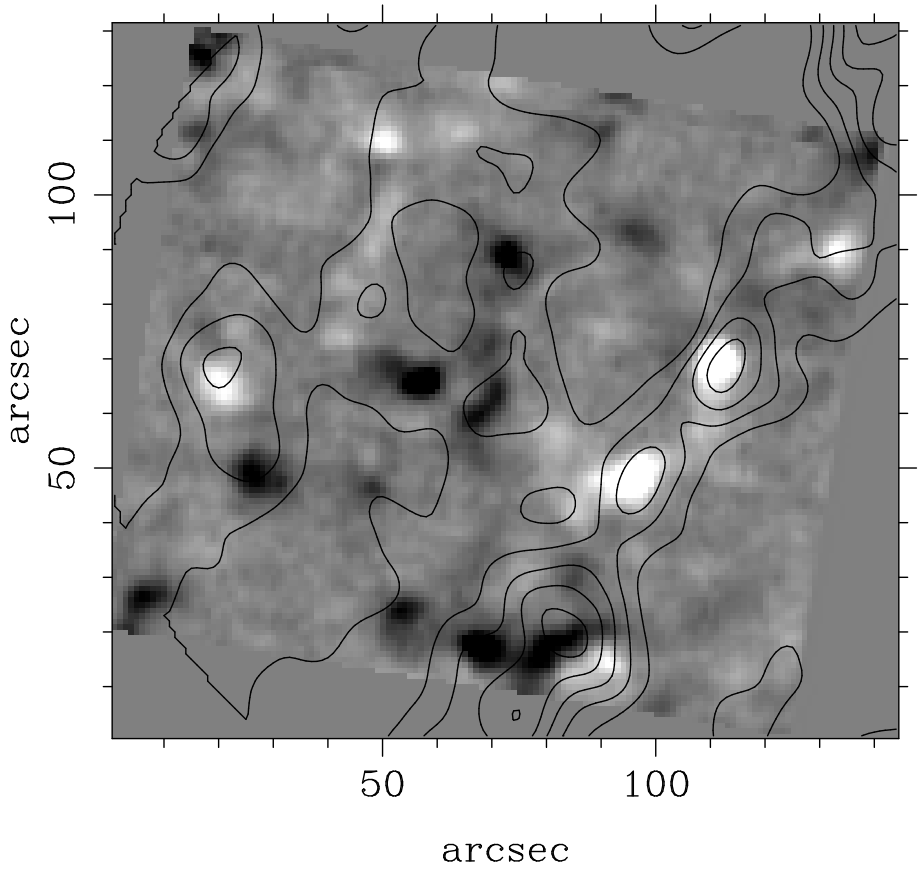


Figure 14.2. A magnetogram of the quiet Sun close to disk center obtained with ZIMPOL at the McMath-Pierce solar telescope with contour lines showing the 2-cm radio emission intensity as observed with the VLA.

increased Hα intensity in radio enhancements. No such enhancements in Hα were detected in the coronal hole outside of radio enhancement regions. This indicates that areas of increased Hα intensity are responsible for the enhanced radio emission and place the origin of the radio enhancement in the chromosphere. At 37 and 87 GHz, the enhanced radio emission in the polar areas is associated with polar faculae, indicating that they are different manifestations of the same underlying activity (Riehokainen *et al.* 2001).

Another interesting development of microwave observations of the quiet Sun has recently been opened by the development of the theory and observational tools to use the birefringence of the free-free emission to make radio magne-

tograms at the base of the quiet Sun corona (Grebinskij *et al.* 2000, see also Chapter 6 by Gelfreikh).

4. Thermal stratification of the quiet Sun

Measuring the temperature stratification of the solar atmosphere has traditionally been done using spectral lines in the optical regime. However, the temperature dependence of spectral line shapes is often highly nonlinear, which requires extensive atomic and radiative transfer modeling to deduce temperatures. The problem becomes particularly severe for very strong lines such as the Ca II H and K lines that are formed in the lower chromosphere. The formation of these lines cannot be assumed to occur in local thermal equilibrium (LTE). The line core that is formed highest in the atmosphere is dominated by the local radiation field and becomes independent of the local temperature. Temperature measurements using strong lines in the visible spectrum as well as EUV lines are therefore not good temperature diagnostics of the upper photosphere and the lower chromosphere. The infrared continuum provides a good measurement of the temperature throughout the photosphere because of the simple relation between the local temperature at optical depth unity and the infrared continuum formation, which is dominated by the H^- opacity and is rather devoid of spectral lines.

In the quiet Sun, thermal free-free (also called thermal bremsstrahlung), which is due to individual electrons being accelerated by the Coulomb field of ions, is the main emission mechanism at radio wavelengths. This incoherent radiation comes mainly from an optically thick source. Therefore the measured intensity only depends on the temperature of the emitting electrons.

In solar radio physics, observed (unpolarized) intensities are expressed in terms of the brightness temperature T_b, which is defined as

$$T_b = \frac{I_\nu c^2}{2k_B\nu^2} \ , \tag{14.1}$$

with c being the speed of light, k_B the Boltzmann constant, and I_ν the intensity observed at the frequency ν. For a given atmospheric stratification, the brightness temperature of the quiet sun is thus given by

$$T_b = \int_0^{\tau_{max}} T e^{-\tau} d\tau \ , \tag{14.2}$$

where T is the temperature, τ is the optical depth, and τ_{max} is a suitably large optical depth, typically $\gg 1$. The optical depth is the integral of the absorption coefficient, κ, along the line of sight. An extensive treatment of the subject can been found in Dulk (1985). Assuming a frequency of 0.1 GHz and a temperature of 10^6 K, typical conditions for observing the solar corona, the

absorption coefficient κ is given by Dulk (1985) as

$$\kappa(\nu) = 0.2 n_e^2 T^{-\frac{3}{2}} \nu^{-2} (\mathrm{cm}^{-1}) \ . \tag{14.3}$$

To calculate the bremsstrahlung emission from a model atmosphere with a known temperature and the electron density stratification, one calculates the absorption coefficient and integrates it from the top of the model along the line of sight to obtain the optical depth τ as a function of geometrical height. The temperature can then be expressed as a function of optical depth, and the integration along the line of sight can be carried out. For oblique paths such as when calculating the center-to-limb variation, the cosine of the heliocentric angle has to be taken into account in the calculation of the optical depth and the integration over the temperature stratification. Very close to the limb, the curvature of the atmosphere also has to be taken into account.

This approach has historically been taken to test models of the quiet Sun. The observed and the predicted brightness temperatures as a function of frequency and center to limb distance are compared. The models can then be tuned to minimize the difference between observations and theoretical prediction. Unfortunately, the temperature stratification cannot be directly deduced from radio measurements because the latter do not provide a measure of the optical depth or opacity. Either one makes certain assumptions or uses additional observations to estimate the opacity.

Another limitation of the one-dimensional line-of-sight approach outlined above becomes evident when dealing with optically thick, filamentary objects such as prominences at the limb that are also seen as filaments on the disk. Because of the filamentary nature of the prominences, only a fraction of the emission in the spatial resolution element comes from the optically thick prominence. This fraction is called the filling factor, and it influences the interpretation of the observed brightness temperature. Unfortunately, radio observations alone are insufficient to determine the filling factor without making additional assumptions. Yet another limitation has to do with optically thin structures such as hot plasma in quiet Sun coronal loops. The increase in brightness temperature due to the optically thin, hot plasma only goes as one over the square root of the plasma temperature, which is rather insensitive. The quiet Sun radio emission therefore has two contributions: one from the optically thin corona, and one from the layer where optical depth unity is reached.

Models of the average quiet Sun have often made use of the measured center-to-limb variation of the absolute brightness temperature (e.g. Vernazza *et al.* 1976). These models are one-dimensional, hydrostatic models that balance the heat flux and the radiative losses. As far as microwave brightness temperatures are concerned, the FAL model C (Fontenla *et al.* 1993) fits the data best. Measurements between 1.4 and 18 GHz (Zirin *et al.* 1991) indicate that the

measured brightness temperature of the quiet Sun between 1.4 and 10 GHz can be modeled by an optically thick component in the chromosphere and an optically thin coronal component. Above 10 GHz, the transition region needs to be taken into account, and spatial variations become important. Furthermore, the phase of the solar cycle must be considered since the coronal contribution increases during periods of high solar activity even in the quiet Sun (Bastian *et al.* 1996).

However, all of these static models ignore the fact that the upper solar atmosphere is highly dynamic and spatially structured. Microwave observations tend to show the cooler structures in the chromosphere because the measured brightness temperature (Bastian *et al.* 1996) is well explained by a chromospheric model that can reproduce the carbon monoxide lines originating from the cool part of the chromosphere (e.g. Avrett 1995). Indeed, until very recently, temperature stratifications of the quiet Sun derived from UV spectral line intensities by far overestimate the observed radio brightness temperature (Zirin *et al.* 1991). By differently analyzing the UV line intensities and distinguishing network and cell-interior as different contributions to the measured radio brightness temperature, it has finally been possible to bring the UV and the radio measurements into agreement (Landi & Chiuderi Drago 2003).

5. Filaments and prominences

Filaments and prominences are different manifestations of the same phenomenon. Filaments are prominences seen on the solar disk. They can be well observed in the microwave domain because they are optically thick at those frequencies. This makes radio observations very suitable for estimating the temperature in filaments. Indeed, radio observations are much better than the traditional Hα observations because the former do not suffer from Doppler shifts and rather complicated spectral line formation processes. Filaments typically occur over extended neutral lines in the quiet Sun and show temperatures well below the temperature of the surrounding quiet corona. Filaments can be quiescent or they can erupt. Since the Hα line is rather limited in temperature range, only radio observations can follow an erupting filament from its quiescent state at temperatures of about 10^4 K to the ambient coronal temperature of the order of 10^6 K.

The first simultaneous radio and EUV observations of a filament (Chiuderi Drago *et al.* 2001) showed that the Lyman continuum absorption is responsible for the lower intensity observed above the filament in the EUV lines that are formed in the transition region. The lower intensity of coronal lines and the depression in brightness temperature at radio wavelengths is due to the lack of

coronal emission. These observations are consistent with a prominence model of cool threads embedded in the hot coronal plasma, with a sheath-like transition region around them.

Hanaoka *et al.* (1999) used the Nobeyama array at 17 GHz to measure the temperature of erupting filaments on the disk. They found that the brightness temperature of the filaments increases to the temperature of the quiet Sun at the beginning of the abrupt eruptions, while the filaments keep their large optical thickness. After the rapid increase, the brightness temperature does not change significantly while the filaments erupt. Heating of the surface of the cool core of the prominences up to the transition-region temperature is the most plausible explanation of the observed increase in the brightness temperature at 17 GHz.

Marqué & Lantos (2002) used the Nançay Radioheliograph to detect brightness depressions around filaments, which are believed to be the signature of a coronal cavity that surrounds the filament. After a filament erupts, even when signatures of only minor energy release are present, the decimetric observations indicate the coronal restructuring on the disk that follows the filament eruption. This suggests the close relation of filament eruptions and coronal mass ejections (see also Chapter 11 by Vourlidas).

6. Coronal heating events in the quiet Sun

More than fifty years after the million-Kelvin temperatures in the corona had been discovered, their cause is still not settled. Many heating mechanisms have been proposed (see the reviews in Ulmschneider *et al.* 1991), including a very large number of discrete heating events in the form of very small flares (microflares and/or nanoflares), various types of waves, and continuous electric currents. While radio observations have been used for almost two decades to study coronal heating events in the quiet Sun, the combination of sensitive radio observations with powerful EUV and X-ray instruments in space has provided us with new insight. Here I will concentrate on summarizing some of the important developments during the last five years.

Initial indications for a relation between compact radio sources in the quiet Sun and coronal brightenings were based on an apparent association of enhanced radio emission with HeI 1083 nm dark points (a proxy for X-ray bright points) at 20 cm (Habbal *et al.* 1986, Habbal & Harvey 1988) and at 6 cm (Fu *et al.* 1987). Sources seen in HeI 1083 nm and at radio wavelengths have been observed to change on time scales of a few minutes. Nevertheless, there were always many more HeI 1083 nm dark points observed than radio sources.

A direct relation between X-ray and radio measurements was first reported by Nitta *et al.* (1992) at 20 cm and by Kundu *et al.* (1994) at 2 cm. About half of the sources seen as enhanced features at radio wavelengths correspond to

X-ray bright points. The other half seems to be associated with concentrated unipolar magnetic flux (e.g. Nitta *et al.* 1992). The temperature of these areas as deduced from X-ray measurements is on the order of 1–2$\times 10^6$ K, while the radio brightness temperature is about a factor of 20 less because the sources are optically thin at radio wavelengths. X-ray bright points tend to be associated with two magnetic elements of opposite polarity that evolve together (e.g. Harvey 1985).

A weak correlation between enhanced radio emission and the magnetic network was discovered by Kundu *et al.* (1988) and Gary & Zirin (1988) at 20 cm. The correlation becomes much better at 6 cm and shorter wavelengths. As seen before, radio emission at these wavelengths originates predominantly from the upper chromosphere with the corona making only a small contribution. Discrete radio sources in the chromospheric network are variable on time scales of a few minutes (Gary & Zirin 1988; Gary *et al.* 1990), such as in Figure 14.3. Nevertheless, the overall evolution of the radio emission is consistent with the evolution of the supergranular network itself (Bastian *et al.* 1996).

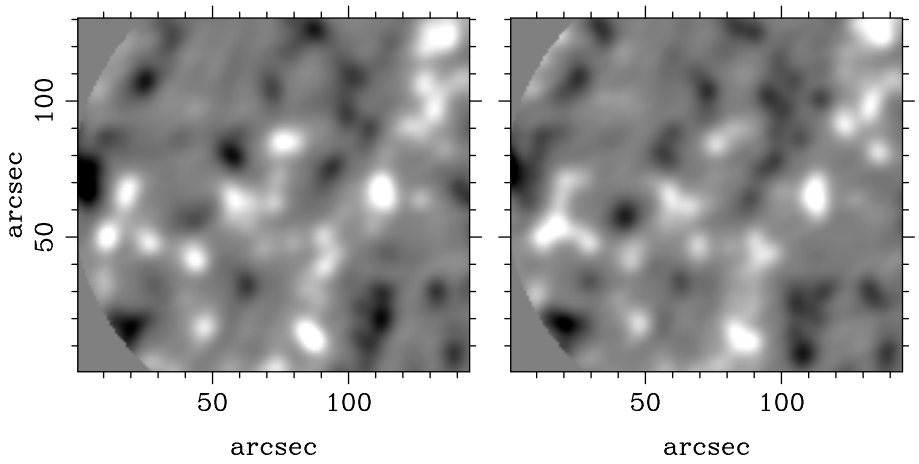


Figure 14.3. Two radio maps of the quiet Sun obtained with the VLA at 2 cm spaced 2 minutes apart.

Benz *et al.* (1997) compared long-exposure soft X-ray images from Yohkoh with VLA maps at 3.6, 2, and 1.3 cm and photospheric magnetograms. Their X-ray observations are more than three orders of magnitude more sensitive than previous observations of X-ray bright points. They find that soft X-ray sources are often associated with bipolar features in the magnetogram, similar to the much brighter X-ray bright points. As previous authors had reported, they find the best correlation between the magnetogram and the radio observations at the shortest wavelengths which originate from the deepest atmospheric layers. The

correlation decreases for the longer wavelengths coming from higher layers, and is also not pronounced for the soft X-ray photons, which originate exclusively from the corona. Interestingly, the X-ray and radio emissions observed close to disk center are often displaced by a few arcsec, indicating inclined magnetic field lines.

Krucker *et al.* (1997) studied the temporal variations in the soft X-ray and radio emissions (see Figure 14.4) using the same data set as Benz *et al.* (1997). X-ray brightenings of at least an order of magnitude less than previous observations show a corresponding radio source correlating in space and time. The authors call these events *network flares* because of the similarities they share with standard solar flares: Variations in temperature and emission measure during the soft X-ray enhancements are consistent with evaporation of cooler material from the transition region and the chromosphere; the ratio of the total energies radiated in X-rays and at radio frequencies is similar to that observed in flares, at least one of the four radio events shows a degree of polarization as high as 35%; in three out of four cases the centimeter radio emission peaks several tens of seconds earlier than in the X-ray emission; and the associated radio emission tends to be more structured and to have faster rise times.

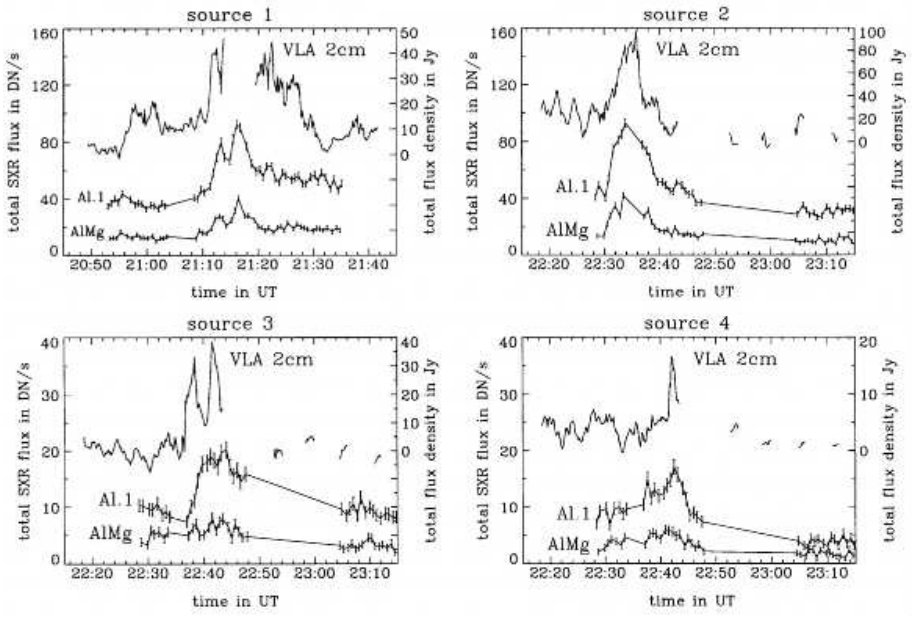


Figure 14.4. Comparison of network flares in soft X-ray and radio waves at 2 cm (from Krucker *et al.* (1997).

In contrast, Nindos *et al.* (1999) selected transient radio brightenings at frequencies between 0.33 and 4.5 GHz and compared them with soft X-ray images from Yohkoh and SOHO EIT images. While most of the events were related to active regions, one of the cases was clearly in the quiet Sun. All events were consistent with the radio emission being due to nonthermal, mildly relativistic electrons.

Benz & Krucker (1999) extended their previous work on the temporal evolution of microflares by statistically studying the faintest fluctuations in the corona and relating them to the layers below. They combined VLA observations with SUMER, CDS, EIT, and MDI data from SOHO. Their analysis indicates that the first emissions due to coronal events occur in spectral lines originating in the transition region and the upper chromosphere. These emissions are assumed to be due to electron beams impinging on the chromosphere. The coronal line EUV emission lags by about 5 minutes, similar to what is seen in regular flares. This coronal line emission is likely due to the evaporating plasma expanding into the corona. The temporal correlation of the radio measurements with respect to the other observations is not as well established. The authors suggest the presence of two different emission processes at work radiating both thermal emission and nonthermal gyrosynchrotron emission at various fluxes. Their statistical results show that the coronal heating events follow the properties of regular solar flares and thus may be interpreted as microflares or nanoflares.

Similar comparisons between radio and transition region lines also indicate the similarity of network flares and the much larger active-region flares (Krucker & Benz 2000). The differences between these two types of flares seem to be mainly quantitative, and the relatively large heating events may in principle be considered as microflares or large nanoflares, thus small versions of regular flares.

7. FASR and the quiet Sun

FASR will provide many new capabilities to answer important questions about the Sun. From a technical point of view, the fact that FASR will be a solar-dedicated instrument should not be underestimated. Past and current combined observing runs between space-based assets and ground-based optical and radio-telescopes are very difficult to arrange because the allocation of observing time on non-solar-dedicated radio telescopes is inflexible. If one wants to study a certain quiet Sun phenomenon such as a filament, one has at most a few days between noticing the interesting object and the time that observations have to be carried out. Furthermore, one often only gets a few hours observing time at telescopes such as the VLA, which might not be sufficient for the event to happen that one would like to study (e.g. the eruption of a filament).

In addition to the flexible scheduling of FASR, its full-disk capability is another advantage for quiet Sun studies. In particular when active regions are also present on the solar disk, a restricted field of view will always suffer to some degree from signals outside of the field of view, which can be very strong in the case of active regions.

From a scientific point of view, the large simultaneous wavelength coverage and the spectral capabilities of FASR will allow new approaches to quiet Sun studies. For instance, using the birefringence of the free-free emission at various frequencies, one will be able to obtain magnetograms at the corresponding levels in the upper solar atmosphere, something that is not feasible with any other known approach.

FASR will also have an impact on modeling of the quiet solar atmosphere. By the time that FASR will be operational, the quiet Sun must be modeled as a time-dependent, three-dimensional atmosphere that is permeated by magnetic fields. The one-dimensional hydrostatic models that are still used today will not be sufficient to explain FASR observations of the quiet Sun. It is therefore important that, along with the development and construction of FASR, the necessary modeling tools are developed to interpret the data to be delivered by FASR.

Current riddles posed by the quiet Sun that will be addressed by a combination of FASR and other ground and space-based assets include:

- What is the magnetic field topology above the photosphere?
- How is energy moved from the photosphere through the chromosphere and transition region into the corona?
- What determines the location of filaments and filaments channels, what is their structure, and what determines their stability?
- What are spicules?
- How is magnetic flux removed (an important ingredient in any solar dynamo theory)?

Acknowledgments

CUK acknowledges support from the Humboldt Foundation while finishing this chapter. The National Solar Observatory is operated by the Association of Universities for Research in Astronomy (AURA), Inc. under cooperative agreement with the National Science Foundation.

References

Avignon, Y., Bonmartin, J., Bouteille, A., Clavelier, B. & Hulot, E. 1989, Solar Phys, 120, 193

Avrett, E. H. 1995, In Infrared tools for solar astrophysics: What's next?, p303
Bastian, T. S. 2002, Astronomische Nachrichten, 323, 271
Bastian, T. S., Dulk, G. A. & Leblanc, Y. 1996, ApJ, 473, 539
Bastian, T. S., Ewell, M. W. & Zirin, H. 1993, ApJ, 415, 364
Bastian, T. S., Gopalswamy, N. & Shibasaki, K., editors 1999, Solar Physics with Radio Observations
Benz, A. O., Krucker, S., Acton, L. W. & Bastian, T. 1997, A&A, 320, 993
Benz, A. O. an Krucker, S. 1999, A&A, 341, 286
Boreiko, R. T. & Clark, T. A. 1986, A&A, 157, 353
Borovik, V. N., Livshitz, M. A. & Medar', V. G. 1997, Astronomy Reports, 41, 836
Chiuderi Drago, F., Alissandrakis, C. E., Bastian, T., Bocchialini, K. & Harrison, R. A. 2001, Solar Phys, 199, 115
Dravskikh, A. F. & Dravskikh, Z. V. 1988, Soviet Astronomy, 32, 104
Ewell, M. W., Zirin, H., Jensen, J. B. & Bastian, T. S. 1993, ApJ, 403, 426
Fontenla, J. M., Avrett, E. H. & Loeser, R. 1993, ApJ, 406, 319
Fu, Q., Kundu, M. R. & Schmahl, E. J. 1987, Solar Phys, 108, 99
Gary, D. E. & Zirin, H. 1988, ApJ, 329, 991
Gary, D. E., Zirin, H. & Wang, H. 1990, ApJ, 355, 321
Grebinskij, A., Bogod, V., Gelfreikh, G., Urpo, S., Pohjolainen, S. & Shibasaki, K. 2000, A&AS, 144, 169
Habbal, S. R. & Harvey, K. L. 1988, ApJ, 326, 988
Habbal, S. R., Ronan, R. S., Withbroe, G. L., Shevgaonkar, R. K. & Kundu, M. R. 1986, ApJ, 306, 740
Hanaoka, Y. & Shinkawa, T. 1999, ApJ, 510, 466
Harvey, K. L. 1985, Australian Journal of Physics, 38, 875
Kaplan, S. A., Kleiman, E. B. & Oiringel, I. M. 1977, Soviet Astronomy, 21, 742
Krucker, S. & Benz, A. O. 2000, Solar Phys, 191, 341
Krucker, S., Benz, A. O., Bastian, T. S. & Acton, L. W. 1997, ApJ, 488, 499
Kundu, M. R., Schmahl, E. J. & Fu, Q.-J. 1988, ApJ, 325, 905
Kundu, M. R., Shibasaki, K., Enome, S. & Nitta, N. 1994, ApJ, 431, L155
Landi, E. & Chiuderi Drago, F. 2003, ApJ, 589, 1054
Lantos, P. 1999, In Proceedings of the Nobeyama Symposium, held in Kiyosato, Japan, Oct. 27-30, 1998, Eds.: T. S. Bastian, N. Gopalswamy & K. Shibasaki, NRO Report No. 479., p.11-24, pages 11
Lindsey, C. A. & Jefferies, J. T. 1991, ApJ, 383, 443
Lindsey, C. A., Yee, S., Roellig, T. L., Hills, R., Brock, D., Duncan, W., Watt, G., Webster, A. & Jefferies, J. T. 1990, ApJ, 353, L53
Marque, C. & Lantos, P. 2002, In SF2A-2002, Semaine de l'Astrophysique Francaise

Moran, T., Gopalswamy, N., Dammasch, I. E. & Wilhelm, K. 2001, A&A, 378, 1037

Nindos, A., Kundu, M. R. & White, S. M. 1999a, ApJ, 513, 983

Nindos, A., Kundu, M. R., White, S. M., Gary, D. E., Shibasaki, K. & Dere, K. P. 1999b, ApJ, 527, 415

Nitta, N., Bastian, T. S., Aschwanden, M. J., Harvey, K. L. & Strong, K. T. 1992, PASJ, 44, L167

Riehokainen, A., Urpo, S., Valtaoja, E., Makarov, V. I., Makarova, L. V. & Tlatov, A. G. 2001, A&A, 366, 676

Shibasaki, K. 1999, In Proceedings of the Nobeyama Symposium, held in Kiyosato, Japan, Oct. 27-30, 1998, Eds.: T. S. Bastian, N. Gopalswamy & K. Shibasaki, NRO Report No. 479., p.1-9, p1

Tsvetkov, L. I. 1986, Izvestiya Ordena Trudovogo Krasnogo Znameni Krymskoj Astrofizicheskoj Observatorii, 75, 77

Ulmschneider, P., Priest, E. R. & Rosner, R., editors 1991, Mechanisms of Chromospheric and Coronal Heating

Vernazza, J. E., Avrett, E. H. & Loeser, R. 1976, ApJ Supp., 30, 1

Zirin, H., Baumert, B. M. & Hurford, G. J. 1991, ApJ, 370, 779

Chapter 15

INTERPLANETARY RADIO BURSTS

N. Gopalswamy
Laboratory for Extraterrestrial Physics NASA/GSFC, Greenbelt, MD

Abstract Nonthermal radio bursts in the interplanetary medium indicate the far-reaching effect of solar eruptions that inject energetic particles, plasmas and shock waves into the inner heliosphere. More than half a century of ground-based observations and subsequent space-based observations exist on this phenomena. In this paper, I summarize the understanding we have gained on the type III and type II radio bursts, which are indicative of electron beams and shocks, respectively. Observations in the new radio window (1-14 MHz) from Wind/WAVES have not only confirmed previous results, but also led to a number of new discoveries. Availability of simultaneous white light (SOHO) and radio (Wind) observations from the same spatial domain in the near-Sun IP medium is largely responsible for these discoveries on the IP propagation of CMEs, so this paper discusses radio bursts in the context of white light observations. After exploring the origin of normal, complex and storm type III bursts, I discuss the type II bursts and their relation to coronal mass ejections. Finally I discuss some of the recent developments on IP radio emission.

1. Introduction

Nonthermal radio bursts in the interplanetary (IP) medium are caused by energetic electrons from the Sun, which convert part of their energy into electromagnetic radiation via an emission mechanism. How exactly these electrons are accelerated during solar eruptions is not fully understood, and is one of the outstanding issues of solar physics. Most of the long-wavelength radio bursts are due to coherent plasma processes, so the frequency of emission is closely related to the plasma frequency (and hence the plasma density) of the medium through which the electrons propagate. Since the plasma density decreases away from the Sun, the plasma frequency also decreases, so radio emission at longer wavelengths originate at greater distances from the Sun. For example, radio emission at metric wavelengths originates close to the Sun, while

the kilometric radio emission comes from IP medium close to 1 AU. A proper understanding of the radio bursts can provide useful information about the solar source (where electrons are accelerated) and the IP medium (through which the accelerated electrons propagate).

The day-time peak of the ionospheric electron density is a few times 10^5 cm^{-3}, which corresponds to a plasma frequency of several MHz. Radio emission from the Sun at longer decametric and kilometric wavelengths cannot penetrate the ionosphere, so we must go to space to observe such radiation. Coronal densities similar to the ionospheric densities occur at a heliocentric distance of $\sim 3R_{\odot}$. The approximate location of the upper source surface of the solar magnetic field is supposed to be near this distance. The ambient medium beyond the source surface may be considered to be that of IP space. In general, therefore, ground based radio telescopes typically access coronal radio emission below the source surface, whereas space based ones must be used to detect radio emission from IP space. Plasma levels at frequencies > 10 MHz are considered coronal, and the lower-frequency levels are taken as IP. Figure 15.1 shows a plot of the level of IP radio emission as compared to the quiet Sun and cosmic background emissions. While the quiet Sun radio emission is very small compared to the galactic background, the solar radio bursts are brighter by several orders of magnitude and hence can be detected easily.

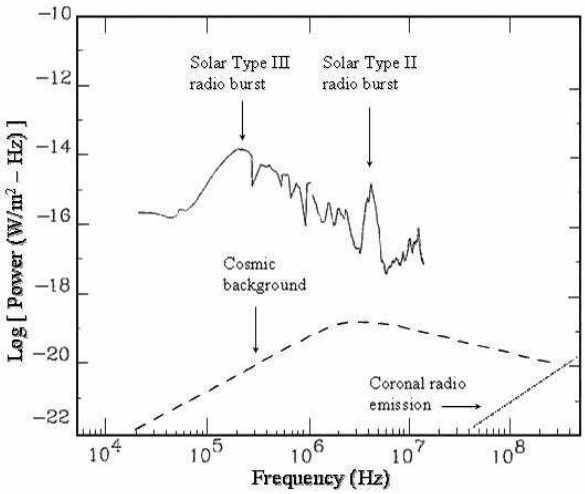


Figure 15.1. Plot showing the level of IP radio burst (types II and III) flux as compared to the cosmic background noise and the quiet coronal emission. The low-frequency end of the solid curve represents *in-situ* plasma frequency. The high-frequency end corresponds to the ionospheric cut-off.

Coronal radio emission has been observed extensively with a variety of ground-based instruments since its discovery by Hey in 1942 but the IP ra-

dio observations became possible only in the space era. The radio instruments on board the Alouette-I satellite observed type III bursts in the 1–8 MHz range and it was possible to infer electron beams with speeds in the range 0.1–0.15c (where c is the speed of light, Hartz 1964). Type II bursts were first identified from IMP-6 data and then from Voyager 2 data (Boischot *et al.* 1980). Extensive observations of coronal mass ejections (CMEs), which became available in the ISEE-3 era, helped enormously in understanding the relationship among shocks, CMEs, and electron beams. Unfortunately, many of the later radio instruments operated at frequencies below 2 MHz, which made it difficult to connect the phenomena observed by ground-based and space-based instruments. The launch of the Wind spacecraft in 1994 essentially closed the gap because the Radio and Plasma Wave (WAVES, Bougeret *et al.* 1995) experiment has a larger frequency range (20 kHz–14 MHz). The spatial domain corresponding to the high-frequency (1–14 MHz) WAVES receiver (RAD2) overlaps with the field of view of the Solar and Heliospheric Observatory (SOHO) mission's Large Angle and Spectrometric Coronagraph (LASCO, Brueckner *et al.* 1995). This synergism has led to the confirmation of a number of old results and enabled new discoveries. The topics in this chapter are mainly concerned with radio phenomena at frequencies below 14 MHz and their relation to solar disturbances such as CMEs. For details on the basic properties of radio bursts, the readers may consult articles in the monograph by Stone *et al.* (2000).

2. Type III Bursts

Type III bursts were first discovered at metric wavelengths by ground-based telescopes in the frequency range 10 to 500 MHz (Wild, 1950). It was recognized early on that electron beams propagating through the coronal and IP plasma can produce these radio bursts (Ginzburg & Zheleznyakov 1958; Wild & Smerd 1972). A beam-plasma system is unstable to the generation of Langmuir waves, which are high frequency plasma waves at the local plasma frequency. Langmuir waves scattered off of ions or low-frequency turbulence result in radiation at the fundamental of the local plasma frequency. Two Langmuir waves can also coalesce to produce electromagnetic waves at twice the local plasma frequency, commonly known as second harmonic emission.

In a dynamic spectrum, the type III bursts appear as almost vertical features because of the high drift rate from high to low frequencies. Since the corona and the IP medium are essentially magnetized plasmas, propagation of electrons occur along open magnetic field lines. Thus, type III bursts continuing from the corona into the IP medium are indicative of open magnetic field lines emanating from the vicinity of the acceleration region and extending into the IP medium. In the inner corona, where closed magnetic field lines are common, one observes a couple of variants of type III bursts such as the J and U bursts,

due to electron beams propagating along curved (or closed) field lines. In the inner corona, one often observes type III bursts with reverse drift. The reverse-drift bursts are due to electrons propagating towards the Sun. The reverse-drift bursts are closely associated with hard X-ray bursts because the latter are also produced by electrons precipitating from the corona and stopped by the chromosphere. Direct observation of nonthermal electrons and plasma waves in space, in association with type III bursts, provided the hard evidence for the plasma emission mechanism (Lin *et al.* 1973). The distribution function of these nonthermal electrons indeed demonstrated the generation of Langmuir waves. Since Langmuir waves derive their energy from the nonthermal electrons, the intensity of the radio bursts depends on the nonthermal electron density and energy (Fitzenreiter *et al.* 1976; Dulk *et al.* 1998).

Type III bursts in the IP space were first detected by the radio instruments on Alouette-I and routinely by later space radio experiments such as ISEE-3, Ulysses, Geotail, and Wind (see Hartz 1964; 1969; Hartz & Gradel 1970; Slysh 1967*ab*; Alexander *et al.* 1969; Fainberg & Stone 1970; Bougeret *et al.* 1998). Radio instruments on board the ATS-II satellite and the Venus 2 Probe observed type III bursts in the 0.45–3 MHz range (Alexander *et al.* 1969), and 0.2–2 MHz (Slysh, 1967*ab*), respectively. The Radio Astronomy Explorer (RAE-I), the first dedicated radio astronomy mission, led to a number of advances in studying electron beams as well as inferring the Archimedean spiral structure of the IP magnetic field (e.g., Fainberg & Stone 1970). When more than one radio instrument was available, it became possible to track the type III radio source: using the RAE-2 and IMP-6 observations, Fitzenreiter *et al.* (1977) obtained the north-south structure in the IP magnetic field. Type III bursts in the IP medium can be grouped into three broad classes representing three different situations of electron beam production and propagation: (i) isolated type III bursts from flares and small-scale energy releases, (ii) complex type III bursts during CMEs, and (iii) type III storms. We discuss them in turn in the next three subsections.

2.1 Isolated type III bursts

Isolated type III bursts are the most common type, produced by energetic electrons escaping from small-scale energy release sites on the Sun. The energy release can occur in regions ranging from small bright points to large active regions. Figure 15.2 shows an example of type III bursts in the metric domain with and without IP counterparts (Gopalswamy *et al.* 1998). The initial type III bursts and the type II burst in the metric domain originated from active region (AR) 7817 with heliographic coordinates, N00E49. However, we do not know the origin of the later intense type III bursts that continued into the Wind/WAVES domain. The isolated kilometric type III bursts are known to be closely associated with He^3-rich events (Reames *et al.* 1988), the class of solar

energetic particle (SEP) events now known as "impulsive" events in contrast to the long-duration (high intensity) SEP events, which are not rich in He^3. Investigation of the source regions of these type III bursts in comparison with the solar sources of the hard X-ray bursts (also due to energetic electrons flowing towards the Sun from the acceleration site) is underway by the RHESSI team.

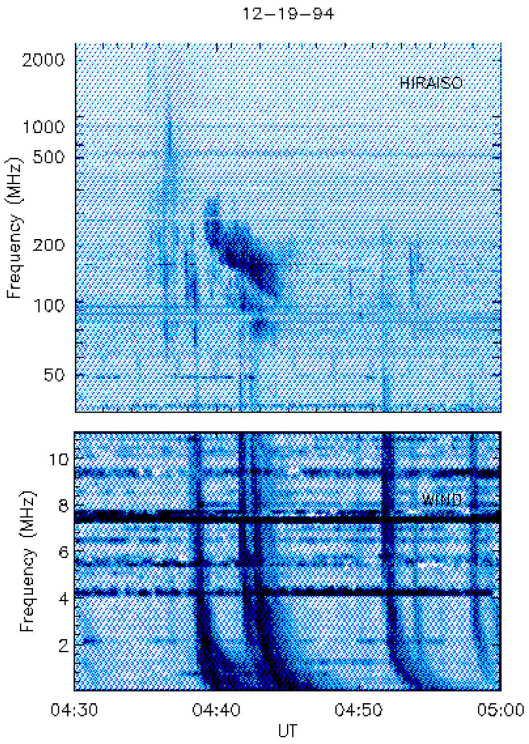


Figure 15.2. A combination of ground-based (Hiraiso; top) and Wind/WAVES (bottom) dynamic spectra showing a number of isolated type III bursts (vertical features). The slanted feature is the type II burst. It is clear that some metric type III bursts continue to lower frequencies, while some do not.

2.2 Complex type III bursts

The complex type III bursts occur in conjunction with CMEs. The bursts were first identified at hectometric wavelengths in the ISEE-3 data (Cane *et al.* 1981) who named them "shock-accelerated" (SA) events. They deduced that the bursts were produced by electron beams accelerated in blast-wave shocks and injected along open magnetic field lines, similar to the herringbone bursts at metric wavelengths. MacDowall *et al.* (1987) introduced a working definition of the SA events: the intensity profile contains five or more peaks of very high intensity

(>100,000 sfu) with an overall duration exceeding 20 min. Figure 15.3 shows an example of the complex type III bursts that occurred on 1997 December 12 from Gopalswamy *et al.* (2000*a*). The event has a group of several bursts in quick succession at high frequencies, which merge to form a single long duration event at lower frequencies.

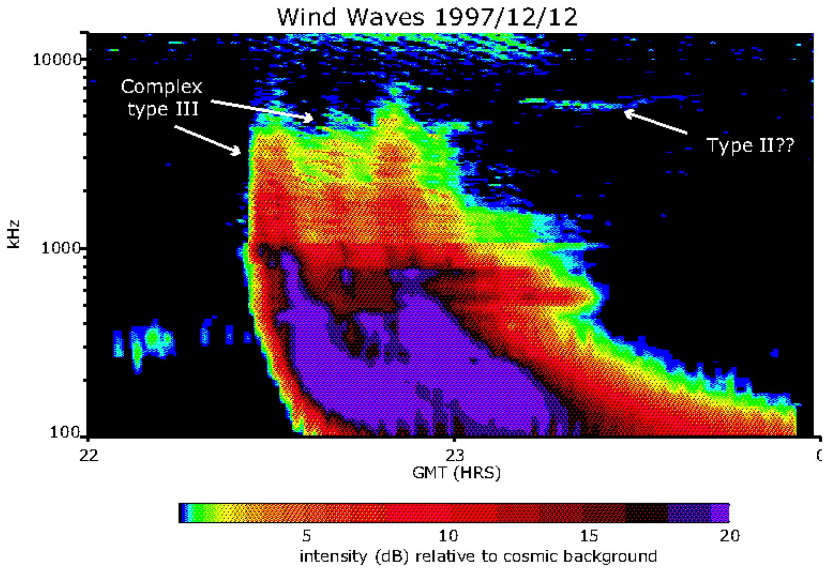


Figure 15.3. The 1997 December 12 complex type III burst that started below about 7 MHz, but was very intense at kilometric wavelengths (from Gopalswamy *et al.* 2000).

2.2.1 Origin of nonthermal electrons. The blast wave origin of the electron acceleration responsible for the complex type III bursts was questioned by Kundu & Stone (1984), who found that the onset times of the complex type III bursts and microwave bursts were identical. These authors concluded that the responsible electrons were accelerated by the common flare process. They also called these bursts "shock-associated" rather than "shock-accelerated" (the acronym SA remained the same!) because of the different origin of the non-thermal electrons. A comparison of SA events with microwave and hard X-ray bursts led Klein (1995) to arrive at similar conclusions. However, Kahler *et al.* (1986) studied a set of metric type II bursts associated with SA events and found that about half of them were not associated with type III bursts in the metric domain, contradicting the low-coronal origin for the SA events. They also found a good association between proton events and SA events, suggesting the involvement of shocks because energetic protons are accelerated by shocks.

Bougeret *et al.* (1998) preferred the term "shock-associated," which could include the possibility that electron beams, accelerated low in the corona, may encounter a shock along their path causing the radio emission to turn on. Reiner *et al.* (2000) noted the similarity in the complexity and duration of the time profiles of 5 complex type III bursts and decimetric (3 GHz) nonthermal emissions, which they presented as further evidence for a flare origin of the electron acceleration. Bougeret et al (1998) showed a complex type III burst, which appeared to start from a metric type II burst with no 3-GHz counterpart. This example is consistent with shock acceleration, unless the decimetric emission was suppressed for some reason. We must point out that relatively smooth decimetric emission, like microwave emission, is due to gyrosynchrotron emission from high energy electrons trapped in closed field lines, while the complex type III bursts are due to low energy electrons propagating along open field lines. Thus the actual duration of decimetric and type III emissions need not agree. One has to compare the lifetime of the trapped particles in closed magnetic field lines with the decay time of plasma waves in the open field region before the time-profile similarity can be used as evidence for the common origin of the nonthermal electrons (Reiner *et al.* 2000). It is not clear if the Reiner *et al.* result would hold for a larger sample of complex type III bursts. Reiner & Kaiser (1999) also argued against the blast-wave origin (Cane *et al.* 1981) for complex type III bursts based on the observation that there are complex type III events without metric type II bursts.

2.2.2 Complex type III bursts and CMEs. In their study of 25 radio-rich CMEs, Gopalswamy *et al.* (2000) found that 23 (92%) of them were associated with SA events (they had incorrectly marked two events—May 2 and 3, 1998—as non-SA events). On the other hand, only half of the SA events associated with front-side CMEs had microwave bursts, while all of them had IP type II bursts. From this they concluded that the presence of CME-driven shocks is essential for the SA events. This clearly brings CMEs into the picture of complex type III bursts. Recently, Cane *et al.* (2002) have changed their interpretation of the SA events to agree with Reiner *et al.* (2000), and have proposed that the electrons are accelerated in reconnection sites behind fast CMEs. However, this does not completely resolve the issue of shock or flare origin, because the presence of fast CMEs also implies the presence of IP shocks near the Sun. In a recent study, MacDowall *et al.* (2003) found that complex type III bursts occurred during almost all large solar energetic particle (SEP) events of solar cycle 23. They also searched for complex type III bursts during impulsive (flare-associated) SEP events and did not find any. Since all large SEP events are associated with fast and wide CMEs with IP type II bursts, the MacDowall *et al.* result also confirms the involvement of CMEs.

The close association between complex type III bursts and shock-driving CMEs (Gopalswamy *et al.* 2000) may have implications for the intensity diminution at 7 MHz, a curious spectral feature reported by Reiner & Kaiser (1999). The intensity diminution has been attributed to complex disturbed magnetic fields around the 7 MHz plasma layer. Not all complex type III bursts show this diminution. Since the associated CMEs are typically fast and wide, one may have to consider the propagation of type III radiation in the presence of high-density CMEs occupying a large volume in the vicinity of complex type III bursts. The CME may affect the propagation of electrons or the propagation of radio waves, depending on where the CME is located with respect to the source of nonthermal electrons and the observer. The magnetically disturbed region invoked by Reiner & Kaiser (1999) may indeed be the associated CME itself.

Irrespective of how the electrons are accelerated (shock or flare site) the occurrence of a CME during the complex type III bursts seems to be required. Figure 15.4 shows the radio dynamic spectrum from Wind/WAVES with the height-time plots of a large number of CMEs on 2000 November 24. Note that all the fast CMEs have associated complex type III bursts. Some CMEs do not have type III association, while some weak type III bursts have no associated CMEs.

In some cases, the complex type III bursts start at much lower frequencies and definitely after the associated type II bursts (Gopalswamy 2000). An example with complex type III bursts starting at lower frequencies after the onset of the metric type II burst is shown in Figure 15.5 (see also Klassen *et al.* 2002). The type II burst was associated with a CME and a filament eruption. The flare in this case was extremely weak and gradual. This event is not inconsistent with electrons accelerated at the shock front and released along open magnetic field lines. The origin of the electrons is thus inconclusive. It is quite possible that both mechanisms could operate to varying degrees.

2.3 Type III storms

Type III storms consist of thousands of short-lived type III-like bursts in rapid succession (Fainberg & Stone 1970; Moller-Pederson 1974). The activity can last for days to weeks. The high frequency counterparts of type III storms are known as “noise storms” or type I storms consisting of narrow-band bursts often superposed on weak continuum emission (see Elgaroy 1977). The storm bursts are thought to be due to electrons from small-scale, quasi-continuous energy releases into closed magnetic structures of active regions. Boishot *et al.* (1970) found a correlation of 80% between type I and decametric type III activity. At coronal heights corresponding to decametric wavelengths, a type I

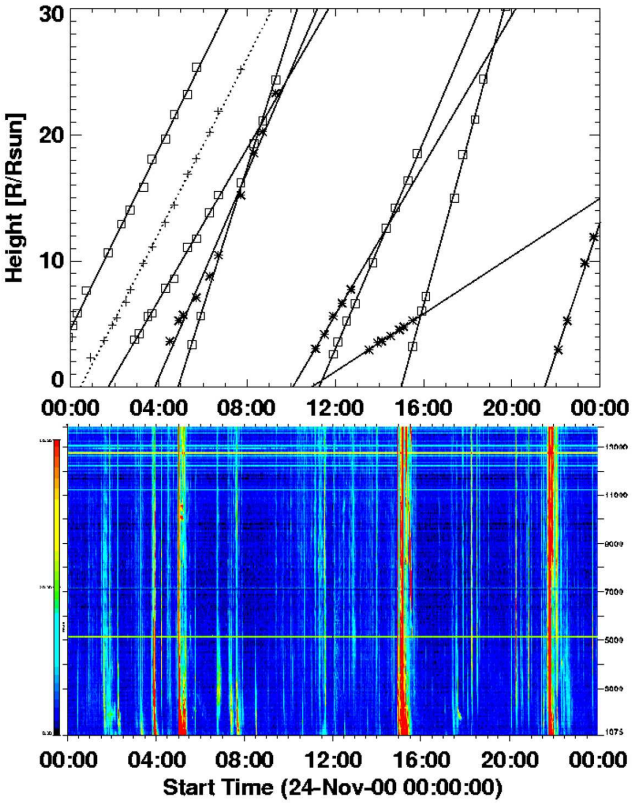


Figure 15.4. Height-time plots of all the CMEs that occurred on 2000 November 24 (top), along with the WAVES/RAD2 dynamic spectrum. Note that all of the complex type III bursts are associated with major CMEs.

storm makes a transition to type III storm (Aubier *et al.* 1978), indicating that electrons gain access to open magnetic field lines of the so-called active region streamers (Stewart & Labrum 1972; Bougeret *et al.* 1984). The occurrence rate of the storm bursts was found to increase as the associated active region crossed the central meridian (Fainberg & Stone 1971). Thus these storms represent energy releases without an eruption of the associated magnetic field structure.

2.3.1 Cessation and recovery of type III storms. What happens when there is an eruption in the active region that has a storm in progress? As one might expect, the type III storms are completely disrupted by large CMEs. After disruption, the type III storms often return to the original level. The cessation and recovery of type III storms may hold the key to understanding how the corona responds to the eruption of large CMEs. Figure 15.6 shows a type III storm during 2000 July 07–08 as observed by Wind/WAVES. On July 07, the

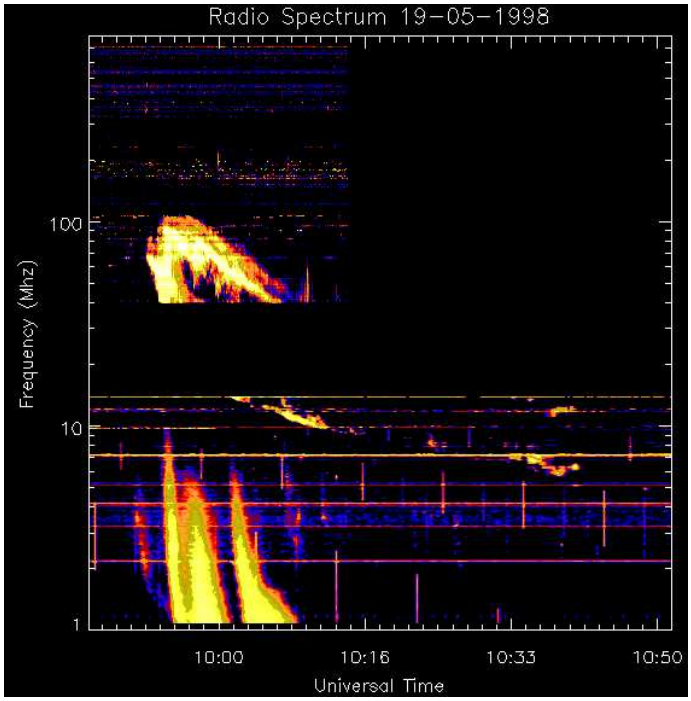


Figure 15.5. A hybrid dynamic spectrum consisting of Potsdam data (top, above 40 MHz) and Wind/WAVES (bottom, below 14 MHz). The Complex type III bursts start only below 10 MHz and delayed with respect to the onset of the type II burst.

storm ceased for about 10 hours from the time of a halo CME from the disk center. The storm came back to its original state by about 20 UT. The storm continued to rage until the end of next day, when there was another CME from the same region and the storm was again interrupted for approximately 8 h. There was also another storm from AR 9077, which continued until the onset of the Bastille Day CME, which disrupted it (see Reiner *et al.* 2001a). After the Bastille Day event, the storm recovery took a much longer time of 17 h.

3. Type II Bursts

The slow-drifting radio bursts were first identified by Payne-Scott *et al.* (1947) from the records at 200, 100, and 60 MHz frequencies. The frequency drift was correctly recognized to represent the motion of an exciting agency in the corona, later identified as an MHD shock by Uchida (1960). Wild & McCready (1950) classified the slowly-drifting bursts as type II bursts. These are relatively rare bursts and have been studied extensively at meter-decameter wavelengths using ground based telescopes (see Nelson & Melrose 1985 for a

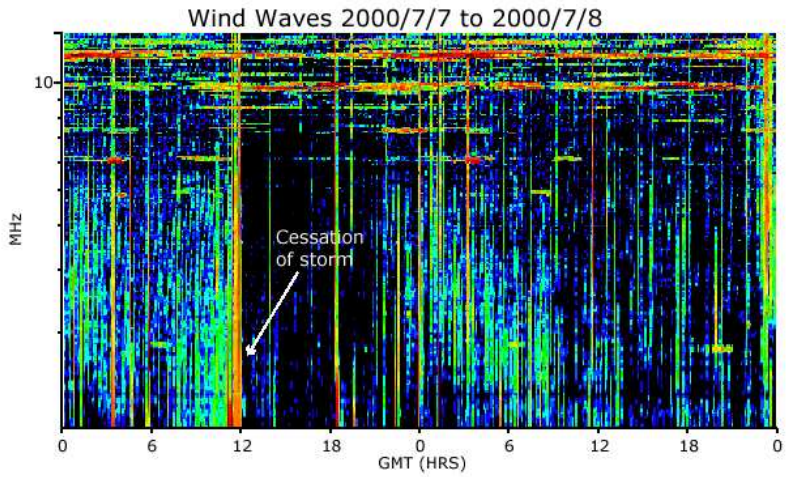


Figure 15.6. Type III storm activity (vertical streaks) observed by Wind/WAVES during 2000 July 7–8. The noise storm was interrupted by a CME on July 7 around 12 UT, but recovers by 20 UT to the original intensity.

review). The current interpretation of the type II burst emission is as follows: electrons accelerated in the MHD shock front generate plasma waves, which get converted into electromagnetic radiation at the fundamental and harmonic of the local plasma frequency.

Type II bursts in the IP medium were first detected by Malitson *et al.* (1973) using IMP 6 data. Voyager data also provided information on IP type II bursts (Boischot *et al.* 1980). The ISEE-3 spacecraft observed about 47 IP type II bursts in the frequency range 30 kHz to 2 MHz over a 50-month period from the L1 point (Lengyel-Frey & Stone 1989). The bursts are intense (up to 1000 sfu at 100 kHz) and have a typical relative bandwidth of 70%. Wind/WAVES data indicates that the IP type II bursts occur more frequently than what ISEE-3 detected. This is likely to be due to the more limited frequency coverage of the ISEE-3 radio instrument (Kaiser, 2003). Figure 15.7 shows an intense IP type II burst extending from 14 MHz down to *in-situ* frequencies (30 KHz). The shock was also detected *in situ* by the WAVES experiment right at the time the type II burst drifts to *in-situ* frequencies ($\sim$20 kHz). The plasma emission process involving electron beams and Langmuir waves (as in the terrestrial electron foreshock and type III radio bursts) was recently verified when Wind spacecraft passed through a type II burst source (Bale *et al.* 1999; Knock *et al.* 2003).

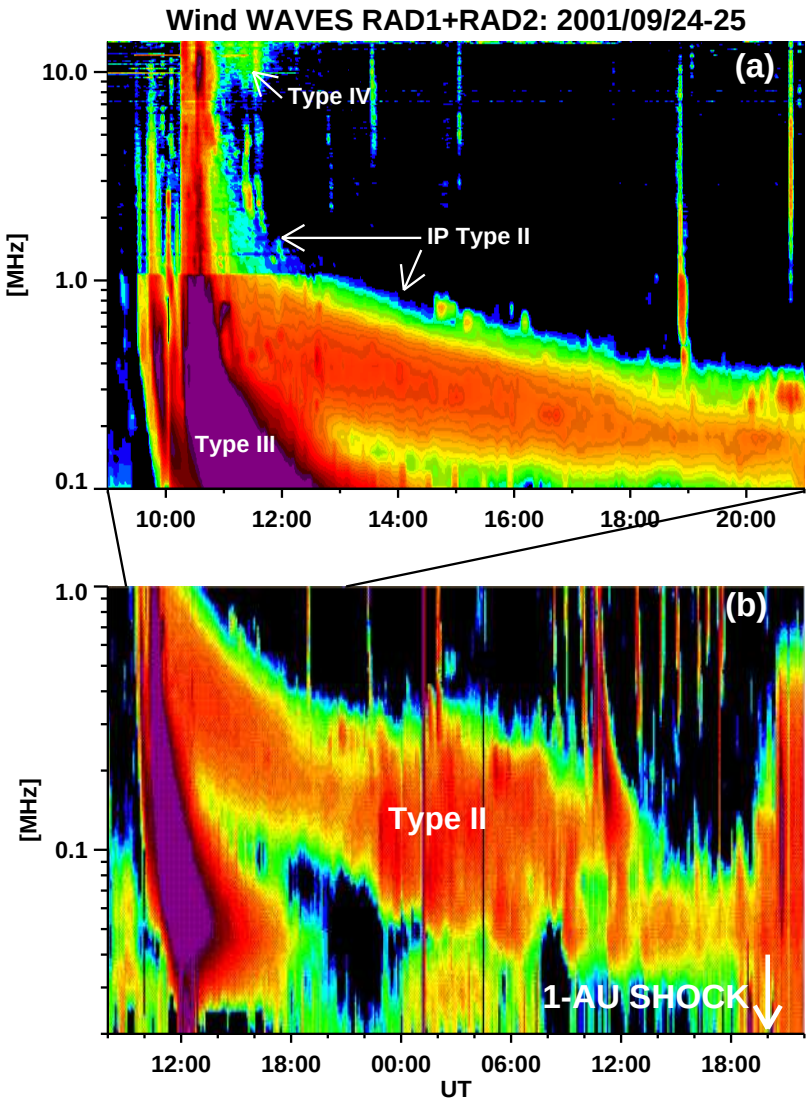


Figure 15.7. IP Type II burst of 2001 September 24-25. The top panel shows the dynamic spectrum over the entire WAVES spectral range. The bottom panel shows the complete evolution of the type II burst until the shock arrived at 1 AU (marked by arrow). The complex Type III, which appeared at the beginning of the event and the associated type IV burst are marked. The collecting area of the antenna in the high-frequency domain is smaller, so the type II burst is faint.

3.1 IP shocks, CMEs and type II radio bursts

The realization that the IP shocks are CME-driven came about when they were found to be closely associated with white-light CMEs (Sheeley *et al.*

1985). At the same time, kilometric type II bursts were also found to be closely associated with IP shocks (Cane *et al.* 1987), so it became clear that the kilometric type II bursts are produced by CME-driven shocks (Cane *et al.* 1987). This confirms the well known *in-situ* observations that many IP shocks are followed by "driver gas" (see, e.g., Borrini *et al.* 1982).

From the inconsistency in the drift rates of type II bursts at frequencies below and above 1 MHz, Cane (1983) concluded that type II bursts above 1 MHz are the continuation of the metric type II bursts and those below 1 MHz are caused by IP shocks. This is consistent with idea of Wagner & MacQueen (1983) that solar eruptions can result in two shocks—a blast wave from the flare and a preceding CME-driven shock due to the CME. According to this idea, the high frequency (metric) type II bursts are caused by the flare shocks (see also Gary *et al.* 1984), while the IP type II bursts are due to CME-driven shocks. Robinson *et al.* (1984) and Cane & Stone (1984) found good correspondence between kilometric type II bursts and metric type II/type IV bursts (70% association), although only 7% of the metric type II bursts were followed by kilometric type II bursts (Robinson *et al.* 1984). Metric type II bursts originate from very close to the solar surface, typically at a height of 0.5 $R_{\odot}$. On the other hand the kilometric type II bursts start beyond 10 $R_{\odot}$. This large gap is a direct result of the lack of frequency coverage between 2 MHz and about 20 MHz.

3.1.1 DH type II bursts. The WAVES/RAD2 frequencies correspond to 2–10 $R_{\odot}$ and hence closed the gap between the kilometric and metric observations. For more than two years after the launch of Wind, no type II bursts were observed in the decametric-hectometric (DH) domain, even though several were observed at metric and kilometric wavelengths (Reiner *et al.* 1998). Gopalswamy *et al.* (1998) noted that none of the 34 metric type II bursts had DH counterparts, but there were IP shocks detected *in situ*. Their analysis also indicated that the IP shocks and metric type II bursts did not come from the same solar source. Starting on 1997 April 01 type II bursts were frequently observed in the DH domain. When Gopalswamy *et al.* (2001a) repeated their study of metric type II bursts and their association with DH and kilometric type II bursts, they found that only 18% and 25% of the metric type II bursts were associated with DH and km type II bursts, respectively. Moreover, 93% of metric type II bursts did not have *in-situ* IP events (shocks or ejecta) and a similar (80%) fraction of IP events had no metric counterparts. Only a small fraction (9%) of metric type II bursts originating from the disk (central meridian distance, CMD $< 60^{\circ}$) were associated with IP shocks; in each of these cases, a halo or partial halo CME was involved (width $> 120^{\circ}$). Thus, even with complete frequency coverage from metric to kilometric wavelengths, the poor correlation between metric and longer wavelength type II bursts was confirmed.

3.2 Are type II bursts CME-driven?

SOHO/LASCO CMEs associated with DH type II bursts had the following properties (see, Gopalswamy *et al.* 2000; 2001*b*): (1) All the DH type II bursts were associated with CMEs. (2) The average speed of the associated CMEs was 1030 km s^{-1}, 2–3 times faster than average CMEs (see Figure 15.8 for the speed distribution of CMEs associated with DH type II bursts). (3) The average width of non-halo CMEs exceeded 100°, nearly twice as wide as the average CMEs. (4) There was a weak correlation between the speed and width of CMEs. (5) The majority (60%) of the CMEs decelerated within the LASCO field of view, with an average value of -11.3 m s^{-2}. (6) The deceleration was proportional to the square of CME speed, as expected when the drag due to the interaction between the ambient medium and the CME becomes important. (7) Only 40% of the fast ($>$ 900 km s^{-1}) CMEs were associated with DH type II bursts.

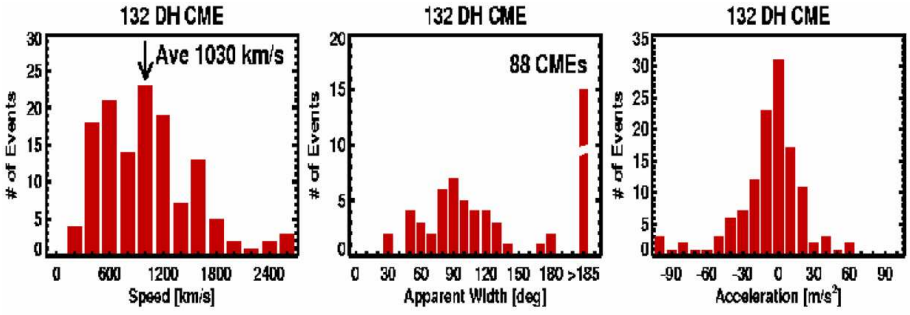


Figure 15.8. Speed, width and acceleration of 132 CMEs associated with DH type II bursts. Note that 88 CMEs were halo events.

A closer examination revealed that fast CMEs without DH type II bursts were not wide; the average width of these CMEs was only 66° as compared to 102° for the ones associated with DH type II bursts (see Figure 15.9). These results prove beyond doubt that DH type II bursts are due to CME-driven shocks, consistent with the high degree of association between kilometric type II bursts and CMEs (see also Kaiser *et al.* 1998; Reiner & Kaiser 1999). It is tempting to extend this association to metric type II bursts also. Gopalswamy *et al.* (2001*a*) reported that a third (34%) of the metric type II bursts originating from the disk were not associated with white light CMEs, as in Kahler *et al.* (1984). However, an EIT wave transient was observed in all these cases, indicating a CME from the disk, probably not observed by the coronagraph by virtue of the solar source location and the nature of coronagraphic observations. This observation supports the conclusion of Cliver *et al.* (1999) that all the metric type II bursts are associated with fast CMEs.

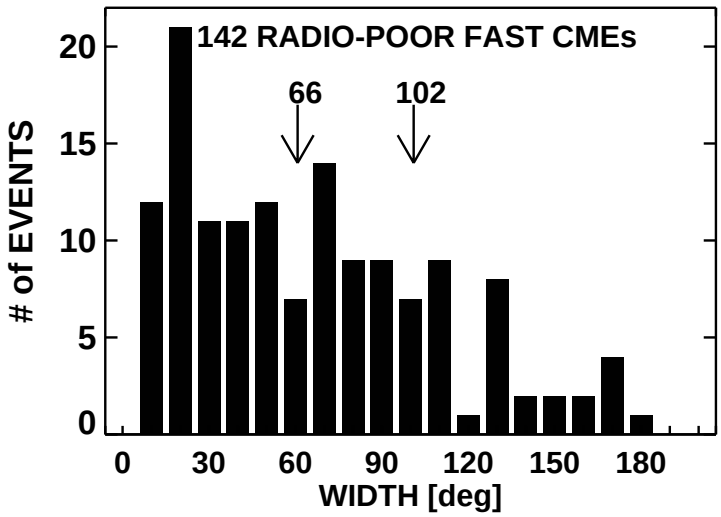


Figure 15.9. Histogram of fast CMEs ($>$ 900 km/s) that did not have associated DH type II bursts. These have an average width of 66°, compared to the 102° for DH type II CMEs.

The close association between DH type II bursts and CMEs on the one hand and the metric type II bursts and CMEs on the other is not consistent with the poor correlation between metric type II bursts and DH type II bursts noted in Gopalswamy *et al.* 2001*b*). Therefore, in addition to the presence of CMEs, additional special conditions need to be satisfied before a metric type II burst can be produced. According to Gosling *et al.* (1976) and Cliver *et al.* (1999) one special condition is a high speed for the CME (fast CMEs). For DH type II bursts, this condition was shown to be fast and wide CMEs (Gopalswamy *et al.* 2001*b*) because 60% of the fast CMEs were radio-poor. In order to see the distinguishing characteristics of CMEs associated with metric type II bursts, Lara *et al.* (2003) considered a set of 80 metric type II bursts that did not have DH counterparts and identified the associated CMEs. They found that the CMEs associated with metric type II bursts are faster ($\sim$ 450 km s^{-1}) than the common CMEs ($\sim$ 350 km s^{-1}), but they are slower than the CMEs associated with DH type II bursts (see Figure 15.10). The average width of all CMEs ($\sim$ 50°) was found to be lower than that ($\sim$70°) for CMEs with metric type II bursts; the latter was, in turn, lower than the average width ($\sim$100°) of CMEs with DH type II bursts. The general population of CMEs had an average acceleration close to zero, while the average had progressively larger negative values for CMEs associated with metric and DH type II bursts. Thus, it appears that type II bursts in all domains are a CME-associated phenomenon.

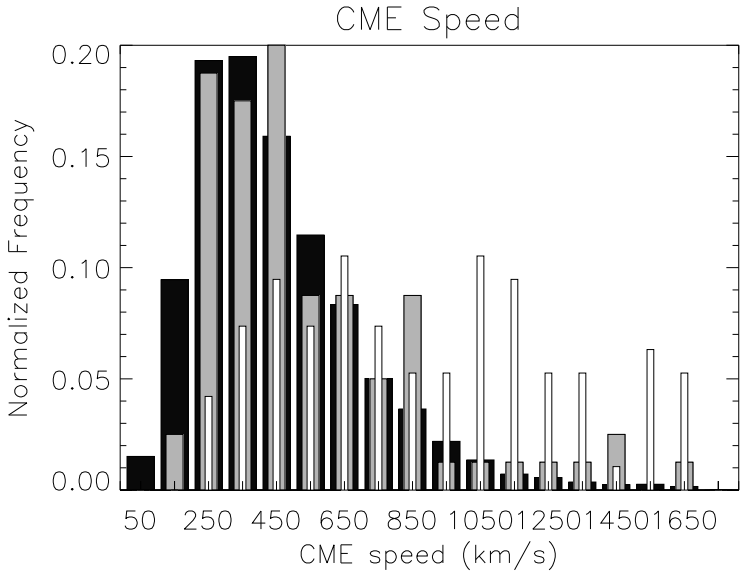


Figure 15.10. Speed distribution of CMEs associated with metric type II bursts as compared to that of general population of CMEs (dark), and DH CMEs (white).

However, there are many fast and wide CMEs without associated DH type II bursts. Gopalswamy *et al.* (2003*b*) investigated a set of fast (> 900 km s^{-1}) and wide (> 60 deg) CMEs that lacked solar energetic particles and DH type II bursts. When they examined the coronagraph images they found that the CMEs were ejected into a tenuous corona. A tenuous corona is expected to have a greater Alfvén speed and hence it is difficult for the CME to drive a shock. Thus the physical properties of the ambient medium such as density and magnetic field (and hence the Alfvén speed) also play a role in deciding the shock-driving capability of CMEs (Uchida *et al.* 1974; Kahler *et al.* 1984), contrary to the conclusion by Cliver *et al.* (1999) that the Alfvén speed is not important.

3.3 What is a fast CME?

In the past, only a single characteristic value was used to define "fast" CMEs: > 400 km s^{-1} (Cliver *et al.* 1999). This number can be traced to Gosling *et al.* (1976) who arrived at the conclusion that, "the characteristic speed with which MHD signals propagate in the lower (1.1 to 3 solar radii) corona, where metric wavelength bursts are generated, is about 400 to 500 km s^{-1}." Some metric type II bursts are known to be produced by CMEs moving with a speed of only 250 km s^{-1} (see Fig. 1 of Gopalswamy *et al.* 2001*a*), which represents a significant departure from the characteristic speed 400-500 km s^{-1}. From

in-situ observations, we know that the Alfvén speed is very low ($\sim$ 50 km s^{-1}) close to 1 AU as compared to the solar wind speed, so the latter is the primary characteristic speed in deciding shock formation. On the other hand, in the equatorial low corona ($<$2 $R_\odot$) the fast magnetosonic speed (V_F, determined by the Alfvén speed V_A and the sound speed V_S) is dominant because the solar wind is not fully formed (the solar wind speed picks up at around 6 $R_\odot$). Typical V_A at the coronal base for a magnetic field of 1 G and a density of $\sim 5 \times 10^8$ cm^{-3} is $\sim$ 175 km s^{-1} while V_S is about 110 km s^{-1}, resulting in $V_F \sim$ 207 km s^{-1}. The Alfvén speed is known to have a peak in the outer corona (around 3.5 $R_\odot$) with a value of several hundred km s^{-1} (see, Krogulec *et al.* 1994; Hollweg 1978; Mann *et al.* 1999; Gopalswamy *et al.* 2001a). Clearly, drivers of moderate speed cannot form shocks in this region. In addition to this outer coronal peak, there is another peak in the inner (active region) corona because V_A could be as high as $\sim$4000 km s^{-1} (Gopalswamy *et al.* 2001a). Between these two peaks (within about 1.5 R$_\odot$), the quiet-Sun V_A dominates, resulting in a low-V_A region in the metric corona (see Fig. 15.11). We can immediately infer that a CME of modest speed (250 km s^{-1}) could drive a shock in the inner corona, while higher speeds are needed in the outer corona. In other words, it is easy for a CME to drive a shock in the inner corona, consistent with the abundant metric type II bursts and progressively smaller number of DH and kilometric type II bursts.

Mann *et al.* (1999) used the quiet-Sun Alfvén speed profile (without the AR part) to study the relation between EIT waves and metric type II bursts. They required that shocks related to metric type II bursts need to have speeds exceeding 408 km s^{-1} (corresponding to region 2 in Figure 15.11). They assumed that EIT waves and shocks were responsible for metric type II bursts from the same flare and concluded that, "a coronal shock wave must have a velocity exceeding 800 km s^{-1} in order to penetrate into the IP space." Contrary to this, Gopalswamy *et al.* (2001a) proposed the possibility of slow and accelerating CMEs driving shocks in the IP medium without a metric type II burst. In fact, the V_F profile in Figure 15.11 can explain most of the observed characteristics of metric, DH and kilometric type II bursts: (1) In the active region corona, V_F is very high, so it is difficult to form shocks. This might explain the low starting frequency of $\sim$ 150 MHz for metric type II bursts. (2) It is easy to produce metric type II bursts in the inner corona because V_F is very low (region 2 in Fig. 15.11). Only a small number of such shocks can continue beyond $\sim 3R_\odot$. (3) A long-lived driver, such as a CME, has more opportunity to produce a type II burst because it goes through a low V_F region, especially in the outer corona. (4) CMEs with intermediate speeds can drive shocks in the metric domain, lose the shock in the regions of V_{Fmax}, and again set up a shock in the outer corona (Gopalswamy & Kaiser 2002). (5) Accelerating, low-speed CMEs may produce shocks in the DH and kilometric domains even though they do not drive

shocks in the metric domain. (6) Blast waves and shocks driven by short-lived drivers have less chance to go beyond the metric domain, unless their initial speed exceeds V_{Fmax}. No blast wave shocks have ever been observed *in situ*, although Leblanc *et al.* (2001) claimed that the blast wave and the CME-driven shock merge somewhere in the solar wind (beyond 30 $R_\odot$). Shocks observed at 1 AU without a driver (Schwenn 1996) have been shown to be flanks of shocks driven by limb CMEs (Gopalswamy *et al.* 2001a).

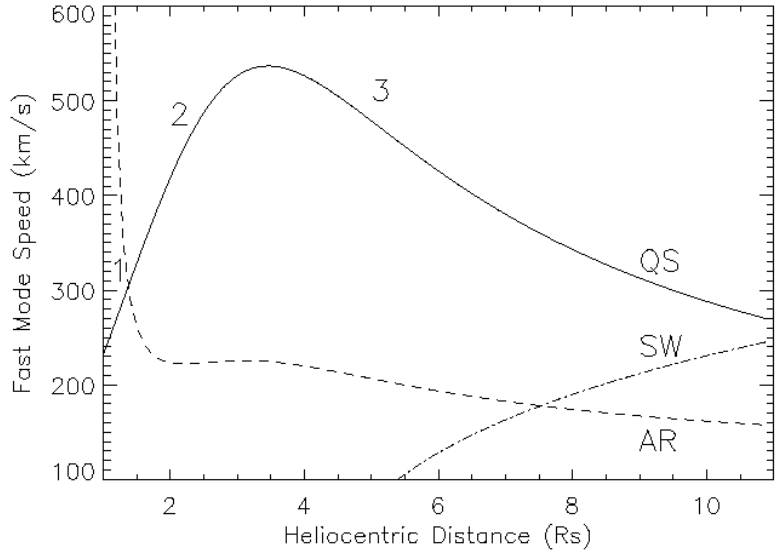


Figure 15.11. Radial profile of the fast mode speed (V_F) in the active region (AR) and quiet (QS) corona. The solar wind speed profile (SW) is also shown. The sharp increase of V_F in region 1 prevents shock formation in the core of active regions. Shock formation is easier in regions 2 and 3 because of lower V_F.

The good correlation between shock speed parameters derived from the DH type II bursts and CME plane-of-the-sky speeds (correlation coefficient = 0.71) and the lack of correlation between the shock speed parameters derived from the metric type II radio bursts and the corresponding CME speeds (correlation coefficient $= -0.07$) found by Reiner *et al.* (2001b) can be reconciled if we note that the CME speed changes rapidly in the inner corona and the CME is propagating through the region of highly variable Alfvén speed profile. Another possibility is that the metric type II bursts come from the flanks of the CME-driven shock (Holman & Pesses 1983) while the IP type II bursts come from the nose of the same shock. This would also account for the lower heliocentric distance of the type II source compared to the CME leading edge—an argument

used to discount CME-driven shock for metric type II bursts (Gopalswamy & Kundu 1992).

4. Recent Developments

In this section we discuss two IP radio signatures detected by Wind/WAVES that are closely related to the topics discussed in this chapter: (1) The radio signatures of CME interaction, and (2) long-lasting continuum at very low frequencies. These observations illustrate the complexity of the IP medium imposed by multiple solar eruptions and other large-scale structures such as coronal holes and streamers.

4.1 Radio signatures of CME interaction

Gopalswamy *et al.* (2001c) reported intense continuum-like radio enhancement at the low-frequency end of a DH type II burst. At the time of the radio enhancement, coronagraphic images revealed a fast (660 km s^{-1}) CME overtaking a slow (290 km s^{-1}) CME in the IP medium. The type II burst preceding the radio enhancement was due to the fast CME. The duration of the radio enhancement corresponded to the transit time of the CME-driven shock through the core of the slow CME. Exactly at the time of interaction, the core of the slow CME changed its trajectory. The radio enhancement was interpreted to be due to shock strengthening when it propagated through the dense material of the slow CME. From radio observations, Gopalswamy *et al.* (2001c) were able to determine the density of the core of the preceding CME to be 4×10^4 cm^{-3}, about 4 times greater than that of the ambient medium at a heliocentric distance of $6.5R_\odot$.

4.1.1 Radio signature solely due to CME interaction. In addition to the modification of a normal type II radio burst, generation of new nonthermal emission at the time of CME collision has also been found (Gopalswamy *et al.* 2002a). The radio emission occurred at a distance beyond $10R_\odot$ from the Sun, where the two CMEs came in contact. There was no type II radio burst (metric or IP) preceding the nonthermal emission. Using Hα and EUV images, the two CMEs were found to be ejected along the same path. The first CME was rather slow (290 km s^{-1}), while the second CME was twice as fast (590 km s^{-1}). Figure 15.12 shows the two CMEs (CME1 and CME2) in a single LASCO image. CME1 was at a heliocentric distance of $\sim 15R_\odot$, while CME2 was at a distance of $\sim 8R_\odot$. At the time of the radio burst, the leading edge of CME2 just caught up with the trailing edge of CME1 at a projected heliocentric distance of $\sim 10R_\odot$. The close temporal association between the onset of the radio burst and the time of interaction between the two white-light CMEs

suggests that the radio emission is a direct consequence of the CME interaction. CME1 was too slow to drive any shock in the outer corona due to the hump in the fast-mode speed (Gopalswamy *et al.* 2001a). The ability of CME2 to drive a shock is marginal because of the relatively high fast-mode speed, and increasing solar wind flow. The nonthermal electrons responsible for the new type of radio emission must have been accelerated due either to the reconnection between the two CMEs or to the formation of a new shock at the time of the collision between the two CMEs. The latter situation is a variant of the previous case, in that the shock is newly formed rather than getting a boost.

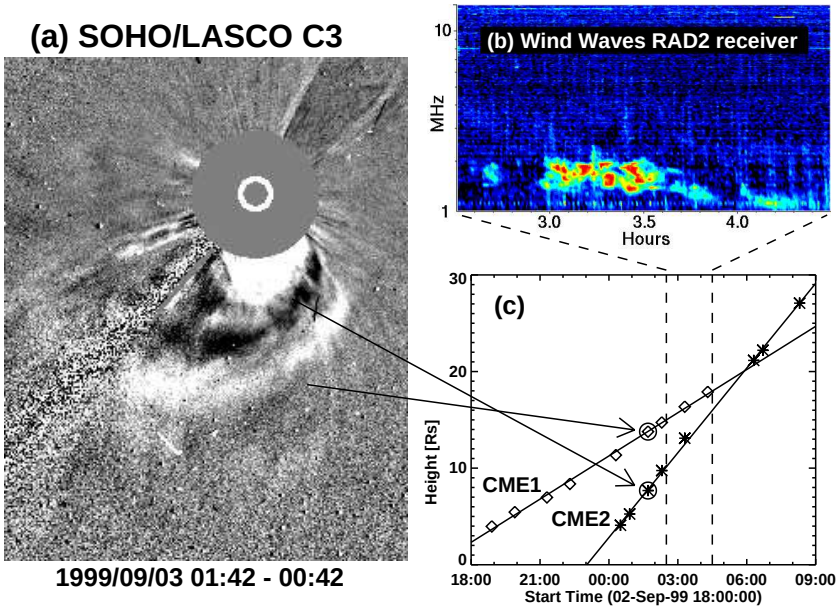


Figure 15.12. (a) Two CMEs on 1999 September 03 as observed by SOHO/LASCO, and (b) the associated continuum radio emission detected by Wind/WAVES around 2 MHz. (c) The height-time plots of the two CMEs with the duration of the radio emission marked by vertical lines.

4.1.2 Medium modification: Interaction between two fast CMEs.

We now discuss the interaction between two fast CMEs that occurred on 2001 January 20. The WAVES dynamic spectrum, LASCO CMEs and their height-time plots are shown in Figure 15.13. The first CME had a speed of 830 km s^{-1} and produced a narrowband type II burst with fundamental-harmonic structure. The second CME followed within two hours and was much faster (1460 km s^{-1}). Near-surface imaging data such as SOHO/EIT revealed that the two CMEs originated from the same active region (AR 9313). Note that the slow-drift type II burst following the second CME is very intense and the

bandwidth (>100%) was much larger than usual for DH type II bursts. There is no fundamental-harmonic structure. Broadband structure means that radio emission is produced from a large range of plasma level at the same time. The long decay time at a given frequency suggests that the shock traverses a given plasma level (at different spatial locations) for a long time. This situation is consistent with the shock of the second CME passing through the material of the first CME.

4.1.3 Interaction between CMEs with high but nearly equal speeds. On 2001 November 22, two CMEs lifted off from AR 9704 (S25W67) and AR 9698 (S15W34), within 3 h of each other. The two solar sources were separated by just 10° in latitude and 33° in longitude. Both were halo CMEs (their true widths are likely to greatly exceed 60°) so interaction between them is expected. The two CMEs had almost the same sky-plane speed (1443 km s^{-1} for CME1 and 1437 km s^{-1} for CME2). The two events were also associated with major flares and solar energetic particle events. The radio emission associated with the two CMEs consisted of the two standard features: a set of complex type III bursts and a type II burst. The first type II burst was close to a normal one with a band width of $\sim$ 10% (see Figure 15.14). The second type II was extremely broad band ($>$ 100%) with a complex structure. The type II burst associated with the second CMEs was spectacular, while the first type II was barely visible on the scale of the spectrum. The shock of CME1 must have propagated through a normal ambient medium while the shock driven by CME2 propagated through the material of CME1—a different ambient medium. Since both CMEs are propagating with roughly the same speed, the relative situation must have persisted for a long time (Gopalswamy *et al.* 2003a).

4.1.4 What we mean by CME interaction. The CME interaction discussed above concerns only the modification of electron acceleration in shocks. CME interactions can also take place without radio emission, especially when the interacting CMEs are slow. Near the Sun a CME is observed as a density enhancement above the ambient corona. This enhancement is thought to be the material in closed magnetic loops overlying the neutral line in the pre-eruption phase. Many CMEs have substructures such as a cavity, and a core of high-density cool material. As CMEs move away from the Sun, they expand and the density decreases. How these substructures result in the observed IP CMEs (or ICMEs) is a topic of current research (Gopalswamy 2003) For example, magnetic clouds are one type of ICME consisting of a flux rope structure. Shocks ahead of fast CMEs that catch up with slow ones might strengthen or weaken depending on the Alfvén speed (V_A) in the preceding CME because $dV_A/V_A = dB/B - 1/2\, dn_e/n_e$, where B and n_e are the mag-

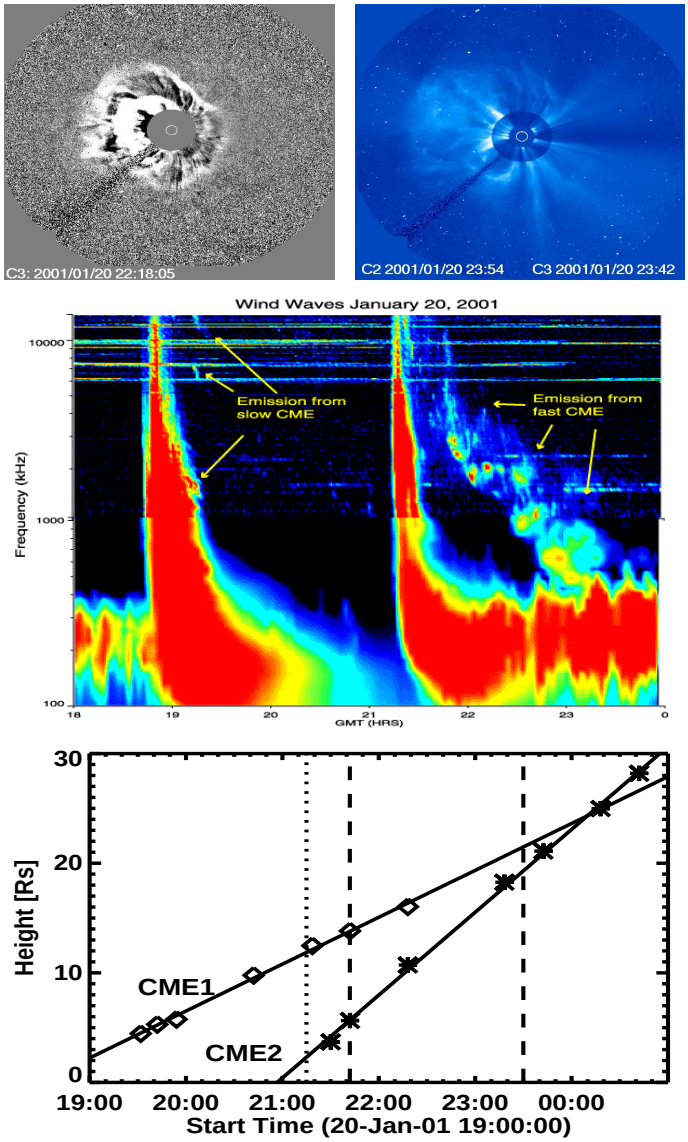


Figure 15.13. *top*: SOHO/LASCO difference image at 22:18 UT on 2001 January 20 showing two CMEs that became indistinguishable in the 23:42 UT image. *middle*: DH type II bursts associated with the two fast CMEs. The type II burst of CME1 was weak and of narrow band compared to the intense broadband type II associated with CME2. *bottom*: Height-time plots of the two CMEs with the vertical dashed lines showing the duration of the type II burst of CME2. The vertical dotted line shows the onset of the complex type III burst that mark the onset of CME2.

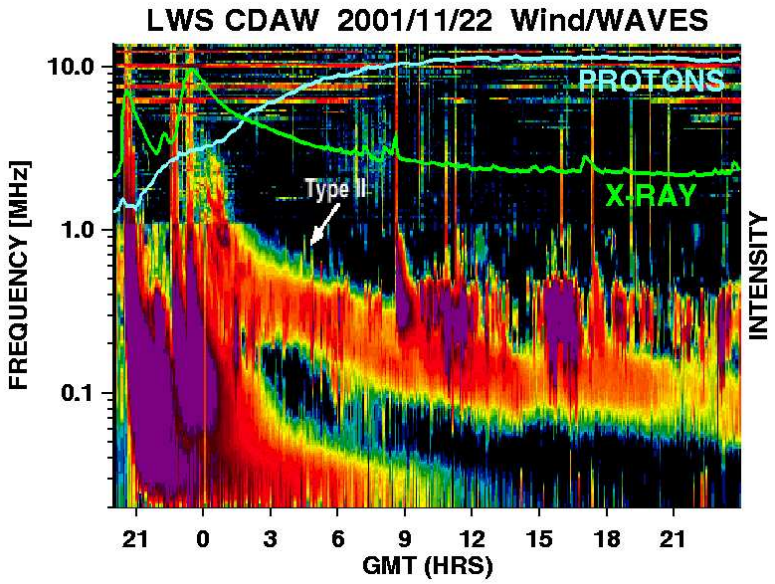


Figure 15.14. Wind/WAVES dynamic spectrum of the 2001 November 22 events. The type II burst (marked by arrow) of the second CME was intense and broadband. Both CMEs were associated with major flares as indicated by the GOES light curve (X-RAY) and the solar energetic particle time profile.

netic field and density in the preceding CME. Some numerical simulations have shown that shocks strengthen when passing through preceding CMEs (Wu *et al.* 2002; Odstrcil *et al.* 2003). Others have shown weakening of the shock, especially close to 1 AU (Vandas *et al.* 1997). Various signatures may be expected depending on the location of the interaction region between Sun and the observing spacecraft. Obviously, we cannot observe CME interactions beyond the LASCO field of view. At present, only *in-situ* observations can detect CME interactions, but by that time the CMEs will have already evolved considerably. Interaction between ICMEs have been discussed before by Burlaga *et al.* (1987). Complex extended ejecta may result due to merger of ejecta at 1 AU (Burlaga *et al.* 2002). CME interaction has important implications for space weather prediction based on halo CMEs: some of the false alarms could be accounted for by CME interactions. The observed CME interaction could also explain some of the complex ejecta at 1 AU, which have unusual composition. More work is needed to classify and recognize radio signatures for a deeper understanding of the phenomenon.

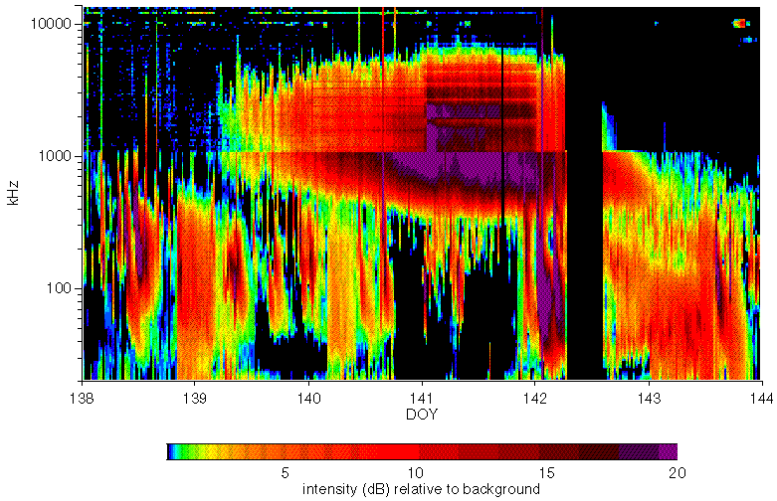


Figure 15.15. Wind/WAVES dynamic spectrum of the unusual and broadband radio emission that lasted for 4 days from 2002 May 18 (DOY 138) to May 23 (DOY 143).

4.2 Unusual radio signatures

An intense, broadband (350 kHz–7 MHz) solar radio event was observed from 2002 May 19–23 by Wind/WAVES (see Figure 15.15). The radio emission had frequency fine structures with 1.5–2 h periodicity and 100% circular polarization. The frequency spectrum has a peaked distribution, with peak frequency decreasing with time. The high frequency level remained constant, while the low frequency end drifted to lower frequencies until the middle of May 21 and remained at this level for the rest of the time (see Figure 15.15).

There was a sudden decline of the continuum at the high frequency end following two CMEs from the southwest quadrant towards the end of May 21 and beginning of May 22. The radio emission disappeared completely on May 23 at 9 UT. There was an unfortunate data gap just at the time of the onset of the decline. The direction-finding analysis reported by Reiner *et al.* (2002) indicates that the radio source may lie somewhere between 4 and 40 $R_{\odot}$ from the Sun and that the source is relatively small. Although Reiner *et al.* (2002) suggested that this could be a unique kilometric manifestation of a moving type IV burst, the high degree of polarization points to a hectometric storm continuum. A similar continuum identified by Fainberg & Stone (1970) in the RAE-1 data (0.54–2.8 MHz) was found to be related to decametric and metric

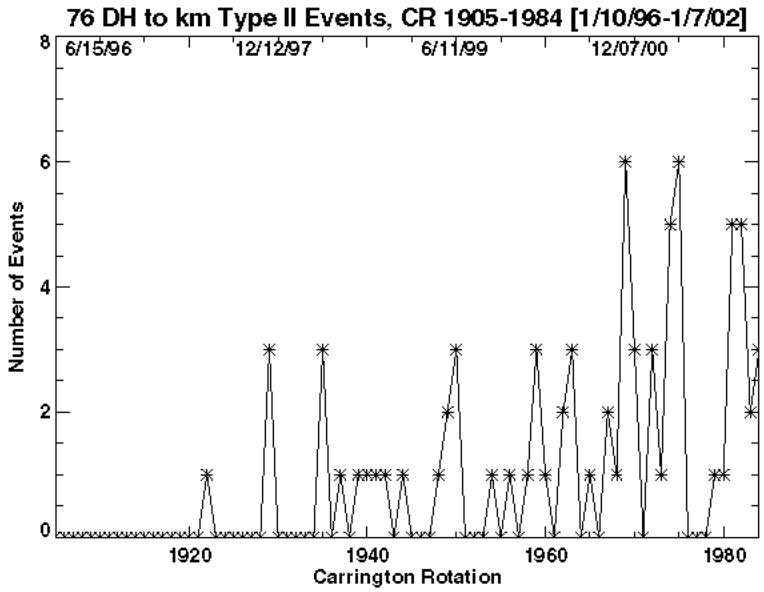


Figure 15.16. Number of type II bursts that begin in the DH domain and continue to the kilometric domain plotted as a function of time (Carrington Rotation number and UT). Note that there are several rotations with no such long-lasting type II bursts.

noise storms (Sakurai 1976). When we examined the solar disk, we found that the onset of the continuum coincided with the appearance of a rapidly changing active region complex (AR 9957 and 9958) located at the edge of an equatorial coronal hole. When continuum started, AR 9957 was at N14E45 and at N10W15 when it ended. The number of sunspots and the active region area were growing rapidly and reached maximum around May 21-22. The radio event disappeared when the active region area dropped to the pre-burst value on May 23. The sunspot number declined at a slightly lower rate.

5. Concluding Remarks

Research on IP radio bursts started in the sixties and tremendous progress has been made, thanks to the series of space missions with radio instruments on board. While early studies concentrated on the radio phenomenon in isolation, connecting them to solar disturbances started in the eighties. We now see that the complex type III bursts and type II bursts are intimately connected to CMEs. This has opened up new opportunities to study the propagation of CME-related disturbances far into the IP medium because radio emission can be observed over the whole Sun-Earth connected space and beyond. These two burst types

also serve as proxies to the two commonly accepted sources of solar energetic particles: flare reconnection and shocks. The simple picture of CMEs and shocks propagating through a plain solar wind may not happen all the time, especially during solar maximum.

With the CME rate averaging to more than 5 per day, the IP medium is expected to be highly disturbed whenever CMEs are ejected in rapid succession from the same region. The radio signatures during CME interaction have opened a new avenue to study the disturbed IP medium. Between 1996 and 2002, SOHO/LASCO detected nearly 7000 CMEs. Yet, there were only about 600 metric type II bursts and about 300 IP type II bursts. Out of the latter 300, only 76 produced radio emission over the entire stretch of the Sun-Earth space (see Figure 15.16). Most of them were also associated with major SEP events. Thus, the IP type II bursts provide unique information on geo-effective CMEs. We were able to make tremendous progress using radio observations with little positional information. Imaging the complex type III bursts, IP type II bursts and the interaction signatures from space is a logical next step to get direct information on shocks and electron beams. Such a possibility with the Solar Imaging Radio Array (SIRA) is within our reach. With the anticipated synergistic contributions from LOFAR and FASR on the ground, solar radio astronomy is poised for a leap.

Acknowledgments

I thank S. Yashiro, A. Lara, and S. Nunes for help with figures and M. J. Reiner, P. K. Manoharan, and S. Nunes for a critical reading of the manuscript.

References

Alexander, J. K., Malitson, H. H. & Stone, R. G., 1969, Solar Phys., 8, 388

Aubier, M. G., Leblanc, Y. & Moller-Pederson, B., 1978, A&Ap, 70, 685

Bale, S. D. and Reiner, M. J. and Bougeret, J.-L. and Kaiser, M. L. and Krucker, S. and Larson, D. E. and Lin, R. P. 1999, GRL, 26, 1573

Boishot, A., de la Noe, J. & B. Moller-Pederson, 1970, A&Ap, 4, 159

Boischot, A., Riddle, A. C., Pearce. J. B., & Warwick, J. W., 1980, Solar Phys., 5, 397

Bougeret, J.-L., Fainberg, J., & Stone, R. G., 1984, A&Ap, 141, 17

Bougeret, J.-L., Kaiser, M. L., Kellogg, P. J., Manning, R., Goetz, K., Monson, S. J., Monge, N., Friel, L., Meetre, C. A., Perche, C., Sitruk, L. & Hoang, S. 1995, Space Sci. Rev., 71, 231

Bougeret, J.-L., Zarka, P., Caroubalos, C., Karlický, M., Leblanc, Y., Maroulis, D., Hillaris, A., Moussas, X., Alissandrakis, C. E., Dumas, G. & Perche, C. 1998, GRL, 25, 2513

Brueckner, G.E. *et al.* 1995, Solar Phys., 162, 357

Burlaga, L. F., Behannon, K. W. & Klein, L. W. 1987, JGR, 92, 5725
Burlaga, L. F., Plunkett, S. P. & St. Cyr, O. C. 2002, JGR, 107, A10, SSH 1-1
Cane, H. V., Stone, R. G., Fainberg, J., Steinberg, J. L., Hoang, S. & Stewart, R. T. 1981, GRL, 8, 1285
Cane, H. V., 1983, Solar Wind Five, NASA Conf. Publ., CP-2280, 703
Cane, H. V. & Stone, R. G., 1984, ApJ, 282, 339
Cane, H. V., Sheeley, N. R. & Howard, R. A. 1987, JGR, 92, 9869
Cane, H. V., Erickson, W. C. & Prestage, N. 2002, JGR, 107, A10
Cliver, E. W., Webb, D. F. & Howard, R. A. 1999, Solar Phys., 187, 89
Dulk, G. A., Leblanc, Y., Robinson, P. A., Bougeret, J. & Lin, R. P. 1998, JGR, 103, 17223
Elgaroy, O. 1977, Solar Noise Storms, Pergamon, New York
Fainberg, J. & Stone, R. G. 1970, Solar Phys., 15, 433
Fainberg, J. & Stone, R. G. 1971, Solar Phys., 17, 392
Fainberg, J., Evans, R. G. & Stone, R. G. 1972, ApJ, 178, 743
Fitzenreiter, R., Evans, R. G. & Lin. R. P. 1976, Solar Phys., 46, 437
Fitzenreiter, R. J., Fainberg, J., Weber, R. R., Alvarez, H., Haddock, F. T. & Potter, W. H. 1977, Solar Phys., 52, 477
Gary, D. E., Dulk, G. A., House, L., Illing, R., Sawyer, C., Wagner, W. J., McLean, D. J. & Hildner, E. 1984, A&A, 134, 222
Ginzbursg, V. L. & Zheleznakov, V., V. 1958, Soviet Astron. A. J. 2, 653
Gopalswamy, N. 2000, in Radio Astronomy at Long Wavelengths, Geophysical Monograph 119, AGU, Washington DC, 123
Gopalswamy, N. 2003, Adv. Space Res., 31(4), 869
Gopalswamy, N. & Kundu, M. R. 1992, in AIP Conference Proceedings # 264: Particle Acceleration in Cosmic Plasmas, ed. by G. P. Zank & T. K. Gaisser, American Institute of Physics, New York, 257
Gopalswamy, N., Kaiser, M. L., Lepping, R. P., Kahler, S. W., Ogilvie, K., Berdichevsky, D., Kondo, T., Isobe, T. & Akioka, M. 1998, JGR, 103, 307
Gopalswamy, N., Kaiser, M. L., Thompson, B. J., Burlaga, L. F., Szabo, A., Vourlidas, A., Lara, A., Yashiro, S. & Bougeret, J.-L. 2000, GRL, 27, 1427
Gopalswamy, N., Lara, A., Kaiser, M. L. & Bougeret, J.-L. 2001*a*, JGR, 106, 25261
Gopalswamy, N., Yashiro, S., Kaiser, M. L., Howard, R. A. & Bougeret, J.-L. 2001*b*, JGR, 106, 29219
Gopalswamy, N. & Kaiser, M. L. 2002, Adv. Space Res. 29, 307
Gopalswamy, N., Yashiro, S., Kaiser, M. L., Howard, R. A. & Bougeret, J.-L. 2001*c*, ApJ, 548, L91
Gopalswamy, N. *et al.* 2003*a*, GRL, 30, No. 12, 8015
Gopalswamy, N. *et al.* 2003*b*, in Solar Wind X, ed. M. Velli, in press
Gosling, J. T., Hildner, E., MacQueen, R. M., Munro, R. H., Poland, A. I. & Ross, C. L. 1976, Solar Phys., 48, 389

Hartz, T. R. 1964, Ann. Astrophys. 27, 831
Hartz, T. R. 1969, Planetary Space Sci., 7, 267
Hartz, T. R. & Gradel, T. E. 1970, ApJ, 160, 293
Holman, G. D. & Pesses, M. E. 1983, ApJ, 267 837
Hollweg, J. V. 1978, Solar Phys. 56, 305
Kahler, S. W., Sheeley, N. R., Howard, R. A., Michels, D. J. & Koomen, M. J. 1984, Solar Phys., 93, 133
Kahler, S. W., Cliver, E. W. & Cane, H. V. 1986, Adv. Space Res., 6(6), 319
Kaiser, M. L., 2003, Adv. Space Res., in press
Kaiser, M. L., Reiner, M. J., Gopalswamy, N., Howard, R. A., St. Cyr, O. C., Thompson, B. J. & Bougeret, J.-L. 1998, GRL, 25, 2501
Klassen, A., Bothmer, V., Mann, G., Reiner, M. J., Krucker, S., Vourlidas, A. & Kunow, H. 2002, A&A, 385, 1078
Klein, K.-L. 1995, in Coronal Magnetic Energy Releases, Lecture Notes in Physics, volume 444, 55
Knock, S. A., Cairns, I. H., Robinson, P. A. & Kuncic, Z. 2003, JGR, 108 (A3), SSH 6-1
Krogulec, M., Musielak, Z. E., Suess, S. T., Nerney, S. F. & Moore, R. L. 1994, JGR, 99, 23489
Kundu, M. R. & Stone, R. G. 1984 Adv. Space Res., 4, 261
Lara, A., Gopalswamy, N., Nunes, S., Muñoz, G. & Yashiro, S. 2003, GRL, 30, No.12, SEP 4-1
Leblanc, Y., Dulk, G. A., Cairns, I. H. & Bougeret, J.-L. 2000, JGR, 105, 18215.
Lengyel-Frey, D. & Stone, R. G. 1989, JGR, 94, 159
Lin, R. P., Evans, R. G. & Fainberg, J. 1973, Astrophys. Lett. & Comm., 14, 191
MacDowall, R. J., Stone, R. G. & Kundu, M. R. 1987, Solar Phys., 111, 397
MacDowall, R. J., Lara, A., Manoharan, P. K., Nitta, N. V., Rosas, A. M. & Bougeret, J. L. 2003, GRL, 30, No. 12, SEP 6-1
Malitson, H. H., Fainberg, J., & Stone, R. G., 1973 Observation of a Type II Solar Radio Burst to 37 Rsun, Astrophys. Lett., 14, 111
Mann, G., Klassen, A., Estel, C. & Thompson, B. J. 1999, in Proc. of 8th SOHO Workshop, Edited by J.-C. Vial & B. Kaldeich-Schmann., p.477
Moller-Pederson, B. 1974, A&A, 37, 163
Nelson, G. J. & Melrose, D. B. 1985, in Solar Radio Physics, edited by D. J. McLean & N. R. Labrum, Cambridge, New York, p. 333
Odstrcil, D., Vandas, M. & Pizzo, V. 2003, Solar Wind 10, in press
Payne-Scott, R., Yabsley D. E. & Bolton, J. G. 1947, Nature, 160, 256
Reames, D. V., Ramaty, R. & von Rosenvinge, T. T. 1988, ApJ, 332, L87
Reiner, M. J., Kaiser, M. L. & Fainberg, J. 1998, JGR, 103, 29651
Reiner, M. J. & Kaiser, M. L. 1999, JGR, 104, 16979

Reiner, M. J., Karlický, M., Jiricka, K., Aurass, H., Mann, G. & Kaiser, M. L. 2000, ApJ, 530, 1049

Reiner, M. J., Kaiser, M. L., Karlický, M., Jiricka, K. & Bougeret, J.-L. 2001a, Solar Phys., 204, 121

Reiner, M. J., Kaiser, M. L., Gopalswamy, N., Aurass, H., Mann, G., Vourlidas, A. & Maksimovic, M. 2001b, JGR, 106, 25279

Reiner, M. J., Kaiser, M. L. & Fainberg, J. 2002, AGU Fall Meeting 2002, abstract #SH72C-02

Robinson, R. D., Stewart, R. T. & Cane, H. V. 1984, Solar Phys., 91, 159

Schwenn, R. 1996, Astrophys. Space Sci., 243, 187

Sakurai, K. 1976, Astrophys. Space Sci., 42, 349

Sheeley, N. R., Jr., Howard, R. A., Michels, D. J., Koomen, M. J., Schwenn, R., Muehlhaeuser, K. H. & Rosenbauer, H. 1985, JGR, 90, 163

Slysh, V. I. 1967a, Soviet Astron. 11, 389

Slysh, V. I. 1967b, Cosmic Res., 5, 759

Stewart, R. T. & Labrum, N. R. 1972, Solar Phys., 27, 192

Stone, R. G., Weiler, K. W., Goldstein, M. L. & Bougeret, J.-L. 2000, Radio astronomy at long wavelengths, AGU, Washington, DC

Uchida, Y. 1960, PASJ, 12, 376

Uchida, Y. 1974, Solar Phys., 39, 431

Vandas, M. Fischer, S., Dryer, M., Smith, Z., Detman, T. & Geranios, A. 1997, JGR, 102, 22295

Wagner, W. J. & MacQueen, R. M. 1983, A&Ap, 120, 136

Wild, J. P. 1950, Aust. J. Sci. Ser. A, 3, 541

Wild, J. P. & McCready, L. L. 1950, Austral. J. Sci. Res., A3, 387

Wild, J. P. & Smerd, S. F. 1972, Ann. Rev. Astron. Astrophys., 10, 159

Wu, S. T., Wang, A. H. & Gopalswamy, N. 2002, in SOLMAG 2002, Ed. H. Sawaya-Lacoste, ESA SP-505. Noordwijk, Netherlands, p. 227

Chapter 16

SOLAR RADAR

William A. Coles
Department of Electrical and Computer Engineering, University of California at San Diego
bcoles@ucsd.edu

Abstract

A serious long-term attempt to study the corona using radar was made between 1961 and 1969, but it was unsuccessful because the characteristics of the radar echo could not be explained. In retrospect it was not possible to adequately model the radar echoes because we did not know enough about the corona at that time. Further observations became impossible as radar astronomy evolved and the technique has been almost forgotten. In this chapter we propose to revive the solar radar technique. We discuss the theory, review the early observations, provide a tenable explanation of them, propose new experiments, and outline the likely development of the technique.

1. Introduction

The Sun was the second target attempted in the development of radar astronomy (after the Moon). The first detailed calculations of the expected echo and the radar parameters required were done by Kerr (1952), and echoes were first detected at 25 MHz by a Stanford group in 1959 (Eshleman *et al.* 1960). A dedicated 38 MHz solar radar was built at El Campo, Texas by an MIT group and regular observations were made between 1960 and 1969 (James *et al.*1970). Unfortunately the observations were not fully understood, and they have not contributed much to our present understanding of the corona. An excellent discussion of solar radar theory and the early observations, is in Chapter 7 of the book *Radar Astronomy* by Evans & Hagfors (James 1968). A more recent review is given by Rodriguez (2000).

In retrospect the early observers faced several insurmountable difficulties. First, the large scale structure of the corona is often dominated by features, such as coronal holes and coronal mass ejections, which were unknown at the time. Second, the microstructure that governs the angular spread of the backscattered

radiation was also unknown. Third, the radar turning point is at the base of the solar wind, which had just been discovered and was largely unknown. Finally, they did not have simultaneous optical observations to help constrain the coronal geometry. Eventually interest in the solar observations waned, the radar was scrapped, and radar astronomy evolved towards the use of higher frequencies. Higher frequencies penetrate through the transition region into the cool dense plasma of the chromosphere where they are heavily attenuated, so it became impossible to repeat the observations and solar radar has been almost forgotten.

It is probable that new radar observations with modern signal processing, dual polarization, and multiple frequencies, combined with modern optical, UV, and X-ray observations, could make a significant contribution to the fundamental questions of coronal heating and solar wind acceleration. Solar radar observations near 50 MHz are possible at present with at least two radars, the Jicamarca ionospheric radar in Peru and the Gadanki atmospheric radar in India. It may soon be possible to observe between 18 and 26 MHz using a new ionospheric heater planned for the Arecibo observatory. The radar echos from Gadanki could be imaged with the GMRT radio telescope, and both Arecibo and Jicamarca echos could be imaged with the proposed LOFAR array. So prospects for revival of solar radar are encouraging.[1]

2. Theory

The propagation constant $k = n\omega/c = \beta + j\alpha$ for a radio wave in a warm plasma, such as the corona, depends on the density, magnetic field, and electron temperature. A normally incident radar wave is reflected at the height H at which β becomes zero. This depends only on the density and the magnetic field. The loss term α depends on the collision frequency and thus T_e as well. To the accuracy necessary here, the refractive index is given by $n^2 = 1 - \omega_p^2/\omega(\omega \pm \omega_{ce})$, where $\omega_p^2 = n_e e^2/m_e\epsilon_0$ gives the electron plasma frequency, and $\omega_{ce} = eB/m_e c$ is the electron cyclotron frequency. The refractive index $n < 1$ so the phase velocity $V_p = c/n > c$, but the wave is highly dispersive and the group velocity $V_g = d\omega/dk = nc < c$. The power loss term $2\alpha = \nu(1 - n^2)/(nc)$, where ν is the collision frequency. In the corona $\nu = 1.81 \times 10^{-6} n_e A_1(2)/T_e^{1.5}$ where $A_1(2) = ln(1 + (10^7 4kT_e/c^2e^2n_e^{0.333})^2)$. The two-way delay T_d and optical depth τ are determined by the integrals given below.

$$T_d = 2\int_{Earth}^{H} ds/V_g \quad and \quad \tau = \int_{Earth}^{H} 2\alpha\, ds\,. \tag{16.1}$$

[1]Note added in proof: A series of new 50 MHz observations has been made at Jicamarca by Coles *et al.* (2004) using the same modulation and pulse width as El Campo. These observations have not shown any valid echoes. This negative result suggests that the echo amplitude may have been significantly overestimated and makes prospects for revival of solar radar less encouraging than when the chapter was written.

We have used these expressions, with estimates of the and temperature in the coronal holes and the equatorial streamers, to obtain the reflection height H, delay T_d, and loss $\exp(2\tau)$ for the two circular polarizations vs. frequency. The density models and the height of the turning points are shown in Figure 16.1. The coronal hole density is from Guhathakurta *et al.* (1999), and the streamer density is from Parenti *et al.* (2000). The kinetic temperature of the electrons is not as well known, so we used rough values of $T_e = 1 \times 10^6 K$ in the coronal holes and $T_e = 2 \times 10^6 K$ in the streamers. The magnetic field is even less well known. We assumed that it was the same in the coronal holes and streamers and extrapolated inwards using $B_r \propto R^{-2}$. This undoubtedly underestimates the field. The left-handed mode (LH) has smaller refractive index change than the RH mode so it turns deeper in the corona (increasing the delay). Likewise the coronal hole plasma is less dense so the reflection points are deeper than in the equatorial plasma.

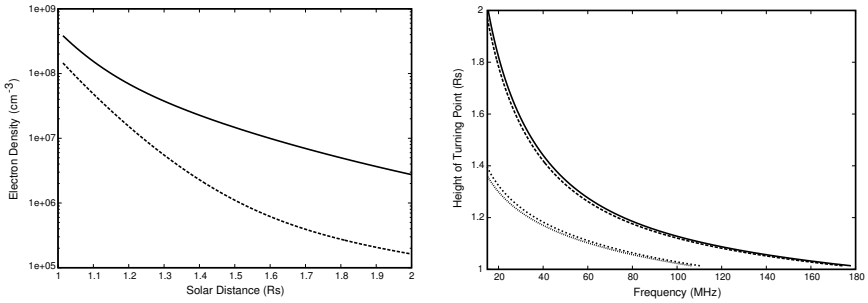


Figure 16.1. Plasma density versus solar distance (left panel) and reflection height versus frequency (right panel). Two plasma models, corresponding to streamers with $T_e = 2 \times 10^6 K$ and coronal holes with $T_e = 1 \times 10^6 K$ are given. The upper traces are from the streamer model in both panels. The magnetic field is the same in both. The free space delay is 4.64 s/$R_\odot$.

The total path-integrated contribution of the plasma to the delay is the almost same for both polarizations. Thus the differential delay between the polarizations ($\approx$ 150 ms at 38 MHz) is almost entirely due to the different height of the turning points. The delays can be measured with sufficient accuracy to provide good estimates of both the density and the magnetic field near the turning points. Since the density is already reasonably well-known from optical observations, the most important result will be the magnetic field estimate.

The loss increases dramatically if the wave "punches through" the corona into the transition region where the temperature decreases and the density increases. This will probably occur near 110 MHz in the coronal holes and 180 MHz in the streamers but we do not have sufficient information to model the effect. The lower frequency limit, $\sim$ 15 MHz, is set by the ionospheric cutoff, but

increasing noise, refraction and scintillation will make operation down near the cutoff unattractive. The plasma delay and the signal loss are shown in Figure 16.2. The loss is higher in the coronal holes because the temperature is lower and the collision frequency is higher, however the plasma delay is lower because the turning point is nearer the Sun where the density gradient is higher.

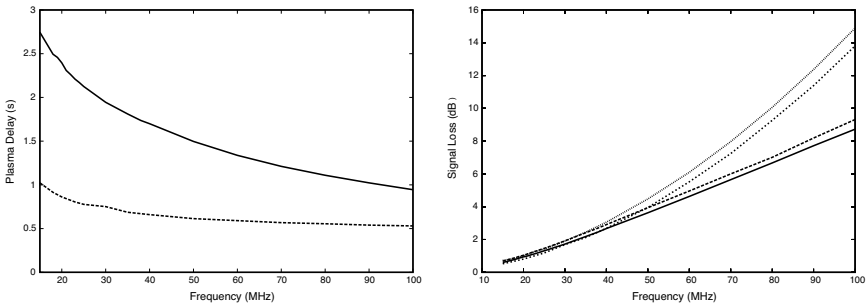


Figure 16.2. Plasma delay versus frequency (left panel) and loss versus frequency (right panel) for the models given in Figure 16.1. The coronal hole model gives less plasma delay and more loss.

The effect on delay of a step density increase, such as would occur during a fast Earthward CME, is plotted in Figure 16.3. When the step passes the turning point it carries the turning point outward, reducing the free space delay abruptly. When both polarizations reflect from the edge of the step the differential delay is entirely due to the differential plasma contribution so the sense of the difference is reversed. When the step moves far enough outward the turning points of the two polarizations separate again and the differential delay changes back to the normal sense. The total delay then increases slowly as the remainder of the line of sight fills with denser plasma.

The returned echo will be scattered into a Doppler spectrum by motion of the plasma at the turning point. The Doppler spectrum will be shifted by the velocity of the solar wind and broadened by the random thermal and wave motions in the plasma. The reflection process is an electron resonance but it is a collective effect of many electrons. In this case the broadening is not due to the thermal velocity of the electrons but to that of the ions. This phenomenon has been studied in the case of Bragg backscattering in the ionosphere (Vanzandt & Bowles 1960; Fejer 1960), but does not appear to have been studied in the case of coherent reflections such as solar echoes.

Radars normally transmit and receive with the same antenna, and the antenna beam illuminates the entire target. The antenna area A and gain G are related by $G = 4\pi A/\lambda^2$. In this case we can calculate the received power in terms of

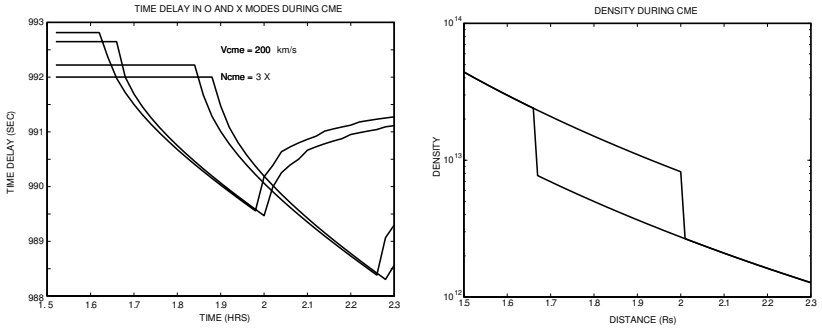


Figure 16.3. Simulation of a spherically symmetric density step of three times the background density, moving outwards at 200 km/s = $1R_\odot$/h. The delays are shown for RH and LH polarizations at 18 and 26 MHz. The density profile is shown at 1.68 h and 2.0 h.

the target cross-section σ, which is the area of the equivalent isotropic reflector. (The radar cross section of a large sphere is equal to its cross sectional area, regardless of the surface roughness.) The transmitted flux is $S_t = P_t G/4\pi R^2$. The reflected power $S_t\sigma$ is reradiated isotropically, so the total returned power at the antenna is

$$P_r = P_t\sigma\frac{GA}{(4\pi R^2)^2} = P_t\sigma\frac{A^2}{4\pi\lambda^2 R^4}. \tag{16.2}$$

The reflected power is further reduced by the loss due to propagation through warm plasma as discussed earlier. The returned signal is weak, because the gain of the transmitting antenna is low at the low frequencies necessary to obtain a coronal reflection, so the antennas must be physically large. This means that the noise for all practical antennas will be dominated by solar noise. Thus we can calculate the signal to noise ratio directly from the solar flux $S_s = 2kT_e\Omega_s B/\lambda^2$ W/m^2. Here B is the bandwidth and $\Omega_s = \pi(R_\odot/R)^2$ is the solid angle subtended by the Sun. The resulting signal to noise ratio is

$$\frac{P_r}{P_s} = \frac{P_t A}{8\pi kTBR^2}. \tag{16.3}$$

It is interesting that the signal to noise ratio (except for plasma loss) is independent of frequency. This is because both the solar noise and the antenna gain increase with frequency at the same rate.

If the reflecting surface were a smooth sphere the echo would come entirely from a small region in the center of the apparent disk called the specular reflection. The cross section of such a reflection is $\sigma = \pi R_c^2$, where R_c is the radius of the reflecting surface. The actual area contributing to the specular reflection would be roughly that of the first Fresnel zone $\approx \pi R_c\lambda/2$.

If the reflecting surface is rough on a small scale, the wave will be backscattered into an angular spectrum of width θ_{rms}. Each specular reflection will be broadened into a patch of diameter $\approx \theta_{rms} R_c$. If the surface is very rough, such as the surfaces of the terrestrial planets, moons, and asteroids, the echo will be distributed more or less uniformly over the half of the reflecting surface that faces the radar.

To determine the backscattering angular spectrum for the corona one must characterize the surface roughness to obtain an estimate of the rms gradients of the surface. The density fluctuations can be described by their structure function $D_{ne}(\mathbf{s}) = \langle (n_e(\mathbf{r}) - n_e(\mathbf{r}+\mathbf{s}))^2 \rangle$, so the rms density gradient on a scale s is given by $\delta n_e/s = D_{ne}^{0.5}(s)/s$. The structure function $D_{ne}(s)$ is power law in nature but the exponent changes at the inner scale $s = \ell_i$. At scales $s < \ell_i$, $D_{ne}(s) \propto s^2$ so $\delta n_e/s$ is independent of s. At scales $s > \ell_i$, $D_{ne}(s) \propto s^\alpha$ where $\alpha < 2$, so $\delta n_e/s$ drops with increasing scale s. We have measurements of $D_{ne}(s)$ near $s = \ell_i$ from radio scattering observations and we can use a recent model (Armstrong *et al.* 2000) to obtain a lower bound at a typical radar turning point of $1.4 R_\odot$. At that distance the model gives $D_{ne}(s < \ell_i) \geq 2.1 \times 10^{-6} n_e^2 (s/\ell_i)^2$ and $\ell_i \approx 1040$ m.

The gradient of the reflecting surface can be obtained by translating the density fluctuation δn_e into a height fluctuation $\delta H = \delta n_e/(dn_e/dR)$ where dn_e/dR is the radial gradient. The rms surface gradient is then $dH/dR = (D_{ne}^{0.5}(\ell_i)/\ell_i)/(dn_e/dR)$. The density gradient at $1.4 R_\odot$ is $dn_e/dR \approx n_e/6R$ so $dH/dR \approx 220$! The effect of anisotropy will increase this by about an order of magnitude, but it is very large in any case. The coronal reflecting surface is very different from other targets in the solar system. It is smooth on scales smaller than the inner scale, which is about 100 times larger than the wavelength. However the surface gradients are extremely large. It appears that the incident wave will be backscattered into a very wide angular spectrum by reflection from a violently undulating smooth surface, rather than a rough surface.

To help visualize the nature of the reflecting surface we show simulated one-dimensional cuts $n_e(r)$ in the radial and tangential directions in Figure 16.4. The Fourier transform of $n_e(r)$ was generated from a sampled gaussian random process and scaled so its squared magnitude matches the anisotropic spectrum measured by radio scattering near the Sun (Grall *et al.* 1997). It was then Fourier transformed back and the mean radial gradient was added. The fluctuations in $n_e(r)$ are normalized to the mean value of the simulation. The two-dimensional spectra at this distance have an axial ratio of about 50, so the two cuts have very different spatial scales. The smallest scales in the tangential direction are about 1 km, whereas in the radial direction they are about 50 km. The reflecting surface will be at the rising edge of one of these radial bumps. It will be carried outward until the peak density drops below the critical value, then it will jump

back to the following bump. If these density bumps are convected with the plasma flow (velocity V_f), then the mean Doppler shift will be $\Delta\nu = 2V_f\nu/c$, however they could be traveling density waves (wave velocity V_w), which would increase the Doppler shift to $\Delta\nu = 2(V_f + V_w)\nu/c$.

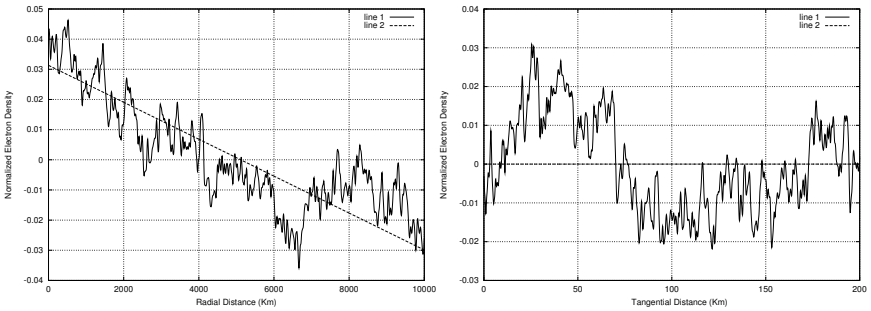


Figure 16.4. Simulation of n_e vs radial distance (left panel), and n_e vs tangential distance (right panel). The mean radial gradient is shown as a dashed line in the left panel.

The radial gradients of the fluctuations are very much larger than the mean radial gradient. Thus the height of the reflecting surface will vary by 1000's of km as these structures move outward. The structure of the reflecting surface is illustrated in Figure 16.5, which is a two-dimensional cut through the equatorial plane. The region where the wave can propagate is white, where the wave is cutoff it is black. The wave is incident from the right and is reflected by the black structure. However, in order to display the plot conveniently we increased the radial gradient by a factor of 20. Thus the highly filamentary radial structures in Figure 16.5, should actually be even more elongated. This is an unusual type of reflecting surface which apparently has not been studied before. It seems likely that it will scatter the incident wave into a wide angular spectrum, but it is also possible that multiple reflections in the low density channels will greatly increase the loss in the manner of an optical beam trap. Study of the cross polarized echo may be useful here. Evidently some analysis and perhaps simulation of this situation will be necessary.

The corona has a great deal of large-scale structure controlled by the coronal magnetic field. The gradients in such structures are small compared with the turbulent gradients, but the changes in the mean density and temperature are significant. Near solar maximum the height of the reflecting surface at 38 MHz will be about 1.4 $R_\odot$ so the radar cross section will be about $\sigma = 2\pi R_\odot^2$. Near solar minimum the large scale structure is characterized by a high density equatorial streamer belt and coronal holes over both poles. The height of the reflecting surface will be about 1.4 $R_\odot$ over the streamer belt and 1.2 $R_\odot$ over the polar holes. The polar hole echo is weaker, as shown in Figure 16.2, so

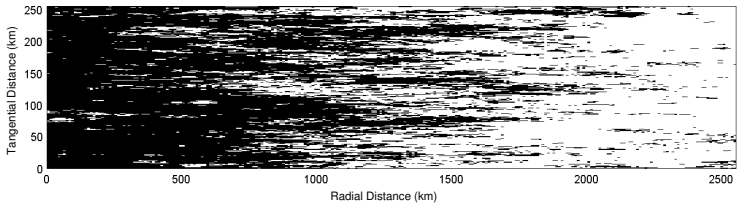


Figure 16.5. Simulation of n_e in the equatorial plane. In the dark regions the wave frequency is above the plasma frequency and the wave cannot propagate. The wave is incident from the left and reflects from the black structures. The pixel size is 1 km by 10 km. The radial gradient has been increased by a factor of 20 to keep the plot on a convenient scale.

the average cross section at solar minimum will be about half that at solar maximum.

At all phases of the solar cycle coronal mass ejections (CMEs) are common, although the rate is higher at solar maximum and during the declining phase of solar activity. CMEs often have a roughly spherical geometry comparable in size with the solar disk. However, they are far from a smooth sphere and many irregular events occur. One of the simplest large CMEs observed with LASCO is shown in Figure 16.6 below. Such a CME would have a stronger echo than the background corona because it will not only increase the area, it will push the reflecting surface out and reduce the loss.

We have considered only the total reflection that occurs at the location where the refractive index goes to zero. The wave can also be reflected from periodic density fluctuations that satisfy the Bragg condition. The density fluctuations can be thermal fluctuations or MHD waves. In either case, only a small amount of the incident power will be reflected at any distance, so the echo is distributed over range. This is a very useful phenomenon in the ionosphere but Bragg reflections from the corona are too weak to be measurable with an Earth-based radar.

3. Other Coronal Observations

Solar observations, by any method, are complex and difficult to interpret because there is a large range of spatial structure; the Sun is not constant; and the observations inevitably average over some finite region. It will be essential to interpret solar radar observations in conjunction with other coronal observations. Here we outline the other coronal data that are most likely to be useful in this regard. These include: (1) white light observations of Thomson scattered solar radiation; (2) radio forward-scattering observations; (3) UV

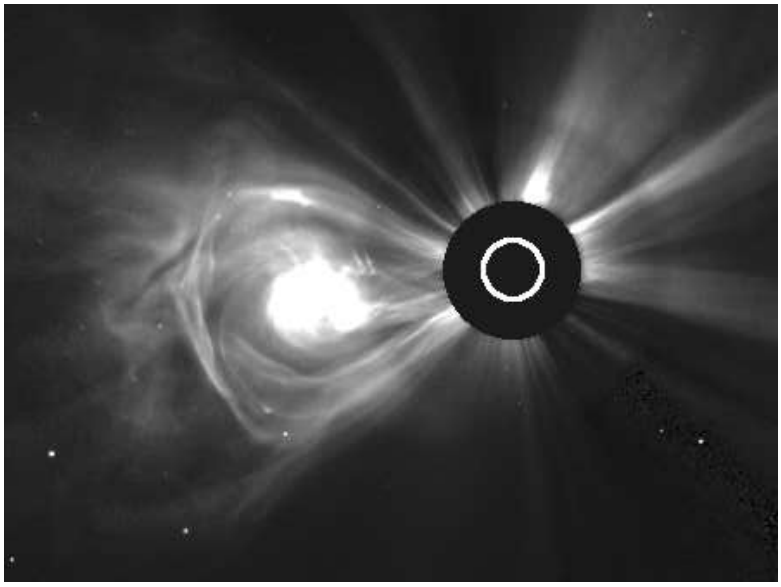


Figure 16.6. A relatively simple large CME known as "the lightbulb" as observed by LASCO C2 and C3. This CME was directed to the north and has been rotated east for convenience. The SOHO/LASCO data are produced by a consortium of the Naval Research Laboratory (USA), Max-Planck-Institut fuer Aeronomie (Germany)), Laboratoire d'Astronomie (France), and the University of Birmingham (UK). SOHO is a project of international cooperation between ESA and NASA.

emission line observations; (4) soft X-ray continuum observations; (5) radio emission observations. All of these observations involve important line of sight integrations, and the effect of this is different for each observation. It is usually less severe for observations made on the disk than for observations made off the limbs.

The white light observations are made off the limbs where the direct solar radiation can be blocked with occulting disks. They provide an image of the path integrated coronal electron density. These are the best measurements of large-scale coronal structures such as streamers, coronal holes, and CMEs. An example of a CME observation is shown in Figure 16.6. No existing space-born coronagraph can reach the turning point of feasible solar radars because the occulting disks are too large. Fortunately, the new COR1 coronagraph of the SECCHI instrument on STEREO will reach 1.4 $R_{\odot}$. The velocity of well-defined structures like CMEs can be measured by tracking the motion of the feature over time. Smaller structures in streamers have also been tracked, but it has not been possible to measure the velocity in coronal holes by this method because no distinct features can be tracked. White light observations

are not directly sensitive to the magnetic field, but lines of enhanced brightness appear to follow magnetic field lines, and they are believed to be a tracer of the magnetic field.

Radio forward-scattering measurements are also limb observations sensitive to density or density fluctuations. One can, in principle, measure Faraday rotation and thus the magnetic field. However, in the normal limb observation the mean Faraday rotation cancels out and only fluctuations can be observed. If a coherent source, such as a space-craft transponder or a pulsar, is available one can measure the column density. Otherwise one can measure the density fluctuations. These measurements can be very precise but only in the direction of the radio source. In this respect they are complementary to the white light observations, which provide an image but less precision. Radio scattering measurements can measure the micro-turbulence and also the velocity of the microstructure. However the microstructure might be moving with respect to the mean flow, if the density fluctuations are caused by traveling waves, and this potential bias can be very important in the sub-Alfvénic flow near the Sun. The primary value of radio scattering measurements for solar radar is that they can be used to estimate the small-scale density gradients, which determine the angular spread of the radar echo.

Soft X-ray observations can be made both on disk and off the limbs. The emission is free-free bremsstrahlung and the characteristic temperature of the radiating electrons is about 7×10^6 K. This is far above the kinetic temperatures of $1-2\times10^6$ K, so the soft X-ray emission is really a measure of the high-speed tail of the electron velocity distribution. Such superheating of electrons occurs when they are trapped on closed field lines. Absence of soft X-ray emission is a clear signal of open field lines and this is how coronal holes, which are characterized primarily by open field lines, were discovered.

Ultraviolet emission lines can be observed both on disk and off the limbs. They are sensitive to density, temperature and composition. A great deal of information can be derived from these observations but very careful modeling is required. They are particularly valuable in the transition region where one can trace the temperature by observation of different ionization states. There is great potential for comparing details of the radar echoes with TRACE and UVCS observations.

Meter wavelength radio emissions have been observed since the dawn of radio astronomy, because the Sun is a very strong radio source at low frequencies. Continuous thermal emission comes from the hot plasma above the reflection point. However, strong transient emissions occur at the local plasma frequency or its harmonics. They are caused by a disturbance, such as a shock or a stream of relativistic electrons. By observing emission at different frequencies one can measure the local density and trace the disturbance outward (and occasionally inward). These local emissions are often much stronger than the thermal

emission from the entire Sun. They can be observed with spectrometers, which average over the entire Sun. However one can also image the emission with a radio-heliograph, which allows one to separate emissions in position, and to compare with other imaging observations. These observations are primarily traces of solar activity and have not been as useful in outlining the quiet regions. They may prove very useful in comparisons with radar echoes.

4. Previous Radar Measurements

The first radar echoes from the Sun were detected by in 1959 (Eshleman *et al.* 1960). They transmitted 40 kW at 25.6 MHz using an antenna with 3450 m^2 collecting area. The detection was marginally significant in an integration time of 18 min. Regular measurements were made from 1961 to 1969 with a much more powerful system (James *et al.* 1970). They transmitted 500 kW at 38 MHz using an antenna with 20,000 m^2 collecting area. The signal was much weaker than had been expected on the basis of the 1959 detection—less than one would expect of a spherically symmetric Sun. The only other apparent radar detection was made at 40 MHz using Arecibo in 1965 (Campbell, private communication, 2001). Solar observations at Arecibo were not continued. Attempts to detect a Raman scattered echo at 2380 MHz with the Arecibo radar were unsuccessful (Fitze & Benz 1981).

The El Campo antenna was a manually-phased array with a rather narrow bandwidth. It was steered in declination by changing the length of the transmission lines. The beam width was 8° E-W by 2° N-S, which is enough to transmit for 18 min, then receive for 18 min, once a day. The antenna declination was changed every few days to track the seasonal change in solar declination. The transmitter was frequency-shift (FSK) modulated between frequencies separated by 8 kHz because it was originally thought that the Doppler shift would not exceed this value. However it was increased in subsequent years to 16, 40, and finally 60 kHz. Even 60 kHz, which corresponds to 237 km/s, was not always sufficient and some of the data show evidence of aliasing in the form of negative echo power. Although part of the antenna had two polarizations, measurements of cross polarization were not reported. The signal processing was done with repeated passes of an analog tape through an analog filter bank. The design and operation of this radar was a tour de force with the technology of the day.

The results were a surprise in many respects. The mean delay was close to the expected value, but echoes were received much earlier and much later than the mean. A long-term average of the delay distribution (James 1968) is shown in Figure 16.7. The observations confirmed that the mean electron density used to model the observations was reasonably accurate, which was not surprising since the density model used (Pottasch 1960) was the result of a great many

optical observations. The early echoes must arise from high density structures near the center of the disk. These could come from equatorial streamers but much stronger echoes would come from Earth-directed fast CMEs, which would carry the reflecting surface further outward than normal. The late echoes must have come from the limbs. They could be either high inclination streamers or CMEs on the limb.

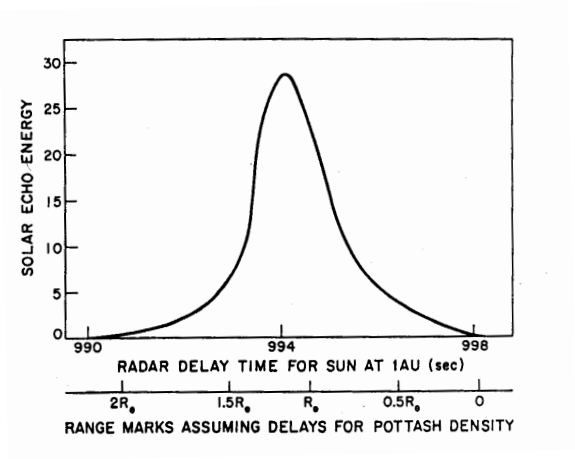


Figure 16.7. Average range distribution of echoes observed with El Campo radar.

The echo strength was weaker than expected and was also highly variable. The annual averages (James 1970), shown in Figure 16.8 are clearly correlated with solar activity. The observations were started as solar activity was declining and the mean echo strength continued to decline with solar activity. It began to increase in 1968 as the solar activity picked up, but the observations were stopped before solar activity reached maximum. This behavior is evidently caused by the reduced cross-section of the polar coronal holes that form at solar minimum as discussed earlier.

The echo strength was also more variable than expected, with daily variations sometimes exceeding a factor of 10. This is apparent in several years of daily observations (James 1968) as shown in Figure 16.9. Some of the unusually large echoes are probably due to large fast CMEs. Those directed toward the Earth will have strong echoes and short delays. Limb CMEs will also show enhanced echoes but longer delays. Other large echoes will occur when a highly inclined streamer is near the limb, and these will also show longer delays.

The most informative displays are the range-Doppler spectra, some of which are shown in Figure 16.10. These were selected from those with high echo amplitude at normal or higher heights (James 1968), which suggests that they

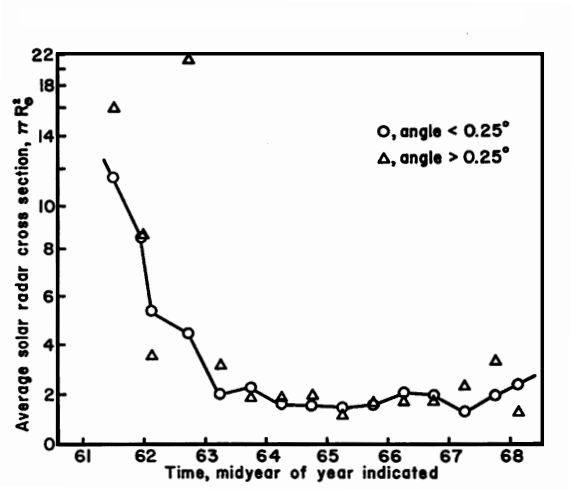


Figure 16.8. Annual average echo strength.

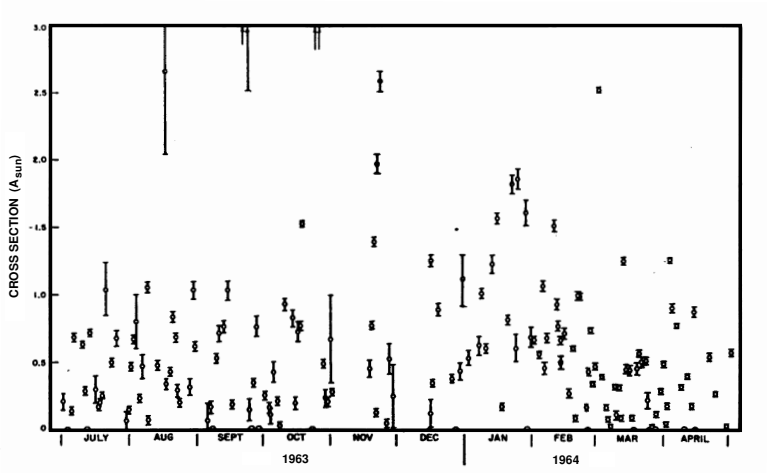


Figure 16.9. Daily measurements of echo strength.

are Earth-directed fast CMEs. The spectra all show a large Doppler broadening corresponding to rms radial velocities of about 100 km/s, consistent with ion temperatures of the order of 2×10^6 K. The spectra clearly shift to the right with elevation, which is consistent with an acceleration. However the echoes

from lower ranges are probably from the flanks of the CME where the velocity is not directed toward Earth. This would cause an apparent acceleration. The mean shift of the higher echoes, of the order of 50 to 100 km/s, is probably a good measure of the radial velocity and is consistent with measurements of fast CME at these heights. These spectra provide some guidance for planning future observations. The Doppler resolution of 5 kHz is sufficient but the finer range resolution would be useful.

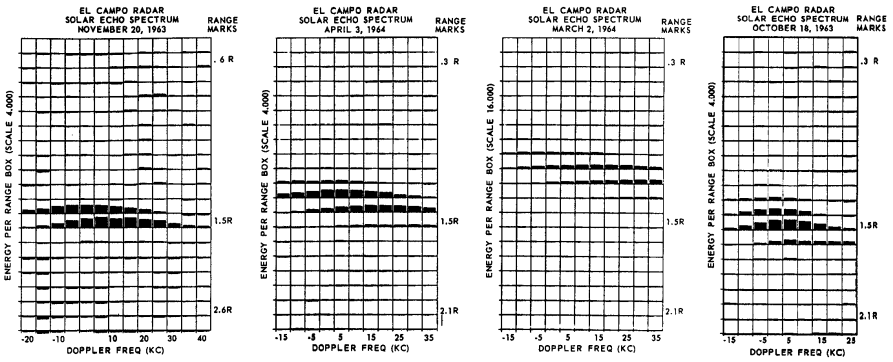


Figure 16.10. Range-Doppler spectra of selected strong echoes. At 38 MHz a velocity of 4 km/s gives a Doppler shift of 1 kHz, so the 5 kHz grid corresponds to 20 km/s.

More typical spectra, such as those in Figure 16.11, show a rich variety of structure (James, 1968). Some features in Figure 16.11 show much less broadening and the broadening is not as smooth as in Figure 16.10. Evidently this must be cool material extending into the corona. Chromospheric material with a kinetic temperature of 10^4 K would have a thermal velocity of about 10 km/s and a Doppler broadening of about 2.5 kHz. Such cool features should be observable in H_α which is regularly monitored on the disk. These spectra suggest that it would be valuable to have finer Doppler resolution, perhaps 1 kHz, in future observations.

5. New Observations

There are a few ionospheric and atmospheric radars which could observe echoes from the Sun with sensitivity comparable with that of El Campo. New radars will have to use pulse amplitude modulation PAM which only provides a maximum 50% duty cycle, because we now know that potential Doppler shifts can exceed the maximum possible FSK shift. It may be possible to use polarization modulation if the cross polarization of the echo is very small. Since

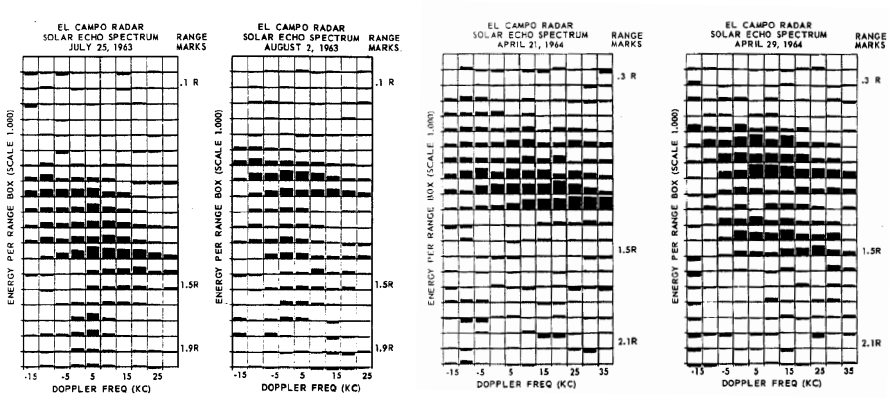


Figure 16.11. Typical Range-Doppler spectra. Notable on theses plots are multiple clusters in range and some rather narrow Doppler features. The narrowest features on these spectra could be chromospheric material.

the coherence time of the corona is less than the range resolution, the range decoding must be done incoherently. Thus the effective transmitting power is the peak power P_{pk} times the square root of the duty cycle D. Thus a figure of merit is $F_m = P_{pk}A(DN_p)^{0.5}$, where N_p is the number of polarizations. The echo is probably unpolarized so the signal to noise ratio increases by $\sqrt{2}$ if both polarizations can be measured.

The signal to noise ratio also depends on the pulse width T_p. If the pulse width of the radar is much smaller than the intrinsic width of the echo T_s, the signal to noise ratio decreases as $(T_p/T_s)^{0.5}$. If the intrinsic pulse width exceeds the pulse repetition rate of T_p/D, then it is better to operate in a CW mode where the effective power is P_{avg} but the pulse can be matched to the echo. Estimated values of F_m are given in Table 16.1 for pulse lengths of 2 ms and 500 ms, for existing and potential radars. These have been corrected for the expected signal loss for the streamer model in Figure 16.2 and referenced to El Campo.

The signal to noise ratio does not depend on the frequency resolution because frequency smoothing can be applied either before or after range decoding. Most of the El Campo data were taken with T_p = 500 ms and a frequency resolution of 5 kHz. The data may have finer structure in both range and Doppler, so higher resolution in both coordinates would be useful.

The most sensitive existing radar for solar observation is the 50 MHz radar at Jicamarca in Peru. However its maximum pulse width is only 2 ms and the duty cycle is 5%. So if the intrinsic pulse width exceeds 40 ms it should be operated in CW mode. Like El Campo, Jicamarca is a transit instrument that can be steered manually $\pm 3.5^\circ$ from the zenith in either direction. It is bigger than El Campo,

Table 16.1. Comparison of Solar Radar Parameters.

Parameter	Arecibo	Jicamarca	El Campo	NMRF
Frequency (MHz)	15-26	50	38	53
Peak Power (MW)	2.4	2.25	0.5	2.5
Avg Power (kW)	600	112	500	60
Area (1000 m^2)	30	63	20	10
Sensitivity F_m (2ms)	6.7	3.4	-	0.4
Sensitivity F_m (500ms)	2.4	0.5	1	0.04

and it also has dual polarization. However the Jicamarca beam is less than 1° in diameter, so if it were pointed at the Sun to transmit, it would be pointing off the Sun by the time the echo returned. Fortunately the antenna can be separated into sub-arrays and it is possible to use separate sub-arrays for transmitting and receiving. Even with the antenna split Jicamarca has higher sensitivity than El Campo, so solar observations appear to be feasible. Jicamarca is at $-7°$ latitude, so the Sun is within the steering range during two 13-day periods—Oct. 19 to 31; and Feb. 11 to 23. The daily declination change is about 1.6 $R_\odot$/day, so the Sun can only be observed for a few days without repointing the beam. An unsuccessful attempt to observe the Sun with Jicamarca was made in the early 1960's (Bowles, private communication, 2002). This is puzzling because Jicamarca made the first detection of echoes from Venus about the same time, and the Venus detection appears to be more difficult.

Jicamarca is probably best configured with most of the array devoted to transmitting, and only a few modules used for the receiver. However only three of the four original transmitters are presently operational, so it is presently optimal to use three quadrants for transmitting and one for receiving. The transmitters are presently operated at about 75% of their original rating, so the sensitivity is less than that available in the 1960s. The modular nature of Jicamarca allows the use of interferometry to obtain some spatial resolution.

The 53 MHz National MST radar facility (NMRF) at Gadanki near Bangalore in India is another possibility. It has a peak power of 2.5 MW with a duty cycle of 2.5%, and dual polarization. Although it is considerably less sensitive than Jicamarca, it might be possible to use the "Giant Meter Wavelength Radiotelescope" GMRT near Pune as an imaging receiver. With GMRT the sensitivity would not increase, but imaging the echo would be so valuable that this possibility should be explored.

It may soon be possible to use Arecibo as a solar radar. It is likely that a proposed ionospheric heater will be constructed in the next few years, and this heater can be used as a solar radar with minor modifications. The design of

the proposed heater is not complete at this time, but the primary features are becoming clear. The transmitter will operate from 3.0 MHz to 26 MHz. It will have a peak power of about 2.4 MW with a 25% maximum duty cycle, and it will probably be connected to a fixed-feed in the 305 m primary reflector. This will be a very sensitive and flexible system because of the high average power. The heating feed or feeds will only operate up to 9 MHz, so a new high-power feed will have to be constructed for the 18 to 26 MHz band. However we can use an existing dual-polarization 25 MHz receiving-feed mounted on carriage house 2. The beam width would be more than twice that of Jicamarca so there is little possibility of separating the echos from the limbs without an additional receiving antenna.

If the transmitter feed is fixed, then the transmit time will be 18 min, but if the transmitting feed were also mounted on carriage house 2 the total observation time could be increased to 2 h. This would be a real advantage for observing transient events like CMEs. It is feasible to route the transmitter power to the carriage house using an existing high power coaxial-line which is presently unused. This would also simplify the setup considerably and make it much easier to interleave solar observations with other uses of the telescope.

The Arecibo system would have several advantages over Jicamarca: the antenna can be pointed at the Sun any time between March 22 and September 22; the observing time per day is longer; any frequency from 18 to 26 MHz can be used; and sensitivity is better. However observations at Jicamarca will remain interesting because the frequency is different, and the angular resolution is significant.

The analysis of single-antenna data will remain complex because the echo is integrated over the entire Sun. The reflecting surface will have to be located by model fitting, which will have to include correlative optical, UV, and soft X-ray data to constrain the large scale geometry. However some geometries will be unambiguous, for example that of a fast Earth-directed CME. Such a case will be particularly valuable in measuring the pre-CME corona, because the incident wave will be reflected at the leading edge of the density compression. The CME will act as a test reflector moving out through the pre-existing corona. The location of cool filaments may also be unambiguous as they can be observed on the disk with an H_α monitor.

6. Use of an Imaging Receiver

The most serious weaknesses of the single antenna radars: (1) the ambiguity in the location of the reflections and the resulting complexity in echo analysis; (2) the limited frequency range and thus height coverage; (3) limited tracking time. The ambiguity problem could be eliminated by receiving the echo with an imaging array capable of spatially resolving the coronal features of interest.

Such an array would provide a range-Doppler spectrum for each beam, mapping the reflecting surface in velocity, density, and magnetic field. This would be possible using the NMRF and GMRT in India, although the planned 53 MHz receiver at GMRT has not yet been implemented. Another possibility is the LOFAR array, now being designed primarily for radio astronomy. LOFAR would be ideal for receiving the solar echo (provided it is located reasonably close to the transmitter) because it is designed to have a good instantaneous beam shape. Most imaging arrays, including GMRT, have rather high sidelobes on their "instantaneous beam." They synthesize a clean beam by Earth-rotation averaging, which typically takes at least half a day. A LOFAR array in the south-west USA could work with both Arecibo and Jicamarca transmitters. Unfortunately Arecibo and Jicamarca cannot point at the Sun at the same time because Arecibo cannot point south of 0° declination and Jicamarca cannot point north of -5° declination.

The LOFAR goal is to have the instantaneous beam sidelobes $< 0.5\%$ of the peak so the dynamic range of the map could exceed 100. Since the signal to noise ratio is limited by the transmitter flux, rather than the sensitivity of the receiver, it is unlikely that LOFAR could reach a dynamic range of 100 with existing transmitters. Even if the sidelobe levels are somewhat higher LOFAR should be able to produce excellent maps of the reflecting surface. The GMRT/NMRF combination cannot provide the high spatial resolution and high dynamic range of LOFAR, but it would be capable of resolving the major coronal features of interest, i.e. coronal holes, CMEs, streamers, etc. Furthermore a 53 MHz system at GMRT could be ready long before LOFAR, so serious consideration should be given to NMRF. The main uncertainty appears to be the coronal loss at 50 MHz. This could be resolved by observations at Jicamarca which would help judge the feasibility of NMRF/GMRT observations.

Acknowledgments

The author wishes to thank Barney Rickett, Mike Sulzer, John Harmon, Brett Isham, Don Campbell, Ernie Hildner, Mukul Kundu, Ken Bowles, and Jesse James for helpful comments, suggestions, and discussions.

References

Armstrong, J. W., W. A. Coles, & B. J. Rickett, 2000, JGR105, 5149

Coles, W. A., Sulzer, M. P., Harmon, J. K., Chau J. L. & Woodman R. F. 2004, presented at "Ionospheric Interactions Workshop," Santa Fe, NM, 2004 April 18-21

Eshleman, V. R., R. C. Barthle, & P. B Gallagher, 1960, Science, 131, 329

Fejer, J.A., 1960, JGR65, 2635

Fritze, H. R. & A. O. Benz, 1981, ApJ, 250, 782

Grall, R. R., W. A. Coles, S. R. Spangler, T. Sakurai, & J. K. Harmon, 1997, JGR102, 263

Guhuthakurta, M, A. Fludra, S. E. Gibson, D. Biesecker, & R. Fisher, 1999, JGR, 104, 9801

James, J. C., 1968, Chapter 7 in Radar Astronomy, (eds J. V. Evans & T. Hagfors), McGraw-Hill, New York

James, J. C., 1970, Solar Phys12, 143

Kerr, F. J., 1952, Proc. IRE, 40, 660

Parenti, S., B. J. I. Bromage, G. Poletto, G. Noci, J. C. Raymond, & G. E. Bromage, 2000, A&A, 363, 800

Pottasch, S. R., 1960, ApJ, 131, 68

Rodriguez, P., 2000, in Radio Astronomy at Long Wavelengths, AGU Geophysical Monograph 119, 155

Vanzandt, T.E., & Bowles, K.L., 1960, JGR, 65, 2627

Chapter 17

THREE-DIMENSIONAL TOMOGRAPHY OF INTERPLANETARY DISTURBANCES

Bernard V. Jackson
University of California at San Diego
bvjackson@ucsd.edu

P. Paul Hick
University of California at San Diego
phick@ucsd.edu

Abstract We have developed a Computer Assisted Tomography (CAT) program that modifies a three-dimensional kinematic heliospheric model to fit interplanetary scintillation (IPS) or Thomson scattering observations. The tomography program iteratively changes this global model to least-squares fit the data. Both a corotating and time-dependent model can be reconstructed. The short time intervals of the time-dependent modeling (to shorter than 1 day) force the heliospheric reconstructions to depend on outward solar wind motion to give perspective views of each point in space accessible to the observations, allowing reconstruction of interplanetary Coronal Mass Ejections (CMEs) as well as corotating structures. We show these models as velocity or density Carrington maps and remote views. We have studied several events, including the 2000 July 14 Bastille-Day halo CME and several intervals using archival Cambridge IPS data, and we have also used archival *Helios* photometer data to reproduce the heliosphere. We check our results by comparison with additional remote-sensing observations, and *in-situ* observations from near-Earth spacecraft. A comparison of these observations and the Earth forecasts possible using them is available in real time on the World Wide Web using IPS data from the Solar Terrestrial Environment Laboratory, Japan.

1. Introduction

In coronal and heliospheric physics there have been numerous attempts to reconstruct the corona and heliosphere in three dimensions. Near the Sun there is good reason to determine the three-dimensional shapes of structures in order to learn about their initiation and source of energy. Coronal mass ejections (CMEs) often have a loop-like appearance. As helical loops driven by currents, as proposed by Anzer (1978) or Mouschovias & Poland (1978), the shape of a CME should follow a very specific pattern. If, however, a CME is a spherical bubble, then it might very well be the remnant of a large addition of energy at a single point in the low corona (Wu, Dryer & Han 1976). Various techniques used to determine CME shapes from the single perspective of Earth, including polarization (Munro 1977; Crifo, Picat & Cailloux 1983) and depletion of the corona (MacQueen 1993) indicate that CMEs are extensive coronal structures. Studies using multiple perspectives from spacecraft viewing from different vantage points (Jackson *et al.* 1985) reach the same conclusion. The extent and the shape of the background corona are also important. For instance, the shapes and positions of coronal streamers can indicate their location and extents relative to the magnetic structures on the Sun. This in turn can give an indication of whether all streamers are formed by the effects of a global solar current "pinch" effect or some more local magnetic phenomena. For studies of the solar wind and the processes that supply its energy, these studies can only be carried out if the global solar wind parameters can be determined.

Forecast ideas in heliospheric physics demand remote sensing techniques that determine the three-dimensional and evolving shapes of solar and interplanetary structures. The three-dimensional morphology of solar features allows a determination of whether or not a solar structure will affect Earth. In the case of flares and other large transient changes near the solar surface this information can tell whether that structure will erupt and then whether or not this eruption is placed in a location to affect the Earth. This premise, more than any other, has promoted the three-dimensional observations that will be possible from NASA's two STEREO spacecraft that are now under construction. When global heliospheric data are available from one or more data sources, a new type of computer assisted tomography is possible that allows a model of corotating and outward-expanding solar wind to reconstruct its shape by the rearrangement of features along each line of sight (LOS). These ideas follow a lengthy heritage of such analyses.

Tomography is best-known for its application in the medical profession, where it is used as a non-invasive way to probe the human body, and reconstruct its internal structure in three dimensions (Gilbert 1972). Most other tomographic applications are limited in the ability to view objects from a large number of directions. However, depending on the choice of orientation and res-

olution of the three dimensional matrix shape relative to the input images, even a single perspective view can provide a unique solution for an object's three dimensional structure (Katz 1978). One of the earliest uses of tomography was in solar radio astronomy (Bracewell 1956). Other areas where tomographic reconstruction techniques have been successfully applied are in studies of binary star systems (Marsh & Horne 1988) and accretion disks in astrophysics (Gies *et al.* 1994), acoustic sounding in oceanography (Worcester, Corunelle & Spindel 1991), seismic studies in geology (Anderson & Dziewonski 1984), auroral studies (Frey 1996) and coronal studies in solar physics (Hurlburt *et al.* 1994). An application in atmospheric modeling, somewhat similar to our model in its use of an irregular sampling of refractometric sounding observations is discussed in Gorbunov (1996).

Some of the first coronal tomographic analyses from Skylab coronagraph observations (Wilson 1977; Jackson 1977) used solar rotation to provide perspective views of the corona. Coronal tomography has been enhanced recently by Zidowitz, Inhester & Epple (1995) using rotational tomographic techniques to reconstruct coronal densities from Mark III coronagraph observations. Corotational tomography of SOHO UVCS data (Panasyuk 1999; Frazin 2000; Frazin & Jansen 2002) has shown considerable improvement over techniques that simply assume the structure is on the limb at the time of observation. A two-perspective-view tomography analysis of CMEs by Jackson & Hick (1994) and Jackson & Froehling (1995) performed using Solwind coronagraph and *Helios* spacecraft photometer observations show the extended three dimensional shape of two CMEs.

Since the 1960s, interplanetary scintillation (IPS) measurements have been used to probe solar wind features with ground-based meter-wavelength radio observations (Hewish, Scott & Wills 1964; Houminer 1971). Observations from the UCSD (Coles & Kaufman 1978) and Nagoya (Kojima & Kakinuma 1987) multi-site scintillation array systems have been used to determine velocities in the interplanetary medium since the early 1970s. The scintillation-level intensity IPS observations, which arise from small-scale ($\sim$200 km) density variations, highlight heliospheric disturbances of larger scale that vary from one day to the next and are often associated with geomagnetic storms on Earth (Gapper *et al.* 1982). These 80 MHz scintillation-level IPS observations show a preponderance of disturbances that appear to corotate with the Sun as inferred from a list of events, their shapes, and their solar surface associations (Hewish & Bravo 1986).

Often, only a rudimentary determination of the location of solar wind structures (an assumption that all material is present at the location of LOS closest approach) has been used to determine several parameters through purely remote sensing. For instance, from IPS velocity data it was determined that the polar solar wind has high speed (Kakinuma 1977; Coles *et al.* 1980; Kojima & Kak-

inuma 1990) long before observations from the Ulysses spacecraft (McComas *et al.*1995) measured these velocities *in situ*. Regions of slow solar wind are generally found near the solar equator especially at solar minimum, and thus near the location of the magnetic neutral line as determined by the potential magnetic field model (Hoeksema, Wilcox & Scherrer 1983). Scintillation level data from the Cambridge scintillation array have been analyzed in the same manner (Hick *et al.* 1995) to produce detailed Carrington maps.

Heliospheric tomography of transient heliospheric structures using global IPS data (Gapper *et al.* 1982; Behannon, Burlaga & Hewish 1991) has often been attempted without the aid of sophisticated computer techniques. A more sophisticated approach has been pursued by Tokumaru *et al.* (2003) or Hayashi *et al.* (2003) who fit assumed model structures to data from one day's observation of IPS data.

The techniques described here apply computer assisted tomography methods to data primarily obtained from one location in space. The corotational analyses (Jackson *et al.* 1997*b*; 1998; Kojima *et al.* 1997; Kojima *et al.* 1998; Asai *et al.* 1998; Jackson & Hick 2002) using these techniques improve upon the inherent averages made by assuming all material lies at the point of closest approach of the LOS to the Sun.

The next section gives a background for both the global IPS and *Helios* photometer Thomson-scattering observations that have inspired these tomographic techniques. The third section describes the solar wind model used and the tomographic program that has been developed to fit this model. The forth section gives a comparison of observations with small portions of the kinematic model that have been reconstructed from them showing that the models do indeed fit observations. The fifth section compares the tomographic models to *in-situ* data from Earth and in the Thomson-scattering analysis, *Helios* spacecraft density data. The sixth section displays and discusses the kinematic model values in a variety of ways including remote observer views of the data and as Carrington synoptic maps. We conclude in the last section.

2. Global Data Analyses

The IPS technique relies on several assumptions to relate changes in scintillation level and velocity integrated along each LOS to local changes in the scintillation level and velocity. In weak scattering (assumed here exclusively), the Born approximation holds and the scintillation pattern at Earth is a sum of contributions from each thin scattering layer perpendicular to the LOS (Tatarski 1961). At any given radio frequency at solar elongations close to the Sun, and depending on the radio source size and the scintillation level, the weak scattering approximation breaks down and IPS observations are no longer optically thin.

This effect provides an effective limit to IPS observations of a given frequency close to the Sun.

Heliospheric Thomson scattering (sunlight scattered from electrons) present along each LOS, on the other hand, is optically thin to elongations within a small fraction of a solar radius out to 180°. However, unlike ground-based interplanetary scintillation measurements, heliospheric brightness is only a tiny component of the brightness of the night sky. At elongations of a few degrees Thomson scattering brightness is at best only a few percent of the zodiacal light, and this percentage becomes less at even greater elongations. Stellar signals can also be hundreds of times brighter than those from heliospheric Thomson scattering. From the surface of the Earth, mesopheric air glow at even the darkest sites presents a time-variable signal that is several times larger (Garcia, Taylor & Kelley 1997; James *et al.* 1997) than heliospheric signals. Mesospheric air glow has effectively limited ground-based Thomson scattering observations to elongations within a few solar radii of the Sun and the best of these at times of total solar eclipses obtained by high-flying aircraft (Chapman 1979).

The tomographic program employed here requires that the contribution of a solar wind model be estimated along each LOS. This model is iteratively changed to fit observations at each LOS by following each LOS contribution back to its origin on an inner boundary and formally inverting the contributions to this inner boundary according to weights provided along each LOS. The solar wind model provides each three-dimensional LOS contribution, and the inner boundary or source surface makes the tomographic inversion a two-dimensional problem in order to maximize the information from each LOS observation. This technique estimates LOS weighting from an IPS or Thomson scattering weight function separate from the solar wind and then includes allowance for the solar wind model. The following two subsections give LOS weighting details that provide modeled IPS g-levels, velocities, and Thomson-scattering brightness.

2.1 IPS measurements

Scintillation-level measurements are available digitally from 1990 October through 1994 September from nearly 1000 sources observed daily at 80 MHz by the Cambridge array telescope. In recent years radio source scintillation-level observations have been obtained from several tens of sources measured each day by the group at the Solar-Terrestrial Environment Laboratory (STELab), Toyokawa City (Nagoya University), Japan. These observations have been available from the STELab Kiso radio telescope from 1997 to the present and more recently (since mid-2002) from the STELab Fuji and Sugadaira radio telescopes. The IPS analysis shown here uses data from a relatively short time intervals from the Cambridge, England and STELab telescopes in 1994 and

from STELab during 2000 July. The value of the disturbance factor g is defined as

$$g = m/\langle m \rangle, \tag{17.1}$$

where m is the fractional scintillation level $\Delta I/I$, the ratio of source intensity variation to intensity and $\langle m \rangle$ is the mean level of $\Delta I/I$ for the source at that elongation. Scintillation level measurements from the STELab radio facility analyses are available at a given sky location as an intensity variation of the source signal strength. For each source, data are automatically edited to remove any obvious interference discerned in the daily observations. To yield g-levels in real time, the white noise P_{WN} is subtracted from the scintillation signal spectrum $P(\nu)$, and then system gain corrections are determined by automatically calibrating with the white noise level at the high frequency end of the power spectrum. To obtain m, the white noise is subtracted from the scintillation signal,

$$m = \int (P(\nu) - P_{WN})/P_{WN} d\nu. \tag{17.2}$$

At UCSD, STELab g-values for a source are determined in real time from m by a least square fit to the axially symmetric solar wind model. We assume that it is sufficient to fit 8 daily measurements in order to obtain a value of $\langle m \rangle$ for a given source.

The scintillation level weighting factor along the LOS $W_I(s)$ can be approximated in weak scattering (Young 1971) at the 327 MHz frequency of the STELab IPS observations and at the 80 MHz frequency of the Cambridge, England array as

$$W_I(s) = 2\pi \int \sin^2\left(\frac{q^2 \lambda s}{4\pi}\right) \exp\left(-\frac{\theta_0^2 q^2 s^2}{2}\right) q^{-3} dq. \tag{17.3}$$

In this general IPS weight integral, q is the wave vector. We use a single power law for the spectrum, the same for slow and fast solar wind, with an average power index of 3. The average angular size of a radio source is set at $\theta_0 = 0.3''$at the wavelength $\lambda = 3.68$ m (81.5 MHz) of the Cambridge IPS observations and at $\theta_0 = 0.1''$at the wavelength $\lambda = 0.917$ m (327 MHz) of the STELab IPS observation. These weights are plotted in Figure 17.1.

The scintillation level m is related to the small-scale density variations along the LOS by

$$m^2 = \int \Delta n_e(s)^2 W_I(s) ds. \tag{17.4}$$

Here, $\Delta n_e(s)$ are the small-scale density variation values at distance s along the LOS. The density values along the LOS are not *a priori* known, but we

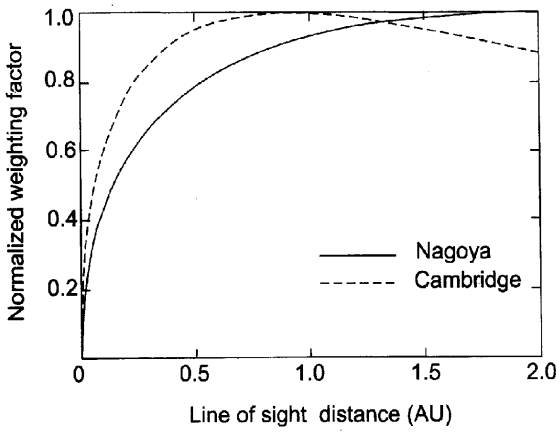


Figure 17.1. Normalized weighting functions for Cambridge and Nagoya interplanetary scintillation (IPS).

assume that the small-scale variations scale with a power law of heliospheric density,

$$\Delta n_e = A_C R^{PWR} n_e^{PWN}, \tag{17.5}$$

where A_C is a proportionality constant, PWR is a power of the radial falloff (Asai *et al.* 1998) and PWN is the power of the density. In the present analysis, we have determined values of PWR and PWN that best fit the data over the interval chosen. For instance, for the time period presented for the Nagoya-observed Bastille-Day CME, A_C is set equal to 1 and the two powers PWR and PWN are -3.5 and 0.7, respectively, to best fit *in-situ* density over a ten-day time interval centered on the time the Bastille-Day CME reaches Earth. These constants depend to some extent on the model used as the mean g-level response of a source with elongation at various frequencies. Other similar constants are used to fit the *in-situ* data for the 80 MHz Cambridge scintillation-level measurements for given time intervals.

Generally, valid IPS velocity data from the Nagoya scintillation arrays are available from the same radio sources as observed in scintillation level each day. IPS velocities are based on observations from up to four scintillation arrays operated from STELab, Japan and have been available since 1985. To use these data our tomography program assumes that the LOS IPS velocity follows a similar LOS weighting relationship to that of the intensity scintillation found for the STELab data, and the powers PWR and PWN are assumed the same

for the STELab velocity measurements. When STELab velocity and Cambridge g-level data are used, the constants PWR and PWN are assumed from data observed at other times for velocity and fit for the Cambridge data for that time interval for g-level. We approximate the velocity observed at Earth as in Jackson *et al.* 1998 (see Kojima *et al.* 1998, for a more complete formulation and validity tests) as the weighted integral,

$$V = \frac{\int V_{\perp}(s)\Delta n_e(s)^2 W_N(s) ds}{\int \Delta n_e(s)^2 W_N(s) ds}, \tag{17.6}$$

where $V_{\perp}(s)$ is the component of the solar wind velocity perpendicular to the LOS. The quantity $\Delta n_e(s)$ is the small-scale electron density variation at distance s along the LOS as determined by the level of intensity scintillation, and the weighting factor W_N for the STELab arrays is indicated.

There is extensive editing of the IPS data using a variety of techniques before it is used in the tomographic analysis. The Cambridge, England 80 MHz source observations are in weak scattering beyond about 30° elongation and are not used in the analysis at distances closer than this. For these g-level data there was considerable attention paid to the removal of ionospheric scintillation, and at UCSD this resulted in the elimination of all data at greater than 80° elongation since ionospheric scintillation at a single radio site at this radio frequency is difficult to detect in the scintillation-level data automatically. Further, solar radio noise was sometimes detected as a band of higher noise at a single time in Cambridge data. When this noise level was suspected, the data for the entire time was eliminated. In all about 10% of the data between 30° and 80° elongation was eliminated for these reasons in the Cambridge data. Even more extensive editing procedures, developed and refined over many years of data taking at STELab, have been largely computerized so that man-made, solar, ionospheric scintillation, and other natural (*i.e.*, lightening) noise sources are removed as completely as possible from the final data set. At UCSD we use the data from STELab velocities and g-level from elongations only greater than 11.5° to insure that the radio source lines of sight are in the weak scattering regime. Currently, scintillation-level data are available from three radio arrays, at Kiso, Fuji, and Sugadaira stations in Japan. At UCSD we analyze all three of these data sources for g-level as above, and then choose the lowest of the three g-level values for use in the tomography analysis if measurements exist for the same source from the three stations.

2.2 Helios spacecraft Thomson scattering measurements

The *Helios* spacecraft, launched in December 1974 (*Helios* 1) and January 1976 (*Helios* 2), each contained three zodiacal-light photometers which were originally intended to measure the distribution of dust in the interplanetary

medium between the Sun and the Earth (Leinert *et al.* 1975, Leinert, Link & Salm 1981). However, these photometers also measured brightness variations produced by Thomson scattering from large-scale structures in the interplanetary electron density. The three photometers were fixed on the spacecraft and rotated at its 1 s spin period on an axis perpendicular to the plane of the ecliptic; they pointed 16°, 31° and 90° south (*Helios* 1) or north (*Helios* 2) of the ecliptic plane. Data from the 16° and 31° photometers were binned into 32 longitude sectors at constant ecliptic latitude around the sky. The data were integrated over 8.6-min periods in turn from each of the three photometers, through a set of broad-band ultraviolet, blue, and visual light filters and a set of one clear and three polarizing filters, with a time interval of about five hours between the same combination of color and polarization filters. All *Helios* photometer data are available from the National Space Science Data Center (NSSDC).

Richter, Leinert & Planck (1982) first described use of these data to follow plasma ejections detected by Thomson scattering out to 90° solar elongation. Since then Jackson & Leinert (1985) and Jackson (1985) used these data to study characteristics of mass ejections and trace their motion outward from the Sun into the anti-solar hemisphere (Figure 17.2). Jackson (1991) also used these data to study the longer-lasting corotating regions in the solar wind. The *Helios* spacecraft orbited the Sun with 6-month periods from 0.3 to 1 AU, and its photometers viewed heliospheric structures from a non-Earth location. Interpretation of these observations must take this non-Earth viewpoint into account to match observed brightness to heliospheric structure.

LOS Thomson-scattering brightness for a column of electrons follows the relationship,

$$B = \int n_e(s) W_T(s) ds, \tag{17.7}$$

where $n_e(s)$ is the electron density per cm^{-3}, at distance s in cm, along the LOS; $W_T(s)$, the scattered intensity per electron, serves as a brightness "weight factor" for the density. For the large distances from the Sun viewed by the *Helios* photometers,

$$W_T(s) = \frac{1}{2}\sigma F_s \left(\frac{r_0}{r}\right)^2 (2 - \sin^2\chi), \tag{17.8}$$

where σ is the Thomson-scattering cross section, F_s is the flux received from the solar disk at a distance r_0, r is the distance of the electron from the Sun, and χ is the angle between the incident solar radiation and the direction of scattering (Billings 1966). To evaluate (17.8) both r and χ are determined as functions of the distance R of the observer from the Sun, elongation ϵ of the LOS, and distance s along the LOS. Using R, ϵ and s as independent variables W_T scales as R^{-2}. For a fixed R and ϵ the function W_T has a maximum at $s = R\cos\epsilon$,

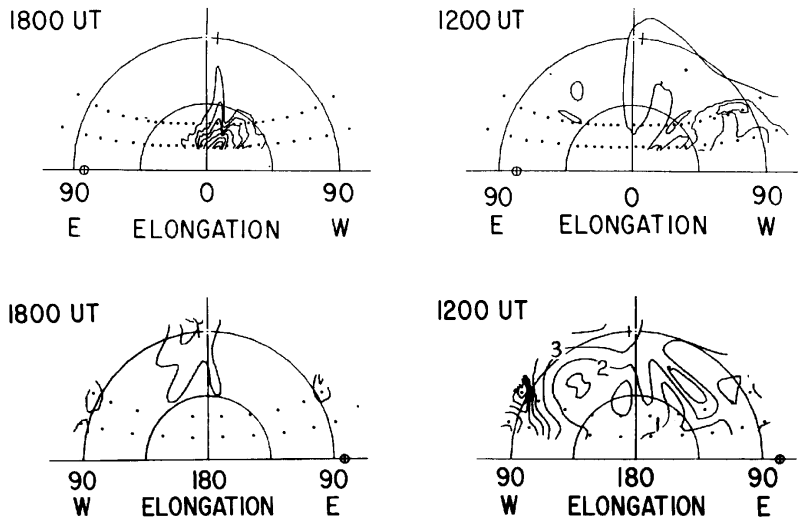


Figure 17.2. Contour plot images obtained from the *Helios* photometers of the 1979 May 07 CME on May 08 and May 09 at the times indicated. In the top two images the Sun is centered and 90° marked as the outer semi-circle above the ecliptic plane (represented by the horizontal line). Electron density is plotted in contour levels of 3×10^{14} e$^-$ cm^{-2} The position of the Earth is marked as $\oplus$ near east 90° Positions of the sector centers are marked by dots. The bottom two images view directly away from the Sun and are contoured in levels of 10^{14} e$^-$ cm^{-2}.

and is symmetric around this point. For $\epsilon < 90^\circ$ the maximum is at the point of closest approach of the LOS to the Sun. Figure 17.3 shows the weight function at $\epsilon = 16^\circ$, 31° and 90° for $R = 1$ AU.

Helios photometer brightness data are usually specified in S10 units, the brightness within one square degree of sky scaled to the equivalent brightness of a tenth-magnitude solar-type star. Expressing (17.7) and (17.8) in S10 units requires that the flux F_s received from the Sun (17.8) also be specified in S10 units:

$$\frac{1}{2}\sigma F_s = \frac{1}{2}\sigma(\Delta\Gamma/\Omega_s)10^{(10-m)/2.5}, \tag{17.9}$$

where $\Delta\Gamma = 3.046 \times 10^{-4}$ is the solid angle in steradians subtended by one square degree, and Ω_s and m are the solid angle and apparent magnitude of the Sun, respectively. These quantities, at 1 AU are $m = -26.73$, $\Omega_s = 6.800 \times 10^{-5}$ (Allen 1964) and thus,

$$\frac{1}{2}\sigma F_s = 8.76 \times 10^{-11}\mathrm{cm}^2\mathrm{S10}. \tag{17.10}$$

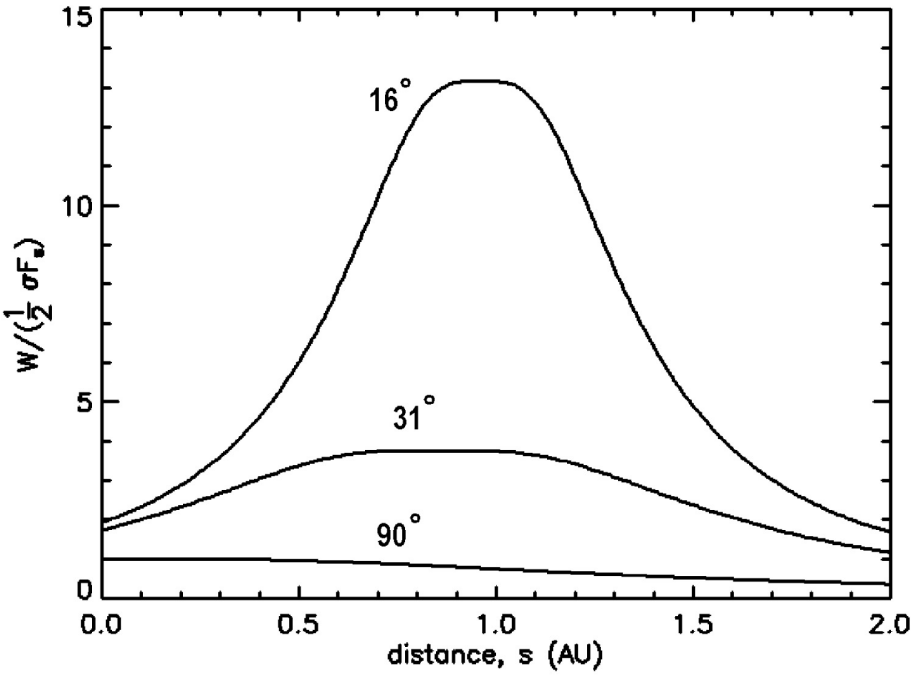


Figure 17.3. Thomson-scattering weight function W from equation (17.8) as a function of distance s along the LOS for the elongations given. The observer is assumed to be at $R = 1$ AU from the Sun.

The data from the *Helios* photometers is brightness time-series information in heliocentric coordinates mapped relative to the Sun. These time series (see next section) have had a zodiacal light model (Leinert, Link & Salm 1981) removed and stellar signals eliminated. To further refine these time series for use with the tomography, we remove an 8-day running mean. This filter removes a portion of the low-frequency response not otherwise accounted for. At this level, the *Helios* systems act as differential photometers for high-frequency heliospheric signals. In addition, the final time series is searched for "glitches." These generally appear as spikes in the data that are more prominent above the background in the direction opposite the Sun. These spikes are often correlated with high-energy particle flux observed in the *Helios* particle detectors (Jackson & Hick 2002). When these spikes are detected in the photometer data, the whole period of time from the *Helios* photometers is considered suspect and eliminated from consideration even though the high-energy particle spike is not prominent in the photometer observations nearer the Sun. Although Thomson scattering observations are valid to nearly photospheric heights, the *Helios* photometer observations get no closer than 15° from the Sun, and from the innermost orbital

position of the *Helios* spacecraft (0.3 AU) this amounts to a closest approach distance of $\sim$17 $R_{\odot}$.

Because the heliospheric time series signal is inseparable from the very bright zodiacal light component except by its rapid ($\lesssim$ 8-day) variation over time, the tomographic analysis must deal with the fact that there is a steady background Thomson-scattering signal component as well as the time-varying one. Several techniques have been devised to include an estimate of this signal in our Thomson-scattering analysis. One of the first methods was to simply analyze the variations relative to the mean datum formed by the running 8-day average (Jackson & Hick, 2000; 2002). After the 3-D analysis was complete, a small additional r^2 density was added to the data to provide a total density at 1 AU commensurate with the mean value for that time interval at Earth. In the current tomographic analysis shown here, an additional r^{-P} density with a constant value at 1 AU is added to the model data prior to the tomographic analysis. The sum of the modeled background brightness and the variable component above the mean datum are now compared with total modeled brightness from the three-dimensional model. The *Helios* spacecraft densities (rather than those at Earth) are now also compared over the time interval in question with the densities derived by our model in order to provide a best interval fit to the value of P and the density at 1 AU. For the period of time during May 1979, P was found to be 2.07 with a density at 1 AU of 7.0 e^- cm^{-2}. For a less active time in 1977 (Carrington rotation 1653) P was found to be ~ 2.10 with a 1 AU value of 8.5 e^- cm^{-2}. The different techniques used in background density fitting make little difference in the location of the heliospheric structures reconstructed, but they do somewhat change the overall density.

3. Model and Tomographic Analysis

The heliospheric model in our analysis and the iterative procedure that provides the three-dimensional results are explained more thoroughly in Jackson *et al.* (1998). The UCSD tomography program currently applies corrections to a kinematic model, modifying the model until there is a least squares best fit match with the observations. The solar wind model provides two parameters to fit in three dimensions: the radial outward solar wind velocity and the solar wind density as described previously. Density rather than the small-scale density variations are used in the IPS analyses and propagated outward in the UCSD kinematic model, and thus density is related to density variation as in (17.5), to be used in the LOS integral. IPS velocity is related to its perpendicular component, as in (17.6), and used in the LOS integral as well. In the Thomson-scattering case, density is related to brightness directly in (17.7) and used in the LOS integral.

3.1 Solar wind model

The solar wind is currently mapped from a source surface at the lower boundary of the model by projecting it radially outward from below the lowest lines of sight (unlike the UCSD model described in Jackson *et al.* (1998), where this surface was at 0.3 AU). Consistent approximately with *in-situ* spacecraft observations (Hundhausen 1970), the solar wind motion is assumed to be strictly radial, and thus, for example, faster solar wind catches up with slower wind that is flowing along its Archimedean spiral. The resultant solar wind speed is then continued after merging by assuming mass flux conservation of the plasma within the latitudinal band resolved by the model. At each heliocentric distance and especially at the source surface, the velocity structure of the model is smoothed so that some information from neighboring latitudes and longitudes is retained. The smoothing incorporates adjacent pixels in the map using a gaussian filter weighted according to the angular distance of the adjacent resolution elements at the same heliocentric distance. Since the resolution of a rectangular Carrington coordinate map increases spatially in longitude with increasing latitude, this filter is used to even the spatial resolution over the whole of the map.

In the kinematic model described here, we either assume that the solar wind corotates, so that for the period of observation there is no temporal variation, or else that the source surface boundary can change over evenly spaced time intervals. This latter time-dependent tomography allows changes of the source surface boundary of some specified length that can be shorter than one day. The corotation assumption allows robust tomographic convergence when the numbers of lines of sight are small and when the data are noisy. The time-dependent assumption requires less noisy data and more lines of sight to provide the same spatial resolution, but essentially limits the tomographic reconstruction to rely on outward solar wind flow to form the perspective views. For each observed LOS at a given time, the location of the position along this line in the model is calculated. The model g-levels along each LOS defined by the densities are summed using the weighting described in (17.3) or in the case of the Thomson scattering data, by the weighting described in (17.8). These model values are then compared with the observed g-levels, or brightness and this comparison is used to change the model. For one solar rotation from the Nagoya STELab data there are typically between 500 to 1000 lines of sight that can be used to determine model density from the scintillation-level measurements and velocity. This implies that for STELab data between 20 and 40 crossed LOS components typically input to latitude and longitude positions each day subject to the gaussian spatial filter described earlier, and a similar gaussian filter that combines data from one day to the next. This implies a possibility of determining the density/g-level values for 20 to 40 latitude and

longitude locations and a similar number of velocity locations from STELab data each day. The Cambridge IPS lines of sight are as numerous as several hundred per day as are the Thomson scattering data from each *Helios* spacecraft. These greater LOS numbers can in theory provide better temporal and spatial resolution in density.

The amount and quality of the available observations and the heliographic coordinate resolution and temporal cadence dictate this resolution even more strongly. For corotational IPS tomography the STELab data can be resolved with at least 10° by 10° heliographic latitude and longitude digital resolution as can the Thomson scattering data from the *Helios* photometers. For the UCSD time dependent tomographic program using STELab data, 20° by 20° resolution is used. For the Cambridge and *Helios* photometer data 10° by 10° resolution has also been used for the time-dependent tomography. This resolution is modified by the gaussian spatial and temporal filters that limit structure extent in latitude, longitude and (in the case of the time-dependent tomography) height, commensurate with the data amounts and quality. In practice it is important that the lines of sight used to determine the value of each resolved point within the model cross each other at different angles and from different elongations. The regions near the Earth are those most frequently crossed by different lines of sight while those far from it, especially over the solar poles, are not. Where the computational aspects of the tomography differ from those given in (Jackson *et al.* 1998) they are discussed further in the following sub-section.

3.2 Computer analysis

As in Jackson *et al.* (1998) the computational aspects of the tomography program necessarily deal with the detailed geometry for each LOS, the location of each within the three-dimensional solar wind model and its projection to the heliocentric source surface. In the tomographic analysis scheme used here, the Carrington map at a given reference surface below all of the lines of sight provides input to the three-dimensional velocity and density model to use along each LOS. In the corotational tomography only a single reference is provided. In the time-dependent tomography a new reference surface is provided at evenly spaced time intervals. A LOS projects to a given heliocentric distance at a given time as shown for the schematic and several actual STELab IPS Carrington map examples during the Bastille-Day CME in Figure 17.4. Lines of sight from different elongations and different time project to each location on a given reference surface. Each LOS projection is weighted according to the scheme presented in the preceding sections. A model LOS g-level and V change are calculated for each source surface, respectively. The weights of all changes are accumulated as a ratio of observed to model value for each coordinate position

on the reference surface. After all the changes have been accumulated, the three dimensional model is formed with regard to these changes to allow further iterative changes to be determined. In our analysis we presume a measurement at one elongation is as valid as at any other, and we weight each LOS (but not the points along them) equally. These least squares differences from the mean for each coordinate position are summed and used, along with the differences of the source observation, to model LOS ratio differences to indicate the rate of convergence.

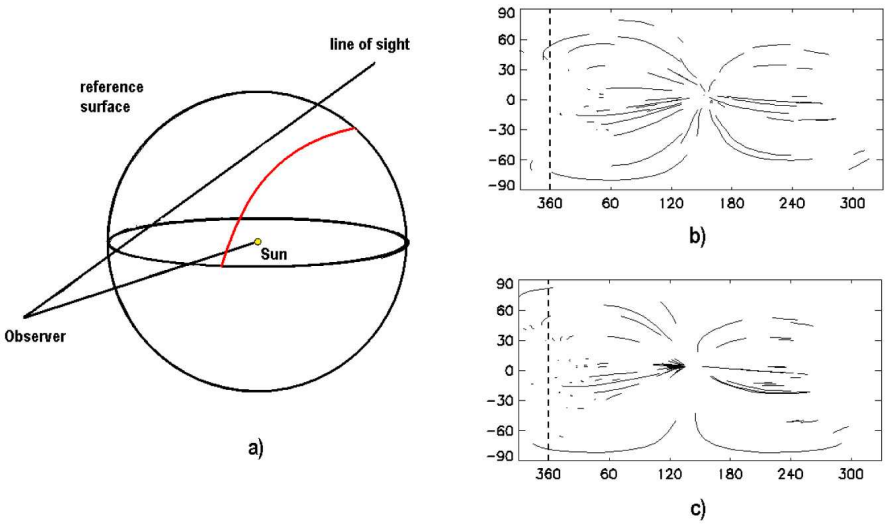


Figure 17.4. (a) Schematic of a LOS and its projection to a constant heliocentric distance here shown as a reference surface below the LOS. The reference surface is set so that all lines of sight are above it. The curved line below the LOS on the reference surface is the LOS projection after taking outward solar wind motion into account. (b) and (c) Consecutive-day (2000 July 13 and 14) latitude and longitude LOS projections onto the source surface. Lines of sight are depicted which begin near the Earth and extend outward from it for 2 AU. Different perspectives are obtained where the lines of sight cross and as the weights of the different line segments indicate.

In the tomographic analysis used here, first the velocity corrections are made to the more preliminary velocities on the reference surface. Secondly, the three dimensional model is updated and the new projected locations of each LOS point on the reference surface are determined. This is done to assure that the newest values of velocity and density from the assumption of mass continuity are used to determine the small-scale density variations along each LOS. Finally, the preliminary model density corrections are made on the reference surface and then the three dimensional model is again updated (unlike the earlier scheme reported in Jackson *et al.* (1998) where only one update of the model is made per iteration). In order that several different perspective lines of sight produce

changes in the modeled values, we require more than one LOS crossing within the digital ($20^\circ \times 20^\circ$ for STELab IPS) heliographic spatial interval for changes to be made at any given coordinate position. These LOS crossings are given by an accumulated average of all contributions as derived from the two (space and time) gaussian filters used. Where the sum of all contributors are less than one, in order to obtain continuity along lines of sight, the source surface value from known locations is interpolated from locations where the data can be changed. Where the model cannot be changed at some location, these coordinate positions are left blank in the final result. The reference surface maps are smoothed on each iteration using a gaussian spatial filter that incorporates equal solar surface areas and a gaussian temporal filter. These spatial and temporal filters can be varied to insure convergence. Filter changes by large percentages have a significant effect on the result. These spatial and temporal filters can be varied to insure convergence when the data are noisy, but (for instance) were set to a $1/e$ width of 13.5° and 0.85 days, for the $20^\circ \times 20^\circ$ spatial resolution and 1-day model digitization, respectively, during intervals shown here for the 2000 July 14 time period using STELab data.

The tomography program (written in Fortran) iterates to a solution, generally converging to a slowly changing model within several iterations. For a typical rotation, a set of velocity and density iterations generally takes about five minutes on a 2.4 GHz Pentium IV computer using 20° by 20° resolution digitization. The UCSD tomography program operates for 9 iterations to be certain the program has converged. Those source velocity observations each day that do not fit within a 3σ limit of the mean ratio change are removed from the data set. This same criterion is also used to remove daily g-level or Thomson-scattering data that vary beyond the three-sigma model limit. The program is then allowed to operate for another 9 iterations. Convergence is monitored using techniques as described in Jackson *et al.* (1998). Tests of the program show that the model solutions are not sensitive to the starting input model, and that after a few iterations any signature of the input model is lost. Other tests (see Jackson *et al.* 1998) show that pseudo observation inputs to the three-dimensional model can be reproduced in the tomography.

That the models reproduce the velocity and g-level data are shown in Figure 17.5 and *Helios* brightness is shown in Figure 17.6. The data points show a sample time series of the observations for an IPS radio source in velocity and g-level compared with the model values obtained using the UCSD kinematic model after 18 program iterations. Except for the data from some sources that are missing on some days, during this time interval the time series for over 50 sources were fit simultaneously in both velocity and g-level in the STELab IPS tomography. For the *Helios* Thomson scattering observations, 130 sky position photometer values obtained approximately every 5 hours (some locations and

times are missing from this analysis) were fit simultaneously over the 48-day time period.

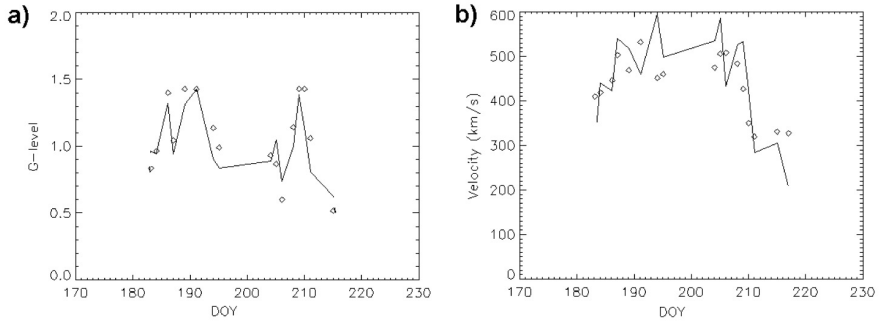


Figure 17.5. Time series (a) showing a sample of the final (18^{th} iteration) velocity and (b) g-level model (open circles) and observations (solid lines) for a time-dependent tomographic run for 48 days from in 2000 June-July, which includes the Bastille-Day CME event. The model fits data from radio source 3C273 on 2000 July 14 (DOY 196). There were a total of 46 radio sources fit in velocity and density during this time interval.

The model currently fits all sources observed in the analysis with equal weight. Other sources within the same time interval contribute to the model and are the main reason for the discrepancy between the specific source shown and the model values. An idea of how well the model reproduces the global structure can be gotten simply by correlation of the individual model values with the data points. Figure 17.5 shows the correlation for a 48-day time series in IPS velocity and g-level during 2000 June–July. Figure 17.6 shows the correlation in a 48-day time series of *Helios* spacecraft photometer brightness data.

4. *In-situ* Comparisons

Tomographic model densities and velocities are available in three dimensions and can be extrapolated to any heliocentric distance, for example to 1 AU. At present they compare directly to the measured results from, e.g., the Advanced Composition Explorer (ACE) spacecraft near Earth (see Figure 17.7). We smooth the ACE data into 18-hour averages, consistent with the approximate spatial resolution present from the longitudinal and temporal binning of the time-dependent tomography data. The time series are fit by varying the two powers PWR and PWN in (17.5) and the spatial and temporal gaussian filters as mentioned earlier. The densities mapped to 1 AU are shown as a time series for rotation 1965 in Figure 17.2. The correlation for rotation 1965 in model relative to ACE *in-situ* values is 0.82 and 0.85 respectively for velocity and density over the 10-day period centered on the Earth arrival time of the July 14 CME (Figure 17.7). For IMP *in-situ* data, fits to the corotational tomography

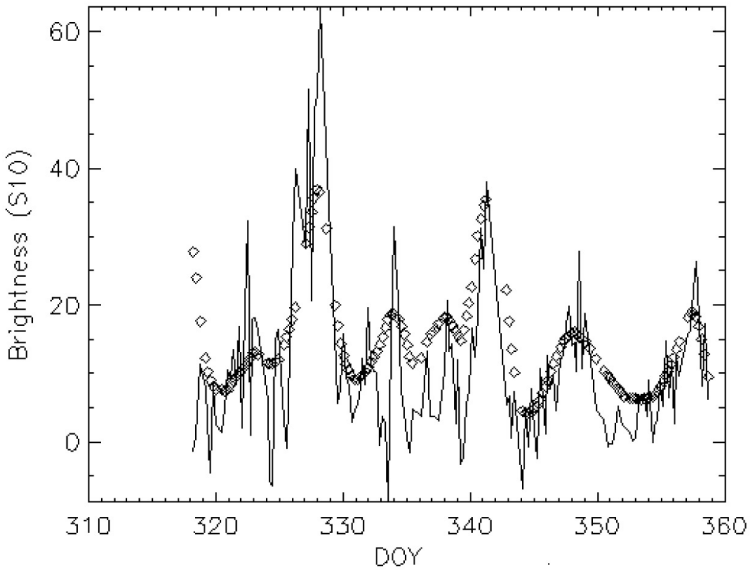


Figure 17.6. Time series showing a sample of the final (18^{th} iteration) model and photometer brightness comparison for a time-dependent tomographic run for *Helios* data in 1977 November. The observed brightness is shown as a solid line; the model brightness as open circles. The *Helios*-2 16° photometer observations viewing 2° west of the Sun-spacecraft line is shown. November 24 is DOY 328.

model using Cambridge, England IPS data and STELab IPS velocity data are not as good as these. See the analysis by Jackson *et al.* (1998).

Tomographic time-dependent modeling of Thomson-scattering brightness also allows measurement of changes in large-scale heliospheric density to be extrapolated to any location in space. During times of *Helios* spacecraft operation the spacecraft *in-situ* monitors regularly measured proton density, and by assuming that there is one electron present per proton, the daily changes in proton density map electron density-derived brightness variation at the *Helios* spacecraft. Figure 17.8 is a comparison plot of heliospheric density at the *Helios* 2 spacecraft and the reconstructed density from only that spacecraft from the time-dependent kinematic model extracted at the location of the spacecraft during 1979 April and May (see next section). The *in-situ* density values at *Helios* 2 are averaged using an 18-hour filter in order that they have the same approximate temporal resolution as the $10^\circ \times 10^\circ$ latitude and longitude daily spatial model. The only adjustments that are allowed in the density tomography model used to fit *in-situ* measurements are changes in the gaussian temporal and spatial filters used to reconstruct the data and an adjustment of the background non-varying heliospheric density component. Even better correlations

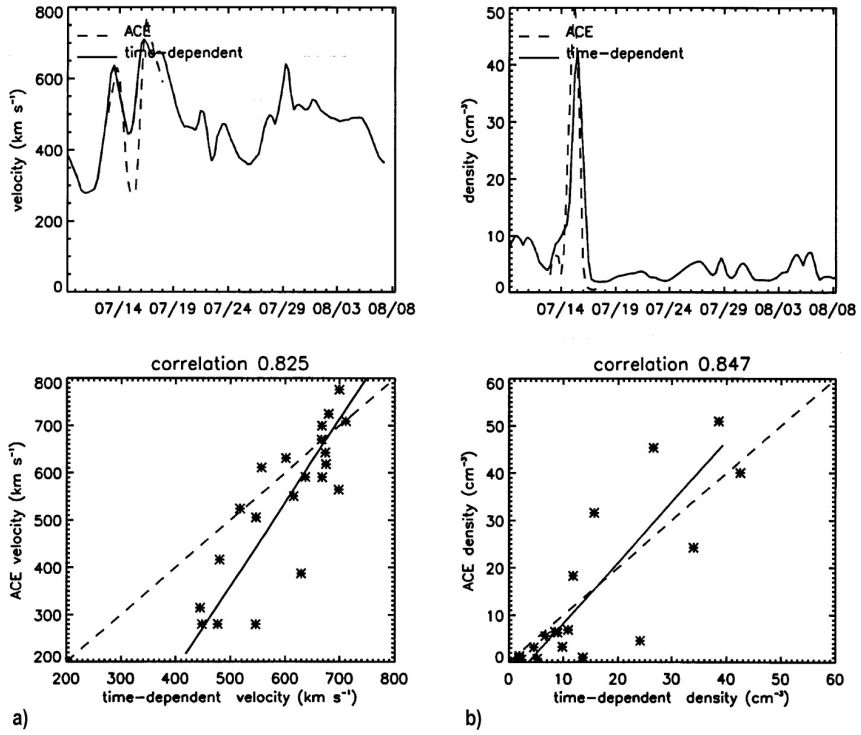


Figure 17.7. Rotation 1965. (a) 10-day velocity time series from the three dimensional time-dependent model projected to 1 AU compared to the velocity time series from the ACE spacecraft (dashed line) and its correlation. (b) Model and ACE density correlation.

are possible between model and *in-situ* density (Jackson, Buffington & Hick 2001) when both *Helios* spacecraft are used to reconstruct the three-dimensional density.

Once a three-dimensional result is available, it can be viewed from any perspective or extrapolated to any position in space with the most accurate values present presumably where data coverage is most complete with the greatest signal relative to the many sources of observational noise. These tomographic reconstructions are shown as Carrington plots at a given height and as remote-observer views in the next section.

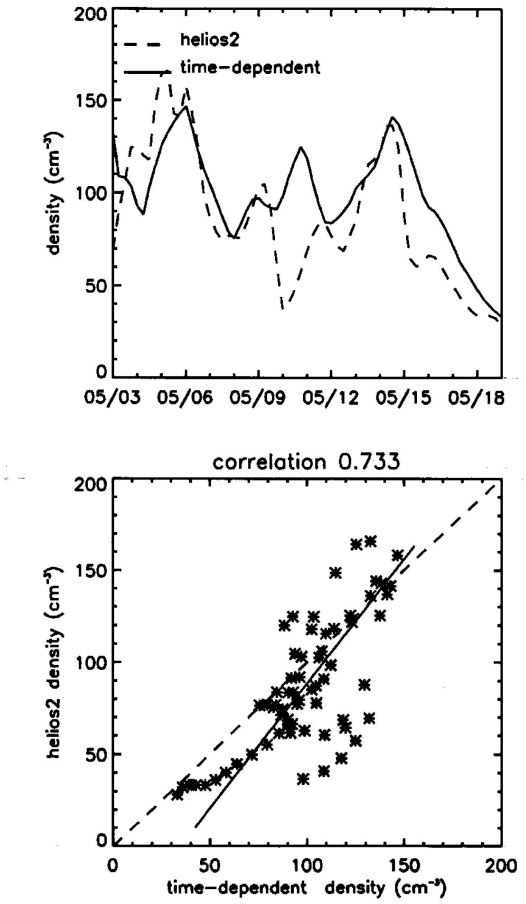


Figure 17.8. Comparison plot of heliospheric densities at the *Helios* 2 spacecraft and least squares correlation.

4.1 Reconstructed global observations

The fits to *in-situ* observations only guarantee that the three-dimensional model constructed remotely by the IPS and Thomson scattering analysis over a large portion of the heliosphere agrees with *in-situ* data near Earth or, when observations exist, at the *Helios* spacecraft. However, we can also view the reconstructed time-dependent model shapes for these events and see if they match remotely sensed data from other instruments including coronagraph observations obtained closer to the Sun.

The first IPS data used in the corotating and time-dependent tomography were combinations of Cambridge, England and STELab IPS velocity data. These data form the basis for the analyses shown in Figure 17.9a (from Jackson *et al.* 1998). The same time interval from Carrington rotation 1884 during the year 1994 is reconstructed in both of these analyses. In the corotational analyses, which assumes an unchanging source surface with time, there are clear discrepancies (see Jackson *et al.* 1998) that could be better dealt with if the model were allowed to evolve with time. Indeed, when the time-dependent tomography began to work, both corotating structures and CMEs (see Figure 17.9b) were observed in the models. Unfortunately, during these time periods no space-based coronagraph was operating to certify the CME shapes in the lower corona. It wasn't until after the Cambridge array was closed in 1994 September that the LASCO coronagraphs on SOHO began operation.

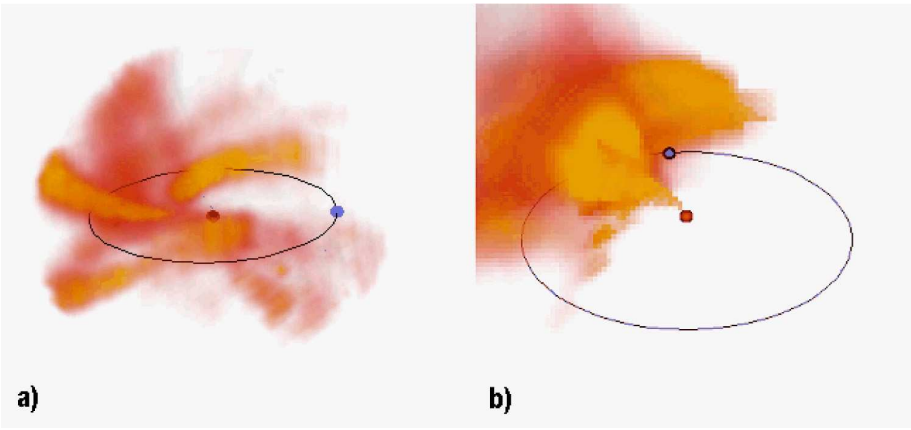


Figure 17.9. (a) View of the corotating component of the plasma density in the inner heliosphere (out to 1.5 AU) derived by tomographic reconstruction from IPS intensity level data (Cambridge, UK) and IPS velocity data (Nagoya, Japan) for Carrington rotation 1884 (1994 June 23 to July 20). The density is normalized by the removal of a r^{-2} distance dependence. The Sun is at the center; the Earth is marked in blue in its orbit around the Sun. The view is from 15° above the plane of the solar equator. The scintillation intensity level is calibrated in terms of density by comparison with IMP spacecraft densities at Earth. Clearly seen is the Archimedean spiral structure of the solar wind (as presented in Jackson *et al.* 1998). (b) A three dimensional model projection of the heliosphere from an observer's perspective situated at 3 AU, 30° above the ecliptic opposite the position of Earth on 1994 July 07. As in (a), density is normalized by the removal of an r^{-2} distance dependence. A solar ejection is observed moving outward to the west of the Sun as seen from Earth.

The STELab IPS observations are available during periods when the LASCO coronagraphs operate, and at the best of times the 40 or so sources per day that these radio telescopes observe are sufficient to reconstruct a global model daily

using the time-dependent tomography. Figure 17.10a shows a LASCO C2 coronagraph image of the July 11 halo CME compared with a remote observer view of the modeled tomographic density as the CME is about to reach 1 AU. The reconstruction shows that this CME moves mostly to the east and north of the Earth as also indicated in the coronagraph image. Similarly, Figure 17.10b shows the Bastille-Day CME compared with a remote observer view of the reconstructed density as the CME is about to hit Earth. Given the expanse of heliosphere that the CMEs have traversed to reach 1 AU, the comparisons with LASCO near-Sun observations are excellent. The results of the present three-dimensional reconstruction are in good agreement for the Bastille-Day CME with an alternate reconstruction analysis by Tokumaru *et al.* (2003).

The *Helios* Thomson scattering time-dependent tomography also gives excellent agreement with Solwind coronagraph observations in 1979 where these two sets of data exist simultaneously. The major structure observed in Figure 17.11a is a coronal mass ejection that was observed by the Solwind coronagraph (Poland *et al.* 1981) to arise from the Sun to the solar northwest at midday 1979 May 07. This well-studied CME (Jackson & Leinert 1985; Jackson 1985; Jackson, Rompolt & Svestka 1988; Jackson & Froehling 1995) was termed "three-pronged" by the Solwind coronagraph group. At the time of Figure 17.11b, the front portion of the CME is estimated to have a solar distance of at least 1.0 AU (Jackson, Rompolt & Svestka 1988). This compares with the shape of the outer portion of this CME obtained by the two-spacecraft tomographic reconstruction technique (Jackson & Froehling 1995). This is the same time period in 1979 May as shown in the *in-situ* data comparison in the last section. In both 3D reconstruction techniques, the northern portion of the CME is directed away from Earth and northerly while the southern feature is directed primarily northwest of the Sun-Earth line. The 1979 time period during Carrington rotation 1681 is at the extreme maximum of CME activity for Solar Cycle 21. Far more CMEs can be observed throughout this period and related to CMEs observed by the Solwind coronagraph, and some of these CMEs and CME sequences are far more extensive than the single isolated May 07 CME. In particular this is the case with a CME that erupted from the Sun on 1979 May 25 that has also been reconstructed by both the two spacecraft (Jackson & Hick, 1994) and single spacecraft reconstruction techniques.

Although no coronagraph data exist during the period in 1977 November shown in Figure 17.12a, the period has been well studied using *in-situ* data from 5 different spacecraft (Burlaga *et al.* 1980). Figure 17.12b is a remote observer view of the *Helios* data at this same time period. The *Helios* photometer time-dependent tomographic model density satisfactorily depicts both the corotating structure and the assumed CME piston that were studied and postulated using *in-situ* observations.

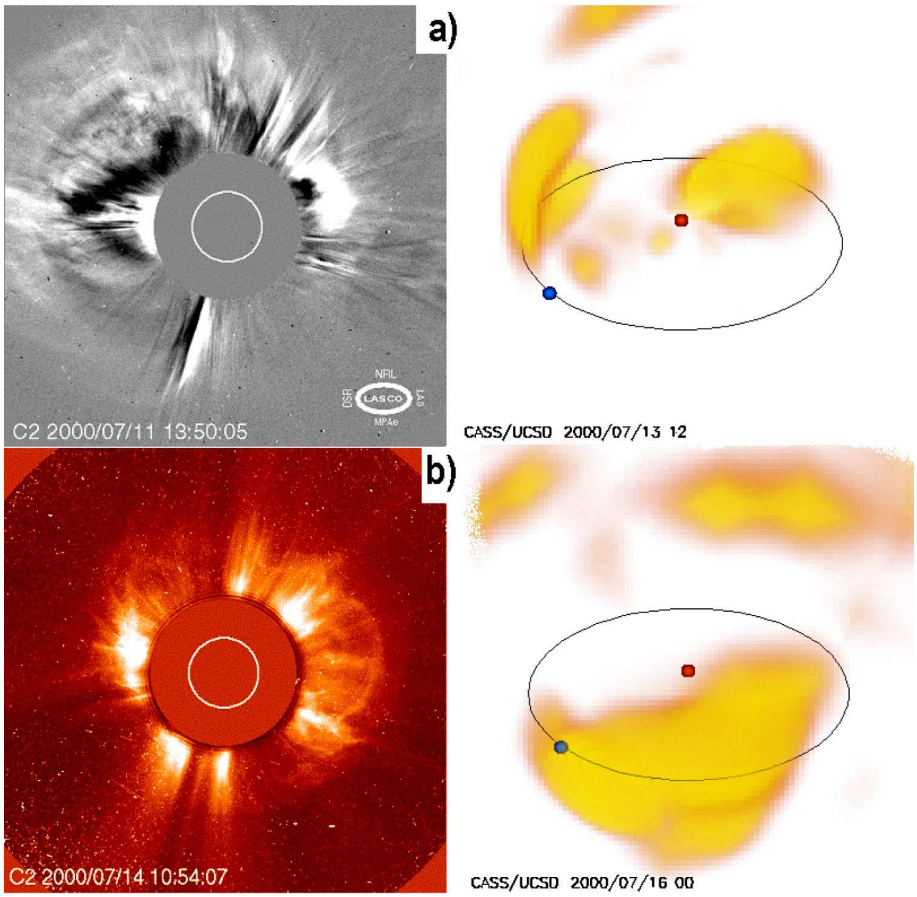


Figure 17.10. LASCO C2 images and a view of the reconstruction of the halo CMEs in 2000 July with $N_e > 30$ e$^-$ cm^{-3} normalized to 1 AU shown. Views (left to right) are 3° across from 1 AU; 55° across from 3 AU, 30° above the ecliptic plane 45° west of the Sun-Earth line. (a) 2000 July 11 CME in LASCO reconstructed July 13 at 12 UT. (b) July 14 CME in LASCO reconstructed July 16 at 0 UT.

More precise measurement of these global models is possible by forming a Carrington map surface at a constant solar height and providing a contour plot of the model at this height. Figure 17.13 shows two Carrington contour maps of velocity and two of density during the July 11–14 CME sequence from the time-dependent tomography model. The heights and times chosen show the model density when the front portions of the disturbances reach 1 AU at 12 UT on 2000 July 13 and at 0 UT 2000 July 16. Velocities are shown at these same times at a solar distance of 0.3 AU. We have purposely chosen these times to demonstrate one aspect of the observations—namely that both of the reconstructed disturbances show a high velocity region centered below the

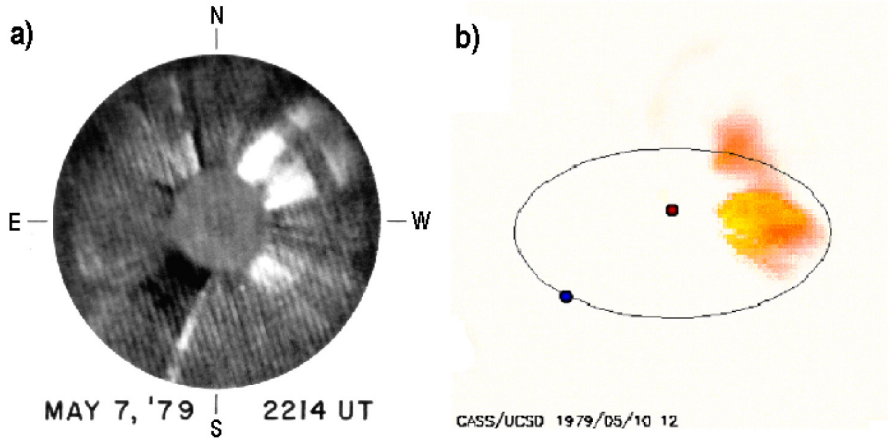


Figure 17.11. (a) Solwind coronagraph image of the May 7 CME observed at the time indicated. The coronagraph outer field of view extends to 8 $R_\odot$. (b) Remote observer view of heliospheric density at the time indicated. An $r^{-2.07}$ density gradient fit to the observations over the Carrington rotation 1681 interval has been removed from the kinematic model ambient (fit from *Helios* 2 *in-situ* measurements at 7.0 e^- cm^{-3} at 1 AU), and to the reconstructed structures to aid in viewing them. The observer is located at 3.0 AU 30° above the ecliptic plane $\sim 45°$ west of the Sun-Earth line.

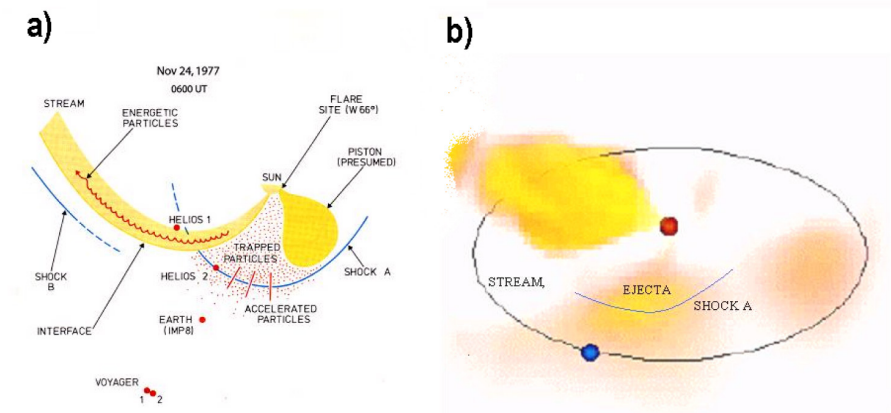


Figure 17.12. 1977 Nov 24 reconstruction at 6 UT. (a) using *in-situ* observations from 5 spacecraft (Burlaga *et al.* 1980). (b) Using the IPS time-dependent Thomson scattering tomography.

disturbance and filling in below the disturbance with a following high-speed wind. The high speed wind fills in behind the CME at ever increasing longitude consistent with a source region that temporarily rotates with the solar surface. This region is larger and higher-speed in the case of the July 14 event. These

high velocity plumes were first noticed in the time-dependent tomographic analyses, and are either associated with the transient coronal holes studied by others (*e.g.*, Rust, 1983) as a dimming in Yohkoh spacecraft X-ray or EIT data or else are associated with reconnection following a CME (Riley *et al.* 2002), or both. Each high velocity plume has some structure, is generally small compared with the size of the major disturbance that proceeds it into the heliosphere, and appears following most CME disturbances viewed to date with the approximate location and orientation of the solar surface dimming following a CME. In any case these transient high velocity plumes are uniquely present for study only in the velocity IPS time-dependent tomography.

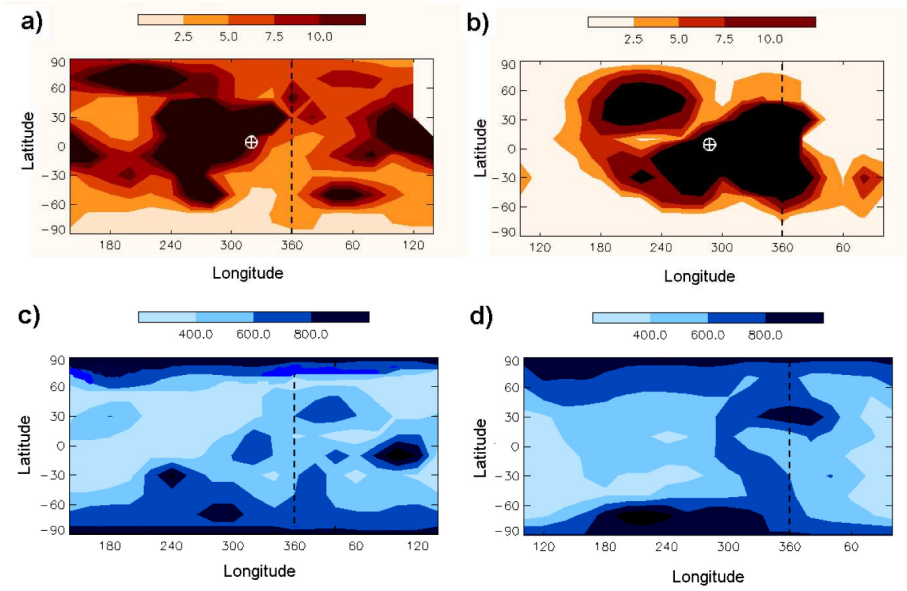


Figure 17.13. Carrington synoptic maps of time periods during the two halo CMEs in 2000 July. Density maps and are presented at 1.0 AU, velocity maps are presented at 0.3 AU for the same time interval for each event. The Earth $\oplus$ is centered in each 1.0 AU density map. Both reconstructions are at the same time as the remote observer views in Figure 17.10. The (a) density and (c) velocity maps of the 2000 July 11 CME are shown on July 13 at 12 UT. The CME density is centered at latitude 270° longitude 20°N latitude in the maps. The high speed velocity beneath the CME is centered at 320° longitude at the same latitude. The (b) density and (d) velocity maps of the 2000 July 14 CME are shown on July 16 at 0 UT. The CME density is centered at latitude 330° longitude 0° latitude. The high speed velocity beneath the CME is centered at 360° longitude and 30° N latitude.

For the *Helios* spacecraft photometer volume for the CME of 1979 May 07 we show a Carrington map on 12 UT 1979 May 10 in Figure 17.14 at the same time as the reconstruction remote view of Figure 17.11. Poland *et al.* (1981) estimate that this CME had an excess mass of 10^{16} g assuming that its entire

excess mass was located in the plane of the sky observed by Solwind. The CME underwent considerable evolution by the time it reached the *Helios* viewing position, expanding both outward and in north-south size. By summing over time and space in the 3D matrix using the current tomographic reconstruction, this CME is estimated to have an excess mass of $\sim 4 \times 10^{16}$ g at 1.0 AU. If the total CME mass above zero within the CME volume is included, the CME mass is estimated to be $\sim 1 \times 10^{17}$ g and the CME takes from 18 UT 1979 May 09 to 18 UT May 13 to completely pass 1 AU! This compares with values of 6×10^{15} g and 9×10^{15} g respectively for the outer portion of this CME obtained by the two-spacecraft tomographic reconstruction technique (Jackson & Froehling 1995).

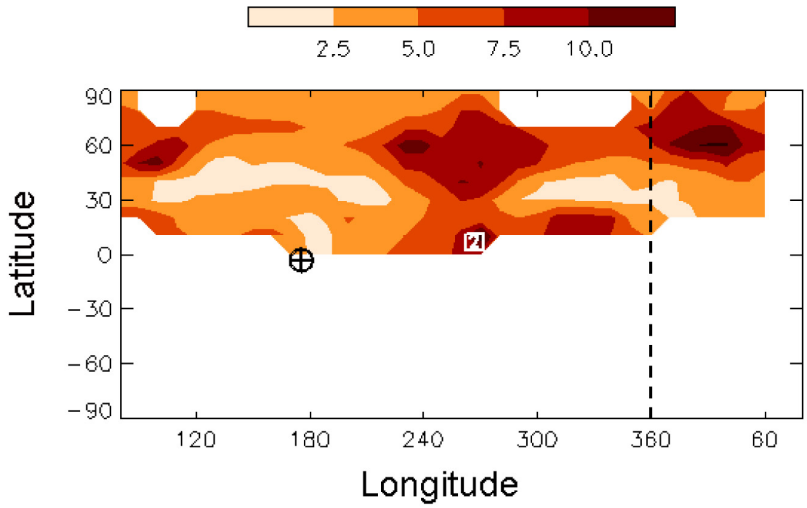


Figure 17.14. Carrington synoptic map of the heliospheric structure at 1.0 AU on 12 UT 1979 May 10. At this time the *Helios* 2 spacecraft is $\sin 90^\circ$ west of Earth in heliographic longitude (centered as indicated) at a solar distance of 0.3 AU. The Earth $\oplus$ is shown to the left near 180° in the 1.0 AU density map.

The time interval depicted on 6 UT 1977 November 24 in Figure 17.12 is shown as a Carrington synoptic map at 0.6 AU slightly following that time at 12 UT 1977 November 25 in Figure 17.15. A shock observed *in situ* at *Helios* was observed to pass both spacecraft about one day earlier than the time of this synoptic map. The density enhancement reconstructed in the tomographic model in this synoptic map is approximately consistent in location with the *in-situ* enhancment observed following the shock front.

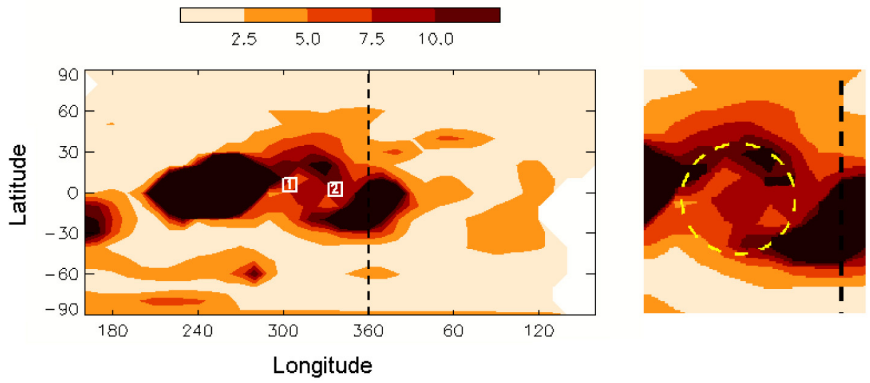


Figure 17.15. Carrington synoptic map of the heliospheric structure at 0.6 AU on 12 UT 1977 November 25. The positions of the two *Helios* spacecraft at 0.69 (*Helios* 1) and 0.64 AU (*Helios* 2) are indicated on the full map that shows that the primary dense structure at this time in the ascending phase of the solar cycle is centered around the solar equator. An enlargement at the right of the center of the map shows a ring-like structure that is approximately 40° in size, centered between the two *Helios* spacecraft.

5. Conclusion

The tomographic analysis handles density both nearby and distant from the spacecraft as accurately as the modeling and data precision allows. From comparison with *in-situ* data at Earth, and at the *Helios* spacecraft the time-dependent tomographic analysis (Jackson, Buffington, & Hick, 2001; Jackson *et al.* 2003) gives superior results to the previous corotating analyses (Jackson *et al.* 1998; Kojima *et al.* 1998), but only when the data are precise and quantitative enough to warrant the necessary degradation in spatial resolution needed to insure convergence. We reconstruct as complete as possible a global three-dimensional model in order to obtain a good fit to observations at Earth, even though these global models amount to only a few tens of lines of sight per day. In real-time analysis, data dropouts and noise make the task of forecasting CME arrival using this technique with the present STELab arrays even more problematic.

In fact, we operate these two tomographic reconstruction techniques in near real time and regularly present some of the images shown here using IPS observations from STELab, Japan. Since 2002 July, when the IPS array telescopes are operating they have been able to view all the major CMEs observed by the LASCO coronagraphs (Rappoport, Hick & Jackson 2003), and the tomography can determine their approximate three-dimensional extents as they move outward into the heliosphere. However, we expect that only when new and bigger IPS systems are available will the IPS technique provide a more refined

tomographic analysis to accurately forecast CME arrival to within a few hours. Other large array systems at different Earth longitudes will also be helpful, since coverage using a single IPS array system can obviously only view heliospheric structures heading towards the Earth when it can view sources near the Sun. At any one Earth longitude this observation period is limited to within a few hours of local noon. The Solar Mass Ejection Imager (SMEI) (Jackson, *et al.* 1989; 1992; 1996; Jackson, Gold & Altrock 1991; Keil *et al.* 1996ab; Jackson *et al.* 1997a; Eyles *et al.* 2003; Jackson *et al.* 2004) will theoretically be able to reconstruct density over the entire heliosphere with approximately $1^\circ \times 1^\circ$ heliospheric latitude-longitude spatial resolution and a 90-minute temporal cadence. Near the Earth the SMEI data, with updates every 100 minute orbit, can revise a real time density estimate forecast at Earth so that accuracy at Earth's position can be maintained. However, the SMEI analyses alone cannot completely determine the velocities required to complete a global solar wind model and only velocity information such as available from the IPS velocity measurements can do this in order to help complete the SMEI far-field view.

Thus, we expect that by using SMEI analyses alone the structures near the Earth can be more accurately reconstructed in density than can those more distant from it. Other spacecraft instruments such as those on board STEREO may operate during the same times as SMEI. If so these other instruments may help fill in heliospheric region density not observed well from the SMEI spacecraft or from ground-based IPS observations and provide far more information about plasma structures in regions of the heliosphere distant from Earth.

The kinematic model currently fit by the tomography can be improved significantly by using a technique whereby the boundary condition (source surface) for a 3D-MHD model is adjusted to give a best fit to the three-dimensional tomographic analysis. One such attempt has been pioneered for corotating tomography by Hayashi *et al.* (2003). We have our own procedure to incorporate any heliospheric MHD model into our analysis, but these are not needed for forecast purposes until global data become more numerous and precise.

Acknowledgments

The work of B. V. Jackson and P. P. Hick was supported at the UCSD by AFOSR grant AF49620-01-1-0054, NSF grant ATM 98-199947 and NASA grant NAG5-8504.

References

Anderson, D. L. & Dziewonski, A. M. 1984, Sci. Am., 251(4), 60
Allen, C. W. 1964, Astrophysical Quantities, Athlone, London
Anzer, U. 1978, Solar Phys., 57, 111

Asai, K., Kojima, M., Tokumaru, M., Yokobe, A., Jackson, B. V., Hick, P. L. & Manoharan, P. K. 1998, J. Geophys Res., 103, 1991
Behannon, K. W., Burlaga, L. F. & Hewish, A. 1991, J. Geophys. Res., 96, 21213
Billings, D. E. 1966, A Guide to the Solar Corona, p. 150, Academic, New York
Bracewell, R. N. 1956, Australian J. Phys., 9, 198
Burlaga, L., Lepping, R., Weber, R., Armstrong, T, Goodrich, C., Sullivan, J., Gurnett, D., Kellogg, P., Keppler, E., Mariani, F., Neubauer, F., Rosenbauer, H. & Schwenn, R. 1980, J. Geophysical Res., 85 (A4), 2227
Chapman, R. W. 1979, Sky & Telescope, 58 (3), 223
Coles, W. A. & Kaufman, J. J. 1978, Radio Science, 13, 591
Coles, W. A., Rickett, B. J., Rumsey, V. H., Kaufman, J. J., Turley, D. G., Anathakrishnan, S., Armstrong, J. W., Harmon, J. K., Scott, S. L. & Sime, D. G. 1980, Nature, 286, 239
Crifo, F., Picat, J. P. & Cailloux, M. 1983, Solar Phys., 83, 143
Eyles, C. J., Simnett, G. M., Cooke, M. P., Jackson, B. V., Buffington, A., Hick, P. P., Waltham, N. R., King, J. M., Anderson, P. A. & Holladay, P. E. 2003, Solar Phys., 217, 319
Frazin, R. A. 2000, Astrophys. J., 530, 1026
Frazin, R. A. & Janzen, P. 2002, Astrophys. J., 570, 408
Frey, S., Frey, H. U., Barnes, O. H. & Haerendel, G. 1996, J. Geophys. Res., 101, 2173
Gapper, G. R., Hewish, A., Purvis, A. & Duffet-Smith, P. J. 1982, Nature, 296, 633
Garcia, F. J., Taylor, M. J. & Kelley, M. C. 1997, Applied Optics, 36, 7374
Gies, D., Fullerton, A. W., Boulton, C. T., Bagnuolo, W. G., Jr., Hahula, M. E. & Wiemker, R. 1994, Astrophys. J., 422, 823
Gilbert, P. 1972, J. Theor. Biol., 36, 105
Gorbunov, M. E. 1996, Radio Sci., 31(1), 95
Hayashi, K., Fujiki, K., Kojima M. & Tokumaru, M. 2003, in M. Velli, R. Bruno & F. Malara (eds.), Solar Wind Ten, AIP Conf. Proc. 679, Melville, New York, p. 144
Hewish, A., Scott, P. F. & Wills, D. 1964, Nature, 203, 1214
Hewish, A. & Bravo, S. 1986, Solar Phys., 106, 185
Hick, P., Jackson, B. V., Rappoport, S., Woan, Slater, G., Strong, K. & Uchida, Y. 1995, Geophys. Res. Lett., 22, 643
Hurlburt, E., Martens, C. H., Slater, G. & Jaffey, S. M. 1994, in Solar Active Region Evolution, Comparing Models With Observations, ASP Conf. Ser., 68, Balasubramaniam, K.S. & Simon, G.W., eds., p. 30
Hoeksema, J. T., Wilcox, J. M. & Scherrer, P. H. 1983, J. Geophys. Res., 88, 9910
Houminer, Z. 1971, Nature Phys. Sci., 231, 165

Hundhausen, A. J., Bame, S. J., Ashbridge, J. R. & Sydoriak, S. J. 1970, J. Geophys. Res., 75, 4643
Jackson, B. V. 1977, in a Topical Conference on Solar and Interplanetary Physics, Tucson, Arizona, January 12-15, 7
Jackson, B. V. 1985, Solar Phys., 100, 563
Jackson, B. V. 1991, J. Geophys. Res., 96, 11,307
Jackson, B. V. & Leinert, C. 1985, J. Geophys. Res., 90, 10,759
Jackson, B. V. & Hick, P. P. 1994, in the Third SOHO Workshop, Solar Dynamic Phenomena & Solar Wind Consequences, ESA SP-373, 199
Jackson, B. V. & Hick, P. 2000, Advances Space Res., 25 (9), 1875
Jackson, B. V. & Hick, P. P. 2002, Solar Phys., 211, 344
Jackson, B. V. & Froehling, H. R. 1995, Astron. Astrophys., 299, 885
Jackson, B. V., Rompolt, B. & Svestka, Z. 1988, Solar Phys., 115, 327
Jackson, B., Gold, R. & Altrock, R. 1991, Adv. Space Res. 11, 377
Jackson, B. V., Buffington, A. & Hick P. P. 2001, in the Proc. of "Solar Encounter, The First Solar Orbiter Workshop", ESA SP-493, 251
Jackson, B. V., Howard, R. A., Sheeley, N. R., Jr., Michels, D. J., Koomen, M. J. & Illing, R. M. E. 1985, J. Geophys. Res., 90, 5075
Jackson, B. V., Hudson, H. S., Nichols, J. D. & Gold, R. E. 1989, Waite J. H., Jr., Burch J. L. & Moore, R. L., eds., Geophysical Monograph 54, 291
Jackson, B. V., Webb, D. F., Altrock R. C. & Gold, R. 1992, Eruptive Solar Flares Svestka, Z., Jackson, B. V. & Machado M. E., (eds.), Springer-Verlag, Heidelberg, 322
Jackson, B. V., Buffington, A., Hick, P. L., Kahler, S. W., Altrock, R. C., Gold, R. E. & Webb, D. F. 1996, in D. Winterhalter, J. T. Gosling, S. R. Habbal, W. S. Kurth & M. Neugebauer (eds.), Solar Wind Eight, AIP Conf. Proc. 382, Woodbury, New York, p. 536
Jackson, B. V., Buffington, A., Hick, P., Kahler, S. W., Keil, S. L., Altrock, R. C., Simnett, G. M. & Webb, D. F. 1997*a*, Phys. Chem. Earth, 22, 441
Jackson, B. V., Hick, P. L., Kojima M. & Yokobe, A. 1997*b*, Adv. Space Res., 20, (1), 23
Jackson, B. V., Hick, P. L., Kojima, M. & Yokobe, A. 1998, J. Geophys. Res., 103, 12,049
Jackson, B. V., Hick, P. P., Buffington, A., Kojima, M., Tokumaru, M., Fujiki, K., Ohmi T. & Yamashita, M. 2003, in M. Velli, R. Bruno & F. Malara (eds.), Solar Wind Ten, AIP Conf. Proc. 679, Melville, New York, p. 75
Jackson, B. V., Buffington, A., Hick, P. P., Kahler, S. W., Price, S., Johnston, J. C., Holladay, P., Sinclair, D., Radick, R. R., Mozer, J., Altrock, R. C., Sagalyn, R., Anderson, P., Keil, S. L., Gold, R., Simnett, G. M., Eyles, C.J., Cooke, M. P., Tappin, J., Waltham, N. R., Kuchar, T., Mizumo, D. & Webb, D. F. 2004, Solar Phys. (in press).

James, J. F., Mukai, T., Watanabe, T., Ishigura, M. & Nakamura, R. 1997, Mon Not. R. Astron. Soc., 288, 1022

Katz, M. B. 1978, Lecture Notes in Biomathematics, 26, Levin, S., ed., Springer-Verlag, New York

Kakinuma, T. 1977, in Study of Travelingf Interplanetary Phenomena, Shea, M. A., Smart, D. F. & Wu, S. T., eds., D. Reidel, Norwell, Mass.,101

Keil, S. L., Altrock, R. C., Kahler, S., Jackson, B. V., Buffington, A., Hick, P. L., Simnett, G. M., Eyles, C. J., Webb, D. & Anderson, P. 1996*a*, S.P.I.E. proc., 2804, 78

Keil, S. L., Altrock, R. C., Kahler, S. W., Jackson, B. V., Buffington, A., Hick, P. L., Simnett, G., Eyles, C., Webb, D. F. & Anderson, P. 1996*b*, in Solar Drivers of Interplanetary and Terrestrial Disturbances, Balasubramaniam, K.S., Keil S.L. & Smartt R.N., eds., ASP Conference Series, 95, 158

Kojima, M. & Kakinuma, T. 1987, J. Geophys. Res., 92, 7269.

Kojima, M. & Kakinuma, T. 1990, Space Sci. Rev., 53, 173

Kojima, M., Asai, K., Hick, P. L., Jackson, B. V., Tokumaru, M., Watanabe, H. & Yokobe, A. 1997, in S. R. Habbal (ed.), Robotic Exploration close to the Sun, Scientific Basis, AIP Conference Proceedings 385, 97

Kojima, M., Tokumaru, M., Watanabe, H., Yokobe, A., Asai, K., Jackson, B. V. & Hick, P. L. 1998, J. Geophys. Res., 103, 1981.

Leinert, C., Link, H. & Salm, N. 1981, J. Space Sci. Instr. 5, 257

Leinert, C., Link, H., Pitz, E., Salm, N. & Knuppelberg, D. 1975, Raumfahart-forschung, 19, 264

McComas, D. J., Phillips, J. L., Bame, S. J., Gosling, J. T., Goldstein, B. E. & Neugebauer, M. 1995, Space Sci. Rev., 72, 93

MacQueen, R. M. 1993, Solar Phys., 145, 169

Marsh, T. R. & Horne, K. 1988, Mon. Not. R. Astron. Soc., 235, 269

Mouschovias, T. & Poland, A. I. 1978, Astrophys. J., 220, 675

Munro, R. H. 1977, in Topical Conference on Solar and Interplanetary Physics, Tucson, Arizona, January 12-15, 10

Panasyuk, A. V. 1999, J. Geophys. Res., 104, 9721

Poland, A. I., Howard, R. A., Koomen, M. J., Michels, D. J. & Sheeley, N. R., Jr, 1981, Solar Phys., 69, 169

Rappoport, S., Hick, P. P. & Jackson, B. V. 2003, BAAS, 34 (4), 1242

Richter, I., Leinert, C. & Planck, B. 1982, Astron. Astrophys., 110, 115

Riley, P., Linker, J. A., Mikic, Z., Odstrcil, D., Pizzo, V. J. & Webb, D. F. 2002, Astrophys. J., 578, 972

Rust, D. M. 1983, Rev. Geophys. Space Phys., 21(2), 349

Tatarski, V. I. 1961, Wave propagation in a turbulent medium, McGraw-Hill, New York

Tokumaru, M., Kojima, M., Fujiki, K. & Yamashita, M. 2003, in M. Velli, R. Bruno & F. Malara (eds.), Solar Wind Ten, AIP Conf. Proc. 679, Melville, New York, p. 729

Young, A. T. 1971, Astrophys. J., 168, 543

Wilson, D. C. 1977, NCAR Cooperative Thesis No. 40, Ph.D. thesis to the University of Colorado, Boulder, Colorado

Worcester, P., Corunelle, B. D. & Spindel, R. C. 1991, U.S. Natl. Rep. Int. Union Geod. Geophys. 1987-1991, Rev. Geophys., 29, 557

Wu, S. T., Dryer, M. & Han, S. M. 1976, Sol. Phys., 49, 187

Zidowitz, S., Inhester, B. & Epple, A. 1995, in D. Winterhalter, J. T. Gosling, S. R. Habbal, W.S. Kurth & M. Neugebauer (eds.), Solar Wind Eight, AIP Conf. Proc. 382, Woodbury, New York, p. 165

Index

Absorption, 49–51, 82, 209, 218, 257, 271
  coefficient, 49, 52, 93, 116–117, 247, 253, 257, 295
Abundance
  coronal, 39, 272
  iron, 268, 272
Acceleration, 27, 30–31, 34, 39–40, 53, 90, 115, 127, 157, 163–164, 179, 182–183, 193, 197, 199, 203, 206, 214–215, 217–219, 231, 234, 236–237, 307
  particle, 8, 75
  stochastic, 164
Active region, 21, 64, 76, 79, 90, 96, 108, 110, 122, 124–125, 136, 140–141, 150, 156, 169, 172, 193, 211, 231, 243, 245–246, 249, 256, 265, 268, 270, 272, 275, 282–283, 300, 313, 322, 329
  loop, 56, 252–253, 261
Air glow, 359
ALMA, 289–290
Amplifier, 65
Antenna gain, 11, 339
Aperture synthesis, 21, 60, 62, 248
Arcade
  double, 246
  event, 162
  flare, 34, 156, 159
Arch, 131
Arecibo, 336, 345, 350–352
Array configuration, 63
Atmosphere
  model, 78
  solar, 25, 30, 58, 73, 76, 85, 90, 119–120, 122, 125, 268, 273, 276, 294
Atmospheric drag, 55
Attenuator, 65
Aurora, 2
Background corona, 157, 251–252, 342, 356
Backscattering, 340
Balance
  energy, 104, 247, 261
  pressure, 81, 257
Bandwidth, 41, 61, 63, 65, 145, 205–206, 208, 210, 219, 238, 315, 339
Baseline, 59, 64
Bastille-Day
  CME, 314, 355, 361, 368, 371, 376
  flare, 187, 190
Beam
  antenna, 50, 338
  clean, 352
  dilution, 251–253
  dirty, 60
  electron, 19–20, 54, 75, 164, 206–207, 211, 214, 300, 307–309, 315
  flux density per, 50
  optical trap, 341
  proton, 208
  trajectory, 75, 206, 216, 308
  velocity, 75
  width, 10–11, 59, 345, 350
Bidirectional burst, 215–216
Blackbody radiation, 10
Blast wave, 35, 56, 168–169, 310, 317, 322
Boundary value problem, 91
Bow shock, 36, 41
Bragg Crystal Spectrometer (BCS), 159
Bragg
  backscattering, 338
  reflection, 342
Bremsstrahlung, 19, 21, 30, 75, 90, 115, 118–119, 121, 132, 265, 294
Brightening, 300
  coronal, 297
  diffuse, 34
  flare, 157, 167
  limb, 292
  polar, 292
  transient, 170
  X-ray, 299
Brightness temperature, 19, 22, 72, 75, 79, 96–98, 106, 116, 119–120, 245, 247–248, 251–252, 258, 265–267, 269, 272, 277–278, 291–292, 294–296, 298
  filament, 297
  spectra, 21, 72, 76, 79, 82, 101, 106, 244, 253, 256–258, 261
Broadband emission, 203, 208, 210

Bump-on-tail instability, 207, 217
Burst, 305
  bidirectional, 215–216
  interplanetary, 315, 329
  J and U, 20
  reverse-drift, 211, 214, 308
  reverse slope, 20
  type I, 204
  type II, 19–20, 34–35, 38–39, 50–51, 54, 56, 165, 168–169, 227, 231, 233, 236, 306–307, 309–311, 314, 316, 320–323, 325–327, 329–330
  type III, 19–20, 26, 39, 41, 50–51, 54, 165, 203–207, 209, 211, 214–218, 306–314, 316, 325–326, 329
  type IV, 20, 34, 39, 54, 203–204, 208, 227, 316, 328
  type V, 20, 204–205
Calibration, 62, 64–65, 67, 272, 274
Caltech Submillimeter Observatory, 292
Cascade, 188
Cavity, 31, 224, 233, 235, 297
CDS, 272, 274–275, 300
Cell, 57, 105
Cellular, 11
Center-to-limb variation, 295
Channel, 210
Charge
  electron, 118, 210, 270
  ion, 76
  states, 39
Chromosphere, 57, 76, 121, 124, 131, 156, 184, 211, 228, 257–259, 288, 291, 293, 296, 298–299
Cloud, 37
CME, 15, 24, 31, 34, 36–38, 40, 55, 131, 156, 204, 223–225, 229, 307, 311, 313, 316, 318–319, 324, 326, 330, 342–343, 348, 351, 355–356, 375, 379–380
  3-part, 224, 235
  acceleration, 157, 318–319
  and type II bursts, 233
  associated, 31, 166, 318–319
  collision, 323
  discovery, 223
  driven, 35, 37, 40, 169, 311, 321
  Earth-directed, 38, 224, 236, 338, 346, 376
  event, 168, 228, 233, 376–377, 379
  fast, 320
  flare relationship, 156–157, 167
  halo, 32, 38, 224, 230, 314, 317, 325, 327, 355, 376, 379
  interaction, 41, 323, 325
  limb, 346
  precursor, 234
  propagation, 329
  radio, 225, 227, 234
Collision, 82, 92
  frequency, 336, 338
Collisionless, 92
  plasma, 92
  trap, 182, 191
Condensation, 123, 147
Corona, 17, 20, 24, 41–42, 47, 51, 53, 61, 76, 78, 89, 92, 105, 121, 130–131, 137, 140, 151, 157, 160, 164, 184, 203, 206, 215, 224, 234–235, 251–252, 257–258, 261–262, 290–291, 294, 297, 300, 307, 313, 320–322, 335, 340–341, 349, 356–357
  active region, 78, 321
  density, 104, 225, 336, 357
  heating, 24–25, 56
  isothermal, 76
  magnetic field, 20, 92, 105
  model, 74
  temperature, 81, 104, 106, 226
Coronagraph, 156, 168, 223, 235, 357
Coronal heating, 261
Coronal hole, 18, 115, 127, 131, 245, 337–338
  equatorial, 292
  polar, 292, 341, 346
  transient, 167
Coronal magnetogram, 58, 106
Coronal magnetography, 20, 135–136, 144, 147, 265, 267, 272, 274–275
Coronal
  scattering, 61, 63, 248, 340
  seeing, 63
Correlator, 63, 66
Cosmic background noise, 306
Coulomb collisions, 180–181, 187, 190–191, 197–198
Critical frequency, 251, 253, 255–256
Cross-section, 255, 339, 346
Culgoora, 48
Current
  coronal, 92, 107, 139, 163
  electric, 297
  instability, 218
  sheet, 35, 139
Cusp, 29, 160–161, 172
Cyclotron
  emission, 218–219
  frequency, 19, 210
  resonance, 93
Density, 22, 28, 74, 91, 96, 130, 148, 165, 182, 190, 207, 210, 217, 243, 246, 251–253, 255, 257, 259, 262, 267, 274, 276, 281, 320–321, 323, 325, 336–341, 344, 346, 355, 366, 372, 379, 382
  diagnostic, 53, 190, 227, 253, 255
  electron, 157
  irregularities, 38, 344
  model, 35, 75

scale height, 96, 252
variation, 360, 362, 369
Depolarization line, 142–145, 147
Differential emission measure, 271–272, 275
Digitizers, 65
Dimming
coronal, 224
EUV, 31, 33–34, 56, 167, 230–231, 379
X-ray, 167, 379
Dipole sunspot model, 96–97, 100
Dispersion relation, 266
Earth-rotation synthesis, 60, 289
EIT, 33–34, 55, 160, 169, 223, 231, 235, 274–275, 292, 300, 379
Ejecta, 35, 37, 56, 189, 216, 230, 234, 327
El Campo, 345
Electron cyclotron maser, 83
Electron cyclotron
maser, 51
frequency, 210, 336
maser, 19, 218–219
Electron
acceleration, 19, 27–28, 34, 39, 42, 48, 54, 90, 163, 180, 182, 197, 214, 217, 219, 231, 236, 310, 325
beam, 48, 51, 54, 206, 211, 214, 300, 307–309, 315
bremsstrahlung, 54
density, 22, 31, 38, 73, 75, 79, 116, 128, 151, 157, 182, 190, 207, 210, 225, 232, 236, 245, 253, 257, 259, 261, 266–267, 291, 295, 306, 308, 345, 362, 364
energy, 82, 181, 187, 191, 197
gyrofrequency, 19, 73, 118, 120, 210, 218–219, 266–267
nonthermal, 51, 54, 57, 166, 308, 324
propagation, 307, 312
resonance, 338
suprathermal, 54
temperature, 73, 76–77, 80–81, 116, 118, 157, 245, 251, 253, 257, 261, 266–267, 337
transport, 180, 199
Electronics
front-end, 63
space, 8
Emission measure, 76, 225, 262, 266–268, 277, 299
Emission
coherent, 19–20, 50, 53, 72–73, 75, 83, 203, 208, 210, 217
coronal, 300
cyclotron, 90
electron-cyclotron, 85
free-free, 20–21, 51, 73, 75–77, 85, 115, 126, 217, 225–226, 236, 253, 255, 259, 262, 301
gyroresonance, 19, 21, 51, 61, 79, 89–90, 96, 104, 111, 121, 132, 244, 255, 262
gyrosynchrotron, 19, 28, 81, 84, 205, 210, 225–226, 232, 236, 311
harmonic, 216, 218–219
incoherent, 20, 50, 53, 72, 85, 205, 217
mechanism, 12, 20–22, 50–51, 61, 81, 118, 151, 225, 227, 236, 305, 308
nonthermal, 53
plasma, 19, 42, 73, 85, 218, 225, 308
radio, 8, 13, 17, 19, 22, 48–51, 54, 56, 59–60, 63, 67, 73, 81, 85, 89, 98, 107, 115, 124, 131, 157, 203–204, 210, 212, 214, 218, 256, 265, 292–293, 297–299, 305–306, 324–325, 328, 330
synchrotron, 34
transition radiation, 85
Emissivity, 49, 116–117, 193
Energy
balance, 247, 261
dissipation, 261
distribution, 25, 82, 191, 236
flare, 24, 164, 169, 219
kinetic, 161
magnetic, 24, 26, 158, 161, 172
release, 24, 32, 39, 48, 53–54, 56, 172, 181, 203, 210, 214–215, 219, 224, 308, 313
Eruption, 154, 157, 165–166, 172, 230, 232–233, 238, 262, 313
Escape rate, 182, 197
EUV, 22, 25, 31, 34, 53, 55, 58, 67, 85, 91, 111, 127, 130, 155, 159–160, 170, 187, 189, 203–204, 220, 225, 235, 255, 257, 261, 265, 267–268, 271–272, 282, 294, 296, 300, 323
wave, 34, 169, 231, 238, 321
Evaporation, 24, 29, 154, 158, 165, 299
EVLA, 290
Faraday rotation, 145, 151, 344
FASR, 15, 23, 42, 47–48, 52, 56, 60, 62, 64, 66, 72–73, 75–76, 79, 82, 85, 106–107, 111, 136, 140, 143, 150, 153–154, 173, 200, 203–204, 223, 225, 235, 237, 245, 248, 252, 255, 257, 261–262, 267, 272, 278, 281, 283, 290, 300–301, 330
Fast-mode, 165, 168–169, 324
Feed, 63–64, 351
Fiber optic, 6
Filament, 296
disappearance, 234
eruption, 160, 233
Filter bank, 66, 345
FIP, 272–273, 283
Flare, 308, 310, 325
and CMEs, 24, 31–32, 35, 40, 156–157, 167, 233
Bastille Day, 159, 163, 190
classification, 156, 180
concept, 155
energy, 24, 28, 53, 154, 158, 164, 169, 219
gradual phase, 157–158, 162

impulsive phase, 30, 39, 41, 157–158, 162–163, 165, 169
loop, 34, 154, 156–159, 163, 219, 260
Masuda, 158, 165
model, 26–27, 29, 156, 172
network, 299–300
reconnection, 161, 330
spotless, 160
Flux rope, 37, 160, 163, 325
Fokker-Planck, 182, 191
Footpoint, 29, 84, 158, 163–165, 183, 186, 191, 196, 219, 246
Free-free, 294
absorption, 52, 218, 247, 257
emission, 20–21, 73, 75–77, 85, 115, 126, 217, 225–226, 236, 253, 255, 259, 262, 293, 301, 344
opacity, 251–252, 258
polarization, 269
Frequency band, 57
Frequency
agility, 61
characteristic, 73
collision, 92
cyclotron, 210
drift, 75, 314
plasma, 19, 51, 73, 76, 92, 206, 210, 217, 227, 291, 305, 315
Gas pressure, 157, 169
Geomagnetic
field, 169
storm, 13, 55, 357
Gyroemission, 74, 265, 283
Gyrofrequency, 19, 73, 79, 81, 85, 118, 210, 219, 262, 266
Gyromagnetic, 51
Gyroresonance
absorption, 51–52
emission, 19, 21, 51, 61, 78–79, 89–90, 96, 104, 111, 121, 132, 244, 255, 262
harmonics, 272
layer, 96, 104
opacity, 78, 89, 93, 267, 277
Gyrosynchrotron, 19, 81, 205, 210, 225–226, 232, 236, 300
Harmonic
layer, 95, 106, 108
number, 93, 106–107, 267, 277
Heat transport, 109
Heating
coronal, 24–25, 52, 56, 104, 111, 171, 204, 261, 288, 297
quiet Sun, 294
Heliosphere, 20, 37, 157, 163, 223, 355–356, 374
inner, 42, 375
Hydrostatic
equilibrium, 57, 257, 259, 261–262
model, 258–259
Imaging spectroscopy, 50, 54, 71–72, 159, 199
Incoherent emission, 205, 217
Index
of refraction, 226, 266, 336
spectral, 118, 120, 122, 196
Injection
function, 180, 183–185
pitch angle, 191
rate, 182
spectrum, 29, 181, 197
Instability, 51, 207, 217–219
Interference, 10
radio frequency, 66
terrestrial, 237
Interferometer, 59–60
Interplanetary
coronal mass ejection, 37
medium, 18–19, 35, 40, 53, 55–56, 167, 305, 307, 357, 363
radio bursts, 50, 56
scintillation, 38, 355, 357, 359
shock, 56, 169
Inversion
double, 144
multiple, 136, 144–145
Ion
acceleration, 30, 40
charge, 76
density, 76
energetic, 166
sound wave, 218
Ionization
equilibrium, 268, 271, 276
Ionosphere, 306, 338, 342
Isothermal, 120, 252, 257, 259, 268
corona, 76, 79, 258, 261
James Clerk Maxwell Telescope, 292
Jansky
Karl, 7
Jets, 26, 162, 166
Jicamarca, 336, 349
LASCO, 168, 223, 235, 307, 318, 323–324, 326, 343, 376
LOFAR, 330, 336, 352
Loop
coronal, 115, 131, 136, 158, 164, 166, 173, 245–246, 255, 261, 295
density, 247–248
flare, 26, 193, 219, 260
geometry, 75
model, 253
temperature, 248
thin, 251
top, 181, 183, 187, 193–195, 247
trans-equatorial, 167
Loss-cone, 203, 219

angle, 183, 191
instability, 51
Magnetic field, 50–52, 54–55, 73, 116, 118–120, 126, 135–136, 139, 148–149, 151, 154, 183, 189, 199, 223, 225, 232, 236, 244–245, 266, 268, 306, 320, 336–337, 344, 358
CME, 327
coronal, 20–22, 47, 52–53, 59, 89–91, 104, 122, 151, 163, 166, 172, 259, 261, 267–268, 273, 278, 312, 321, 337, 341
direction, 75, 82, 93
extrapolation, 22, 24, 108, 243, 262, 268, 270
interplanetary, 308
lines, 19, 103, 109, 167, 216–217, 246, 266, 299, 307, 309, 313
longitudinal, 78, 143
photospheric, 91
strength, 19, 21, 58, 76, 79–80, 82, 89–92, 95, 104, 109, 124, 128, 183, 193, 210, 266, 275, 283
structure, 128, 191
topology, 53, 172, 288, 301
Magnetic
scale height, 267, 275, 279, 283
structure, 125, 150
twist, 163
Magnetogram, 78, 125, 138, 143, 147, 149, 151, 181, 245–246, 293
coronal, 106, 147, 149, 268, 281, 283–284, 301
photospheric, 107–108, 164, 172, 274, 293, 298
Magnetosonic speed, 321
Magnetosphere, 149
active region, 136, 149
disturbance, 15
Maser, 19, 51, 83, 218–219
Maunder minimum, 58
MDI, 274, 300
MHD, 31, 56, 172, 233, 281, 382
catastrophe, 172
shock, 165, 314
wave, 33, 342
Microflare, 24–26, 166, 169–171, 297, 300
Mode
extraordinary, 78, 93–94, 116, 120
ordinary, 78, 93–94, 116, 120
Moreton wave, 168–169
Morse
Samuel, 1
Nagoya, 357, 361, 367
Nançay Radioheliograph, 27, 71, 155, 290
Nanoflare, 56, 169–170, 297, 300
Network, 298
Neutral line, 108, 140, 143, 149–150, 296, 358
Nobeyama Radioheliograph, 21, 72, 115, 136, 155, 200, 289, 292
Noise storm, 31, 232, 234, 312, 315
Number problem, 165
Observations
in-situ, 37–38, 157, 234, 376
multi-frequency, 58
radio, 17, 21, 23, 31, 34, 47, 49, 67, 90, 104, 126, 136, 141, 149, 151, 154, 225, 227, 229, 233–236, 238, 258–259, 267, 288, 295–297, 343–344, 357
X-ray, 42, 157, 164, 169, 267, 343–344
Opacity, 75, 89–90, 93–94, 118, 245, 247, 251–252, 257–259, 269, 276, 294
Optical depth, 294
Optically thick, 20, 47, 49–51, 53, 72, 76–77, 79–80, 82, 85, 89, 91, 108, 119–120, 122–123, 193, 196, 198–199, 232, 251, 253, 255, 259, 276, 278, 294–296
Optically thin, 49–50, 53, 79–80, 82, 85, 91, 119–121, 123, 193–194, 196, 198–199, 225–226, 251, 253, 255, 258, 271, 295–296, 298
Oscillation, 92
OSO-7, 223
OVSA, 72, 79, 192, 200
Owens Valley Solar Array, 72, 104–105, 155, 268, 290
Particle
acceleration, 8, 39, 52, 56, 75, 163–165, 204, 212
nonthermal, 163–164, 173
oscillations, 217
solar energetic, 40, 55–56, 159, 309, 311, 325
wave interaction, 50, 82
Penumbra, 102, 110
Photosphere, 10, 90, 105, 136–137, 145, 279, 288, 294
Pitch angle, 82–83, 181–183
anisotropic, 196
diffusion, 181, 189, 192, 199
distribution, 183, 189, 196
scattering, 183, 190, 193, 196
Plage, 125, 268
Planck function, 72, 116
Plasma
density, 53, 270, 279, 305, 337, 375
emission, 19–20, 42, 73, 75, 218, 225, 308
frequency, 19, 51, 73, 75–76, 84–85, 92, 206, 210, 217, 227, 305, 315, 342, 344
instability, 19
thermal, 20, 34, 55, 82, 115
Plasmoid, 227, 232
Plume, 379
Polarization, 337
circular, 22, 81–82, 93, 96, 106, 116–117, 123, 135–137, 139–140, 143–145, 147, 150, 208, 245, 262, 266, 270, 288, 290, 328, 337
degree of, 119, 125, 299, 328
inversion, 22, 135, 137, 140, 143, 145–146, 148, 150, 270–271
linear, 145, 290

Potential field, 106, 280
  approximation, 92
  extrapolation, 245–246, 280
Precipitation, 24, 159, 164, 181–186, 188–191, 193–194, 198
Pressure, 276
  balance, 81, 257
Prominence, 31, 131, 232, 295–296
  eruption, 59, 232–233, 238
  magnetic field, 125
  model, 297
Propagation, 3, 19–20, 33, 37, 42, 53, 71, 90, 117, 135–137, 140, 181, 189, 200, 204, 216–217, 266–267, 269–270, 336
Proton
  density, 372
Pulse
  amplitude modulation, 348
  width, 349
QT, 22, 136, 140, 149, 265, 270–271
Quasi-transverse
  layer, 267
  propagation, 132, 135, 139
Quiet Sun, 17, 51–52, 56–57, 66, 125, 170, 226, 283, 287–291, 295–296, 298, 301, 306, 321
  brightness temperature, 291–292, 296
  heating, 297
Radar, 8, 15, 43, 335, 345
  cross-section, 339, 341
Radiation
  coherent, 51, 212
  field, 294
  incoherent, 51, 294
  plasma, 51, 53, 227
  synchrotron, 55
  transition, 51
Radiative transfer, 49, 76, 96, 119, 184, 289, 294
Radio
  diagnostic, 49, 52–53, 58, 67, 73, 261
  emission, 8, 13, 17, 19, 22, 28, 34, 39, 48–51, 54, 56, 59–60, 63, 67, 73, 85, 115, 124, 131, 157, 203–204, 210, 212, 214, 218, 256, 265, 292–293, 297–300, 305, 324, 330
  emission mechanism, 265, 277
  telescope, 47, 60, 63, 66–67, 93, 128
Radiometric calibration, 272
RATAN-600, 105, 115, 128, 144, 245, 262, 290
Rayleigh-Jeans approximation, 72, 116
Reber
  Grote, 7
Receiver, 145, 290
Reconnection, 24–27, 34, 40, 57, 156, 158, 161, 164–165, 172, 181, 200, 212, 215, 218, 283, 311, 324, 379
Reconstruction
  tomographic, 357, 367, 373, 376, 381
Reflection
  height, 337
  specular, 339
  total, 342
Refraction, 226, 338
Resolution
  angular, 50, 59–61, 63, 249, 251
  frequency, 66, 72
  spatial, 28
  temporal, 28, 289, 372
Resonance, 92, 99, 266
RHESSI, 18, 30, 155, 166, 173, 214, 259–260
Rotation, 62, 111, 140, 145, 244, 248, 357, 370
Satellite, 10
Scattering, 183, 189–190, 194, 196, 344, 358, 362
  coronal, 61, 63, 248, 340
  mechanism, 190–191, 193, 197
  rate, 189, 191
  Thomson, 223, 225, 358–359, 363, 374, 376
Scintillation, 7, 43, 338
  array, 357–358
  ionospheric, 362
  level, 358–360
Sensitivity, 57, 60, 63, 122, 125, 128, 139, 151, 184, 191, 199, 210, 229, 236
Separatrix, 35, 172, 181
Shock, 321–322
  acceleration, 75, 311
  bow, 36, 41
  CME-driven, 317
  coronal, 35
  front, 312, 315
  interplanetary, 316
  MHD, 165, 168–169, 233, 314–315
  slow-mode, 165, 168
  speed, 35, 37, 322
  wave, 37, 39, 164, 168, 309, 321
Siberian Solar Radio Telescope, 136, 233
SIRA, 330
Slow-mode, 165
SMEI, 382
Soft X-ray, 24, 26, 31, 39, 154, 156–157, 159, 164, 167–168, 170, 186, 192, 204, 220, 255, 257, 265, 271, 298–300, 344
SOHO, 18, 25, 37, 55, 66, 130, 154–155, 159, 223, 245, 272, 274, 292, 300, 307, 343, 357, 375
Solar-B, 159, 282
Solar cycle, 10, 229, 296, 376, 381
Solar event distribution, 12, 25, 169
Solar flux unit, 10, 49
Solar Probe, 15
Solar rotation, 367
  stereoscopy, 244–245
Solar wind, 8, 38, 55, 73, 127, 321–322, 324, 330, 355–357
  fast, 37, 55, 357, 360, 367
  model, 356, 358–360, 366–367
  slow, 37, 55, 358, 360, 367

speed, 39, 321–322, 338, 362, 367
Solar
rotation, 111
Solwind, 357, 376, 380
Spectrogram, 206
Spectrograph, 42
Spectroscopy, 30, 47–50, 53–54, 56–57, 66, 71, 84, 154, 159, 166, 236, 290
Spectrum, 328
brightness, 21, 244, 253–254, 256
Doppler, 338, 346, 348–349
dynamic, 307
STEREO, 343, 356, 382
Stereoscopy, 111
Stokes parameters, 61
Storm
geomagnetic, 13, 55, 357
noise, 31, 232, 234, 312, 315
type I, 20, 312–313
type III, 20, 312–313, 315
Streamer, 32, 161, 229, 237, 291, 313, 337, 343, 346
belt, 341
SUMER, 300
Sunspot
group, 166
number, 4, 58, 329
Surface
reference, 368–369
reflecting, 339–341, 351
source, 306, 359, 367, 375
SXR, 53, 55, 57, 66
SXT, 154–155, 160, 163, 170
Synoptic
map, 58, 358, 380
studies, 42, 52, 58
T-interval, 276–279
Telegraph, 1, 3, 5
Temperature
brightness, 19, 22, 49, 72, 75, 77, 79, 82, 96–97, 106, 116, 119–120, 225, 233, 244–245, 247–249, 251–253, 255, 258, 262, 265–267, 269, 272, 277–278
distribution, 275
effective, 49, 72, 193, 198
electron, 157
kinetic, 47
structure, 100, 161, 243
Theory
magneto-ionic, 116
mode coupling, 137
solar radar, 335
transition radiation, 84
type III, 218
wave propagation, 151, 169
Thick target, 182
Thickness
optical, 76, 119–120, 227, 233, 266–267, 277, 295
Thin-target bremsstrahlung, 165
Thin target, 182
Three-dimensional
model, 366, 370, 374, 381
tomography, 355, 382
Time-dependent
model, 355, 372, 374
tomography, 367–368, 371, 375–376, 381
Time-of-flight, 172, 184
TRACE, 18, 25, 67, 105, 154–155, 160, 187, 189, 214
Transition radiation, 84
resonant, 84
Transition region, 91, 104, 121, 218, 262, 288, 297, 299–300, 337
Transmission
cross-Atlantic, 3
Transmitter, 345, 351
Transport, 29, 42, 48, 52–54, 82, 109, 180, 199, 273, 283
Trap-and-precipitation, 29, 181–184, 189, 197–198, 200
Trap
magnetic, 198
Trapped electrons, 180, 182–184, 186, 199, 203, 213–214, 217, 219
Turbulence
Whistler, 196–197
Ulysses, 8, 18, 37, 358
Umbra, 91, 96, 101
UVCS, 357
Vector
magnetogram, 107–108, 111
Velocity
field, 161–162
group, 336
IPS, 357, 361, 366, 382
phase, 196, 217, 336
solar wind, 366
thermal, 218
Venus, 350
Very Large Array, 72
Visibility
complex, 59, 64
VLA, 25, 27, 48, 50, 57, 60, 63, 67, 101, 104, 106, 136, 151, 155, 181, 200, 228–229, 237, 268, 272, 282, 290, 298, 300
Voyager, 307, 315
Wave
coronal, 31, 33–34, 41
EIT, 35, 318, 321
electromagnetic, 20, 137, 266
electron-cyclotron, 72
EUV, 56
global, 168

heating, 56
interaction, 50–51
Langmuir, 19, 42, 72, 203, 207, 217–218, 227, 307–308, 315
MHD, 281
Moreton, 34, 168–169
propagation, 20, 137, 151, 270, 312
transverse, 218, 227, 281
Westerbork Synthesis Radio Telescope, 22, 72, 145
Wind, 307
Wireless
cell, 11, 13
communication, 7
interference, 11
X-class flare, 161
X-ray bright points, 297–298
Yohkoh, 18, 153–154, 159, 164, 172, 298, 300
Zeeman effect, 91
Zeeman
effect, 121
Zodiacal light, 359, 365